UNCLASSIFIED

SE

AD-A241 503

PORT DOCUMENTATION PAGE

1 Unclassified

1b. RESTRICTIVE MARKINGS

2a SECURITY CLASSIFICATION AUTHORITY
N/A

3. DISTRIBUTION / AVAILABILITY OF REPORT
Approved for public release; distribution unlimited.

2b. DECLASSIFICATION / DOWNGRADING SCHEDULE
N/A

ELECTE
OCT 1 0 1991
C

4 PERFORMING ORGANIZATION REPORT NUMBER(S)
PSU-ME-R

5. MONITORING ORGANIZATION REPORT NUMBER(S)

6a. NAME OF PERFORMING ORGANIZATION	6b. OFFICE SYMBOL (If applicable)	7a. NAME OF MONITORING ORGANIZATION
Penn State University		Office of Naval Reasearch Resident Representative N66005

6c. ADDRESS (City, State, and ZIP Code)	7b. ADDRESS (City, State, and ZIP Code)
Department of Mechanical Engineering University Park, PA 16802	Administrative Contracting Officer The Ohio State Univ. Research Center 1314 Kinnear Rd., Columbus, OH 43212-1194

8a. NAME OF FUNDING, SPONSORING ORGANIZATION	8b. OFFICE SYMBOL (If applicable)	9 PROCUREMENT INSTRUMENT IDENTIFICATION NUMBER
Office of Naval Research		N00014-86-K-0468

8c. ADDRESS (City, State, and ZIP Code)	10. SOURCE OF FUNDING NUMBERS			
	PROGRAM ELEMENT NO	PROJECT NO.	TASK NO.	WORK UNIT ACCESSION NO
Code 1513:MBL 800 North Quincy Street Arlington, VA 22217-5000				

11 TITLE (Include Security Classification)

12 PERSONAL AUTHOR(S)
K. K. Kuo, T. A. Litzinger, V. Yang, S. T. Thynell, and W. H. Hsieh

13a. TYPE OF REPORT	13b. TIME COVERED	14. DATE OF REPORT (Year, Month, Day)	15. PAGE COUNT
FINAL	FROM _____ TO _____	May 17, 1990	

16. SUPPLEMENTARY NOTATION
The view, opinions and/or findings contained in this report are those of the author(s) and should not be construed as an official Department of the Navy position, policy, or decision, unless so designated by other documentation.

17 COSATI CODES		
FIELD	GROUP	SUB-GROUP

18. SUBJECT TERMS (Continue on reverse if necessary and identify by block number)
See reverse side.

19 ABSTRACT (Continue on reverse if necessary and identify by block number)
See reverse side.

REPRODUCED BY
U.S. DEPARTMENT OF COMMERCE
NATIONAL TECHNICAL
INFORMATION SERVICE
SPRINGFIELD, VA 22161

20 DISTRIBUTION / AVAILABILITY OF ABSTRACT	21 ABSTRACT SECURITY CLASSIFICATION
☒ UNCLASSIFIED/UNLIMITED ☐ SAME AS RPT ☐ DTIC USERS	Unclassified

22a NAME OF RESPONSIBLE INDIVIDUAL	22b. TELEPHONE (Include Area Code)	22c OFFICE SYMBOL
Prof. Kenneth K. Kuo	(814)863-6270	

DD FORM 1473, 84 MAR — 83 APR edition may be used until exhausted. All other editions are obsolete.

SECURITY CLASSIFICATION OF THIS PAGE
UNCLASSIFIED

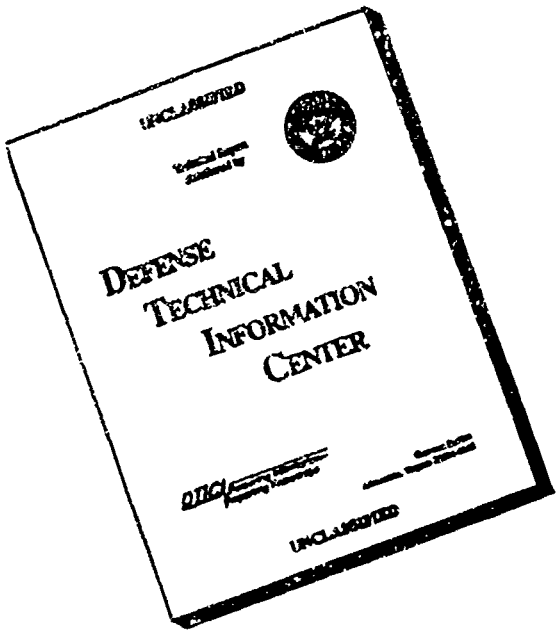
AD-A241503

AD-A241503 MISSING PAGES WILL BE INSERTED AT AN LATER DATE AS ERRATA(S). PAGE(S) 7 & 385.

19 MAY 1992

THIS
PAGE
IS
MISSING
IN
ORIGINAL
DOCUMENT

DISCLAIMER NOTICE



THIS DOCUMENT IS BEST QUALITY AVAILABLE. THE COPY FURNISHED TO DTIC CONTAINED A SIGNIFICANT NUMBER OF PAGES WHICH DO NOT REPRODUCE LEGIBLY.

FUNDAMENTAL COMBUSTION PROCESSES OF PARTICLE-LADEN SHEAR FLOWS IN SOLID FUEL RAMJETS

FINAL REPORT

Submitted to the Office of Naval Research
Under Contract No. N00014-86-K-0468
Dr. Gabriel D. Roy, Contract Monitor
Code 1132P
800 North Quincy Street
Arlington, VA 22217-5000

Prepared by Professors K. K. Kuo, T. A. Litzinger, V. Yang,
S. T. Thynell, and W. H. Hsieh
Department of Mechanical Engineering
The Pennsylvania State University
University Park, PA 16802

July 1991



Accession For
NTIS GRA&I ☑
DTIC TAB ☐
Unannounced ☐
Justification
By
Distribution/
Availability Codes
Dist | Avail and/or Special
A-1

ACKNOWLEDGEMENTS

This advanced research initiative was sponsored by Dr. Richard S. Miller, Chief Scientist of Mechanics Division, and Dr. Gabriel Roy, Scientific Officer, Office of Naval Research, Arlington, Virginia. Their strong support of this research investigation is greatly appreciated. We also would like to acknowledge the supply of solid fuels and propellants from various manufacturers; in particular, Mr. Jerry Manser of Aerojet for providing the energetic BAMO/NMMO copolymer and Mr. B.M. Kosowski of Mach I, Inc. for providing coated boron particles. Some fuel samples were obtained from Mr. Gordon E. Jensen of the United Technologies/Chemical System Division and Mr. Bill Burdette of Naval Weapons Center in China Lake, CA. The authors also would like to thank the many undergraduate and graduate students who participated in this project. They contributed significantly towards the success of this project. The authors would also like to thank Dr. Arie Peretz, Chief Research Engineer of Propulsion Department of RAFAEL, Israel for his participation and valuable contribution in this project during his sabbatical year from Fall of 1988 to Fall of 1989.

TABLE OF CONTENTS

CHAPTER 1

COMBUSTION OF SOLID FUELS UNDER CROSSFLOW CONDITIONS 1

I. Introduction 1

II. Method of Approach 2
A. Experimental 2
B. Numerical 3

III. Discussion of Results 3

IV. Conclusions 8
V. References 8

CHAPTER 2

CO_2 LASER PYROLYSIS AND IGNITION 237

I. Introduction 237
II. Experimental Approach 238
III. Results and Discussion 241
A. B/HTPB Solid Fuels 241
B. Boron-BAMO/NMMO Solid Fuels 242
C. Boron/Mg/PTFE Solid Fuels 244
D. Mg/PTFE/Viton A Solid Fuels 246
E. HTPB-based Solid Fuels 248
IV. Conclusions 248
V. References 249

CHAPTER 3

NONINTRUSIVE FT-IR DIAGNOSTICS FOR SPECIES AND TEMPERATURE MEASUREMENTS OF PRODUCTS FROM SOLID PROPELLANTS 314

I. Introduction 314
II. Objectives of Work 315
III. Method of Approach 316
IV. Discussion of Results 320
A. Emission and Transmission Measurements 320
B. Signal-to-Noise Analysis of High-Pressure Combustion 323
C. A New Approach to Flame Spreading Measurements 326
V. Conclusions 328
VI. References 329
Publications and Presentations 330
Journal Publications and Paper Presentations 331

CHAPTER 4

STEADY-STATE COMBUSTION BEHAVIOR OF MG/PTFE/VITON AND BORON-BASED SOLID FUELS 382
I. Introduction 382
II. Method of Approach 382
III. Discussion of Results 384
IV. Conclusions 387

APPENDICES

1.1 Ignition and Combustion of Solid Fuels Under High-Velocity Crossflows 10

1.2 Analysis of Boron Particle Ignition Above a Burning Solid Fuel in a High-Velocity Environment 140

1.3 A Numerical Study of Solid Fuel Combustion Under Supersonic Crossflows 168

1.4 Effect of Magnesium-Coated Boron Particles on Burning Characteristics of Solid Fuels in High-Speed Crossflows 180

1.5 Experimental Study of Solid Fuel Ignition and Combustion Under High-Velocity Crossflows 195

1.6 Solid Fuel Ignition and Combustion Characteristics Under High-Speed Crossflows 228

2.1 Combustion Characteristics and CO_2 Laser Ignition Behavior of Boron/Magnesium/PTFE Pyrotechnics 250

2.2 Pyrolysis and Ignition of Boron-Based Solid Fuels for Ramjet Applications 271

2.3 Combustion Behavior and Thermophysical Properties of Metal-Based Solid Fuels 283

2.4 Ignition and Combustion Behavior of MTV Igniter Materials for Base Bleed Applications 291

2.5 An Instrument for Measuring High-Power Laser Beam Profiles and Beam Attenuation 310

3.1 Analysis of Plumes of Solid Propellant Combustion Using an FT-IR Spectrometer 332

3.2 Measurements and Theory of Signal-to-Noise Ratio of FT-IR Emission Spectrometry Applied to High Pressure Solid Propellant Combustion 342

3.3 An Approach to Measurements of Flame Spreading Over Solid Propellants 371

4.1 Combustion Behavior of Boron-Based BAMO/NMMO Fuel-Rich Solid Propellants. . 388

4.2 Strand-Burning Characteristics of Advanced Boron-Based BAMO/NMMO Fuel-Rich Solid Propellants 396

4.3 Burning-Rate Characteristics of Boron/[BAMO/NMMO] Fuel-Rich Solid Propellant Under Broad Ranges of Pressure and Temperature. 400

4.4 Combustion Behavior and Thermophysical Properties of Metal-Based Solid Fuels. . 415

CHAPTER I
COMBUSTION OF SOLID FUELS UNDER CROSSFLOW CONDITIONS

I. Introduction

In the modern development of airbreathing propulsion systems for high-speed vehicles, attention is often focused on the solid fuel ramjet (SFRJ). Because of its airbreathing feature, the vehicle avoids the weight penalty associated with carrying oxidants, resulting in a higher specific impulse and longer flight range. The use of solid fuel greatly simplifies the system design, and eliminates problems associated with fuel storage and feeding mechanisms. The fuel may also incorporate energetic additives, such as boron or metallic powders, to maximize performance during volume-limited missions. However, in order to establish the SFRJ as a viable air-breathing engine, it must first demonstrate efficient operation under a wide range of Mach numbers and altitudes.

A detailed review of experimental and numerical works in SFRJ combustion systems is available in the attached Ph.D. thesis of Jarymowycz (Appendix 1.1). A condensed version was presented in Lampoldshausen, Germany, at the *Second International Symposium on Spe ial Topics in Chemical Propulsion: Combustion of Boron-Based Solid Propellants and Solid Fuels*, and is attached here as Appendix 1.2. These studies have provided useful information regarding solid-fuel combustion; however, the majority of these works were conducted in low-speed environments. The primary objective of the research conducted in this area was to investigate the ignition and combustion processes of solid fuels under a wide range of Mach numbers, including both subsonic and supersonic crossflows, using advanced experimental and theoretical techniques.

Ignition and combustion of boron-based solid fuel in a high-speed environment involve many intricate physical and chemical processes including turbulent mixing, multi-phase heat and mass transport, surface pyrolysis, and homogeneous and heterogeneous reactions. Understanding of detailed flow structures, boron particle ignition and combustion processes, and burning characteristics of solid fuels under various freestream conditions is important in advancing the state-of-the-art in solid fuel ramjet propulsion systems.

The work was accomplished using experimental and numerical techniques. Specifically, the objectives in the experimental study were as follows:

1. to determine the feasibility of solid-fuel combustion under high-velocity crossflows;
2. to study the effect of boron particles on the ignition and combustion characteristics of HTPB-based solid fuels; and
3. to determine the effects of freestream conditions such as pressure, temperature, and mass flux on the burning rates of HTPB-based solid fuels.

A comprehensive theoretical model of the combustion of homogeneous solid fuels under supersonic crossflow conditions was also formulated and solved. As a specific example, the combustion behavior of pure HTPB fuel samples was treated in depth. To better understand some of the complex two-phase phenomena occurring above a reacting boron-laden solid fuel, the ignition behavior of boron particles in a ramjet environment was treated. The specific objectives of the numerical study were:

1. to investigate the detailed flowfields and flame structures involved in the combustion of solid fuels in a supersonic flow environment;
2. to determine the burning rates of the fuel samples under various conditions;
3. to examine the effects of the freestream conditions (specifically pressure and temperature) on the pyrolysis and combustion characteristics of the fuel samples;
4. to study the ignition process of individual boron particles ejected from a reacting solid fuel under a high-velocity crossflow;
5. to determine the effect of particle size on the ignition time and location of the particles;
6. to investigate the effects of freestream parameters, including pressure and temperature on the ignitability of the boron particle; and
7. to determine if ignition delay times of boron particles can be minimized by utilizing a particular size range of particles.

II. Method of Approach

A. Experimental

In order to understand the physical and chemical mechanisms involved in the combustion of solid fuels, an experimental study was conducted using a connected-pipe facility which simulates the combustion chamber conditions of a hypersonic vehicle at high altitudes. The rig provides vitiated air over a wide range of conditions with a maximum freestream temperature of 1000 K, static pressure of 0.62 MPa, and Mach number of 1.5. The maximum flow rate attainable

is 8 kg/s with a duration of four minutes at the highest pressure. A detailed description of the facility and test setup are available in the attached papers and thesis of Jarymowycz.

The solid fuels utilized in this study were either processed at Penn State, United Technologies/Chemical System Division (UT/CSD), or Aerojet Corporation. The Penn State fuels were HTPB-based with various loadings (0-20% by weight) of pure boron particles or magnesium-coated boron particles (10% boron by weight, with up to 20% magnesium coating). UT/CSD fuels were HTPB-based with 50% boron by weight. Aerojet provided fuels consisting of a highly energetic copolymer BAMO/NMMO, with 0 or 18% boron loading.

B. Numerical

The combustion of solid fuels under supersonic crossflows was studied using a comprehensive numerical analysis. The formulation was based on the time-dependent multi-dimensional compressible Navier-Stokes equations and species transport equations. Features of this approach included consideration of finite-rate chemical kinetics and variable properties. Turbulence closure was achieved using the Baldwin-Lomax algebraic model. The governing equations were solved numerically using a flux-vector splitting Lower-Upper Symmetric Successive Overrelaxation technique that treats source terms implicitly. The details on the invoked assumptions and corresponding equations in the modelling effort are presented in Appendix 1.1.

The ignition processes of boron particles above a burning solid fuel were also studied by numerical solution of the comprehensive theoretical model. The particle-phase solution was obtained based on a well-established boron particle ignition model. Boron particles were ejected from the surface of the burning fuel into a high-velocity crossflow and their trajectories were traced through the reacting flowfield using a Stochastic Separated Flow approach. The effects of particle size on their ignition time and location were studied.

III. Discussion of Results

The most important accomplishments and major findings of the experimental study of solid fuel ignition and combustion processes are summarized below.

- The transient regression phenomena of solid fuels were observed in-situ using real-time X-ray radiography. HTPB-based fuels with different percentages of boron loading showed layer-by-layer regression without subsurface reactions.

- Fuel surface regression rates were reduced using an advanced digital image processing system. Regression rates were found to be highly dependent on freestream pressure, and less dependent on freestream temperature and mass flux. The results are summarized in Appendix 1.3.
- Fuels with boron particles of high purity (>99%) and small particle diameters (0.04-0.15 μm) experienced higher regression rates than fuels with particles of slightly lower purity and diameters approximately 10 times higher. These results were also presented in Lampoldshausen, and are attached as Appendix 1.4.
- At low pressures (below 0.55 MPa), the addition of magnesium-coated boron particles to the fuel samples increased the burning rates from those of uncoated boron particles. The augmented burning rates were due to the additional heat generated by the magnesium/oxygen reactions which occur more rapidly than boron/oxygen reactions at low pressures. Figure 1.1 shows the burning rates as functions of pressure for fuel samples of various compositions. The fuel samples with 20% magnesium coating on the particles show the highest burning rates at low pressures, whereas at high pressures, the fuels with uncoated boron burn fastest.
- A burning-rate correlation in terms of freestream conditions and boron concentration was established. Such correlations are useful for the design of SFRJ propulsion systems.
- The BAMO/NMMO solid fuels from Aerojet has high gasification rates at low pressures and has the ability to eject boron particles into the oxidizer region; however, this polymer certain drawbacks. The fuel liquefies at low temperatures and cannot retain its rigidity under shear flow conditions. This finding was conveyed to Aerojet.

The following results are detailed in Appendix 1.5.

- The UT/CSD fuels with 50% boron loading do not burn efficiently under low pressures. Even with the addition of combustion aids, the regression rates of these fuels are very low. These findings are important for industrial companies to improve their formulation.
- Combustion of solid fuels under supersonic crossflows was successfully demonstrated with HTPB/B fuels. For these tests, it was necessary to increase

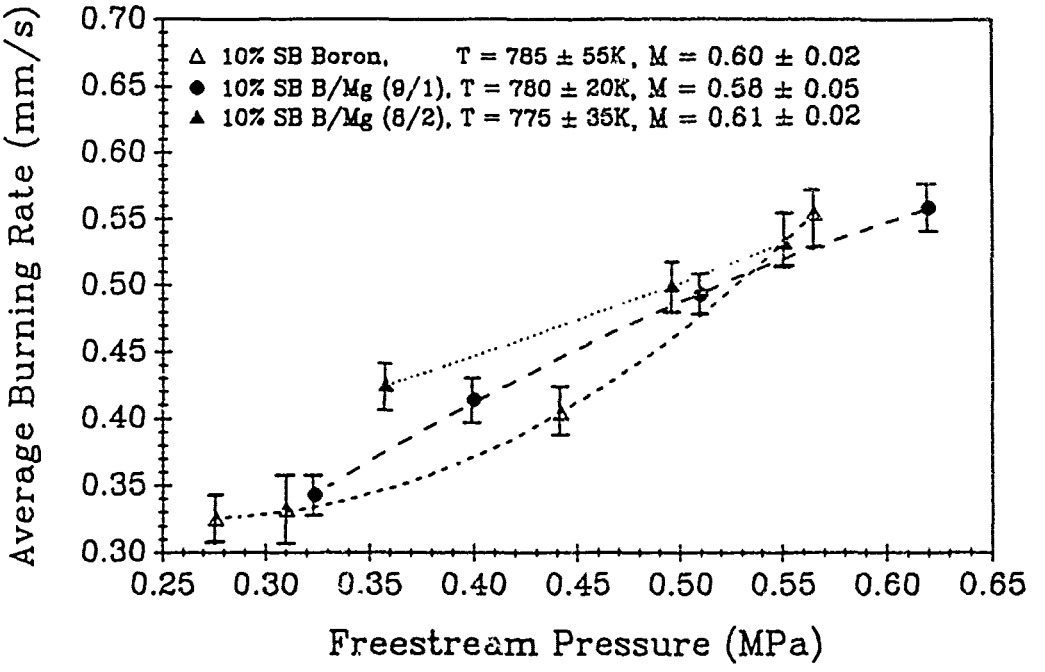


Figure 1.1 Burning-rate dependence on freestream pressure and magnesium-coating percentage for HTPB-based fuels

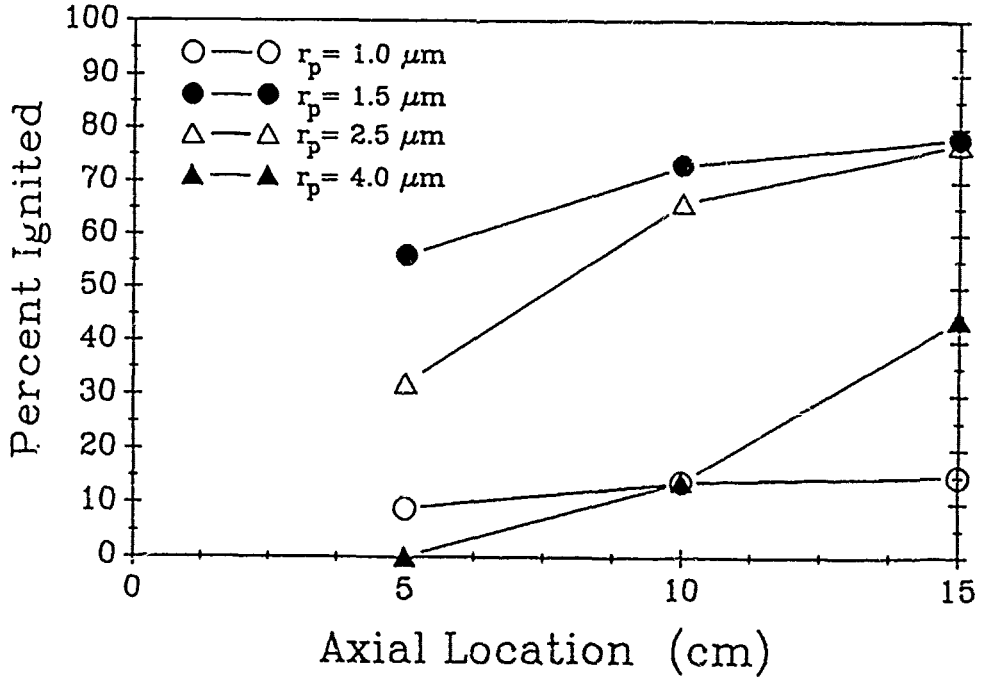


Figure 1.2 Effect of particle radius on ignition percentage at three axial stations

the size of the recirculating region to promote ignition and flame stabilization of the solid fuel sample.

- The effect of fuel ingredients on the ignition, flame spreading, and combustion characteristics was investigated. Autoignition of HTPB solid fuels with no additives was attained with freestream temperatures above 820 K. However, autoignition of HTPB-based solid fuels with boron was attained with freestream temperatures above 725 K. This temperature was lower because reacting boron particles on the fuel surface acted as a heat source for igniting the pyrolyzed fuel-rich species. Addition of boron particles to the fuels (up to 10%) considerably increased the burning rates. Further addition to 15 and 20% decreased the burning rates. The increase was caused by the additional energy release from the boron; the decrease was due to several factors: (1) the heat sink effect of boron particles in the gas phase which reduced the gas-phase temperature, and (2) heat feedback to the surface was effectively shielded by the large number of boron particle above the surface.
- Ignition phenomena of HTPB solid fuels without boron showed a gas-phase ignition mechanism, whereas samples with boron always ignited on the surface. In terms of surface ignition mechanism, no dependence on particle size, loading fraction, or purity of boron was noted in our convective ignition study.
- For a given B/HTPB solid fuel, there exists a pressure deflagration limit, below which self-sustained combustion cannot be achieved. For instance, our results showed momentary ignition of several B/HTPB fuels followed with extinction for pressures below 2 atm.

Results from the comprehensive theoretical analysis of solid-fuel combustion under supersonic crossflows are highlighted below and detailed in Appendix 1.2. Results from the study of boron particle ignition above a reacting solid fuel are also summarized.

- The combustion behavior of solid fuels was studied numerically as a function of freestream conditions, fuel ingredients, and flow geometry, with attention focused on the importance of kinetic- vs. diffusion-controlled reactions. At high pressures, the reaction zone thickness becomes smaller; whereas, at low pressures, the reaction is more distributed. This implies that at high pressures, a single-step forward reaction is sufficient to describe the combustion process; however, at lower pressures, a finite-rate approach must be considered.

environment cannot provide suitable conditions for both ignition and combustion of the particles. In contrast, this study reveals that it is possible for particles to ignite and burn in SFRJ's, provided the particles sizes are kept small (below 10 μm).

IV. Conclusions

The major findings in this study include:

- the successful ignition and sustained combustion of HTPB/B solid fuels under supersonic flow conditions (M = 1.5);
- establishment of an optimum particle size of ~3 μm for minimizing ignition time above a reacting HTPB solid fuel under supersonic crossflow;
- higher burning rates of solid fuels under subsonic conditions and low pressures by substituting magnesium-coated boron particles for uncoated boron particles;
- improved ignition and combustion characteristics of solid fuels by utilizing high-purity (>99%), small diameter (0.04-0.15 μm) boron particles.

V. References

1.1 Jarymowycz, T. A., "Ignition and Combustion of Solid Fuels Under High-Velocity Crossflows," Ph.D. Thesis, The Pennsylvania State University, August 1991.

Journal Publications and Paper Presentations

1.2 Jarymowycz, T. A., Yang, V., and Kuo, K. K., "A Numerical Study of Solid Fuel Combustion Under Supersonic Crossflow," Presented at the *AIAA/SAE/ASME/ASEE 26th Joint Propulsion Conference*, AIAA Paper No. 90-2076, Orlando, FL, 1990, accepted for publication in the *Journal of Propulsion and Power.*

1.3 Jarymowycz, T. A., Yang, V., and Kuo, K. K., "Analysis of Boron Particle Ignition Above a Burning Solid Fuel in a High-Velocity Environment," accepted for publication in the *Proceedings of the Second International Symposium on Special Topics in Chemical Propulsion: Combustion of Boron-Based Solid Propellants and Solid Fuels*, Lampoldshausen, Germany, March 1991.

1.4 Pace, K. K., Jarymowycz, T. A., Yang, V., and Kuo, K. K., "Effect of Magnesium-Coated Boron Particles on Burning Characteristics of Solid Fuels in High Speed Crossflows, accepted for publication in the *Proceedings of the Second International Symposium on Special Topics in Chemical Propulsion: Combustion of Boron-Based Solid Propellants and Solid Fuels*, Lampoldshausen, Germany, March 1991.

1.5 Jarymowycz, T. A., Pace, K. K., Snyder, T. S., Yang, V., and Kuo, K. K., "Experimental Study of Solid Fuel Combustion Under High-Velocity Crossflow Conditions," *27th JANNAF Combustion Meeting*, Cheyenne, WY, Nov. 1990, accepted for publication in the *Journal of Propulsion and Power.*

1.6 Snyder, T. S., Jarymowycz, T. A., Pace, K. K., and Kuo, K. K., "Solid Fuel Ignition and Combustion Characteristics Under High-Speed Crossflows," presented at the *AIAA/SAE/ASME/ASEE 26th Joint Propulsion Conference*, AIAA Paper No. 90-2075, Orlando, FL, 1990.

The Pennsylvania State University

The Graduate School

College of Engineering

IGNITION AND COMBUSTION OF SOLID FUELS UNDER HIGH-VELOCITY CROSSFLOWS

A Thesis in

Mechanical Engineering

by

Taras A. Jarymowycz

Submitted in Partial Fulfillment
of the Requirements
for the Degree of

Doctor of Philosophy

August 1991

We approve the thesis of Taras A. Jarymowycz.

Date of Signature

Kenneth K. Kuo — May 14, 1991

Kenneth K. Kuo
Distinguished Professor of Mechanical Engineering
Thesis Co-Advisor
Co-Chair of Committee

Vigor Yang — May 14, 1991

Vigor Yang
Associate Professor of Mechanical Engineering
Thesis Co-Advisor
Co-Chair of Committee

Thomas A Litzinger — May 14, 1991

Thomas A. Litzinger
Associate Professor of Mechanical Engineering

Robert J. Santoro — May 15, 1991

Robert J. Santoro
Associate Professor of Mechanical Engineering

Dennis K McLaughlin — May 16, 1991

Dennis K. McLaughlin
Professor of Aerospace Engineering

Harold R Jacobs — 5/14/91

Harold R. Jacobs
Head of the Department of Mechanical Engineering
Professor of Mechanical Engineering

ABSTRACT

The solid-fuel ramjet (SFRJ) has great potential as an advanced propulsion system because of its compactness and simplicity. An understanding of the important physical and chemical mechanisms involved in the ignition and combustion processes is necessary in order to further the state-of-the-art of SFRJ propulsion systems. In this investigation, the ignition and combustion of solid fuels under high-velocity crossflows have been studied using comprehensive numerical and experimental analyses.

In the numerical analysis, the formulation is based on the multidimensional compressible Navier-Stokes equations and species transport equations. Features of this approach include consideration of finite-rate chemical kinetics and variable properties. The effects of various operating conditions on the combustion behavior of the HTPB-based solid fuel samples are treated in detail. Results indicate the detailed flame structures and flowfields associated with solid-fuel combustion.

The ignition processes of boron particles above a burning solid fuel have also been studied by numerical solution of Lagrangian equations of motion. Boron particles are ejected from the surface of the burning fuel into a high-velocity crossflow and their trajectories are traced through the reacting flowfield. The effects of particle size on their ignition time and location are determined.

The combustion behavior of hydroxyl terminated polybutadiene (HTPB) based solid fuels with boron particles were studied experimentally under both subsonic and supersonic crossflows, using a connected-pipe test facility. The Mach numbers ranged from 0.47 to 0.74 for subsonic tests, while supersonic tests were conducted at a fixed Mach number of 1.5. Instantaneous surface profiles of the solid fuels were obtained using a real-time x-ray radiography system. Boron particle addition to

the fuels greatly diminished the minimum ambient temperature required for solid-fuel ignition, since reacting boron particles on the sample surface served as a local heat source for igniting the pyrolyzed fuel-rich species. Subsonic combustion studies revealed that regression rates were highly dependent on freestream static pressures, and less dependent on temperature and mass flux. The addition of boron particles (up to 10 percent by weight) to the HTPB fuels considerably increased the burning rates of the fuels. A burning-rate correlation was obtained in terms of pressure, temperature, mass flux, and boron concentration. Combustion of solid fuels under supersonic crossflows was also successfully demonstrated.

TABLE OF CONTENTS

LIST OF FIGURES vii

LIST OF TABLES ix

NOMENCLATURE x

ACKNOWLEDGEMENTS xiv

Chapter 1. INTRODUCTION 1

1.1. Survey of Previous Works 3

1.1.1. Experimental Study of Solid Fuel Combustion 3
1.1.2. Effect of Boron Additives 5

1.1.2.1. Single-Particle Studies 5
1.1.2.2. Boron-Based Solid Fuel Studies 8

1.1.3. Numerical Study of Solid-Fuel Combustion 9

1.2. Objectives 10

Chapter 2. EXPERIMENTAL APPROACH 12

2.1. Test Facility 12

2.1.1. Air Supply System 12
2.1.2. Test Rig 13
2.1.3. Data Acquisition and Control Systems 17

2.2. Solid Fuels 18
2.3. Igniter 19
2.4. Real-Time X-Ray Radiography and Video System 19

CHAPTER 3. EXPERIMENTAL RESULTS AND DISCUSSION 22

3.1. Ignition Sequence 25
3.2. Combustion Characteristics 31

3.2.1. Subsonic Results 31
3.2.2. Supersonic Results 39

CHAPTER 4. THEORETICAL FORMULATION 43

4.1. Gas-Phase Analysis 45
4.2. Solid-Fuel Analysis 47
4.3. Boundary Conditions 48
4.4. Turbulence Model 50
4.5. Gas-Phase Combustion Model 52

4.6. Boron Particle Analysis 54

4.6.1. Particle Ignition Model 54
4.6.2. Particle Tracking 59

CHAPTER 5. NUMERICAL METHOD 63

CHAPTER 6. DISCUSSION OF NUMERICAL RESULTS 74

6.1. Gas-Phase Solution 76
6.2. Boron Particle Ignition Results 90

CHAPTER 7. SUMMARY AND CONCLUSIONS 109

REFERENCES 112

LIST OF FIGURES

Figure		
1	Schematic Diagram of Solid-Fuel Ramjet	2
2	Schematic Diagram of Connected-Pipe Facility	14
3	Schematic Diagram of Combustion Chamber Showing Temperature and Pressure Measurement Locations	16
4	Schematic Diagram of Real-Time X-Ray Radiography System	20
5	Temperature-Time History of Thermocouple B from a Typical Subsonic Test	23
6	Pressure-Time Histories of a Typical Subsonic Test	24
7	Autoignition Sequence of a B/HTPB (5/95) Solid Fuel Viewed through Top Window at a Framing Rate of 30 pps	27
8	Autoignition Sequence of a B/HTPB (0/100) Solid Fuel Viewed through Top Window at a Framing Rate of 30 pps	30
9	Instantaneous Surface Profiles of B/HTPB (5/95) Solid Fuel under Subsonic Crossflow	32
10	Burning Rate Dependence on Freestream Pressure for B/HTPB Solid Fuels at Various Temperatures	34
11	Burning Rate Dependence on Freestream Pressure for B/HTPB Solid Fuels at 815 K	36
12	Burning Rate Dependence on Freestream Temperature for B/HTPB Solid Fuels	37
13	Comparison of Observed and Predicted Burning Rates for B/HTPB Solid Fuels	40
14	Instantaneous Surface Profiles of B/HTPB (10/90) Solid Fuel under Supersonic Crossflow	42
15	Physical Geometry of Two-Dimensional Combustion Chamber	44
16	Boron Particle Ignition Model Processes	56
17	Mach Number, Stagnation Temperature, and Static Pressure Contours for Baseline Case; M_∞=2.0, T_∞=1400 K, p_∞=1 atm	77
18	Species Mass Fractions for Baseline Case; M_∞=2.0, T_∞=1400 K, p_∞=1 atm	79
19	Solid Fuel Burning Rate for Baseline Case; M_∞=2.0, T_∞=1400 K, p_∞=1 atm	81
20	Surface Pressure for Baseline Case; M_∞=2.0, T_∞=1400 K, p_∞=1 atm	82

21	Mach Number and Stagnation Temperature Contours; M_∞=2.0, T_∞=1400 K, p_∞=5 atm	83
22	Solid Fuel Burning Rate; M_∞=2.0, T_∞=1400 K, p_∞=5 atm	85
23	Axial Distribution of Burning Rate Parameter	87
24	Variation of Burning Rate Parameter with Pressure	89
25	Histories of Particle Temperature and Oxide-Layer Thickness	91
26	Mach Number and Temperature Contours; M_∞=1.2, T_∞=2000 K, p_∞=2.5 atm	94
27	Species Mass Fractions; M_∞=1.2, T_∞=2000 K, p_∞=2.5 atm	96
28	Calculated Number Distributions of Particles at Various Temperatures (Station x= $\frac{1}{3}L_c$)	98
29	Calculated Number Distributions of Particles at Various Temperatures (Station x= $\frac{2}{3}L_c$)	99
30	Effect of Particle Radius on Ignition Locations; M_∞=1.2, T_∞=2000 K, p_∞=2.5 atm	101
31	Calculated Number Distributions of Particles at Various Temperatures (Station x= $\frac{1}{3}L_c$)	103
32	Calculated Number Distributions of Particles at Various Temperatures (Station x= $\frac{2}{3}L_c$)	104
33	Effect of Particle Radius on Ignition Percentage at Three Axial Stations	105
34	Effect of Freestream Conditions on Ignition Percentage at Three Axial Stations, r_p= 2.5 μm	107

LIST OF TABLES

1	Heats of Oxidation of Selected Elements	6
2	Kinetic Parameters for Gas-Phase Combustion Model	76

NOMENCLATURE

A = Pre-exponential factor

A^+ = Damping factor

B = Weight percentage of boron in solid fuel

C_D = Drag coefficient

C_i = Molar concentration of species i

c_p = Constant pressure specific heat

C_μ = Turbulence constant

D_{ij} = Binary diffusion coefficient

D_{im} = Effective diffusivity of species i against mixture

e = Total stored energy

E = Activation energy

f = Fraction of boron particle melted

g = Gravitational acceleration

G = Mass flux of oxidizer

h = Convective heat transfer coefficient

h_i = Enthalpy of species i

h_f° = Heat of formation

k = Turbulent kinetic energy

k_i = Reaction rate of species i

l = Turbulent length scale

L_c = Length of combustion chamber

L_f = Length of fuel sample

L_e = Characteristic size of turbulent eddy

M = Mach number

M_i = Molecular weight of species i

$\dot{m}$ = Mass flowrate of oxidizer

N = Total number of species

Nu = Nusselt number

p = Pressure

q = Heat flux

q_{rad} = Radiative heat flux

Q_1 = Energy released in reaction of boron and oxygen

Q_2 = Energy absorbed in water vapor/boron oxide reaction

Q_3 = Energy absorbed in evaporation of boron oxide

r_b = Burning rate of solid fuel

r_p = Boron particle radius

R_B = Molar consumption rate of boron

R_E = Molar consumption rate of boron oxide by evaporation

R_H = Molar consumption rate of boron oxide by reaction with water vapor

R_u = Universal gas constant

Re_d = Reynolds number based on droplet diameter

t = Time

t_e = Eddy lifetime

t_t = Transit time of particle in eddy

T_{su} = Surface temperature

T_{sur} = Surroundings temperature

$T_{s,ref}$ = Temperature of solid fuel at reference state

T_o = Solid fuel temperature at $y = -\infty$

u = Velocity in x direction

u^* = Wall friction velocity

$\tilde{U}_i$ = Diffusion velocity in x direction

v = Velocity in y direction

$\tilde{V}_i$ = Diffusion velocity in y direction

x = Coordinate in axial direction

X = Boron oxide layer thickness

X_i = Mole fraction of species i

y = Coordinate normal to fuel surface

y^+ = Non-dimensional height

Y_i = Mass fraction of species i

Greek Symbols

α = Boron oxide evaporation coefficient

ϵ = Eddy dissipation rate

ϵ_B = Emissivity of boron

λ = Thermal conductivity

λ_{eff} = Effective thermal conductivity

μ = Viscosity

μ_{eff} = Effective viscosity

μ_t = Turbulent eddy viscosity

ρ = Density

σ = Stefan-Boltzmann constant

τ = Viscous shear

ω = Vorticity

$\bar{\omega}_i$ = Rate of production of species i

Subscripts

B = Boron

fu = Fuel species

g = Gas phase

p = Particle

s = Solid phase

w = Wall

Superscripts

T = Transpose

$\tilde{}$ = Favre-averaged quantities

$\bar{}$ = Time-averaged quantities

ACKNOWLEDGEMENTS

The author wishes to express his sincere gratitude to his thesis co-advisors, Professors Kenneth K. Kuo and Vigor Yang, for their invaluable guidance throughout this study. In particular, he would like to thank his advisors for providing the opportunity to attend conferences on a regular basis, which broadened his educational experience.

The author would like to acknowledge the project sponsors, Drs. Richard Miller and Gabriel Roy of the Office of Naval Research, Arlington, VA.

The experimental work performed in this study could not have been possible without the help of Mike DiRosa and Dr. Louis Chang. Although they departed years ago, their efforts in designing and constructing the air supply system at the inception of this project are not forgotten. The author also wishes to thank D. L. Cherng and C. L. Chuang for their help in the construction.

The author would like to thank Tim Snyder and Kirsten Pace for their help in making the fuels and conducting the test firings. Their help is greatly appreciated. Randy Salizzoni is also highly appreciated for assisting with the x-ray. Ginny Smith deserves thanks for her everyday help with office matters.

The author would like to thank Drs. J. S. Shuen and K. C. Hsieh of NASA Lewis Research Center and I. S. Tseng of Penn State for providing helpful information and discussion with the numerical portion of this study. In addition, the author wishes to acknowledge the National Science Foundation for providing CPU time on the CRAY Y-MP at the Pittsburgh Supercomputing Center.

Finally, the author wishes to express his deepest gratitude to his parents, brother, and sister, for their support and encouragement throughout the study.

Chapter 1

INTRODUCTION

In the modern development of airbreathing propulsion systems for high-speed vehicles, attention is often focused on the solid fuel ramjet (SFRJ), because of its potential for achieving high performance levels while being simple and compact. The concept of the SFRJ is shown in the schematic diagram of Fig. 1. Compressed air from the inlet mixes and burns with fuel, and the combustion products are accelerated through an exhaust nozzle to generate thrust. Because of its airbreathing feature, the vehicle avoids the weight penalty associated with carrying oxidants and consequently provides a higher specific impulse and longer flight range. The use of solid fuel greatly simplifies the system design, and eliminates problems associated with fuel storage and feeding mechanisms. The fuel may also incorporate energetic additives such as boron or metallic powders to maximize performance during volume-limited missions. However, for the SFRJ to become a viable air-breathing engine, it must first demonstrate efficient operation under a wide range of Mach numbers and altitudes.

The purpose of this work is to experimentally and numerically study the processes involved in the ignition and combustion of solid fuels, so that these mechanisms can be better understood for SFRJ applications.

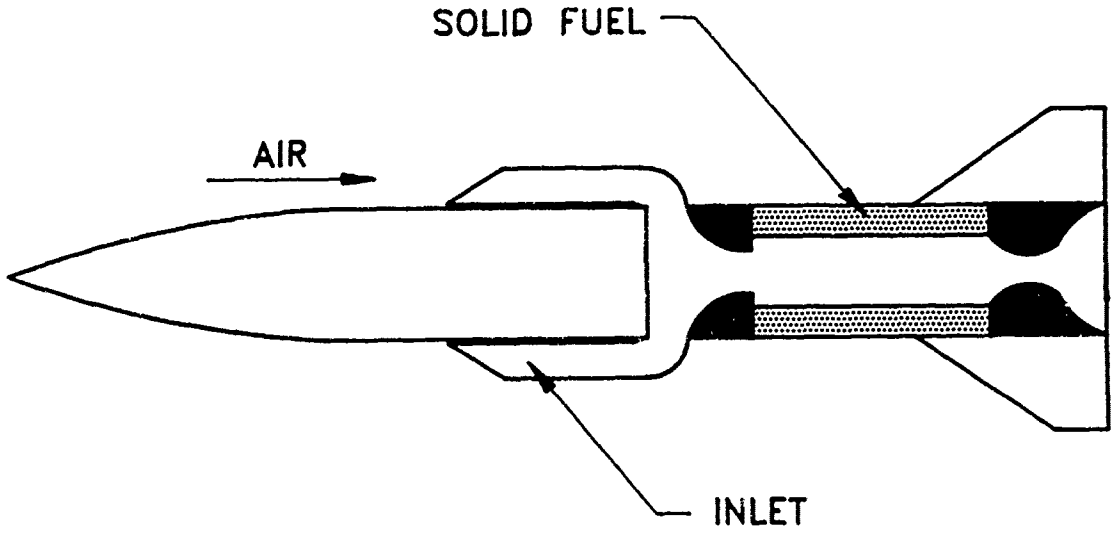


Figure 1. Schematic Diagram of Solid-Fuel Ramjet

1.1. Survey of Previous Works

1.1.1. Experimental Study of Solid Fuel Combustion

Several investigations[1-5] have been conducted to determine the effects of freestream conditions (including pressure, temperature, and flowrate) on the burning rates of homogeneous solid fuels in ramjet environments. The majority of these studies were conducted under low Mach-number flow conditions. Korting et al.[1] studied the combustion behavior of polymethylmethacrylate (PMMA) at low mass flowrates using a connected-pipe test facility. Results indicated that regression rates were hardly dependent on pressure for freestream pressures below 0.65 MPa, but at higher pressures where soot production becomes significant, the burning rate increases with pressure according to the power rule of $p^{0.56}$. This is in reasonable agreement with PMMA combustion studies summarized by Mady et al.[2] Furthermore, at low pressures the burning rates are strongly dependent on the convective heat transfer rates which are influenced by inlet temperature and total mass flux, but at higher pressures this dependence is weaker due to the increase in radiative heat transfer.

In low pressure environments (less than 0.6 MPa), Elands et al.[3] also noticed a slight dependence of burning rate of polyethylene (PE) solid fuels on pressure. The effects of temperature and mass flowrate were greater and in accordance with the relations $T^{0.58}$ and $\dot{m}^{0.56}$, where T and $\dot{m}$ are freestream temperature and flowrate, respectively. These findings compared reasonably well with predicted data from a numerical model which calculated burning rates as functions of T, p, and $\dot{m}$. At higher mass flowrates the temperature dependency was slightly lower, with the exponent decreasing to 0.50.[4]

Schulte[4] also studied flame stabilization in an experimental ramjet motor and determined flame-holding limits based on various ratios of fuel port area to nozzle throat area, and fuel port area to flame holder area. Flame holding was improved by increasing these area ratios and by raising the ram air temperature. In addition, an increase in inlet air temperature enhanced the regression rate of polyethylene solid fuel to a greater extent than did the air mass flux and chamber pressure. Netzer and Gany[5] made similar observations regarding flame stabilization limits and burning-rate dependencies using a miniaturized solid fuel ramjet.

Schulte et al.[6] performed temperature and concentration measurements in an SFRJ combustion chamber and showed that the flowfield in the combustor could be divided into two regions: an air-rich core and a high-temperature zone of combustion products closer to the wall. These two zones did not mix completely, and the addition of an aft mixing chamber would have been beneficial to the combustion process. In addition, the flame position in the redeveloping boundary layer was slightly dependent on the inlet air temperature.

Attempts to experimentally investigate the combustion of solid fuels under transonic and supersonic crossflows were made by Snyder et al.[7] Results indicated that conventional hydrocarbon fuels such as hydroxyl terminated polybutadiene (HTPB) are difficult to ignite at low pressure. However, this situation can be improved significantly with the use of an energetic copolymer such as 3,3-bis [azidomethyl] oxetane/3-nitratomethyl 3-methyl oxetane (BAMO/NMMO), which is readily ignitable because of its lower heat of decomposition and availability of oxygen in the condensed phase.

1.1.2. Effect of Boron Additives

Boron is an attractive candidate as a solid-fuel component for volume-limited propulsion systems because of its high volumetric heating rate. The heats of oxidation of various elements are listed in Table 1, showing boron with the highest value on a volumetric basis, and third highest on a gravimetric basis. For effective utilization, boron particles must ignite and completely burn within the allowed residence time of a combustion chamber. However, since inhibitive boron-oxide layers usually surround these particles, ignition and subsequent combustion are often delayed, thereby hindering the performance of boron-laden fuels. Unless the operating environment is suited toward minimizing the ignition and combustion times, or manufacturing techniques are developed to minimize the particle size and oxide layer effect, boron-containing fuels cannot perform at the desired levels.

1.1.2.1. Single-Particle Studies

To understand some of the difficulties associated with the combustion of boron particles, the ignition and burning processes of individual boron particles have been studied both experimentally and theoretically. Macek[8] determined the burning times of crystalline boron particles with average diameters of 35 and 44 microns in a hot, oxidizing gas stream at atmospheric pressure. The combustion of boron particles was observed to occur in two successive stages, the first being an ignition stage during which the boron-oxide layer is consumed from the surface. Ignition was then followed by a combustion stage in which the boron particle burned vigorously with ambient oxidizer. Burning times were found to decrease with increases in incoming gas temperature and mole fraction of oxygen (X_{O_2}) in the gas. Addition of water vapor to the surrounding gas was shown to decrease the burning times

Table 1. Heats of Oxidation of Selected Elements

Element		Density, gm/cm^3	Gravimetric Heat of Oxidation, kJ/gm	Volumetric Heat of Oxidation, kJ/cm^3
Hydrogen	(H)	–	141.9	–
Lithium	(Li)	0.53	43.2	23.1
Beryilium	(Be)	1.85	66.5	123.0
Boron	(B)	2.34	58.7	137.4
Carbon	(C)	2.25	32.8	73.8
Magnesium	(Mg)	1.74	24.7	43.0
Aluminum	(Al)	2.70	31.1	83.9
Silicon	(Si)	2.33	32.3	75.2
Titanium	(Ti)	4.54	19.7	89.6
Iron	(Fe)	7.86	7.4	58.1
Zirconium	(Zr)	6.49	12.0	78.1

dramatically. Further works by Macek[9,10] provided a substantial data base for particle sizes of 37 to 125 microns in diameter, in pressures from 0.17 to 35.0 atm with a range of oxygen mole fractions from 0.1 to 1.0. For higher values of the diameter (d), pressure (p) and oxygen mole fraction, the burning times were found to be inversely proportional to X_{O_2}, directly proportional to d^2 and independent of p. The burning times deviated from these scaling laws at low values of d, p, and X_{O_2}.

Results from these studies were compared with the predictions of an ignition model by King[11] which described the ignition event in terms of the physical and chemical processes involved in removing the oxide layer from the surface of the particle. Ignition times decreased with increasing initial particle temperature for large particles with radii greater than 10 microns. Decreasing the oxygen partial pressure increased the minimum ambient temperature required for ignition and the total ignition time of the particles. Further refinements of this numerical model[12–14] attempted to fully describe the fundamental heat and mass transfer processes surrounding the particle, including the effects of radiation, oxide-layer thickness, water vapor and oxygen mole fractions in the ambient gas. Comparison of model predictions with the data of Macek[8] were quite reasonable. The ignition model was then linked with a combustion model[15] for clean boron particles under kinetic- or diffusion-limited conditions, leading to a unified model for boron particles. The combustion stage is diffusion-controlled for large particles and kinetics-controlled for small particles, with transition in the region from 15-30 microns in diameter, depending on the ambient pressure.

Mohan and Williams[16] also studied the ignition and combustion of laser-ignited boron particles in the 100 micron diameter range. A diffusion-controlled droplet burning equation was applied to the combustion stage and agreement was attained

between theory and experiment. However, the application of this model is limited to high-temperature (T > 2300 K), dry environments in which the particle diameters are greater than approximately 40 microns and the burning is diffusion-controlled.

Because of the important role which boron oxide (B_2O_3) plays in the ignition process, the gasification process of B_2O_3 droplets was studied in wet and dry oxidizing environments by Turns et al.[17] Droplets with 1000 micron diameters were examined under freestream gas temperatures from 1500-1975 K at atmospheric pressure. Large variations in ambient oxygen concentration produced little or no effect in the droplet lifetimes, whereas the presence of water vapor in the ambient gas significantly increased the gasification rate of the particles. A diffusion-limited equilibrium model provided agreement between oxide drop-life histories and experimental data for particles with temperatures greater than 1350 K.

1.1.2.2. Boron-Based Solid Fuel Studies

Recent experimental studies in boron-based solid fuel combustion have focused on the effect of boron loading on regression rate and combustion efficiency. Snyder et al.[18] studied the effects of boron percentage on the burning rates of hydroxyl terminated polybutadiene (HTPB) solid fuels by adding small fractions of boron powders to enhance the ignition and combustion characteristics of the fuel samples. Regression rates were found to increase with boron addition up to 10 percent, but further addition of boron caused the fuel regression rates to decrease. Pein and Vinnemeier[19] noted similar effects on specific thrust at a boron loading of 20 percent. Specific thrust increased with boron loading to 20 percent; however further addition of boron hampered combustion efficiency and decreased specific thrust. This decrease may be attributed to (1) the heat-sink effect associated with unignited

boron particles in the gas phase which reduced the gas-phase temperature, (2) shielding of heat feedback to the surface by a large number of boron particles above the surface, and (3) decreased gas-phase reactions due to the smaller percentage of HTPB contained in the sample.

Gany and Netzer[20] studied the combustion processes of highly-loaded boron-based fuels in solid fuel ramjets. In this study, the fraction of binder ingredients in the samples was only 30 to 50 percent. Results from direct visualization showed large segments of fuel being ejected from the surface and being swept downstream. Ignition of these pieces ordinarily occurred in the gas phase; however, surface roughness caused by the ejection of the segments allowed for direct impingement of oxygen onto the surface and subsequent surface heating and glowing.

Karadimitris et al.[21] also studied the regression and combustion characteristics of highly loaded boron-containing solid fuels, and noticed similar results with regard to the shedding of flakes of unburned material from the fuel surface. This process played a major role in the overall mass loss rate of the solid fuel. The fuels did not burn well at pressures below 40 psia, primarily due to the lack of adequate gas-phase reactions for complete ignition and combustion of the boron flakes, and inherently poor combustion efficiency of boron at low pressures.

1.1.3. Numerical Study of Solid Fuel Combustion

Turbulent reacting flowfields in solid-fuel combustion chambers have also been studied numerically using finite-rate combustion models. Elands et al.[3] solved a two-dimensional flow over a rearward-facing step, and incorporated a burning-rate equation for a polyethylene solid fuel along one of the wall boundaries. Flame temperatures varied significantly among the finite-rate kinetics and diffusion-flame

models tested; however, the near-wall temperature gradients and corresponding burning rates did not differ substantially. Predictions from the numerical model compared reasonably well with experimental data. Milshtein and Netzer[22] examined the qualitative effects of inlet air location and flow characteristics on solid-fuel regression rate patterns using a three-dimensional computer code with finite-rate kinetics. Predictions showed that regression rates could vary significantly, depending on the manner in which the air was introduced into the combustion chamber. In addition, inlet air swirl could be used to improve fuel utilization.

1.2. Objectives

The previous studies have provided useful information regarding solid-fuel combustion; however, the majority of these studies were conducted in low-speed environments. The primary objective of this research is to investigate the ignition and combustion processes of solid fuels under a wide range of Mach numbers, including both subsonic and supersonic crossflows.

The work was accomplished using experimental and numerical techniques. Specifically, the objectives in the experimental study are as follows:

1. to determine the feasibility of solid-fuel combustion under high-velocity crossflows;
2. to study the effect of boron particles on the ignition and combustion characteristics of HTPB-based solid fuels; and
3. to determine the effects of freestream conditions such as pressure, temperature, and mass flux on the burning rates of HTPB-based solid fuels.

A full description of the experimental apparatus is given in Chapter 2, with discussion of the results in Chapter 3.

A comprehensive theoretical formulation of the combustion of homogeneous solid fuels under supersonic crossflow conditions will also be presented, with a description of the numerical algorithm. As a specific example, the combustion behavior of pure HTPB fuel samples is treated in depth. To better understand some of the complex two-phase phenomena occurring above a reacting boron-laden solid fuel, the ignition behavior of boron particles in a ramjet environment is treated. The approach presented herein should furnish a more realistic indication of the varying conditions surrounding a particle as it travels through a turbulent reacting flowfield into an oxidizing core region. The specific objectives of the numerical study are:

1. to investigate the detailed flowfields and flame structures involved in the combustion of solid fuels in a supersonic flow environment;
2. to determine the burning rates of the fuel samples under various conditions;
3. to examine the effects of the freestream conditions (specifically pressure and temperature) on the pyrolysis and combustion characteristics of the fuel samples;
4. to study the ignition process of individual boron particles ejected from a reacting solid fuel under a high-velocity crossflow;
5. to determine the effect of particle size on the ignition time and location of the particles;
6. to investigate the effects of freestream parameters, including pressure and temperature on the ignitability of the boron particle; and
7. to determine if ignition delay times of boron particles can be minimized by utilizing a particular size range of particles.

The comprehensive formulation of the numerical model is given in Chapter 4, with a description of the solution algorithm in Chapter 5, and finally the discussion of results in Chapter 6. Conclusions of this study are summarized in Chapter 7.

Chapter 2

EXPERIMENTAL APPROACH

2.1. Test Facility

In order to study the physical and chemical mechanisms involved in the combustion of solid fuels, a test facility was constructed consisting of the following major components: an air supply system, test rig, and data acquisition and control systems. These components are described in the following subsections.

2.1.1. Air Supply System

The air supply system serves as an air reservoir for blowdown tests. A detailed description of this facility is given in DiRosa,[23] therefore, only a short summary is provided here.

The system consists of a compressor plant, two air storage tanks, and gas supply lines to the test rig. The compressor plant houses a primary compressor, an intermediate receiver, and a booster compressor. All three of these units were manufactured by Ingersoll-Rand. The primary compressor, otherwise known as ESH, is a double-acting, horizontal compressor. The ESH is a nonlubricated unit that provides two stages of compression with a maximum discharge of 2.5 MPa (350 psig) to the intermediate receiver. The receiver dissipates the discharge pulses from the ESH and feeds the booster compressor. The booster (or ESV) is a double-acting compressor, and like the ESH, is also a non-lubricated unit. The booster provides an additional stage of compression and is capable of discharging up to 4.9 MPa (700

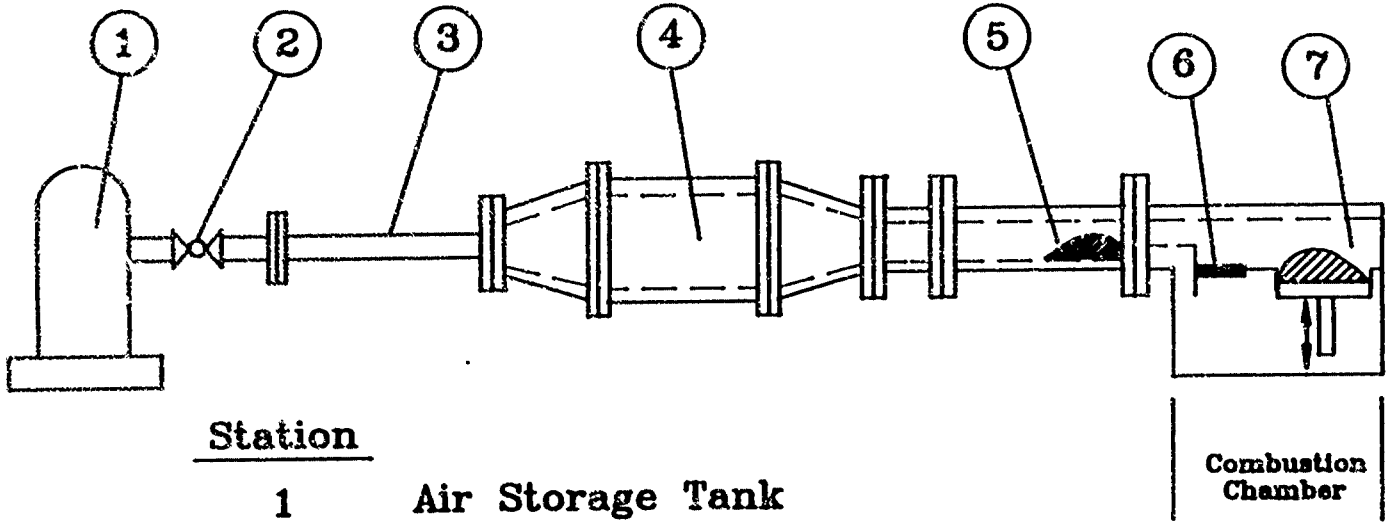
psig) of air to the storage tanks.

The air storage tanks have a dry capacity of 72 cubic meters (19,000 gallons), and have a rated working pressure of 5.3 MPa (750 psig). The tanks stand six meters (20') high and weigh approximately twenty-nine tons each. The storage tanks can discharge the compressed air to the test rig through 5.1 cm (2") and 10.2 cm (4") diameter gas supply lines, which are rated at 4.9 MPa. The rate of discharge is regulated by pneumatic ball valves, which are described in the following section.

2.1.2. Test Rig

The connected-pipe facility is shown schematically in Fig. 2. The rig consists of several major components including: a pneumatic ball valve, vitiator, settling chamber, converging-diverging nozzle, and combustion chamber.

Primary air flow for the rig is released from the storage tanks through the 10 cm discharge line, and is regulated by a 7.5 cm (3") pneumatically controlled Fisher ball valve. To simulate flight conditions at high altitude, the temperature of the primary air must be increased. This is accomplished by mixing and burning the air with an appropriate amount of liquid propane in the vitiator, achieving a maximum temperature of 1000 K. Preheating the air also improves the ignitability of the fuel sample in the combustion chamber. For the majority of tests, the mole fraction of oxygen in the vitiated air is fixed at approximately 0.17. After passing through a diverging section, the gas flows through the settling chamber, which contains a series of perforated plates, screens, and honeycomb for breaking-up the large-scale turbulent structures and flow straightening. The Mach number in the settling chamber is quite low (less than 0.05), therefore stagnation pressure and temperature are measured at this location. The inner diameter of the settling



Station	
1	Air Storage Tank
2	Pneumatic Ball Valve
3	Vitiator
4	Settling Chamber
5	Converging–Diverging Nozzle
6	Test Section (Fuel Sample)
7	Downstream Adjustable Nozzle

Figure 2. Schematic Diagram of Connected-Pipe Facility

chamber is 33 cm (13") with an inner surface coating of Hydrecon, an insulating material for reducing heat loss to the chamber walls. Further downstream, a transition section between the settling chamber and converging-diverging nozzle changes the flow configuration from axisymmetric to 2-D rectangular. The hot gas then passes through the convergent-divergent nozzle which accelerates the flow to a supersonic Mach number of 1.5, or as in most cases, a subsonic Mach number in the vicinity of 0.7. The inlet channel to the combustion chamber is 3.175 cm ($1\frac{1}{4}$") in height and 10.2 cm (4") in width. A rearward-facing step provides a recirculating region for flame stabilization above the fuel sample. The final product gases pass through the adjustable nozzle and are released to the ambient surroundings. The purpose of the exhaust nozzle is to choke the flow and control the Mach number in the test section for subsonic operation. For supersonic operation, the downstream nozzle is removed, since the combustion chamber operates at static pressures above one atmosphere and the flow is already choked by the upstream nozzle.

A detailed diagram of the combustion chamber is provided in Fig. 3, showing the dimensions and features of the test section. The high-enthalpy flow enters the combustion chamber through a short and straight rectangular inlet measuring 3.18 cm in height, 10.16 cm in width, and 10.8 cm in length. The inlet flow has a Reynolds number based on the inlet height of approximately 1×10^6 before passing over a rearward-facing step into the test section. The solid fuel sample is placed directly behind this step. The initial step height is kept constant for all subsonic tests at 1.27 cm, creating a recirculation zone with sufficient dimensions for achieving ignition and stable combustion of the fuel sample, and leaving adequate space for boundary layer redevelopment in the downstream portion of the fuel sample. During supersonic operations, the step height is increased to 1.91 cm to provide a larger recirculation zone for flame stabilization. After ignition, an electronic actuator may

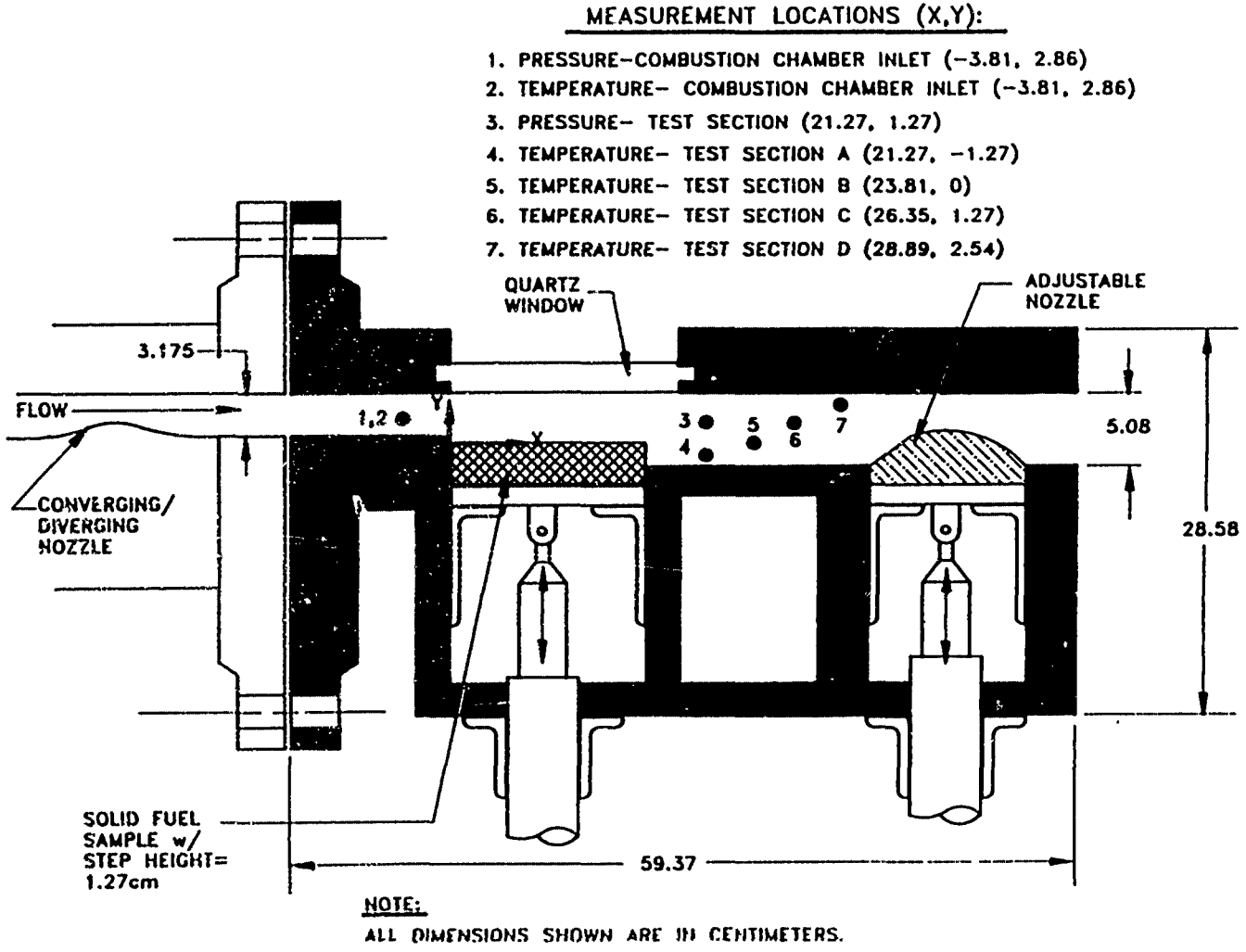


Figure 3. Schematic Diagram of Combustion Chamber Showing Temperature and Pressure Measurement Locations

be used to feed the fuel sample upward in order to study the effect of step height on combustion behavior. The sample feeding rate is on the order of 2.5 cm/s.

The facility is capable of providing vitiated air at a high-velocity crossflow with a static pressure range of 0.1 to 0.62 MPa in the test section, simulating the combustion chamber conditions of a hypersonic vehicle at high altitudes. The maximum flowrate attainable at Mach 1.5 is 8 kg/s with a duration of four minutes at the highest pressure.

2.1.3. Data Acquisition and Control Systems

Pressure and temperature measurements are taken at several locations: the settling chamber, upstream of the convergent-divergent nozzle, the inlet of the combustion chamber, and downstream of the solid fuel sample. Data are not taken in the regions surrounding the fuel sample, since measurements in these locations would interfere with the video systems. Combustion chamber temperature and pressure are monitored at the locations shown in Fig. 3. Temperature measurements are obtained using R-type (platinum/platinum-13% rhodium) thermocouples. Radiative and catalytic effects on the thermocouple beads are found to be negligible because of the high convective velocity and small bead size of 200 microns; therefore, no corrections are made to the temperature readings. The pressure measurements are taken using high output transducers from Setra Systems, Inc. An IBM PC/AT computer records all temperature and pressure measurements using a Metrabyte DAS-16 high-speed data acquisition system. A Metrabyte EXP-16 expansion board provides an additional 16 channels of differential analog input.

Steady flow conditions are achieved by means of a feedback control loop between the pneumatic ball valve in the air supply line, a single-loop digital controller,

and a pressure transducer in the settling chamber, with a maximum fluctuation of 1 percent in the stagnation pressure. The controller is manufactured by Moore Products and the model type is MYCRO-352. A 4-20 mA signal from the controller is converted to a pneumatic pressure via a 546 Electro-Pneumatic Transducer (Fisher), which regulates the supply pressure for the ball valve. The air flowrate to the test rig is therefore regulated by changing the output current from the Moore controller.

The liquid propane flowrate to the vitiator is regulated by a Worcester Controls V-seat $\frac{1}{2}$" control valve. A 1075 electric actuator from Worcester drives the valve based on a 4-20 mA signal provided from the test operator. The propane flowrate is monitored by an Omega FTB-100 Series turbine flowmeter.

2.2. Solid Fuels

All fuels studied in this work are processed by mixing liquid HTPB binder (ARCO R45-M) and various percentages (0-20 by weight) of boron powder with the curing agent isophorone diisocyanate (IPDI). Amorphous boron powders added to the fuels have a purity of 99.9% and a size range of 0.04 to 0.15 microns in diameter. The fuels are prepared by thoroughly blending all of the ingredients in a vacuum mixer at 50°C for one hour. After mixing, the fuels are poured into a mold, placed in a vacuum desiccator for three hours, then cured at 65°C for at least four days. The samples measure 15.2 cm in length, 5.1 cm in width, and 3.2 cm in height for the subsonic tests. During supersonic operations, the width of the samples is increased to the full width of the chamber (10.16 cm) in order to prevent expansion of the gas to the sides of the fuel sample and to maintain a high pressure above the fuel surface. The narrower samples are used for subsonic tests to avoid direct impingement of the flame onto the side windows and prolong the lifetime of the windows.

2.3. Igniter

A pyrophoric liquid, triethylborane (TEB), is injected into the recirculation zone to achieve ignition of the solid fuels. A stainless steel tube with an outer diameter of 0.32 cm is extended slightly above the sample surface to inject TEB parallel to the top surface of the sample at an angle approximately 60 degrees from the side walls. The injection time is ordinarily on the order of one second, then the TEB is turned off after solid fuel ignition is attained. In some cases, the solid fuel samples are ignited by the hot crossflow gas without the aid of TEB, but this is highly dependent upon freestream conditions and fuel composition.

2.4. Real – Time X – Ray Radiography and Video System

Instantaneous surface profiles of the solid fuels are obtained using a real-time x-ray radiography system. The system, shown in Fig. 4, consists of an x-ray source, an image intensifier which receives the x-ray image through the graphite windows, and a video camera. After completion of each test, the regression rate of the fuel sample is deduced using a digital image processing system. This non-intrusive technique offers several advantages over the conventional optical methods in measuring the instantaneous surface profiles of fuel samples. First, x-rays easily identify the fuel surface by penetrating through the two-phase combustion products surrounding the sample, which are usually opaque for other visualization techniques. The flame does not interfere with the interpretation of the surface profiles, since the luminous flame zone is not visible on the x-ray images. Second, gas purging of the viewing windows, as required by the direct photography technique, is not necessary since deposits of fuel and/or char on the windows are easily penetrated by the x-rays. The elimination of gas purging also simplifies the design of the combustion chamber.

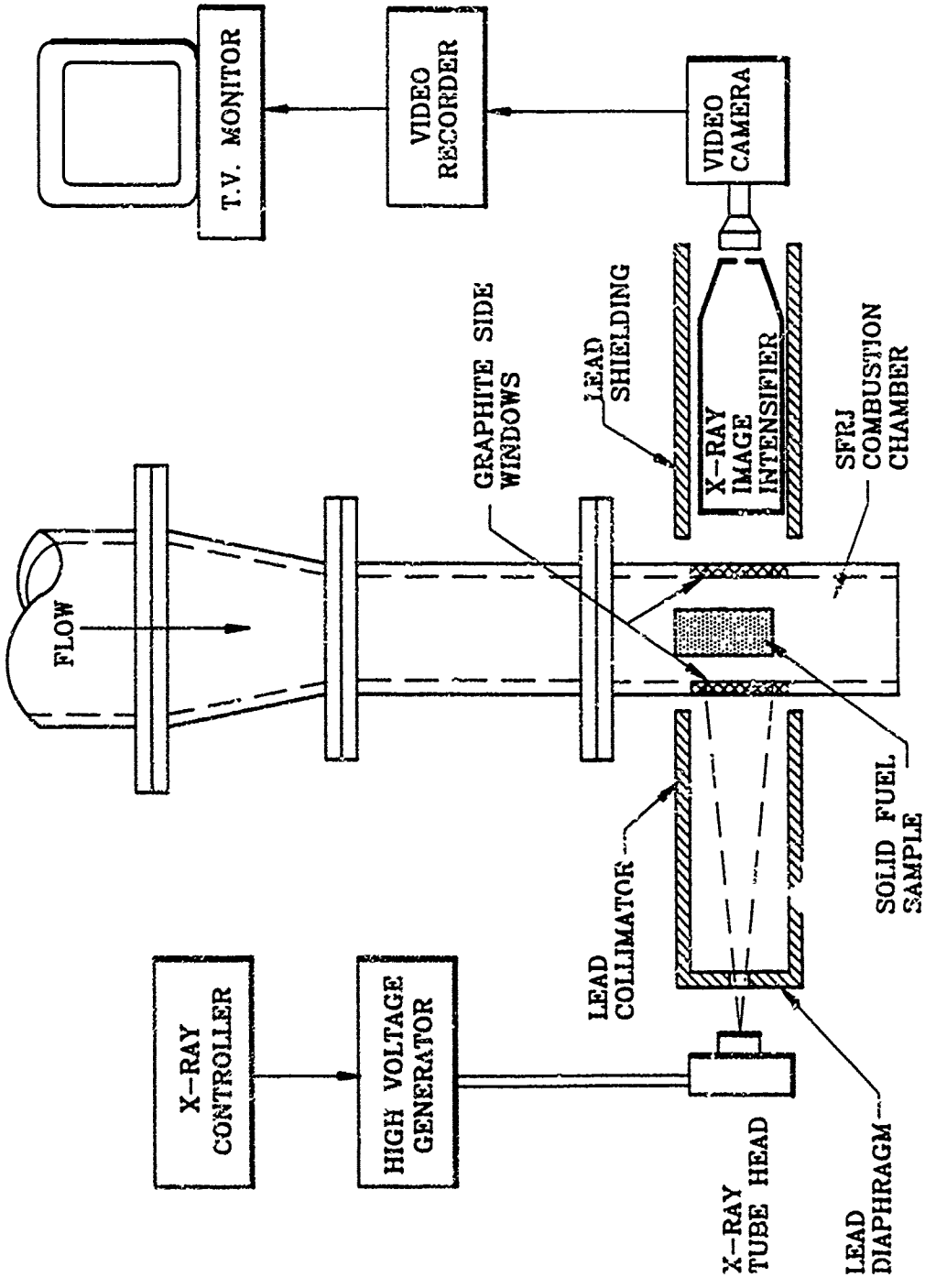


Figure 4. Schematic Diagram of Real-Time X-Ray Radiography System

Third, the viewing area (6.35 cm in height × 13.3 cm in length) encompasses a large portion of the fuel sample and its associated reacting flowfield, so that the complete surface profile is contained on one image.

Direct video is also employed to study the burning phenomena of the solid fuels. The top view of the solid fuel is captured through a quartz window (see Fig. 3) to study the surface ignition, flame spreading, and combustion processes. Another video camera records the exhaust plume emanating from the combustion chamber.

Chapter 3

EXPERIMENTAL RESULTS AND DISCUSSION

A series of subsonic and supersonic tests were performed using the facility described in Chapter 2. For subsonic crossflow conditions, the inlet static pressures and freestream temperatures ranged from 0.26 to 0.57 MPa and 550 to 1080 K, respectively. Vitiated air entered the combustion chamber at flowrates ranging from 1.1 to 3.1 kg/s and Mach numbers from 0.47 to 0.74. Figures 5 and 6 show typical temperature and pressure histories recorded from a subsonic test with a sample consisting of 5 percent (by weight) boron in the HTPB binder (denoted as B/HTPB, 5/95). Ignition of the propane/air mixture in the vitiator occurs forty seconds into the test, as indicated by the abrupt increase in temperature shown in Fig. 5. Prior to this time, the cold air is slowly introduced into the test section. After ignition in the vitiator, the propane and air flowrates are steadily increased to raise the temperature and pressure of the hot gas. Heat transfer to the solid-fuel sample raises the surface temperature of the sample, and the fuel begins to slowly release pyrolyzed fuel-rich gaseous species from its surface. According to the thermogravimetric analysis of B/HTPB fuels at a heating rate of 100 deg/min,[24] decomposition starts at approximately 520 K, and reaches a peak weight loss in the neighborhood of 680 K, with boron having only a very limited effect. A dashed vertical line at t=64 seconds in Fig. 5 represents the time at which the gas temperature exceeds 520 K. For this particular test, TEB injection is not necessary because the temperature of the vitiated air is sufficiently high to promote exothermic surface reactions of boron particles which serve as a local ignition source for the air and pyrolyzed fuel mix-

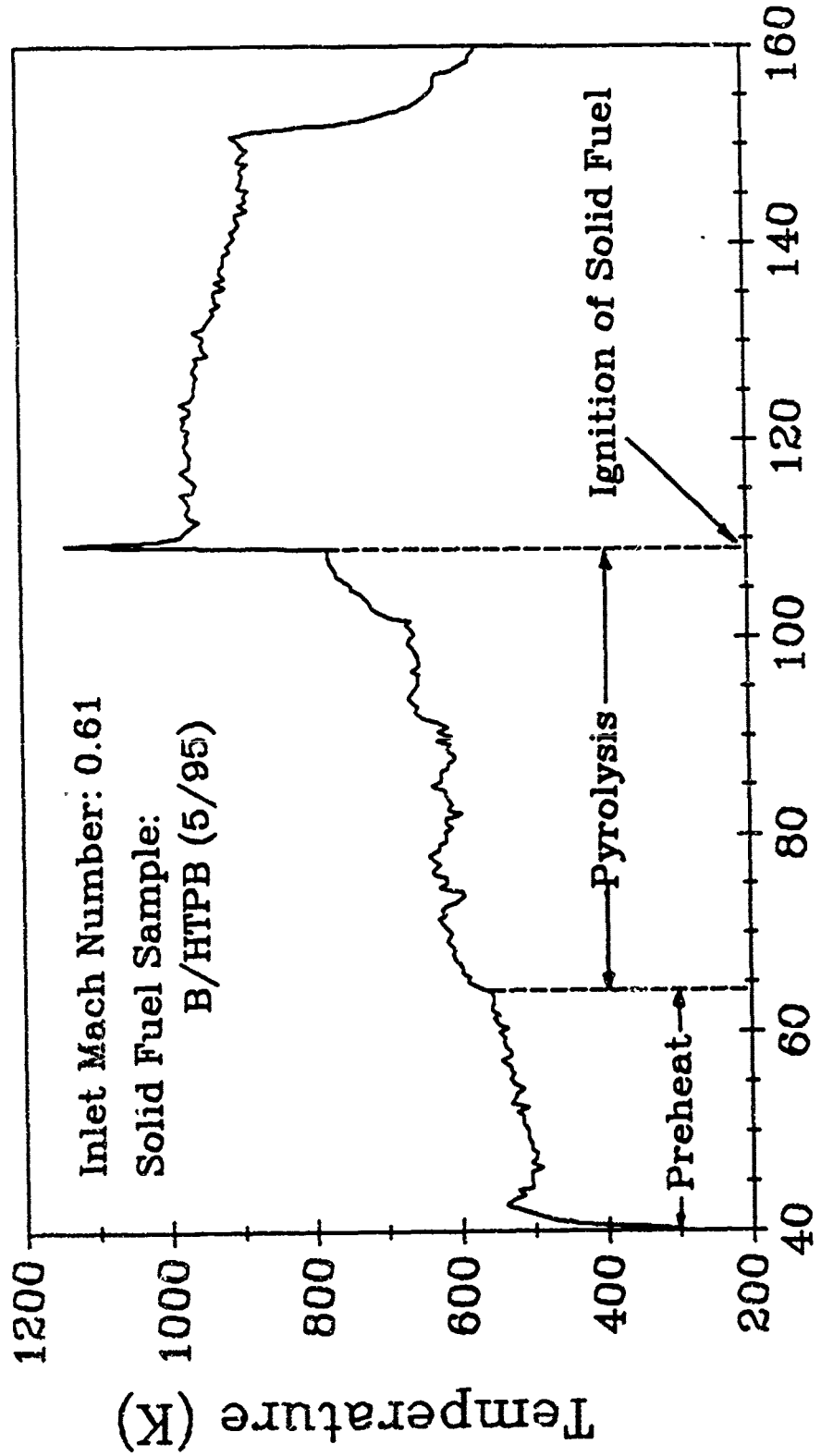


Figure 5. Temperature-Time History of Thermocouple B from a Typical Subsonic Test

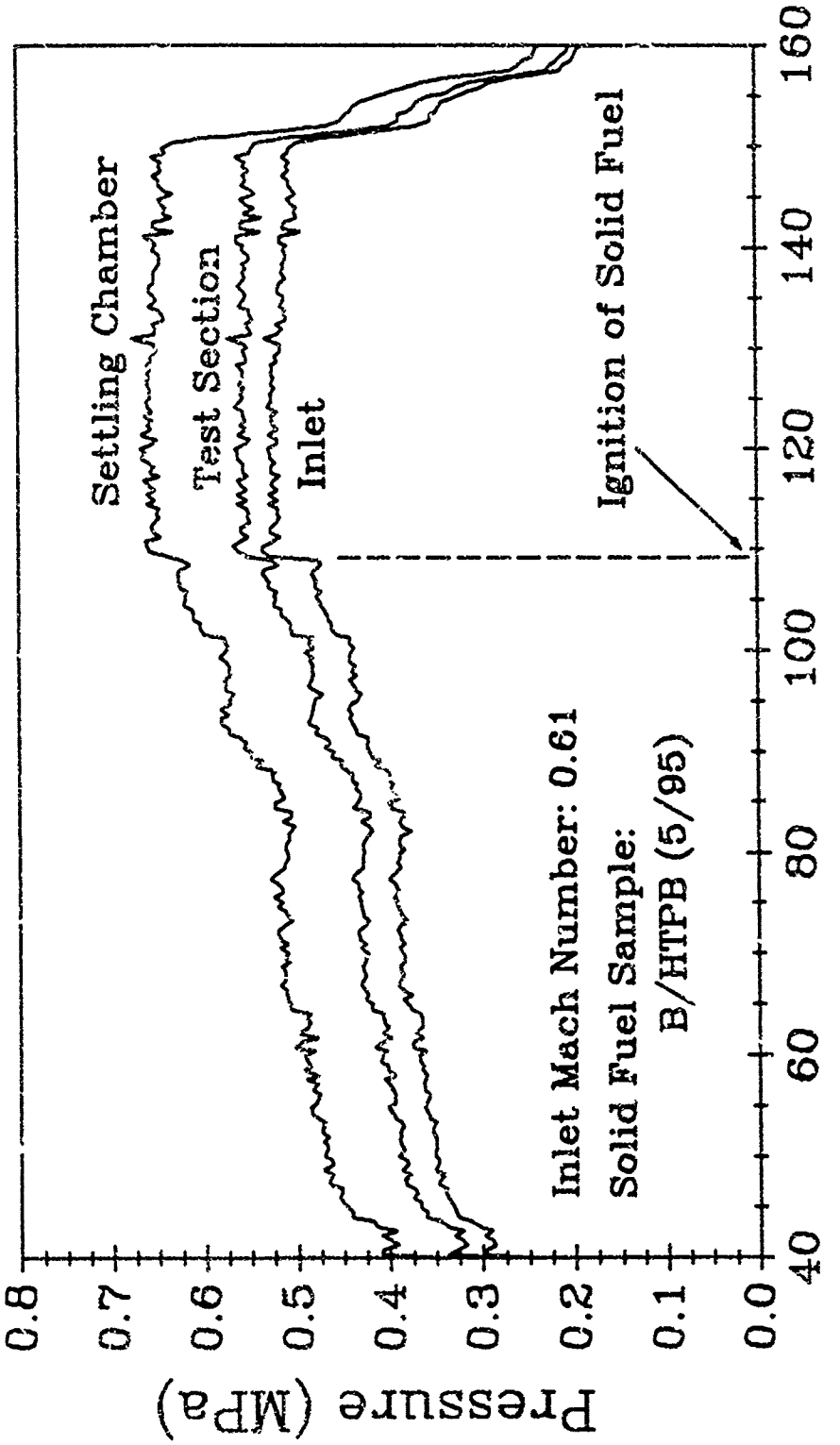


Figure 6. Pressure-Time Histories of a Typical Subsonic Test

ture. Following ignition of the fuel sample, the flowrates of propane and air remain fixed, resulting in a constant pressure for the duration of the combustion event. The occurrence of ignition is indicated by a large spike in the test-section thermocouple B reading, as shown in Fig. 5. The height of the thermocouple is initially aligned with the sample surface prior to the test. When the fuel sample ignites, the flame is in close proximity to the thermocouple; however, as the sample regresses, the flame zone moves down with the surface of the sample, thereby increasing the distance between the flame and thermocouple and reducing the temperature reading. The abrupt drop in temperature at the end of the test is caused by shutdown of the test facility.

Figure 6 shows three separate pressure-time traces measured in the settling chamber, combustion chamber inlet, and test section. As shown in these traces, ignition of the solid fuel sample causes a small, abrupt increase in each pressure reading. During the combustion event, the Mach number at the inlet is fixed at 0.61. This value is calculated using the static to stagnation pressure ratio, then verified by determining the correct pressure ratio based on the inlet to nozzle area ratio.

3.1. Ignition Sequence

As mentioned previously, autoignition of the solid fuel can be initiated by reactions of boron particles on the surface of the fuel sample. This ignition process relies on several important physical and chemical mechanisms, including pyrolysis of the solid fuel, mixing of the pyrolyzed fuel-rich species with the oxygen, and subsequent ignition of the mixture by the reacting boron particles. In order to describe this sequence in more detail, the ignition process of the boron particle is briefly summarized below.

Previous studies of ignition and combustion of individual boron particles[8,25] indicate that boron undergoes a two-stage ignition process. The first stage begins with the removal of a thin inhibitive oxide layer from the particle surface. Heat transfer to the particle melts the oxide layer at 723 K, thereby allowing oxygen to diffuse across the molten oxide layer. The boron/oxygen reactions produce additional boron oxide which thicken the oxide layer, but also raise the temperature of the particle due to the exothermicity of the reactions. This initial rise in temperature is accompanied by the appearance of luminosity, and marks the onset of the first stage of particle ignition. In order for the ignition process to continue, the particle temperature must continue to rise. This occurs by further convective or radiative heat transfer to the particle, which evaporates the oxide layer from the surface. In addition, self-heating from boron/oxygen reactions raises the particle temperature at the expense of boron oxide production. At a sufficiently high freestream temperature (ca. 1900 K), the evaporation rate of the boron oxide is high enough to completely remove the oxide layer. The elemental boron is then directly exposed to the oxygen, giving rise to highly exothermic heterogeneous reactions and the second stage of particle ignition. This results in full-fledged combustion and a much brighter flame surrounding the particle.

Figure 7 shows the top view of the ignition sequence of a B/HTPB (5/95) fuel sample. The flow conditions are given in Figs. 5 and 6. The viewing area of the window spans 19 cm in length by 7 cm in width, and the flow direction is from left to right. Since the fuel sample is 15 cm in length, a small portion of the downstream section of the combustion chamber is visible on the right side of the window. The temperature of the crossflow gas is approximately 750 K, sufficient to melt the oxide layers on the particles and promote the first step of particle ignition. Figure 7a reveals glowing spots on the fuel surface which appear to be boron particles in

a. t=0.000 s

b. t=0.033 s

c. t=0.067 s

d. t=0.100 s

e. t=0.133 s



Figure 7. Autoignition Sequence of a B/HTPB (5/95) Solid Fuel Viewed through Top Window at a Framing Rate of 30 pps

the first stage of ignition. As shown in the sequential Figs. 7a through 7c taken at a framing rate of 30 pictures per second, the glowing particles on the surface provide the heat necessary to ignite the pyrolyzed fuel-rich gas and air mixture. Ignition of the gas phase begins in the recirculation zone formed by the rearward facing step, and spreads downstream very quickly as shown in Figs. 7c and 7d. The flame-spreading process ordinarily occurs in less than 0.05 seconds for the B/HTPB fuels used in this study. Finally, Fig 7e shows full-fledged ignition of the solid fuel sample. The erratic edges of the window are video distortions caused by the high noise level in the test room.

After ignition of the solid fuel, the glowing boron particles are ejected with pyrolyzed fuel-rich species into the gas-phase reaction zone. In order for the particles to achieve full-fledged ignition and combustion, they must pass through the flame zone. In summary, the ignition process of the boron-laden solid fuels is as follows. The high-temperature crossflow gas promotes the first stage of boron particle ignition. The regions surrounding the reacting particles create a reaction site for the pyrolyzed fuel-rich species and air mixture, which results in flame spreading and stabilization above the solid-fuel surface. Once the fuel sample sustains combustion, ejected boron particles can achieve their second stage of ignition by passing through the established flame zone.

Within the Mach number range tested in this work, the majority of boron-laden solid fuels can ignite at inlet temperatures between 725 and 820 K without the use of TEB. This temperature range is conducive to ignition, since HTPB pyrolyzes below this temperature range, and boron particles begin their ignition process with the melting of the oxide layer at 723 K. All of these fuels ignited in the recirculating region, even though some had glowing boron particles on the sides and in the downstream region of the sample. In addition, ignition of the

solid fuel did not instantaneously occur when these glowing spots were formed in the recirculation zone, but occurred only after a sufficient amount of gas pyrolyzed from the fuel surface. An attempt was made to establish a correlation between the time allowed for pyrolysis and the ignition temperature, but none was found because the elapsed time between these two events was primarily dependent on the test procedure and the sequence in supplying propane and air to the test rig.

The ignition sequence for B/HTPB (0/100) fuels without the aid of TEB was slightly different than that for boron-containing fuels, since boron particles were not available on the surface to promote ignition. The HTPB fuels did ignite in the recirculation zone; however, the required inlet temperatures were beyond 820 K. The ignition event of a B/HTPB (0/100) fuel is shown in Figs. 8a through 8e. Figure 8a reveals onset of ignition of the gas-phase mixture in the recirculation zone, and the next three figures show the flame-spreading phenomenon which is similar to that of the B/HTPB (5/95) fuel. The B/HTPB (0/100) fuels showed no indication of a localized ignition source to initiate the ignition process; instead ignition seemed to occur spontaneously over a distributed region in the recirculation zone. The flame spread slightly faster compared to the boron-laden fuels, but this might be due to the faster gas-phase kinetics caused by a higher inlet temperature.

As previously mentioned, TEB was available to ignite the solid fuel; however, it was used only under conditions which necessitated its use. Typically, TEB was used for those tests with low inlet temperatures in which auto-ignition of the fuel species in the gas phase was difficult to achieve. When the operating conditions matched the desired test temperature and pressure, the TEB was injected and the fuel samples ignited within one second from the start of injection, with the exception of one test employing B/HTPB (0/100) fuel at a low inlet temperature. For this particular test at 620 K, the fuel sample ignited momentarily when TEB



Figure 8. Autoignition Sequence of a B/HTPB (0/100) Solid Fuel Viewed through Top Window at a Framing Rate of 30 pps

was injected for ten seconds above the surface; however, the sample extinguished after the igniter was turned off. A B/HTPB (10/90) fuel sample tested at a lower inlet temperature of 550 K did ignite and sustain combustion after TEB injection. The successful ignition of this fuel is most likely caused by the increased surface absorptivity due to the addition of boron particles. Another factor contributing to the flame stabilization at low inlet temperatures is the increase in heat feedback to the surface from the ejected boron particles reacting above the solid fuel.

3.2. Combustion Characteristics

3.2.1. Subsonic Results

Figure 9 shows the instantaneous surface profiles deduced from the x-ray radiography system for a B/HTPB (5/95) sample burning under a subsonic crossflow. The profiles are taken at axial locations 4.5 to 13.5 cm from the rearward-facing step at intervals of 1.5 cm. These profiles are not extended to the full length of the sample because all of the fuels experience some degree of end burning; therefore, data at the 15 cm location are not always available. In addition, the region upstream of the 2.8 cm location was not visible due to restrictions in the size of the graphite side window (the graphite window was 13 cm in length, whereas the fuel was 15 cm long). The dashed line corresponds to the fuel surface profile before the test, and the solid lines are the contours of the sample taken after ignition at five second intervals. The first profile taken immediately after ignition of the entire fuel sample at t=110 seconds shows the degree of fuel pyrolysis prior to ignition. Since each test necessitates some start-up time to achieve operating conditions, all solid fuels exhibit similar pre-ignition pyrolysis. The fuel surface profiles show a slight increase in regression rate in the downstream region caused by enhanced heat feedback

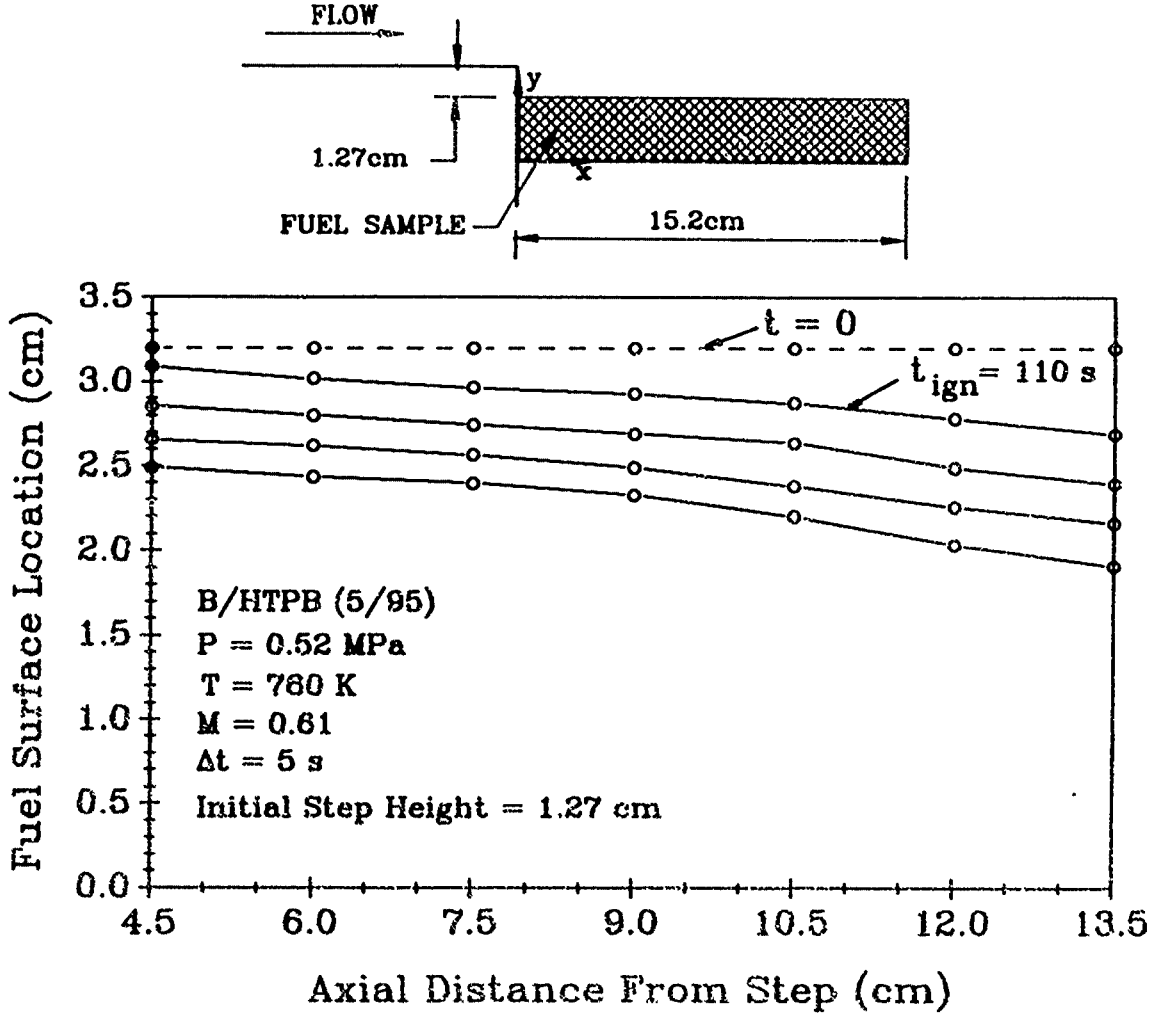


Figure 9. Instantaneous Surface Profiles of B/HTPB (5/95) Solid Fuel under Subsonic Crossflow

from the diffusion flame zone. Although Fig. 9 does not indicate a large variation in burning rate along the length of the sample, some tests indicate a variation as large as 10 percent. The reason for the uneven burning may be attributed to larger amounts of fuel-rich species being reacted in downstream locations rather than at upstream stations. This occurs because the majority of the pyrolyzed gases are transported downstream by the shear flow before chemical reactions occur. Thus, heat release in the diffusion flame is greater in the downstream region.

Figure 10 shows the influence of freestream pressure on the regression rates of HTPB-based solid fuels with boron loadings of 0 and 10 percent. The regression rates are averaged values from the locations at 6.0, 9.0, and 12.0 cm from the rearward-facing step, which cover a significant portion of the fuel sample. The error bars on the data are based on uncertainties in locating the top surface of the solid fuel when using the digital image processing system (1 to 2 pixels). This uncertainty results in an error of 2 to 4 percent in the total burning rates. For the fuels shown in Fig. 10, the burning rates increase substantially with pressure. Two mechanisms can be attributed to the enhanced burning rates at higher pressures. First, the increase in pressure corresponds to an increase in oxidizer-to-fuel ratio, allowing additional reactions of oxidizers with the fuel-rich pyrolysis products and boron particles. This results in higher flame temperatures and greater heat transfer to the fuel surface, thus increasing the regression rate of the solid fuel. Second, the gas-phase kinetics are faster, which also intensify the reactions above the fuel surface resulting in enhanced heat feedback to the fuel sample. Unfortunately, what cannot be shown by the x-ray images is the change in the height of the diffusion flame above the surface. This standoff height may be altered by changes in molecular diffusion rates, surface blowing, and turbulent mixing, which can be functions of pressure. Diagnostic procedures other than x-ray may reveal the effect of pressure

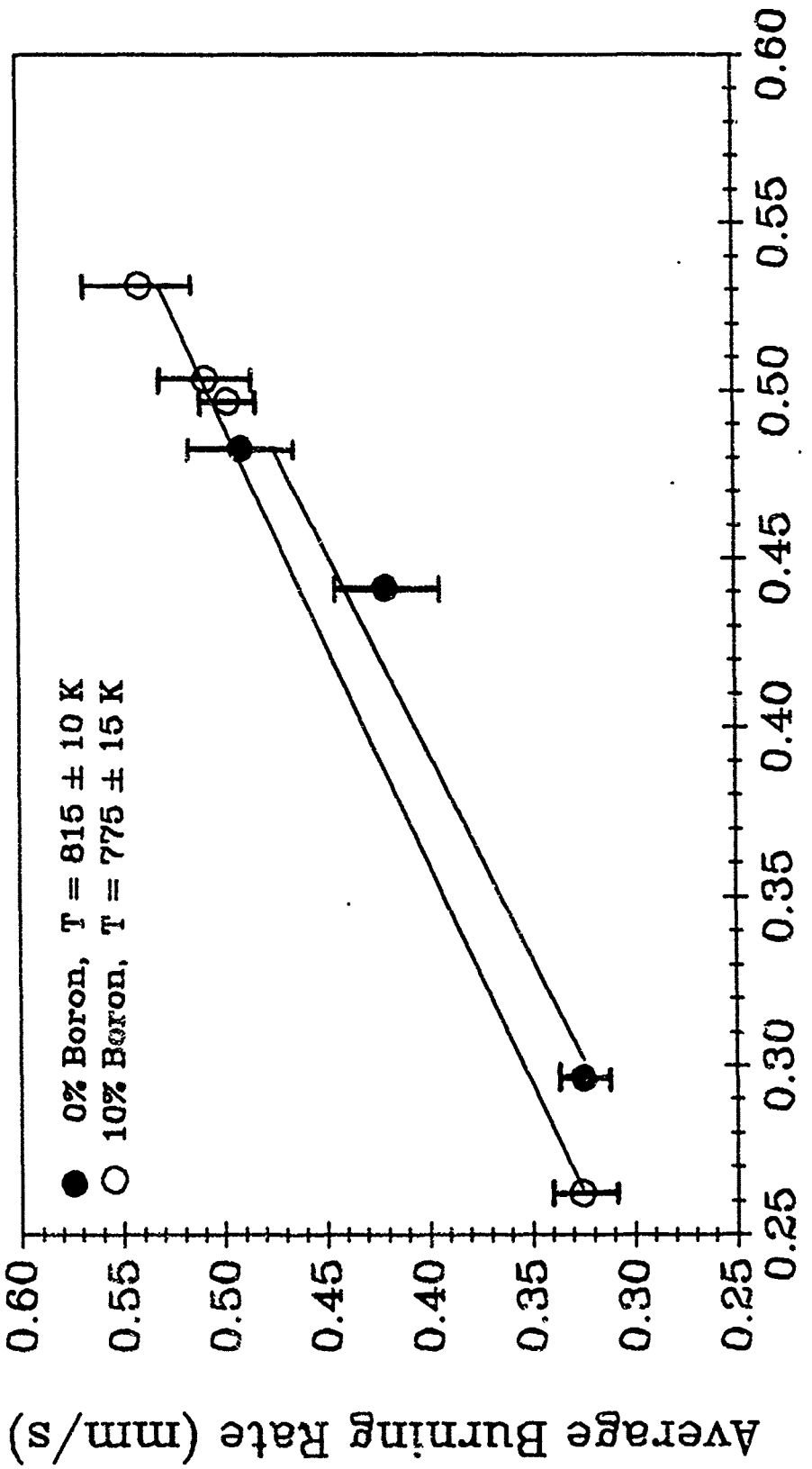


Figure 10. Burning Rate Dependence on Freestream Pressure for B/HTPB Solid Fuels

on the flame height.

The effect of boron on the regression rate of the HTPB fuels can also be determined from Fig. 10. In order to compare the 0 and 10 percent boron data, the burning rates must first be independent of freestream temperature. Therefore, the regression rates of the 10 percent boron are adjusted from the 775 K freestream temperature to corresponding burning rates at 815 K by employing the power rule: $r_b \propto T^{0.28}$. The value of the exponent will be justified later in this chapter. The new curves are shown in Fig. 11, with additional points coming from data at temperatures other than those shown in Fig. 10. The addition of 10 percent boron to a pure HTPB fuel increases the burning rate by approximately 10 percent. This increase can be attributed to the additional convective and radiative heat transfer from the reacting particles to the fuel surface, as well as the increased radiation absorptivity of the fuel surface.

Fuels with boron loadings greater than 10 percent were also tested. A higher boron particle loading of 15 percent slightly decreased the burning rate compared with the 10 percent boron fuel. This may be due to the following reasons: (1) the decreased HTPB content in the fuel diminishes the gas-phase reactions and reduces the energy supply for complete ignition and combustion of boron particles, (2) the higher boron percentage increases the heat-sink effect in the gas phase, which reduces the flame temperature and results in incomplete ignition and combustion of the particles, thereby reducing the heat feedback from the ejected particles, and (3) the heat feedback is diminished due to shielding caused by accumulated particles on the surface. Only a few tests were conducted at these higher loadings and more data may be needed to support these statements.

The effect of freestream temperature on the burning rates of B/HTPB fuels with particle loadings of 0, 5, and 10 percent is presented in Fig. 12. The burning

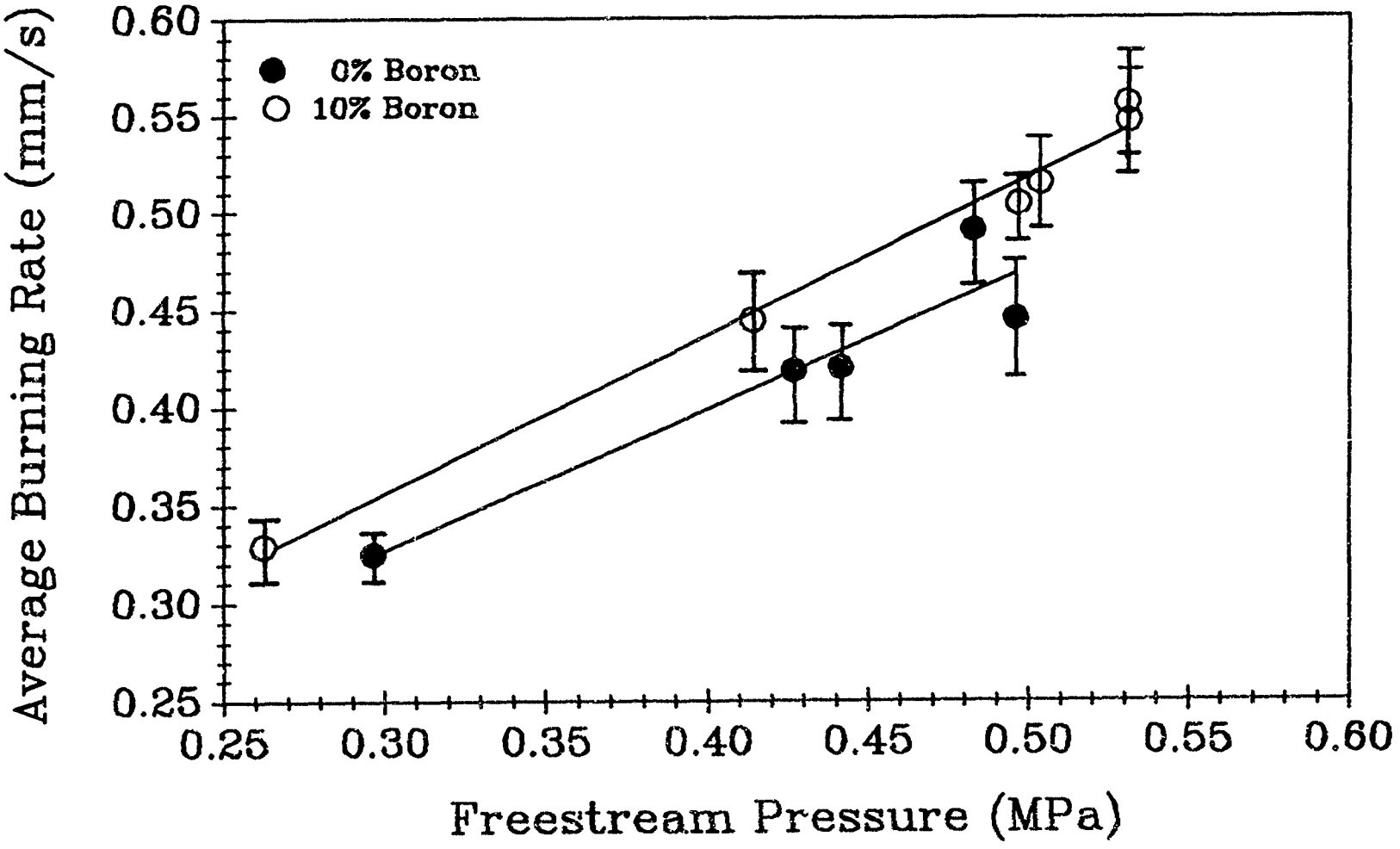


Figure 11. Burning Rate Dependence on Freestream Pressure for B/HTPB Solid Fuels at 815 K

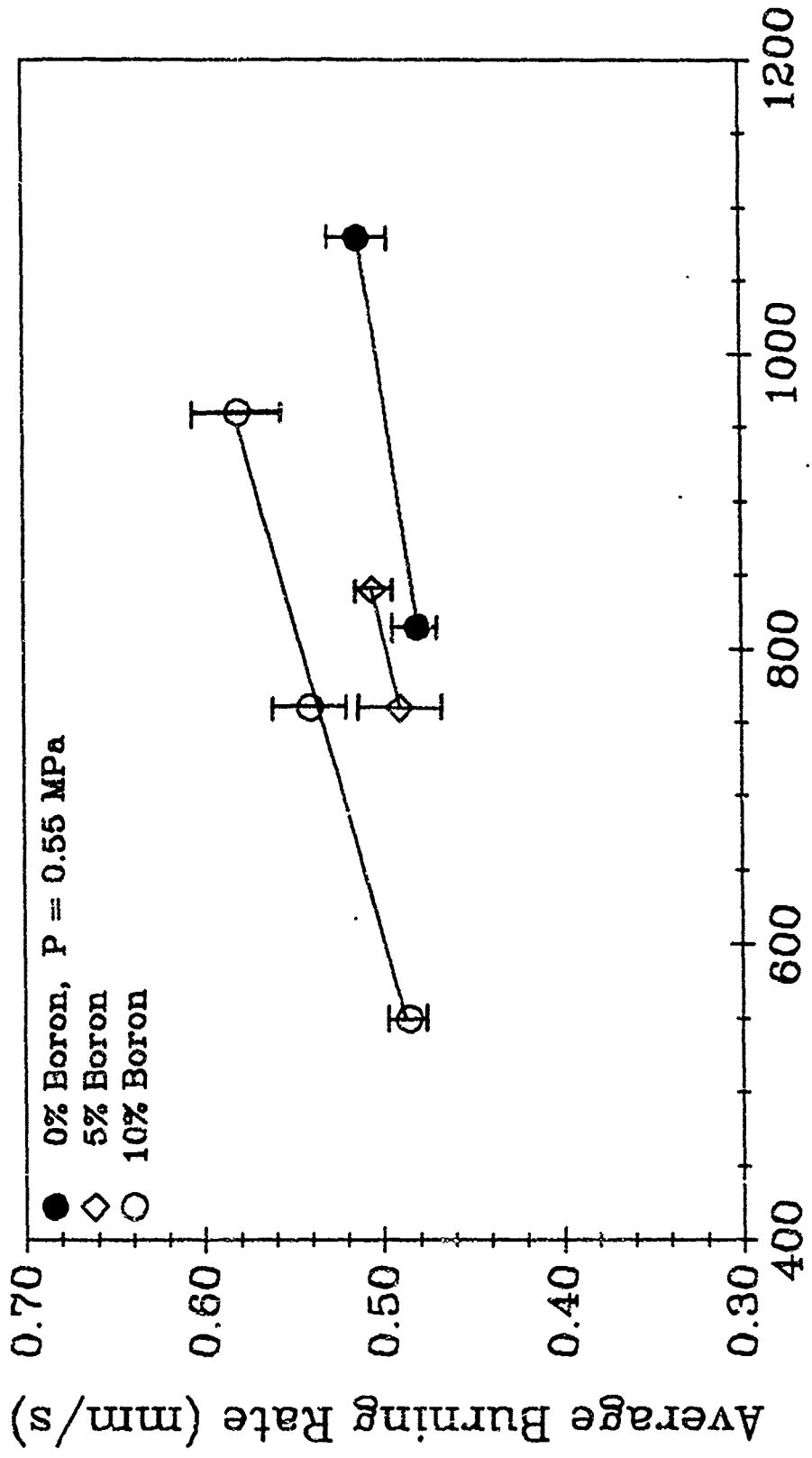


Figure 12. Burning Rate Dependence on Freestream Temperature for B/HTPB Solid Fuels

rates increase with freestream temperature due to enhanced convective heat transfer to the fuel surface from the crossflow and faster chemical reaction rates at elevated temperatures. The rise in freestream temperature not only increases the gas-phase reaction rates, but also increases the convective heat transfer to the boron particles, which subsequently decreases the heatup and ignition delay of boron in the gas-phase reaction zone above the fuel sample. At lower inlet temperatures the particles may ignite but not until they are convected downstream of the solid fuel where less energy can be directly transferred back to the fuel. If the particles achieve ignition sooner due to the higher inlet temperatures, they can supplement the heat feedback to the fuel surface with radiative and convective heat transfer from the condensed-phase reactions. Figure 12 also supports the observation of higher burning rates with increased boron loadings to 10 percent.

In order to assess the effects of temperature, pressure, and boron loading percentage on the burning rates in a more general and quantified sense, the independent variables were input into a power law of the form:

$$r_b = a\, p^b\, T^c\, G^d \tag{1}$$

where the pre-exponential constant a and the pressure exponent b are functions of boron percentage. The units of pressure, temperature, and burning rate are MPa, K, and mm/s, respectively. In this work, boron loading varied from 0 to 20 percent, pressures from 0.26 to 0.57 MPa, temperatures from 550 to 1080 K, mass flux from 337 to 965 kg/m^2/s, and Mach number from 0.47 to 0.74, with an initial combustion chamber step height of 1.27 cm. The correlation determined from a least-squares estimation of nonlinear parameters[26] is shown below.

$$r_b = (0.06 + 0.93B)\, p^{0.6(1.0-0.23B)}\, T^{0.28}\, G^{0.09} \tag{2}$$

Results from this correlation are shown in Fig. 13, where the fitted power law is shown on the horizontal axis, and the observed burning rates on the vertical axis. The diagonal line signifies agreement between fitted and observed burning rates. The data correlates reasonably well for the wide range of pressures and temperatures, with pressure exhibiting the most dominating effect on the burning rate. This equation was utilized to adjust the data shown in Fig. 10, such that the effects of pressure and boron concentration on burning rates could be compared, without regard to temperature effects. According to the power-law expression, addition of boron to an HTPB fuel increases the burning rate; however, relatively few data are available for boron loadings greater than 10%, and care must be taken before extrapolating this equation to higher boron concentrations.

Efforts were made to incorporate the effect of mass flux into the correlation, but the current results indicate only a very weak effect on the burning rate, with an exponent of 0.09 for the mass flux in the power-law expression. Since mass flux is a function of pressure, temperature, and Mach number, and no direct attempts were made to keep the pressure and temperature constant while changing the Mach number, it is possible that the major effects of the mass flux are represented in the pressure or temperature exponents. Future tests should incorporate variations in Mach number while keeping the remaining independent variables constant.

3.2.2. Supersonic Results

The combustion of solid fuels under supersonic crossflows was also achieved with B/HTPB (10/90) and B/HTPB (0/100) samples at a Mach number of 1.5. The first test was conducted with B/HTPB (0/100) to determine the effect of the step height on flame stabilization. The initial step height was 1.27 cm prior to the test. Under Mach 1.5 crossflow with a freestream temperature of 900 K and

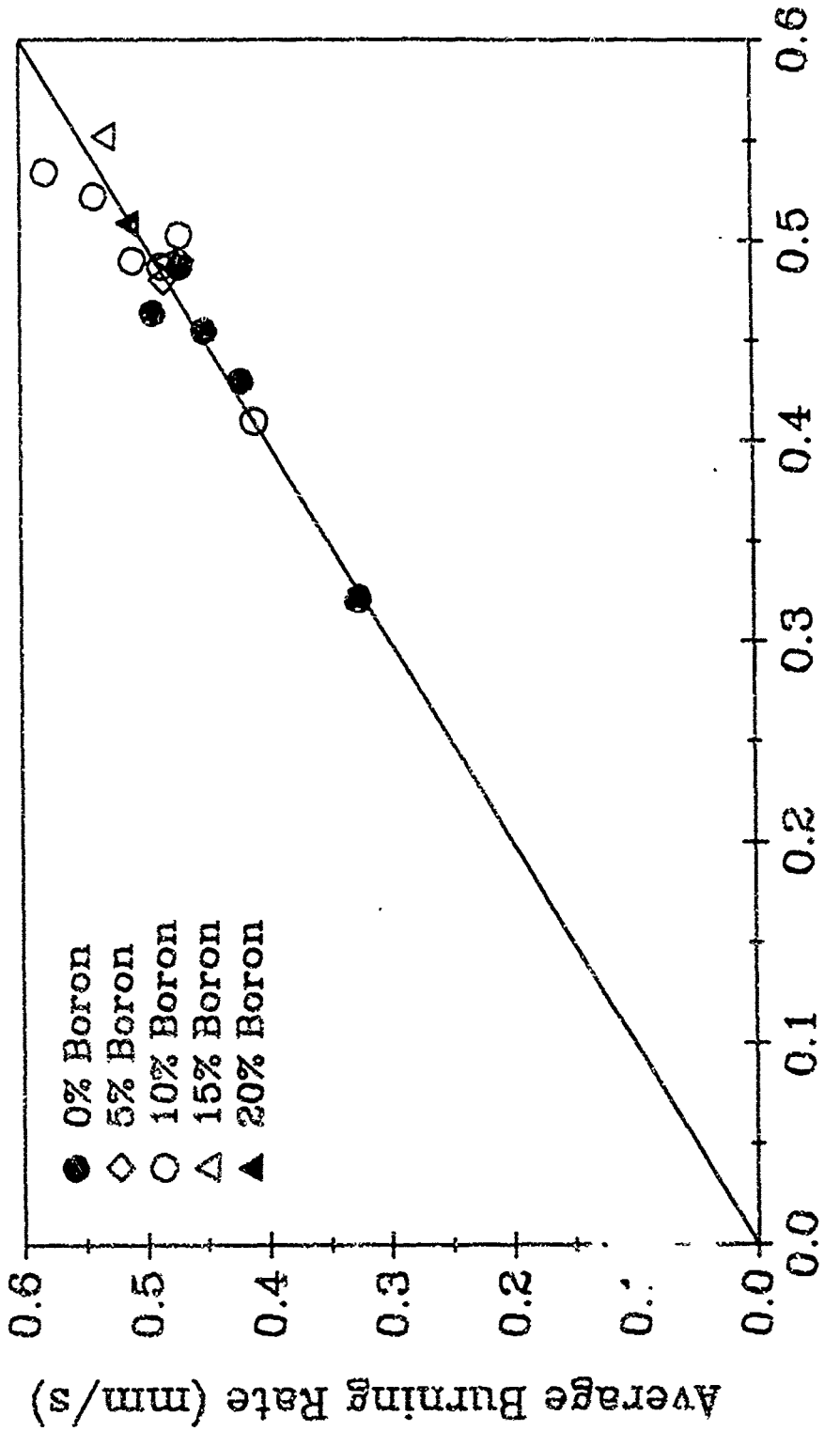


Figure 13. Comparison of Observed and Predicted Burning Rates for B/HTPB Solid Fuels

static pressure of 0.30 MPa, the fuel sample did not ignite with TEB injection. To achieve ignition, the step height was increased to 1.9 cm by lowering the fuel. With a larger flame stabilization region, the fuel ignited with TEB injection. After ignition, the TEB injection was turned off and the sample burned for approximately seven seconds. No further attempts to ignite the fuel sample were made because the fuel sample had pyrolyzed significantly.

In order to promote ignition of the B/HTPB (10/90) fuel sample, the initial height of the rearward-facing step was increased to 1.91 cm prior to the succeeding test. In this arrangement, the top surface of the fuel was directly in line with the exit channel of the combustion chamber. TEB was injected onto the surface of the fuel sample in order to achieve ignition. As the sample regressed, a forward-facing step was formed at the rear of the sample with the exit channel. A set of instantaneous surface profiles from a supersonic crossflow test is presented in Fig. 14. The dashed line corresponds to the surface profile taken before the test, while the solid lines are contours taken during combustion of the fuel. The first profile is taken immediately after ignition of the entire fuel sample at t=85 seconds. This profile indicates a significant amount of pyrolysis in the downstream region before ignition, with most of the pyrolysis occurring 10.5 to 12.0 cm from the rearward-facing step. After ignition, the average burning rate of the sample is approximately 0.49 mm/s. Visual observation of the exit plume confirms that reactions also occur downstream of the sample in the supersonic flow.

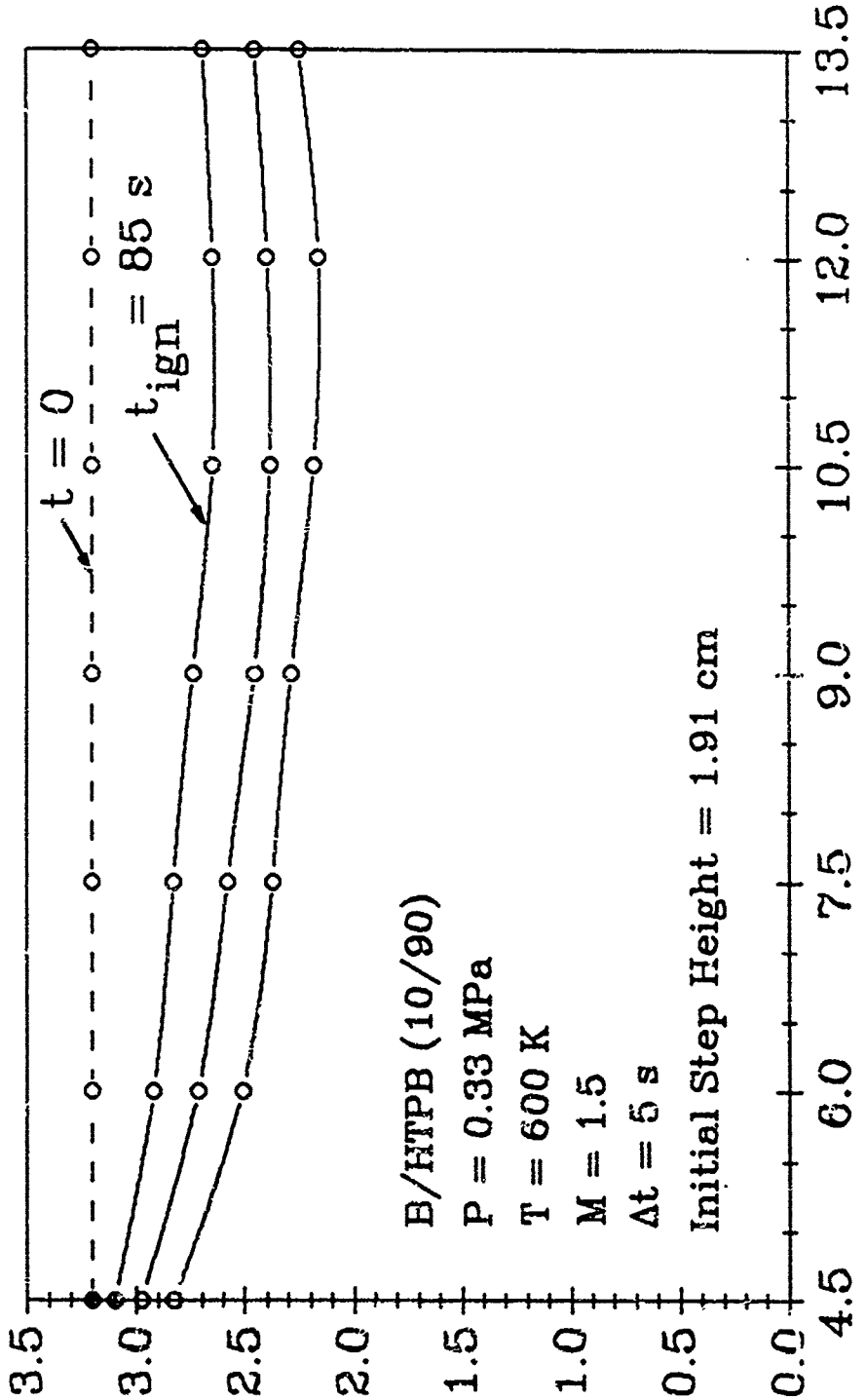


Figure 14. Instantaneous Surface Profiles of B/HTPB (10/90) Solid Fuel under Supersonic Crossflow

Chapter 4

THEORETICAL FORMULATION

The physical geometry considered in the analysis is shown in Fig. 15. A uniform supersonic air flow enters a two-dimensional chamber in which a solid fuel sample pyrolyzes and reacts with the ram air in the gas phase. To facilitate formulation, the gas phase, solid fuel, and boron particles are treated separately. The gas and solid phases are linked together through the balance of mass and energy fluxes at their interface. In order to achieve steady-state conditions in the gas phase and at the fuel boundary, the fuel is fed at a rate of r_b equal to the local burning rate, which keeps the surface of the burning sample stationary. A single boron particle is then ejected from the fuel surface into the surrounding gas, and tracked through the turbulent flowfield to the exit of the chamber. The instantaneous gas properties surrounding the particle are incorporated into the boron particle ignition model, but mass and energy fluxes from the particle are not included in the gas-phase solution since the effect of an individual particle on the flowfield is minimal. The gaseous flowfield is therefore decoupled from the influence of the particle. This assumption is justified for two-phase flowfields with high void fractions.

The single-particle model presented here is a first-step approach to solving flowfields above solid fuels with high boron loadings. For high boron mass fractions, particle-particle interactions as well as gas-particle coupling must be considered. These phenomena would be added to the current model, should treatment of high loadings be necessary. This type of single-particle trajectory analysis has been performed by Natan and Gany[27] in a low-speed environment with Mach numbers

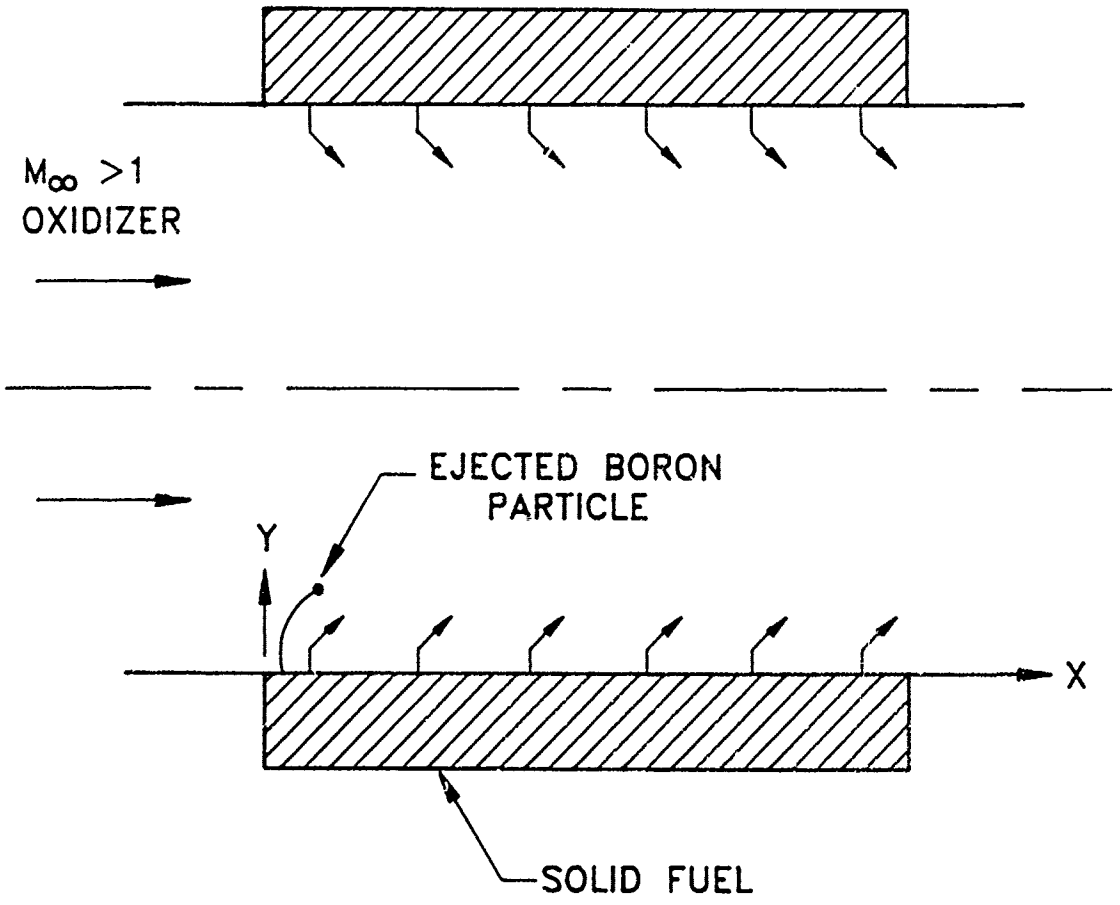


Figure 15. Physical Geometry of Two-Dimensional Combustion Chamber

less than 0.1 and particle sizes greater than 25 microns in diameter. The work presented here considers much smaller particle sizes on the order of 5 microns in a high-velocity environment (M > 0.8). The smaller sizes are treated since these particles have a higher probability of being consumed efficiently within the allowed residence time of a supersonic or highly subsonic combustor. Because of the small particle size, the turbulence effect on dispersion of the particle trajectories is also included.

In the following formulation, equations governing the gas phase and solid fuel are given first. Afterwards, the boron particle ignition model is summarized along with the particle-tracking equations.

4.1. Gas – Phase Analysis

The gas-phase analysis is based on the Favre-averaged conservation equations of mass, momentum, energy, and species transport for a multicomponent system in Cartesian coordinates. They can be written conveniently in the vector form

$$\frac{\partial Q}{\partial t} + \frac{\partial E}{\partial x} + \frac{\partial F}{\partial y} = \frac{\partial E_v}{\partial x} + \frac{\partial F_v}{\partial y} + H \tag{3}$$

where

$$Q \equiv \left[\bar{\rho}_g,\ \bar{\rho}_g\tilde{u},\ \bar{\rho}_g\tilde{v},\ \bar{\rho}_g\tilde{e},\ \bar{\rho}_g\tilde{Y}_i\right]^T$$

$$E \equiv \left[\bar{\rho}_g\tilde{u},\ \bar{\rho}_g\tilde{u}^2+\bar{p},\ \bar{\rho}_g\tilde{u}\tilde{v},\ \tilde{u}\left(\bar{\rho}_g\tilde{e}+\bar{p}\right),\ \bar{\rho}_g\tilde{u}\tilde{Y}_i\right]^T$$

$$F \equiv \left[\bar{\rho}_g\tilde{v},\ \bar{\rho}_g\tilde{u}\tilde{v},\ \bar{\rho}_g\tilde{v}^2+\bar{p},\ \tilde{v}\left(\bar{\rho}_g\tilde{e}+\bar{p}\right),\ \bar{\rho}_g\tilde{v}\tilde{Y}_i\right]^T$$

$$E_v \equiv \left[0,\ \bar{\tau}_{xx},\ \bar{\tau}_{xy},\ \tilde{u}\bar{\tau}_{xx}+\tilde{v}\bar{\tau}_{xy}-\bar{q}_x,\ -\bar{\rho}_g\tilde{U}_i\tilde{Y}_i\right]^T$$

$$F_v \equiv \left[0,\ \bar{\tau}_{xy},\ \bar{\tau}_{yy},\ \tilde{u}\bar{\tau}_{xy}+\tilde{v}\bar{\tau}_{yy}-\bar{q}_y,\ -\bar{\rho}_g\tilde{V}_i\tilde{Y}_i\right]^T$$

$$H \equiv \left[0,\ 0,\ 0,\ 0,\ \bar{\omega}_i\right]^T$$

for $i = 1, 2, \ldots$ N-1, with N being the total number of species considered. The diffusion terms in E_v and F_v are defined as

$$\bar{\tau}_{xx} = 2\mu_{eff}\frac{\partial \tilde{u}}{\partial x} - \frac{2}{3}\mu_{eff}\left(\frac{\partial \tilde{u}}{\partial x} + \frac{\partial \tilde{v}}{\partial y}\right) \tag{4}$$

$$\bar{\tau}_{xy} = \mu_{eff}\left(\frac{\partial \tilde{u}}{\partial y} + \frac{\partial \tilde{v}}{\partial x}\right) \tag{5}$$

$$\bar{\tau}_{yy} = 2\mu_{eff}\frac{\partial \tilde{v}}{\partial y} - \frac{2}{3}\mu_{eff}\left(\frac{\partial \tilde{u}}{\partial x} + \frac{\partial \tilde{v}}{\partial y}\right) \tag{6}$$

$$\bar{q}_x = -\lambda_{eff}\frac{\partial \tilde{T}}{\partial x} + \bar{\rho}_g \sum_{i=1}^{N} \tilde{h}_i \tilde{Y}_i \tilde{U}_i \tag{7}$$

$$\bar{q}_y = -\lambda_{eff}\frac{\partial \tilde{T}}{\partial y} + \bar{\rho}_g \sum_{i=1}^{N} \tilde{h}_i \tilde{Y}_i \tilde{V}_i \tag{8}$$

where $\tilde{U}_i$ and $\tilde{V}_i$ stand for the diffusion velocities and are determined by Fick's law. The effective transport properties μ_{eff} and λ_{eff} contain contributions from both the laminar and turbulent diffusion processes. Full account is taken of the variation of specific heat with temperature, giving the static enthalpy of each species as

$$h_i = \int_{T_{ref}}^{T} c_{p,i}\, dT + h^o_{f,i} \tag{9}$$

where $h^o_{f,i}$ is the enthalpy of formation. Consequently, the specific total internal energy e of the mixture becomes

$$e = \sum_{i=1}^{N} Y_i h_i - \frac{p}{\rho_g} + \frac{1}{2}\left(u^2 + v^2\right) \tag{10}$$

Finally, the equation of state determines the pressure from the temperature, density, and species mass fractions.

$$p = \rho_g R_u T \sum_{i=1}^{N} \frac{Y_i}{M_i} \tag{11}$$

The binary mass diffusivity is determined using the Chapman-Enskog theory along with the Lennard-Jones intermolecular potential-energy functions.[28] The effective diffusivity is then calculated through the following formula.[29]

$$D_{im} = \frac{1 - X_i}{\sum_{j=1}^{N} X_j / D_{ij}} \quad for\ i \neq j, \tag{12}$$

where X_i is the molar fraction of species i.

Thermodynamic and other transport properties of each constituent species are evaluated using fourth-order polynomials of temperature[30] which are valid for the range from 300 to 5000 K. For a mixture, specific heat is determined by mass-concentration weighing of each species; viscosity and thermal conductivity are calculated using Wilke's mixing rule.[31]

4.2. Solid – Fuel Analysis

If we ignore the bulk motion, subsurface chemical reaction, and axial thermal diffusion, the equation governing the condensed-phase process reduces to a one-dimensional heat conduction equation for each axial station. Under steady-state conditions, this equation takes the form

$$\frac{d}{dy}\left(\lambda_s \frac{dT_s}{dy}\right) - \rho_s r_b \frac{d}{dy}\left[c_{p,s}\left(T_s - T_{s,ref}\right) + h^{\circ}_{f,s}\right] = 0 \tag{13}$$

subject to the boundary conditions

$$T_s = T_o \qquad \text{as} \qquad y \to -\infty$$

$$T_s = T_{su} \qquad \text{at} \qquad y = 0$$

where the subscript "s" denotes the properties of the solid phase. Since the thermophysical properties of most solid fuels are not well characterized with respect to temperature, these properties are treated as constants. For HTPB-based solid fuels, the condensed-phase reactions such as thermal decomposition usually occur in a very thin layer immediately beneath the surface (about several hundred microns). This effect can be incorporated in the gas-solid interface conditions to simplify the analysis. Integration of Eq. (13) yields the steady-state temperature distribution at a given axial location in the solid phase.

$$T_s = T_o + (T_{su} - T_o)\, exp\left(\frac{\rho_s r_b c_{p,s}}{\lambda_s} y\right) \tag{14}$$

Since the ejection of an individual boron particle is addressed in this work, the effect of a single particle on the global thermophysical properties of the solid fuel is negligible. In the event that a high loading of particles is treated, then fuel properties should be modified accordingly.

4.3. Boundary Conditions

The heat and mass transfer processes between the gas and condensed phases must be matched at the fuel surface to provide the necessary interface conditions for both phases. This procedure will eventually determine the temperature, regression rate, and species concentrations at the surface. The analysis is simplified by neglecting (a)

subsurface species diffusion; (b) kinetic energy of escaping gases; and (c) Dufour effect. With some straightforward manipulation, the matching conditions are as follows.

Mass

$$\rho_s r_b = \rho_g v_g|_+ \tag{15}$$

Species Mass Fraction

$$\rho_s r_b Y_i|_- = \rho_g v_g Y_i|_+ - \rho_g D_{im} \frac{\partial Y_i}{\partial y}\Big|_+ \tag{16}$$

Energy

$$-\lambda_s \frac{\partial T}{\partial y}\Big|_- + \rho_s r_b \left(\int_{T_{ref}}^{T_{su}} c_{p,s} dT + h^o_{f,s} \right) = -\lambda_g \frac{\partial T}{\partial y}\Big|_+ + \rho_g \sum_{i=1}^{N} Y_i h_i \left(v_g - \frac{D_{im}}{Y_i} \frac{\partial Y_i}{\partial y} \right)\Big|_+ - q_{rad} \tag{17}$$

where "+" and "–" represent, respectively, the conditions immediately above and below the surface. It is worth mentioning that h_i contains both the sensible and chemical enthalpies of the gaseous species. The difference in enthalpy across the interface accounts for the latent heat of gasification and chemical energy release associated with the thermal decomposition immediately beneath the solid-fuel surface. The pyrolysis rate of solid fuel is evaluated using a zeroth-order Arrhenius expression.

$$r_b = \frac{A_s}{\rho_s} exp\left(\frac{-E_a}{R_u T_{su}} \right) \tag{18}$$

where A_s is the pre-exponential factor, ρ_s the fuel density, E_a the activation energy, and T_{su} the surface temperature. Radiant heat transfer to the surface due to emission from the gas phase is calculated using a Stefan-Boltzmann relation in terms of the averaged gas-phase temperature. The total gas emissivity is estimated using a method developed by Hottel[32] and is a function of the species mole fractions, gas-phase temperature, pressure, and mean beam length. The incorporation of a boron particle into the gas/solid interface conditions is also neglected, since only an individual particle is addressed here.

The flow at the upstream boundary is supersonic, with pre-specified temperature, pressure, Mach number, and species mass fraction. The inlet velocity profile is assumed to be uniform in the y-direction, and has no vertical velocity component. Since the flow at the downstream boundary is also supersonic, except in the region immediately above the fuel surface, all of the exit conditions are extrapolated from their counterparts within the combustion chamber. However, in the event that the flow at the exit is subsonic (i.e. due to shock waves), the static pressure may be specified as an additional boundary condition. The upper boundary is taken to be a line of symmetry. Therefore, the vertical velocity component and the derivatives of all the other dependent variables across the boundary are set to zero. The no-slip condition is employed at the surface of the fuel sample.

4.4. Turbulence Model

The Baldwin-Lomax algebraic model[33] along with constant turbulent Prandtl and Schmidt numbers ($Pr_t = Sc_t = 0.9$) are chosen to achieve the turbulence closure because of their computational efficiency and simplicity. This algebraic model calculates the turbulent eddy viscosity, using the Prandtl-Van Driest formulation and the local vorticity distribution for the near-wall and outer regions, respectively.

Namely,

$$\mu_t = \begin{cases} (\mu_t)_{\text{inner}} & y \leq y_{\text{crossover}} \\ (\mu_t)_{\text{outer}} & y > y_{\text{crossover}} \end{cases}$$

where y is the normal distance from the fuel surface and $y_{\text{crossover}}$ is the minimum value of y at which the turbulent viscosity of the inner and outer regions are equal.

Within the inner region, the Prandtl-Van Driest formulation gives

$$(\mu_t)_{\text{inner}} = \rho_g l^2 |\omega| \tag{19}$$

where ρ_g is the gas density, $|\omega|$ is the magnitude of the vorticity, l is the turbulent length-scale given by

$$l = \kappa y \left[1 - exp\left(- \frac{y^+}{A^+} \right) \right]$$

and κ equals 0.4. The term y^+ is the non–dimensional height

$$y^+ = \frac{\rho_w u^*}{\mu_w} y$$

and A^+ is the damping factor corrected for blowing at the surface:[34]

$$A^+ = 26.0 \; exp\left(- 5.9 \frac{v_w}{u^*} \right)$$

The friction velocity u^* is calculated from the wall shear stress and gas density:

$$u^* = \sqrt{\frac{\tau_w}{\rho_w}}$$

For the outer layer

$$(\mu_t)_{\text{outer}} = \rho_g K C_{cp} F_{\text{wake}} F_{\text{KLEB}}(y) \tag{20}$$

where K=0.0168, $C_{cp} = 1.6$ and

$$F_{\text{wake}} = \text{Min}\left(y_{max} F_{max}, C_{wk}\, y_{max} \frac{u_{dif}^2}{F_{max}} \right)$$

in which $u_{dif} = \sqrt{u_g^2 + v_g^2}$ and $C_{wk} = 0.25$.

The quantities y_{max} and F_{max} are determined from

$$F(y) = y|\omega| \left[1 - exp\left(-\frac{y^+}{A^+} \right) \right]$$

where y_{max} is the value of y where F is a maximum in the profile. The Klebanoff intermittency factor in Eq. (20) is given by:

$$F_{\text{KLEB}}(y) = \left[1 + 5.5 \left(\frac{y C_{\text{KLEB}}}{y_{max}} \right)^6 \right]^{-1}$$

with $C_{\text{KLEB}} = 0.30$.

4.5. Gas – Phase Combustion Model

For combustion of gaseous hydrocarbon fuels with oxygen, Westbrook and Dryer[35] suggested a simplified two-step reaction mechanism that reasonably predicts reaction rates for a large number of hydrocarbons over a wide range of equivalence ratios and pressures.

$$C_nH_m + \left(\frac{n}{2} + \frac{m}{4}\right) O_2 \rightarrow nCO + \frac{m}{2} H_2O \tag{21}$$

$$CO + \frac{1}{2} O_2 \rightleftharpoons CO_2 \tag{22}$$

This two-step mechanism is adopted without the reverse reaction of Eq.(22) since its reaction rate is slower than the forward reaction by six orders of magnitude, and in light of the short residence time of the flowfield, it has little effect on the overall kinetics. Equations (21) and (22) are satisfactory expressions for the gas-phase reactions, provided the flame temperature is not high enough to promote dissociation to free radical species such as H, O, and OH. For flame temperatures above 3000 K, a multi-step mechanism will be recommended to account for dissociation.

Westbrook and Dryer[35] consider the reaction rate of a hydrocarbon to be of the form

$$k_{fu} = A_{fu}\, exp\left(\frac{-E_{fu}}{R_u T}\right) C_{fu}^{a} C_{O_2}^{b} \tag{23}$$

where C is the molar concentration and the subscript fu represents the fuel. The factors a and b are dependent on the type of fuel species considered. The CO reaction rate is similarly expressed:

$$k_{CO} = A_{CO}\, exp\left(\frac{-E_{CO}}{R_u T}\right) C_{CO}\, C_{H_2O}^{\frac{1}{2}}\, C_{CO_2}^{\frac{1}{4}} \tag{24}$$

The production rates of the species are

$$\dot{\omega}_{fu} = -M_{fu} A_{fu}\, exp\left(\frac{-E_{fu}}{R_u T}\right) C_{fu}^{a} C_{O_2}^{b} \tag{25}$$

and

$$\bar{\omega}_{CO} = nM_{CO}A_{fu}\,exp\left(\frac{-E_{fu}}{R_uT}\right)C_{fu}^{a}\,C_{O_2}^{b}$$
$$-M_{CO}A_{CO}\,exp\left(\frac{-E_{CO}}{R_uT}\right)C_{CO}\,C_{H_2O}^{\frac{1}{2}}\,C_{CO_2}^{\frac{1}{4}} \qquad (26)$$

Similarly the rate of production $\bar{\omega}_i$ for each of the remaining species is written:

$$\bar{\omega}_{O_2} = M_{O_2}\left[-\left(\frac{n}{2}+\frac{m}{4}\right)k_{fu} - \frac{1}{2}k_{CO}\right] \qquad (27)$$

$$\bar{\omega}_{H_2O} = M_{H_2O}\left(\frac{m}{2}k_{fu}\right) \qquad (28)$$

$$\bar{\omega}_{CO_2} = M_{CO_2}k_{CO} \qquad (29)$$

Nitrogen is also considered since air is the oxidizer; however, it is treated inert with its production rate being zero. In summary, N-1 species conservation equations and one algebraic expression relating these species to nitrogen are solved:

$$\tilde{Y}_{N_2} = 1 - \sum_{i=1}^{N-1}\tilde{Y}_i \qquad (30)$$

In this study, multiplicative effects between chemical kinetics and turbulence are not included. This is justified due to the lack of experimental or analytical information in the area of supersonic reacting flows. A much more comprehensive treatment is required to fully account for these interactions

4.6. Boron Particle Analysis

4.6.1. Particle Ignition Model

The ignition of the boron particle is treated according to the model of King[12] with the most recent modifications.[14,37] This model assumes a particle radius of

r_p with an initial boron oxide layer thickness X surrounding the particle (see Fig. 16). Convective and radiative heat transfer to the particle begin to liquify and evaporate the oxide layer, while oxygen and water vapor diffuse through the layer to react with boron and raise the temperature of the particle. These processes correspond to the first stage of particle ignition mentioned previously. Additional surface reactions of water vapor with the oxide layer further aid in the removal of the oxide. Provided that the heat transfer to the particle is high enough to promote the complete removal of oxide and the melting of the particle, thermal runaway should occur. If the surrounding temperature is too low, or if the oxygen concentration is not high enough to allow sufficient exothermic reactions with boron, the particle will not ignite. The equations for the rate of change of particle radius and oxide thickness based on the processes discussed above are as follows.

$$\frac{dr_p}{dt} = -\frac{R_B M_B}{\rho_B} \tag{31}$$

where R_B is the molar consumption rate of boron per unit area due to the reaction with O_2.

$$\frac{dX}{dt} = \frac{\left(\frac{R_B}{2} - R_H - R_E\right) M_{B_2O_3}}{\rho_{B_2O_3}} \tag{32}$$

R_H is the molar removal rate of B_2O_3 per unit area due to reaction with H_2O, and R_E is the molar evaporation rate of B_2O_3 per unit area. The energy equation for the particle at the bulk temperature of T_p is given as

$$\frac{dH}{dt} = 4\pi r_p^2 \left(R_B Q_1 - R_H Q_2 - R_E Q_3 + h(T_g - T_p) + \sigma \epsilon_B \left(T_{sur}^4 - T_p^4\right)\right) \tag{33}$$

Boron–Particle Ignition Model (M. King):

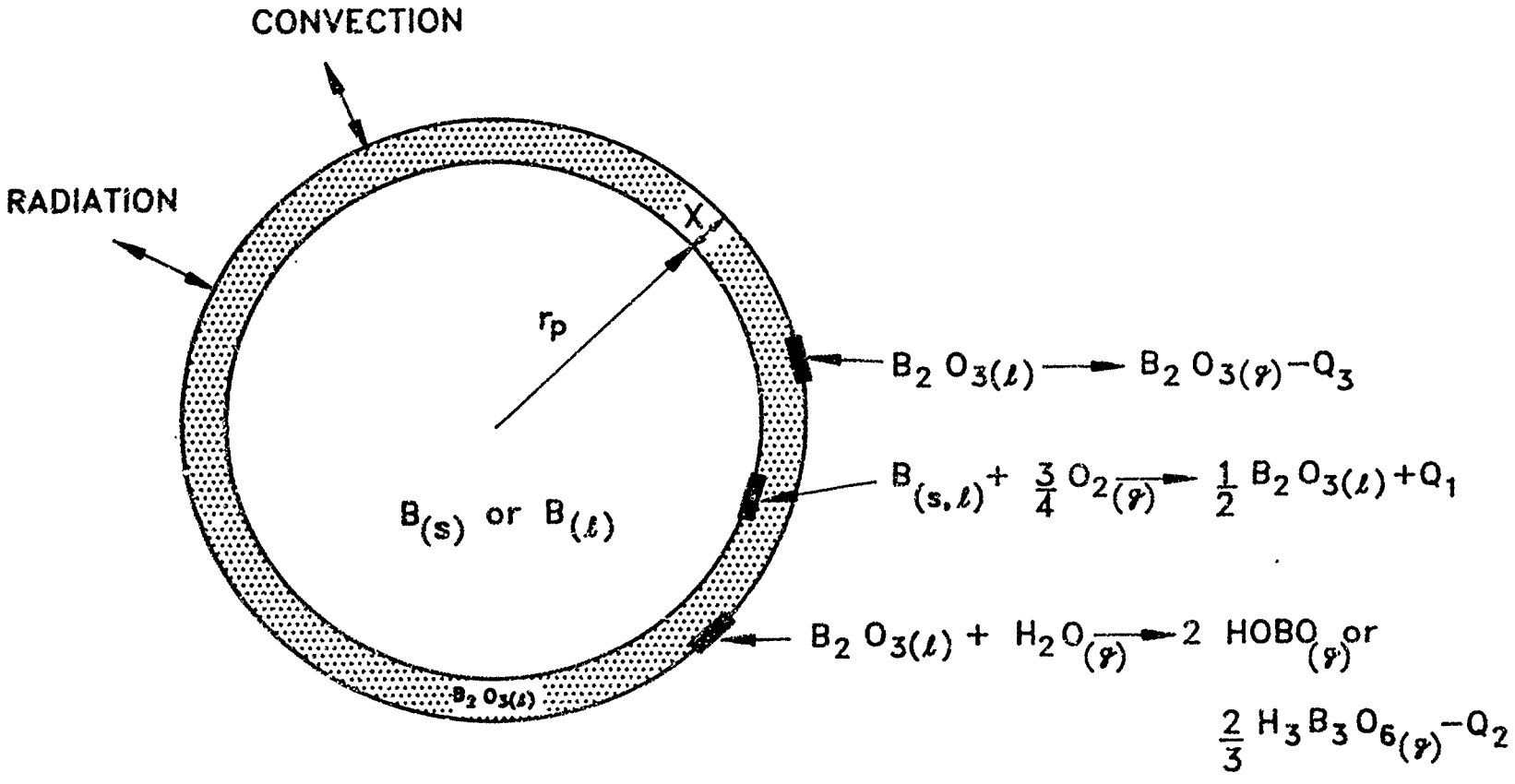


Figure 16. Boron Particle Ignition Model Processes (after King[12])

where Q_1 is the heat of reaction of the solid or liquid boron with oxygen, and Q_2 is the endothermic heat of reaction of water vapor with boron oxide which depends on the resulting product (either HOBO or $H_3B_3O_6$). For gas temperatures below 1400 K, the product is solely $H_3B_3O_6$, whereas above 2000 K the result is HOBO; at intermediate temperatures there is a product mix. In this study, HOBO was used as the reaction product, since the surrounding temperatures were greater than 2000 K. The term Q_3 in Eq. (33) represents the heat of vaporization of $B_2O_{3(l)}$. An additional water vapor reaction with $B_{(s)}$ and $B_2O_{3(l)}$

$$H_2O_{(g)} + \frac{4}{3}B_{(s,l)} + \frac{1}{2}B_2O_{3(l)} \rightarrow \frac{2}{3}H_3B_3O_{3(l)} \tag{34}$$

may be included in the ignition model; however, this reaction does not affect the ignition times in mixed O_2/H_2O atmospheres[14] and is therefore neglected here.

The convective heat transfer coefficient is calculated by the product of the Nusselt number[38] and thermal conductivity of the gas phase divided by the particle diameter, where

$$Nu = 2.0 + 0.60 Re_d^{\frac{1}{2}} \tag{35}$$

$$\text{and} \qquad Re_d = \frac{2r_p |u_g - u_p| \rho_g}{\mu} \tag{36}$$

Equations describing the rate of change of the particle bulk temperature and the fraction of boron melted are given below.

$$\frac{dT_p}{dt} = \frac{\frac{dH}{dt}}{\frac{4}{3}\pi r_p^3 \rho_B c_{pB(s)} + 4\pi r_p^2 X \rho_{B_2O_3} c_{pB_2O_3}} \qquad \text{for} \quad T_p < T_{melt} \tag{37}$$

$$\frac{dT_p}{dt} = \frac{\frac{dH}{dt}}{\frac{4}{3}\pi r_p^3 \rho_B c_{pB(l)} + 4\pi r_p^2 X \rho_{B_2O_3} c_{pB_2O_3}} \qquad \text{for} \quad T_p > T_{melt} \qquad (38)$$

$$\frac{df}{dt} = \frac{\frac{dH}{dt}}{\frac{4}{3}\pi r_p^3 \rho_B Q_{melt}} \qquad \text{for} \quad T_p = T_{melt} \qquad (39)$$

where T_{melt} is the boron melting temperature of 2450 K and Q_{melt} is the heat of fusion of boron.

The molar rate of conversion of boron to boron oxide incorporates several series resistances: the diffusion of oxygen through the surrounding gas to the outer surface of the oxide layer, the dissolving of oxygen within boron oxide, the diffusion of oxygen across the molten oxide layer to the B/B_2O_3 interface, and the resulting kinetics of the reaction at that interface. Details of the origin of the expression for R_B are given by King[14] and the resulting equation is given below.

$$R_B = \frac{p_{O_2}}{\frac{1}{f_1} + \frac{X}{f_2} + \frac{1}{f_3}} \qquad (40)$$

where

$$f_1 = 3.89\, exp\left(-\frac{1700}{T_p}\right) \qquad (41)$$

$$f_2 = 7.0 \times 10^{-8} exp\left(-\frac{9800}{T_p}\right) \qquad (42)$$

$$f_3 = \frac{4.68 \times 10^{-4} T_g^{\frac{1}{2}} Nu}{r_p p} \qquad (43)$$

The following units are used in Eqns. (40-45): R_B (kg-mole/m^2/sec), p (atm), r_p (m), X (m), T (K), f_1 and f_3 (kg-mole/m^2/atm/sec), and f_2 (kg-mole/m/atm/sec). The evaporation rate of B_2O_3 liquid contains two series resistances: evaporation kinetics and the diffusion of B_2O_3 gas away from the particle. Derivation of the expression for R_E can be found in King.[12]

$$R_E = \frac{8 \times 10^9\, \alpha\, exp\left(-\frac{44000}{T_p}\right)}{T_p^{0.5}\left(1 + \frac{4.5 \times 10^9 \alpha r_p p}{T_g Nu}\right)} \qquad (44)$$

The rate of reaction of water vapor with boron oxide to produce HOBO was given by King[37]

$$R_H = \frac{1.816 \times 10^5}{T_p} exp\left(-\frac{16900}{T_p}\right) p_{H_2O} \tag{45}$$

where p_{H_2O} is the partial pressure of water vapor.

4.6.2. Particle Tracking

To track the particles through the flowfield, Lagrangian equations of motion are solved. The calculations assume that the particle is spherical, and the effects of static pressure gradients, virtual mass, and Basset forces (deviation from steady flow pattern around the sphere) are negligible. The resulting momentum equations consider the drag force on the sphere, which contains both the skin friction and form drag, and the body force in the vertical direction.

$$\frac{du_p}{dt} = \frac{3C_D\rho_g}{8r_p\rho_p}(u_g - u_p)\,|u_g - u_p| \tag{46}$$

$$\frac{dv_p}{dt} = \frac{3C_D\rho_g}{8r_p\rho_p}(v_g - v_p)\,|v_g - v_p| + g \tag{47}$$

The drag coefficients are approximated as follows.[39]

$$C_D = \frac{24}{Re_d}\left(1 + \frac{Re_d^{\frac{2}{3}}}{6}\right) \qquad \text{for} \quad Re_d \leq 1000 \tag{48}$$

$$C_D = 0.44 \qquad \text{for} \quad Re_d > 1000 \tag{49}$$

The position of the particle is determined by integrating the equations below.

$$\frac{dx}{dt} = u_p \tag{50}$$

$$\frac{dy}{dt} = v_p \tag{51}$$

The effects of dispersion on the particle trajectories should also be considered, since the particles are small and their paths are influenced by turbulent fluctuations in the flowfield. To incorporate these effects, the Stochastic Separated Flow (SSF) model for spray combustion is utilized.[40] The SSF model involves finding the trajectories of a statistically significant number of individual particles ejected from the fuel sample into a flowfield containing a random distribution of turbulent eddies. For each eddy, the translational velocity of the bulk motion of the gas phase is considered uniform, but this property changes randomly from one eddy to the next. Changes in particle trajectories are observed by substituting the instantaneous velocities of the eddies into Eqs. (46) and (47). Specification of eddy properties and the interaction time between a particle and eddy are therefore crucial elements in this model, and they are summarized below.

The velocities of each eddy are determined at the start of the particle-eddy interaction by random sampling from the probability density function (PDF) of velocity. The velocities in the axial, vertical, and transverse directions are assumed to have normal distributions, with mean values of $\bar{u}$, $\bar{v}$, and 0, respectively. Velocity fluctuations in the axial direction have a magnitude of u', but because of anisotropic behavior near the wall, the magnitudes of fluctuations in the vertical and transverse directions are only fractions of u'.[41] For simplicity, they are approximated throughout the boundary layer region as

$$v' = \frac{1}{2}u' \tag{52}$$

$$w' = \frac{3}{4}u' \tag{53}$$

The instantaneous velocities of the eddies in the x and y directions are $\bar{u} + \sigma u'$ and $\bar{v} + \sigma v'$, respectively, where σ, the standard deviation, is randomly sampled from a standard normal distribution.

The values for u' and v' cannot be obtained from the algebraic turbulence model. To solve for these turbulent fluctuations, the turbulent kinetic energy and eddy dissipation rate must first be found using the following equations.

$$U\frac{\partial k}{\partial x} + V\frac{\partial k}{\partial y} = \frac{\partial}{\partial y}\left[\frac{1}{\rho}\left(\mu + \frac{\mu_t}{\sigma_k}\right)\frac{\partial k}{\partial y}\right] + \frac{\mu_t}{\rho}\left(\frac{\partial U}{\partial y}\right)^2 - \epsilon \tag{54}$$

$$U\frac{\partial \epsilon}{\partial x} + V\frac{\partial \epsilon}{\partial y} = \frac{\partial}{\partial y}\left[\frac{1}{\rho}\left(\mu + \frac{\mu_t}{\sigma_\epsilon}\right)\frac{\partial \epsilon}{\partial y}\right] + c_1\frac{\epsilon}{k}\frac{\mu_t}{\rho}\left(\frac{\partial U}{\partial y}\right)^2 - c_2 f_2\frac{\epsilon^2}{k} + \frac{2\mu\mu_t}{\rho^2}\left(\frac{\partial^2 U}{\partial y^2}\right)^2 \tag{55}$$

where c_1 and c_2 are constants and f_2 is a function to modify c_2. The details of the formulation and solution to these equations are given in the thesis by Tseng.[42] Under isotropic conditions, turbulent fluctuations are equal in magnitude in all three dimensions. However, the conditions imposed here by Eqs. (52-53) result in $u' = (1.10\,k)^{\frac{1}{2}}$. Equation (52) is then employed to obtain v'.

The k-ϵ equations described above are utilized expressly for determining k, which then yields u' and v'. The values of μ_t obtained from Eqs. (54) and (55) are checked with the algebraic solution, but are not substituted back into the gas-phase analysis since the algebraic approach is acceptable for these purposes.

A particle interacts with an eddy for a duration which is either the time required for the particle to traverse the eddy or the eddy lifetime. The eddy lifetime can be estimated from Shuen[40] using

$$t_e = \frac{L_e}{\left(\frac{2}{3}k\right)^{\frac{1}{2}}} \tag{56}$$

in which L_e, the characteristic size of an eddy, is assumed to be the dissipation length scale.

$$L_e = \frac{C_\mu^{\frac{3}{4}} k^{\frac{3}{2}}}{\epsilon} \tag{57}$$

where $C_\mu = 0.09$. The time required for the particle to traverse the eddy is not directly calculated; however, the distance the particle travels within the eddy is continuously monitored such that it remains less than the eddy size. The particle/eddy interaction is terminated if (1) the distance the particle travels within the eddy $|\Delta x|$ is greater than the length scale of the eddy, or (2) the time of interaction (Δt) is greater than the eddy lifetime. These criteria are represented as follows.

$$|\Delta x| > L_e \quad , \quad \Delta t > t_e \tag{58}$$

Upon completion of the interaction, the particle then enters a new eddy with properties determined from another random sampling of the PDF. Mean dispersion rates of the particles are obtained by averaging over a statistically significant number of particle trajectories.

Chapter 5

NUMERICAL METHOD

The theoretical formulation is solved using a numerical scheme based on the lower-upper symmetric successive overrelaxation (LU-SSOR) technique.[43,44] This scheme solves the two- or three-dimensional Navier-Stokes equations and species transport equations by means of the finite volume approach. It has proven to be very robust and efficient for highly reactive systems such as the combustion of hydrogen and oxygen.[45] The algorithm was validated previously for mixing and reacting supersonic flows by comparing predicted results with both experimental results and other numerical calculations.

The advantage of the LU-SSOR technique lies in the manner of solving the chemical source terms implicitly with the inviscid fluxes. Most other implicit schemes require the inversion of block banded matrices for the entire set of equations, but the LU-SSOR method requires only a scalar diagonal inversion of the flow equations and a diagonal block inversion for the species equations. Consequently, it has an operational count comparable to explicit schemes in addition to a fast convergence rate, thereby saving a considerable amount of CPU time. Furthermore, the scheme can also be fully vectorized.

To improve numerical efficiency and accuracy, the governing equations in Cartesian coordinates are transformed to the generalized coordinates

$$\xi = \xi(x, y) \qquad \text{and} \qquad \eta = \eta(x, y). \tag{59}$$

The transformation is chosen so that the grid spacing in the computational domain

is uniform and of unit length, i.e., $\Delta\xi$ and $\Delta\eta$=1. The governing equation then takes the following form,

$$\frac{\partial \hat{Q}}{\partial t} + \frac{\partial \hat{E}}{\partial \xi} + \frac{\partial \hat{F}}{\partial \eta} = \hat{H} + \frac{\partial \hat{E}_v}{\partial \xi} + \frac{\partial \hat{F}_v}{\partial \eta} \tag{60}$$

where the new dependent variables $\hat{Q}$, $\hat{E}$, $\hat{F}$, etc. are the transformed vectors in general coordinates, defined as

$$\hat{Q} = \frac{Q}{J}$$

$$\hat{E} = \frac{\xi_x E + \xi_y F}{J}$$

$$\hat{F} = \frac{\eta_x E + \eta_y F}{J}$$

$$\hat{H} = \frac{H}{J}$$

$$\hat{E}_v = \frac{\xi_x E_v + \xi_y F_v}{J}$$

$$\hat{F}_v = \frac{\eta_x E_v + \eta_y F_v}{J}$$

and J is the Jacobian of the coordinate transformation

$$J = \xi_x \eta_y - \xi_y \eta_x$$

The inviscid flux and source vectors are treated implicitly, giving

$$\frac{\partial \hat{Q}}{\partial t} + \frac{\partial \hat{E}^{n+1}}{\partial \xi} + \frac{\partial \hat{F}^{n+1}}{\partial \eta} - \hat{H}^{n+1} = \frac{\partial \hat{E}_v^n}{\partial \xi} + \frac{\partial \hat{F}_v^n}{\partial \eta} \tag{61}$$

where n+1 is the new time level, and n is the present time level. The diffusion vectors $\hat{E}_v$ and $\hat{F}_v$ are not solved implicitly because their effect on the convergence

rate would be much smaller than that of the source and convective terms, and solving them implicitly is considerably more difficult and cumbersome.

The governing equation is expressed in strongly conservative form with the primary dependent variable $\hat{Q}$. Vectors $\hat{E}$, $\hat{F}$, and $\hat{H}$ can be expressed as functions of $\hat{Q}$ using a truncated Taylor Series expansion:

$$\hat{E}^{n+1} = \hat{E}^n + \frac{\partial \hat{E}}{\partial \hat{Q}} \frac{\partial \hat{Q}}{\partial \hat{t}} \Delta t + \ldots$$

$$\hat{F}^{n+1} = \hat{F}^n + \frac{\partial \hat{F}}{\partial \hat{Q}} \frac{\partial \hat{Q}}{\partial \hat{t}} \Delta t + \ldots$$

$$\hat{H}^{n+1} = \hat{H}^n + \frac{\partial \hat{H}}{\partial \hat{Q}} \frac{\partial \hat{Q}}{\partial \hat{t}} \Delta t + \ldots$$

where Δt is the time increment. The terms $\frac{\partial \hat{E}}{\partial \hat{Q}}$, $\frac{\partial \hat{F}}{\partial \hat{Q}}$, $\frac{\partial \hat{H}}{\partial \hat{Q}}$ are known as the Jacobian matrices and are represented by A, B, and D, respectively. Eliminating terms of the second and higher orders gives:

$$\hat{E}^{n+1} = \hat{E}^n + A\,\delta\hat{Q} \tag{62}$$

$$\hat{F}^{n+1} = \hat{F}^n + B\,\delta\hat{Q} \tag{63}$$

$$\hat{H}^{n+1} = \hat{H}^n + D\,\delta\hat{Q} \tag{64}$$

Substituting the Eqs. (62) – (64) into Eq. (61) yields

$$\left[I - D\Delta t + \Delta t\left(\frac{\partial}{\partial \hat{\xi}} A \cdot + \frac{\partial}{\partial \eta} B \cdot\right)\right]^{n+1} \delta\hat{Q} = -\Delta t \left(\frac{\partial \hat{E}}{\partial \xi} + \frac{\partial \hat{F}}{\partial \eta} - \hat{H} - \frac{\partial \hat{E}_v}{\partial \xi} - \frac{\partial \hat{F}_v}{\partial \eta}\right)^n$$

$$= -\Delta t\, R \tag{65}$$

where R is the residual and I is the identity matrix. The Jacobians A, B, and D are given on the following pages with the term $\bar{\gamma}$ being the ratio of specific heats given by

$$
A = \begin{pmatrix}
0 & \xi_x & \xi_y & 0 & 0 & 0 & \cdots & 0 \\
\xi_x\Phi \\ -\tilde{u}_g\tilde{U} & \tilde{U}- \\ (\tilde{\gamma}-2)\,\tilde{u}_g\xi_x & \tilde{u}_g\xi_y- \\ (\tilde{\gamma}-1)\,\xi_x\tilde{v}_g & \xi_x(\tilde{\gamma}-1) & -\xi_x(\tilde{\gamma}-1) \\ \cdot\Delta h^{\circ}_{f,1} & -\xi_x(\tilde{\gamma}-1) \\ \cdot\Delta h^{\circ}_{f,2} & \cdots & -\xi_x(\tilde{\gamma}-1) \\ \cdot\Delta h^{\circ}_{f,N-1} \\
\xi_y\Phi \\ -\tilde{v}_g\tilde{U} & \tilde{v}_g\xi_x- \\ (\tilde{\gamma}-1)\,\tilde{u}_g\xi_y & \tilde{U}- \\ (\tilde{\gamma}-2)\,\xi_y\tilde{v}_g & \xi_y(\tilde{\gamma}-1) & -\xi_y(\tilde{\gamma}-1) \\ \cdot\Delta h^{\circ}_{f,1} & -\xi_y(\tilde{\gamma}-1) \\ \cdot\Delta h^{\circ}_{f,2} & \cdots & -\xi_y(\tilde{\gamma}-1) \\ \cdot\Delta h^{\circ}_{f,N-1} \\
\tilde{U}\cdot & -\tilde{U}\tilde{u}_g(\tilde{\gamma}-1) & -\tilde{U}\tilde{v}_g(\tilde{\gamma}-1) & \tilde{U}\tilde{\gamma} & -\tilde{U}(\tilde{\gamma}-1) & -\tilde{U}(\tilde{\gamma}-1) & \cdots & -\tilde{U}(\tilde{\gamma}-1) \\
\left(\Phi-\tilde{e}-\frac{p}{\rho_g}\right) & +\xi_x\left(\tilde{e}+\frac{p}{\rho_g}\right) & +\xi_y\left(\tilde{e}+\frac{p}{\rho_g}\right) & & \cdot\Delta h^{\circ}_{f,1} & \cdot\Delta h^{\circ}_{f,2} & & \cdot\Delta h^{\circ}_{f,N-1} \\
-\tilde{Y}_1\tilde{U} & \tilde{Y}_1\xi_x & \tilde{Y}_1\xi_y & 0 & \tilde{U} & 0 & \cdots & 0 \\
-\tilde{Y}_2\tilde{U} & \tilde{Y}_2\xi_x & \tilde{Y}_2\xi_y & 0 & 0 & \tilde{U} & 0\ \cdots & 0 \\
\cdot & \cdot & \cdot & \cdot & \cdot & 0 & & \cdot \\
\cdot & \cdot & \cdot & \cdot & \cdot & \cdot & & \cdot \\
\cdot & \cdot & \cdot & \cdot & \cdot & \cdot & & 0 \\
-\tilde{Y}_{N-1}\tilde{U} & \tilde{Y}_{N-1}\xi_x & \tilde{Y}_{N-1}\xi_y & 0 & 0 & 0 & 0\ \cdots & \tilde{U}
\end{pmatrix}
$$

Equation (66)

$$
B = \begin{pmatrix}
0 & \eta_x & \eta_y & 0 & 0 & 0 & \cdots & 0 \\
\eta_x \Phi \\ -\tilde{u}_g \tilde{V} & \tilde{V} - (\bar{\gamma}-2)\,\tilde{u}_g \eta_x & \tilde{u}_g \eta_y - (\bar{\gamma}-1)\,\eta_x \tilde{v}_g & \eta_x (\bar{\gamma}-1) & -\eta_x (\bar{\gamma}-1) \cdot \Delta h^o_{f,1} & -\eta_x (\bar{\gamma}-1) \cdot \Delta h^o_{f,2} & \cdots & -\eta_x (\bar{\gamma}-1) \cdot \Delta h^o_{f,N-1} \\
\eta_y \Phi \\ -\tilde{v}_g \tilde{V} & \tilde{v}_g \eta_x - (\bar{\gamma}-1)\,\tilde{u}_g \eta_y & \tilde{V} - (\bar{\gamma}-2)\,\eta_y \tilde{v}_g & \eta_y (\bar{\gamma}-1) & -\eta_y (\bar{\gamma}-1) \cdot \Delta h^o_{f,1} & -\eta_y (\bar{\gamma}-1) \cdot \Delta h^o_{f,2} & \cdots & -\eta_y (\bar{\gamma}-1) \cdot \Delta h^o_{f,N-1} \\
\tilde{V} \cdot \left(\Phi - \tilde{e} - \frac{\phi}{\tilde{\rho}_g}\right) & -\tilde{V}\tilde{u}_g (\bar{\gamma}-1) + \eta_x \left(\tilde{e} + \frac{p}{\tilde{\rho}_g}\right) & -\tilde{V}\tilde{v}_g (\bar{\gamma}-1) + \eta_y \left(\tilde{e} + \frac{p}{\tilde{\rho}_g}\right) & \tilde{V}\bar{\gamma} & -\tilde{V}(\bar{\gamma}-1) \cdot \Delta h^o_{f,1} & -\tilde{V}(\bar{\gamma}-1) \cdot \Delta h^o_{f,2} & \cdots & -\tilde{V}(\bar{\gamma}-1) \cdot \Delta h^o_{f,N-1} \\
-\tilde{Y}_1 \tilde{V} & \tilde{Y}_1 \eta_x & \tilde{Y}_1 \eta_y & 0 & \tilde{V} & 0 & \cdots & 0 \\
-\tilde{Y}_2 \tilde{V} & \tilde{Y}_2 \eta_x & \tilde{Y}_2 \eta_y & 0 & 0 & \tilde{V} & 0 \cdots & 0 \\
\cdot & \cdot & \cdot & \cdot & \cdot & 0 & & \cdot \\
\cdot & \cdot & \cdot & \cdot & \cdot & \cdot & & \cdot \\
\cdot & \cdot & \cdot & \cdot & \cdot & \cdot & & 0 \\
-\tilde{Y}_{N-1} \tilde{V} & \tilde{Y}_{N-1} \eta_x & \tilde{Y}_{N-1} \eta_y & 0 & 0 & 0 & 0 \cdots & \tilde{V}
\end{pmatrix}
$$

Equation (67)

$$
D = \begin{pmatrix}
0 & 0 & 0 & 0 & 0 & \cdots & 0 \\
0 & 0 & 0 & 0 & 0 & \cdots & 0 \\
0 & 0 & 0 & 0 & 0 & \cdots & 0 \\
0 & 0 & 0 & 0 & 0 & \cdots & 0 \\
\frac{\partial \dot{\omega}_1}{\partial q_1} & \frac{\partial \dot{\omega}_1}{\partial q_2} & \frac{\partial \dot{\omega}_1}{\partial q_3} & \frac{\partial \dot{\omega}_1}{\partial q_4} & \frac{\partial \dot{\omega}_1}{\partial q_5} & \cdots & \frac{\partial \dot{\omega}_1}{\partial q_{N+3}} \\
\frac{\partial \dot{\omega}_2}{\partial q_1} & \frac{\partial \dot{\omega}_2}{\partial q_2} & \frac{\partial \dot{\omega}_2}{\partial q_3} & \frac{\partial \dot{\omega}_2}{\partial q_4} & \frac{\partial \dot{\omega}_2}{\partial q_5} & \cdots & \frac{\partial \dot{\omega}_2}{\partial q_{N+3}} \\
\cdot & \cdot & \cdot & \cdot & \cdot & & \cdot \\
\cdot & \cdot & \cdot & \cdot & \cdot & & \cdot \\
\cdot & \cdot & \cdot & \cdot & \cdot & & \cdot \\
\frac{\partial \dot{\omega}_{N-1}}{\partial q_1} & \frac{\partial \dot{\omega}_{N-1}}{\partial q_2} & \frac{\partial \dot{\omega}_{N-1}}{\partial q_3} & \frac{\partial \dot{\omega}_{N-1}}{\partial q_4} & \frac{\partial \dot{\omega}_{N-1}}{\partial q_5} & \cdots & \frac{\partial \dot{\omega}_{N-1}}{\partial q_{N+3}}
\end{pmatrix}
$$

Equation (68)

$$\bar{\gamma} = \frac{\sum_{i=1}^{N} Y_i \int_{T_{ref}}^{T} c_{p,i} dT}{\sum_{i=1}^{N} Y_i \int_{T_{ref}}^{T} c_{v,i} dT}$$

The parameter Φ in A and B is

$$\Phi = (\bar{\gamma} - 1) \left[\frac{1}{2} \left(\tilde{u}_g^2 + \tilde{v}_g^2 \right) - h_{f,N}^{o} \right]$$

and $\tilde{U}$ and $\tilde{V}$ are the contravariant velocities where

$$\tilde{U} = \xi_x \tilde{u}_g + \xi_y \tilde{v}_g$$

and

$$\tilde{V} = \eta_x \tilde{u}_g + \eta_y \tilde{v}_g$$

In Eq. (68), the derivatives of the source terms with respect to the independent variables are determined in the following manner:

$$\frac{\partial \bar{\omega}_1}{\partial q_1} = \frac{\partial \bar{\omega}_{fu}}{\partial \rho_g} = \frac{\partial}{\partial \rho_g} \left\{ - M_{fu} A_{fu} \, exp \left(\frac{-E_{fu}}{R_u T} \right) \left[\frac{\rho_g Y_{fu}}{M_{fu}} \right]^a \left[\frac{\rho_g Y_{O_2}}{M_{O_2}} \right]^b \right\}$$

which equals zero, since $\rho_g Y_{fu}$ and $\rho_g Y_{O_2}$ are treated as separate independent variables. Similarly, no other source terms contain ρ_g as an individual independent variable, and all other $\frac{\partial \bar{\omega}_i}{\partial q_1}$ are set to zero. Terms in the second and third columns ($\frac{\partial \bar{\omega}_i}{\partial q_2}$ and $\frac{\partial \bar{\omega}_i}{\partial q_3}$) are taken as zero because they are usually small, although they can be evaluated by the chain rule:

$$\frac{\partial \bar{\omega}_i}{\partial \rho_g u} = \left(\frac{\partial \bar{\omega}_i}{\partial T} \right)_{\rho_g Y_i} \left(\frac{\partial T}{\partial \hat{e}} \right)_{\rho_g, \rho_g Y_i} \left(\frac{\partial \hat{e}}{\partial \rho_g u} \right)_{\rho_g, \rho_g v, \rho_g c, \rho_g Y_i}$$

where $\hat{e}$ is the specific internal energy. The terms of $\frac{\partial \bar{\omega}_i}{\partial q_4}$ are also determined using a chain rule formula:

$$\frac{\partial \bar{\omega}_i}{\partial e} = \left(\frac{\partial \bar{\omega}_i}{\partial T}\right)_{\rho_g, \rho_g Y_i} \left(\frac{\partial T}{\partial \hat{e}}\right)_{\rho_g, \rho_g Y_i} \left(\frac{\partial \hat{e}}{\partial e}\right)_{\rho_g, \rho_g u, \rho_g Y_i}$$

Finally, the most dominant terms of D are calculated in the following manner:

$$\frac{\partial \bar{\omega}_1}{\partial q_5} = \frac{\partial \bar{\omega}_{fu}}{\partial (\rho_g Y_{fu})} = -M_{fu} A_{fu} \, exp\left(\frac{-E_{fu}}{R_u T}\right) \frac{a(\rho_g Y_{fu})^{a-1}}{{M_{fu}}^a} \left[\frac{\rho_g Y_{O_2}}{M_{O_2}}\right]^b$$

The source term Jacobians $\frac{\partial \bar{\omega}_1}{\partial q_5}$ to $\frac{\partial \bar{\omega}_{N-1}}{\partial q_{N+3}}$ are solved in a similar fashion using Eqs. (25) – (29).

At this point, Eq. (65) can be solved by directly inverting the large block-banded matrix on the left-hand side; however, this would be inefficient and require a great computational effort. Instead, many researchers have opted to solve this governing equation using the popular alternating-direction implicit (ADI) scheme, which is less costly but still requires block-tridiagonal or pentadiagonal matrix inversions. A third alternative is the lower-upper (LU) factored implicit scheme developed by Yoon and Jameson,[43] which is described here.

In this method, the Jacobian matrices A and B are split such that their eigenvalues are positive for the A^+ and B^+ matrices and negative for the A^- and B^- matrices. There are many ways in which this splitting can be accomplished. One possibility which increases the diagonal dominance of Eq. (65) is

$$\begin{aligned} A^+ &= \frac{1}{2}(A + \nu_A I) \quad , \; A^- = \frac{1}{2}(A - \nu_A I) \\ B^+ &= \frac{1}{2}(B + \nu_B I) \quad , \; B^- = \frac{1}{2}(B - \nu_B I) \end{aligned} \tag{69}$$

where ν_A is greater than or equal to the maximum eigenvalue of the A Jacobian matrix (λ_A), $\nu_A \geq max(|\lambda_A|)$. Similarly, ν_B is chosen such that $\nu_B \geq max(|\lambda_B|)$. Equation (70) is then obtained with D_ξ^- and D_η^- as backward difference operators for matrices with positive eigenvalues and D_ξ^+ and D_η^+ as forward difference operators for matrices with non-positive eigenvalues:

$$\left[I + \Delta t \left(D_\xi^- A^+ + D_\xi^+ A^- + D_\eta^- B^+ + D_\eta^+ B^- - D\right)\right] \delta\hat{Q} = -\Delta t\, R \qquad (70)$$

Adding and subtracting like terms to the diagonal on the LHS gives

$$\begin{aligned}
&\left[I + \Delta t \left[\left(\frac{A^+}{\Delta\xi} - \frac{A^-}{\Delta\xi}\right) + \left(\frac{B^+}{\Delta\eta} - \frac{B^-}{\Delta\eta}\right)\right]\right. \\
&+ \Delta t \left[D_\xi{}^- A^+ + D_\xi{}^+ A^- + D_\eta{}^- B^+ + D_\eta{}^+ B^-\right] \\
&\left. - \Delta t \left[\left(\frac{A^+}{\Delta\xi} - \frac{A^-}{\Delta\xi}\right) + \left(\frac{B^+}{\Delta\eta} - \frac{B^-}{\Delta\eta}\right) + D\right]\right] \delta\hat{Q} = -\Delta t\, R
\end{aligned} \qquad (71)$$

This equation may be factorized using the relations

$$A^+ - A^- = \nu_A I, \qquad B^+ - B^- = \nu_B I, \qquad C = \left[1 + \Delta t \left(\frac{\nu_A}{\Delta\xi} + \frac{\nu_B}{\Delta\eta}\right)\right] I$$

to give

$$\begin{aligned}
&\left[C + \Delta t \left(D_\xi{}^- A^+ + D_\eta{}^- B^+ - \frac{A^+}{\Delta\xi} - \frac{B^+}{\Delta\eta} - D\right)\right] \cdot C^{-1} \cdot \\
&\left[C + \Delta t \left(D_\xi{}^+ A^- + D_\eta{}^+ B^- + \frac{A^-}{\Delta\xi} + \frac{B^-}{\Delta\eta}\right)\right] \delta\hat{Q} = -\Delta t\, R
\end{aligned} \qquad (72)$$

Taking the limit in which $\Delta t \to \infty$, we obtain

$$\begin{aligned}
&\left(D_\xi{}^- A^+ + D_\eta{}^- B^+ - \frac{A^-}{\Delta\xi} - \frac{B^-}{\Delta\eta} - D\right) \cdot \left[\left(\frac{\nu_A}{\Delta\xi} + \frac{\nu_B}{\Delta\eta}\right) I\right]^{-1} \cdot \\
&\left(D_\xi{}^+ A^- + D_\eta{}^+ B^- + \frac{A^+}{\Delta\xi} + \frac{B^+}{\Delta\eta}\right) \delta\hat{Q} = -R
\end{aligned} \qquad (73)$$

which, with the use of Eq. (69), may be written in two steps as the final version of the governing equation:

$$\left[DIAG_{i,j} - \frac{A^{+}_{i-1,j}}{\Delta\xi} - \frac{B^{+}_{i,j-1}}{\Delta\eta}\right]\delta Q^{*} = -\left(\frac{\nu_A}{\Delta\xi} + \frac{\nu_B}{\Delta\eta}\right)R \qquad (74a)$$

$$\left[\left(\frac{\nu_A}{\Delta\xi} + \frac{\nu_B}{\Delta\eta}\right)I + \frac{A^{-}_{i+1,j}}{\Delta\xi} + \frac{B^{-}_{i,j+1}}{\Delta\eta}\right]\delta\hat{Q} = \delta Q^{*} \qquad (74b)$$

where

$$DIAG_{i,j} = \left[\left(\frac{\nu_A}{\Delta\xi} + \frac{\nu_B}{\Delta\eta}\right)I - D\right]_{i,j}$$

Equation (74a) is solved by forward marching since the left-hand side is lower bidiagonal, then Eq. (74b) is solved by backward marching to complete one iteration. It is interesting to note that for non-reacting systems the source Jacobian D is zero which reduces DIAG to a scalar, and the solution procedure for Eq. (74a) requires only a scalar diagonal inversion. For reacting cases such as this, however, DIAG is a non-zero matrix, and a block diagonal matrix inversion is necessary.

The inversion method for Eq. (74a) can be simplified to some extent for reacting cases, because only the lower right corner of D is non-zero. Equation (68) shows that the first four flow equations do not contain a source term Jacobian (i.e. D is zero for these cases), and a scalar diagonal inversion is applied. The remainder of the equations contain finite values in D, therefore no simplifications are made in their solution and a block diagonal matrix inversion is performed.

After the solution to the gas phase is attained, an individual boron particle is ejected from the solid fuel into the high temperature flowfield. Local values of pressure, temperature, and species mass fractions are used for the conditions surrounding the particle. The equations governing the boron particle history are solved

by a fourth-order Runge-Kutta scheme.[46] The time step for stable convergence of the continuity and energy equations for this application is found to be approximately 0.01 milliseconds: however, the time scales for the turbulent eddies are much smaller. For this reason, the eddy lifetimes are first determined, then one-fifth of t_e is utilized as the time step for the calculation. The particle trajectory is traced to the exit of the chamber, after which another particle is ejected from the same location as the first. The new particle is also traced to the exit of the combustion chamber, but due to the randomness of the turbulent fluctuations, the trajectory is different. The procedure is repeated 2000 times to achieve a statistically significant number of trajectories. The properties of the particles are recorded at three axial stations, at $x = \frac{1}{3}L_c$, $\frac{2}{3}L_c$, and L_c, where L_c is the length of the combustion chamber.

Chapter 6

DISCUSSION OF NUMERICAL RESULTS

Calculations were performed with HTPB-based solid fuel samples located along the bottom surface of a 2-D chamber with an inlet height of 3.175 cm and a length of 15.24 cm, as shown in Fig. 15. The sample spans 7.62 cm along the lower boundary of the chamber, thus allowing space for chemical reactions downstream of the fuel. HTPB was chosen for this study because it has been characterized for its wide use in composite propellants,[47] and it is an energetic binder commonly found in solid fuels.[4–7]

The inlet conditions to the combustion chamber were obtained from the high-speed end of the flight envelope for a solid-fueled scramjet, by assuming an adiabatic deceleration from the flight Mach number to the combustor Mach number. With real-gas effects taken into account, a flight Mach number of 7.3 in the tropopause (T=216.7 K) is required to attain a combustor inlet static temperature of 1400 K with a Mach number of 2. Since this inlet temperature is high enough to promote ignition and flame stability above the fuel sample, it was chosen as a baseline condition. A static pressure of 1 atmosphere was also utilized at the inlet since some experimental facilities operated at this condition;[7] however, the appropriate inlet pressure based on pressure recovery is much higher. For this reason, additional cases were calculated with higher pressures and compared with the baseline.

To facilitate the gas-phase analysis, it is assumed that butadiene (C_4H_6) is the only product released from the fuel surface. This simplification is justified for the following reasons. First, butadiene and vinylcyclohexene are respectively the first- and

second-most abundant pyrolysis products of HTPB.[48,49] Since the monomer and dimer have similar molecular structures and kinetic parameters, vinylcyclohexene can be adequately represented by butadiene. Second, the majority of hydrocarbons tabulated in Ref. 35 have equal activation energies and only a slight variation in preexponential factor. Thus the consideration of additional fuel species would not alter the kinetic behavior of the gas phase. Finally, in the limit of fast kinetics with respect to the diffusion process, one hydrocarbon may be sufficient to represent the fuel species, and additional hydrocarbons would not change the fundamental characteristics of the sample. With the two-step reaction mechanism of Eqs. (21) and (22), the gas phase contains six species: C_4H_6, O_2, CO, H_2O, CO_2, and N_2. The kinetic parameters for both the gas and solid phases are summarized in Table 2, where the values for ethylene are adopted for Eq. (23) since the parameters for butadiene were not available and ethylene and butadiene have similar molecular structures. The exponents for Eq. (23) are 0.1 and 1.65 for a and b, respectively.

Each calculation employed a 120×80 grid. The numerical grid was uniform in the horizontal direction, with a spacing of 0.129 cm. Since many important physical processes occur in the region immediately above the sample surface, the numerical grid was clustered vertically near the surface, with the smallest grid measuring 45 microns in height. For each computation, the total mass flowrate of the ram air and pyrolyzed fuel was conserved to within 0.1% at the exit. The scheme required approximately 40 μsec of CPU time per iteration per grid point on a Cray Y-MP machine.

To determine the influence of the inlet flow distributions on the burning characteristics of the solid fuel, calculations were performed with two different sets of inlet conditions. Flow properties were assumed to be uniformly distributed at the inlet for one case, and an inlet velocity profile based on the one-seventh law was assumed

Table 2. Kinetic Parameters for Gas-Phase Combustion Model

	Activation Energy, E	Pre-exponential Factor, A
Gas-phase Eq. (23)	30 $\frac{kcal}{mole}$	2.4×10^{12} $\frac{\left(\frac{cm^3}{mole}\right)^{.75}}{sec}$
Gas-phase Eq. (24)	40 $\frac{kcal}{mole}$	$1.0\times10^{14.6}$ $\frac{\left(\frac{cm^3}{mole}\right)^{.75}}{sec}$
Burning rate Eq. (28)	16.9 $\frac{kcal}{mole}$	2990. $\frac{kg}{m^3}$

for the other. Variation in the solutions were found to be minimal in the resulting flow structures and fuel regression rates. Thus, for convenience of discussion, only results with uniform conditions are presented herein.

6.1. Gas – Phase Solution

Figure 17 shows the contour plots for Mach number, stagnation temperature, and static pressure for the baseline case, with an inlet Mach number of 2, an inlet static temperature of 1400 K, and an inlet static pressure of 1 atmosphere. The stagnation temperature contours are plotted instead of the static temperatures so that heat release is distinguishable from temperature recovery near the surface. Mach-number contours are incremented by 0.1, temperature contours by 100 K, and pressure contours by 0.02 atm. These figures show only the bottom sixth of the

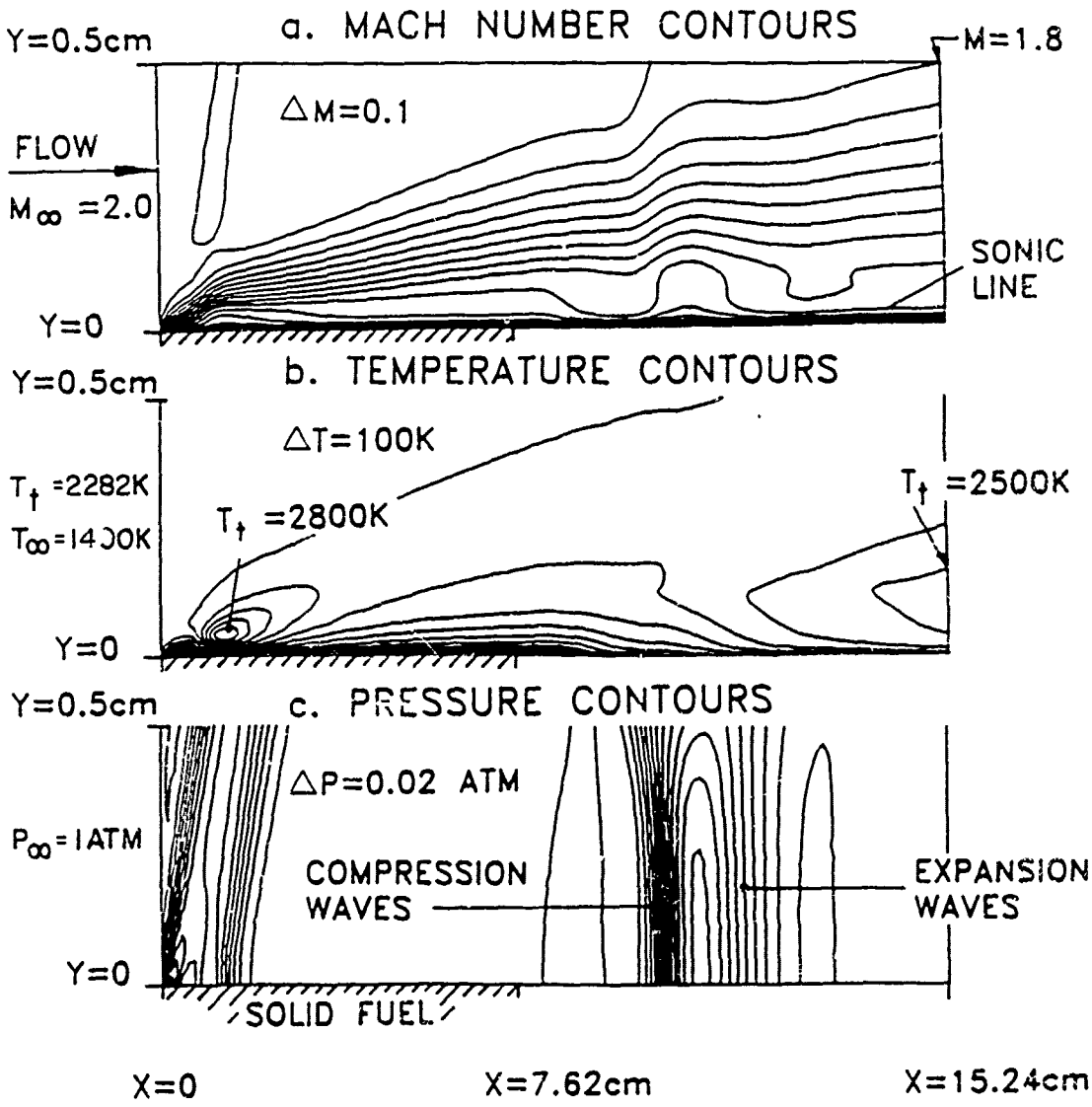


Figure 17. Mach Number, Stagnation Temperature, Static Pressure Contours for Baseline Case; M_∞=2.0, T_∞=1400 K, p_∞=1 atm

combustion chamber and have been magnified in the y-direction by a factor of ten to resolve the flow structures nearest the surface. In Fig. 17a, a weak inlet shock occurs at the entrance due to the abrupt deceleration of the flow at the surface to satisfy the no-slip condition. This deceleration enhances temperature recovery and heat transfer at the surface. Immediately downstream of the entrance, the temperature plot shows a series of closely spaced contours, indicating the leading edge of the flame with a maximum stagnation temperature of 2800 K. The heat released by chemical reactions causes another oblique shock wave originating from the flame zone, which is evidenced in Fig. 17c. This wave travels upward to the line of symmetry and meets a similar wave coming down from the upper half of the chamber. The right-running wave then reflects off the bottom surface, moves upward again, and finally exits the chamber. These reflected waves cause the fluctuating Mach-number contours shown in Fig. 17a. As the flow crosses this shock structure, it first decelerates by passing through a reflected compression wave, then accelerates through an expansion caused by the distributed reaction zone near the surface.

The mass fractions of butadiene and oxygen are presented in Fig. 18. The fuel species are generated from the sample surface, then diffuse toward the freestream to mix and burn with oxygen. At the inlet to the chamber, the oxygen is uniformly distributed with a mass fraction of 0.23. It is then consumed by the chemical reaction which generates a maximum stagnation temperature of 2800 K. The flame temperature diminishes downstream because of heat transfer back to the fuel sample and a reduction in chemical reactions caused by an oxygen deficiency at the fuel surface. The maximum temperature at each axial station occurs in a region where mass fractions of oxygen and butadiene are near stoichiometric. The temperature then drops off from this region due to fuel-rich conditions toward the surface and oxygen-rich conditions toward the freestream. The vertical location of maximum

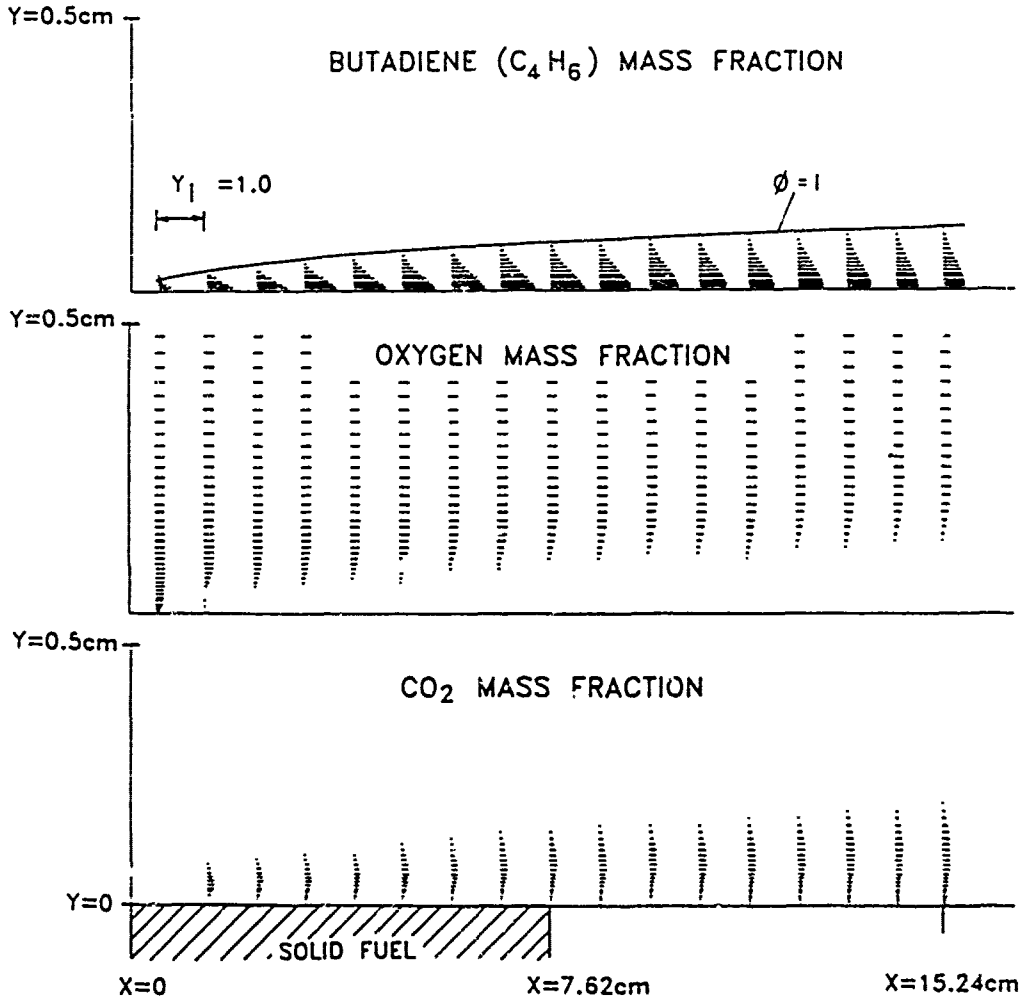


Figure 18. Species Mass Fractions for Baseline Case;
M_∞=2.0, T_∞=1400 K, p_∞=1 atm

temperature is determined by the rate of diffusion and blowing of pyrolyzed fuel-rich gases into the crossflow. Finally, the species distributions show incomplete consumption of butadiene at the exit along with the complete consumption of oxygen near the surface, which suggests that further entrainment of oxygen or perhaps better mixing between the fuel and oxidizer will improve combustion efficiency.

Figure 19 shows the burning rate of HTPB for the baseline case. At the inlet, the leading edge of the fuel sample experiences temperature recovery and enhanced heat transfer due to the abrupt deceleration of the flow; the result is a burning rate slightly higher than succeeding locations along the sample. Immediately downstream of the inlet is a large peak with a burning rate of 1.13 mm/sec and surface temperature of 1060 K. This is caused by the intense convective and radiative heat feedback from the flame to the fuel surface. As the flame temperature decreases downstream, the heat transfer to the solid boundary is reduced, resulting in a decaying profile of the burning rate.

A plot of surface pressure is shown in Fig. 20. The first two peaks in this curve are due to the inlet shock and burning phenomenon mentioned previously. After passing the second peak, the pressure abruptly decreases, then increases slowly along the length of the fuel sample from x = .020 to x = .075 m. The slight pressure rise can be explained qualitatively by comparing this situation to a constant-area tube with supersonic flow and heat addition (by external means or chemical reaction), in which a similar pressure increase occurs along the length of the tube. Finally, the third peak in the curve results from the reflected oblique shock wave and subsequent expansion evident in Fig. 17c.

In order to study the effect of freestream conditions on the burning characteristics of the sample, calculations were also carried out with different pressures and temperatures. Figures 21a and 21b show the results for an inlet pressure of

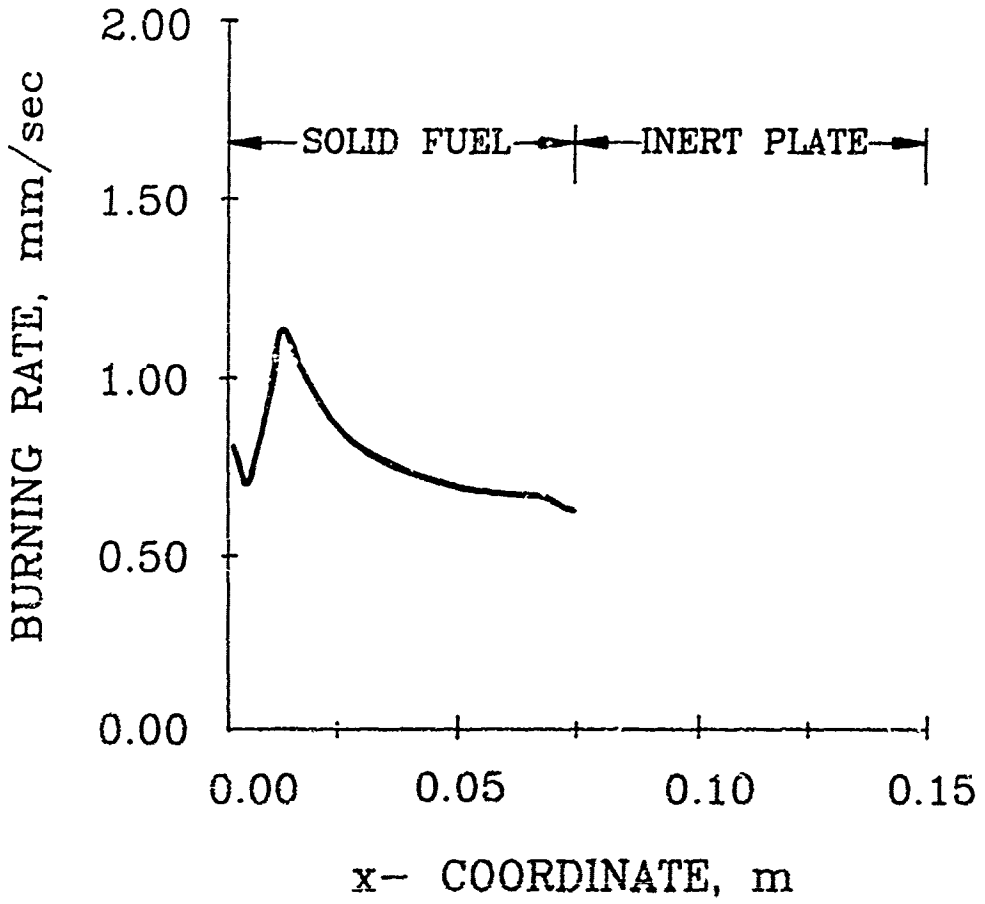


Figure 19. Solid Fuel Burning Rate for Baseline Case; M_∞=2.0, T_∞=1409 K, p_∞=1 atm

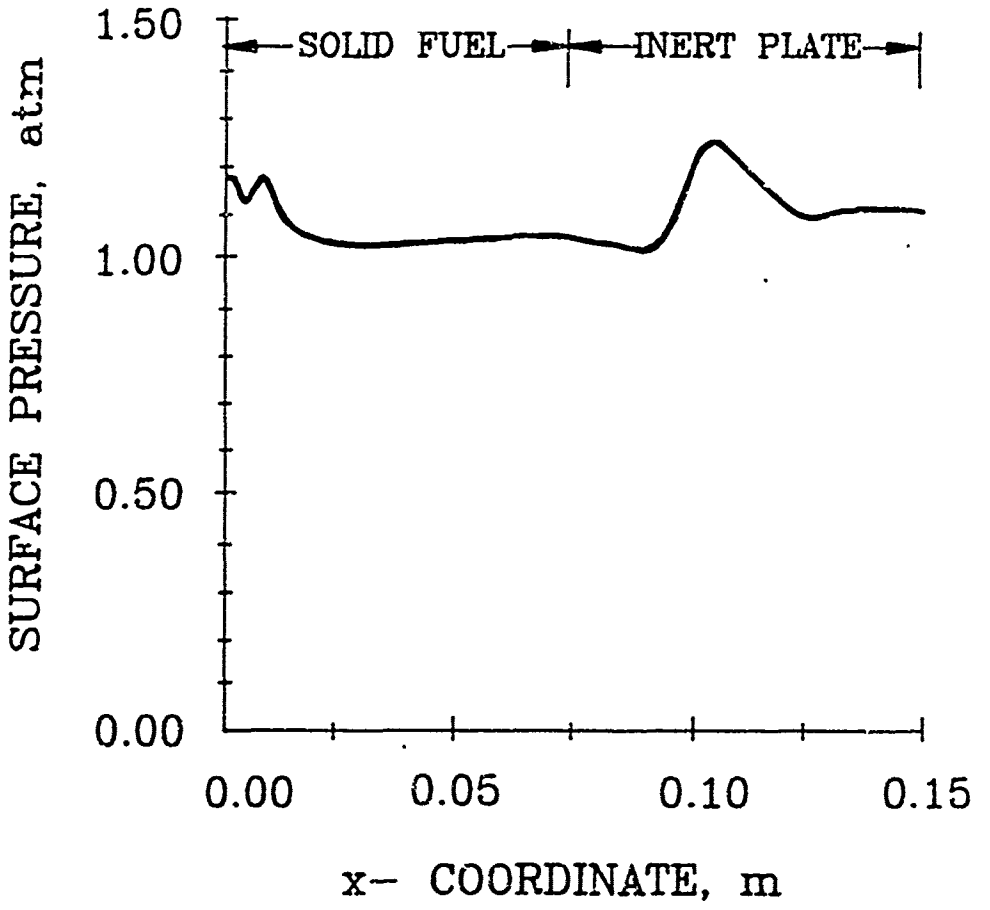


Figure 20. Surface Pressure for Baseline Case;
M_∞=2.0, T_∞=1400 K, p_∞=1 atm

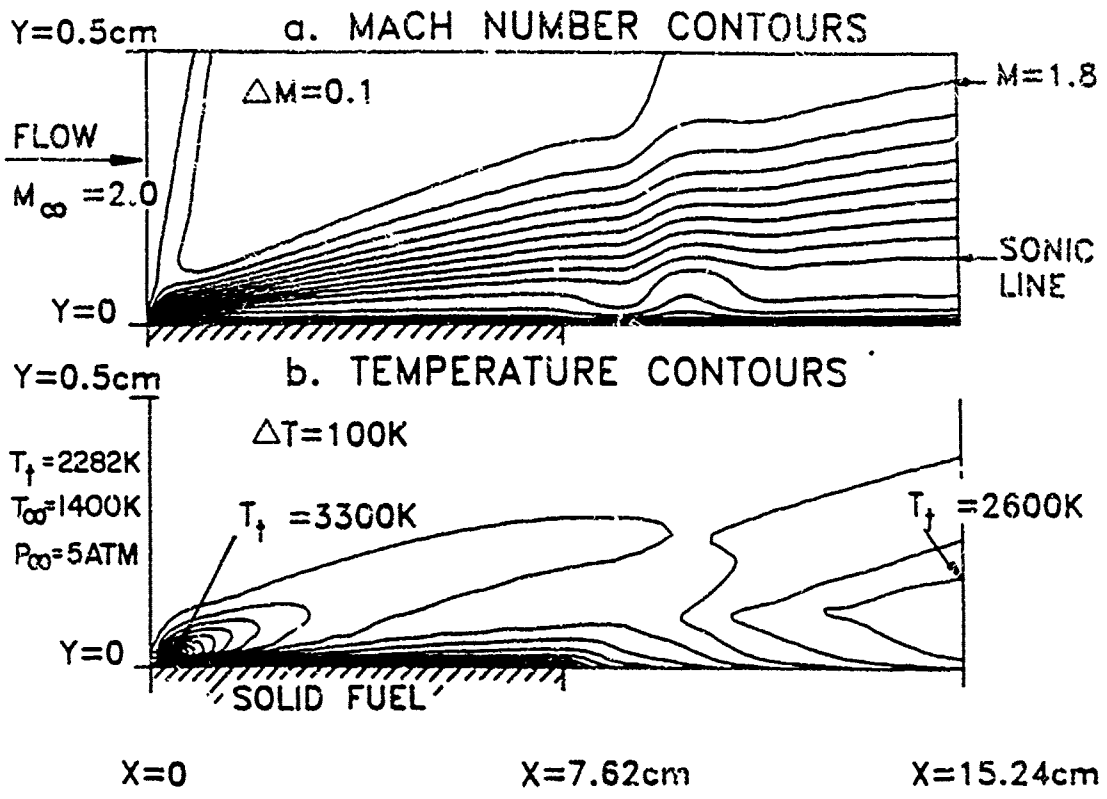


Figure 21. Mach Number, Temperature Contours;
M_∞=2.0, T_∞=1400 K, p_∞=5 atm

five atmospheres, with other conditions remaining the same as those of the baseline case. Compared to the baseline case, the flame front is shifted slightly upstream with a shorter stand-off distance from the fuel surface. Furthermore, the maximum flame temperature is increased by 350 K, with the corresponding increase in the stagnation temperature being 500 K. The shift in the flame-front location and the decrease in stand-off distance are due to the increasing gas-phase reaction rates with pressure, whereas the rise in flame temperature can be attributed to the fivefold increase in oxidizer molar concentration. Because more oxygen was supplied to the combustion chamber for reaction, the exit temperature near the surface has also increased by approximately 100 K. In addition to the faster kinetics, the burning rate of the solid fuel has increased considerably since the flame is at a higher temperature and is closer to the boundary, causing the radiative and convective heat feedback to increase significantly. The curve shown in Fig. 22 has a peak burning rate of 1.55 mm/sec, nearly 40% higher than that in the baseline case.

A calculation with an increased inlet static temperature of 1800 K was also performed. Results for this case were similar to the previous calculation with a higher pressure, in which the flame-front was shifted upstream due to enhanced chemical reaction rates at elevated pressure. Compared to the baseline case, the maximum flame temperature increased by nearly 400 K, corresponding to the 400 K rise in the inlet temperature. On the average, the burning rate of the solid fuel increased by 15% along the length of the sample because of the higher flame temperature and intensified heat transfer from the flame to the surface.

Increased inlet temperature and pressure have been shown to enhance the regression rate of the fuel sample. To further assess the effects of these freestream variables on the combustion behavior of the solid fuel, a burning rate parameter r_b^* was established for comparison of cases. This parameter is formulated so that

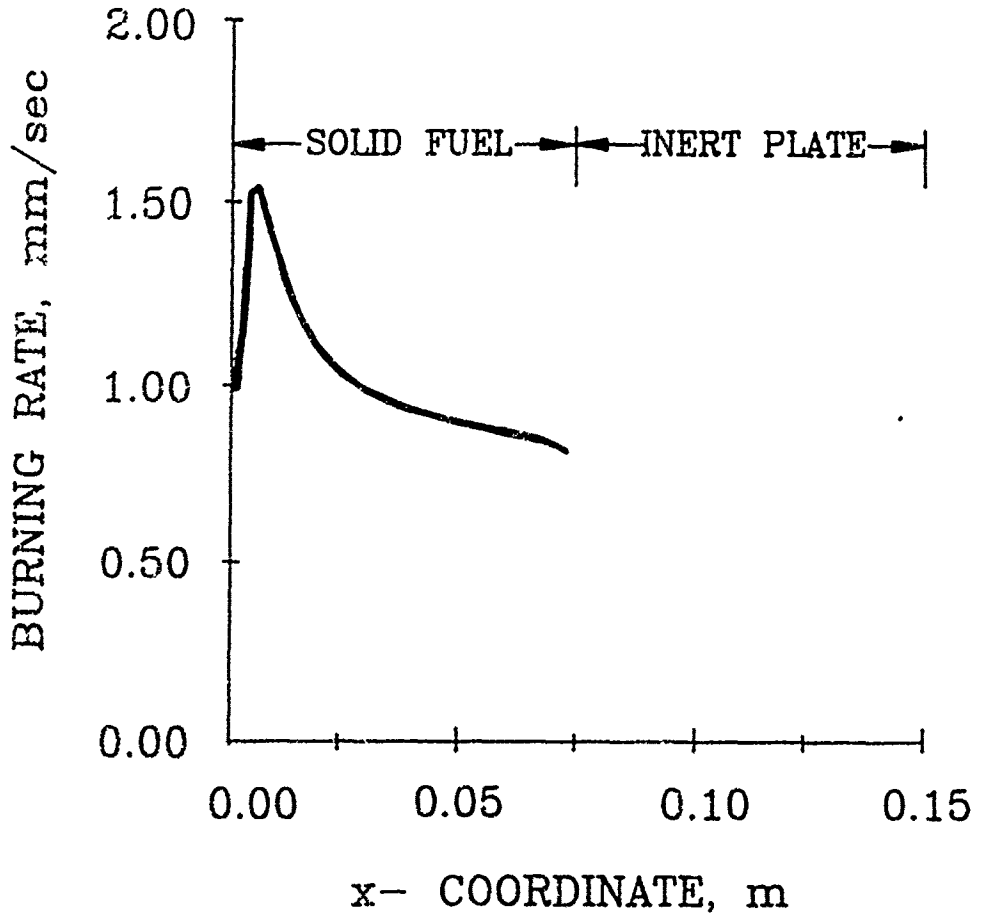


Figure 22. Solid Fuel Burning Rate; M_∞=2.0, T_∞=1400 K, p_∞=5 atm

its value remains constant along the length of the sample, starting from the axial position of the leading edge of the flame to the downstream end of the fuel. It is evaluated by multiplying the burning rate of the sample by a local dimensionless parameter, namely

$$r_b^* = r_{b,x}\left(\frac{x}{L_f}\right)^{\frac{1}{3}} \tag{75}$$

where x is the axial distance from the inlet, L_f the total length of the fuel sample, and $r_{b,x}$ the local solid-fuel burning rate. The exponent of $\frac{1}{3}$ was chosen to minimize the variation in r_b^* along the length of the sample as shown in Fig. 23. The burning rate parameter versus pressure was also plotted for two different inlet temperatures, giving the result in Fig. 24. The burning rate increases with pressure for several reasons. First, the molar concentration of oxygen in the freestream increases with inlet pressure, so more oxidizer is available for reaction with the fuel-rich region near the surface. A subsequent rise in flame temperature intensifies heat transfer to the surface and increases the burning rate. Second, the gas-phase reaction rates are proportional to the 1.75 power of pressure and have a profound effect on flame thickness. At low pressures, kinetic rates are relatively slow with regard to the diffusion and mixing processes of the fuel and oxidizer, so the two species may overlap to form a widely distributed reaction zone. However, at higher pressures the kinetic rates are fast enough for the fuel and oxidizer to react upon contact, thereby collapsing the reaction zone to a thin sheet and increasing local heat of reaction, flame temperature, and subsequent convective heat transfer rates to the fuel surface. Finally, the molecular diffusion rate of fuel species decreases with an increase in pressure, thus bringing the flame closer to the surface and increasing the burning rate of the solid fuel. This effect may only be secondary, since other processes such as turbulence and blowing also govern the flame stand-off heig

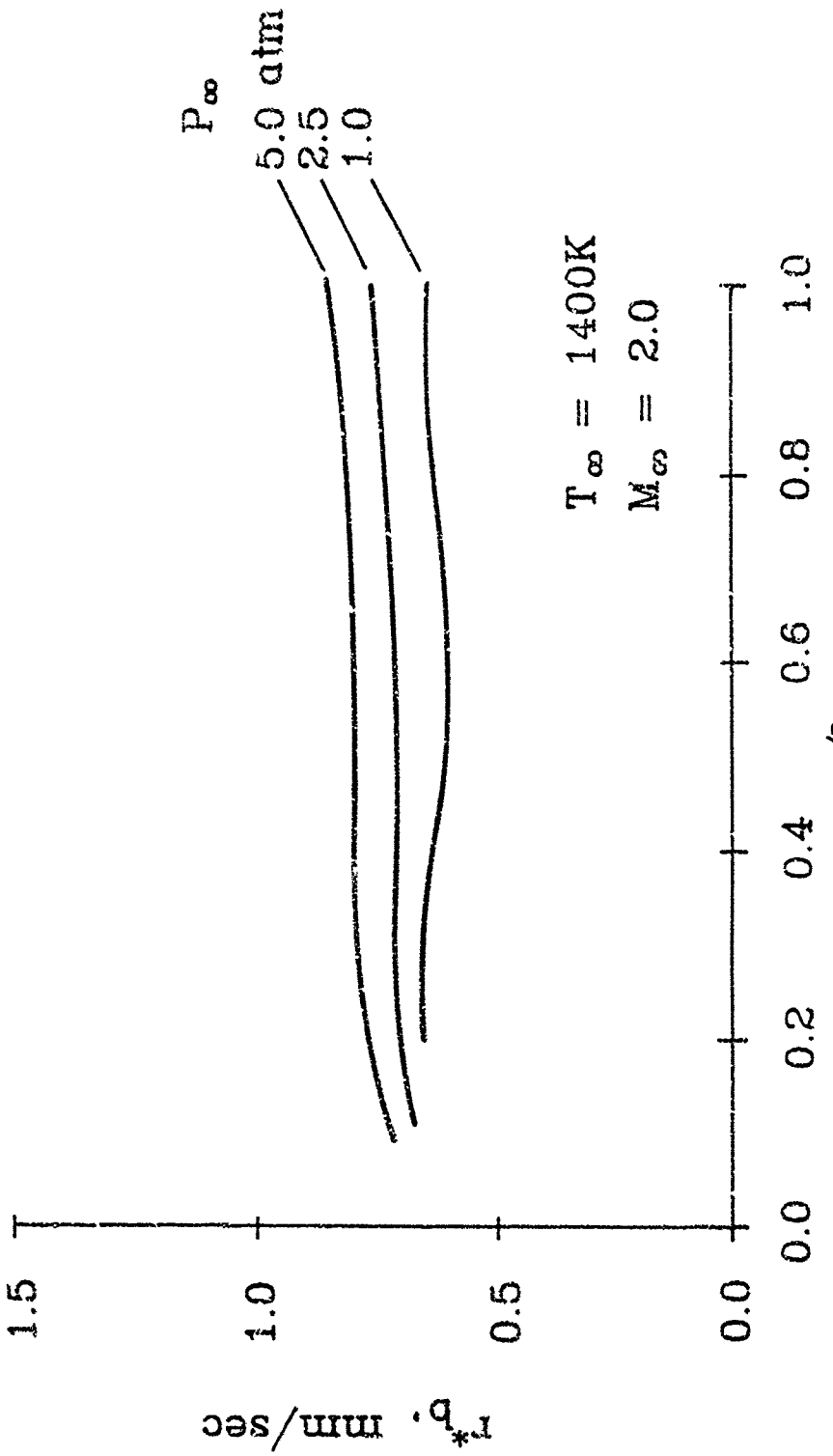


Figure 23. Axial Distribution of Burning Rate Parameter

For the operating range of 1-4 atmospheres, the dependence of the regression rate on ambient pressure and temperature can be expressed by an empirical power law.

$$r_b^* \propto p^{0.19} T^{0.57} \tag{76}$$

The ambient temperature appears to have a stronger influence on the burning rate than does pressure; this corresponds closely to results obtained under subsonic crossflow conditions with polyethylene fuels.[4] The pressure and temperature exponents were 0.28 and 0.50, respectively, for subsonic crossflow conditions. Results under supersonic conditions show similar freestream effects; however, caution must be exercised in extrapolating Eq. (76) to other cases because of differences in operating range and fuel composition.

The burning rate decreases at an inlet pressure of five atmospheres as shown in Fig. 24. This reversal in the burning rate may be explained as follows. As the pressure increases from four to five atmospheres, the mass flow of air also increases, necessitating an increase in the heat released by combustion to raise the total enthalpy of the product gases. Although the reaction rate is enhanced with pressure, the overall heat release may not increase accordingly due to the lack of additional fuel in the reactions. The mixture may reach a considerably fuel-lean condition, and cannot supply the energy necessary to raise the enthalpy of the flow. Consequently, a decrease in heat feedback to the solid fuel occurs, causing a reversal of the burning rate trend with pressure. The burning rate will achieve a maximum value at some threshold pressure, then diminish due to the finite energy released by combustion. It is interesting to note that the combustion of solid propellants does not encounter this type of pressure threshold in the burning rate. The burning rates

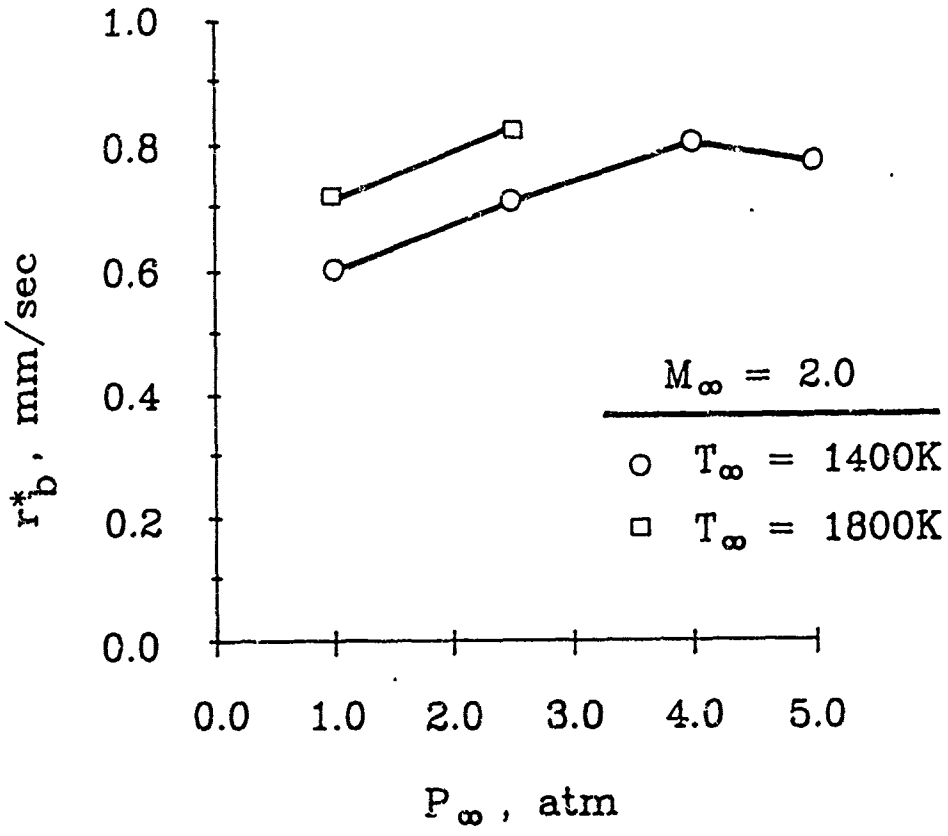


Figure 24. Variation of Burning Rate Parameter with Pressure

are proportional to certain powers of pressure throughout a wide range of chamber pressures because the oxidizer-to-fuel ratio is fixed within the propellant.

6.2. Boron Particle Ignition Results

Calculations were first performed with boron particles in stagnant surroundings in order to verify the operation of the numerical scheme, and to determine the approximate particle size which would most likely result in ignition within the confines of the combustion chamber. Typical results of such a calculation are shown in Fig. 25, where the particle temperature and oxide-layer thickness are plotted versus time. The initial particle radius is 2.5 microns with an oxide thickness of 0.03 microns, and initial temperature of 900 K. The ambient temperature, pressure, oxygen mole fraction and water vapor mole fraction are 2200 K, 2.5 atm, 0.21, and 0.0, respectively. Figure 25 shows an abrupt increase in particle temperature within the first 0.2 ms due to conductive heat transfer from the surroundings, then a gradual increase when the particle reaches the ambient temperature. While the particle temperature rises, the oxide layer thickens due to the diffusion of oxygen across the oxide layer to react with boron at the B/B_2O_3 interface. At a sufficiently high particle temperature (at t=0.18 ms), the evaporation rate of boron oxide begins to dominate over other modes of B_2O_3 generation, and the oxide layer becomes thinner. The particle temperature continues to slowly rise due to the self-heating from the interfacial reactions between B and O_2. Eventually, the particle temperature reaches 2450 K at t=0.45 ms and the boron particle begins to melt. After melting, the remaining oxide is quickly removed and thermal runaway occurs, resulting in full-fledged ignition of the particle at t= 0.66 ms. The change in the particle radius throughout the ignition event is almost negligible, with the radius at thermal runaway equal to 2.45 microns.

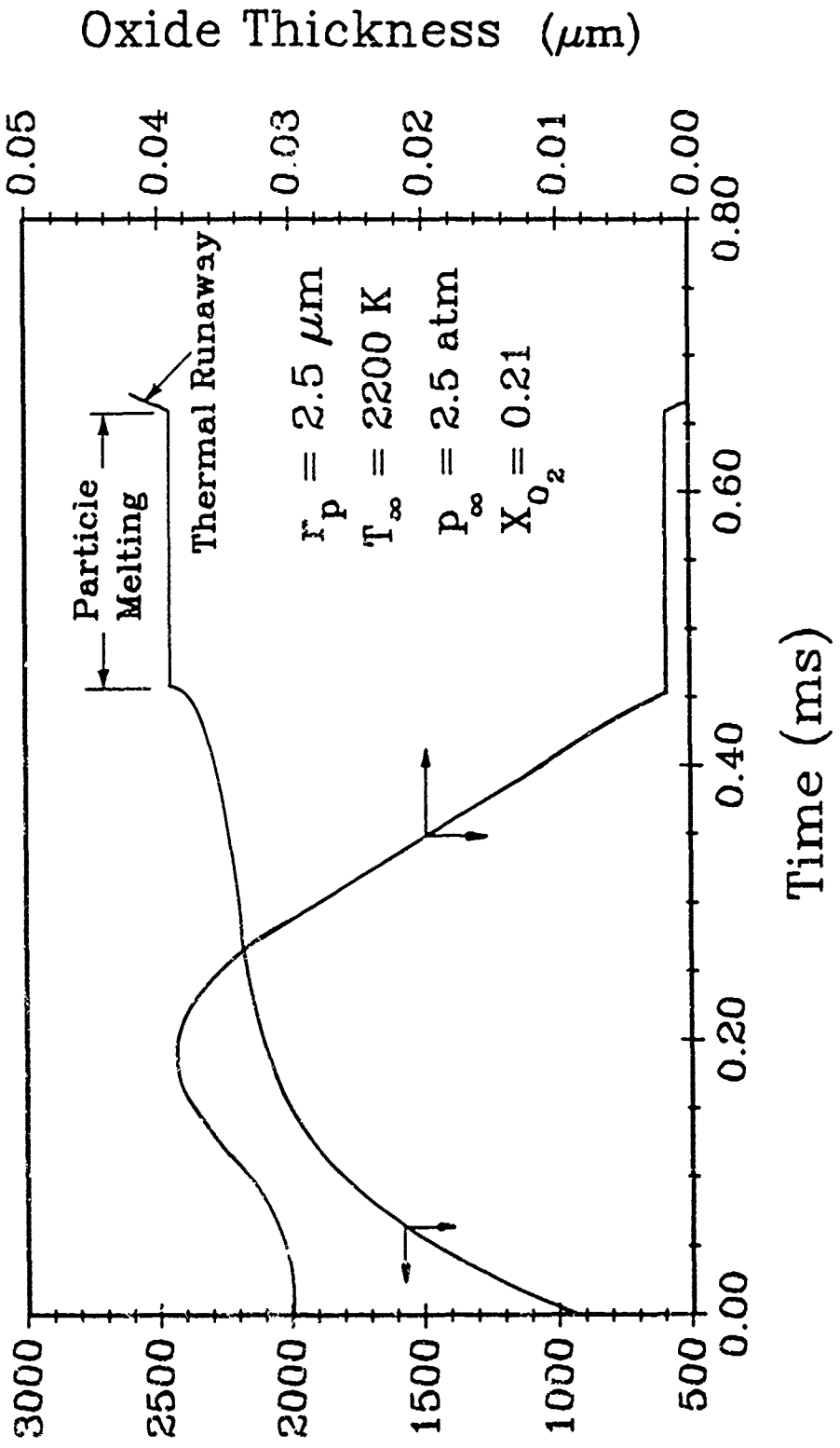


Figure 25. Histories of Particle Temperature and Oxide-Layer Thickness

Choices in the initial conditions of the particle may have some bearing on the ignition time of the particle. The initial temperature of 900 K was based on the anticipated temperature of the particle when it is ejected from the solid fuel. A slight variation in this initial condition should have negligible effects, because the increase in particle temperature at the onset is very steep. The initial oxide thickness, on the other hand, may have some consequence on the final ignition time of the particle. According to previous studies[12] a fivefold increase in oxide thickness from 0.02 - 0.10 microns with a particle radius of 2.5 microns results in a 50 percent increase in ignition time. The value of 0.03 microns was chosen to keep the mass fraction of oxide below 5 percent of the total weight of the particle. This value was not varied in the remainder of the numerical cases studied, since the effect of the initial oxide thickness is already known.

Several key points should be addressed concerning the results from the previous example, keeping in mind that the following comments refer to dry oxidizing environments. First, the rise in particle temperature from the initial to the ambient temperature is predominantly due to conductive heat transfer from the surroundings. The presence of oxygen during this short time has some adverse effect on the ignition process, since the oxygen mostly serves to thicken the oxide layer, thereby requiring additional time to eventually evaporate the thickened layer. Second, when the particle is heated to the ambient temperature in the neighborhood of 2200 K, the exothermic reactions between boron and oxygen are responsible for generating heat to evaporate the oxide layer, melt the particle, and subsequently cause thermal runaway. These processes account for a large portion of the ignition time, as evidenced in Fig. 25, because increases in particle temperature are slowed by heat losses through evaporation and conduction to the surroundings (for $T_p > T_\infty$). Finally, the criterion for ignition is thermal runaway. Thermal runaway cannot occur

before the oxide layer is removed, nor can it occur before the particle is completely melted. The choice of a high temperature (2600-3000 K) to terminate the calculation is not crucial, since the temperature increases rapidly during this stage. In this work, the particle temperature chosen to stop the ignition calculations after thermal runaway is 2600 K. When water vapor is present in the surrounding gases, thermal runaway will occur sooner due to the increase in the consumption rate of B_2O_3.

In order to achieve ignition of boron particles in the flowfields discussed above, the residence times of the particles in the combustion chamber and heat transfer to the particles must be sufficient. Preliminary calculations with the inlet conditions of T= 1400 K, p=1 atm, and M= 2.0 did not result in particle ignition; therefore, these conditions were adjusted such that they would ignite the particles.

Figure 26 shows the contour plots for Mach number and static temperature with an inlet Mach number of 1.2, a static temperature of 2000 K, and static pressure of 2.5 atmospheres. Static temperatures are plotted in this figure since these values give a better indication of the direction of heat-transfer to or from the particle. Mach-number contours are incremented by 0.1 and temperature contours by 100 K. These figures show only the bottom 3 mm of the combustion chamber and have been magnified in the y-direction by a factor of twenty to resolve the flow structures nearest the surface. Results from this calculation are similar to those in Fig. 17, with the exception of the inlet shock, which reduces the freestream Mach number to 0.89 and increases the static temperature and pressure to 2100 K and 3.4 atm, respectively. The flame region has a maximum temperature of 3300 K. Although this temperature is high enough to promote dissociation, the high-temperature region is very small and it is unlikely that neglecting dissociation in this region would significantly affect the results from the particle-phase solution.

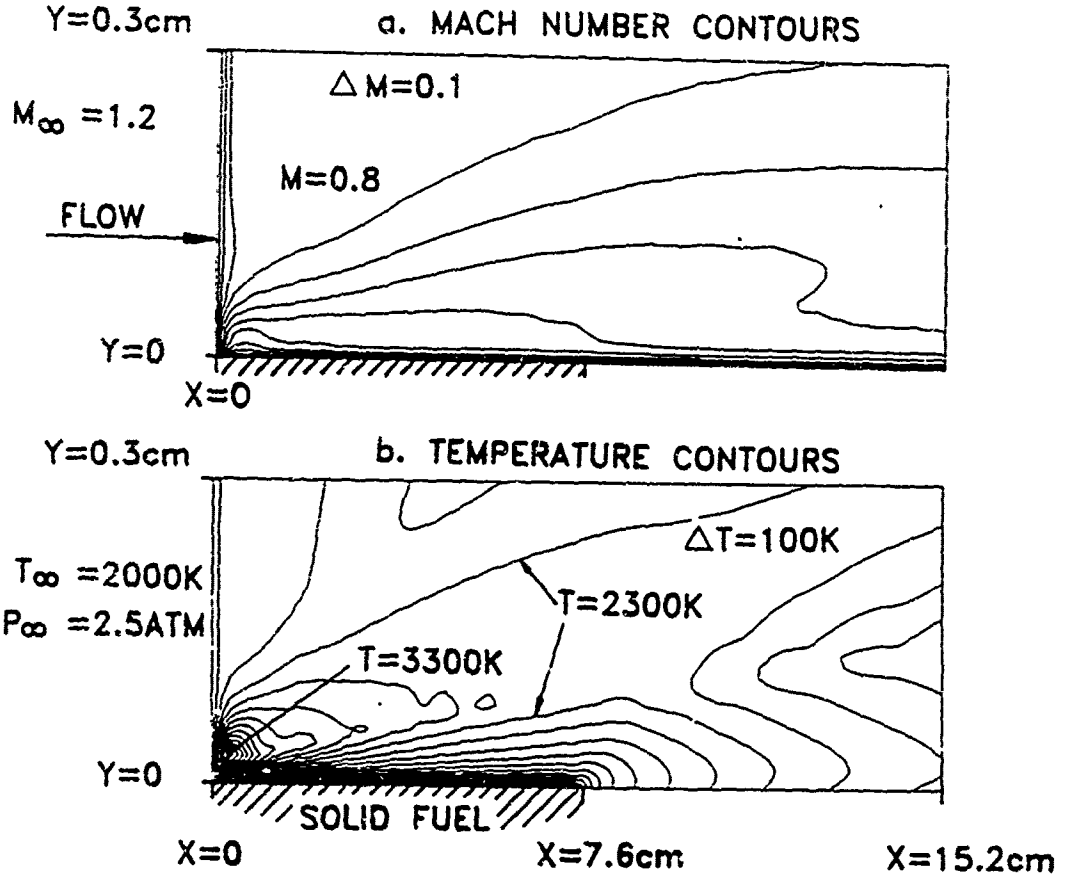


Figure 26. Mach Number and Temperature Contours; M_∞=1.2, T_∞=2000 K, p_∞=2.5 atm

Further downstream of the fuel sample, the temperatures are in the neighborhood of 2300 K.

The mass fractions of butadiene, oxygen, and water vapor are presented in Fig. 27. This figure is qualitatively similar to Fig. 18, and is provided for later discussions concerning the particle ignition mechanism.

The conditions for the baseline case of a boron particle ejected from the fuel sample are as follows. The initial particle radius is 2.5 microns with an oxide-layer thickness of 0.03 microns and temperature of 900 K. The particle is ejected vertically from the front of the fuel sample with a velocity of 0.3 m/s. This velocity is approximately one half of the velocity of the pyrolyzing gases. Depending on the entrainment and the size of the particle in the pyrolyzing gas, this initial velocity may vary. Typically, smaller particles will have higher ejection velocities. Furthermore, the ejection angle of the particle may vary, such as shown by Natan and Gany.[27] In order to minimize the number of input variables, the velocity and angle of ejection of the particles are not varied. The particle is ejected into the reacting flowfield for which the Mach number contours, temperature contours, and species mass fractions have been given (Figs. 26 and 27). The ejection process is repeated two thousand times to achieve a statistically significant number of trajectories.

For each particle, the equations for the rate of change of radius, oxide-layer thickness, and temperature are solved at each time step. The particle location and velocity at each time step are also determined. In some cases, the particles may hit the lower wall boundary somewhere downstream of the ejection station. In this instance, the particle is assumed to adhere to the surface and the calculation is terminated. Particles which satisfy the ignition criterion of thermal runaway continue to be traced through the combustion chamber at a constant particle temperature of 2600 K. This assumes that the particle has ignited and does not extinguish during

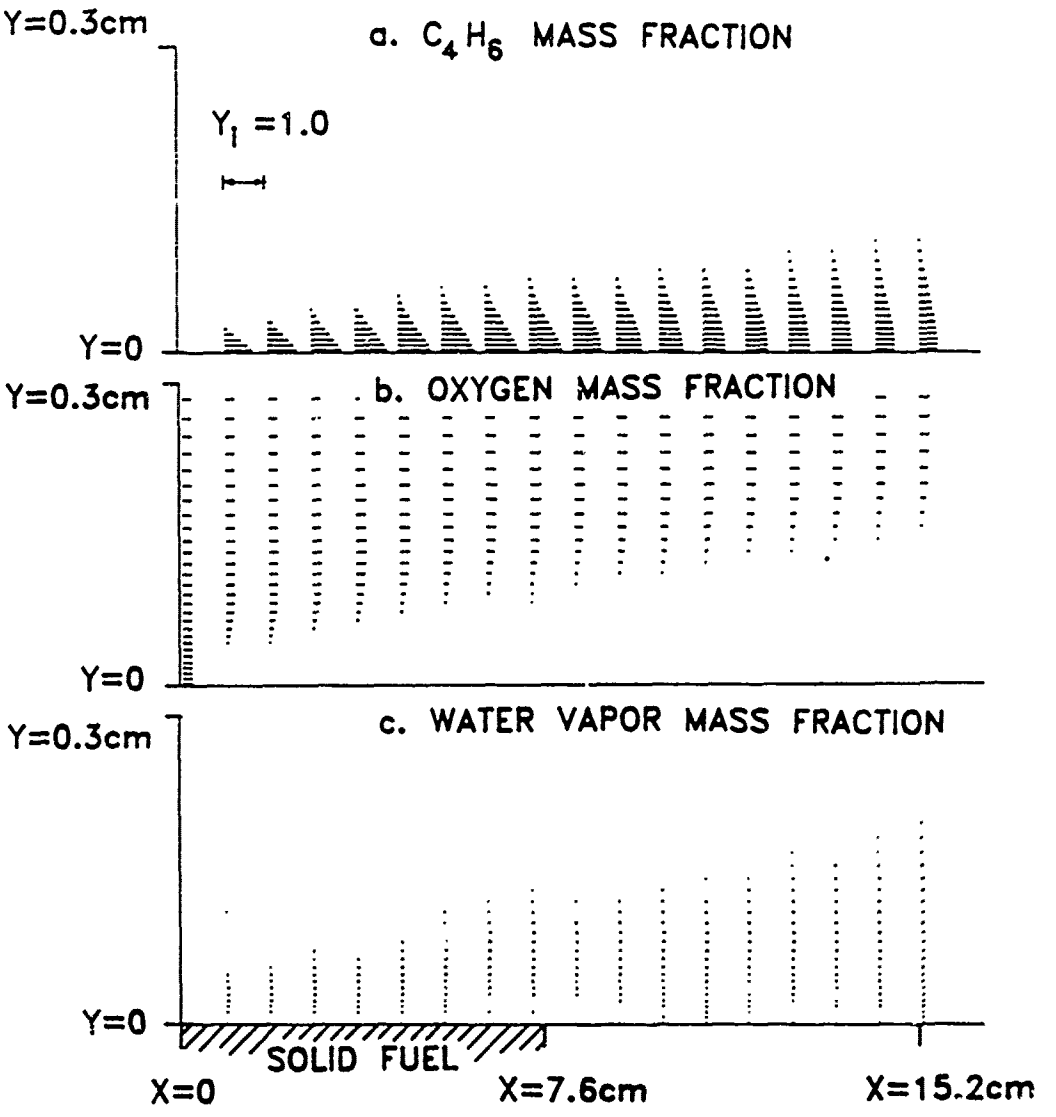


Figure 27. Species Mass Fractions; M_∞=1.2, T_∞=2000 K, p_∞=2.5 atm

its remaining time within the combustion chamber.

The distributions of the particle height above the lower wall are plotted according to temperature in Fig. 28, at an axial location of x= 5 cm ($\frac{1}{3}L_c$). Of the 2000 ejected particles, 1512 remain in the flowfield while the rest have hit the surface due to the influence of random turbulent fluctuations in the downward direction. The majority of the remaining particles are either melting or have already ignited, as shown in Fig. 28, with few particles at temperatures below 2450 K. The trajectories associated with the melting and ignition of the particle are such that most trajectories pass through the high-temperature region at the front of the sample shown in Fig. 26; therefore, these particles are subject to a very high convective heating immediately after ejection. Particles whose trajectories are closer to the surface do not experience such a high temperature increase from convection. These lower trajectories are within 0.6 mm from the surface, which is within the fuel-rich region of the boundary layer (shown in Fig. 27). Along these paths, the particles are not exposed to oxygen; therefore, the possibility of their ignition is slim. Further downstream at x=$\frac{2}{3}L_c$, the number distributions are more broadly spread as shown in Fig. 29, with 65% of the particles ignited. All particles above the 1.4 mm location have ignited. This indicates that particles ignite if they are able to penetrate the gas-phase flame region, since their temperatures are high and the surroundings provide sufficient oxygen for ignition. Results also show that at the exit, 77% of the particles remaining in the flowfield have ignited. The average horizontal velocity of these particles leaving the chamber is 582 m/s, indicating that these particles are almost fully entrained into the flow which has an average gas-phase velocity of 650 m/s.

In order to determine the most probable location for ignition of the particles, the number of occurrences of ignition were recorded according to the spatial location

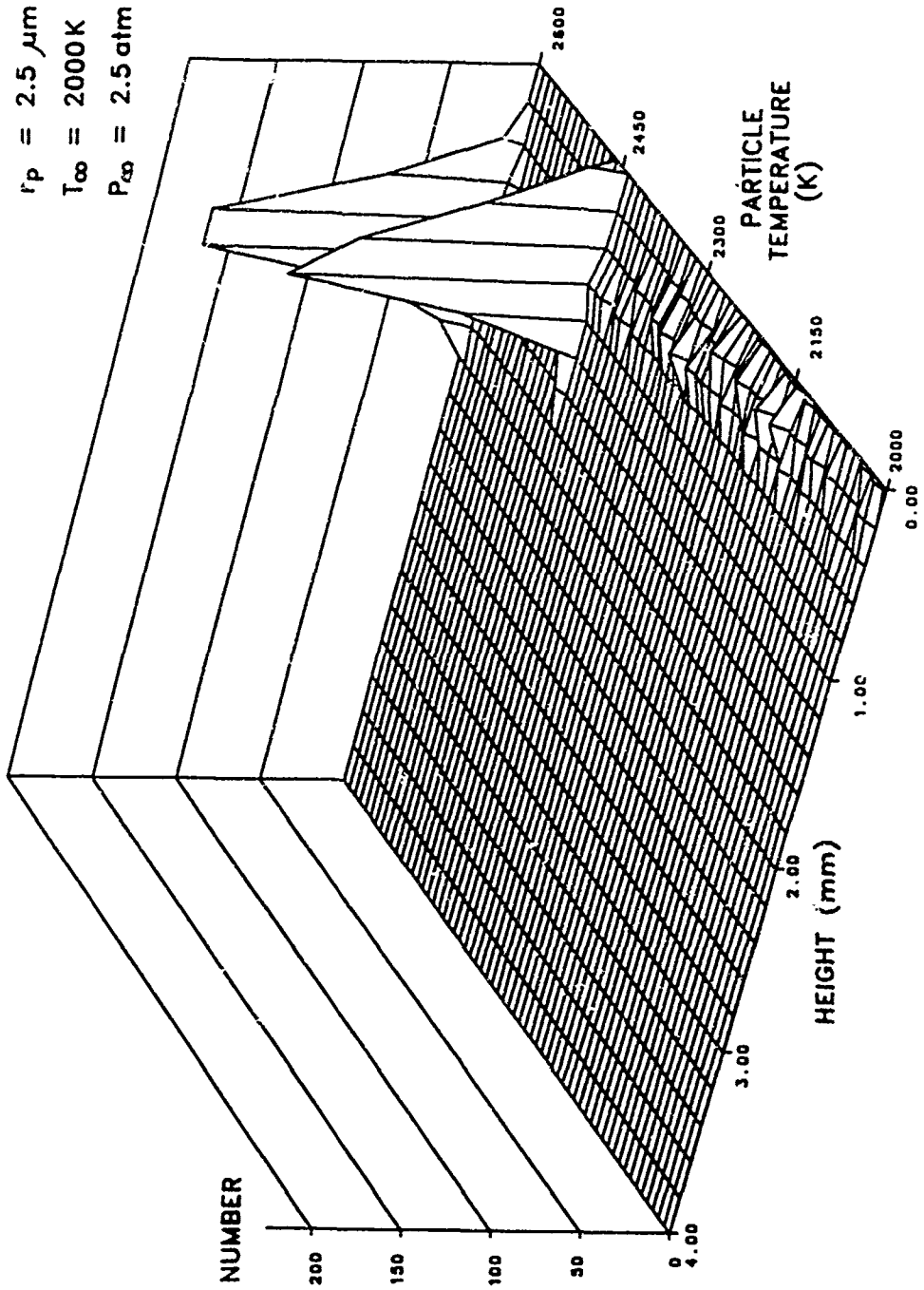


Figure 28. Calculated Number Distributions of Particles at Various Temperatures (Station x= $\frac{1}{3}L_c$)

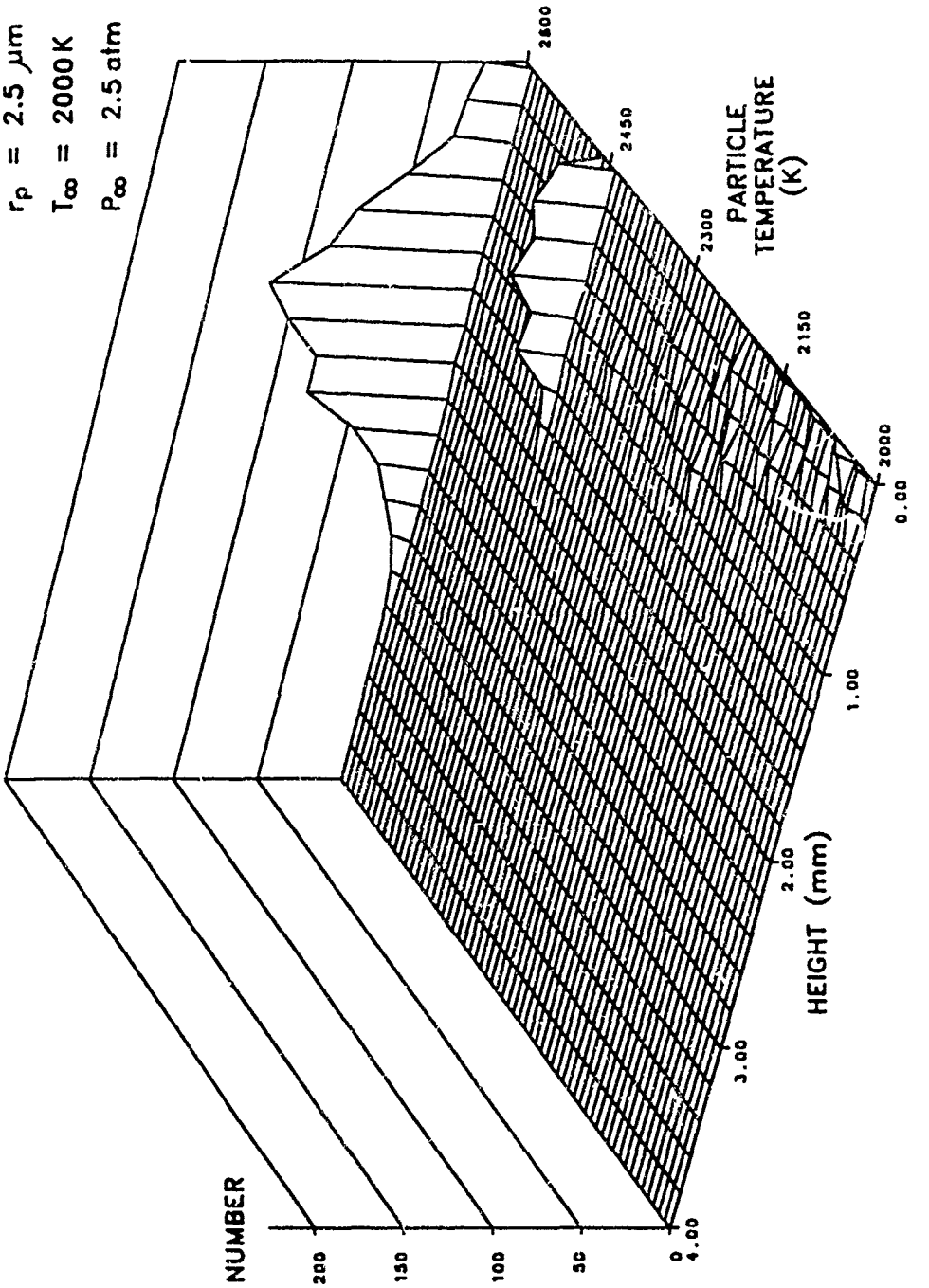


Figure 29. Calculated Number Distributions of Particles at Various Temperatures (Station x= $\frac{2}{3}L_c$)

within the flowfield. Contours of the number of occurrences for the baseline case are plotted in Fig. 30a, with the outermost contour line representing the ignition of at least one particle, and each succeeding line representing an additional three occurrences of ignition. The lines are closely spaced within the region between 3.0 and 4.5 cm from the inlet and 0.7 to 0.9 mm from the fuel surface, where 37 percent of the particles ignited. The average time for ignition at this location is 0.13 ms. When compared with oxygen mass fractions in Fig. 27, the ignition locations indicate the importance of O_2, since the particles ignite when they come in contact with oxygen after passing through the high-temperature zone. The effect of water vapor on the ignition time is insignificant in this case, because the mass fractions shown in Fig. 27 are quite small.

The effect of particle size on the ignition time and location was investigated. Additional cases were studied with smaller particle radii of 1.5 and 1.0 microns, and larger radii of 4.0 microns, with all other initial conditions remaining the same. For both of the smaller particle sizes, the ignition locations moved upstream to 1.75 cm, as shown in Fig. 30b and 30c. For the 1.5 micron particles, 56 % of the particles ignited by the time they reached $x=\frac{1}{3}L_c$ and 78 % by the time they reached the exit. The likelihood of ignition for this size is greater in comparison to the 2.5 micron particles because the smaller size requires less energy to be heated to the ignition temperature. The approximate ignition time for these particles is 0.06 ms. For even smaller particles with a 1.0 micron radius, the ignition time is nearly the same. This occurs since the particles cannot ignite any sooner due to the lack of oxygen near the surface. Both the 1.5 and 1.0 micron particles heat up and completely remove their oxide layers within the fuel-rich region near the surface, then ignite when they come in contact with O_2. Although the ignition times and locations are the same, a tremendous decrease in the number of ignited particles is

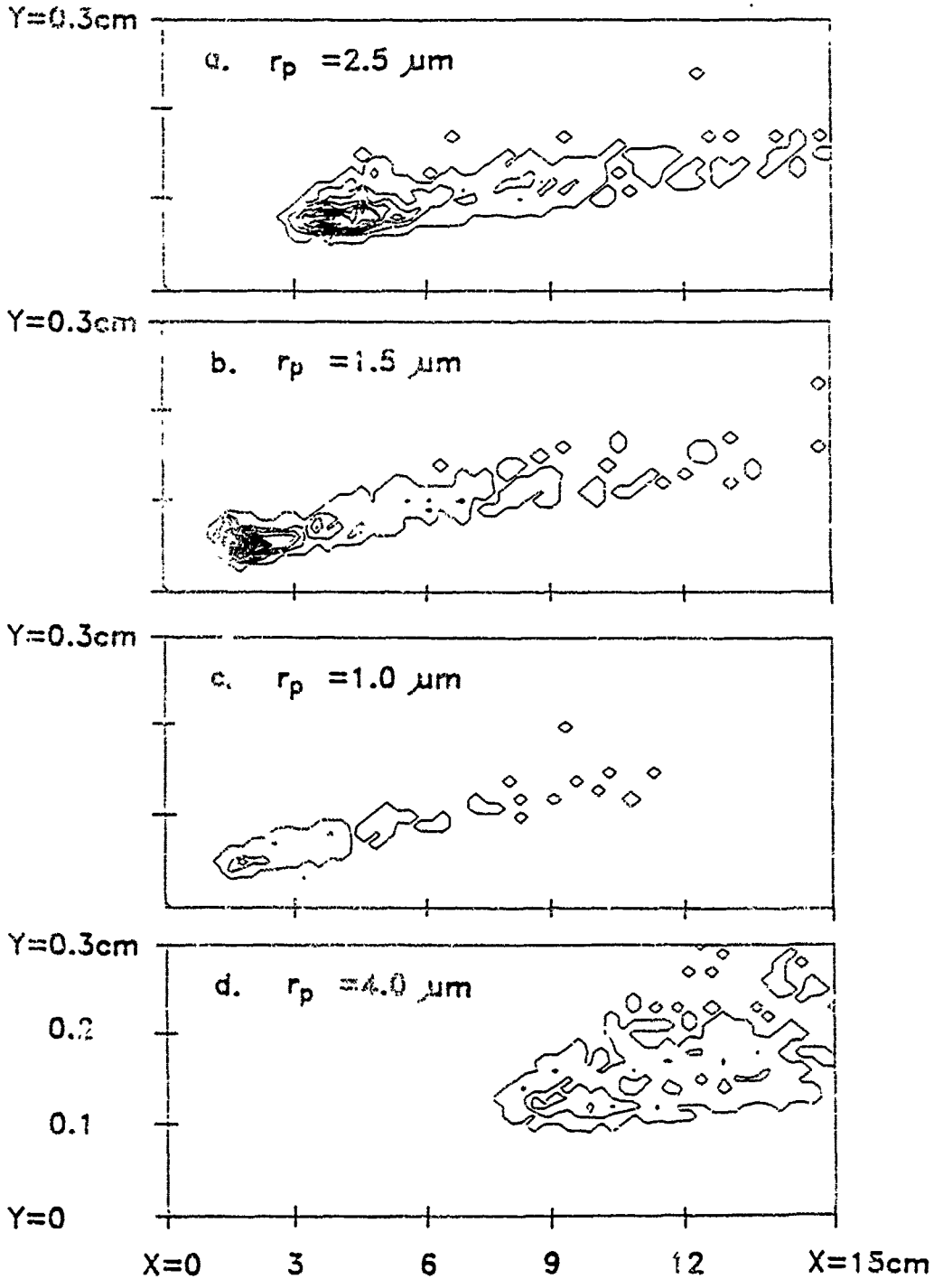


Figure 30. Effect of Particle Radius on Ignition Locations;
M_∞=1.2, T_∞=2000 K, p_∞=2.5 atm

noticed for the particles with 1.0 μm radius. At x=$\frac{1}{3}L_c$, only 9% have ignited, and at the exit only 15% have experienced thermal runaway. These results are partly due to the lower inertia of the smaller particles, which allows the majority of them to be swept downstream before reaching the high temperature region above the fuel sample. Another cause for the smaller number of ignited particles is convective heat loss of the unignited particles after they pass into the oxidizing region. The surrounding gas temperature is in the neighborhood of 2300 K, which should be sufficient to ignite the particles; however, for smaller particles, both the specific surface area and the convective heat-transfer coefficient become greater, resulting in a more dominating effect of heat loss from the particle. The energy supplied by the exothermic reactions may not be sufficient to compensate for the heat-loss effect. Therefore, in some instances a smaller particle size would not benefit the ignition process. If the surrounding temperature was greater than the ignition temperature of the boron particles, then the convective heat losses could be avoided and the ignition times would be shortened for the smaller particles.

Larger particles with radii of 4.0 microns ignited much further downstream at x= 8.75 cm and y=1.3 mm as shown in Fig. 30d. The ignition time at this location is 0.32 ms. At x=$\frac{1}{3}L_c$ no particles were ignited, and at the exit only 44 % were ignited. In comparison with small particles (r_p= 2.5 μm), less dispersion in the trajectories was noticed at the x=$\frac{1}{3}L_c$ and x=$\frac{2}{3}L_c$ stations, as shown in Figs. 31 and 32, since the particles were heavier and not able to follow the turbulent fluctuations as well as the smaller particles.

Figure 33 summarizes the effect of particle size and axial location on the ignition probability. The percent of ignited particles is plotted at three axial stations for the four different particle sizes. For particles with radii equal to 1.0 micron, 9 percent ignited by passing through the flame region, and only 6 percent more ignited

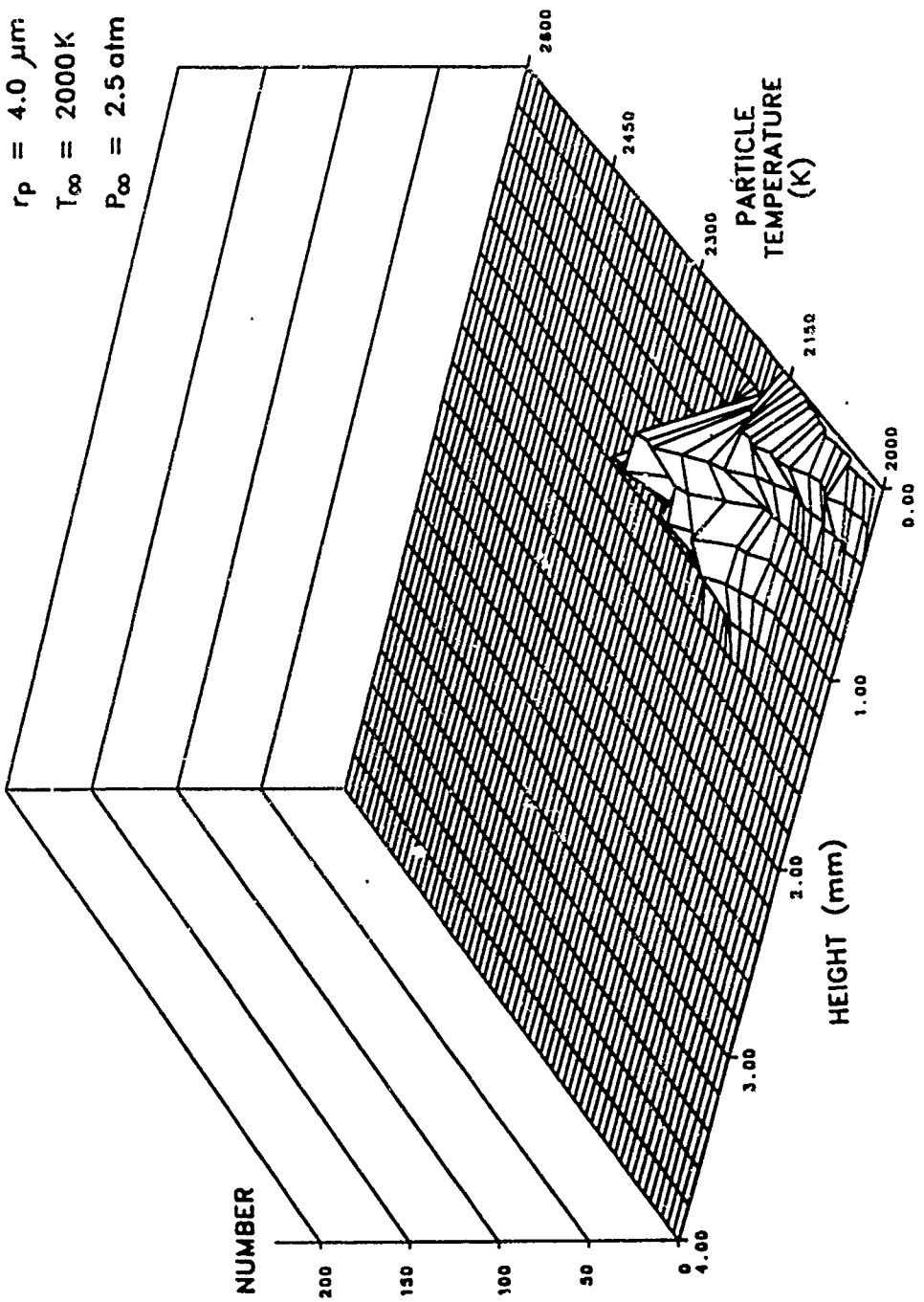


Figure 31. Calculated Number Distributions of Particles at Various Temperatures (Station x= $\frac{1}{3}L_c$)

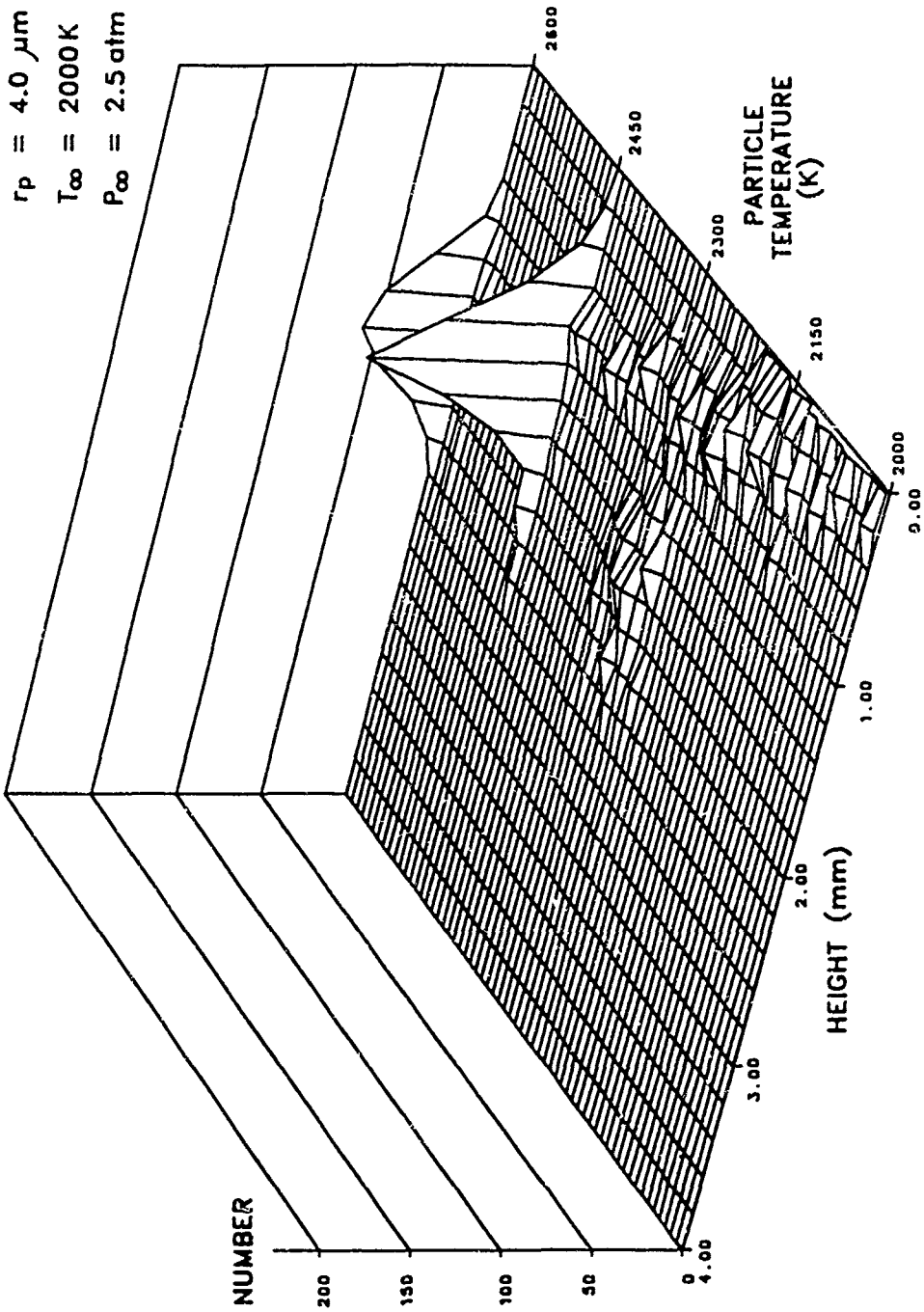


Figure 32. Calculated Number Distributions of Particles at Various Temperatures (Station x= $\frac{2}{3}L_c$)

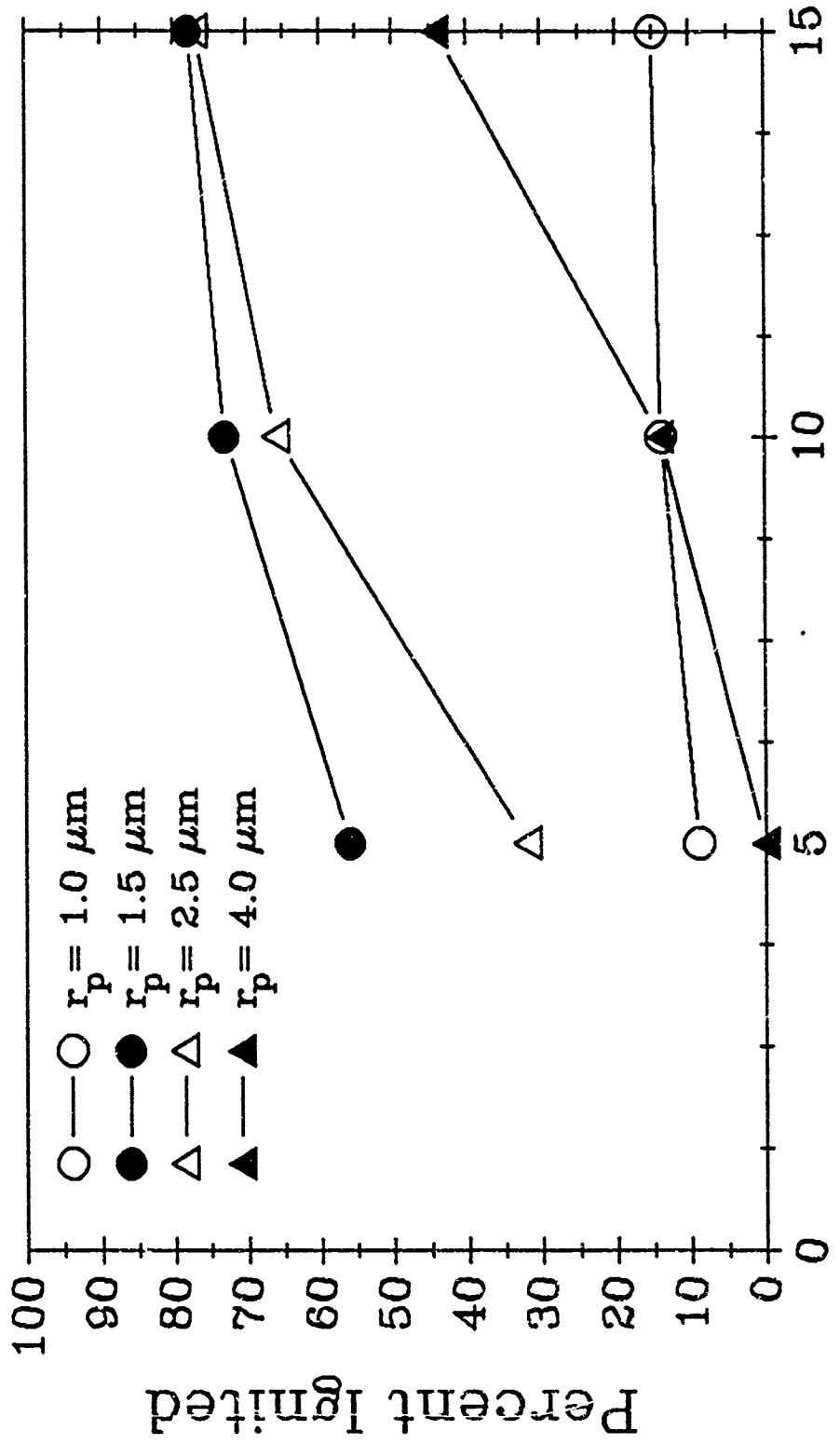


Figure 33. Effect of Particle Radius on Ignition Percentage at Three Axial Stations

afterwards. For larger particles of 1.5 and 2.5 microns in radius, dramatic increases were noticed in the ignition percentages. The particles with 1.5 micron radius ignited in the upstream regions of the combustion chamber, whereas the slightly larger particles of 2.5 microns required more time to ignite. Nevertheless, the results at the exit of the chamber are comparable. A total of 78 percent of these particles ignited. For even larger particles of 4 micron radius, the percentages decreased because of the increased energy and time required to ignite the particles.

The effect of ambient conditions on the ignition of the boron particles was also studied and compared to the baseline case. The gas-phase equations were solved again based on a lower inlet temperature of 1900 K, with the Mach number and pressure remaining at 1.2 and 2.5 atm, respectively. Boron particles were ejected in the same manner as discussed above, with 2.5 micron radius, 0.03 initial oxide thickness, and 900 K initial temperature. The new freestream conditions resulted in a decrease to 69% in the number of ignited particles, with a slight increase of 0.04 ms in the ignition time. The particles most frequently ignited at the station 5.25 cm from the front edge of the sample. This location is 1.75 cm downstream from the results of the baseline case at the higher inlet temperature of 2000 K. The slower ignition response is primarily due to increased convective heat loss caused by the 100 K cooler surroundings when the particle temperature rises above the gas-phase temperature. Results from this calculation are plotted in Fig. 34, where a noticeable decrease in the percent ignited is shown in comparison with the baseline case. Another case with lower freestream pressure of 1.5 atm was calculated, with all other conditions the same as the baseline. Similar effects on the ignition results are evident. The poorer performance stems from the decline in freestream pressure which decreases the oxygen partial pressure and the flame temperature, resulting in a delayed ignition of the particle.

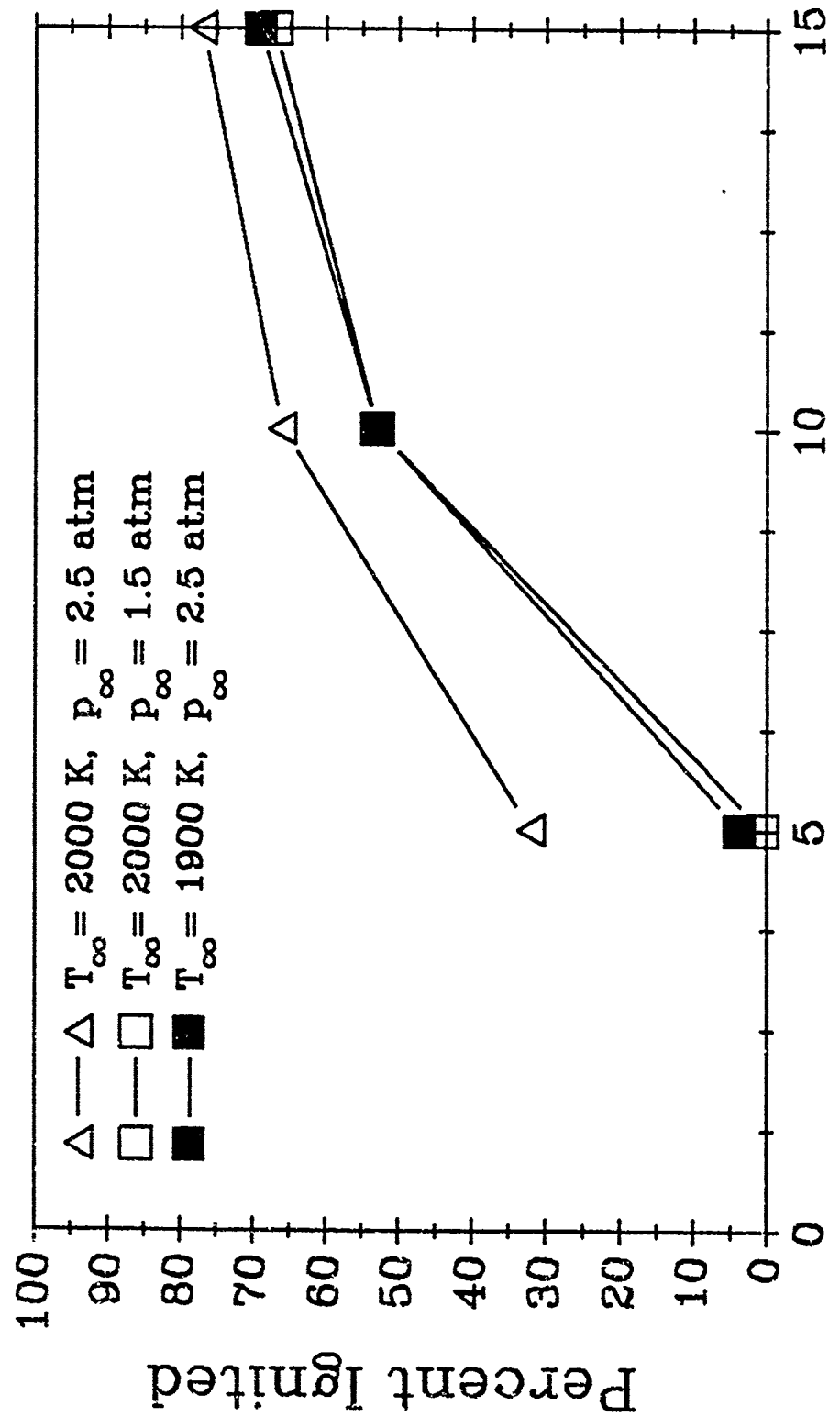


Figure 34. Effect of Freestream Conditions on Ignition Percentage at Three Axial Stations, r_p= 2.5 μm

Results discussed in this work show that the minimization of ignition time can be accomplished by optimizing the environmental conditions at certain periods during the ignition process. King[14] originally suggested such a scenario which involved the initial heatup and removal of the oxide layer in a mixed H_2O/N_2 atmosphere, then exposure to an O_2/N_2 environment for melting and complete ignition. In this manner, the buildup of the oxide layer during the heatup process (as evidenced in Fig. 25) can be avoided, and ignition can occur sooner. A similar scenario is presented here. With the initial heatup occurring in the fuel-rich mixture below the reaction zone, boron particles avoid oxide layer build-up as they are ejected into the reacting boundary layer. Since the particles do not ignite or burn within the fuel-rich layer, the near-surface region heats the particle and removes the oxide layer, so that the particles achieve thermal runaway immediately upon contact with the oxidizer. When this occurs, the ignition delay time is governed by the residence time required for the particles to travel from the sample surface to the region where sufficient oxidizers exist. Otherwise, if the oxide layer is not completely removed before the particle contacts oxygen, ignition delay time will be prolonged, thereby reducing the chances for achieving a high combustion efficiency.

Chapter 7

SUMMARY AND CONCLUSIONS

The combustion behavior of HTPB-based solid fuels with various percentages of boron loading were studied on an experimental basis under both subsonic and supersonic crossflows, using a connected-pipe facility. A non-intrusive real-time x-ray radiography system was used to obtain instantaneous surface profiles of the solid fuels. New findings in the area of solid-fuel ignition and combustion are summarized below.

Visual observation of the ignition sequence of boron-loaded fuels under high-temperature crossflows revealed the presence of glowing boron particles in the early stages of particle ignition on the fuel surface. These localized hot spots served as the ignition source for the solid-fuel sample. The ignition sequence for B/HTPB (0/100) fuels was different from that of boron-laden fuels, since only pyrolyzed HTPB fuel was involved in the ignition process. Ignition of pyrolysis products of HTPB began in the recirculation zone; however, the required inlet temperatures were much higher. The addition of boron particles to the solid fuels resulted in a reduced minimum ambient temperature required for ignition of the solid fuels.

The subsonic crossflow tests revealed that regression rates were highly dependent on freestream static pressures, and less dependent on the temperature and mass flux. Two mechanisms are attributed to enhanced burning rates at higher pressures: (1) faster gas-phase kinetics which lead to higher gas-phase temperatures and increased heat feedback to the fuel surface, and (2) increased oxidizer-to-fuel ratio which allows additional reactions of oxidizers with fuel-rich pyrolysis products and

ejected boron particles. The addition of small percentages of boron (up to 10 percent by weight) significantly enhanced the ignition and combustion characteristics of the sample and increased the regression rates. The increase in the regression rate is believed to be caused by the increase in convective and radiative heat transfer from the reacting particles to the fuel surface, as well as the increased radiation absorptivity of the fuel surface. A burning-rate correlation was also obtained in terms of pressure, temperature, and boron concentration.

Combustion of solid fuels under supersonic crossflows was, for the first time, successfully demonstrated. For these tests, it was necessary to increase the size of the recirculating region to promote ignition and flame stabilization of the solid fuel sample.

The combustion of HTPB solid fuel samples under supersonic crossflow was also studied using a comprehensive numerical analysis. The formulation was based on the full two-dimensional Navier-Stokes equations with finite-rate chemistry and variable properties. The Baldwin-Lomax algebraic model was employed for turbulence closure. The governing equations were solved numerically using a flux-vector splitting LU-SSOR technique that treated source terms implicitly. Results showed a distinct flame region above the fuel sample. Inlet conditions were varied for several cases to determine the effect of pressure and temperature on the combustion behavior. For the operating range considered, results indicated that both pressure and temperature had a strong influence on the solid-fuel burning rate, and that the burning rate increased with pressure at low inlet pressures from 1-4 atmospheres. At a higher pressure, the energy released by combustion was not sufficient to further raise the temperature of the crossflow. This resulted in a decrease in heat feedback to the fuel sample, causing, in turn, a reversal of the burning-rate trend with pressure. This finding is a departure from the conventional understanding in

solid-propellant studies that burning rates always increase with pressure.

The ignition processes of boron particles above a burning solid fuel were also modeled. The effects of particle size on the ignition times and locations of the particles were determined. Under certain operating conditions, an optimum particle size was attained for minimizing ignition delay times. The study also showed that the solid-fuel ramjet (SFRJ) provides a suitable environment for reducing ignition delay times of small particles by staging their ignition process. In this manner, ignition occurs in a very short time period, allowing ample time for complete combustion of the particle. Previous studies of boron-particle ignition in solid-fuel ramjet systems concluded that the ramjet environment cannot provide suitable conditions for both ignition and combustion of the particles. This study reveals that it is possible for particles to ignite and burn in SFRJ's, provided the particles sizes are kept small (below 10 μm).

REFERENCES

1. Korting, P. A. O. G., van der Geld, C. W. M., Wijchers, T., and Schoyer, H. F. R., "Combustion of Polymethylmethacrylate in a Solid Fuel Ramjet," *Journal of Propulsion and Power*, Vol. 6, No. 3, May-June 1990, pp. 263-270.

2. Mady, C. J., Hickey, P. Y., and Netzer, D. W., "Combustion Behavior of Solid-Fuel Ramjets," *Journal of Spacecraft and Rockets*, Vol. 15, No. 3, May-June 1978, pp 131-132.

3. Elands, P. J. M., Korting, P. A. O. G., Wijchers, T., and Dijkstra, F., "Comparison of Combustion Experiments and Theory in Polyethylene Solid Fuel Ramjets," *Journal of Propulsion and Power*, Vol. 6, No. 6, Nov.-Dec., 1990, pp. 732-739.

4. Schulte, G., "Fuel Regression and Flame Stabilization Studies of Solid-Fuel Ramjets," *Journal of Propulsion and Power*, Vol. 2, No. 4, July-August 1986, pp. 301-304.

5. Netzer, A. and Gany, A., "Burning and Flameholding Characteristics of a Miniature Solid Fuel Ramjet Combustor," AIAA Paper No. 88-3044, AIAA/SAE/-ASME/ASEE 24th Joint Propulsion Conference, Boston, MA, July 1988.

6. Schulte, G., Pein, R., and Högl, A., "Temperature and Concentration Measurements in a Solid Fuel Ramjet Combustion Chamber," *Journal of Propulsion and Power*, Vol. 3, No. 2, March-April 1987, pp. 114-120.

7. Snyder, T. S., Jarymowycz, T. A., Hsieh, W. H., Peretz, A., Yang, V., and Kuo, K. K., "Pyrolysis and Combustion of Solid Fuels under Subsonic and Supersonic Conditions," Proceedings of 26th JANNAF Combustion Meeting, Pasadena, California, 1989, CPIA Publication 529, Vol. I, Johns Hopkins University, Laurel, MD, pp. 371-380.

8. Macek, A. and Semple, J. M., "Combustion of Boron Particles at Atmospheric Pressure," *Combustion Science and Technology*, Vol. 1, 1969, pp. 181-191.

9. Macek, A. and Semple, J. M., "Combustion of Boron Particles at Elevated Pressures," *Thirteenth Symposium (International) on Combustion*, The Combustion Institute, Pittsburgh, 1971, pp. 859-868.

10. Macek, A., "Combustion of Boron Particles: Experiment and Theory," *Fourteenth Symposium (International) on Combustion*, The Combustion Institute, Pittsburgh, 1972, pp. 1401-1411.

11. King, M. K., "Boron Ignition and Combustion in Air-Augmented Rocket Afterburners," *Combustion Science and Technology*, Vol. 5, 1972, pp. 155-164.

12. King, M. K., "Boron Particle Ignition in Hot Gas Streams," *Combustion Science and Technology*, Vol. 8, 1974, pp. 255-273.

13. King, M. K., "Ignition and Combustion of Boron Particles and Clouds," *Journal of Spacecraft and Rockets*, Vol. 19, 1982, pp. 294-306.

14. King, M. K., "Single Particle Boron Ignition Modeling," 19th JANNAF Combustion Meeting, CPIA Publication 366, Vol. II, 1982, pp. 27-42.

15. King, M. K., "A Unified Model of Ignition, Burning, and Extinguishment of Single Boron Particles," 20th JANNAF Combustion Meeting, CPIA Publication 383, Vol. II, 1983, pp. 97-115.

16. Mohan, G. and Williams, F. A. "Ignition and Combustion of Boron in O_2/Inert Atmospheres," *AIAA Journal*, Vol. 10, 1972, pp. 776-783.

17. Turns, S. R., Holl, J. T., Solomon. A. S. P., and Faeth, G. M., "Gasification of Boron Oxide Drops in Combustion Gases," *Combustion Science and Technology*, Vol. 43, 1985, pp. 287-300.

18. Snyder, T. S., Jarymowycz, T. A., Pace, K. K., and Kuo, K. K., " Solid Fuel Ignition and Combustion Characteristics Under High-Speed Crossflows" AIAA Paper No. 90-2075, AIAA/SAE/ASME/ASEE 26th Joint Propulsion Conference, July 16-18, 1990, Orlando, FL.

19. Pein, R., and Vinnemeier, F., "The Influence of Swirl and Fuel Composition of Boron-Containing Fuels on Combustion in a Solid Fuel Ramjet Combustion Chamber," AIAA Paper No. 89-2885, AIAA/SAE/ASME/ASEE 25th Joint Propulsion Conference, July 10-12, 1989, Monterey, CA.

20. Gany, A. and Netzer, D. W., "Combustion Studies of Metallized Fuels for Solid Fuel Ramjets," AIAA Paper 85-1177, 21st Joint Propulsion Conference, July 8-10, 1985, Monterey, California.

21. Karadimitris, A., Scott, C.K., II, Netzer, D.W., and Gany, A., "Regression and Combustion Characteristics of Boron-Containing Fuels for Solid Fuel Ramjets," 26th JANNAF Combustion Meeting, Pasadena, CA, Oct. 1989, CPIA Publication 529, Vol. I, pp. 355-369.

22. Milshtein, T. and Netzer, D. W., "Three-Dimensional, Primitive-Variable Model for Solid-Fuel Ramjet Combustion," *Journal of Spacecraft and Rockets*, Vol. 23, No. 1, January-February, 1986, pp. 113-117.

23. DiRosa, M. D., *Air Supply and Storage Facility Design and Description*, M.S. Paper, The Pennsylvania State University, 1988, University Park, PA.

24. Chen, D. M., "Pyrolysis, Ignition and Combustion of Solid Fuels for Ramjet Applications," Ph.D. Thesis, The Pennsylvania State University, 1988, pp. 104-105.

25. Faeth, G. M., "Status of Boron Combustion Research," Report of the Boron Combustion Specialists Workshop, Air Force Office of Scientific Research, October, 1984.

26. Marquardt, D. W., "An Algorithm for Least-Squares Estimation of Nonlinear Parameters," *Journal of the Society for Industrial and Applied Mathematics*, Vol. 11, No. 2, 1963, pp. 431-441.

27. Natan, B, and Gany, A., "Ignition and Combustion Characteristics of Individual Boron Particles in the Flowfield of a Solid Fuel Ramjet," AIAA Paper 87-2034, AIAA/SAE/ASME/ASEE 23th Joint Propulsion Conference, 1987, San Diego, CA.

28. Sherwood, T. K., Pigford, R. L., and Wilke, C. R., *Mass Transfer*, McGraw-Hill Publishing Co., New York, NY, 1975.

29. Williams, F. A., *Combustion Theory*, 2nd Edition, Benjamin/Cummings Publishing Co., Menlo Park, CA, 1985, pp. 631-645.

30. McBride, B. J., and Gordon, S., "FORTRAN IV Program for Calculation of Thermodynamic Data," NASA TN D-4097, 1967.

31. Reid, R. C., Prausnitz, J. M., and Sherwood, T. K., *The Properties of Gases and Liquids*, 3rd Edition, McGraw-Hill Publishing Co., New York, NY, 1977.

32. Incropera, F. P. and DeWitt, D. P., *Fundamentals of Heat and Mass Transfer*, 2nd Ed., John Wiley and Sons, NY, 1985, pp. 657-661.

33. Baldwin, B. S., and Lomax, H., "Thin Layer Approximation and Algebraic Model for Separated Turbulent Flows," AIAA Paper 78-257, 16th Aerospace Sciences Meeting, Jan. 16-18, 1978, Huntsville, Alabama.

34. Yam, C., and Dwyer, H., "Investigation of the Influence of Blowing and Combustion on Turbulent Wall Boundary Layers," *AIAA Journal*, Vol. 27, No. 3, March 1989, pp. 370-372.

35. Westbrook, C. K., and Dryer, F. L., "Simplified Reaction Mechanisms for the Oxidation of Hydrocarbon Fuels in Flames," *Combustion Science and Technology*, Vol. 27, 1981, pp. 31-43.

36. Dryer, F. L., and Glassman, I., "High-Temperature Oxidation of CO and CH_4," *Fourteenth Symposium (International) on Combustion*, The Combustion Institute, Pittsburgh, p. 987.

37. King, M. K., "Modification of Boron Ignition Model to Include Recent Liquid Boron Oxide – Water Gas Kinetics," 26th JANNAF Combustion Meeting, Pasadena, CA, 1989, CPIA Publication 529, Vol. I, Johns Hopkins University, Laurel, MD, pp. 203-211.

38. Bird, R. B., Stewart, W. E., and Lightfoot, F. N., *Transport Phenomena*, John Wiley and Sons, New York, 1960.

39. Kuo, K. K., *Principles of Combustion*, John Wiley and Sons, New York, 1986, p. 579.

40. Shuen, J. S., "A Theoretical and Experimental Investigation of Dilute Particle-Laden Turbulent Gas Jets," Ph. D. Thesis, The Pennsylvania State University, 1984, University Park, PA, pp. 26-29.

41. Hinze, J. O., *Turbulence*, McGraw-Hill, New York, 2nd ed., 1976, pp. 639-640.

42. Tseng, I. S., *Velocity-Coupled Combustion Instabilities in Solid-Propellant Rocket Motors*, Ph.D. Thesis, The Pennsylvania State University, 1991, University Park, PA.

43. Yoon, S., and Jameson, A., "An LU-SSOR Scheme for the Euler and Navier-Stokes Equations," AIAA Paper 87-0600, 25th Aerospace Sciences Meeting, Jan. 12-15, 1987, Reno, Nevada.

44. Jameson, A., and Yoon, S., "Lower-Upper Implicit Schemes with Multiple Grids for the Euler Equations," *AIAA Journal*, Vol. 25, No. 7, July 1987, pp. 929-935.

45. Shuen, J. S., and Yoon, S., "A Numerical Study of Chemically Reacting Flows Using an LU-SSOR Scheme," AIAA Paper 88-0436, 26th Aerospace Sciences Meeting, Jan. 11-14, 1988, Reno, Nevada.

46. Hornbeck, R. W., *Numerical Methods*, Prentice-Hall Inc., Chapter 5, 1975.

47. Cohen, N. S., Fleming, R. W., and Derr, R. L., "Role of Binders in Solid Propellant Combustion," *AIAA Journal*, Vol. 12, No. 2, Feb. 1974, pp. 212-218.

48. Ericsson, I., "Sequential Pyrolysis Gas Chromatographic Study of the Decomposition Kinetics of Cis-1,4-Polybutadiene," *Journal of Chromatographic Science*, Vol. 16, 1978, pp. 340-344.

49. Brazier, D. W., and Schwartz, N. V., "The Effect of Heating Rate on the Thermal Degradation of Polybutadiene," *Journal of Applied Polymer Science*, Vol. 22, 1978, pp. 113-124.

VITA

Taras Andrew Jarymowycz was born in Philadelphia, PA, on November 1, 1963. He graduated from Central High School in Philadelphia, PA, in June of 1981. Taras received his B.S. degree in Mechanical Engineering from Drexel University in Philadelphia in June of 1986. As part of his undergraduate education, he was employed at the Naval Air Propulsion Center in Trenton, NJ. In the summer of 1990, Taras received his Master's Degree in Mechanical Engineering from Penn State. He is a member of the American Institute of Aeronautics and Astronautics and the American Society of Mechanical Engineers.

ANALYSIS OF BORON PARTICLE IGNITION ABOVE A BURNING SOLID FUEL IN A HIGH-VELOCITY ENVIRONMENT

T. A. Jarymowycz, V. Yang, K. K. Kuo
Department of Mechanical Engineering
The Pennsylvania State University
University Park, PA 16802

ABSTRACT

The ignition processes of boron particles above a burning solid fuel have been studied by numerical solution of a comprehensive theoretical model. The gas-phase formulation is based on the time-dependent multi-dimensional compressible Navier-Stokes equations and species transport equations. The particle-phase solution is obtained using a well-established boron particle ignition model. Boron particles are ejected from the surface of the burning fuel into a high-velocity crossflow and their trajectories are traced through the reacting flowfield using a Stochastic Separated Flow approach. The effects of particle size on their ignition time and location are determined. Results indicate that small particles ($d < 3\mu m$) ignite as soon as they pass through the gas-phase reaction zone and come in contact with oxygen. Larger particles ignite further downstream, since they require more energy to remove their oxide layers and achieve thermal runaway. The effects of ambient conditions on the ignition times are also investigated. The study shows that minimization of ignition time can be accomplished by optimizing the environmental conditions during the ignition process.

1. INTRODUCTION

The high volumetric energy density of boron makes it an attractive candidate as a solid-fuel component for volume-limited propulsion systems. For effective utilization, boron particles must ignite and completely burn within the allowed residence time of a combustion chamber. However, since inhibitive boron-oxide layers usually surround these particles, ignition and subsequent combustion are often delayed, thereby hindering the performance of boron-laden fuels. Unless the operating environment is suited toward minimizing the ignition and combustion times, or manufacturing techniques are developed to minimize the particle size and oxide layer-effect, boron-containing fuels cannot perform at the desired levels.

To understand some of the difficulties associated with the combustion of boron particles, the ignition and burning processes of individual boron particles have been studied both experimentally and theoretically. Macek (1969) determined the burning times of crystalline boron particles with average diameters of 35 and 44 microns in a hot, oxidizing gas stream at atmospheric pressure. The combustion of boron particles was observed to occur in two successive stages, the first being an ignition

stage during which the boron oxide layer is consumed from the surface. Ignition was then followed by a combustion stage in which the boron particle burned vigorously with ambient oxidizer. Burning times were found to decrease with increases in incoming gas temperature and mole fraction of oxygen in the gas. Addition of water vapor to the surrounding gas was shown to decrease the burning times dramatically. Further works by Macek (1971, 1972) provided a substantial data base for particle sizes of 37 to 125 microns in diameter, in pressures from 0.17 to 35.0 atm with a range of oxygen mole fractions from 0.1 to 1.0. For higher values of the diameter (d), pressure (p) and oxygen mole fraction (X_{O_2}), the burning times were found to be inversely proportional to X_{O_2}, directly proportional to d^2 and independent of p. The burning times deviated from these scaling laws at low values of d, p, and X_{O_2}.

Results from these studies were compared with the predictions of an ignition model by King (1972), which described the ignition event in terms of the physical and chemical processes involved in removing the oxide layer from the surface of the particle. Ignition times decreased with increasing initial particle temperature for large particles with radii greater than 10 microns. Decreasing the oxygen partial pressure increased the minimum ambient temperature required for ignition and the total ignition time of the particles. Further refinements of this numerical model proposed by King (1974, 1982a, 1982b, 1989) attempted to fully describe the fundamental heat and mass transfer processes surrounding the particle, including the effects of radiation, oxide-layer thickness, water vapor and oxygen mole fractions in the ambient gas. Comparison of model predictions with the data of Macek (1969) were quite reasonable. The ignition model was then linked with a combustion model (King, 1983) for clean boron particles under kinetic- or diffusion-limited conditions, thereby resulting in a unified model for boron particles. The combustion stage is diffusion-controlled for large particles and kinetics-controlled for small particles, with transition in the region from 15-30 microns in diameter, depending on the ambient pressure.

Mohan and Williams (1972) also studied the ignition and combustion of laser-ignited boron particles in the 100 micron diameter range. A diffusion-controlled droplet burning equation was applied to the combustion stage and agreement was attained between theory and experiment. However, the application of this model is limited to high-temperature
(T > 2300 K), dry environments in which the particle diameters are greater than approximately 40 microns and the burning is diffusion-controlled.

Because of the important role which boron oxide (B_2O_3) plays in the ignition process, the gasification process of B_2O_3 drops was studied in wet and dry oxidizing environments (Turns et al., 1985). Drops with 1000 micron diameters were examined under freestream gas temperatures from 1500-1975 K at atmospheric pressure. Large variations in ambient oxygen concentration produced little or no effect in the droplet lifetimes, whereas the presence of water vapor in the ambient gas significantly increased the gasification rate of the particles. A diffusion-limited equilibrium model provided agreement between oxide drop-life histories and experimental data for particles with temperatures greater than 1350 K.

Recent experimental studies in boron-based solid fuel combustion have focused on the effect of boron loading on regression rate and combustion efficiency. Snyder et al. (1990) studied the effects of boron percentage on the burning rates of hydroxyl terminated polybutadiene (HTPB) solid fuels by adding small fractions of boron powders to enhance the ignition and combustion characteristics of the fuel samples. Regression rates were found to increase with boron addition up to 10 percent, but further addition of boron caused the fuel regression rates to decrease. Pein and Vinnemeier (1989) noted similar effects on specific thrust at a boron loading of 20 percent. Specific thrust increased with boron loading to 20 percent; however

further addition of boron hampered combustion efficiency and decreased specific thrust. This decrease in may be attributed to (1) the heat-sink effect associated with unignited boron particles in the gas phase which reduced the gas-phase temperature, (2) shielding of heat feedback to the surface by a large number of boron particles above the surface, (3) reduced pyrolysis caused by the accumulation of unreacted boron particles on the surface, and (4) decreased gas-phase reactions due to the smaller percentage of HTPB contained in the sample.

Jarymowycz et al. (1990b) also studied the effect of boron on the ignition and combustion behavior of solid fuels under high-velocity crossflows. The addition of boron decreased the minimum freestream temperature required for ignition, since reacting particles on the sample surface acted as a local heat source for igniting the fuel sample. The dependence of regression rate on temperature also increased with boron addition due to the enhanced radiative and convective heat feedback from the particle-phase reactions at elevated temperatures.

To better understand some of the complex two-phase phenomena occurring above a reacting boron-laden solid fuel, a numerical study was conducted to determine the ignition behavior of individual boron particles in a ramjet environment. The approach presented herein should furnish a more realistic indication of the varying conditions surrounding a particle as it travels through a turbulent reacting flowfield into an oxidizing core region. The specific objectives of this study are:
1. to study the ignition process of individual boron particles ejected from a reacting solid fuel under a high-velocity crossflow,
2. to determine the effect of particle size on the ignition time and location of the particles,
3. to investigate the effects of freestream parameters, including pressure and temperature on the ignitability of the boron particle, and
4. to investigate the possibility of an optimum particle size for minimizing the ignition delay time.

This type of particle trajectory analysis has been performed by Natan and Gany (1987) in a low-speed environment with Mach numbers less than 0.1 and particle sizes greater than 25 microns in diameter. This work considers much smaller particle sizes on the order of 5 microns in a high-velocity environment ($M > 0.8$). Because of the small particle size, the turbulence effect on dispersion of the particle trajectories is also included.

2. THEORETICAL FORMULATION

The physical geometry considered in the analysis is shown in Fig. 1. A uniform supersonic air flow enters a two-dimensional chamber in which a solid-fuel sample pyrolyzes and reacts with the ram air in the gas phase. To facilitate formulation, the gas phase, solid fuel, and boron particles are treated separately. The gas and solid phases are linked together through the balance of mass and energy fluxes at their interface. In order to achieve steady-state conditions in the gas phase and at the fuel boundary, the fuel is fed at a rate of r_b equal to the local burning rate, which keeps the surface of the burning sample stationary. A single boron particle is then ejected from the fuel surface into the surrounding gas, and tracked through the turbulent flowfield to the exit of the chamber. The instantaneous gas properties surrounding the particle are incorporated into the boron particle ignition model, but mass and energy fluxes from the particle are not included in the gas-phase solution since the effect of an individual particle on the flowfield is minimal. The gaseous flowfield is therefore decoupled from the influence of the particle. This assumption is justified for two-phase flowfields with high void fractions

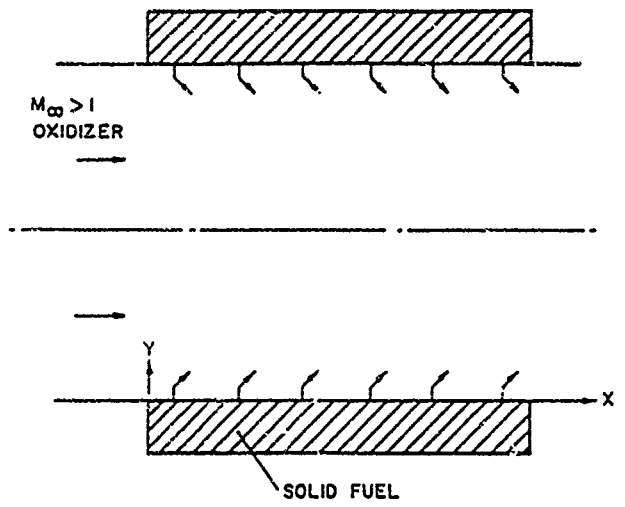


FIGURE 1. Physical Geometry of Two-Dimensional Combustion Chamber

In the following formulation, equations governing the gas phase and solid fuel are given first. Afterwards, the boron particle ignition model is summarized along with the particle-tracking equations.

2.1 Gas-Phase Analysis

The gas-phase analysis is based on the Favre-averaged conservation equations of mass, momentum, energy, and species transport for a multicomponent system in Cartesian coordinates. They can be written conveniently in the vector form

$$\frac{\partial Q}{\partial t} + \frac{\partial E}{\partial x} + \frac{\partial F}{\partial y} = \frac{\partial E_v}{\partial x} + \frac{\partial F_v}{\partial y} + H \tag{1}$$

where

$$Q \equiv \left[\bar{\rho}_g,\ \bar{\rho}_g\tilde{u},\ \bar{\rho}_g\tilde{v},\ \bar{\rho}_g\tilde{e},\ \bar{\rho}_g\tilde{Y}_i\right]^T$$

$$E \equiv \left[\bar{\rho}_g\tilde{u},\ \bar{\rho}_g\tilde{u}^2 + \bar{p},\ \bar{\rho}_g\tilde{u}\tilde{v},\ \tilde{u}\left(\bar{\rho}_g\tilde{e} + \bar{p}\right),\ \bar{\rho}_g\tilde{u}\tilde{Y}_i\right]^T$$

$$F \equiv \left[\bar{\rho}_g\tilde{v},\ \bar{\rho}_g\tilde{u}\tilde{v},\ \bar{\rho}_g\tilde{v}^2 + \bar{p},\ \tilde{v}\left(\bar{\rho}_g\tilde{e} + \bar{p}\right),\ \bar{\rho}_g\tilde{v}\tilde{Y}_i\right]^T$$

$$E_v \equiv \left[0,\ \bar{\tau}_{xx},\ \bar{\tau}_{xy},\ \tilde{u}\bar{\tau}_{xx} + \tilde{v}\bar{\tau}_{xy} - \bar{q}_x,\ -\bar{\rho}_g\tilde{U}_i\tilde{Y}_i\right]^T$$

$$F_v \equiv \left[0,\ \bar{\tau}_{xy},\ \bar{\tau}_{yy},\ \tilde{u}\bar{\tau}_{xy} + \tilde{v}\bar{\tau}_{yy} - \bar{q}_y,\ -\bar{\rho}_g\tilde{V}_i\tilde{Y}_i\right]^T$$

$$H \equiv \left[0,\ 0,\ 0,\ 0,\ \bar{\omega}_i\right]^T$$

for $i = 1, 2, \ldots$ N-1, with N being the total number of species considered. The diffusion terms in E_v and F_v are defined as

$$\bar{\tau}_{xx} = 2\mu_{eff}\frac{\partial\tilde{u}}{\partial x} - \frac{2}{3}\mu_{eff}\left(\frac{\partial\tilde{u}}{\partial x} + \frac{\partial\tilde{v}}{\partial y}\right) \tag{2}$$

$$\tilde{\tau}_{xy} = \mu_{eff}\left(\frac{\partial \tilde{u}}{\partial y} + \frac{\partial \tilde{v}}{\partial x}\right) \tag{3}$$

$$\tilde{\tau}_{yy} = 2\mu_{eff}\frac{\partial \tilde{v}}{\partial y} - \frac{2}{3}\mu_{eff}\left(\frac{\partial \tilde{u}}{\partial x} + \frac{\partial \tilde{v}}{\partial y}\right) \tag{4}$$

$$\tilde{q}_x = -\lambda_{eff}\frac{\partial \tilde{T}}{\partial x} + \bar{\rho}_g \sum_{i=1}^{N} \tilde{h}_i \tilde{Y}_i \tilde{U}_i \tag{5}$$

$$\tilde{q}_y = -\lambda_{eff}\frac{\partial \tilde{T}}{\partial y} + \bar{\rho}_g \sum_{i=1}^{N} \tilde{h}_i \tilde{Y}_i \tilde{V}_i \tag{6}$$

where $\tilde{U}_i$ and $\tilde{V}_i$ stand for the diffusion velocities and are determined by Fick's law. The effective transport properties μ_{eff} and λ_{eff} contain contributions from both the laminar and turbulent diffusion processes. Full account is taken of the variation of specific heat with temperature, giving the static enthalpy as

$$h_i = \int_{T_{ref}}^{T} c_{p,i}\, dT + h^o_{f,i} \tag{7}$$

where $h^o_{f,i}$ is the enthalpy of formation. Consequently, the specific total internal energy e becomes

$$e = \sum_{i=1}^{N} Y_i h_i - \frac{p}{\rho_g} + \frac{1}{2}\left(u^2 + v^2\right) \tag{8}$$

Finally, the equation of state determines the pressure from the temperature, density, and species mass fractions.

$$p = \rho_g R_u T \sum_{i=1}^{N} \frac{Y_i}{M_i} \tag{9}$$

The binary mass diffusivity, D_{ij}, is determined using the Chapman-Enskog theory along with the Lennard-Jones intermolecular potential-energy functions (Sherwood et al., 1975). The effective diffusivity is then calculated through the following formula (Williams, 1985).

$$D_{im} = \frac{1 - X_i}{\sum_{j=1}^{N} X_j / D_{ij}} \quad for\ i \neq j, \tag{10}$$

where X_i is the molar fraction of species i.

Thermodynamic and other transport properties of each constituent species are evaluated using fourth-order polynomials of temperature (McBride and Gordon, 1967)

which are valid for the range from 300 to 5000 K. For a mixture, specific heat is determined by mass-concentration weighing of each species; viscosity and thermal conductivity are calculated using Wilke's mixing rule (Reid et al., 1987).

2.2 Solid-Fuel Analysis

If we ignore the bulk motion, subsurface chemical reaction, and axial thermal diffusion, the equation governing the solid-fuel sample reduces to a one-dimensional heat conduction equation for each axial station. Under steady-state conditions, this equation takes the form

$$\frac{d}{dy}\left(\lambda_s \frac{dT_s}{dy}\right) - \rho_s r_b \frac{d}{dy}\left[c_{p,s}(T_s - T_{s,ref}) + h^o_{f,s}\right] = 0 \tag{11}$$

subject to the boundary conditions

$$T_s = T_o \quad \text{as} \quad y \to -\infty$$
$$T_s = T_{sur} \quad \text{at} \quad y = 0$$

where the subscript "s" denotes the properties of the solid phase. Since the thermophysical properties of most solid fuels are not well characterized with respect to temperature, these properties are treated as constants. For solid fuels, the condensed-phase reactions such as thermal decomposition usually occur in a very thin layer immediately beneath the surface (about several hundred microns). This effect can be incorporated in the gas-solid interface conditions to simplify the analysis. Integration of Eq. (11) yields the steady-state temperature distribution at a given axial location in the solid phase.

$$T_s = T_o + (T_{sur} - T_o)\, exp\left(\frac{\rho_s r_b c_{p,s}}{\lambda_s} y\right) \tag{12}$$

Since the ejection of an individual boron particle is addressed in this work, the effect of a single particle on the properties of the solid fuel is negligible. In the event that a high loading of particles is treated in a future study, then fuel properties should be modified accordingly.

2.3 Boundary Conditions

The heat and mass transfer processes between the gas and condensed phases must be matched at the fuel surface to provide the necessary interface conditions for both phases. This procedure will eventually determine the temperature, regression rate, and species concentrations at the surface. With some straightforward manipulation, the matching conditions are as follows.

Mass

$$\rho_s r_b = \rho_g v_g|_+ \tag{13}$$

Species Mass Fraction

$$\rho_s r_b Y_i|_- = \rho_g v_g Y_i|_+ - \rho_g D_{im} \frac{\partial Y_i}{\partial y}|_+ \tag{14}$$

Energy

$$-\lambda_s \frac{\partial T}{\partial y}|_- + \rho_s r_b \left(\int_{T_{ref}}^{T_{sur}} c_{p,s} dT + h^o_{f,s} \right) =$$

$$-\lambda_g \frac{\partial T}{\partial y}|_+ + \rho_g \sum_{i=1}^{N} Y_i h_i \left(v_g - \frac{D_{im}}{Y_i} \frac{\partial Y_i}{\partial y} \right)|_+ - q_{rad} \tag{15}$$

where "+" and "–" represent, respectively, the conditions immediately above and below the surface. It is worth mentioning that h_i contains both the sensible and chemical enthalpies of the gaseous species. The difference in enthalpy across the interface accounts for the latent heat of gasification and chemical energy release associated with the thermal decomposition immediately beneath the solid-fuel surface. The pyrolysis rate of solid fuel is evaluated using a zeroth-order Arrhenius expression.

$$r_b = \frac{A_s}{\rho_s} exp\left(\frac{-E_a}{R_u T_{sur}} \right) \tag{16}$$

where A_s is the pre-exponential factor, ρ_s the fuel density, E_a the activation energy, and T_{sur} the surface temperature. Radiant heat transfer to the surface due to emission from the gas phase is calculated using a Stefan-Boltzmann relation in terms of the averaged gas-phase temperature. The total gas emissivity is estimated using a method developed by Hottel (Incropera and DeWitt, 1985), and is a function of the species mole fractions, gas-phase temperature, pressure, and mean beam length. Again, since only an individual particle is addressed here, the incorporation of a boron particle into the gas/solid interface conditions is neglected.

The flow at the upstream boundary is supersonic, with pre-specified temperature, pressure, Mach number, and species mass fraction. The inlet velocity profile is assumed to be uniform in the y-direction, and has no vertical velocity component. Since the flow at the downstream boundary is also supersonic, all of the exit conditions are extrapolated from their counterparts within the combustion chamber. However, in the event that the flow at the exit is subsonic (i.e. due to shock waves), the static pressure may be specified as an additional boundary condition. The upper boundary is taken to be a line of symmetry. Therefore, the vertical velocity component and the derivatives of all the other dependent variables across the boundary are set to zero. The no-slip condition is employed at the surface of the fuel sample.

2.4 Turbulence Model

The Baldwin-Lomax algebraic model (Baldwin et al., 1978) along with constant turbulent Prandtl and Schmidt numbers ($Pr_t = Sc_t = 0.9$) are chosen to achieve the turbulence closure because of their computational efficiency and simplicity. This algebraic model calculates the turbulent eddy viscosity, using the Prandtl-Van Driest

formulation and the local vorticity distribution for the near-wall and outer regions, respectively.

2.5 Gas-Phase Combustion Model

For combustion of gaseous hydrocarbon fuels with oxygen, Westbrook and Dryer (1981) suggested a simplified two-step reaction mechanism that reasonably predicts reaction rates for a large number of hydrocarbons over a wide range of equivalence ratios and pressures.

$$C_nH_m + \left(\frac{n}{2} + \frac{m}{4}\right) O_2 \rightarrow nCO + \frac{m}{2}H_2O \tag{17}$$

$$CO + \frac{1}{2}O_2 \rightleftharpoons CO_2 \tag{18}$$

This two-step mechanism is adopted without the reverse reaction of Eq.(18) since its reaction rate is slower than the forward reaction by six orders of magnitude, and in light of the short residence time of the flowfield, it has little effect on the overall kinetics. Equations (17) and (18) are satisfactory expressions for the gas-phase reactions, provided the flame temperature is not high enough to promote dissociation to free radical species such as H, O, and OH. For flame temperatures above 3000 K, a multi-step mechanism will be recommended to account for dissociation.

The production rates of the species are

$$\bar{\omega}_{fu} = -M_{fu}A_{fu}\,exp\left(\frac{-E_{fu}}{R_uT}\right) C_{fu}^a\, C_{O_2}^b \tag{19}$$

and

$$\bar{\omega}_{CO} = nM_{CO}A_{fu}\,exp\left(\frac{-E_{fu}}{R_uT}\right) C_{fu}^a\, C_{O_2}^b$$

$$-M_{CO}A_{CO}\,exp\left(\frac{-E_{CO}}{R_uT}\right) C_{CO}\, C_{H_2O}^{\frac{1}{2}}\, C_{O_2}^{\frac{1}{4}} \tag{20}$$

where the subscript fu represents the fuel species, and the factors a and b are dependent on the type of fuel species considered. The source term for each of the remaining species is similarly determined. Nitrogen is also considered since air is the oxidizer; however, it is treated as inert with a production rate of zero. In summary, N-1 species conservation equations and one algebraic expression relating these species to nitrogen are solved.

In this study, multiplicative effects between chemical kinetics and turbulence are not included. This is justified due to the lack of experimental or analytical information in the area of supersonic reacting flows. A much more comprehensive treatment is required to fully account for these interactions.

2.6 Boron Particle Analysis

The ignition of the boron particle is treated according to the model of King (1982a) with the most recent modifications (King, 1982b, 1989). This model assumes a

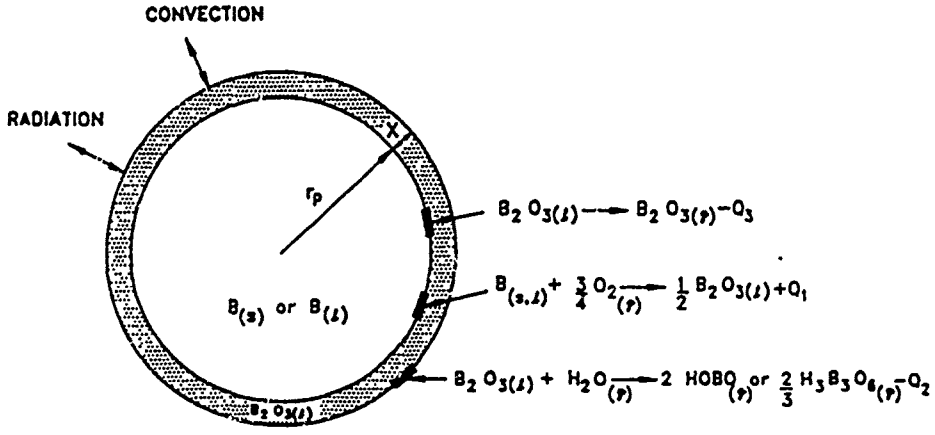


FIGURE 2. Boron Particle Ignition Model Processes

particle radius of r_p with an initial boron oxide layer thickness X surrounding the particle (see Fig. 2). Convective and radiative heat transfer to the particle begin to liquify and evaporate the oxide layer, while oxygen and water vapor diffuse through the layer to react with boron and raise the temperature of the particle. Additional surface reactions of water vapor with the oxide layer further aid in the removal of the oxide. Provided that the heat transfer to the particle is high enough to promote the complete removal of oxide and the melting of the particle, thermal runaway should occur. If the surrounding temperature is too low, or if the oxygen concentration is not high enough to allow sufficient exothermic reactions with boron, the particle will not ignite. The equations for the rate of change of particle radius and oxide thickness based on the processes discussed above are as follows.

$$\frac{dr_p}{dt} = -\frac{R_B M_B}{\rho_B} \tag{21}$$

where R_B is the molar consumption rate of boron per unit area due to the reaction with O_2.

$$\frac{dX}{dt} = \frac{\left(\frac{R_B}{2} - R_H - R_E\right) M_{B_2O_3}}{\rho_{B_2O_3}} \tag{22}$$

R_H is the molar removal rate of B_2O_3 per unit area due to reaction with H_2O, and R_E is the molar evaporation rate of B_2O_3 per unit area. The energy equation for the particle at the bulk temperature of T_p is given as

$$\frac{dH}{dt} = 4\pi r_p^2 \left(R_B Q_1 - R_H Q_2 - R_E Q_3 + h(T_g - T_p) + \sigma \epsilon_B \left(T_{amb}^4 - T_p^4\right)\right) \tag{23}$$

where Q_1 is the heat of reaction of the solid or liquid boron with oxygen, and Q_2 is the endothermic heat of reaction of water vapor with boron oxide which depends on the resulting product (either HOBO or $H_3B_3O_6$). For gas temperatures below 1400 K, the product is solely $H_3B_3O_6$, whereas above 2000 K the result is HOBO; at intermediate temperatures there is a product mix. In this study, HOBO was used

as the reaction product, since the surrounding temperatures were greater than 2000 K. Q_3 in Eq. (23) represents the heat of vaporization of $B_2O_{3(l)}$. An additional water vapor reaction with $B_{(s)}$ and $B_2O_{3(l)}$

$$H_2O_{(g)} + \frac{4}{3}B_{(s,l)} + \frac{1}{2}B_2O_{3(l)} \rightarrow \frac{2}{3}H_3B_3O_{3(l)} \tag{24}$$

may be included in the ignition model; however, this reaction does not affect the ignition times in mixed O_2/H_2O atmospheres (King, 1982b) and is therefore neglected here.

The convective heat-transfer coefficient is calculated by the product of the Nusselt number (obtained from Bird et al., 1960) and thermal conductivity of the gas phase divided by the particle diameter, where

$$Nu = 2.0 + 0.60 Re_d^{\frac{1}{2}} \tag{25}$$

$$\text{and} \qquad Re_d = \frac{2r_p |u_g - u_p| \rho_g}{\mu}. \tag{26}$$

Equations describing the rate of change of the particle bulk temperature and the fraction of boron melted are given below.

$$\frac{dT_p}{dt} = \frac{\frac{dH}{dt}}{\frac{4}{3}\pi r_p^3 \rho_B c_{pB(s)} + 4\pi r_p^2 X \rho_{B_2O_3} c_{pB_2O_3}} \qquad \text{for} \quad T_p < T_{melt} \tag{27a}$$

$$\frac{dT_p}{dt} = \frac{\frac{dH}{dt}}{\frac{4}{3}\pi r_p^3 \rho_B c_{pB(l)} + 4\pi r_p^2 X \rho_{B_2O_3} c_{pB_2O_3}} \qquad \text{for} \quad T_p > T_{melt} \tag{27b}$$

$$\frac{df}{dt} = \frac{\frac{dH}{dt}}{\frac{4}{3}\pi r_p^3 \rho_B Q_{melt}} \qquad \text{for} \quad T_p = T_{melt} \tag{28}$$

where T_{melt} is the boron melting temperature of 2450 K and Q_{melt} is the heat of fusion of boron.

The molar rate of conversion of boron to boron oxide incorporates several series resistances: the diffusion of oxygen through the surrounding gas to the outer surface of the oxide layer, the dissolving of oxygen within boron oxide, the diffusion of oxygen across the molten oxide layer to the B/B_2O_3 interface, and the resulting kinetics of the reaction at that interface. Details of the origin of the expression for R_B are given by King (1982b) and the resulting equation is given below.

$$R_B = \frac{p_{O_2}}{\frac{1}{f_1} + \frac{X}{f_2} + \frac{1}{f_3}} \tag{29}$$

$$\text{where} \qquad f_1 = 3.89 \exp\left(-\frac{1700}{T_p}\right) \tag{30}$$

$$f_2 = 7.0 \times 10^{-8} \exp\left(-\frac{9800}{T_p}\right) \tag{31}$$

$$f_3 = \frac{4.68 \times 10^{-4} T_g^{\frac{1}{2}} Nu}{r_p p} \tag{32}$$

The following units are used in Eqns. (29-34): R_B (kg-mole/m^2/sec), p (atm), r_p (m), X (m), T (K), f_1 and f_3 (kg-mole/m^2/atm/sec), and f_2 (kg-mole/m/atm/sec). The evaporation rate of B_2O_3 liquid contains two series resistances: evaporation kinetics and the diffusion of B_2O_3 gas away from the particle. Derivation of the expression for R_E can be found in King (1974).

$$R_E = \frac{8 \times 10^9 \ \alpha \ exp\left(-\frac{44000}{T_p}\right)}{T_p^{0.5}\left(1 + \frac{4.5 \times 10^9 \alpha r_p p}{T_p N_2}\right)} \tag{33}$$

The rate of reaction of water vapor with boron oxide to produce HOBO was updated by King (1989).

$$R_H = \frac{1.816 \times 10^5}{T_p} exp\left(-\frac{16900}{T_p}\right) p_{H_2O} \tag{34}$$

where p_{H_2O} is the partial pressure of water vapor.

To track the particles through the flowfield, Lagrangian equations of motion are solved. The calculations assume that the particle is spherical, and the effects of static pressure gradients, virtual mass, and Basset forces (deviation from steady flow pattern around the sphere) are negligible. The resulting momentum equations consider the drag force on the sphere, which contains both the skin friction and form drag, and the body force in the vertical direction.

$$\frac{du_p}{dt} = \frac{3C_D\rho_g}{8r_p\rho_p}(u_g - u_p)\,|u_g - u_p| \tag{35}$$

$$\frac{dv_p}{dt} = \frac{3C_D\rho_g}{8r_p\rho_p}(v_g - v_p)\,|v_g - v_p| + g \tag{36}$$

The drag coefficients are approximated as follows (Kuo, 1986).

$$C_D = \frac{24}{Re_d}\left(1 + \frac{Re_d^{\frac{2}{3}}}{6}\right) \qquad \text{for} \quad Re_d \leq 1000 \tag{37}$$

$$C_D = 0.44 \qquad \text{for} \quad Re_d > 1000 \tag{38}$$

The position of the particle is determined by integrating the equations below.

$$\frac{dx}{dt} = u_p \tag{39}$$

$$\frac{dy}{dt} = v_p \tag{40}$$

The effects of dispersion on the particle trajectories should also be considered, since the particles are small and their paths are influenced by turbulent fluctuations in

the flowfield. To incorporate these effects, the Stochastic Separated Flow (SSF) model for spray combustion is utilized (Shuen, 1984). The SSF model involves finding the trajectories of a statistically significant number of individual particles ejected from the fuel sample into a flowfield containing a random distribution of turbulent eddies. For each eddy, the translational velocity of the bulk motion of the gas phase is considered uniform, but this property changes randomly from one eddy to the next. Changes in particle trajectories are observed by substituting the instantaneous velocities of the eddies into Eqs. (35) and (36). Specification of eddy properties and the interaction time between a particle and eddy are therefore crucial elements in this model, and they are summarized below.

The velocities of each eddy are determined at the start of the particle-eddy interaction by random sampling from the probability density function (PDF) of velocity. The velocities in the axial, vertical, and transverse directions are assumed to have normal distributions, with mean values of $\bar{u}$, $\bar{v}$, and 0, respectively. Velocity fluctuations in the axial direction have a magnitude of u', but because of anisotropic behavior near the wall, the magnitudes of fluctuations in the vertical and transverse directions are only fractions of u'(Hinze, 1975). For simplicity, they are approximated throughout the boundary layer region as

$$v' = \frac{1}{2}u' \tag{41}$$

$$w' = \frac{3}{4}u'. \tag{42}$$

The instantaneous velocities of the eddies in the x and y directions are $\bar{u} + \sigma u'$ and $\bar{v} + \sigma v'$, respectively, where σ is randomly sampled from a standard normal distribution.

The values for u' and v' cannot be obtained from the algebraic turbulence model. To solve for these turbulent fluctuations, the turbulent kinetic energy and eddy dissipation rate must first be found using the following equations.

$$U\frac{\partial k}{\partial x} + V\frac{\partial k}{\partial y} = \frac{\partial}{\partial y}\left[\frac{1}{\rho}\left(\mu + \frac{\mu_t}{\sigma_k}\right)\frac{\partial k}{\partial y}\right] + \frac{\mu_t}{\rho}\left(\frac{\partial U}{\partial y}\right)^2 - \epsilon \tag{43}$$

$$U\frac{\partial \epsilon}{\partial x} + V\frac{\partial \epsilon}{\partial y} = \frac{\partial}{\partial y}\left[\frac{1}{\rho}\left(\mu + \frac{\mu_t}{\sigma_\epsilon}\right)\frac{\partial \epsilon}{\partial y}\right] + c_1\frac{\epsilon}{k}\frac{\mu_t}{\rho}\left(\frac{\partial U}{\partial y}\right)^2 - c_2 f_2\frac{\epsilon^2}{k} + \frac{2\mu\mu_t}{\rho^2}\left(\frac{\partial^2 U}{\partial y^2}\right)^2 \tag{44}$$

where c_1 and c_2 are constants and f_2 is a function to modify c_2. The details of the formulation and solution to these equations are given in the thesis by Tseng (1991). Under isotropic conditions, turbulent fluctuations are equal in magnitude in all three dimensions. However, the conditions imposed here by Eqs. (41-42) result in $u' = (1.10\,k)^{\frac{1}{2}}$. Equation (41) is then employed to obtain v'.

A particle interacts with an eddy for a duration which is either the time required for the particle to traverse the eddy or the eddy lifetime. The eddy lifetime can be estimated from Shuen (1984) using

$$t_e = \frac{L_e}{\left(\frac{2}{3}k\right)^{\frac{1}{2}}} \tag{45}$$

in which L_e, the characteristic size of an eddy, is assumed to be the dissipation length scale.

$$L_s = \frac{C_\mu^{\frac{3}{4}} k^{\frac{3}{2}}}{\epsilon} \tag{46}$$

where $C_\mu = 0.09$. The time required for the particle to traverse the eddy is not directly calculated; however, the distance the particle travels within the eddy is continuously monitored such that it remains less than the eddy size. The particle/eddy interaction is terminated if (1) the distance the particle travels within the eddy $|\Delta x|$ is greater than the length scale of the eddy, or (2) the time of interaction (Δt) is greater than the eddy lifetime. These criteria are represented as follows.

$$|\Delta x| > L_s \quad , \quad \Delta t > t_e \tag{47}$$

Upon completion of the interaction, the particle then enters a new eddy with properties determined from another random sampling of the PDF. Mean dispersion rates of the particles are obtained by averaging over a statistically significant number of particle trajectories.

3. NUMERICAL METHOD

The theoretical formulation for the gas phase is solved using a numerical scheme based on the Lower-Upper Symmetric Successive Overrelaxation (LU-SSOR) technique (Yoon and Jameson, 1987, and Jameson and Yoon, 1987). This scheme solves the two- or three-dimensional Navier-Stokes equations and species transport equations by means of the finite-volume approach. It has proven to be very robust and efficient for highly reactive systems such as the combustion of hydrogen and oxygen. The algorithm was previously validated for supersonic mixing and reacting flows by comparing predicted results with both experimental results and other numerical calculations (Shuen and Yoon, 1989). A summary of the solution technique for this application is given in Jarymowycz et al. (1990a).

After the solution to the gas phase is attained, an individual boron particle is ejected from the solid fuel into the high-temperature flowfield. Local values of pressure, temperature, and species mass fractions are used for the conditions surrounding the particle. The equations governing the boron particle history are solved by a fourth-order Runge-Kutta scheme (Hornbeck, 1975). The time step for stable convergence of the continuity and energy equations is approximately 0.01 milliseconds; however, the time scales for the turbulent eddies are much smaller. For this reason, the eddy lifetimes are first determined, then one-fifth of t_e is utilized as the time step for the calculation. The particle trajectory is traced to the exit of the chamber, after which another particle is ejected from the same location as the first. The new particle is also traced to the exit of the combustion chamber, but due to the randomness of the turbulent fluctuations, the trajectory is different. The procedure is repeated 2000

times to achieve a statistically significant number of trajectories. The properties of the particles are recorded at three axial stations, at x = $\frac{1}{3}$L, $\frac{2}{3}$L, and L, where L is the length of the combustion chamber.

4. RESULTS AND DISCUSSION

4.1 Gas-Phase Solution

Calculations were performed with HTPB (hydroxyl-terminated polybutadiene) solid fuel samples located along the bottom surface of a 2-D chamber with an inlet height of 3.175 cm and a length of 15.24 cm, as shown in Fig. 1. The sample spans 7.62 cm along the lower boundary of the chamber, thus allowing space for chemical reactions downstream of the fuel. HTPB was chosen for this study because it has been characterized for its wide use in composite propellants (Cohen et al., 1974), and it is an energetic binder commonly found in solid fuels.

To facilitate the gas-phase analysis, it is assumed that butadiene (C_4H_6) is the only product released from the fuel surface. This simplification is justified for the following reasons. First, vinylcyclohexene, the second-most abundant pyrolysis product, (Ericsson, 1978, and Brazier and Schwartz, 1978) can be adequately represented by butadiene, since the monomer and dimer have similar molecular structures and kinetic parameters. Second, the majority of hydrocarbons tabulated in Westbrook and Dryer (1981) have equal activation energies and only a slight variation in pre-exponential factor. Thus, the consideration of additional fuel species would not alter the kinetic behavior of the gas phase. Finally, in the limit of fast kinetics with respect to the diffusion process, one hydrocarbon may be sufficient to represent the fuel species, and additional hydrocarbons would not change the fundamental characteristics of the sample. With the two-step reaction mechanism of Eqs. (17) and (18), the gas phase contains six species: C_4H_6, O_2, CO, H_2O, CO_2, and N_2. The rate constants for these reactions are given in Westbrook and Dryer (1981) and Dryer and Glassman (1972).

Each calculation employed a 120×80 grid. The numerical grid was uniform in the horizontal direction, with a spacing of 0.129 cm. Since many important physical processes occur in the region immediately above the sample surface, the numerical grid was clustered vertically near the surface, with the smallest grid measuring 45 microns in height. For each computation, the total mass flowrate of the ram air and pyrolyzed fuel was conserved to within 0.1% at the exit. The scheme required approximately 40 μsec of CPU time per iteration per grid point on a Cray Y-MP machine.

Figure 3 shows the contour plots for Mach number and static temperature with an inlet Mach number of 1.2, a static temperature of 2000 K, and static pressure of 2.5 atmospheres. Mach-number contours are incremented by 0.1 and temperature contours by 100 K. These figures show only the bottom 3 mm of the combustion chamber and have been magnified in the y-direction by a factor of twenty to resolve the flow structures nearest the surface. In Fig. 3a, an inlet shock occurs at the entrance due to the abrupt deceleration of the flow at the surface to satisfy the no-slip condition. This deceleration enhances temperature recovery and heat transfer at the surface. This shock decelerates the flow to a subsonic Mach number of 0.89, with corresponding increases in static temperature and pressure to 2100 K and 3.4 atm, respectively. Immediately downstream of the entrance, the temperature plot shows a series of closely spaced contours near the surface, indicating the leading edge of the flame with a maximum temperature of 3300 K. Although this temperature is

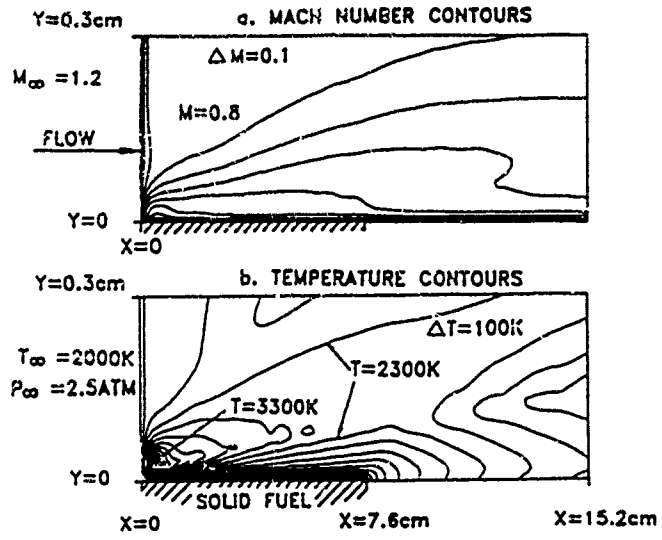


FIGURE 3. Mach Number and Temperature Contours; $M_\infty = 1.2$, $T_\infty = 2000$ K, $p_\infty = 2.5$ atm

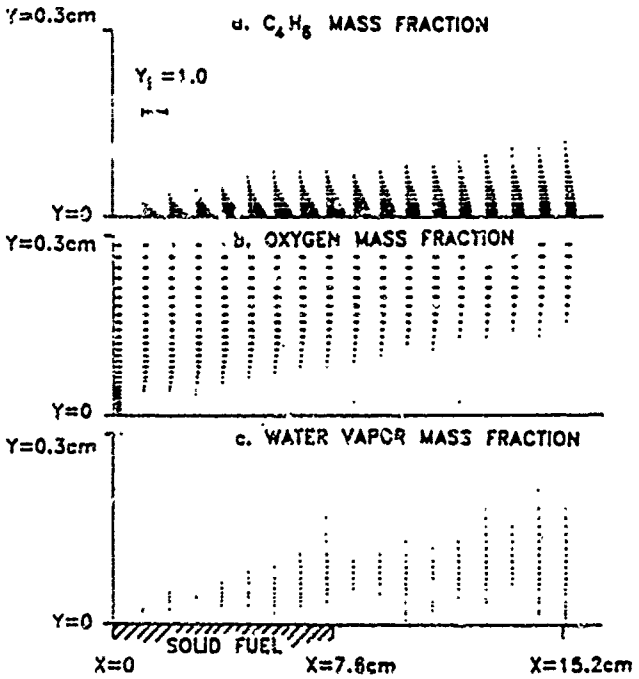


FIGURE 4. Species Mass Fractions; $M_\infty = 1.2$, $T_\infty = 2000$ K. $p_\infty = 2.5$ atm

high enough to promote dissociation, the high-temperature region is very small and it is unlikely that neglecting dissociation in this region would significantly affect the results from the particle-phase solution. Further downstream of the fuel sample, the temperatures are in the neighborhood of 2300 K.

The mass fractions of butadiene, oxygen, and water vapor are presented in Fig. 4. The fuel species are generated from the sample surface, then diffuse toward the freestream to mix and burn with oxygen. At the inlet to the chamber, the oxygen is uniformly distributed with a mass fraction of 0.23. It is then consumed by the chemical reaction which generates a maximum temperature of 3300 K, shown in Fig. 3b. The gas-phase temperature diminishes downstream of the T_{max} location because of heat transfer back to the fuel sample and a reduction in chemical heat release caused by an oxygen deficiency near the fuel surface. The maximum temperature at each axial station occurs in a region where mass fractions of oxygen and butadiene are near stoichiometric. The temperature then drops off from this region due to fuel-rich conditions toward the surface and oxygen-rich conditions toward the freestream. The vertical location of maximum temperature is determined by the rate of diffusion and blowing of pyrolyzed fuel-rich gases into the reacting boundary layer. Finally, the species distributions show incomplete consumption of butadiene at the exit along with the complete consumption of oxygen near the surface, which suggests that further entrainment of oxygen or perhaps better mixing between the fuel and oxidizer will improve combustion efficiency.

4.2 Particle Ignition Results

Preliminary calculations were performed with boron particles in quiescent surroundings in order to verify the operation of the numerical scheme, and to determine the approximate particle size which would most likely result in ignition within the confines of the combustion chamber. Typical results of such a calculation are shown in Fig. 5, where the particle temperature and oxide-layer thickness are plotted versus time. The initial particle radius is 2.5 microns with an oxide thickness of 0.03 microns, and initial temperature of 900 K. The ambient temperature, pressure, oxygen mole fraction and water vapor mole fraction are 2200 K, 2.5 atm, 0.21, and

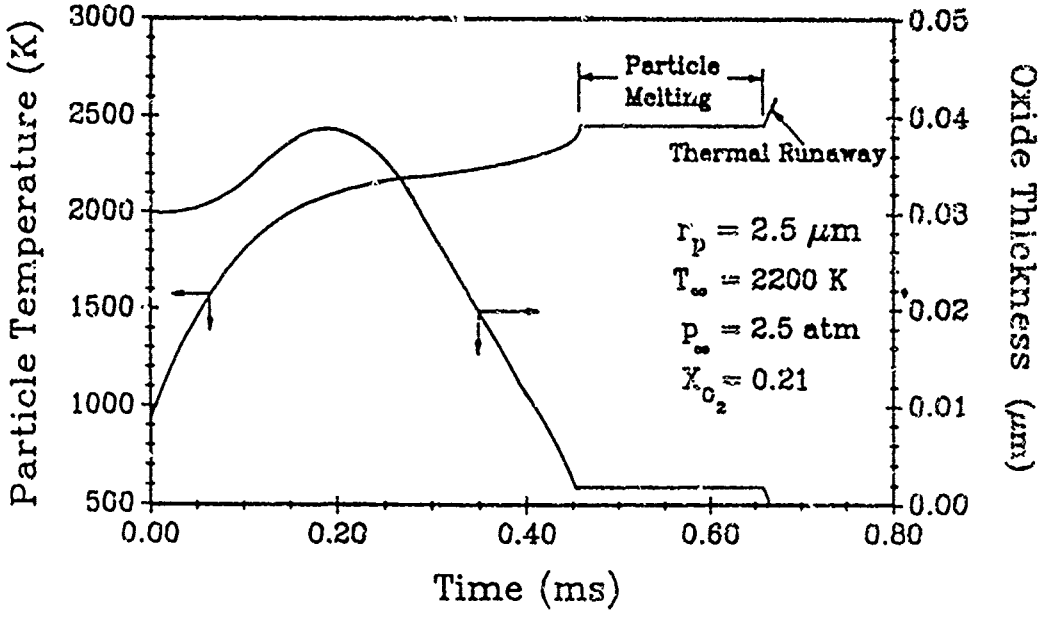


FIGURE 5. Histories of Particle Temperature and Oxide Layer Thickness

0.0, respectively. Figure 5 shows an abrupt increase in particle temperature within the first 0.2 ms due to convective heat transfer from the surroundings, then a gradual increase when the particle reaches the ambient temperature. While the particle temperature rises, the oxide layer thickens due to the diffusion of oxygen across the oxide layer to react with boron at the B/B_2O_3 interface. At a sufficiently high particle temperature (at t=0.18 ms), the evaporation rate of boron oxide begins to dominate over other modes of B_2O_3 generation, and the oxide layer becomes thinner. The particle temperature continues to slowly rise due to the self-heating from the interfacial reactions between B and O_2. Eventually, the particle temperature reaches 2450 K at t=0.45 ms and the boron particle begins to melt. After melting, the remaining oxide is quickly removed and thermal runaway occurs, resulting in full-fledged ignition of the particle at t= 0.66 ms. The change in the particle radius throughout the ignition event is almost negligible, with the radius at thermal runaway equal to 2.45 microns.

Choices in the initial conditions of the particle may have some bearing on the ignition time of the particle. The initial temperature of 900 K was based on the anticipated temperature of the particle when it is ejected from the solid fuel. A slight variation in this initial condition should have negligible effects, because the increase in particle temperature at the onset is very steep. The initial oxide thickness, on the other hand, may have some consequence on the final ignition time of the particle. According to previous studies (King, 1974), a five-fold increase in oxide thickness from 0.02 - 1.0 microns with a particle radius of 2.5 microns results in a fifty percent increase in ignition time. The value of 0.03 microns was chosen to keep the mass fraction of oxide below five percent of the total weight of the particle. This value was not varied in the remainder of the numerical cases studied, since the effect of the initial oxide thickness is already known.

Several key points should be addressed concerning the results from the previous example, keeping in mind that the following comments refer to dry oxidizing environments. First, the rise in particle temperature from the initial to the ambient temperature is predominantly due to convective heat transfer. The presence of oxygen during this short time has some adverse effect on the ignition process, since the oxygen mostly serves to thicken the oxide layer, thereby requiring additional time to eventually evaporate the thickened layer. Second, when the particle is heated to the ambient temperature in the neighborhood of 2200 K, the exothermic reactions between boron and oxygen are responsible for generating heat to evaporate the oxide layer, melt the particle, and subsequently cause thermal runaway. These processes account for a large portion of the ignition time, as evidenced in Fig. 5, because increases in particle temperature are slowed by heat losses through evaporation and convection (for $T_p > T_\infty$). Finally, the criterion for ignition is thermal runaway. Thermal runaway cannot occur before the oxide layer is removed, nor can it occur before the particle is completely melted. The choice of a high temperature (2600-3000 K) to terminate the calculation is not crucial, since the temperature increases rapidly during this stage. In this work, the particle temperature chosen to stop the ignition calculations after thermal runaway is 2600 K. When water vapor is present in the surrounding gases, thermal runaway will occur sooner due to the increase in the consumption rate of B_2O_3.

As mentioned above, the purpose of the previous example was to ascertain whether or not a certain particle size would ignite during the limited residence time within the combustion chamber. Since the ignition time shown in Fig. 5 is approximately 0.7 ms and the residence time of the particle is on the order of 1 ms, then the particle with a 2.5 μm radius should be appropriate.

The conditions for the baseline case of a boron particle ejected from the fuel sample are as follows. The initial particle radius is 2.5 microns with an oxide-layer thickness

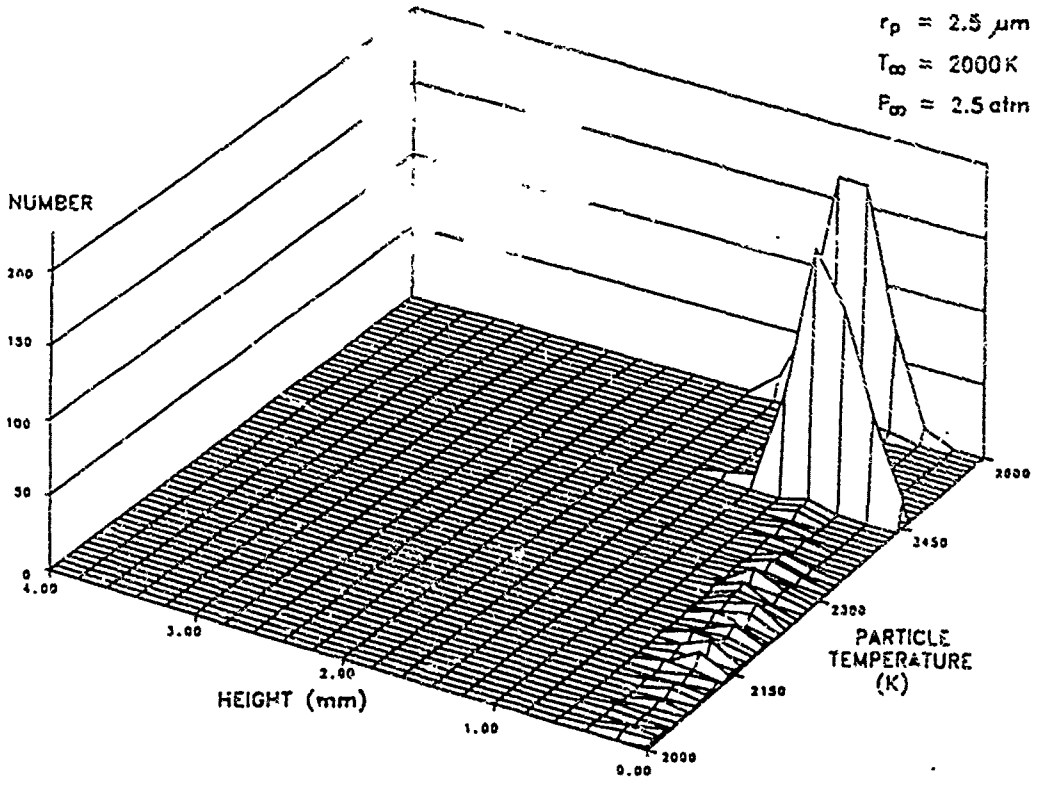


FIGURE 6. Calculated Number Distributions of Particles at Various Temperatures (Station x = $\frac{1}{3}$ L)

of 0.03 microns and temperature of 900 K. The particle is ejected vertically from the front of the fuel sample with a velocity of 0.3 m/s. This velocity is approximately one half of the velocity of the pyrolyzing gases. Depending on the entrainment of the particle in the pyrolyzing gas, this initial velocity may vary. The particle is ejected into the reacting flowfield for which the Mach number contours, temperature contours, and species mass fractions have been given (Figs. 3 and 4). The ejection process is repeated two thousand times to achieve a statistically significant number of trajectories.

For each particle, the equations for the rate of change of radius, oxide-layer thickness, and temperature are solved at each time step. The particle location and velocity at each time step are also determined. In some cases, the particles may hit the lower wall boundary somewhere downstream of the ejection station. In this instance, the particle is assumed to adhere to the surface and the calculation is terminated. Particles which satisfy the ignition criterion of thermal runaway continue to be traced through the combustion chamber at a constant particle temperature of 2600 K. This assumes that the particle has ignited and does not extinguish during its remaining time within the combustion chamber.

The distributions of the particle height above the lower wall are plotted according to temperature in Fig. 6, at an axial location of x= 5 cm ($\frac{1}{3}$L). Of the 2000 ejected

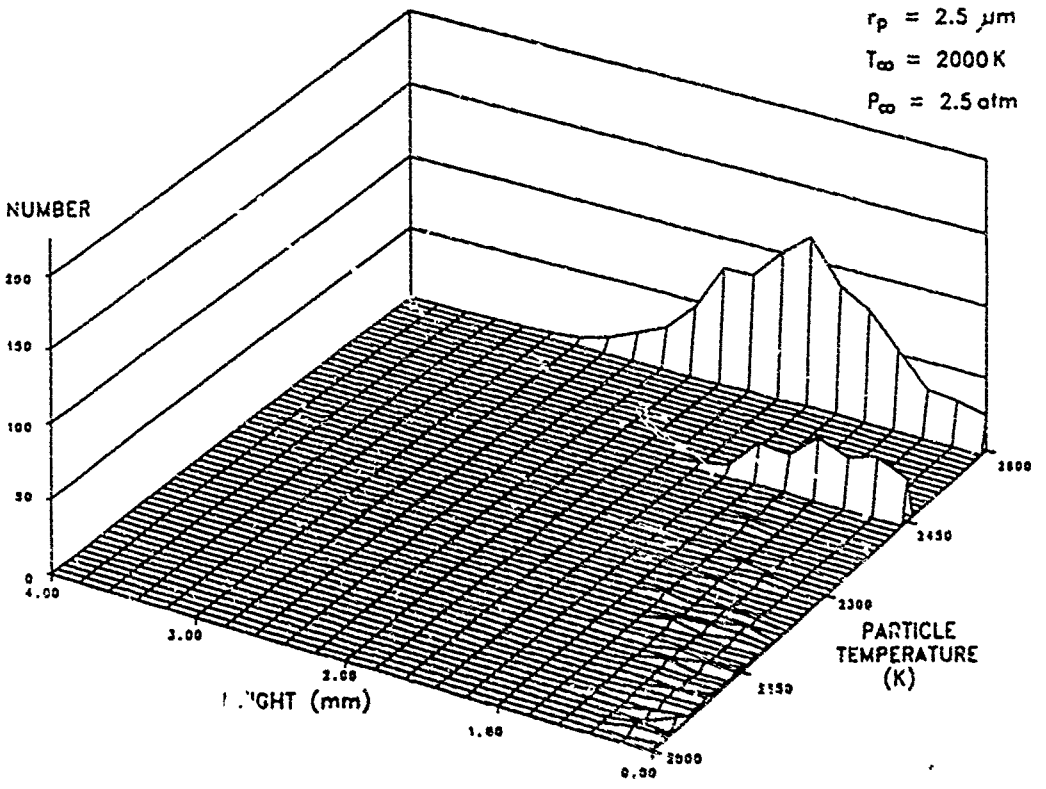


FIGURE 7. Calculated Number Distributions of Particles at Various Temperatures (Station x = $\frac{2}{3}$ L)

particles, 1512 remain in the flowfield while the rest have hit the surface due to the influence of random turbulent fluctuations in the downward direction. The majority of the remaining particles are either melting or have already ignited, as shown in Fig. 6, with few particles at temperatures below 2450 K. The trajectories associated with the melting and ignition of the particle are such that most trajectories pass through the high-temperature region at the front of the sample shown in Fig. 3b; therefore, these particles are subject to a very high convective heating immediately after ejection. Particles whose trajectories are closer to the surface do not experience such a high temperature increase from convection. These lower trajectories are within 0.6 mm from the surface, which is within the fuel-rich region of the boundary layer (shown in Fig. 4a). Along these paths, the particles are not exposed to oxygen; therefore, the possibility of their ignition is slim. Further downstream at x=$\frac{2}{3}$L, the number distributions are more broadly spread as shown in Fig. 7, with 65% of the particles ignited. All particles above the 1.4 mm location have ignited. This indicates that particles ignite if they are able to penetrate the gas-phase flame region, since their temperatures are high and the surroundings provide sufficient oxygen for ignition. Results also show that at the exit, 77% of the particles remaining in the flowfield have ignited. The average horizontal velocity of these particles leaving the chamber is 582 m/s, indicating that these particles are almost fully entrained into the flow which has an average gas-phase velocity of 650 m/s.

In order to determine the most probable location for ignition of the particles, the number of occurrences of ignition were recorded according to the spatial location

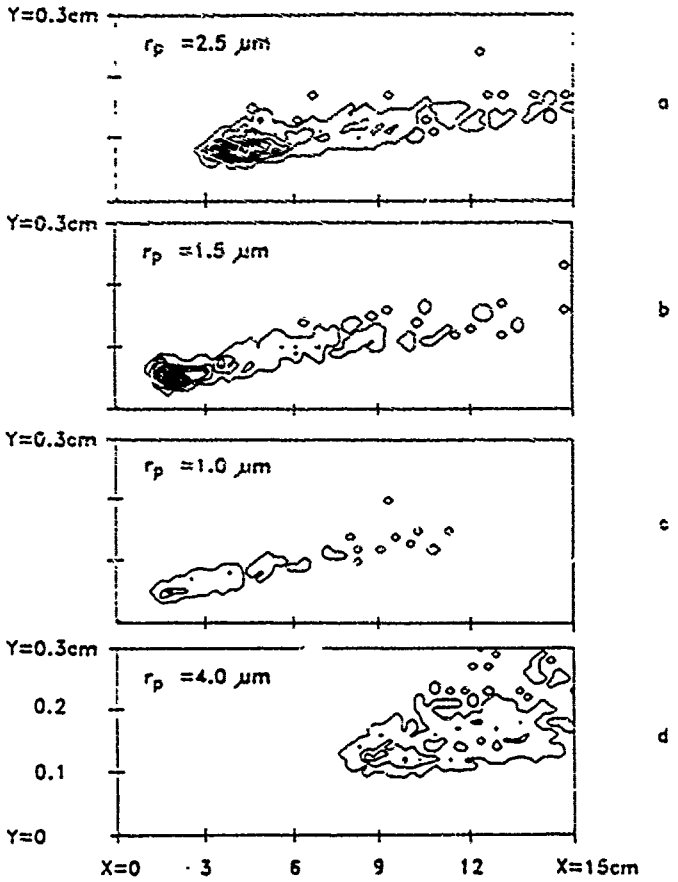


FIGURE 8. Effect of Particle Radius on Ignition Locations;
$M_\infty = 1.2$, $T_\infty = 2000$ K, $p_\infty = 2.5$ atm

within the flowfield. Contours of the number of occurrences for the baseline case are plotted in Fig. 8a, with the outermost contour line representing the ignition of at least one particle, and each succeeding line representing an additional three occurrences of ignition. The lines are closely spaced within the region between 3.0 and 4.5 cm from the inlet and 0.7 to 0.9 mm from the fuel surface, where 37 percent of the particles ignited. The average time for ignition at this location is 0.13 ms. When compared with oxygen mass fractions in Fig. 5b, the ignition locations indicate the importance of O_2, since the particles ignite when they come in contact with oxygen after passing through the high-temperature zone. The effect of water vapor on the ignition time is insignificant in this case, because the mass fractions shown in Fig. 5c are quite small

The effect of particle size on ignition time and location was investigated. Additional cases were studied with smaller particle radii of 1.5 and 1.0 microns, and larger radii of 4.0 microns, with initial conditions remaining the same. For both of the smaller particle sizes, the ignition locations moved upstream to 1.75 cm, as shown in Fig. 8b and 8c. For the 1.5 micron particles, 56 % of the particles ignited by the time they reached $x=\frac{1}{3}L$ and 78 % by the time they reached the exit. The likelihood of ignition for this size is greater in comparison to the 2.5 micron particles because the smaller size requires less energy to be heated to the ignition temperature. The approximate ignition time for these particles is 0.06 ms. For even smaller particles with a 1.0 micron radius, the ignition time is nearly the same. This occurs since the particles cannot ignite any sooner due to the lack of oxygen near

the surface. Both the 1.5 and 1.0 micron particles heat up and completely remove their oxide layers within the fuel-rich region near the surface, then ignite when they come in contact with O_2. Although the ignition times and locations are the same, a tremendous decrease in the number of ignited particles is noticed for the particles with 1.0 μm radius. At x=$\frac{1}{3}$L, only 9% have ignited, and at the exit only 15% have experienced thermal runaway. These results are partly due to the lower inertia of the smaller particles, which allows the majority of them to be swept downstream before reaching the high temperature region above the fuel sample. Another cause for the smaller number of ignited particles is due to convective heat loss of the unignited particles after they pass into the oxidizing region. The surrounding gas temperature is in the neighborhood of 2300 K, which should be sufficient to ignite the particles; however, for smaller particles both the specific surface area and the convective heat-transfer coefficient become greater, resulting in a more dominating effect of heat loss from the particle. The energy supplied by the exothermic reactions may not be sufficient to compensate for the heat-loss effect. Therefore, in some instances a smaller particle size would not benefit the ignition process. If the surrounding temperature was greater than the ignition temperature of the boron particles, then the convective heat losses could be avoided and the ignition times would be shortened for the smaller particles.

Larger particles with radii of 4.0 microns ignited much further downstream at x= 8.75 cm and y=1.3 mm as shown in Fig. 8d. The ignition time at this location is 0.32 ms. At x=$\frac{1}{3}$L no particles were ignited, and at the exit only 44 % were ignited. In comparison with Figs. 6 and 7, less dispersion in the trajectories was noticed at the x=$\frac{1}{3}$L and x=$\frac{2}{3}$L stations, as shown in Figs. 9 and 10, since the particles

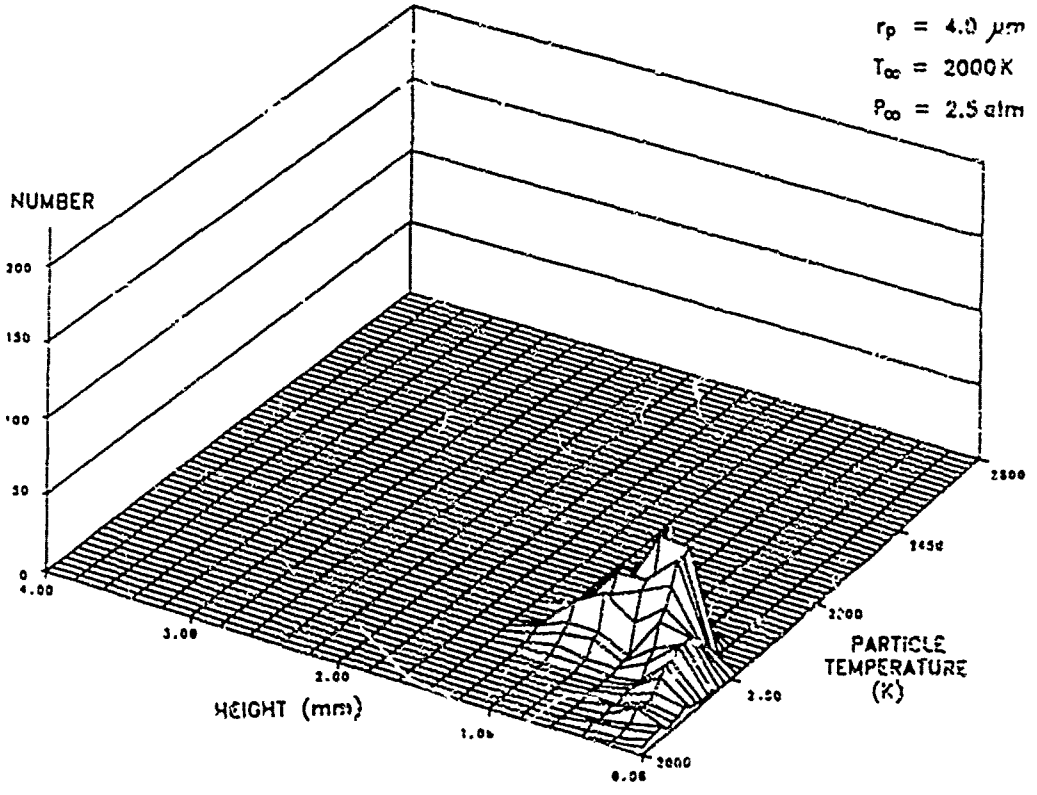


FIGURE 9. Calculated Number Distributions of Particles at Various Temperatures (Station x = $\frac{1}{3}$ L)

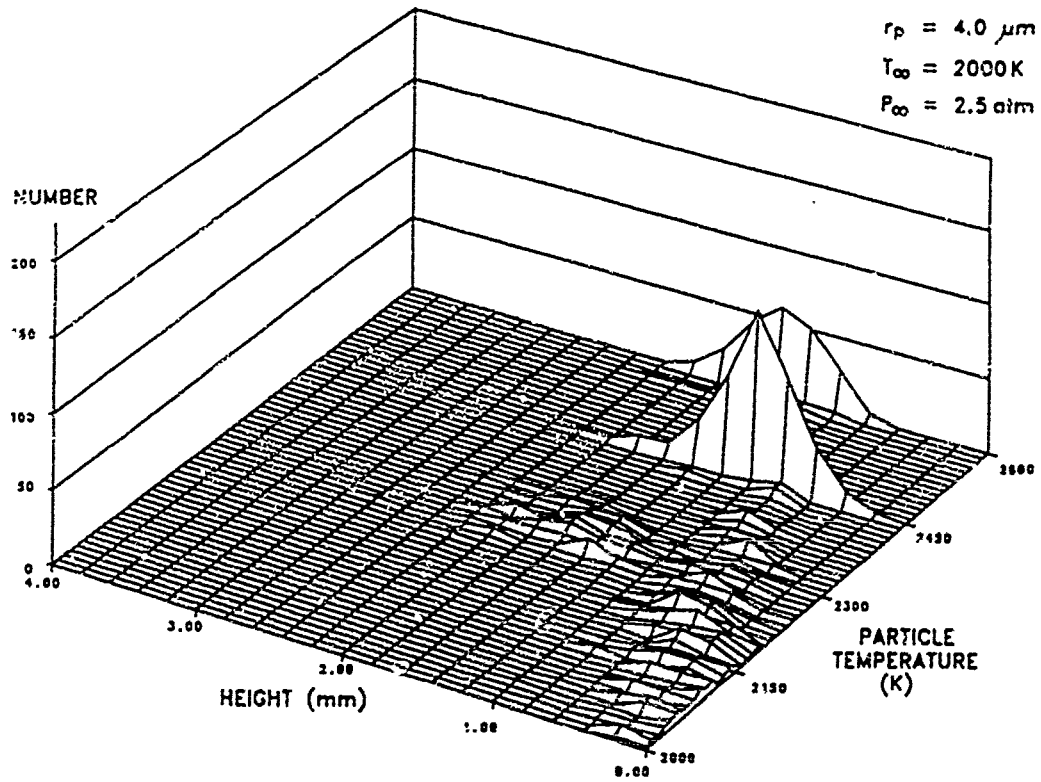


FIGURE 10. Calculated Number Distributions of Particles at Various Temperatures (Station $x = \frac{2}{3}$ L)

were heavier and not able to follow the turbulent fluctuations as well as the smaller particles.

Figure 11 summarizes the effect of particle size and axial location on the ignition probability. The percent of ignited particles is plotted at three axial stations for the four different particle sizes. For particles with radii equal to 1.0 micron, 9 percent ignited by passing through the flame region, and only 6 percent more ignited afterwards. For larger particles of 1.5 and 2.5 microns in radius, dramatic increases were noticed in the ignition percentages. The particles with 1.5 micron radius ignited in the upstream regions of the combustion chamber, whereas the slightly larger particles of 2.5 microns required more time to ignite. Nevertheless, the results at the exit of the chamber are comparable. A total of 78 percent of these particles ignited For even larger particles of 4 micron radius, the percentages decreased because of the increased energy and time required to ignite the particles.

The effect of ambient conditions on the ignition of the boron particles was also studied and compared to the baseline case. The gas-phase equations were solved again based on a lower inlet temperature of 1900 K, with the Mach number and pressure remaining at 1.2 and 2.5 atm, respectively. Boron particles were ejected in the same manner as discussed above, with 2.5 micron radius, 0.03 initial oxide thickness, and 900 K initial temperature. The new freestream conditions resulted in a decrease to 69% in the number of ignited particles, with a slight increase of 0.04 ms in the ignition time. The particles most frequently ignited at the station

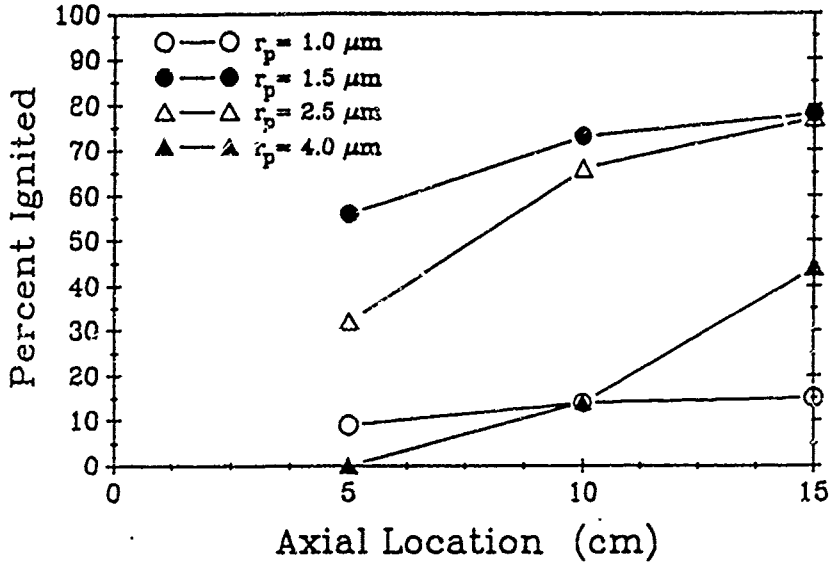


FIGURE 11. Effect of Particle Radius on Ignition Percentage at Three Axial Stations

5.25 cm from the front edge of the sample. This location is 1.75 cm downstream from the results of the baseline case at the higher inlet temperature of 2000 K. The slower ignition response is primarily due to increased convective heat loss caused by the 100 K cooler surroundings when the particle temperature rises above the gas-phase temperature. Results from this calculation are plotted in Fig. 12, where a noticeable decrease in the percent ignited is shown in comparison with the baseline case. Another case with lower freestream pressure of 1.5 atm was calculated, with all other conditions the same as the baseline. Similar effects on the ignition results are evident. The poorer performance stems from the decline in freestream pressure which decreases the oxygen partial pressure and the flame temperature, resulting in a delayed ignition of the particle.

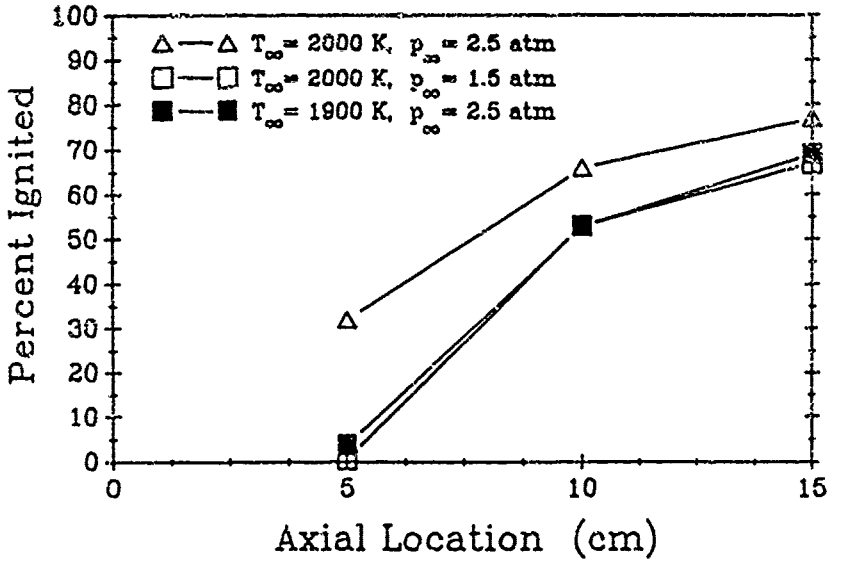


FIGURE 12. Effect of Freestream Conditions on Ignition Percentage at Three Axial Stations

Results discussed in this work show that the minimization of ignition time can be accomplished by optimizing the environmental conditions at certain periods during the ignition process. King (1982b) originally suggested such a scenario which involved the initial heatup and removal of the oxide layer in a mixed H_2O/N_2 atmosphere, then exposure to an O_2/N_2 environment for melting and complete ignition. In this manner, the buildup of the oxide layer during the heatup process (as evidenced in Fig. 5) can be avoided, and ignition can occur sooner. A similar scenario is presented here. With the initial heatup occurring in the fuel-rich mixture below the reaction zone, boron particles avoid oxide layer build-up as they are ejected into the reacting boundary layer. Since the particles do not ignite or burn within the fuel-rich layer, the near-surface region heats the particle and removes the oxide layer, so that the particles achieve thermal runaway immediately upon contact with the oxidizer. When this occurs, the ignition delay time is governed by the residence time required for the particles to travel from the sample surface to the region where sufficient oxidizers exist. Otherwise, if the oxide layer is not completely removed before the particle contacts oxygen, ignition delay time will be prolonged; thereby reducing the chances for achieving a high combustion efficiency.

5. CONCLUSIONS

The ignition processes of boron particles above a burning solid fuel were studied by numerical solution of a comprehensive theoretical model. The effects of particle size on the ignition times and locations of the particles were determined. Under certain operating conditions, an optimum particle size can be attained for minimizing ignition delay times. The study also showed that the solid-fuel ramjet provides an ideal environment for reducing ignition delay times by staging the ignition process. In this manner, ignition occurs in a very short time period, allowing ample time for complete combustion of the particle.

The effects of ambient conditions on the particle ignition times were also investigated. Lower freestream temperatures delayed ignition because of reduced heating of the particles. Lower pressures increased ignition delay times because of a decreased oxygen partial pressure for exothermic reactions.

ACKNOWLEDGEMENTS

This paper represents a part of the research work conducted under the sponsorship of the Office of Naval Research, Arlington, VA, Contract No. N00014-86-K-0468. The support and encouragement of Drs. Richard S. Miller and Gabriel D. Roy are greatly appreciated. The authors would like to thank Drs. J. S. Shuen and K. C. Hsieh of NASA Lewis Research Center for providing helpful information and discussion. In addition, the authors wish to acknowledge the National Science Foundation for providing CPU time on the CRAY Y-MP at the Pittsburgh Supercomputing Center.

NOMENCLATURE

A = Pre-exponential factor
C_D = Drag coefficient
C_i = Molar concentration of species i
c_p = Constant pressure specific heat
C_μ = Turbulence constant
D_{ij} = Binary diffusion coefficient
D_{im} = Effective diffusivity of species i against mixture
e = Total stored energy

E = Activation energy
f = Fraction of boron particle melted
g = Gravitational acceleration
h = Convective heat transfer coefficient
h_i = Enthalpy of species i
h_f^o = Heat of formation
k = Turbulent kinetic energy
k_{eff} = Effective thermal conductivity
L = Length of combustion chamber
L_e = Characteristic size of turbulent eddy
M_i = Molecular weight of species i
N = Total number of species
p = Pressure
q = Heat flux
q_{rad} = Radiative heat flux
Q_1 = Energy released in reaction of boron and oxygen
Q_2 = Energy absorbed in water vapor/boron oxide reaction
Q_3 = Energy absorbed in evaporation of boron oxide
r_b = Burning rate of solid fuel
r_p = Boron particle radius
R_B = Molar consumption rate of boron
R_E = Molar consumption rate of boron oxide by evaporation
R_H = Molar consumption rate of boron oxide by reaction with water vapor
R_u = Universal gas constant
t = Time
t_e = Eddy lifetime
t_t = Transit time of particle in eddy
T_{su} = Surface temperature
T_{sur} = Surroundings temperature
$T_{s,ref}$ = Temperature of solid fuel at reference state
T_o = Solid fuel temperature at $y = -\infty$
u = Velocity in x direction
$\tilde{U}_i$ = Diffusion velocity in x direction
v = Velocity in y direction
$\tilde{V}_i$ = Diffusion velocity in y direction
x = Coordinate in axial direction
X = Boron oxide layer thickness
X_i = Mole fraction of species i
y = Coordinate normal to fuel surface
Y_i = Mass fraction of species i

Greek Symbols

α = Boron oxide evaporation coefficient
ϵ = Eddy dissipation rate
ϵ_B = Emissivity of boron
λ = Thermal conductivity
μ = Viscosity
μ_{eff} = Effective viscosity
ρ = Density
σ = Stefan-Boltzmann constant
τ = Viscous shear
$\dot{\omega}_i$ = Rate of production of species i

Subscripts
B = Boron
fu = Fuel species
g = Gas phase
p = particle
s = Solid phase

Superscripts
T = Transpose
$\tilde{}$ = Favre-averaged quantities
$\bar{}$ = Time-averaged quantities

REFERENCES

Baldwin, B. S. and Lomax, H., (1987). Thin Layer Approximation and Algebraic Model for Separated Turbulent Flows, AIAA Paper No. 78-257, AIAA 16th Aerospace Sciences Meeting, Huntsville, AL.

Bird, R. B., Stewart, W. E., and Lightfoot, F. N., (1960). *Transport Phenomena*, John Wiley and Sons, New York.

Brazier, D. W. and Schwartz, N. V., (1978). The Effect of Heating Rate on the Thermal Degradation of Polybutadiene, *Journal of Applied Polymer Science*, 22, 113-124.

Cohen, N. S., Fleming, R. W., and Derr, R. L., (1974). Role of Binders in Solid Propellant Combustion, *AIAA Journal*, 12, 2, 212-218.

Dryer, F. L. and Glassman, I., (1972). High-Temperature Oxidation of CO and CH_4, *Proceedings of Fourteenth Symposium (International) on Combustion*, The Combustion Institute, Pittsburgh, PA, 987-1003.

Ericsson, I., (1978). Sequential Pyrolysis Gas Chromatographic Study of the Decomposition Kinetics of Cis-1,4-Polybutadiene, *Journal of Chromatographic Science*, 16, 340-344.

Hinze, J. O., (1976). *Turbulence*, McGraw-Hill, New York, 2nd ed., pp. 639-640.

Hornbeck, R. W., (1975). *Numerical Methods*, Prentice-Hall Inc., Englewood Cliffs, NJ.

Incropera, F. P. and DeWitt, D. P., (1985). *Fundamentals of Heat and Mass Transfer*, 2nd Ed., John Wiley and Sons, NY, pp. 657-661.

Jameson, A. and Yoon, S., (1987). Lower-Upper Implicit Schemes with Multiple Grids for the Euler Equations, *AIAA Journal*, 25, 7, 929-935.

Jarymowycz, T. A., Yang, V., and Kuo, K. K., (1990a). A Numerical Study of Solid Fuel Combustion under Supersonic Crossflows, AIAA Paper 90-2076, AIAA/SAE/-

ASME/ASEE 26th Joint Propulsion Conference, Orlando, FL, also accepted for publication in *Journal of Propulsion and Power.*

Jarymowycz, T. A., Pace, K. K., Snyder, T. S., Yang, V., and Kuo, K. K., (1990b). Experimental Study of Solid Fuel Ignition and Combustion under High-Velocity Crossflows, submitted for publication to *Journal of Propulsion and Power*, and presented at 27th JANNAF Combustion Meeting, Cheyenne, WY.

King, M. K., (1972). Boron Ignition and Combustion in Air-Augmented Rocket Afterburners, *Combustion Science and Technology*, 5, 155-164.

King, M. K., (1974). Boron Particle Ignition in Hot Gas Streams, *Combustion Science and Technology*, 8, 255-273.

King, M. K., (1982a). Ignition and Combustion of Boron Particles and Clouds, *Journal of Spacecraft and Rockets*, 19, 294-306.

King, M. K., (1982b). Single Particle Boron Ignition Modeling, 19th JANNAF Combustion Meeting, CPIA Publication 366, II, 27-42.

King, M. K., (1983). A Unified Model of Ignition, Burning, and Extinguishment of Single Boron Particles, 20th JANNAF Combustion Meeting, CPIA Publication 383, II, 97-115.

Kuo, K. K., (1986). *Principles of Combustion*, John Wiley and Sons, New York, pg. 579.

Macek, A. and Semple, J. M., (1969). Combustion of Boron Particles at Atmospheric Pressure, *Combustion Science and Technology*, 1, 181-191.

Macek, A. and Semple, J. M., (1971). Combustion of Boron Particles at Elevated Pressures, *Thirteenth Symposium (International) on Combustion*, The Combustion Institute, Pittsburgh, 859-868.

Macek, A., (1972). Combustion of Boron Particles: Experiment and Theory, *Fourteenth Symposium (International) on Combustion*, The Combustion Institute, Pittsburgh, 1401-1411.

McBride, B. J., and Gordon, S., (1967). FORTRAN IV Program for Calculation of Thermodynamic Data, NASA TN D-4097.

Mohan, G. and Williams, F. A. (1972). Ignition and Combustion of Boron in O_2/Inert Atmospheres, *AIAA Journal*, 10, 776-783.

Natan, B, and Gany, A., (1987). Ignition and Combustion Characteristics of Individual Boron Particles in the Flowfield of a Solid Fuel Ramjet, AIAA Paper 87-2034, AIAA/SAE/ASME/ASEE 23th Joint Propulsion Conference, San Diego, CA.

Pein, R. and Vinnemeier, F., (1989). The Influence of Swirl and Fuel Composition of Boron-Containing Fuels on Combustion in a Solid Fuel Ramjet Combustion

Chamber, AIAA Paper 89-2885, AIAA/SAE/ASME/ASEE 25th Joint Propulsion Conference, Monterey, CA.

Reid, R. C., Prausnitz, J. M., and Poling, B. E., (1987). *The Properties of Gases and Liquids*, 4th Edition, McGraw-Hill Publishing Co., New York, NY.

Shuen, J. S., (1984). A Theoretical and Experimental Investigation of Dilute Particle-Laden Turbulent Gas Jets, Ph. D. Thesis, The Pennsylvania State University, 26-29.

Sherwood, T. K., Pigford, R. L., and Wilke, C. R., (1975). *Mass Transfer*, McGraw-Hill Publishing Co., New York, NY.

Shuen, J. S. and Yoon, S., (1989). Numerical Study of Chemically Reacting Flows Using a Lower-Upper Symmetric Successive Overrelaxation Scheme, *AIAA Journal*, 27, 12, 1752-1760.

Snyder, T. S., Jarymowycz, T. A., Pace, K. K., and Kuo, K. K., (1990). Solid Fuel Ignition and Combustion Characteristics under High-Speed Crossflows, AIAA Paper 90-2075, AIAA/SAE/ASME/ASEE 26th Joint Propulsion Conference, Orlando, FL.

Tseng, I. S. (1991). Velocity-Coupled Combustion Instabilities in Solid- Propellant Rocket Motors, Ph. D. Thesis, The Pennsylvania State University, University Park, PA.

Turns, S. R., Holl, J. T., Solomon, A. S. P., and Faeth, G. M., (1985). Gasification of Boron Oxide Drops in Combustion Gases, *Combustion Science and Technology*, 43, 287-300.

Westbrook, C. K. and Dryer, F. L., (1981). Simplified Reaction Mechanisms for the Oxidation of Hydrocarbon Fuels in Flames, *Combustion Science and Technology*, 27, pp. 31-43.

Williams, F. A., (1985). *Combustion Theory*, 2nd Edition, Benjamin/Cummings Publishing Co., Menlo Park, CA, pp. 631-645.

Yoon, S. and Jameson, A., (1987). An LU-SSOR Scheme for the Euler and Navier-Stokes Equations, AIAA Paper No. 87-0600, AIAA 25th Aerospace Sciences Meeting, Reno, NV.

AIAA 90-2076
A Numerical Study of Solid Fuel Combustion Under Supersonic Crossflows

T. Jarymowycz, V. Yang and K. Kuo
Penn State Univ.
University Park, PA

AIAA/SAE/ASME/ASEE
26th Joint Propulsion Conference
July 16-18, 1990 / Orlando, FL

For permission to copy or republish, contact the American Institute of Aeronautics and Astronautics
370 L'Enfant Promenade, S.W., Washington, D.C. 20024

A NUMERICAL STUDY OF SOLID FUEL COMBUSTION UNDER SUPERSONIC CROSSFLOWS

T. A. Jarymowycz,† V. Yang,‡ K. K. Kuo*
Department of Mechanical Engineering
The Pennsylvania State University
University Park, PA 16802

Abstract

The combustion of solid fuels under supersonic crossflow has been studied using a comprehensive numerical analysis. The formulation is based on the time-dependent multi-dimensional compressible Navier-Stokes equations and species transport equations. Features of this approach are the consideration of finite-rate chemical kinetics and variable properties. Turbulence closure is achieved using the Baldwin-Lomax algebraic model. The governing equations are solved numerically using a flux-vector splitting Lower-Upper Symmetric Successive Overrelaxation technique that treats source terms implicitly. The effects of various operating conditions on the combustion behavior of the HTPB-based solid fuel samples are treated in detail. Results indicate that both the inlet temperature and pressure have strong influences on the burning rate of the fuel sample. For the operating range considered, an optimum pressure is required to maximize the burning rate. The sample burns increasingly faster with pressure from one to four atmospheres. However, at a higher pressure, the energy released by combustion is not sufficient to further raise the temperature of the crossflow. This results in a decrease in heat feedback to the fuel sample, consequently causing a slight reversal of the burning rate trend with pressure.

Nomenclature

A = Pre-exponential factor
C_i = Molar concentration of species i
c_p = Constant pressure specific heat
D_{ij} = Binary diffusion coefficient
D_{im} = Effective diffusivity of species i against mixture
e = Total stored energy
E = Activation energy
h = Enthalpy
h_f° = Heat of formation
k = Thermal conductivity
k_{eff} = Effective thermal conductivity
L = Length of fuel sample
M_i = Molecular weight of species i
N = Total number of species
p = Pressure
q = Heat flux
q_{rad} = Radiative heat flux
r_b = Burning rate of solid fuel
R_u = Universal gas constant
T_w = Surface temperature
$T_{s,ref}$ = Temperature of solid fuel at reference state
T_s = Solid fuel temperature at $y = -\infty$
u = Velocity in x direction
U_i = Diffusion velocity in x direction
v = Velocity in y direction
V_i = Diffusion velocity in y direction
x = Coordinate in axial direction
X_i = Mole fraction of species i
y = Coordinate normal to fuel surface
Y_i = Mass fraction of species i
ϵ = Emissivity
μ = Viscosity
μ_{eff} = Effective viscosity
ρ = Density
σ = Stefan-Boltzmann constant
τ = Viscous shear
$\dot{\omega}_i$ = Rate of production of species i

Subscripts
fu = Fuel species
g = Gas phase
s = Solid phase

Superscripts
T = Transpose
$\tilde{}$ = Favre-averaged quantities
$\bar{}$ = Time-averaged quantities

1. Introduction

In the modern development of airbreathing propulsion systems for hypersonic vehicles, attention is often focused on the supersonic combustion ramjet (commonly known as scramjet) due to its effectiveness in capturing the incoming air with sufficient pressure recovery. Once compressed, the air mixes and burns with fuel, then the combustion products are accelerated through an exhaust nozzle to generate thrust. The principles of the scramjet and solid propellant rocket motor may be linked in sequence to form an integral rocket-ramjet (IRR),[1] as shown schematically in Fig. 1. This design is particularly attractive for its low-volume configuration, since the rocket and scramjet modes utilize a common combustion chamber. In addition, the vehicle avoids a weight penalty associated with carrying oxidants during the airbreathing phase, and consequently provides a higher specific impulse and longer flight range.

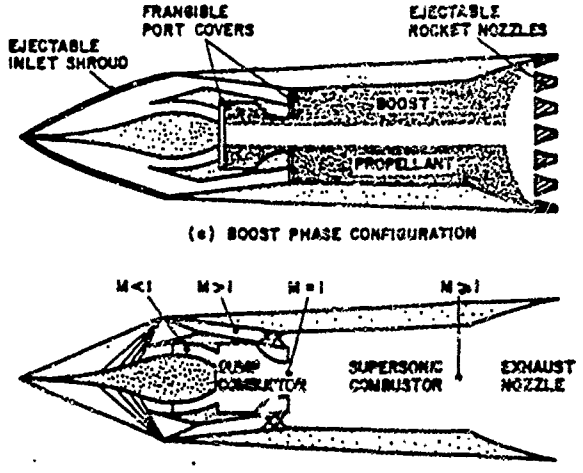


Figure 1. Schematic of Integral Rocket-Ramjet

† Ph. D. Student, Member AIAA
‡ Assistant Professor, Member AIAA
* Distinguished Alumni Professor of Mechanical Engineering, Associate Fellow AIAA

"Copyright ©1990 by Taras A. Jarymowycz. Published by American Institute of Aeronautics and Astronautics, Inc. with permission."

The scramjet engine can be powered by either solid or liquid fuels. The use of solid fuel greatly simplifies the system design and eliminates problems associated with fuel storage and feeding mechanisms. In addition, highly energetic additives such as boron or metallized powders may considerably increase the energy density of a solid fuel beyond that of a liquid fuel, thereby making it particularly attractive for volume-limited missions. The purpose of this work is to study numerically the physical and chemical processes involved in the supersonic combustion of solid fuels and link these phenomena with experimental results discussed in companion papers.[2,3]

Several works have been devoted to the combustion of solid fuels under low Mach-number flow conditions. In References 4 and 5, preliminary results were summarized on the combustion processes in solid-fuel ramjets, including the effects of configuration variables and operating conditions on combustion performance. Schulte[6] studied flame stabilization in an experimental ramjet motor and determined flame holding limits based on various ratios of fuel port area to nozzle throat area, and fuel port area to flame holder area. Flame holding was improved by increasing these area ratios and by raising the ram air temperature. In addition, an increase in inlet air temperature enhanced the regression rate of polyethylene solid fuel to a greater extent than did the air mass flux and chamber pressure. Netzer and Gany[7] made similar observations regarding flame stabilization limits and burning rate dependencies using a miniaturized solid fuel ramjet.

Gany and Netzer[8] studied the combustion of highly metallized, boron containing solid fuels under low Mach-number flow conditions. They observed that the supply of oxygen plays a significant role in the heterogeneous reactions. The decomposing binder ejects heated particles into the crossflow where they react with oxygen, and subsequently ignite and burn. The presence of oxygen in the near-surface region could affect the lifetime of these particles, depending on how long they remain near the surface and to what extent they are heated before ejection occurs. Recently, Scott and Netzer[9] studied the effect of fuel ingredients on the combustion behavior, noting that metallized fuels require higher pressures and longer residence times to achieve better combustion efficiency. In addition, fuels with lower shore hardness could be ignited more easily.

Attempts to investigate the combustion of solid fuels under transonic and supersonic crossflows were made by Snyder et al.[2] Results indicated that conventional hydrocarbon fuels such as hydroxyl terminated polybutadiene (HTPB) are difficult to ignite at low pressure. However, this situation can be improved significantly with the use of an energetic copolymer such as 3,3-bis [azidomethyl] oxetane and 3-nitratomethyl 3-methyl oxetane (BAMO/NMMO), which is readily ignitable because of its lower heat of decomposition and availability of oxygen in the condensed phase. Observations from strand burner tests[10] also revealed that boron/poly (BAMO/NMMO) has an advantage over conventional HTPB based solid fuels, since it pyrolyzes vigorously and disperses boron particles effectively into the main reaction zone.

Since the experimental study of solid fuel combustion under supersonic conditions has been performed only on a very limited basis,[2,3] the present research sheds some light on the feasibility of solid-fuel scramjet propulsion. The specific objectives of this paper are:

1. to investigate the detailed flowfields and flame structures involved in the combustion of solid fuels in a supersonic flow environment;
2. to determine the burning rates of the fuel samples under various conditions;
3. to examine the effects of the freestream conditions (specifically pressure and temperature) on the pyrolysis and combustion characteristics of the fuel samples.

In what follows, a comprehensive theoretical formulation of the combustion of homogeneous solid fuels under supersonic crossflow conditions is given, followed by a description of the numerical algorithm. As a specific example, the combustion behavior of pure HTPB fuel samples is treated in depth. The situation involving two-phase flows will be discussed in future work.

2. Theoretical Formulation

The physical geometry considered in the analysis is shown in Fig. 2. A uniform supersonic air flow enters a two-dimensional chamber in which a solid fuel sample pyrolyzes and reacts with the ram air in the gas phase. To facilitate formulation, the processes in the gas and solid phases are treated separately. They are linked together through the balance of mass and energy fluxes at the gas/solid interface. In order to achieve steady-state conditions in the gas phase and at the fuel boundary, the fuel is fed at a rate r_b equal to the burning rate, which keeps the surface of the burning sample stationary.

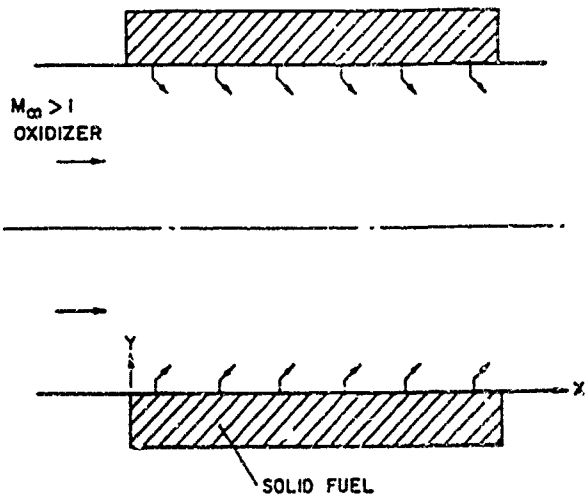


Figure 2. Physical Geometry of Two-Dimensional Combustion Chamber

Gas – Phase Analysis

The gas phase analysis is based on the Favre-averaged conservation equations of mass, momentum, energy, and species transport for a multicomponent system in Cartesian coordinates. They can be written conveniently in the vector form

$$\frac{\partial Q}{\partial t}+\frac{\partial E}{\partial x}+\frac{\partial F}{\partial y}=\frac{\partial E_v}{\partial x}+\frac{\partial F_v}{\partial y}+H \tag{1}$$

where

$$Q \equiv \left[\bar\rho_g,\ \bar\rho_g\tilde u,\ \bar\rho_g\tilde v,\ \bar\rho_g\tilde e,\ \bar\rho_g\tilde Y_i\right]^T$$

$$E \equiv \left[\bar\rho_g\tilde u,\ \bar\rho_g\tilde u^2+\bar p,\ \bar\rho_g\tilde u\tilde v,\ \tilde u(\bar\rho_g\tilde e+\bar p),\ \bar\rho_g\tilde u\tilde Y_i\right]^T$$

$$F \equiv \left[\bar\rho_g\tilde v,\ \bar\rho_g\tilde u\tilde v,\ \bar\rho_g\tilde v^2+\bar p,\ \tilde v(\bar\rho_g\tilde e+\bar p),\ \bar\rho_g\tilde v\tilde Y_i\right]^T$$

$$E_v \equiv \left[0,\ \bar\tau_{xx},\ \bar\tau_{xy},\ \tilde u\bar\tau_{xx}+\tilde v\bar\tau_{xy}-\bar q_x,\ -\bar\rho_g\tilde U_i\tilde Y_i\right]^T$$

$$F_v \equiv \left[0,\ \bar\tau_{xy},\ \bar\tau_{yy},\ \tilde u\bar\tau_{xy}+\tilde v\bar\tau_{yy}-\bar q_y,\ -\bar\rho_g\tilde V_i\tilde Y_i\right]^T$$

$$H \equiv \left[0,\ 0,\ 0,\ 0,\ \dot\omega_i\right]^T$$

for $i = 1, 2, \ldots N-1$, with N being the total number of species considered. The diffusion terms in E_v and F_v are defined as

$$\bar\tau_{xx}=2\mu_{eff}\frac{\delta\tilde u}{\delta x}-\frac{2}{3}\mu_{eff}\left(\frac{\delta\tilde u}{\delta x}+\frac{\partial\tilde v}{\partial y}\right) \tag{2}$$

$$\bar\tau_{xy}=\mu_{eff}\left(\frac{\partial\tilde u}{\partial y}+\frac{\partial\tilde v}{\delta x}\right) \tag{3}$$

$$\tau_{yy} = 2\mu_{eff}\frac{\partial \tilde{v}}{\partial y} - \frac{2}{3}\mu_{eff}\left(\frac{\partial \tilde{u}}{\partial x} + \frac{\partial \tilde{v}}{\partial y}\right) \tag{4}$$

$$q_x = -k_{eff}\frac{\partial \tilde{T}}{\partial x} + \tilde{\rho}_g \sum_{i=1}^{N} \tilde{h}_i \tilde{Y}_i \tilde{U}_i \tag{5}$$

$$q_y = -k_{eff}\frac{\partial \tilde{T}}{\partial y} + \tilde{\rho}_g \sum_{i=1}^{N} \tilde{h}_i \tilde{Y}_i \tilde{V}_i \tag{6}$$

where $\tilde{U}_i$ and $\tilde{V}_i$ stand for the diffusion velocities and are determined by Fick's law. The effective transport properties, μ_{eff} and k_{eff}, contain contributions from both the laminar and turbulent diffusion processes. A full account is taken of the variation of specific heat with temperature, giving the static enthalpy as follows:

$$h_i = \int_{T_{ref}}^{T} c_{p,i}\, dT + h^{\circ}_{f,i} \tag{7}$$

where $h^{\circ}_{f,i}$ is the enthalpy of formation. Consequently, the total internal energy e becomes

$$e = \sum_{i=1}^{N} Y_i h_i - \frac{p}{\rho_g} + \frac{1}{2}\left(u^2 + v^2\right) \tag{8}$$

Finally, the equation of state determines the pressure from the temperature, density, and species mass fractions.

$$p = \rho_g R_u T \sum_{i=1}^{N} \frac{Y_i}{M_i} \tag{9}$$

The binary mass diffusivity is determined using the Chapman-Enskog theory along with the Lennard-Jones intermolecular potential-energy functions.[11] The effective diffusivity is then calculated through the following formula.[12]

$$D_{im} = \frac{1 - X_i}{\sum_{j=1}^{N} X_j / D_{ij}} \quad \text{for } i \neq j, \tag{10}$$

where X_i is the molar fraction of species i.

Thermodynamic and other transport properties of each constituent species are evaluated using fourth-order polynomials of temperature[13] which are valid for the range from 300 to 5000 K. For a mixture, specific heat is determined by a mass-concentration weighing of each species, but viscosity and thermal conductivity are calculated using Wilke's mixing rule.[14]

Condensed – Phase Analysis

If we ignore the bulk motion, subsurface chemical reaction, and axial thermal diffusion, the equation governing the condensed-phase process reduces to a one-dimensional heat conduction equation for each axial station. Under steady-state conditions, this equation takes the form

$$\frac{d}{dy}\left(k_s \frac{dT_s}{dy}\right) - \rho_s r_s \frac{d}{dy}\left[c_{p,s}\left(T_s - T_{s,ref}\right) + h^{\circ}_{f,s}\right] = 0 \tag{11}$$

subject to the boundary conditions

$$T_s = T_o \quad \text{as} \quad y \to -\infty$$
$$T_s = T_{sw} \quad \text{at} \quad y = 0$$

where the subscript "s" denotes the properties of the solid phase. Since the thermophysical properties of most solid fuels are not well characterized with respect to temperature, these properties are treated as constants. Integration of Eq. (11) yields the steady-state temperature distribution at a given axial location in the solid phase.

$$T_s = T_o + \left(T_{sw} - T_o\right) exp\left(\frac{\rho_s r_s c_{p,s}}{k_s} y\right) \tag{12}$$

Boundary Conditions

The heat and mass transfer processes between gas and condensed phases must be matched at the fuel surface to provide the necessary interface conditions for both the gas and condensed phases. This procedure will eventually determine the temperature, regression rate, and species concentrations at the surface. With some straightforward manipulation, the matching conditions are given as follows

Mass

$$\rho_s r_s = \rho_g v_g|_{+} \tag{13}$$

Species Mass Fraction

$$\rho_s r_s Y_i|_{-} = \rho_g v_g Y_i|_{+} - \rho_g D_{im}\frac{\partial Y_i}{\partial y}\Big|_{+} \tag{14}$$

Energy

$$-k_s \frac{\partial T}{\partial y}\Big|_{-} + \rho_s r_s\left(\int_{T_{ref}}^{T_{sw}} c_{p,s}\, dT + h^{\circ}_{f,s}\right) = -k_g \frac{\partial T}{\partial y}\Big|_{+} + \rho_g \sum_{i=1}^{N} Y_i h_i \left(v_g - \frac{D_{im}}{Y_i}\frac{\partial Y_i}{\partial y}\right)\Big|_{+} - q_{rad} \tag{15}$$

where "+" and "–" represent respectively the conditions immediately above and below the surface. The pyrolysis rate of solid fuel is evaluated using a zeroth-order Arrhenius expression.

$$r_s = \frac{A_s}{\rho_s} exp\left(\frac{-E_s}{R_u T_{sw}}\right) \tag{16}$$

where A_s is the pre-exponential factor, ρ_s the fuel density, E_s the activation energy, and T_{sw} the surface temperature. Radiant heat transfer to the surface due to emission from the gas-phase is calculated using a Stefan-Boltzmann relation in terms of the averaged gas-phase temperature. The total gas emissivity ϵ_g is estimated using a method developed by Hottel,[15] and is a function of the species mole fractions, gas-phase temperature, pressure, and mean beam length.

The flow at the upstream boundary is supersonic with pre-specified temperature, pressure, Mach number, and species mass fraction. The inlet velocity profile is assumed to be uniform in the y-direction with no vertical velocity component. Since the flow at the downstream boundary is also supersonic except for a small region near the surface, all of the exit conditions are extrapolated from their counterparts within the combustion chamber. However, the static pressure may be specified for the subsonic region of the boundary layer. The upper boundary is taken to be a line of symmetry. Therefore, the vertical velocity component and the derivatives of all the other dependent variables across the boundary are set to zero. In addition, the no-slip condition is employed at the fuel sample. The pressure at the surface of the fuel sample is determined by the y-momentum equation, giving

$$\frac{\partial\left(\frac{1}{2}v_g^2\right)}{\partial y} = -\frac{1}{\rho}\frac{\partial p}{\partial y}. \tag{17}$$

Turbulence Model

The Baldwin-Lomax algebraic model [16] along with constant turbulent Prandtl and Schmidt numbers ($Pr_t = Sc_t = 0.9$) are chosen to achieve the turbulence closure because of their computational efficiency and simplicity. This algebraic model solves for the turbulent eddy viscosity using the Prandtl-Van Driest formulation and the local vorticity distribution for the near-wall and outer regions, respectively.

Gas – Phase Combustion Model

For combustion of gaseous hydrocarbon fuels with oxygen, Westbrook and Dryer[17] suggested a simplified two-step reaction mechanism that reasonably predicts reaction rates for a large number of hydrocarbons over a wide range of equivalence ratios and pressures.

$$C_nH_m + \left(\frac{n}{2} + \frac{m}{4}\right) O_2 \rightarrow nCO + \frac{m}{2} H_2O \qquad (18)$$

$$CO + \frac{1}{2} O_2 = CO_2 \qquad (19)$$

This two-step mechanism is adopted without the reverse reaction of Eq. (19) since its reaction rate is slower than the forward reaction by six orders of magnitude, and has little effect on the overall kinetics in light of the short residence time of the flowfield. Equations (18) and (19) are satisfactory expressions for the gas-phase reactions, provided the flame temperature is not high enough to promote dissociation to free radical species such as H, O, and OH. For flame temperatures beyond 3000 K, a multi-step mechanism will be recommended to account for dissociation.

The production rates of the species are

$$\dot{\omega}_{fu} = -M_{fu} A_{fu} \exp\left(\frac{-E_{fu}}{R_u T}\right) C_{fu}^{a} C_{O_2}^{b} \qquad (20)$$

and

$$\dot{\omega}_{CO} = nM_{CO} A_{fu} \exp\left(\frac{-E_{fu}}{R_u T}\right) C_{fu}^{a} C_{O_2}^{b} - M_{CO} A_{CO} \exp\left(\frac{-E_{CO}}{R_u T}\right) C_{CO} C_{H_2O}^{\frac{1}{2}} C_{CO_2}^{\frac{1}{2}} \qquad (21)$$

where the subscript fu represents the fuel species, and the factors a and b are dependent on the type of fuel species considered. The source terms for each of the remaining species are similarly determined. Nitrogen is also considered since air is the oxidiser; however, it is treated inert with its production rate being zero. In summary, $N-1$ species conservation equations and one algebraic expression relating these species to nitrogen are solved.

The consideration of multiplicative effects between chemical kinetics and turbulence would require a very sophisticated turbulence closure scheme or Direct Numerical Simulation (DNS). Since DNS methods are still in an early stage of development and turbulent combustion models with finite-rate chemistry are not available, the effects of turbulence on chemistry are not considered in this study.

3. Numerical Method

The theoretical formulation is solved using a numerical scheme based on the Lower-Upper Symmetric Successive Overrelaxation (LU-SSOR) technique.[19-21] This scheme solves the two- or three-dimensional Navier-Stokes equations and species transport equations by means of the finite volume approach. It has proven to be very robust and efficient for highly reactive systems such as the combustion of hydrogen and oxygen. The algorithm was previously validated for supersonic mixing and reacting flows by comparing predicted results with both experimental results and other numerical calculations.[21]

The advantage of the LU-SSOR technique lies in the manner of solving chemical source terms implicitly with inviscid fluxes. Most other implicit schemes require the inversion of block-banded matrices for the entire set of equations, but the LU-SSOR method requires only a scalar diagonal inversion of the flow equations and a diagonal block inversion for the species equations. Consequently, it has an operational count comparable to explicit schemes in addition to a fast convergence rate, thereby saving a considerable amount of CPU time. Furthermore, the scheme can be fully vectorized.

To improve numerical efficiency and accuracy, the governing equations in Cartesian coordinates are transformed to generalized coordinates as follows.

$$\xi = \xi(x,y) \quad \text{and} \quad \eta = \eta(x,y) \qquad (22)$$

The transformation is chosen so that the grid spacing in the computational domain is uniform and of unit length, i.e., $\Delta\xi$ and $\Delta\eta = 1$. The governing equation then takes the following form,

$$\frac{\partial \hat{Q}}{\partial t} + \frac{\partial \hat{E}}{\partial \xi} + \frac{\partial \hat{F}}{\partial \eta} = \hat{H} + \frac{\partial \hat{E}_v}{\partial \xi} + \frac{\partial \hat{F}_v}{\partial \eta} \qquad (23)$$

where the new dependent variables $\hat{Q}$, $\hat{E}$, $\hat{F}$, etc. are the transformed vectors in generalized coordinates. The inviscid flux and source vectors are treated implicitly, giving

$$\frac{\partial \hat{Q}}{\partial t} + \frac{\partial \hat{E}^{n+1}}{\partial \xi} + \frac{\partial \hat{F}^{n+1}}{\partial \eta} - \hat{H}^{n+1} = \frac{\partial \hat{E}_v^{n}}{\partial \xi} + \frac{\partial \hat{F}_v^{n}}{\partial \eta} \qquad (24)$$

where $n+1$ denotes the new time level, and n the present time level. For simplicity, the diffusion vectors $\hat{E}_v$ and $\hat{F}_v$ are solved explicitly.

Linearizing the inviscid flux vectors and source terms reveals the Jacobian matrices $\frac{\partial \hat{E}}{\partial \hat{Q}}$, $\frac{\partial \hat{F}}{\partial \hat{Q}}$, $\frac{\partial \hat{H}}{\partial \hat{Q}}$ which are represented by A, B, and D, respectively. Substitution into Eq. (24) yields

$$\left[I - D\Delta t + \Delta t\left(\frac{\partial}{\partial \xi} A \cdot + \frac{\partial}{\partial \eta} B \cdot\right)\right]^{n+1} \delta\hat{Q} = -\Delta t \left(\frac{\partial \hat{E}}{\partial \xi} + \frac{\partial \hat{F}}{\partial \eta} - \hat{H} - \frac{\partial \hat{E}_v}{\partial \xi} - \frac{\partial \hat{F}_v}{\partial \eta}\right)^{n} = -\Delta t\, R \qquad (25)$$

where R is the residual and I the identity matrix.

Equation (25) can be solved by directly inverting the large block-banded matrix on the left-hand side; however, this would be inefficient and require a great computational effort. Instead, a lower-upper (LU) factored implicit scheme developed by Yoon and Jameson,[19] is employed. In this method, the Jacobian matrices A and B are split such that their eigenvalues are positive for the A^+ and B^+ matrices and negative for the A^- and B^- matrices. There are many ways in which this splitting can be accomplished. One possibility which increases the diagonal dominance of Eq. (25) is

$$A^+ = \frac{1}{2}(A + \nu_A I) \;,\; A^- = \frac{1}{2}(A - \nu_A I)$$

$$B^+ = \frac{1}{2}(B + \nu_B I) \;,\; B^- = \frac{1}{2}(B - \nu_B I) \qquad (26)$$

where ν_A is greater than or equal to the maximum eigenvalue of the A Jacobian matrix (λ_A), $\nu_A \geq \max(|\lambda_A|)$. Similarly, ν_B is chosen such that $\nu_B \geq \max(|\lambda_B|)$. Equation (27) is then obtained with D_ξ^- and D_η^- as backward difference operators for matrices with positive eigenvalues and D_ξ^+ and D_η^+ as forward difference operators for matrices with non-positive eigenvalues.

$$\left[I + \Delta t\left(D_\xi^- A^+ + D_\xi^+ A^- + D_\eta^- B^+ + D_\eta^+ B^- - D\right)\right] \delta\hat{Q} = -\Delta t\, R \qquad (27)$$

This equation may be factorized using the relations

$$A^+ - A^- = \nu_A I \quad , \quad B^+ - B^- = \nu_B I \;,$$

$$C = \left[1 + \Delta t\left(\frac{\nu_A}{\Delta\xi} + \frac{\nu_B}{\Delta\eta}\right)\right] I$$

to give

$$\left[C + \Delta t\left(D_\xi^- A^+ + D_\eta^- B^+ - \frac{A^+}{\Delta\xi} - \frac{B^+}{\Delta\eta} - D\right)\right] \cdot C^{-1} \cdot \left[C + \Delta t\left(D_\xi^+ A^- + D_\eta^+ B^- + \frac{A^-}{\Delta\xi} + \frac{B^-}{\Delta\eta}\right)\right] \delta\hat{Q} = -\Delta t\, R \qquad (28)$$

Taking the limit in which $\Delta t \to \infty$, the final version of the governing equation is obtained

$$\left[DIAG_{i,j} - \frac{A^{+}_{i-1,j}}{\Delta\xi} - \frac{B^{+}_{i,j-1}}{\Delta\eta}\right]\delta Q^{*} = -\left(\frac{\nu_A}{\Delta\xi} + \frac{\nu_B}{\Delta\eta}\right) R \quad (29a)$$

$$\left[\left(\frac{\nu_A}{\Delta\xi} + \frac{\nu_B}{\Delta\eta}\right) I + \frac{A^{-}_{i+1,j}}{\Delta\xi} + \frac{B^{-}_{i,j+1}}{\Delta\eta}\right]\delta\hat{Q} = \delta Q^{*} \quad (29b)$$

where

$$DIAG_{i,j} = \left[\left(\frac{\nu_A}{\Delta\xi} + \frac{\nu_B}{\Delta\eta}\right) I - D\right]_{i,j}$$

Equation (29a) is solved by forward marching since the left-hand side is lower bidiagonal, then Eq. (29b) is solved by backward marching to complete one iteration. The inversion method for Eq. (29a) can be simplified to some extent because only the lower right corner of D is non-zero. A scalar diagonal inversion is applied to the first four flow equations and a block diagonal matrix inversion is performed on the species equations.

4 Discussion of Results

Calculations were performed with HTPB (hydroxyl terminated polybutadiene) solid fuel samples located along the bottom surface of a 2-D chamber with an inlet height of 3.175 cm and a length of 15.24 cm, as shown in Fig. 2. The sample spans 7.62 cm along the lower boundary of the chamber, thus allowing space for adequate mixing and chemical reactions downstream of the fuel. HTPB was chosen for this study since it has been characterised[23] for its wide use in composite propellants, and it is an energetic binder commonly found in solid fuels.[3,6,7,23] In addition, a companion experimental work is conducted with HTPB-based fuels[3] under supersonic crossflow conditions.

To facilitate the gas phase analysis, it is assumed that butadiene (C_4H_6) is the only product released from the fuel surface. This simplification is justified for the following reasons. First, vinylcyclohexene, the second-most abundant pyrolysis product,[24,25] can be adequately represented by butadiene, since the monomer and dimer have similar molecular structures and kinetic parameters. Second, the majority of hydrocarbons tabulated in Ref. 17 have equal activation energies and only a slight variation in pre-exponential factor. Thus the consideration of additional fuel species would not alter the kinetic behavior of the gas phase. Finally, in the limit of fast kinetics with respect to the diffusion process, one hydrocarbon may be sufficient to represent the fuel species, and additional hydrocarbons would not change the fundamental characteristics of the sample. With the two-step reaction mechanism of Eqs. (18) and (19), the gas phase contains six species: C_4H_6, O_2, CO, H_2O, CO_2, and N_2. The rate constants for these reactions are given in Refs. 17 and 18.

Each calculation employed a 120x80 grid. The numerical grid was uniform in the horizontal direction with a spacing of 0.129 cm. Since many important physical processes occur in the region immediately above the sample surface, the numerical grid was clustered vertically near the surface with the smallest grid being 45 microns in height. For each computation, the total mass flowrate of the ram air and pyrolysed fuel was conserved to within 0.1% at the exit. The scheme required approximately 40 μsec of CPU time per iteration per grid point on a Cray Y-MP machine.

Figure 3 shows the contour plots for Mach number, temperature and pressure for the baseline case with a inlet Mach number of 2, an inlet static temperature of 1400 K, and an inlet static pressure of 1 atmosphere. The Mach-number contours are incremented by 0.1, temperature contours by 100 K, and pressure contours by 0.02 atm. These figures only show the bottom third of the combustion chamber and have been magnified in the y-direction by a factor of ten to resolve the flow structures nearest the surface. In Fig. 3a, a weak inlet shock occurs at the entrance due to the abrupt deceleration of the flow at the surface to satisfy the no-slip condition. This deceleration enhances temperature recovery and heat transfer at the surface. Immediately downstream of the entrance, the temperature plot shows a series of closely spaced contours, indicating the leading edge of the flame with a maximum temperature of almost 2500 K. The heat released by chemical reactions causes another oblique shock wave originating from the flame zone, which is evidenced in Fig. 3c. This wave travels upward to the line of symmetry and meets a similar wave coming down from the upper half of the chamber. The right-running wave then reflects off the bottom surface, moves upward again and finally exits the chamber. These reflected waves cause the fluctuating Mach-number contours shown in Fig. 3a. As the flow crosses this shock structure, it first decelerates by passing through a reflected compression wave, then accelerates through an expansion caused by the distributed reaction zone near the surface.

The mass fractions of butadiene and oxygen are presented in Fig 4. These plots show only the bottom sixth of the chamber (y = 0.5 cm). The fuel species are generated from the sample surface, then diffuse toward the freestream to mix and burn with oxygen. At the inlet to the chamber, the oxygen is uniformly distributed with a mass fraction of 0.23. It is then consumed by the chemical reaction which generates a maximum flame temperature of 2500 K. The flame temperature diminishes downstream because of heat transfer back to the fuel sample and a reduction in chemical reactions caused by an oxygen deficiency at the fuel surface. The maximum temperature at each axial station occurs in a region where mass fractions of oxygen and butadiene are near stoichiometric. The temperature then drops off from this region due to fuel-rich conditions toward the surface and oxygen-rich conditions toward the freestream. The vertical location of maximum temperature is determined by the rate of diffusion and blowing of pyrolyzed fuel-rich gases into the crossflow. Finally, the species distributions show incomplete consumption of butadiene at the exit along with the complete consumption of oxygen near the surface, which suggests that further entrainment of oxygen or perhaps better mixing between the fuel and oxidizer will improve combustion efficiency.

Figure 5 shows the burning rate of HTPB for the baseline case. At the inlet, the leading edge of the fuel sample experiences the temperature recovery and enhanced heat transfer due to the abrupt deceleration of the flow, resulting in a burning rate slightly higher than succeeding locations along the sample. Immediately downstream of the inlet is a large peak with a burning rate of 1.13 mm/sec and surface temperature of 1060 K. This is a result of the intense convective and radiative heat feedback from the flame to the fuel surface. As the flame temperature decreases downstream, the heat transfer to the solid boundary is reduced, resulting in a decaying profile of the burning rate.

A plot of surface pressure is shown in Fig. 6. The first two peaks in this curve are due to the inlet shock and burning phenomenon mentioned previously. After passage of the second peak, the pressure abruptly decreases, then increases slowly along the length of the fuel sample from x = .020 to x = .075 m. The slight pressure rise can be explained qualitatively by comparing this situation to a constant-area tube with supersonic flow and heat addition (by external means or chemical reaction), in which a similar pressure increase occurs along the length of the tube. Finally, the third peak in the curve results from the reflected oblique shock wave and subsequent expansion evident in Fig. 3c.

In order to study the effect of freestream conditions on the burning characteristics of the sample, calculations were also carried out with different pressures and temperatures. Figures 7a and 7b show the results for an inlet pressure of five atmospheres, with other conditions remaining the same as the baseline case. Compared to the baseline case, the flame-front is shifted slightly upstream with a shorter stand-off distance from the fuel surface. Furthermore, the maximum flame temperature is increased by 350 K. The shift in the flame-front location and the decrease in stand-off distance are due to the increasing gas-phase reaction rates with pressure, whereas the rise in flame temperature can be attributed to the five-fold increase in oxidizer partial pressure. Because more oxygen was supplied to the combustion chamber for reaction, the exit temperature near the surface has also increased by approximately 250 K. In addition to the faster kinetics, the burning rate of the solid fuel has increased considerably since the flame is at a higher temperature and is closer to the boundary, causing the radiative and convective

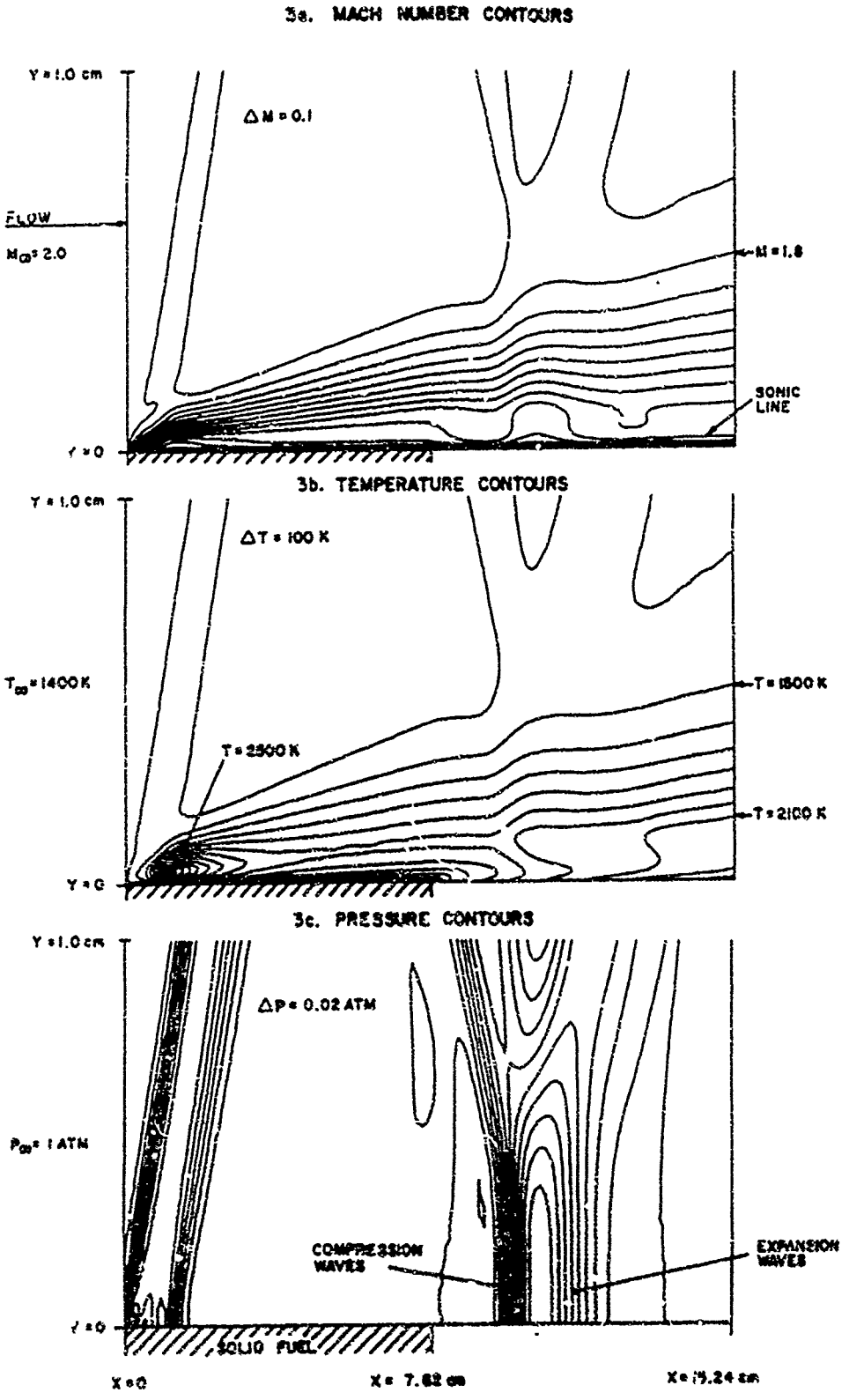


Figure 3. Results from Baseline Case; $M_\infty = 2.0$, $T_\infty = 1400K$, $p_\infty = 1$ atm

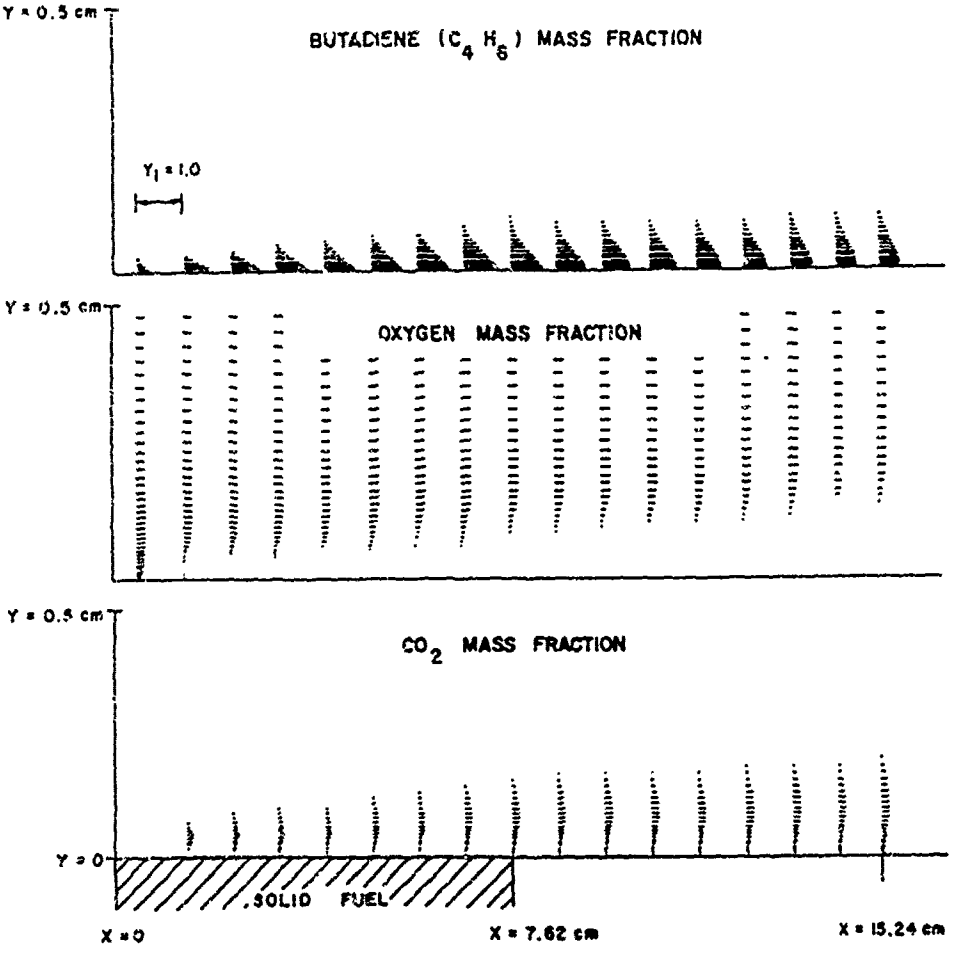


Figure 4. Species Mass Fractions for Baseline Case: M_∞=2.0, T_∞=1400K, p_∞=1 atm

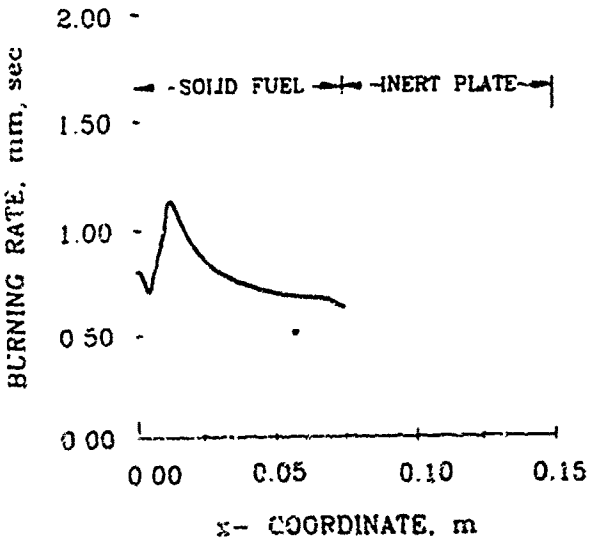


Figure 5. Solid Fuel Burning Rate for Baseline Case; M_∞=2.0, T_∞=1400K, p_∞=1 atm

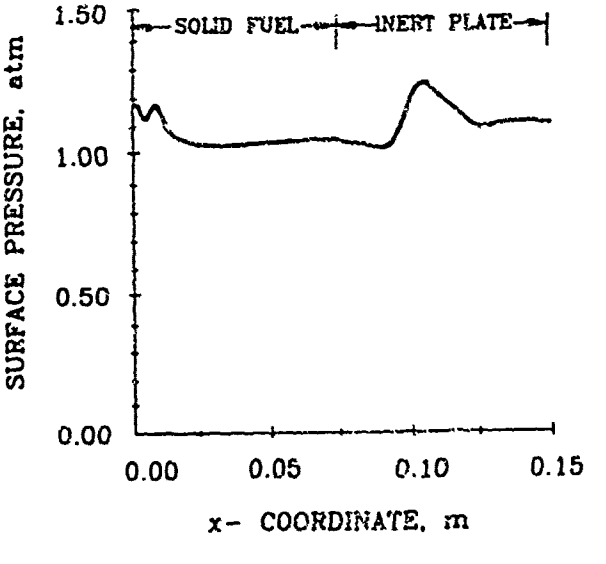
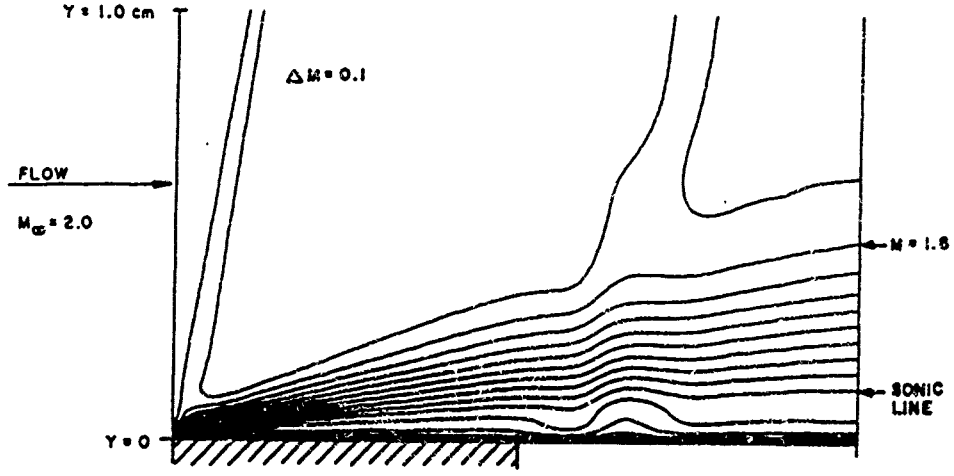


Figure 6. Surface Pressure for Baseline Case; M_∞=2.0, T_∞=1400K, p_∞=1 atm

7a. MACH NUMBER CONTOURS



7b. TEMPERATURE CONTOURS

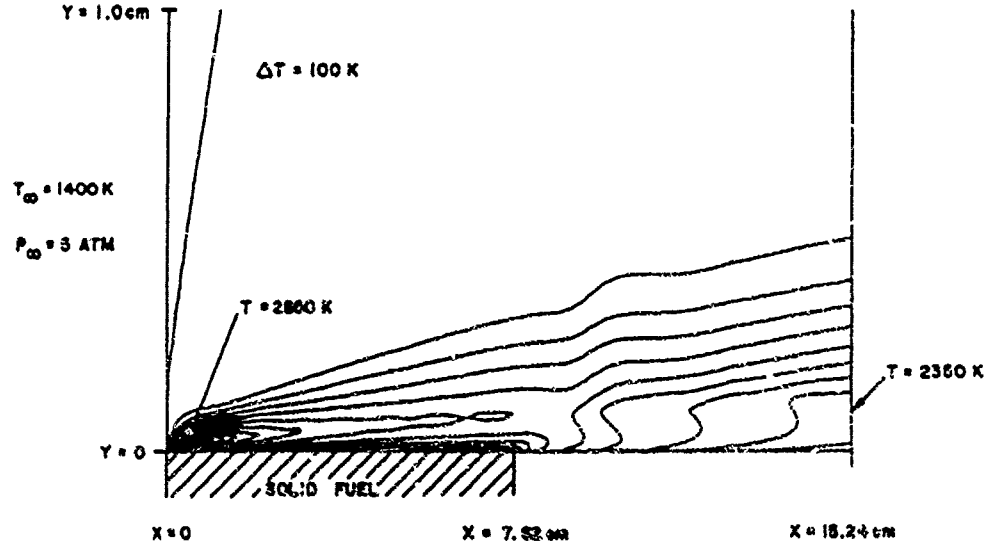


Figure 7. Contours for M_∞=2.0, T_∞=1400K, p_∞=5 atm

heat feedback to increase significantly. The curve shown in Fig. 8 has a peak burning rate of 1.55 mm/sec, nearly 40% higher than that in the baseline case.

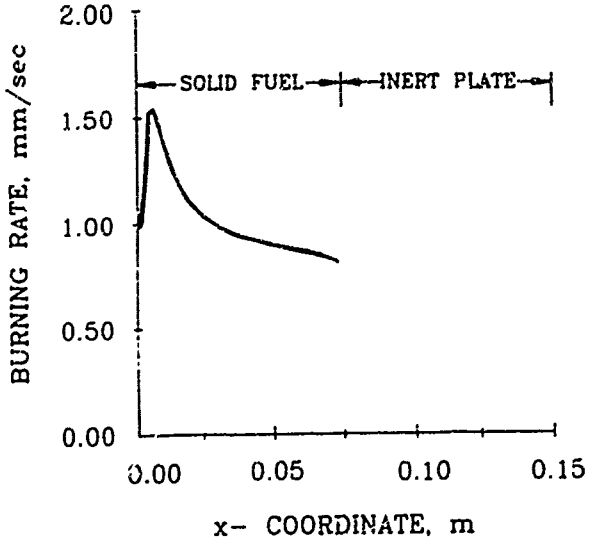


Figure 8. Solid Fuel Burning Rate;
M_∞=2.0, T_{t_∞}=1400K, p_∞=5 atm

A calculation with an increased inlet temperature of 1800 K was also performed. Results for this case were similar to the previous calculation with a higher pressure, in which the flame-front was shifted upstream due to enhanced chemical reaction rates at elevated pressure. Compared to the baseline case, the maximum flame temperature increased by nearly 400 K, corresponding to the 400 K rise in the inlet temperature. On the average, the burning rate of the solid fuel increased by 15% along the length of the sample because of the higher flame temperature and intensified heat transfer from the flame to the surface.

Increased inlet temperature and pressure have shown to enhance the regression rate of the fuel sample. To further assess the effects of these freestream variables on the combustion behavior of the solid fuel, a burning rate parameter r_b^* has been established for comparison among cases. This parameter is formulated so that its value remains constant along the length of the sample, starting from the axial position of the leading edge of the flame to the downstream end of the fuel. It is evaluated by multiplying the burning rate of the sample by a local dimensionless parameter, namely

$$r_b^* = r_{b,x}\left(\frac{x}{L}\right)^{\frac{1}{2}} \qquad (30)$$

where x is the axial distance from the inlet, L the total length of the fuel sample, and $r_{b,x}$ the local solid fuel burning rate of the sample. The exponent of $\frac{1}{2}$ was chosen to give the least variation in r_b^* along the length of the sample. The axial distribution of r_b^* is presented in Fig. 9 for various pressures and is shown to be nearly constant. The burning rate parameter was then plotted versus pressure for two different inlet temperatures, giving the result shown in Fig. 10. The burning rate increases with pressure for several reasons. First, the molar concentration of oxygen in the freestream increases with inlet pressure, so more oxidizer is available for reaction with the fuel-rich region near the surface. A subsequent rise in flame temperature intensifies heat transfer to the surface and increases the burning rate. Second, the gas-phase reaction rates are proportional to the 1.75 power of pressure and have a profound effect on the flame thickness. At low pressures, kinetic rates are relatively slow with regard to the diffusion and mixing processes of the fuel and oxidizer, so the two species may overlap to form a widely distributed reaction zone. However, at higher pressures the kinetic rates are fast enough for the fuel and oxidizer to react upon contact, thereby collapsing the reaction zone to a thin sheet and increasing the local heat of reaction, the flame temperature, and the subsequent radiative and convective heat transfer rates to the fuel surface. Finally, the molecular diffusion rate of fuel species decreases with an increase in pressure, thereby bringing the flame closer to the surface and increasing the burning rate of the solid fuel. This effect may only be secondary, since other processes such as turbulence and blowing also govern the flame stand-off height.

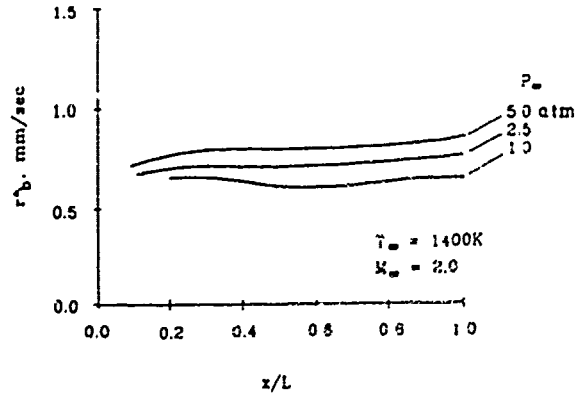


Figure 9. Axial Distribution of the Burning Rate Parameter

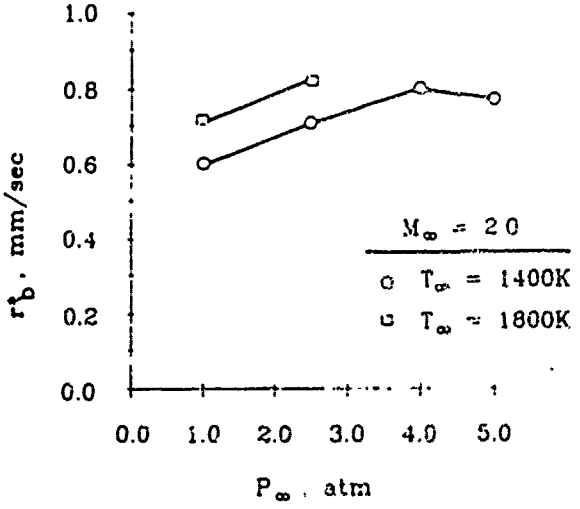


Figure 10. Variation of Burning Rate Parameter with Pressure

For the operating range of 1-4 atmospheres, the dependence of the regression rate on ambient pressure and temperature can be expressed by an empirical power law.

$$r_s \propto p^{0.25} T^{0.87} \tag{31}$$

The ambient temperature appears to have a stronger influence on the burning rate than does the pressure, which closely corresponds to results obtained under subsonic crossflow conditions with polyethylene fuels.[6] The pressure and temperature exponents were 0.25 and 0.50, respectively, for subsonic crossflow conditions. Results under supersonic conditions show similar freestream effects; however, caution must be exercised in extrapolating Eq. (31) to other cases because of the differences in operating range and fuel composition.

At an inlet pressure of five atmospheres, the burning rate decreases slightly as shown in Fig. 10. This reversal in the burning rate trend may be explained as follows. As the pressure increases from four to five atmospheres, the mass flow of air also increases, necessitating an increase in the heat released by combustion to raise the total enthalpy of the product gases. Although the reaction rate is enhanced with pressure, the overall heat release may not increase due to the lack of additional fuel in the reactions. The mixture may reach a considerably fuel-lean condition, and cannot supply the necessary energy to raise the enthalpy of the flow. Consequently, a decrease in heat feedback to the solid fuel is observed causing a reversal of the burning rate trend with pressure. The burning rate will achieve a maximum value at some threshold pressure, then diminish due to the finite energy released by combustion. It is interesting to note that the combustion of solid propellants does not encounter this type of pressure threshold on the burning rate. The burning rates are proportional to pressure throughout a wide range of chamber pressures because the oxidizer-to-fuel ratio is fixed within the propellant.

5. Conclusions

The combustion of HTPB solid fuel samples under supersonic crossflow has been studied using a comprehensive numerical analysis. The formulation is based on the full two-dimensional Navier-Stokes equations with finite-rate chemistry and variable properties. The Baldwin-Lomax algebraic model was employed for turbulence closure. The governing equations were solved numerically using a flux-vector splitting LU-SSOR technique that treats source terms implicitly. Results showed a distinct flame region above the fuel sample. Inlet conditions were varied for several cases to determine the effect of pressure and temperature on the combustion behavior. For the operating range considered, results indicated that both pressure and temperature had a strong influence on the solid fuel burning rate, and that the burning rate increases with pressure at low inlet pressures from 1-4 atmospheres. At a higher pressure, the energy released by combustion is not sufficient to further raise the temperature of the crossflow. This results in a decrease in heat feedback to the fuel sample, causing a reversal of the burning rate trend with pressure.

Acknowledgements

This paper represents a part of the research work conducted under the sponsorship of the Office of Naval Research, Arlington, VA, Contract No. N00014-86-K-0468. The support and encouragement of Drs. Richard S. Miller and Gabriel D. Roy are highly appreciated. The authors would like to thank Drs. J. S. Shuen and K. C. Hsieh of NASA Lewis Research Center, for providing helpful information and discussions. In addition, the authors wish to acknowledge the National Science Foundation for providing CPU time on the CRAY Y-MP at the Pittsburgh Supercomputing Center.

References

1. Billig, F. S., Waltrup, P. J., and Stockbridge, R. D., "Intermal-Rocket Dual-Combustion Ramjets: A New Propulsion Concept," *Journal of Spacecraft and Rockets*, Vol. 17, No. 5, Sept.-Oct. 1980, pp. 4[illegible]424.

2. Snyder, T. S., Jarymowycz, T. A., Hsieh, W. H., Peretz, A., Yang, V., and Kuo, K. K., "Pyrolysis and Combustion of Solid Fuels under Subsonic and Supersonic Conditions," *Proceedings of 26th JANNAF Combustion Meeting*, Oct., 1989.

3. Snyder, T. S., Jarymowycz, T. A., Pace, K. K., and Kuo, K. K., "Solid Fuel Ignition and Combustion Characteristics Under High-Speed Crossflows," AIAA Paper No. 90-2075, AIAA/ASME/SAE/ASEE 26th Joint Propulsion Conference, Orlando, FL, July, 1990.

4. Joulain, P., Most, J., Sztal, B., and Vantelon, J., "Theoretical and Experimental Study of Gas-Solid Combustion in Turbulent Flow," *Combustion Science and Technology*, Vol. 15, 1977, pp. 225-241.

5. Mady, C. J., Hickey, P. Y., and Netzer, D. W., "Combustion Behavior of Solid-Fuel Ramjets," *Journal of Spacecraft and Rockets*, Vol. 15, No. 3, May-June 1978, pp. 13[illegible]132.

6. Schulte, G., "Fuel Regression and Flame Stabilization Studies of a Solid-Fuel Ramjet," *Journal of Propulsion and Power*, Vol. 2, No. 4, July-Aug. 1986, pp. 301-304.

7. Netzer, A., and Gany, A., "Burning and Flameholding Characteristics of a Miniature Solid Fuel Ramjet Combustor," AIAA Paper No. 88-3044, AIAA/ASME/SAE/ASEE 24th Joint Propulsion Conference, Boston, MA, July, 1988.

8. Gany, A., and Netzer, D. W., "Combustion Studies of Metallized Fuels for Solid Fuel Ramjets," AIAA Paper 85-1177, AIAA/ASME/SAE/ASEE 21st Joint Propulsion Conference, Monterey, CA, July, 1985.

9. Scott, C. K., and Netzer, D. W., "Metallized Fuel Burning Characteristics in the Solid Fuel Ramjet," *Proceedings of 23rd JANNAF Combustion Meeting*, CPIA Publication No. 488, Vol. I, October 1986.

10. Hsieh, W. H., Peretz, A., Huang, I. T., and Kuo K. K., "Combustion Behavior of Boron-Based BAMO/NMMO Fuel-Rich Solid Propellants," AIAA Paper 89-2894, AIAA/ ASME/SAE/ASEE 25th Joint Propulsion Conference, Monterey, CA, July, 1989.

11. Sherwood, T. K., Pigford, R. L., and Wilke, C. R., *Mass Transfer*, McGraw-Hill Publishing Co., New York, NY, 1975.

12. Williams, F. A., *Combustion Theory*, 2nd Edition, Benjamin/Cummings Publishing Co., Menlo Park, CA, 1985, pp. 631-645.

13. McBride, B. J., and Gordon, S., "FORTRAN IV Program for Calculation of Thermodynamic Data," NASA TN D-4097, 1967.

14. Reid, R. C., Prausnitz, J. M., and Poling, B. E., *The Properties of Gases and Liquids*, 4th Edition, McGraw-Hill Publishing Co., New York, NY, 1987.

15. Baldwin, B. S., and Lomax, H., "Thin Layer Approximation and Algebraic Model for Separated Turbulent Flows," AIAA Paper 78-257, 16th Aerospace Sciences Meeting, Huntsville, AL, Jan., 1978.

16. Incropera, F. P., and DeWitt, D. P., *Fundamentals of Heat and Mass Transfer*, 2nd Ed., John Wiley and Sons, New York, 1985, pp. 657-661.

17. Westbrook, C. K., and Dryer, F. L., "Simplified Reaction Mechanisms for the Oxidation of Hydrocarbon Fuels in Flames," *Combustion Science and Technology*, Vol. 27, 1981, pp. 31-43.

18. Dryer, F. L., and Glassman, I., "High-Temperature Oxidation of CO and CH_4," *Proceedings of Fourteenth Symposium (International) on Combustion*, 1972, pp. 987-1003.

19. Yoon, S., and Jameson, A., "An LU-SSOR Scheme for the Euler and Navier-Stokes Equations," AIAA Paper 87-0600, 25th Aerospace Sciences Meeting, Reno, NV, Jan., 1987.

20. Jameson, A., and Yoon, S., "Lower-Upper Implicit Schemes with Multiple Grids for the Euler Equations," *AIAA Journal*, Vol. 25, No. 7, July 1987, pp. 929-935.

21. Shuen, J. S., and Yoon, S., "Numerical Study of Chemically Reacting Flows Using a Lower-Upper Symmetric Successive Overrelaxation Scheme," *AIAA Journal*, Vol. 27, No. 12, Dec. 1989, pp. 1752-1760.

22. Cohen, N. S., Fleming, R. W., and Derr, R. L., "Role of Binders in Solid Propellant Combustion," *AIAA Journal*, Vol. 12, No. 2, Feb. 1974, pp. 212-218.

23. Schulte, G., Pein, R., and Högl, A., "Temperature and Concentration Measurements in a Solid Fuel Ramjet Combustion Chamber," *Journal of Propulsion and Power*, Vol. 3, No. 2, March-April 1987, pp. 114-120.

24. Ericsson, I., "Sequential Pyrolysis Gas Chromatographic Study of the Decomposition Kinetics of Cis-1,4-Polybutadiene," *Journal of Chromatographic Science*, Vol. 16, 1978, pp. 340-344.

25. Brazier, D. W., and Schwartz, N. V., "The Effect of Heating Rate on the Thermal Degradation of Polybutadiene," *Journal of Applied Polymer Science*, Vol. 22, 1978, pp. 113-124.

EFFECT OF MAGNESIUM-COATED BORON PARTICLES ON BURNING CHARACTERISTICS OF SOLID FUELS IN HIGH-SPEED CROSSFLOWS

K. K. Pace, T.A. Jarymowycz, V. Yang, and K. K. Kuo
Department of Mechanical Engineering
The Pennsylvania State University
University Park PA 16802

ABSTRACT

An experimental investigation of the ignition and combustion phenomena of boron-laden solid fuels under high subsonic crossflows was conducted. Hydroxyl-terminated polybutadiene (HTPB)-based fuels containing boron particles with and without magnesium coatings were studied using a real-time x-ray radiography system and direct video. The effect of pressure, oxygen mass fraction, and percent of magnesium coating on the regression rates of the solid fuels was determined and burning rate correlation was obtained. At low pressures (below 0.55 MPa), fuels with the magnesium-coated particles experienced higher burning rates than those of the uncoated particles. This is due to the reduction of ignition time of coated boron particles heated by the surface reactions between magnesium and oxygen. However, at higher pressures magnesium coating of the boron particles has diminishing effect on the regression rates of the solid fuels. This trend is caused by the decrease in the contribution of heat generation from surface reactions to the overall heat feedback. The effect of boron type on solid-fuel combustion was also studied. High purity boron with smaller particle size was found to give higher solid fuel regression rates.

1. INTRODUCTION

Many experimental and theoretical studies have been conducted to investigate the feasibility of boron particles as a solid-fuel ingredient for air-breathing propulsion systems, such as solid-fuel ramjet engines and solid-propellant ducted rockets. The interest in boron stems from its high volumetric heating value, which makes it an attractive fuel additive for volume-limited missions. However, problems associated with ignition delay and combustion efficiency often prevent boron particles from delivering their maximum potential. An understanding of boron combustion is necessary to alleviate these problems and to optimize the use of boron.

A study by Jarymowycz et al. (1990) showed that the addition of up to 10% boron particles by weight in HTPB-based fuels increases the burning rates by approximately 10 percent, while further boron addition causes the regression rates to decrease. The increase in burning rates with the addition of small

transfer back to the fuel surface, thereby increasing the regression rate of the fuel. The decrease in performance with boron addition beyond 10% can be attributed to several factors. Unreacted boron particles in the gas phase can act as a heat sink and reduce the gas-phase temperature; accumulation of boron particles on and above the sample surface can block the heat feedback to the surface and thus reduce the surface pyrolysis; and the overall reduction of HTPB in the solid fuel may decrease the amount of exothermic heat release from the gas-phase reactions, thereby preventing complete combustion of the boron particles. Pein et al. (1989) also studied the effects of boron addition on HTPB-based solid fuel combustion and obtained similar results. They noticed an increase in specific thrust and combustion efficiency with boron addition up to 20 percent, and a reversal in this trend for boron addition beyond 20 percent. The observations listed above for the burning rate trends can also be used to describe the changes in specific thrust and efficiency with boron addition. The reasons why the maximum performance levels occur at different boron percentages for the two studies is unclear, but are most likely due to different testing environments or data reduction procedures.

The study by Pein et al. also employed air swirl in the combustion chamber to improve the combustion efficiencies of the boron-laden fuels. Without swirl the maximum efficiency achieved was only 40 percent. However, with the addition of air swirl this efficiency was increased to 60 percent. This improvement can be attributed to enhanced mixing and increased particle residence times in the combustion chamber, which ultimately result in higher temperatures and better performance.

Poor combustion efficiency has also been encountered with boron fuels at low pressures in afterburner applications. These problems have motivated studies of ignition and combustion characteristics of individual boron particles. King (1982) developed a single-particle model which described the removal of the inhibiting boron-oxide (B_2O_3) layer surrounding the boron particle during the ignition process. The ignition sequence allows for convective and radiative heating/cooling of the particle, oxygen diffusion through the oxide layer for exothermic reactions between boron and oxygen in the subsurface regions, endothermic reactions between B_2O_3 and water vapor on the outer surface of the particle, and cooling by evaporation. To achieve ignition, a sufficiently high particle temperature must be reached such that the oxide layer is removed and vigorous heterogeneous reactions between the boron and oxygen occur. Ignition delay times were found to depend strongly on the particle size, oxide layer thickness, and ambient conditions surrounding boron particles. Under the conditions studied by King, ignition times were reduced by raising the ambient temperature, increasing the oxygen concentration, reducing the particle diameter, and minimizing the initial oxide layer thickness.

According to Childs et al. (1971) and Yuasa and Takeno (1982), magnesium can be used in combination with boron in solid fuels to shorten ignition delay times and improve combustion efficiency. Based upon Chen et al.(1988), although magnesium contains a lower heat of combustion than boron, its oxide layer is thinner and more gas permeable, thus the ambient gases can diffuse through to the magnesium more easily. This allows for more abundant exothermic reactions beneath the surface layer, providing shorter ignition delay times. In addition, when used in conjunction with boron, magnesium can react with B_2O_3 to form elementary boron at high temperatures [Nemodruk and Karaleva (1969)]. This reaction (known as the "Moissan Process") may

decrease the delay time needed for the boron particles to ignite because the elementary boron is exposed to an oxidizing atmosphere sooner than it would be under cases without magnesium. Thus, boron and magnesium particles can be used together to generate better performances.

A new technique has recently been developed in which boron particles are coated with magnesium [Criner and Kosowski (1990) and Calcote et al. (1990)]. In Criner and Kosowski's work, the coating is applied before a substantial oxide layer has formed on the boron. This method is proposed to be superior to conventional mixing of boron and magnesium powders because the exothermic reactions between the magnesium and oxidizer promote a fast increase in particle temperature, and the initially thin B_2O_3 layer will be quickly removed through reaction with the magnesium or evaporation. Preliminary observations of the combustion of the boron particles with up to 30 weight percentage of magnesium coating showed that the burning rates increased with magnesium addition. The most significant improvement was found with 20% addition.

Amorphous boron powder can be manufactured and processed using several different techniques. The method used can significantly affect the purity, particle size, shape, and surface characteristics of the boron powder. Variation in these physical and chemical properties can influence the ignition and combustion characteristics of the boron powders.

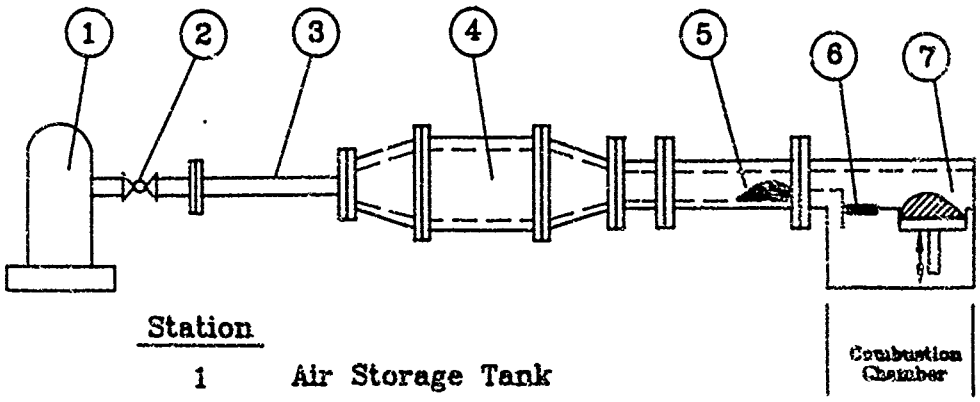
This study is part of an ongoing research effort to investigate ignition and combustion characteristics of boron-containing solid fuels under high-speed crossflows. The specific purpose of this study is to determine the effects of magnesium coating on the combustion of boron-laden solid fuels. Experiments were conducted to study the combustion characteristics of the solid fuels and to determine their burning rates as a function of the percent loading of the magnesium coating, as well as the freestream pressure, temperature, and oxygen concentration. In addition, two different brands of uncoated boron particles were tested.

2. EXPERIMENTAL APPROACH

2.1 Test Facility

An experimental study was conducted using a connected-pipe facility as shown in the schematic diagram of Fig. 1. The test rig receives compressed air from two large storage tanks with a combined capacity of 72 cubic meters and a maximum pressure of 4.9 MPa. Air from these two tanks is mixed and burned with propane in the vitiator to achieve a high temperature in the settling chamber. The hot gases then accelerate through a nozzle. Downstream of the test section, an adjustable nozzle chokes the flow and controls the Mach number in the test chamber. The facility is capable of providing vitiated air at a high-velocity crossflow with a static pressure range of 0.1 to 0.62 MPa in the test section, simulating the combustion chamber conditions of a hypersonic vehicle at high altitudes. The maximum flowrate attainable is 8 kg/s with a duration of four minutes at the highest pressure.

Pressure and temperature measurements are taken at several locations: in the settling chamber, upstream of the first nozzle, at the inlet of the combustion chamber, and downstream of the solid fuel sample. Data are not taken in the



Station	
1	Air Storage Tank
2	Pneumatic Ball Valve
3	Vitiator
4	Settling Chamber
5	Converging–Diverging Nozzle
6	Test Section (Fuel Sample)
7	Downstream Adjustable Nozzle

Fig. 1 Schematic diagram of connected-pipe facility.

regions surrounding the fuel sample, since measurements in these locations would interfere with the x-ray radiography and video systems. Steady flow conditions are achieved by means of a feedback control loop between a pneumatic ball valve in the air supply line and a pressure transducer in the settling chamber, with a maximum fluctuation of 1 percent in the stagnation pressure. Combustion chamber temperature and pressure are monitored at the locations shown in Fig. 2. Temperature measurements are obtained using R-type (platinum/platinum-13% rhodium) thermocouples. An IBM PC/AT computer records all temperature and pressure measurements using a Metrabyte DAS-16 high-speed data acquisition system.

The high-enthalpy flow enters the combustion chamber through a short and straight rectangular inlet measuring 3.18 cm in height, 10.16 cm in width, and 10.8 cm in length, as depicted in Fig. 2. This inlet flow has a Reynolds number based on the inlet height of approximately 1×10^6 before passing over a rearward-facing step into the test section. The solid fuel sample is placed directly behind this step. The initial step height is kept constant at 1.27 cm for all tests, creating a recirculation zone with sufficient dimensions for achieving ignition and stable combustion of the fuel sample, and leaving adequate space for boundary layer redevelopment in the downstream portion of the fuel sample.

2.2 Solid Fuels

All fuels studied in this work were processed by mixing liquid HTPB binder (ARCO R45-M) and 10% of boron powder by weight with the curing agent isophorone diisocyanate (IPDI). Two different brands of amorphous boron powder were studied, one manufactured by Callery Chemical Company and the other by SB Boron Corporation. The Callery boron has a much higher purity than the SB 95 boron and a mean particle diameter approximately ten times smaller, as shown in Table I. Some of the fuel samples were made with

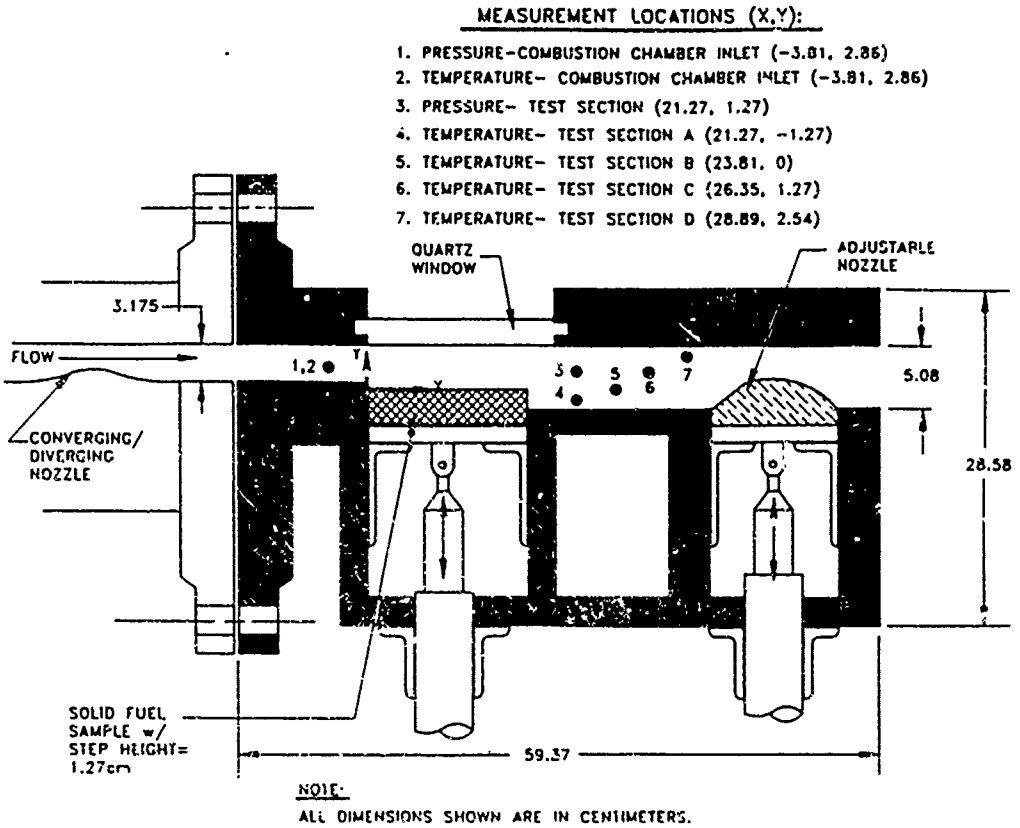


Fig. 2 Schematic diagram of experimental combustion chamber.

SB 95 boron powders coated with magnesium in amounts of 10 and 20 percent by weight. The magnesium-coated boron particles were manufactured by Mach I Inc.

The fuels were prepared by blending the HTPB, IPDI, and boron powder in a vacuum mixer at 50 ^{o}C for one hour. After mixing, the fuels were poured into a mold and degassed in a vacuum desiccator, then cured at 65 ^{o}C for four days. The cured samples measured 15.2 cm in length, 5.1 cm in width, and 3.2 cm in height.

2.3 Ignition System

All of the tests performed in this study utilized the hot crossflow gases to ignite the solid fuel sample. Before ignition, air and propane flowrates were slowly increased to raise the freestream pressure while a steady test section inlet temperature was maintained (generally between 500 and 600 K). When the desired test section inlet pressure was reached, the freestream temperature was adjusted until the hot crossflow gases ignited the fuel sample. The freestream inlet temperatures recorded at the onset of solid-fuel ignition in this study were between 640 and 825 K.

2.4 Real-Time X-Ray Radiography and Video System

To determine the burning rates of solid fuels accurately and non-intrusively, a real-time x-ray radiography system was used, as shown in Fig. 3. A continuous wave x-ray is generated by a constant potential power supply system and is delivered to the x-ray tube head. A lead diaphragm is located at the exit port of

Table 1 Properties of Amorphous Boron Powders*

	Callery Boron	SB 95 Boron
Purity (%)	> 99	95.5-96.5
Impurities (%)	not available	1.0-1.1 Mg, < 0.5 H_2O_2 < 0.25 moisture < 0.2 H_2O soluble
Particle Size (μm)	0.04-0.15	0.8-1.0
Melting Point (deg C)	2,300	2,160

the tube head to limit the angle of divergence of the x-ray beam and to confine the beam to the measuring section of the test rig. Graphite and LEXAN windows are installed on both sides of the viewing area to facilitate x-ray penetration. After passing through the test rig, x-ray signals are transformed to fluorescent light signals on the output screen of a tri-field image intensifier. The intensifier output is recorded by a video camera. After the completion of each test, the regression rate of the fuel sample is deduced using a Quantax 9210 digital image processing system.

Direct video is also employed to study the burning phenomena of the solid fuels. The top view of the solid fuel is captured through a quartz window (see Fig. 2) to study surface ignition, flame spreading, and combustion processes.

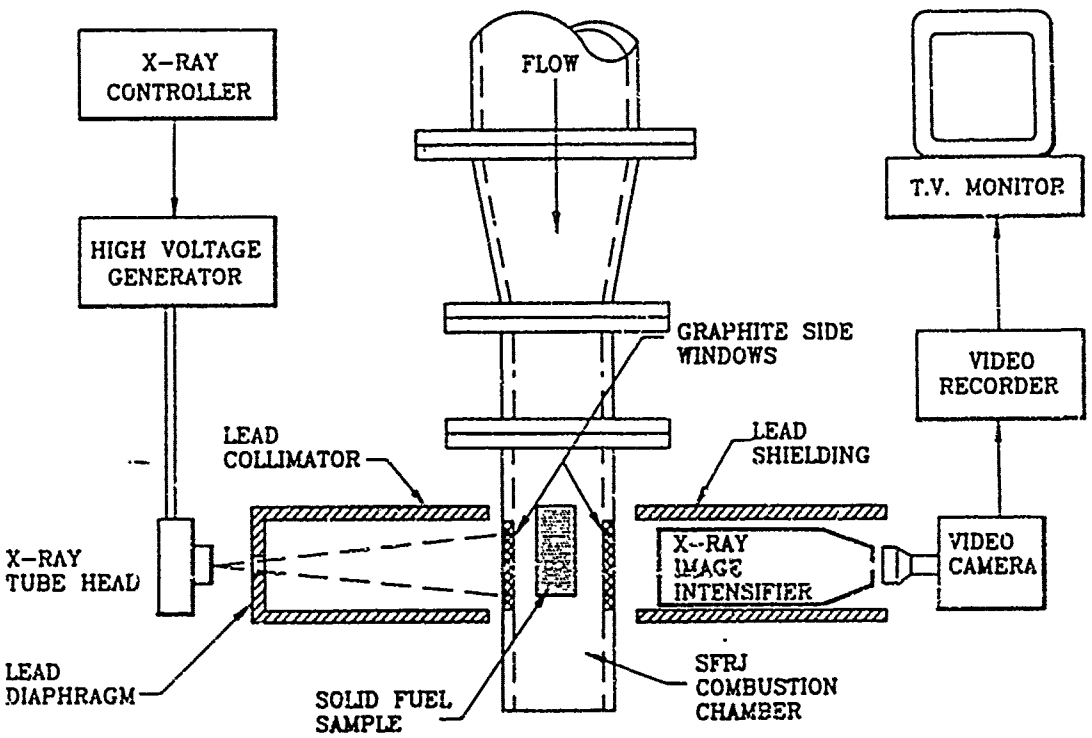


Fig. 3 Schematic diagram of real-time x-ray radiography system.

* obtained from manufacturers' data sheets

Another video camera records the exhaust plume emanating from the combustion chamber. A more detailed description of the experimental setup can be found in the Ph.D. thesis by Jarymowycz (1991).

3. EXPERIMENTAL RESULTS AND DISCUSSION

Tests were performed under a wide range of inlet conditions, with inlet static pressures from 0.28 to 0.62 MPa, freestream temperatures from 640 to 925 K, Mach numbers from 0.53 to 0.66, and oxygen mass fractions from 0.14 to 0.18. Figure 4 shows a set of typical combustion chamber temperature and pressure traces taken from locations 3 and 5, respectively, as shown in Fig. 2. An HTPB-based fuel sample containing 10 percent uncoated Callery boron (denoted as B/Mg/HTPB, 10/0/90) was used for the test and its regression-rate history is superimposed on the figure. The regression rates are averaged values from the locations at 6.0, 9.0, and 12.0 cm from the rearward-facing step. The test begins at t = 0 when air and propane are introduced into the chamber. Approximately 30 seconds into the test, the test-section temperature is increased from 520 to 610 K and pyrolysis of the solid fuel begins. Ignition occurs at 41 seconds, as evidenced by increases in all three readings. The regression rate and temperature both increase very rapidly at the onset of ignition due to the heat release from the combustion of pyrolyzed gases which accumulate in the recirculation zone before ignition. Both parameters decrease following ignition and maintain a fairly steady value during combustion. At the onset of ignition, the pressure experiences a small rise; afterward the pressure maintains a nearly constant level throughout combustion. The pressure increase at ignition is caused by the expansion of combustion gases. The decrease in regression rate at t = 64 seconds is due to the burnout of the fuel sample in the downstream section.

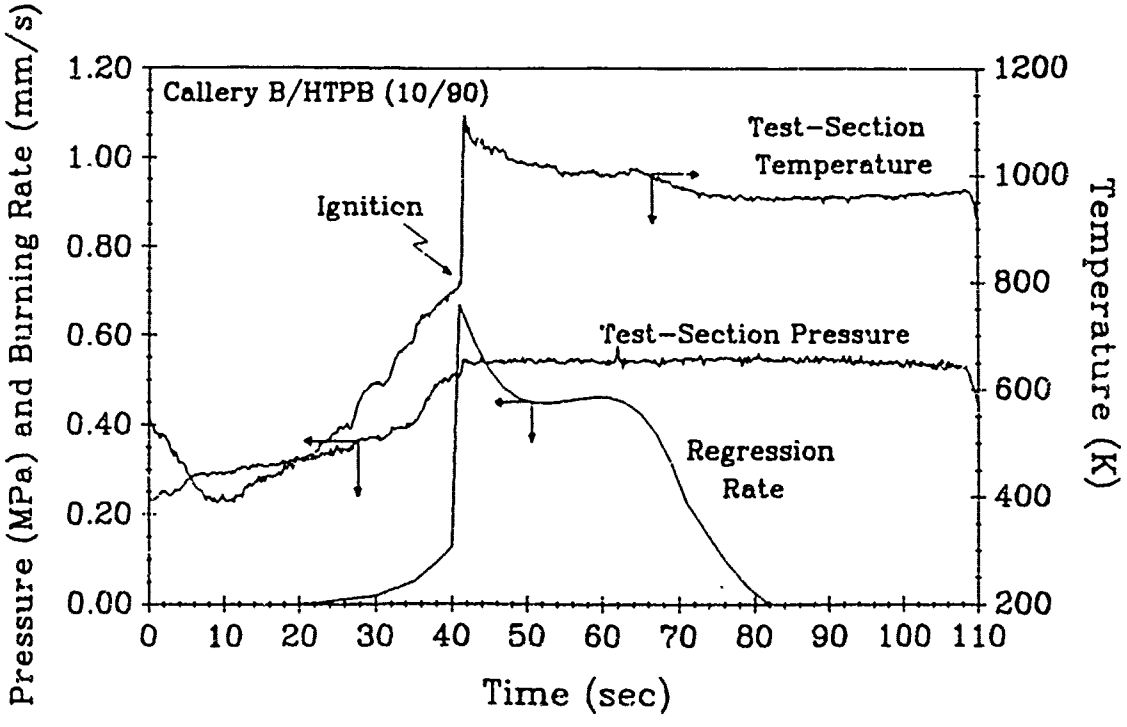


Fig. 4 Combustion chamber pressure, temperature, and regression rate histories.

Ignition of the boron-laden solid fuel is aided by particle reactions on the sample surface. Before ignition, the fuel sample surfaces showed glowing particles in all regions of the samples. However, ignition always occurred in the recirculation region near the rearward facing step, with subsequent flame spreading over the entire surface. The onset of ignition appears to be dependent mainly on the freestream temperature and fuel additives. Ignition occurred at freestream temperatures between 640 and 800 K for the majority of the tests with fuel samples containing magnesium-coated boron particles, and between 725 and 820 K for the samples with uncoated boron particles.

A study by Laurendeau (1968) consistently found the particle ignition temperatures of magnesium to be very close to its melting point (922 K) in a variety of experimental environments. In contrast, the ambient temperatures required for full ignition of boron are generally much higher, above 2500 K [King (1982)]. Thus, higher freestream temperatures are expected for ignition of the boron-laden fuels without magnesium since more energy is needed to ignite these particles. Ignition of the solid fuels at freestream temperatures well below the boron and magnesium particle ignition temperatures is caused by the presence of localized hot spots generated by the exothermic reactions between particles. These spots become reaction sites for the pyrolyzed fuel-rich species and air mixture. Once the fuel sample sustains combustion, ejected particles can fully ignite by passing though the established flame zone.

A limited number of HTPB-based samples containing no boron (B/Mg/HTPB, 0/0/100) were also tested. Without the boron or magnesium reactions to promote ignition of the fuel samples, ignition was not attained below temperatures of 890 K. However, when the first 0.5 cm of the fuel sample (behind the rearward-facing step) was replaced with a section of boron-laden fuel (B/Mg/HTPB, 10/0/90), ignition and sustained combustion was achieved at 800 K. This substantiates the hypotheses that the particle reactions serve as the ignition source for the samples.

Figure 5 compares the influence of freestream pressure on regression rates for SB 95 and Callery boron-laden solid fuels (B/Mg/HTPB, 10/0/90). The regression rates are averaged over the first 12 seconds following the attainment of steady state ignition. During this time period the fuel web thickness is sufficiently thick and the step height relatively constant to ensure consistent results. Similar regression-rate dependencies on pressure are observed for the Callery and SB 95 boron-laden fuels. The regression rates increase with pressure, with the strongest dependency at high pressures. The increased burning-rate dependence at high pressures may be caused by increased radiative heat transfer from the combustion products back to the fuel sample. The formation of soot as a combustion product in hydrocarbon fuels is greatly enhanced at high pressures. According to Sarofim and Hottel (1978), soot can double or triple the heat radiated by the gaseous products to the fuel sample, augmenting the burning rate by increasing the fuel surface temperature. Similar regression-rate dependencies on pressure were found for polymethylmethacrylate (PMMA) solid fuels in a study by Korting et al. (1990).

Figure 5 also shows the effect of boron type on the regression rate of the fuel samples. The regression rates of the Callery boron-laden fuels were found to be approximately 7 to 10 percent higher than those of the SB 95 boron. The different purities of the two boron types is one possible explanation for the differences in the regression rates. The impurities found in the SB 95 boron

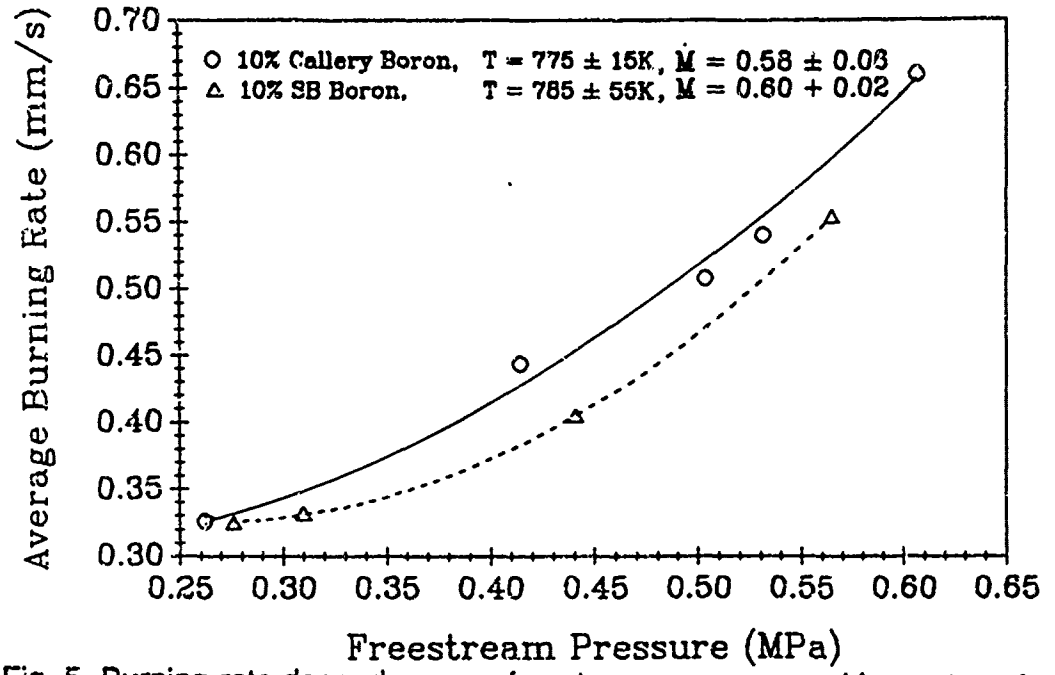


Fig. 5 Burning-rate dependence on freestream pressure and boron type for HTPB-based fuels.

(mainly Mg, H_2O_2, and moisture) diminish the available energy release. In addition, the Callery boron particles are approximately 10 times smaller than the SB 95 boron particles, as listed in Table 1. In the review paper by King (1982), burn-time data for small particles (< 40 μm) were reported to follow the d^1 law, which would predict a much shorter burn time for the Callery boron-laden fuels than the SB 95 boron fuels.

The effective difference in boron particle size may be reduced by particle agglomeration that occurs during storage and in fuel processing. Scanning Electron Microscope (SEM) photographs of the Callery and SB 95 boron-laden fuel samples are shown in Figs. 6 and 7, respectively. In Fig. 6, Callery boron particles smaller than 1 micron are abundant on the sample, while a few larger particles (1-3 microns) are also evident. These micrographs suggest that there is some agglomeration of the particles, which were originally between 0.04 and 0.15 microns, however the average boron particle diameter is still smaller than 1 micron. The micrograph of the SB 95 boron fuel sample of Fig. 7 also shows some agglomeration. The average particle size appears to have increased from the original diameters of 0.8 to 1.0 micron, to around 3 microns in diameter. Thus, after fuel processing there is still a substantial difference in average particle diameters for the two types of boron.

The effect of magnesium coating of boron particles on solid fuel regression versus pressure is shown in Fig. 8. At low pressures, the samples with the magnesium-coated particles experience a higher regression rate than the uncoated boron particle sample. The B/Mg/HTPB (8/2/90) fuel has a burning rate almost 25 percent higher than that of the uncoated boron particle samples at 0.35 MPa. The lower burning rates of samples containing uncoated particles are believed to be caused by longer particle ignition delay times. The uncoated boron particles are surrounded by inhibiting boron-oxide layers, which prevent direct contact between the boron particles and the surrounding oxidizer. For ignition to occur, the boron-oxide layer must first be removed by substantially

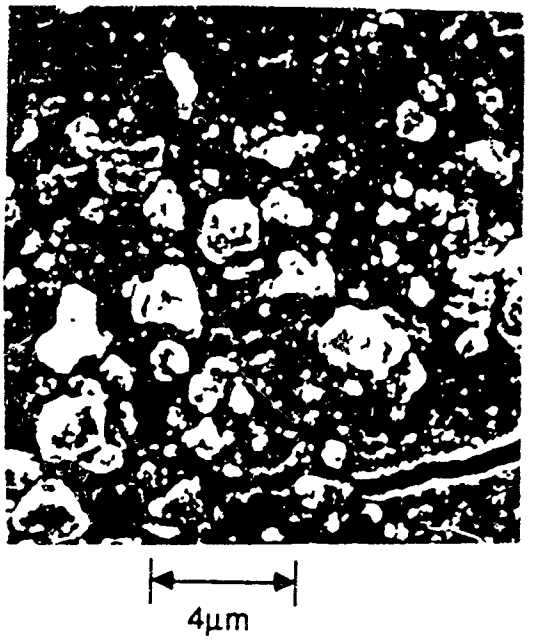


Fig. 6 SEM photograph of Callery boron-laden fuel sampie.

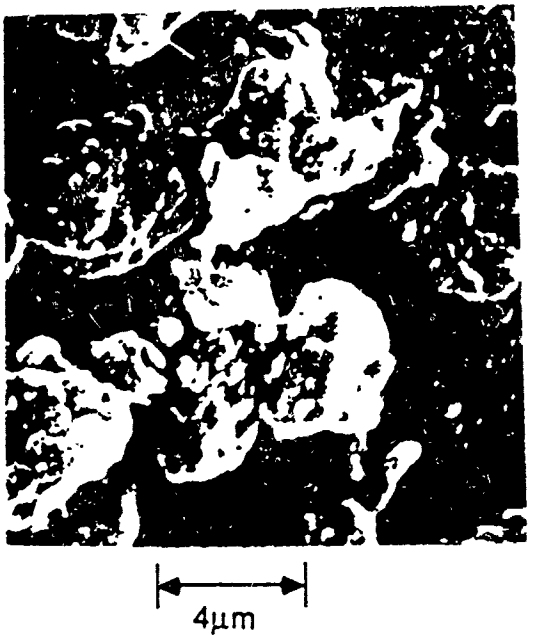


Fig. 7 SEM photograph of SB 95 boron-laden fuel sample.

raising the particle temperature so that the oxide layer evaporates or is consumed by chemical reactions. The time required to remove this layer is governed by rates of convective heating and exothermic or endothermic reactions occurring on or beneath the particle surface. When the boron particles (with B_2O_3 layers) are coated with a layer of magnesium, the magnesium ignites much more readily with the surrounding oxidizer, and transfers a portion of the energy release to the boron particle. The energy transfer from magnesium reactions occurs more efficiently than the convective

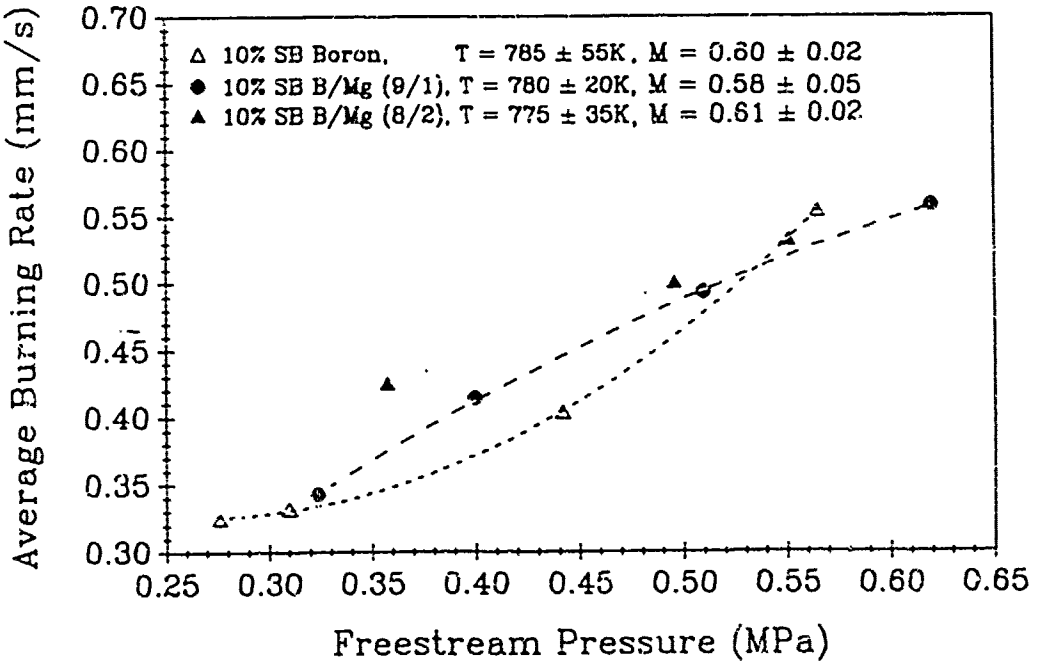


Fig. 8 Burning-rate dependence on freestream pressure and magnesium-coating percentage for HTPB-based fuels.

or self-heating processes which the uncoated particle relies upon. In this manner, the particle temperature rises quickly, resulting in a shorter ignition-delay time and higher burning rates for fuel samples containing magnesium-coated boron particles.

At high pressures, the magnesium coating does not appear to enhance the burning rates of solid fuels. Figure 8 shows that the burning rate curves for fuels with magnesium-coated particles converge to the burning rate curve for fuels with uncoated particles at pressures above 0.55 MPa. This trend is more clear in Fig. 9, where the burning rates are plotted versus the oxygen partial pressure.

At the higher pressures, gas-phase reaction rates increase, resulting in higher temperatures and greater heat transfer to the particles. This minimizes the dependence on the magnesium reactions to provide the required energy for boron particle ignition, leading to the merging of the burning rate curve that is observed.

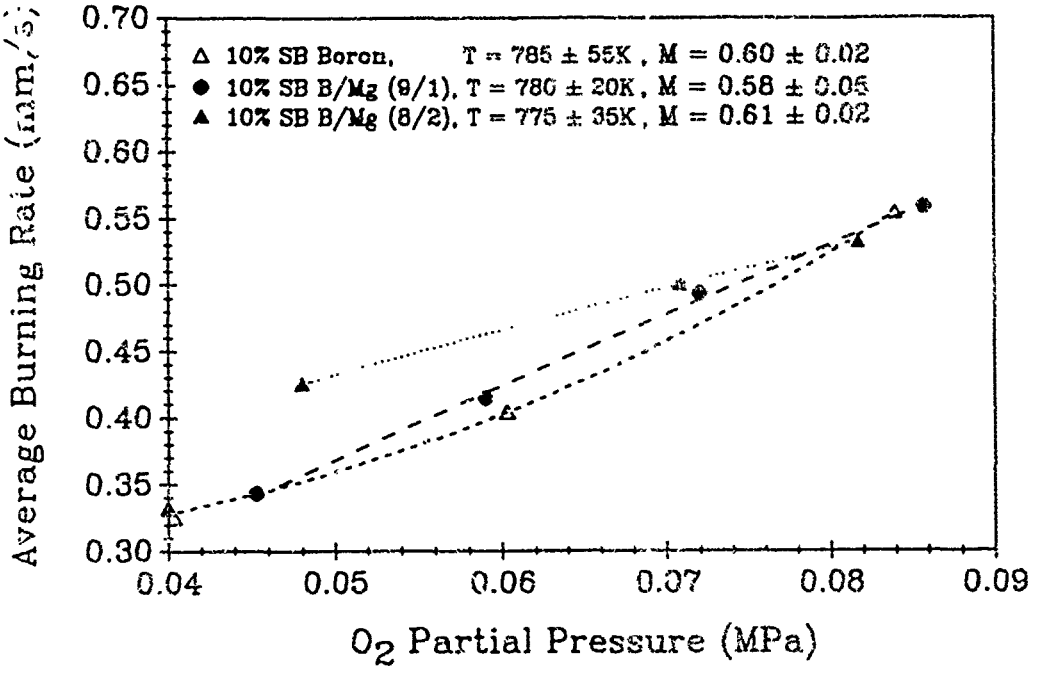


Fig. 9 Burning-rate dependence on oxygen partial pressure and magnesium-coating percentage for HTPB-based fuels.

Another factor in the merging of the three regression rate curves is the decrease in combustion energy of the boron particles with magnesium coating. Magnesium has less than one half the gravimetric heating value of boron. Replacing 20 percent of the boron with magnesium decreases the overall heating value of the particle by slightly more than 10 percent. At conditions for which reduction of ignition delay due to magnesium coating is not substantial, such as at high pressures, the regression rates could even be lower for the magnesium coated boron fuels.

In order to assess the effects of pressure, oxygen mass fraction, and magnesium coating percentage on the burning rates of the SB 95 boron-loaded fuels in a more general and quantified sense, the independent variables were fit to a power law of the following form:

$$r_b = a\,(p/p_{atm})^b\,(Y_{O2}/Y_{O2ref})^c \qquad (1)$$

where the pre-exponential constant a and the pressure exponent b are functions of the fraction of magnesium contained in the fuel (Ψ_{Mg}). The terms P_{atm} and Y_{O2ref} are reference values of 1 atm and 0.233, respectively. Data from 17 tests were entered into an algorithm for least-squares estimation of nonlinear parameters [Marquardt (1963)]. The tests had pressures ranging from .276 to .620 MPa, and oxygen mass fractions from 0.137 to 0.174. There were no significant variations in temperatures or Mach numbers; therefore, they are not included in this data analysis. The correlation obtained is shown below.

$$r_b = (0.17 + 2.4\Psi_{Mg})\,(p/p_{atm})^{0.72(1.0-8.5\Psi Mg)}\,(Y_{O2}/Y_{O2ref})^{0.38} \qquad (2)$$

The pressure exponent of 0.72 for HTPB-based fuels with uncoated SB 95 boron particles is comparable to the burning-rate dependence on pressure for fuels loaded with Callery boron [Jarymowycz (1991)]. The effect of magnesium loading on the pressure exponent appears large; however, the fraction of magnesium in these samples only ranges from 0.0 to 0.02, which would reduce the pressure exponent by a maximum of 17 percent. The power law expression predicts increased burning rate with magnesium addition at low pressures, and a reversal in this trend at high pressures. This is consistent with the results presented in Fig. 8. The freestream oxygen mass-fraction exponent of 0.38 signifies its importance. The comparison of measured and predicted burning rates of B/Mg/HTPB fuels with SB boron is shown in Fig. 10. Equation 2 is highly suitable for predicting fuel regression rates; however, discretion should be used before extrapolating this correlation to higher magnesium concentrations.

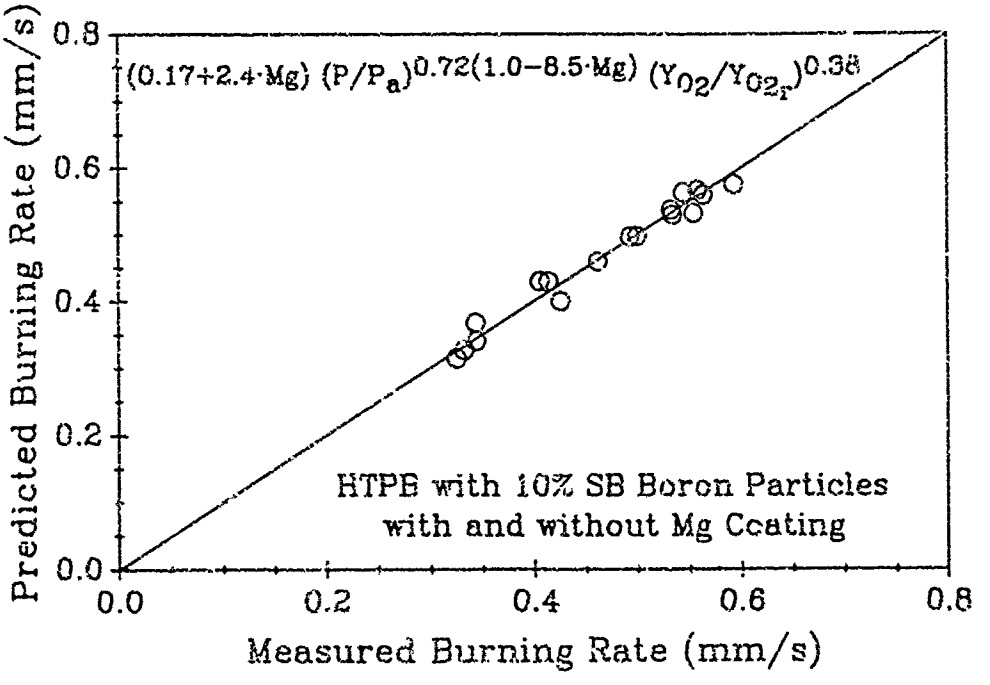


Fig. 10 Comparison of measured and predicted burning rates for SB boron-laden fuels with magnesium coating.

4. SUMMARY AND CONCLUSIONS

An experimental approach was employed to study the combustion behavior of boron-laden solid fuels under high-speed crossflows. Boron particles coated with magnesium were added to HTPB-based solid fuels and the regression rates and burning characteristics were compared to those of solid fuels with uncoated boron particles. In addition, two different types of boron were studied to determine the effect of boron type on the combustion of solid fuels. The regression rates of the solid fuels were determined through instantaneous surface profiles obtained by a non-intrusive real-time x-ray radiography system.

Ignition of the fuel samples was found to be initiated by particle reactions on the sample surface in the recirculation zone. The freestream temperatures required to ignite the magnesium-coated boron fuel samples were lower than those required for the uncoated boron fuels. This is attributed to the lower ambient temperature required for magnesium ignition.

Fuels with boron particles of high purity and small mean diameter experienced higher regression rates than fuels with particles of slightly lower purity and approximately 10 times larger mean diameters. SEM photographs showed that although agglomeration of the particles occurred in the fuel samples, a substantial difference in particle diameters for the two types of boron remained

At low pressures (below 0.55 MPa), the addition of magnesium-coated boron particles to the fuel samples increases the burning rates over those with the uncoated boron particles. The augmented burning rates at low pressures are due to the additional heat generated by magnesium/oxygen reactions which occur more rapidly than boron/oxygen reactions.

At higher pressures, solid fuels with coated boron particles have regression rates similar to those with uncoated-boron samples. At these conditions, gas-phase reaction rates and conductive heat transfer to the particles are higher for both types of particles. Therefore the relative importance of surface heat release by magnesium/oxygen reactions is reduced. In addition, magnesium-coated boron particles contain slightly less combustion energy than the uncoated boron particles.

The effects of pressure, oxygen mass fraction, and percent coating of magnesium on the regression rates of the sold fuels were determined and a burning rate correlation was obtained from this data. Pressure was found to have the greatest influence on the regression rates, with an exponent of 0.72 that decreased slightly with the magnesium coating addition. The oxygen mass fraction exponent was 0.38.

In these tests, magnesium coating was applied to the boron particles of lower purity and larger diameters. Gains incurred by magnesium coating are offset by the lower burning rates of theses particles. Coating the high purity, small diameter boron with magnesium may provide additional regression rate increases.

ACKNOWLEDGEMENTS

This paper represents part of the research work conducted under Contract No. N00014-86 -K-0468 sponsored by the Office of Naval Research, Arlington, VA. The support and encouragement of Drs. Richard S. Miller and Gabriel D. Roy are greatly appreciated. The authors would also like to thank Mr. I-Te Huang for his assistance with the SEM photography.

REFERENCES

Calcote, H.F., Gill, R.J., Berman, C.H., and Felder, W. (1990), "Production and Coating of Pure Boron Powders," Proceedings of 3rd ONR Propulsion Meeting/Contracters Review, Middletown, RI.

Chen, D.M., Hsieh, W.H., Snyder, T.S., Yang, V., and Kuo, K.K. (1988), "Study of the Thermophysical Properties and Combustion Behavior of Metal-Based Solid Fuels," AIAA Paper No. 88-3041, AIAA/ASME/SAE/ASEE 24th Joint Propulsion Conference, Boston, MA; accepted for publication in the Journal of Propulsion and Power.

Childs, L.B., King, M.K., and Martin, I.D. (1971), "Improved Propellants for Throttleable Solid-Air Augmented Rockets," AFRPL-TR-71-127, Vol. 11.

Criner, C.B. and Kosowski, B.M. (1990), "Production and Coating of Pure Boron Powders," Office of Naval Research Report, TR 89-007.

Jarymowycz, T.A., Pace, K.K., Snyder, T.S., Yang, V., and Kuo, K.K. (1990), "Experimental Study of Solid Fuel Ignition and Combustion Under High-Velocity Crossflows," Submitted to Journal of Propulsion and Power, also presented at the 27th JANNAF Combustion Meeting, Cheyenne, WY.

Jarymowycz, T.A. (1991), "Ignition and Combustion of Solid Fuels under High-Velocity Crossflows," Ph.D. Thesis, The Pennsylvania State University, University Park, PA.

King, M.K. (1982), "Ignition and Combustion of Boron Particles and Clouds," Journal of Spacecraft and Rockets, Vol. 19, No. 4, pp. 294-306.

Korting, P.A.O.G., van der Geld, C.W.M., Wijchers, T., and Schoyer, H.F.R. (1990), "Combustion of Polymethylmethacrylate in a Solid Fuel Ramjet," Journal of Propulsion and Power, Vol. 6, No. 3, pp. 263-270.

Laurendau, N.M. (1968), "The Ignition Characteristics of Metals in Oxygen Atmospheres," AMS Report No. 851, Princeton University.

Marquardt, D.W. (1963), "An Algorithm for Least-Squares Estimation of Nonlinear Parameters," Journal of the Society for Industrial and Applied Mathematics, Vol. 11, No. 2, pp. 431-441.

Nemodruk, A.A. and Karalova, Z.K. (1969), Analytical Chemistry of Boron, Translated by Kondor, R., Ann Arbor - Humphrey Science Publishers, Ann Arbor, London.

Pein, R. and Vinnemeier, F. (1989), "The Influence of Swirl and Fuel Composition of Boron-Containing Fuels on Combustion in a Solid Fuel Ramjet Combustion Chamber," AIAA Paper No. 89-2885, AIAA/ASME/SAE/ASEE 25th Joint Propulsion Conference, Monterey, CA.

Sarofim, A. F. and Hottel, H.C. (1978), "Radiative Heat Transfer in Combustion Chambers: Influence of Alternative Fuels," Sixth International Heat Transfer Conference, Toronto, Vol. 6, pp. 199-217.

Yuasa,S. and Takeno, T. (1982), "Ignition and Combustion of Mg/Al Alloy Particle Clouds in a Hot Gas Stream," 19th Symposium (International) on Combustion, pp. 741-748.

FILE COPY

Experimental Study of Solid Fuel Ignition and Combustion Under High-Velocity Crossflows

T. A. Jarymowycz,† K. K. Pace,‡ T. S. Snyder,‡ V. Yang,+ and K. K. Kuo++
Department of Mechanical Engineering
The Pennsylvania State University
University Park, PA 16802

Abstract

The combustion behavior of hydroxyl terminated polybutadiene (HTPB) based solid fuels with boron particles were studied under both subsonic and supersonic crossflows using a connected-pipe test facility. The Mach numbers ranged from 0.47 to 0.74 for subsonic tests, while supersonic tests were conducted at a fixed Mach number of 1.5. Instantaneous surface profiles of the solid fuels were obtained using a real-time x-ray radiography system. For solid fuels without boron, auto-ignition of the pyrolyzed fuel-rich species and air mixture can be achieved in the gas phase at sufficiently high iniet temperatures without the aid of an external ignition source. However, addition of a small amount of boron to the fuels decreases the minimum temperature required for ignition, since reacting boron particles on the sample surface serve as a local heat source for igniting the pyrolyzed fuel-rich species. Subsonic combustion studies revealed that regression rates were highly dependent on freestream static pressures, and less dependent on temperature and mass flux. The addition of boron particles (up to 10 percent by weight) to the HTPB fuels considerably increased the burning rates of the fuels. The dependence of regression rate on temperature also increased with boron addition due to the enhanced radiative and convective heat feedback from the condensed-phase reactions at elevated temperatures. A burning-rate correlation was obtained in terms of pressure, temperature, mass flux, and boron concentration. Combustion of solid fuels under supersonic crossflows was also successfully demonstrated. For these tests, it was necessary to increase the size of the flame stabilization region to promote ignition of the solid-fuel sample.

---

† Ph.D. Candidate, Member AIAA
‡ Graduate Research Assistant, Member AIAA
+ Associate Professor, Member AIAA
++ Distinguished Professor of Mechanical Engineering, Associate Fellow AIAA

Nomenclature

a = Pre-exponential factor

b = Pressure exponent

B = Boron mass fraction in solid fuel

c = Temperature exponent

d = Mass flux exponent

G = Mass flux

$\dot{m}$ = Mass flowrate of oxidizer stream

p = Freestream static pressure

r_b = Burning rate of solid fuel

T = Freestream temperature

1. Introduction

The solid fuel ramjet (SFRJ) has the potential for achieving high performance levels with the advantage of being simple and compact. For the SFRJ to become a viable air-breathing engine, it must demonstrate efficient operation under a wide range of Mach numbers and altitudes. Furthermore, it may incorporate energetic fuel additives such as boron or metallic powders to maximize performance during volume-limited missions.

Several investigations[1-7] have already been conducted to determine the effects of freestream conditions (including pressure, temperature, and flowrate) on the burning rates of homogeneous solid fuels in ramjet environments. Korting et al.[1] studied the combustion behavior of polymethylmethacrylate (PMMA) at low mass flowrates using a connected-pipe test facility. Results indicated that regression rates were hardly dependent on pressure for freestream pressures below 0.65 MPa, but at higher pressures where soot production

becomes significant, the burning rate increases with pressure according to the power rule of $p^{0.56}$. This is in reasonable agreement with PMMA combustion studies summarized by Mady et al.[2] Furthermore, at low pressures the burning rates are strongly dependent on the convective heat transfer rates which are influenced by inlet temperature and total mass flux, but at higher pressures this dependence is weaker due to the increase in radiative heat transfer.

The combustion of polyethylene (PE) fuels has also been studied in SFRJ combustion chambers.[3–5] In low pressure environments (less than 0.6 MPa), Elands et al.[3] noticed a slight dependence of burning rate on pressure. The effects of temperature and mass flowrate are greater and in accordance with the relations $T^{0.58}$ and $\dot{m}^{0.56}$, where T and $\dot{m}$ are freestream temperature and flowrate, respectively. These findings compared reasonably well with predicted data from a numerical model which calculated burning rates as functions of T, p, and $\dot{m}$. At higher mass flowrates the temperature dependency was slightly lower, with the exponent decreasing to 0.50.[4] An additional effect of port diameter on regression rate was also noticed. Increasing the port area, while keeping such influence parameters as temperature, pressure, and mass flux constant, decreased the regression rates. This effect may be due to a change in fuel/oxidizer ratio caused by the increase in oxidizer mass flowrate needed to keep the mass flux constant. The mixture may become fuel lean and cannot supply the necessary energy to raise the enthalpy of the flow, consequently reducing the heat feedback to the fuel sample and decreasing the burning rate. Other possible factors include the increase in radius of curvature, and the change in turbulence structure. Schulte et al.[5] performed temperature and concentration measurements in an SFRJ combustion chamber and showed that the flowfield in the combustor could be divided into two regions: an air-rich core and a high-temperature zone of combustion products closer to the wall. These two zones did not mix completely, and the addition of an aft mixing chamber would have been beneficial to the combustion process.

The effects of energetic additives on the combustion processes of hydroxyl terminated polybutadiene (HTPB) fuels have also been investigated. Snyder et al.[6] studied the effects of boron percentage on the burning rates of HTPB-based fuels by adding small fractions of boron powders to enhance the ignition and combustion characteristics of the fuel samples. Regression rates were found to increase with boron addition up to 10 percent, but further addition of boron caused the burning rates to decrease. This decrease was attributed to (1) the heat-sink effect associated with boron particles in the gas phase which reduces the gas-phase temperature, (2) shielding of heat feedback to the surface by the large number of boron particles above the surface, (3) reduced pyrolysis caused by the accumulation of unreacted boron particles on the surface, and (4) decreased gas-phase reactions due to the smaller percentage of HTPB contained in the sample. Pein et al.[7] also noted that adding small quantities of boron or boron carbide powders to the fuels increased specific thrust considerably because of additional heat generated by the gas-particle reactions. However, further addition of these particles beyond 20 percent hampered combustion efficiency and specific thrust, due to reasons listed above. The effect of air swirl on boron combustion efficiency was found to be beneficial, since swirl enhanced the mixing processes and increased the residence times within the combustor.

The previous studies have provided useful information regarding solid-fuel combustion; however, the majority of these studies were conducted in low-speed environments. The objective of this research is to determine the effect of freestream conditions such as pressure, temperature, and mass flux on the burning rates of HTPB-based solid fuels under a wide range of Mach numbers, including both subsonic and supersonic crossflows. Consequently, the feasibility of solid fuel combustion under high-velocity conditions can be investigated. The effect of boron particle addition on the ignition and combustion characteristics of the fuel samples is also determined.

2. Experimental Approach

Test Facility

In order to understand the physical and chemical mechanisms involved in the combustion of solid fuels, an experimental study was conducted using a connected-pipe facility shown schematically in Fig. 1. The test rig utilizes compressed air from two large storage tanks with a combined capacity of 72 cubic meters and a maximum pressure of 4.9 MPa. Air from these two tanks is mixed and burned with propane in the vitiator to achieve a maximum temperature of 1000 K in the settling chamber, then the hot gas passes through a convergent-divergent nozzle which accelerates the flow to a Mach number of 1.5. In the majority of tests, the mole fraction of oxygen in the vitiated air is fixed at approximately 0.17. The facility is capable of providing vitiated air at a high-velocity crossflow with a static pressure range of 0.1 to 0.62 MPa in the test section, simulating the combustion chamber conditions of a hypersonic vehicle at high altitudes. The maximum flowrate attainable is 8 kg/s with a duration of four minutes at the highest pressure. For subsonic operation, the adjustable exhaust nozzle chokes the flow and controls the Mach number in the test section.

Pressure and temperature measurements are taken at several locations: the settling chamber, upstream of the convergent-divergent nozzle, the inlet of the combustion chamber, and downstream of the solid fuel sample. Data are not taken in the regions surrounding the fuel sample, since mesurements in these locations would interfere with the video systems. Steady flow conditions are achieved by means of a feedback control loop between a pneumatic ball valve in the air supply line and a pressure transducer in the settling chamber, with a maximum fluctuation of 1 percent in the stagnation pressure. Combustion instabilities in the vitiator are sometimes encountered due to fuel-rich conditions during the startup procedure, but are quickly supressed by increasing the air flowrate. At steady

operating conditions, the instabilities are not present. Combustion chamber temperature and pressure are monitored at the locations shown in Fig. 2. Temperature measurements are obtained using R-type (platinum/platinum-13% rhodium) thermocouples. Radiative and catalytic effects on the thermocouple beads are found to be negligible because of the high convective velocity and small bead size of 200 microns; therefore, no corrections are made to the temperature readings. An IBM PC/AT computer records all temperature and pressure measurements using a Metrabyte DAS-16 high-speed data acquisition system. A detailed description of the data acquisition and the flow measurement systems is available in the thesis by Jarymowycz.[8]

The high-enthalpy flow enters the combustion chamber through a short and straight rectangular inlet measuring 3.18 cm in height, 10.16 cm in width, and 10.8 cm in length, as depicted in Fig. 2. The inlet flow has a Reynolds number based on the inlet height of approximately 1×10^6 before passing over a rearward-facing step into the test section. The solid fuel sample is placed directly behind this step. The initial step height is kept constant for all subsonic tests at 1.27 cm, creating a recirculation zone with sufficient dimensions for achieving ignition and stable combustion of the fuel sample, and leaving adequate space for boundary layer redevelopment in the downstream portion of the fuel sample. During supersonic operations, the step height is increased to 1.91 cm to provide a larger recirculation zone for flame stabilization. After ignition, an electronic actuator may be used to feed the fuel sample upward in order to study the effect of step height on combustion behavior. The sample feeding rate is on the order of 2.5 cm/s.

Solid Fuels

All fuels studied in this work are processed by mixing liquid HTPB binder (ARCO R45-M) and various percentages (0-20 by weight) of elemental boron powder with the curing agent isophorone diisocyanate (IPDI). Amorphous boron powders added to the fuels have a purity of 99.9% and an average diameter of 0.9 microns. The fuels are prepared by

thoroughly blending all of the ingredients in a vacuum mixer at 50°C for one hour. After mixing, the fuels are poured into a mold, placed in a vacuum desiccator for three hours, then cured at 65°C for at least four days. The samples measure 15.2 cm in length, 5.1 cm in width, and 3.2 cm in height for the subsonic tests. During supersonic operations, the width of the samples is increased to the full width of the chamber (10.16 cm) in order to prevent expansion of the gas to the sides of the fuel sample and to maintain a high pressure above the fuel surface. The narrower samples are used for subsonic tests to avoid direct impingement of the flame onto the side windows and prolong the lifetime of the windows.

Igniter

A pyrophoric liquid, triethylborane (TEB), is injected into the recirculation zone to achieve ignition of the solid fuels. A stainless steel tube with an outer diameter of 0.32 cm is extended slightly above the sample surface to inject TEB parallel to the top surface of the sample at an angle approximately 60 degrees from the side walls. The injection time is ordinarily on the order of one second, then the TEB is turned off after solid fuel ignition is attained. In some cases, the solid fuel samples are ignited by the hot crossflow gas without the aid of TEB, but this is highly dependent upon freestream conditions and fuel composition.

Real-Time X-Ray Radiography and Video System

Instantaneous surface profiles of the solid fuels are obtained using a real-time x-ray radiography system. The system, shown in Fig. 3, consists of an x-ray source, an image intensifier which receives the x-ray image through the graphite windows, and a video camera. After completion of each test, the regression rate of the fuel sample is deduced using a digital image processing system. This non-intrusive technique offers several advantages over the conventional optical methods in measuring the instantaneous surface profiles of fuel samples. First, x-rays easily identify the fuel surface by penetrating through the two-

phase combustion products surrounding the sample, which are usually opaque for other visualization techniques. The flame does not interfere with the interpretation of the surface profiles, since the luminous flame zone is not visible on the x-ray images. Second, gas purging of the viewing windows, as required by the direct photography technique, is not necessary since deposits of fuel and/or char on the windows are easily penetrated by the x-rays. The elimination of gas purging also simplifies the design of the combustion chamber. Third, the viewing area (6.35 cm in height × 13.3 cm in length) encompasses a large portion of the fuel sample and its associated reacting flowfield, so that the complete surface profile is contained on one image.

Direct video is also employed to study the burning phenomena of the solid fuels. The top view of the solid fuel is captured through a quartz window (see Fig. 2) to study the surface ignition, flame spreading, and combustion processes. Another video camera records the exhaust plume emanating from the combustion chamber.

3. Experimental Results and Discussion

A series of subsonic and supersonic tests were performed using the facility described in the previous section. For subsonic crossflow conditions, the inlet static pressures and freestream temperatures ranged from 0.26 to 0.57 MPa and 550 to 1080 K, respectively. Vitiated air entered the combustion chamber at flowrates ranging from 1.1 to 3.1 kg/s and Mach numbers from 0.47 to 0.74. Figures 4 and 5 show typical temperature and pressure histories recorded from a subsonic test with a sample consisting of 5 percent (by weight) boron in the HTPB binder (denoted as B/HTPB, 5/95). Ignition of the propane/air mixture in the vitiator occurs forty seconds into the test, as indicated by the abrupt increase in temperature shown in Fig. 4. Prior to this time, the cold air is slowly introduced into the test section. After ignition in the vitiator, the propane

and air flowrates are steadily increased to raise the temperature and pressure of the hot gas. Heat transfer to the solid-fuel sample raises the surface temperature of the sample, and the fuel begins to slowly release pyrolyzed fuel-rich gaseous species from its surface. According to the thermogravimetric analysis of B/HTPB fuels at a heating rate of 100 deg/min,[9] decomposition starts at approximately 520 K, and reaches a peak weight loss in the neighborhood of 680 K, with boron having only a very limited effect. A dashed vertical line at t=64 seconds in Fig. 4 represents the time at which the temperature exceeds 520 K. For this particular test, TEB injection is not necessary because the temperature of the vitiated air is sufficiently high to promote exothermic surface reactions of boron particles which serve as a local ignition source for the air and pyrolyzed fuel mixture. Following ignition of the fuel sample, the flowrates of propane and air remain fixed, resulting in a constant pressure for the duration of the combustion event. The occurrence of ignition is indicated by a large spike in the test-section thermocouple B reading, as shown in Fig. 4. The height of the thermocouple is initially aligned with the sample surface prior to the test. When the fuel sample ignites, the flame is in close proximity to the thermocouple; however, as the sample regresses, the flame zone moves down with the surface of the sample, thereby increasing the distance between the flame and thermocouple and reducing the temperature reading. The abrupt drop in temperature at the end of the test is caused by shutdown of the test facility.

Figure 5 shows three separate pressure-time traces measured in the settling chamber, combustion chamber inlet, and test section. As shown in these traces, ignition of the solid fuel sample causes a small, abrupt increase in each pressure reading. During the combustion event, the Mach number at the inlet is fixed at 0.61. This value is calculated using the static to stagnation pressure ratio, then verified by determining the correct pressure ratio based on the inlet to nozzle area ratio.

As mentioned previously, auto-ignition of the solid fuel can be initiated by reactions

of boron particles on the surface of the fuel sample. This ignition process relies on several important physical and chemical mechanisms, including pyrolysis of the solid fuel, mixing of the pyrolyzed fuel rich species with the oxygen, and subsequent ignition of the mixture by the reacting boron particles. In order to describe this sequence in more detail, the ignition process of the boron particle is briefly summarized below.

Previous studies of ignition and combustion of individual boron particles[10] indicate that boron undergoes a two-stage ignition process. The first stage begins with the removal of a thin inhibitive oxide layer from the particle surface. Heat transfer to the particle melts the oxide layer at 723 K, thereby allowing oxygen to diffuse across the molten oxide layer. The boron/oxygen reactions produce additional boron oxide which thicken the oxide layer, but also raise the temperature of the particle due to the exothermicity of the reactions. This initial rise in temperature is accompanied by the appearance of luminosity, and marks the onset of the first stage of particle ignition. In order for the ignition process to continue, the particle temperature must continue to rise. This occurs by further convective or radiative heat transfer to the particle, which evaporates the oxide layer from the surface. In addition, self-heating from boron/oxygen reactions raises the particle temperature at the expense of boron oxide production. At a sufficiently high freestream temperature (ca. 1900 K), the evaporation rate of the boron oxide is high enough to completely remove the oxide layer. The elemental boron is then directly exposed to the oxygen, giving rise to highly exothermic heterogeneous reactions and the second stage of particle ignition. This results in full-fledged combustion and a much brighter flame surrounding the particle.

Figure 6 shows the top view of the ignition sequence of a B/HTPB (5/95) fuel sample. The flow conditions are given in Figs. 4 and 5. The viewing area of the window spans 19 cm in length by 7 cm in width, and the flow direction is from left to right. Since the fuel sample is 15 cm in length, a small portion of the downstream section of the combustion chamber is visible on the right side of the window. The temperature of the crossflow gas

is approximately 750 K, sufficient to melt the oxide layers on the particles and promote the first step of particle ignition. Figure 6a reveals glowing spots on the fuel surface which appear to be boron particles in the first stage of ignition. As shown in the sequential Figs. 6a through 6c taken at a framing rate of 30 pictures per second, the glowing particles on the surface provide the heat necessary to ignite the pyrolyzed fuel-rich gas and air mixture. Ignition of the gas phase begins in the recirculation zone formed by the rearward facing step, and spreads downstream very quickly as shown in Figs. 6c and 6d. The flame-spreading process ordinarily occurs in less than 0.03 seconds for the B/HTPB fuels used in this study. Finally, Fig 6e shows full-fledged ignition of the solid fuel sample. The erratic edges of the window are video distortions caused by the high noise level in the test room.

After ignition of the solid fuel, the glowing boron particles are ejected with pyrolyzed fuel-rich species into the gas-phase reaction zone. The particles pass through the flame zone, where they are further heated to the second-stage ignition temperature. In summary, the first ignition of boron particles aids in the ignition process of the fuel sample by providing a reaction site for the pyrolyzed fuel-rich species and air mixture. Once the fuel sample sustains combustion, ejected boron particles achieve their second stage of ignition by passing through the established flame zone.

Within the Mach number range tested in this work, the majority of boron-laden solid fuels can ignite at inlet temperatures between 725 and 820 K without the use of TEB. This temperature range is very conducive to ignition, since HTPB pyrolyzes below this temperature range, and boron particles begin their ignition process with the melting of the oxide layer at 723 K. All of these fuels ignited in the recirculating region, even though some had glowing boron particles on the sides and in the downstream region of the sample. In addition, ignition of the solid fuel did not instantaneously occur when these glowing spots were formed in the recirculation zone, but occurred only after a sufficient amount of gas pyrolyzed from the fuel surface. An attempt was made to establish a correlation between

the time allowed for pyrolysis and the ignition temperature, but none was found because the elapsed time between these two events was primarily dependent on the test procedure and the sequence in supplying propane and air to the test rig.

The ignition sequence for B/HTPB (0/100) fuels without the aid of TEB was slightly different than that for boron-containing fuels, since boron particles were not available on the surface to promote ignition. The HTPB fuels did ignite in the recirculation zone; however, the required inlet temperatures were beyond 820 K. The ignition event of a B/HTPB (0/100) fuel is shown in Figs. 7a through 7e. Figure 7a reveals onset of ignition of the gas-phase mixture in the recirculation zone, and the next three figures show the flame-spreading phenomenon which is similar to that of the B/HTPB (5/95) fuel. The B/HTPB (0/100) fuels showed no indication of a localized ignition source to initiate the ignition process; instead ignition seemed to occur spontaneously over a distributed region in the recirculation zone. The flame spread slightly faster compared to the boron-laden fuels, but this might be due to the faster kinetics caused by a higher inlet temperature.

As previously mentioned, TEB was available to ignite the solid fuel; however, it was used only under conditions which necessitated its use. Typically, TEB was used for those tests with low inlet temperatures in which auto-ignition of the fuel species in the gas phase was difficult to achieve. When the operating conditions matched the desired test temperature and pressure, the TEB was injected and the fuel samples ignited within one second from the start of injection, with the exception of one test employing B/HTPB (0/100) fuel at a low inlet temperature. For this particular test at 620 K, the fuel sample ignited momentarily when TEB was injected for ten seconds above the surface; however, the sample extinguished after the igniter was turned off. A B/HTPB (10/90) fuel sample tested at a lower inlet temperature of 550 K did ignite and sustain combustion after TEB injection. The successful ignition of this fuel is most likely caused by the increased surface absorptivity due to the addition of boron particles. Another factor contributing to the

flame stabilization at low inlet temperatures is the increase in heat feedback to the surface from the ejected boron particles reacting above the solid fuel.

Figure 8 shows the instantaneous surface profiles deduced from the x-ray radiography system for a B/HTPB (5/95) sample burning under a subsonic crossflow. The profiles are taken at axial locations 4.5 to 13.5 cm from the rearward-facing step at intervals of 1.5 cm. These profiles are not extended to the full length of the sample because all of the fuels experience some degree of end burning; therefore, data at the 15 cm location are not always available. In addition, the region upstream of the 2.8 cm location was not visible due to restrictions in the size of the side window. The dashed line corresponds to the fuel surface profile before the test, and the solid lines are the contours of the sample taken after ignition at five second intervals. The first profile taken immediately after ignition of the entire fuel sample at t=110 seconds shows the degree of fuel pyrolysis prior to ignition. Since each test necessitates some start-up time to achieve operating conditions, all solid fuels exhibit similar pre-ignition pyrolysis. The fuel surface profiles show an increased regression rate in the downstream region caused by enhanced heat feedback from the diffusion flame zone. Larger amounts of fuel-rich species are reacted in downstream locations rather than at upstream stations, because the majority of the pyrolyzed gases are transported downstream by the shear flow before chemical reactions occur. Thus, heat release in the diffusion flame is greater in the downstream region.

Figure 9 shows the influence of freestream pressure on the regression rates of HTPB-based solid fuels with boron loadings of 0, 10, and 15 percent. The regression rates are averaged values from the locations at 6.0, 9.0, and 12.0 cm from the rearward-facing step, which cover a significant portion of the fuel sample. For these boron loadings, the burning rates increase substantially with pressure. Two mechanisms can be attributed to the enhanced burning rates at higher pressures. First, the gas-phase kinetics are faster, thus shortening the flame standoff distance above the fuel surface and enhancing heat feedback

to the fuel sample. Second, the increase in pressure corresponds to an increase in oxidizer-to-fuel ratio, allowing additional reactions of oxidizers with the fuel-rich pyrolysis products and boron particles. This results in higher flame temperature and greater heat transfer to the fuel surface, thus increasing the regression rate of the solid fuel. The increase in pressure also has an inverse effect on the molecular diffusion rate of the fuel species, which may decrease the height of the flame above the surface and consequently alter the burning rate. However, this effect may not be significant because of more pronounced effects of blowing and turbulent mixing above the surface.

The effect of boron on the regression rate of the HTPB fuels is also studied. The addition of 10 percent boron to a pure HTPB fuel increases the burning rate by approximately 10 percent (assuming the slight difference in freestream temperature between the 0 and 10 percent boron curves is negligible). This increase appears to be caused by the additional convective and radiative heat transfer from the reacting particles to the fuel surface, as well as the increased radiation absorptivity of the fuel surface. A higher boron particle loading of 15 percent appears to slightly decrease the burning rate compared with the 10 percent boron fuel. This may be due to the following reasons: (1) the decreased HTPB content in the fuel diminishes the gas-phase reactions and reduces the energy supply for complete ignition and combustion of boron particles, (2) the higher boron percentage increases the heat-sink effect in the gas phase, which reduces the flame temperature and results in incomplete ignition and combustion of the particles, thereby reducing the heat feedback from the ejected particles, and (3) the heat feedback is diminished due to shielding caused by accumulated particles on the surface. Only a few tests were conducted at these higher loadings and more data may be needed to support these statements.

The effect of freestream temperature on the burning rates of B/HTPB fuels with particle loadings of 0, 5, and 10 percent is presented in Fig. 10. The burning rates increase with freestream temperature due to enhanced convective heat transfer to the fuel

surface from the crossflow and faster chemical reaction rates at elevated temperatures. The effect of boron loading on temperature dependence is evidenced by comparing the slopes of the three curves. As boron percentage increases, the slopes of the curves become steeper, demonstrating a greater effect of temperature on the boron-loaded fuels. This may be due to the following factors. The rise in freestream temperature not only increases the gas-phase reaction rates, but also increases the convective heat transfer to the boron particles, which subsequently decreases the heatup and ignition times of the boron in the gas-phase reaction zone above the fuel sample. At lower inlet temperatures the particles may ignite but not until they are convected downstream of the solid fuel where less energy can be directly transferred back to the fuel. If the particles achieve ignition sooner due to the higher inlet temperatures, they can supplement the heat feedback to the fuel surface with radiative and convective heat transfer from the condensed-phase reactions. Thus, the increase in burning rates for boron-laden fuels at elevated temperatures is due to enhanced gas-phase reactions as well as additional convective and radiative heat feedback from the particles.

In order to assess the effects of temperature, pressure, and boron loading percentage on the burning rates in a more general and quantified sense, the independent variables were input into a power law of the form:

$$r_b = a\, p^b\, T^c\, G^d \tag{1}$$

where the pre-exponential constant a and the pressure exponent b are functions of boron percentage. The units of pressure, temperature, and burning rate are MPa, K, and mm/s, respectively. In this work, boron loading varied from 0 to 20 percent, pressures from 0.26 to 0.57 MPa, temperatures from 550 to 1080 K, mass flux from 337 to 965 kg/m/s, and Mach number from 0.47 to 0.74, with an initial combustion chamber step height of 1.27

cm. The correlation determined from a least-squares estimation of nonlinear parameters[11] is shown below.

$$r_b = (0.06 + 0.03B)\, p^{0.6(1.0-0.23B)}\, T^{0.28}\, G^{0.09} \qquad (2)$$

Results from this correlation are shown in Fig. 11, where the predicted power law is shown on the horizontal axis, and the observed burning rates on the vertical axis. The diagonal line signifies agreement between predicted and observed burning rates. The data correlates reasonably well for the wide range of pressures and temperatures, with pressure exhibiting the most dominating effect on the burning rate. According to the power law expression, addition of boron to an HTPB fuel increases the burning rate; however, relatively few data are available for boron loadings greater than 10%, and care must be taken before extrapolating this equation to higher boron concentrations.

Efforts were made to incorporate the effect of mass flux into the correlation, but the current results indicate only a very weak effect on the burning rate, with an exponent of 0.09 for the mass flux in the power-law expression. Since mass flux is a function of pressure, temperature, and Mach number, and no direct attempts were made to keep the pressure and temperature constant while changing the Mach number, it is possible that the major effects of the mass flux are represented in the pressure or temperature exponents. Future tests should incorporate variations in Mach number while keeping the remaining independent variables constant.

The combustion of solid fuels under supersonic crossflows was also achieved with B/HTPB (10/90) and B/HTPB (0/100) samples at a Mach number of 1.5. The first test was conducted with B/HTPB (0/100) to determine the effect of the step height on flame stabilization. The initial step height was 1.27 cm prior to the test. Under Mach 1.5 crossflow with a freestream temperature of 900 K and static pressure of 0.30 MPa,

the fuel sample did not ignite with TEB injection. To achieve ignition, the step height was increased to 1.9 cm by lowering the fuel. With a larger flame stabilization region, the fuel ignited with TEB injection. After ignition, the TEB injection was turned off and the sample burned for approximately seven seconds. No further attempts to ignite the fuel sample were made because the fuel sample had pyrolyzed significantly.

In order to promote ignition of the B/HTPB (10/90) fuel sample, the initial height of the rearward-facing step was increased to 1.91 cm prior to the succeeding test. In this arrangement, the top surface of the fuel was directly in line with the exit channel of the combustion chamber. TEB was injected onto the surface of the fuel sample in order to achieve ignition. As the sample regressed, a forward-facing step was formed at the rear of the sample with the exit channel. A set of instantaneous surface profiles from a supersonic crossflow test is presented in Fig. 12. The dashed line corresponds to the surface profile taken before the test, while the solid lines are contours taken during combustion of the fuel. The first profile is taken immediately after ignition of the entire fuel sample at t=85 seconds. This profile indicates a significant amount of pyrolysis in the downstream region before ignition, with most of the pyrolysis occurring 10.5 to 12.0 cm from the rearward-facing step. After ignition, the average burning rate of the sample is approximately 0.49 mm/s. Study of the exit plume confirms that reactions also occur downstream of the sample in the supersonic flow.

5. Conclusions

The combustion behavior of HTPB-based solid fuels with various percentages of boron loading were studied under both subsonic and supersonic crossflows, using a connected-pipe facility. A non-intrusive real-time x-ray radiography system was used to obtain instantaneous surface profiles of the solid fuels.

The ignition sequence of boron-laden fuels revealed the presence of glowing boron particles in the early stages of particle ignition on the fuel surface. These localized hot spots served as the ignition source for the solid fuel sample. Autoignition of the boron-laden fuels was always initiated by the particles on the sample surface in the recirculation zone formed by the rearward facing step.

The ignition sequence for B/HTPB (0/100) fuels was different from that of boron-laden fuels, since only pyrolyzed HTPB fuel is involved in the gas-phase process. Ignition of pyrolysis products of HTPB began in the recirculation zone; however, the required inlet temperatures were much higher. These fuels showed no indication of a localized ignition source to initiate the ignition process; instead ignition seemed to occur spontaneously over a distributed region in the recirculation zone. Flame spreading over the fuel surface was faster when compared with the boron-laden fuels partly because the freestream temperatures were higher.

All fuels tested under subsonic crossflow exhibited a faster regression rate with increased distance from the rearward-facing step. These tests also revealed that regression rates were highly dependent on freestream static pressures, and less dependent on the temperature and mass flux. Two mechanisms are attributed to enhanced burning rates at higher pressures: (1) faster gas-phase kinetics which lead to shorter flame standoff distance and increased heat feedback to the fuel surface, and (2) increased oxidizer-to-fuel ratio which allows additional reactions of oxidizers with fuel-rich pyrolysis products and ejected boron particles. The addition of small percentages of boron (up to 10 percent by weight) significantly enhanced the ignition and combustion characteristics of the sample and increased the regression rates. The increase in the regression rate is believed to be caused by the increase in convective and radiative heat transfer from the reacting particles to the fuel surface, as well as the increased radiation absorptivity of the fuel surface. A burning-rate correlation was also obtained in terms of pressure, temperature, and boron

concentration.

Combustion of solid fuels under supersonic crossflows was also successfully demonstrated. For these tests, it was necessary to increase the height of the rearward-facing step to promote ignition and flame stabilization of the solid fuel sample.

Acknowledgements

This paper represents a part of the research work conducted under Contract No. N00014-86-K-0468 sponsored by the Office of Naval Research, Arlington, VA. The support and encouragement of Drs. Richard S. Miller and Gabriel D. Roy are greatly appreciated.

References

[1] Korting, P. A. O. G., van der Geld, C. W. M., Wijchers, T., and Schoyer, H. F. R., "Combustion of Polymethylmethacrylate in a Solid Fuel Ramjet," *Journal of Propulsion and Power*, Vol. 6, No. 3, May-June 1990, pp. 263-270.

[2] Mady, C. J., Hickey, P. Y., and Netzer, D. W., "Combustion Behavior of Solid-Fuel Ramjets," *Journal of Spacecraft and Rockets*, Vol. 15, No. 3, May-June 1978, pp 131-132.

[3] Elands, P. J. M., Korting, P. A. O. G., Dijkstra, F., and Wijchers, T., "Combustion of Polyethylene in a Solid Fuel Ramjet– A Comparison of Computational and Experimental Results," AIAA Paper No. 88-3043, AIAA/ASME/SAE/ASEE 24th Joint Propulsion Conference, July 11-13, 1988, Boston, MA.

[4] Schulte, G., "Fuel Regression and Flame Stabilization Studies of Solid- Fuel Ramjets," *Journal of Propulsion and Power*, Vol. 2, No. 4, July- August 1986, pp. 301-304.

[5] Schulte, G., Pein, R., and Högl, A., "Temperature and Concentration Measurements in

a Solid Fuel Ramjet Combustion Chamber," *Journal of Propulsion and Power*, Vol. 3, No. 2, March-April 1987, pp. 114- 120.

[6] Snyder, T. S., Jarymowycz, T. A., Pace, K. K., and Kuo, K. K., " Solid Fuel Ignition and Combustion Characteristics Under High-Speed Crossflows," AIAA Paper No. 90-2075, AIAA/ASME/SAE/ASEE 26th Joint Propulsion Conference, Orlando, FL, July 16-18, 1990.

[7] Pein, R. and Vinnemeier, F., "The Influence of Swirl and Fuel Composition of Boron-Containing Fuels on Combustion in a Solid Fuel Ramjet Combustion Chamber," AIAA Paper No. 89-2885, AIAA/ASME/SAE/ASEE 25th Joint Propulsion Conference, July 10-12, 1989, Monterey, CA.

[8] Jarymowycz, T. A., "Ignition and Combustion of Solid Fuels under High-Velocity Crossflows, " Ph.D. Thesis, The Pennsylvania State University, University Park, PA, 1991.

[9] Chen, D. M., "Pyrolysis, Ignition and Combustion of Solid Fuels for Ramjet Applications," Ph.D. Thesis, The Pennsylvania State University, University Park, PA, 1988, pp. 104-105.

[10] Faeth, G. M., "Status of Boron Combustion Research," Report of the Boron Combustion Specialists Workshop, Air Force Office of Scientific Research, October 1984.

[11] Marquardt, D. W., "An Algorithm for Least-Squares Estimation of Nonlinear Parameters," *Journal of the Society for Industrial and Applied Mathematics*, Vol. 11, No. 2, 1963, pp. 431-441.

List of Figures

Fig. 1 Schematic Diagram of Connected-Pipe Facility.

Fig. 2 Schematic Diagram of Combustion Chamber Showing Temperature and Pressure Measurement Locations.

Fig. 3 Schematic Diagram of Real-Time X-Ray Radiography System.

Fig. 4 Temperature-Time History of Thermocouple B from a Typical Subsonic Test.

Fig. 5 Pressure-Time Histories of a Typical Subsonic Test.

Fig. 6 Autoignition Sequence of a B/HTPB (5/95) Solid Fuel Viewed through Top Window at a Framing Rate of 30 pps.

Fig. 7 Autoignition Sequence of a B/HTPB (0/100) Solid Fuel Viewed through Top Window at a Framing Rate of 30 pps.

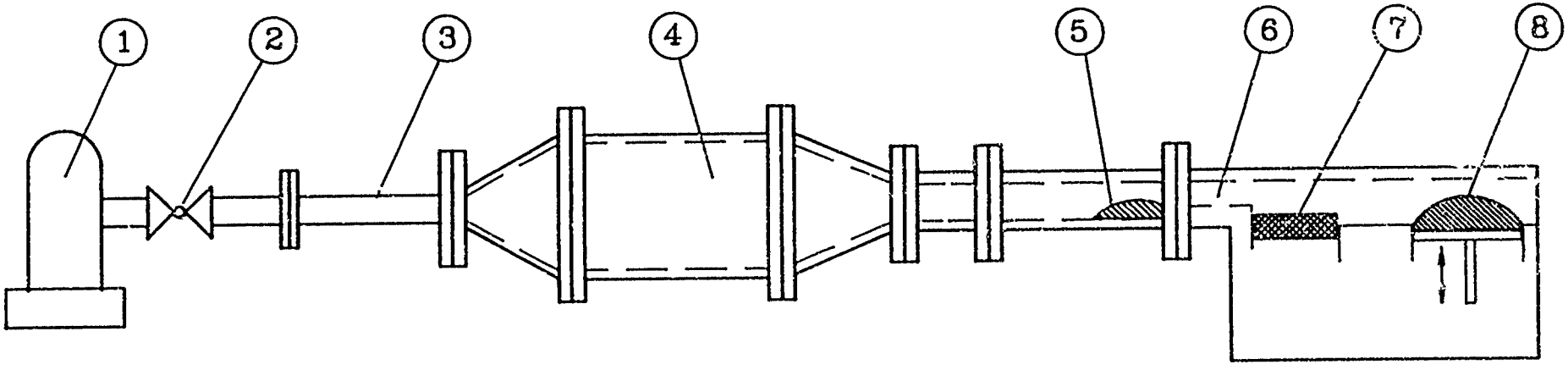
Fig. 8 Instantaneous Surface Profiles of B/HTPB (5/95) Solid Fuel under Subsonic Crossflow.

Fig. 9 Burning Rate Dependence on Freestream Pressure for B/HTPB Solid Fuels.

Fig. 10 Burning Rate Dependence on Freestream Temperature for B/HTPB Solid Fuels.

Fig. 11 Comparison of Observed and Predicted Burning Rates for B/HTPB Solid Fuels.

Fig. 12 Instantaneous Surface Profiles of B/HTPB (10/90) Solid Fuel under Supersonic Crossflow.



Station

1 Air Storage Tank

2 Pneumatic Ball Valve

3 Vitiator

4 Settling Chamber

5 Convergent–Divergent Nozzle

6 Combustion Chamber Inlet

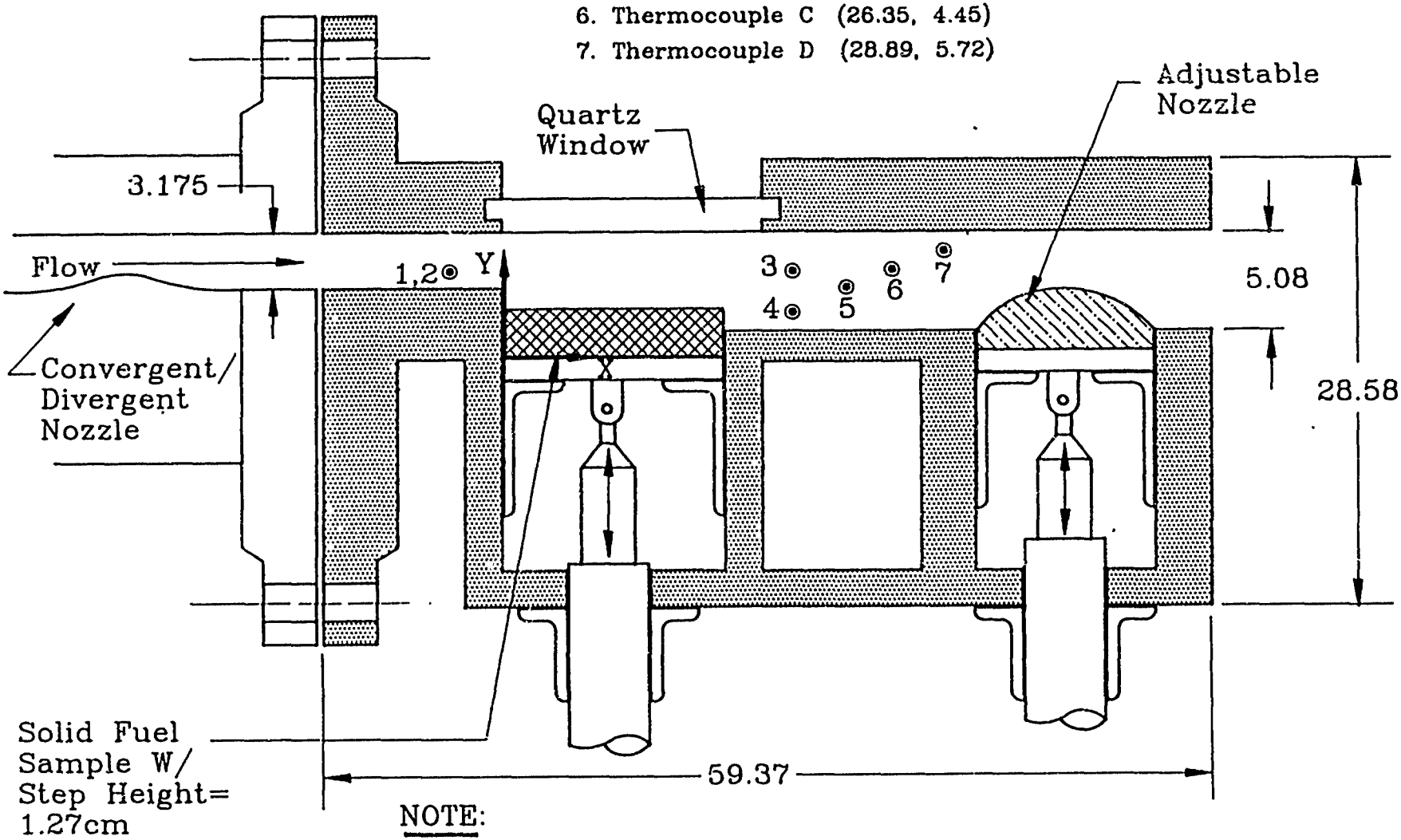
7 Test Secton (Fuel Sample)

8 Adjustable Exhaust Nozzle

Fig 1.

MEASUREMENT LOCATIONS (X,Y)

1. Pressure–Combustion Chamber Inlet (−3.81, 6.04)
2. Thermocouple– Combustion Chamber Inlet (−3.81, 6.04)
3. Pressure (21.27, 4.45)
4. Thermocouple A (21.27, 1.91)
5. Thermocouple B (23.81, 3.18)
6. Thermocouple C (26.35, 4.45)
7. Thermocouple D (28.89, 5.72)



NOTE:

All dimensions shown are in centimeters.

Fig. 2.

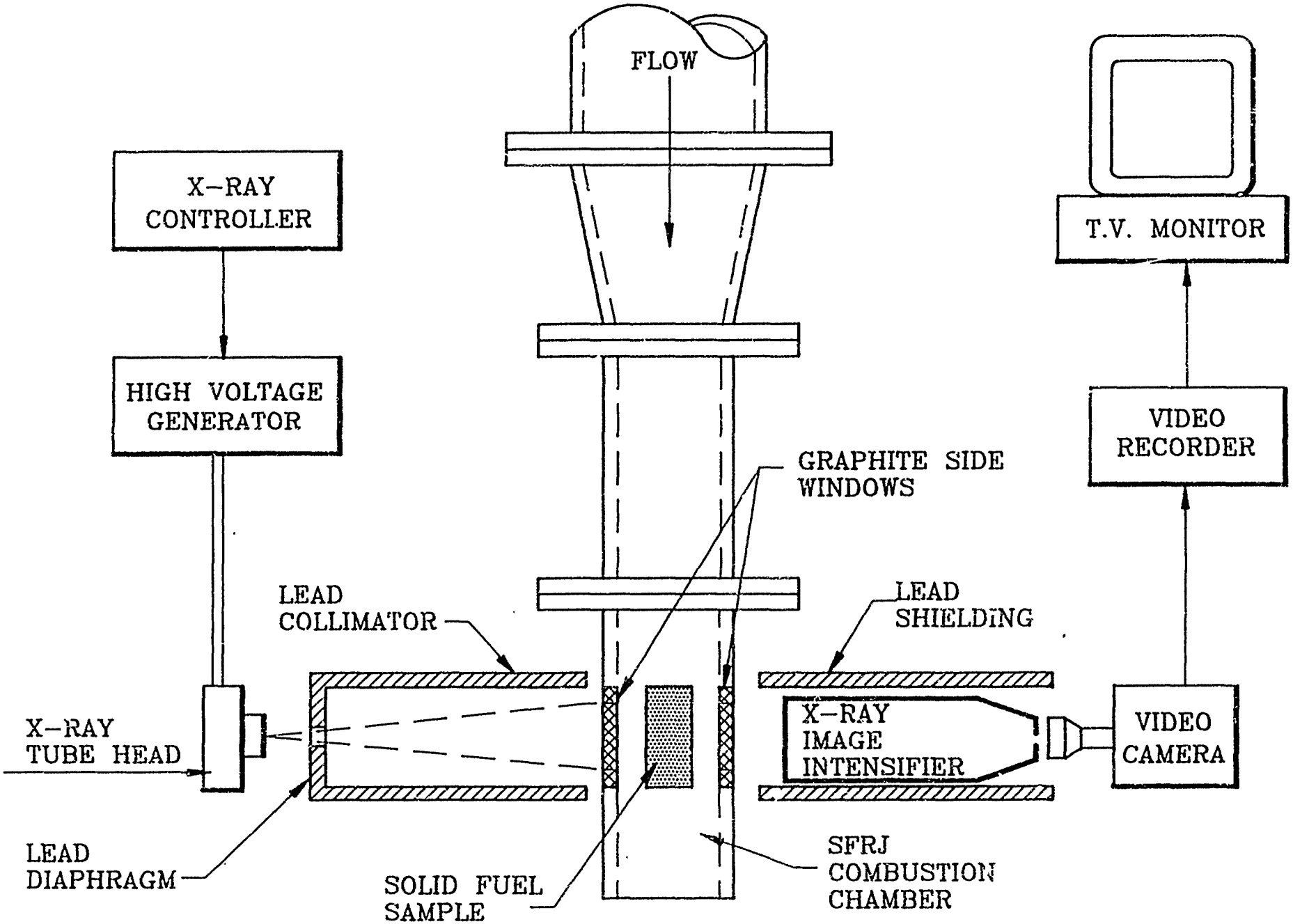

FLOW
X–RAY CONTROLLER
HIGH VOLTAGE GENERATOR
T.V. MONITOR
VIDEO RECORDER
GRAPHITE SIDE WINDOWS
LEAD COLLIMATOR
LEAD SHIELDING
X–RAY TUBE HEAD
X–RAY IMAGE INTENSIFIER
VIDEO CAMERA
LEAD DIAPHRAGM
SOLID FUEL SAMPLE
SFRJ COMBUSTION CHAMBER

Fig. 3

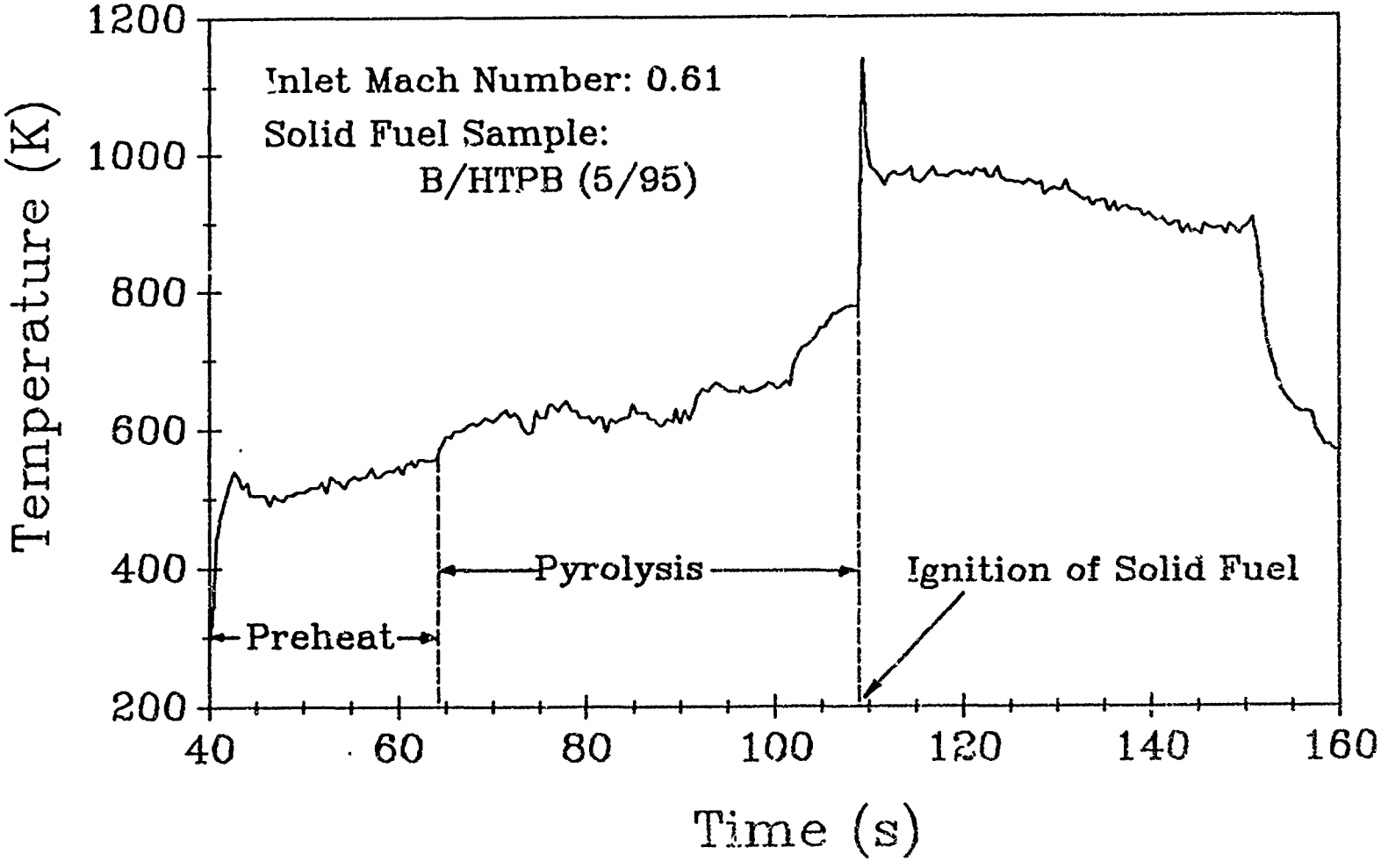

Inlet Mach Number: 0.61
Solid Fuel Sample:
B/HTPB (5/95)
Preheat
Pyrolysis
Ignition of Solid Fuel
Temperature (K)
Time (s)
1200
1000
800
600
400
200
40
60
80
100
120
140
160

Fig 4

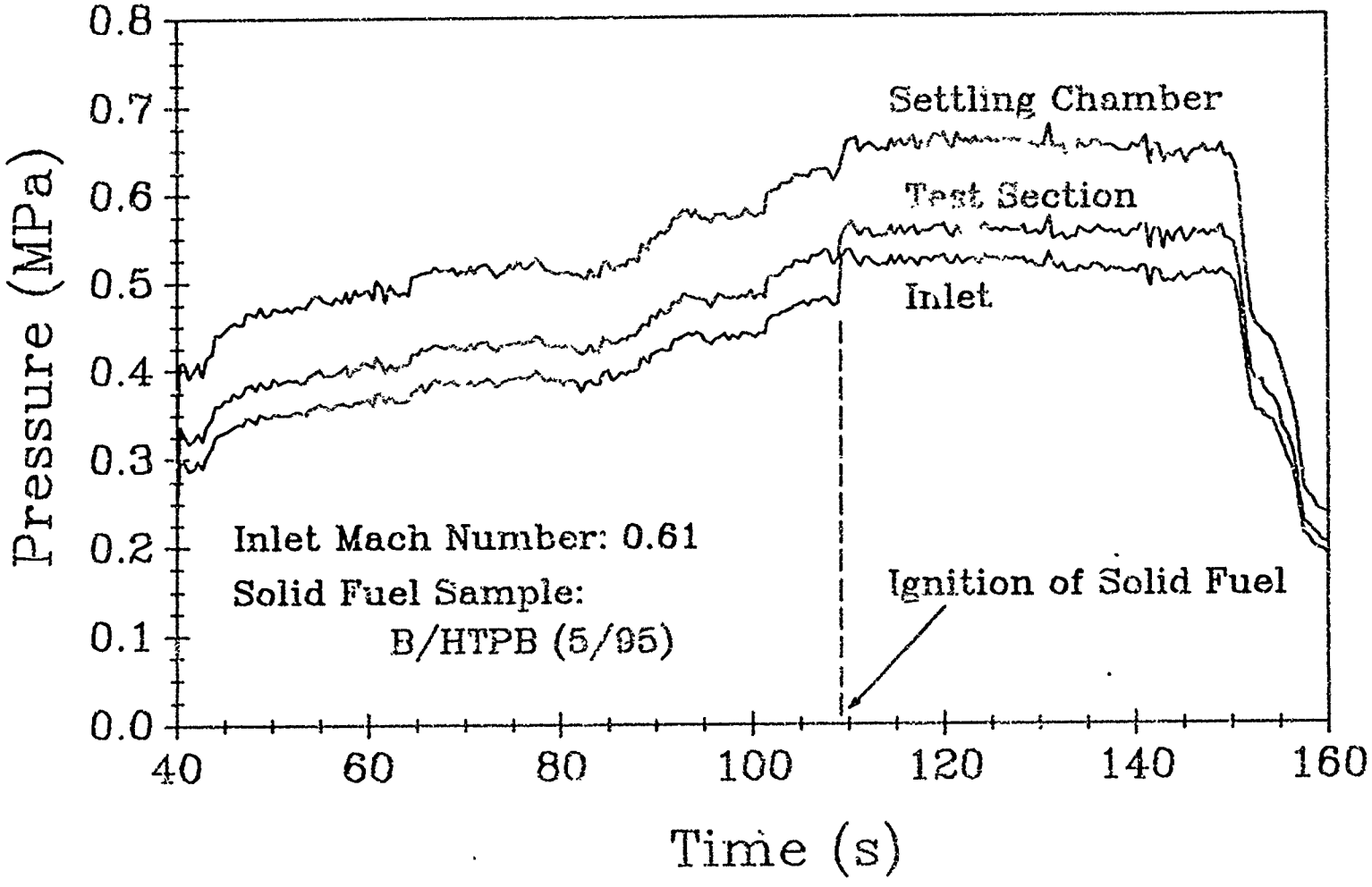

Pressure (MPa)
0.8
0.7
0.6
0.5
0.4
0.3
0.2
0.1
0.0
40
60
80
100
120
140
160
Time (s)
Settling Chamber
Test Section
Inlet
Inlet Mach Number: 0.61
Solid Fuel Sample:
B/HTPB (5/95)
Ignition of Solid Fuel

Fig 5

Fig. 7a

Fig. 7b

Fig. 7c

Fig. 7d

Fig. 7e

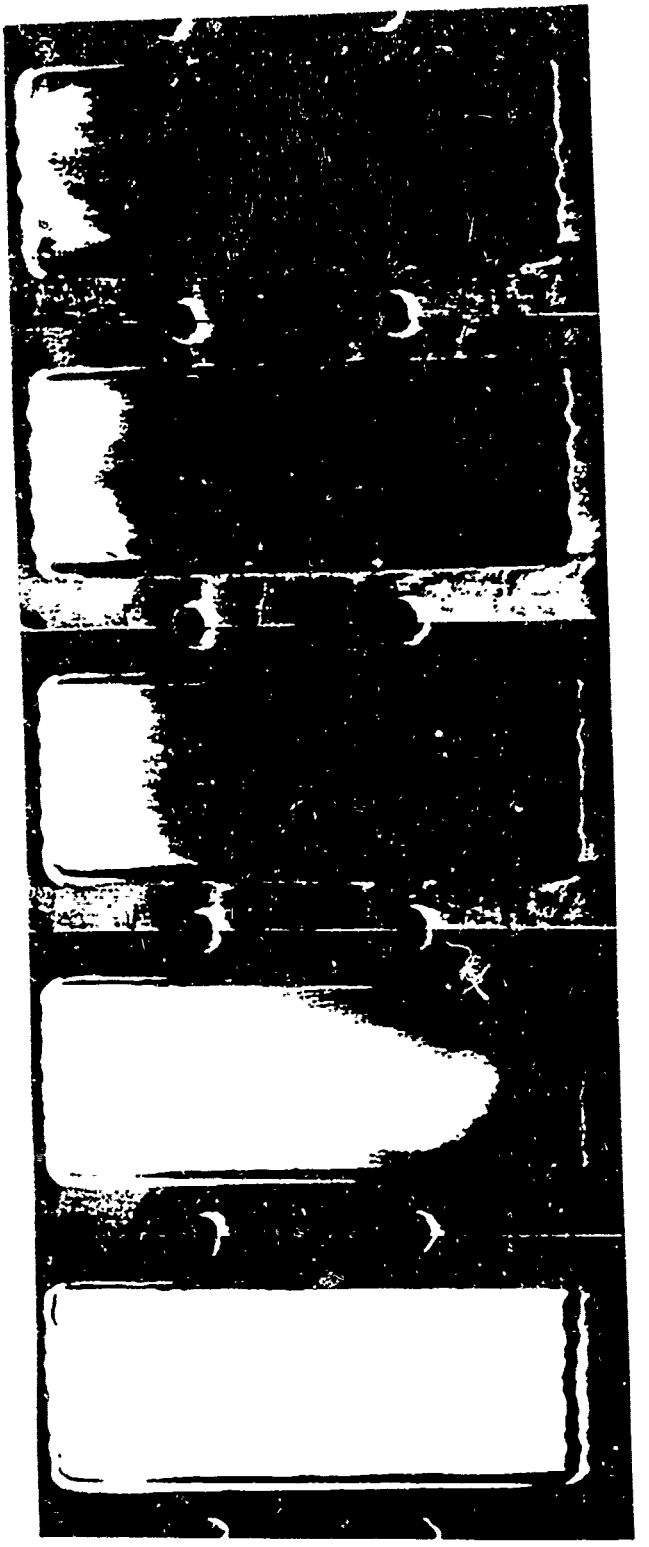


Fig. 6a

Fig. 6b

Fig. 6c

Fig. 6d

Fig. 6e



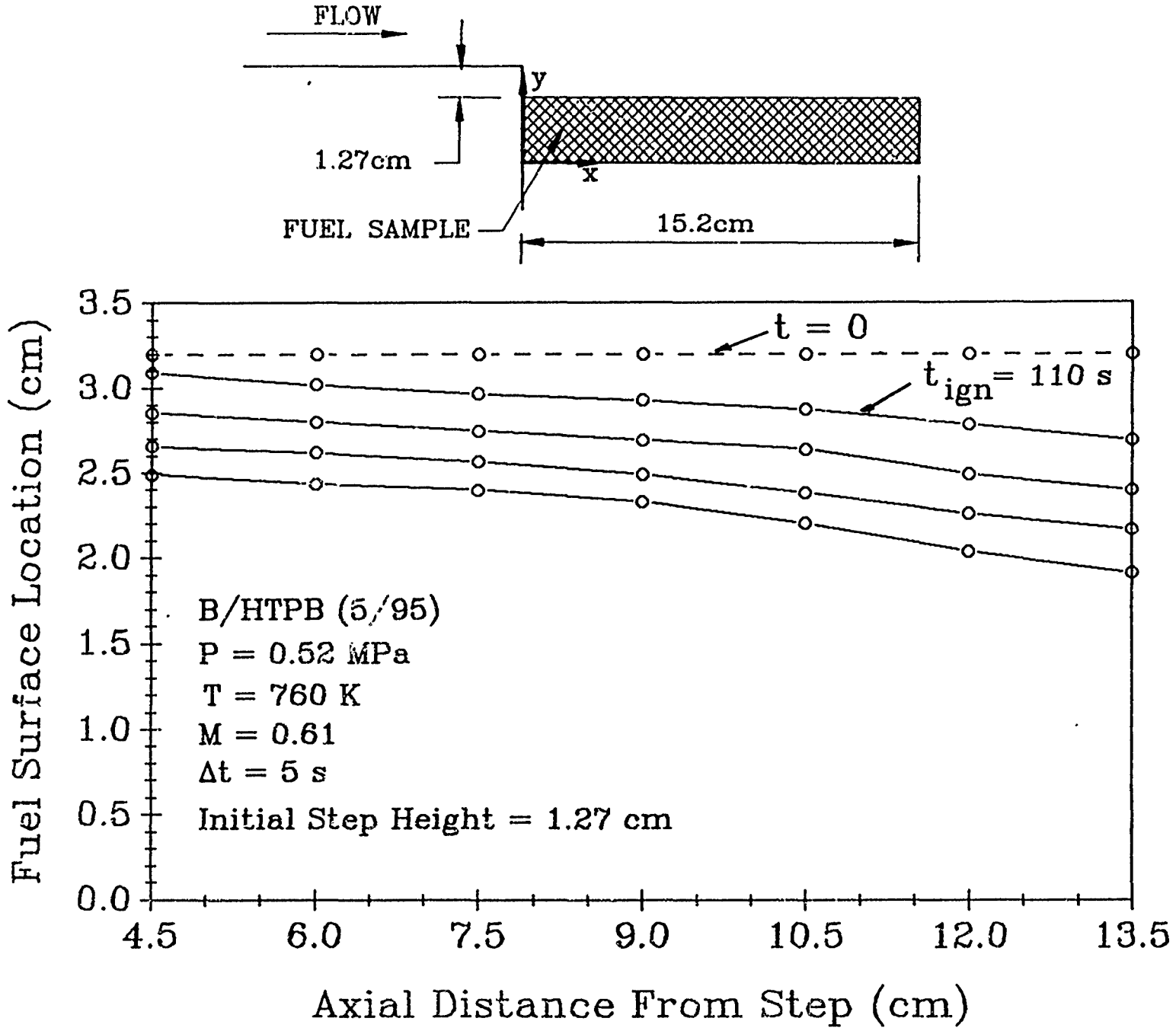
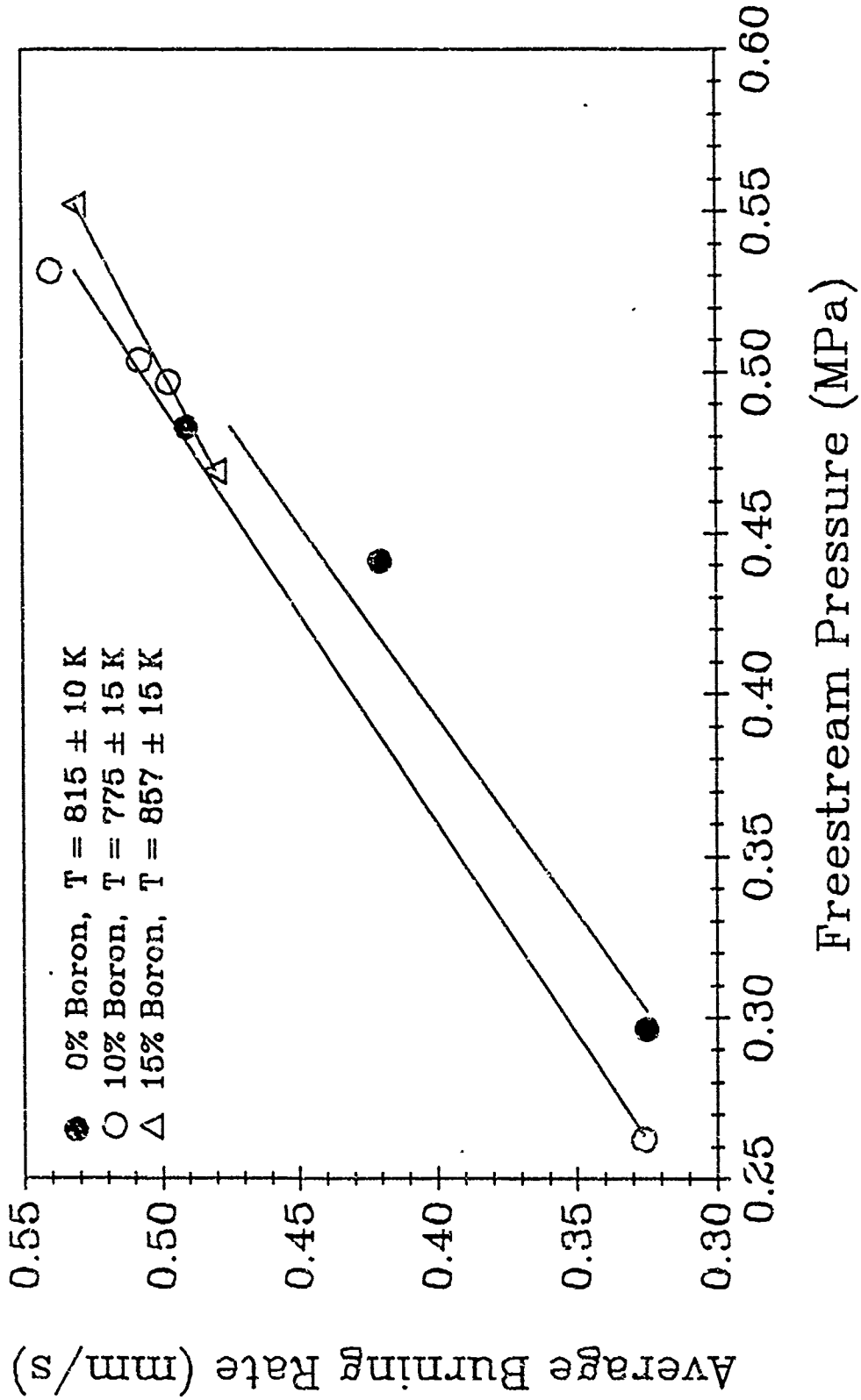

FLOW
y
1.27cm
x
FUEL SAMPLE
15.2cm
t = 0
t_{ign} = 110 s
B/HTPB (5/95)
P = 0.52 MPa
T = 760 K
M = 0.61
Δt = 5 s
Initial Step Height = 1.27 cm
Fuel Surface Location (cm)
Axial Distance From Step (cm)
3.5
3.0
2.5
2.0
1.5
1.0
0.5
0.0
4.5
6.0
7.5
9.0
10.5
12.0
13.5

Fig. 8


Average Burning Rate (mm/s)
0.55
0.50
0.45
0.40
0.35
0.30
0.25
0.30
0.35
0.40
0.45
0.50
0.55
0.60
Freestream Pressure (MPa)
● 0% Boron, T = 815 ± 10 K
○ 10% Boron, T = 775 ± 15 K
△ 15% Boron, T = 857 ± 15 K

F: 9

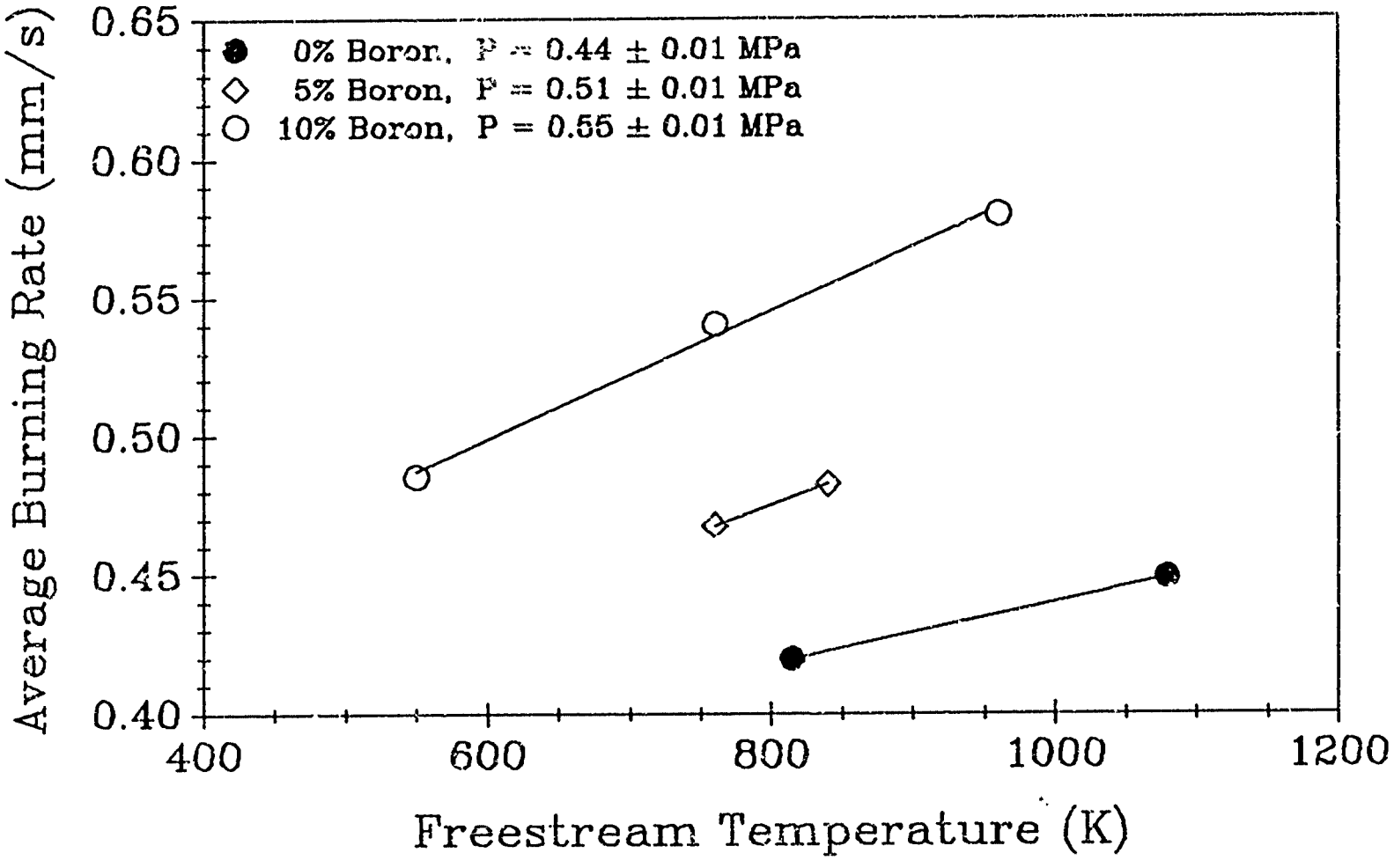

0% Boron, P = 0.44 ± 0.01 MPa
5% Boron, P = 0.51 ± 0.01 MPa
10% Boron, P = 0.55 ± 0.01 MPa
Average Burning Rate (mm/s)
0.65
0.60
0.55
0.50
0.45
0.40
400
600
800
1000
1200
Freestream Temperature (K)

Fig. 10

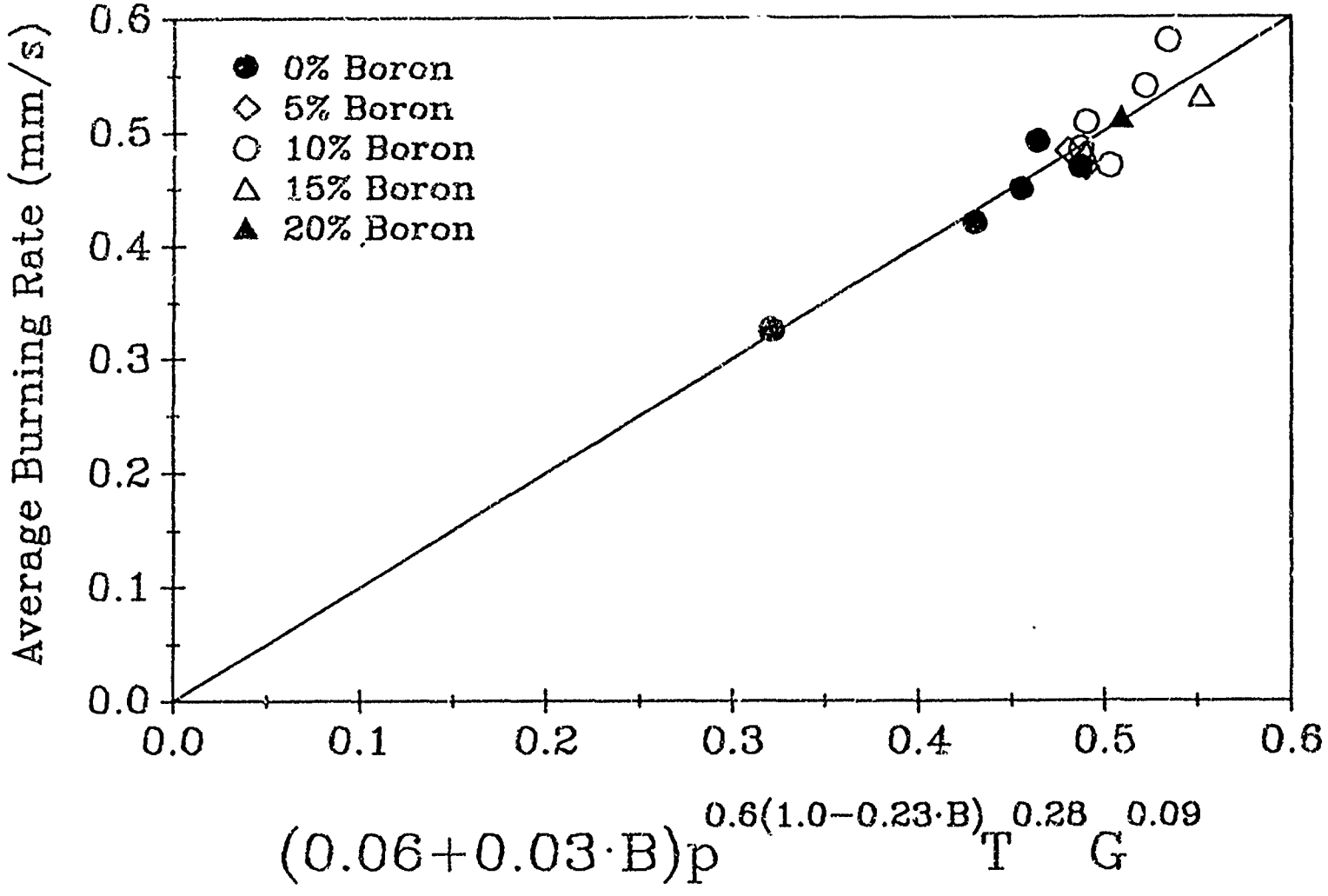

Average Burning Rate (mm/s)
0.6
0.5
0.4
0.3
0.2
0.1
0.0
0.0
0.1
0.2
0.3
0.4
0.5
0.6
0% Boron
5% Boron
10% Boron
15% Boron
20% Boron
$(0.06+0.03\cdot B)p^{0.6(1.0-0.23\cdot B)}\,T^{0.28}\,G^{0.09}$

Fig. 11

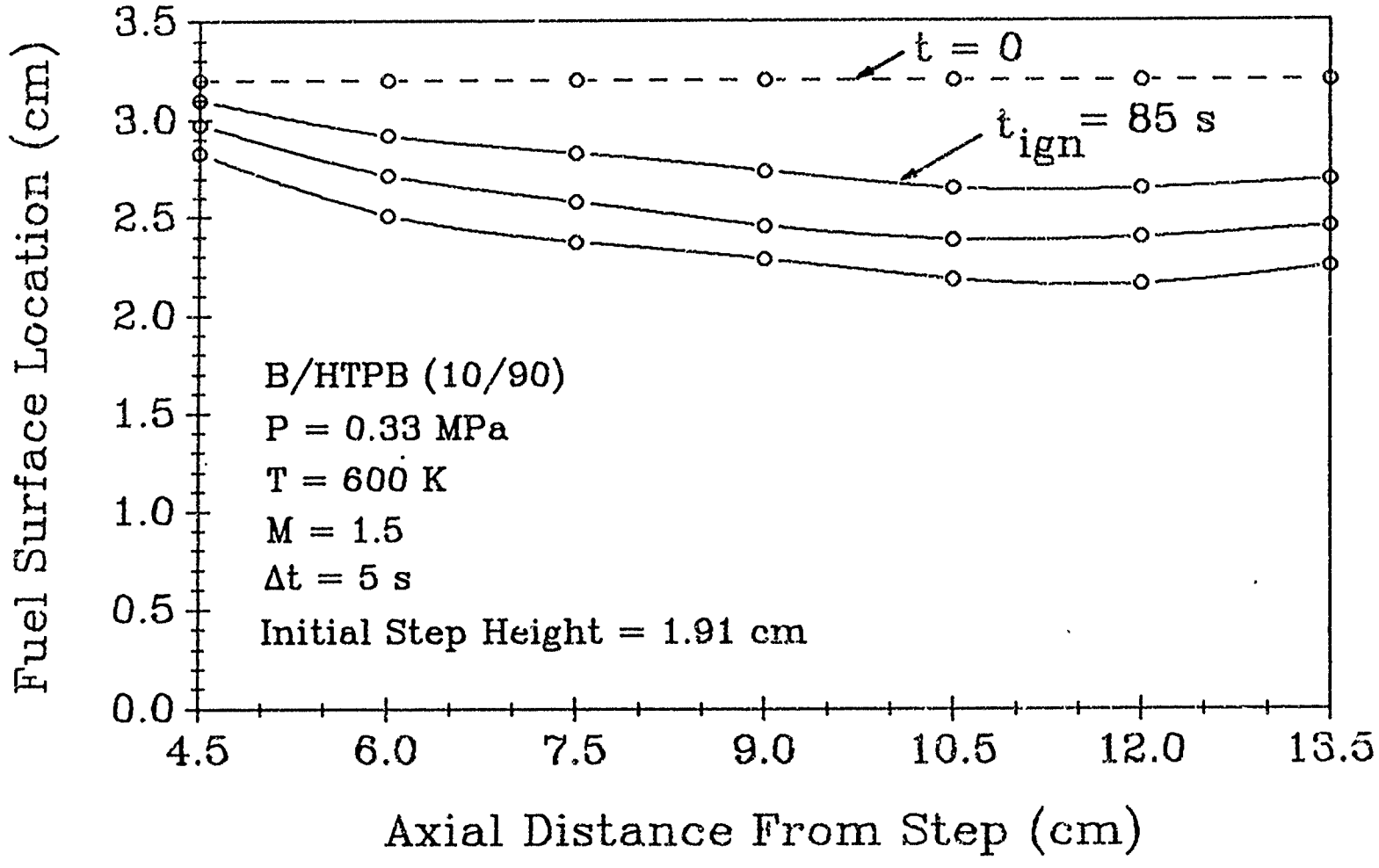

Fuel Surface Location (cm)
3.5
3.0
2.5
2.0
1.5
1.0
0.5
0.0
t = 0
t_{ign} = 85 s
B/HTPB (10/90)
P = 0.33 MPa
T = 600 K
M = 1.5
Δt = 5 s
Initial Step Height = 1.91 cm
4.5
6.0
7.5
9.0
10.5
12.0
13.5
Axial Distance From Step (cm)

Fig. 12

FILE COPY

AIAA 90-2075

Solid Fuel Ignition and Combustion Characteristics Under High-Speed Crossflows

T.S. Snyder, T.A. Jarymowycz, K.K. Pace, and K.K. Kuo

The Pennsylvania State University
University Park, PA 16802

AIAA/SAE/ASME/ASEE
26th Joint Propulsion Conference
July 16-18, 1990 / Orlando, FL

For permission to copy or republish, contact the American Institute of Aeronautics and Astronautics
370 L'Enfant Promenade, S.W., Washington, D.C. 20024

SOLID FUEL IGNITION AND COMBUSTION CHARACTERISTICS UNDER HIGH-SPEED CROSSFLOWS

T.S. Snyder*, T.A. Jarymowycz**, K.K. Pace+, and K.K. Kuo++
Department of Mechanical Engineering
The Pennsylvania State University
University Park, Pennsylvania 16802

ABSTRACT

The ignition and combustion characteristics of HTPB solid fuels with various percentages of boron loadings have been studied under high-speed, high-enthalpy crossflows. A blowdown wind tunnel was utilized to simulate a SFRJ combustor with pressures from 0.26 to 0.55 MPa and temperatures from 620 to 1040 K. Regression rates of the solid fuels were determined as a function of boron percentage and freestream temperature and pressure using a real-time X-Ray radiography system. The addition of 10 percent boron to HTPB enhanced the ignition characteristics of the sample and resulted in the fastest regression rate. Samples loaded with high percentages of boron had lower regression rates. This decrease is caused by the heat sink effect of a large number of boron particles, the shielding of heat feedback from the diffusion flame to the sample surface, and the decreased gas-phase reactions by the reduction in HTPB percentage.

I. INTRODUCTION

The research and development of advanced air-breathing propulsion systems continue to be of great importance because of the advantages of using ambient air as oxidizer. High specific impulse and long range can be achieved by burning solid fuels under subsonic crossflow conditions in ramjets, or under supersonic crossflow conditions in scramjets. Efficient operation of these combustors depends upon: 1) self-sustained combustion of the solid fuel using a rearward facing step for flame holding; 2) adequate freestream temperature, pressure, and mass flowrate; 3) proper mixing of the oxygen in the freestream with the pyrolyzed fuel-rich gases; and 4) uniform regression of the solid fuel grain. Once efficient combustion is demonstrated, practical applications of solid fuels can be incorporated into propulsion systems.

There have been several research efforts dealing with the combustion characteristics of solid fuels under low Mach-number conditions. Netzer and Gany[1] studied the effects of fuel port-to-inlet area ratio, port-to-throat area ratio, and freestream temperature on flame holding of several solid fuels. The fuels studied in their subscale combustor included polymethylmethacrylate (PMMA), polyethylene (PE), and polybutadiene (PB). They found that the flame holding characteristics could be improved by increasing these area ratios and the freestream temperature. Their results also indicate that the flame holding boundary could be broadened to include lower area ratios if the freestream temperature is increased. This implies that as the inlet temperature of the ram air increases (i.e. higher flight Mach number), the step height required for a dump combustor becomes smaller. Similar observations were made by Schulte[2] concerning the effects of area ratio on flame stability. He observed that the regression rate for PE was affected somewhat stronger by an increase in inlet air temperature than by an increase in the air mass flux or chamber pressure.

The results obtained from these works demonstrate the importance of combustor geometry and operating conditions on the combustion of solid fuels. The geometry of the combustor governs the flow characteristics and the mixing processes between the pyrolyzed fuel-rich gases and the inlet air. In addition, the reaction rates between reactants depends strongly on the freestream temperature and chamber pressure.

Gany and Netzer[3] studied the combustion behavior of solid fuels highly loaded with boron, boron carbide, and magnesium particles. They concluded that under regular dump combustor flow conditions almost no oxygen exists at the solid fuel surface. However, flow impingement on the fuel surface caused surface heating and glowing by chemical reactions. These reactions promoted the ejection of hot particles and large fuel segments from the surface reaction layer to the freestream.

Depending upon the reaction time of the particles, ejection of particles from the surface can greatly influence the combustion efficiency of the solid fuels inside a combustor. High combustion efficiency can be attained if the chemical reaction times of the ejected particles are smaller than their residence times in the combustor. In addition, adequate mixing between the fuel-rich reactants and oxidizer species is necessary to decrease the chemical reaction time in the gas-

---

* Graduate Student, Student Member of AIAA
** Ph.D. Candidate, Student Member of AIAA
\+ Graduate Student
++ Distinguished Professor, Associate Fellow of AIAA

Copyright © 1990 by the American Institute of Aeronautics and Astronautics, Inc. All rights are reserved

phase, and to provide a high flame temperature for ignition and combustion of particles.

In a numerical study of solid fuel combustion, Jarymowycz et al.[4] solved a comprehensive model with finite-rate chemical reactions for a hydroxyl-terminated polybutadiene (HTPB) solid fuel under supersonic crossflow conditions. The model predicted steep transverse concentration gradients of oxidizer and fuel-rich species in the diffusion flame zone. In addition, there was a substantial concentration of fuel-rich species which remained unreacted at the exit plane of the combustion chamber, indicating the importance of mixing between the freestream oxidizer and the fuel species.

Schulte et al.[5] made concentration measurements for the combustion of PE in a solid fuel ramjet (SFRJ). They found that at an axial position downstream of the combustor entrance, z/D = 0.6 (where z is the axial distance in the streamwise direction from the step and D is the fuel port diameter), the oxygen concentration was on the order of 1 to 3 percent by volume. The oxygen concentration varied significantly in the radial direction, reaching 21 percent in the core of the freestream. At positions farther downstream, z/D=10.0, the oxygen concentration in the core region dropped to 14 percent, indicating the occurrance of gas-phase reactions. It was concluded that the combustion processes in the recirculation zone take place mainly in the shear layer adjacent to the incoming air flow. In the redeveloping boundary layer downstream of the recirculation zone, the flow could be divided into two regions; a colder air-rich zone in the core and a zone of combustion products and fuel-rich species closer to the wall. These two zones were found not to mix completely which emphasizes the need for proper mixing.

Schadow and Gutmark[6] investigated several different means of enhancing the mixing process in a simulated SFRJ using artificially induced pressure oscillations. Their results indicate that the temperature inside the combustion chamber can be maximized by enhanced mixing. The inherent effect of solid fuel composition on the combustion process and the sites of chemical reactions is also important. Gany and Netzer[3] suggested that as the concentration of volatile ingredients decreases through the increased loading of metallized powders, the gas-phase reactions become less intense and play a less important role in the combustion process. This indicates that the heterogeneous reactions on the surface become more important as particle loading increases.

The relative importance of the heterogeneous reactions have been studied by Snyder et al.[7] using a CO_2 laser as an energy source for ignition.[2] Results from laser ignition of HTPB with boron powders clearly show that ignition of solid fuels under no crossflow conditions occurs in the gas phase rather than on the fuel surface. Following ignition, the flame front propagates toward the surface thus increasing the heat transfer to the surface and enhancing the heterogeneous reactions on the surface. The heterogeneous reactions cause more fuel to pyrolyze and feed additional fuel-rich species to the gas-phase reaction zone. When a low speed crossflow was supplied to a region directly above the sample, ignition was observed in both the gas-phase and on the fuel surface with intensified heterogeneous reactions on the surface. Comparing these results to those obtained under no crossflow, the addition of crossflow to the region above the fuel surface caused the boron to react much more vigorously resulting in increased heat feedback to the surface and the achievement of self-sustained combustion. In similar crossflow tests performed with HTPB samples not containing boron, only gas-phase reactions were observed, and self-sustained combustion could not be achieved. This indicates that the heterogeneous reactions on the surface, caused by the addition of boron particles, enhance both the ignition and combustion processes.

Combustion of boron/HTPB, carbon black/HTPB, and boron mixed with an energetic copolymer, 3,3-bis[azidomethyl] oxetane and 3-nitratomethyl-3-methyl oxetane (BAMO/NMMO), were studied by Snyder et al.[3] under high-speed crossflows at one atmospheric pressure and a freestream temperature of approximately 500 K. Under these conditions, the HTPB-based fuels exibited poor ignition characteristics. Solid fuels containing 50 percent boron were ignited; however, combustion was limited to the recirculation zone immediately behind the rearward facing step. Several bright spots were observed downstream of the reaction zone on the surface of the sample indicating localized heterogeneous reactions. Tests were also performed on HTPB solid fuel samples with the addition of small amounts of carbon black to prevent in-depth radiative heating. Results show that the carbon black/HTPB samples could not be ignited even in the recirculation zone, and there were no signs of heterogeneous reactions on the surface of the solid fuel sample. Based upon the comparison with boron/HTPB fuels, it was concluded that boron particles can considerably enhance the heat release rate and consequently increase the energy transferred to the surface for pyrolysis.

Stable combustion of BAMO/NMMO-based solid fuels were achieved under relatively low pressure and temperature conditions. These fuels were readily ignited under one atmospheric pressure and 500 K freestream temperature because of the lower pyrolysis temperature and the presence of nitrates in the chemical structure. The average regression rate of BAMO/NMMO was found to

be 0.67 mm/sec and increased to 1.05 mm/sec with the addition of 17.6 percent boron, showing the effect of boron in the combustion process.

Based upon the above studies, several parameters have been found to significantly affect the combustion processes inside SFRJ combustors: 1) ratios between the fuel port area, inlet area, and exit throat area; 2) inlet air temperature and pressure; 3) freestream velocity and turbulence intensity; 4) composition of solid fuels and; 5) the type and size distribution of solid particles added to the solid fuel.

The objectives of this paper are:

1. To determine the effect of boron addition (from 0 to 50 weight percent) on the ignitability and regression rate of HTPB-based solid fuels.

2. To determine the effect of freestream temperature and pressure on the ignitability and regression rate of solid fuels.

3. To obtain experimental results as a database for future model validation of solid fuel burning under high-speed, high-enthalpy crossflows.

II. EXPERIMENTAL APPROACH

Blowdown Wind Tunnel

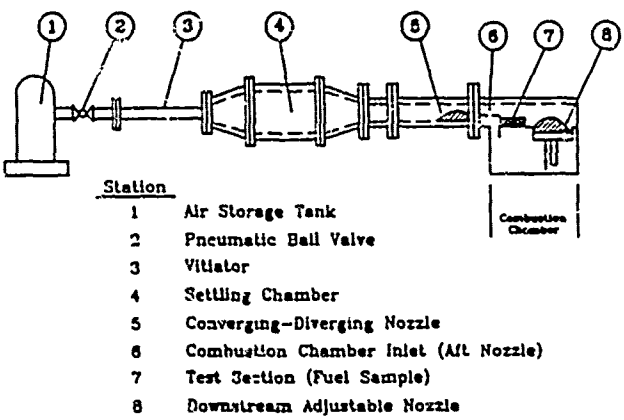


Fig. 1 Schematic diagram of high-enthalpy blowdown wind tunnel

In order acquire a basic understanding of the physical and chemical mechanisms involved in the combustion of solid fuels under high-speed crossflows, a high-enthalpy blowdown wind tunnel was constructed and is shown schematically in Fig. 1. The wind tunnel utilizes compressed air from two large air storage tanks having a combined capacity of 72 cubic meters and a maximum pressure of 4.9 MPa. Air from these two tanks is mixed and burned with propane in the vitiator at an air/fuel ratio of 8:1. The hot gases reach a maximum temperature of 1000 K in the settling chamber, then pass through a converging-diverging nozzle which accelerates the flow. The wind tunnel is capable of providing vitiated air with a static pressure range of 0.1 to 0.62 MPa in the test section at a Mach number of 1.5. During subsonic operations, an adjustable nozzle downstream of the solid fuel sample controls the pressure inside the test section. The maximum flowrate attainable is 8 kg/s with a duration of four minutes at the highest pressure.

Pressure and temperature measurements are taken in the settling chamber, uptream of the converging-diverging nozzle, in the combustion chamber inlet, and downstream of the solid fuel sample. Steady flow conditions are achieved using a feedback control loop between the pressure transducer in the settling chamber and a pneumatic ball valve. An IBM PC/AT computer records all the temperature and pressure measurements for the duration of each test.

The high temperature flow enters the combustion chamber through the rectangular inlet measuring 3.18 cm in height and 10.16 cm in width. The solid fuel sample, (15.24 cm in length, 5.08 cm in width, and 3.18 cm in height), is placed directly behind a rearward facing step forming a step height of 1.27 cm. This corresponds to a fuel port height to inlet height ratio of 1.4. The combustion chamber temperature and pressure measurements are taken at the locations shown in Fig. 2. Temperature profiles in the subsurface, surface, and gas-phase regions of the fuel sample are determined from two embedded thermocouples located 4.60 cm from each end of the solid fuel and 1.90 cm from the initial sample surface. The thermocouples are molded into the solid fuel samples during the curing process.

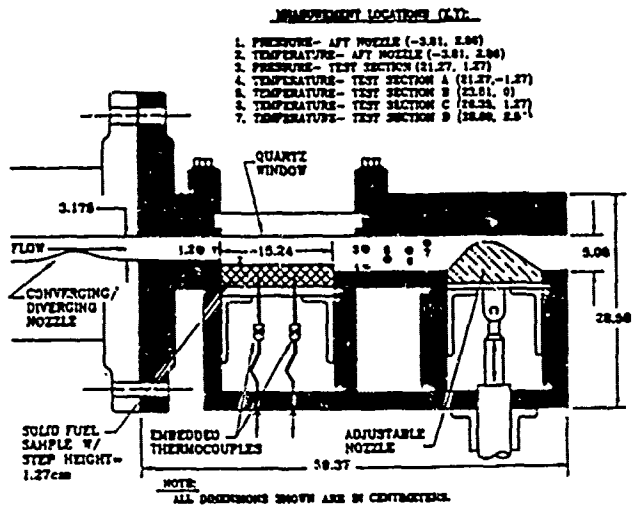


Fig. 2 Schematic diagram of combustion chamber showing pressure and temperature measurement locations

Solid Fuels

The solid fuels of interest in this study include: (1) HTPB with various percentages of boron powder (ranging from 0 to 20 percent) made at the Pennsylvania State University; (2) boron/HTPB (50/50) manufactured by the United Technologies/ Chemical Systems Division (UT/CSD); (3) high density hydrocarbon solid fuels supplied by the Naval Weapons Center (NWC) and; (4) HTPB with boron and aluminum or magnesium powders processed at Penn State University. Amorphous boron powders added to the solid fuel have a 99.9% purity, 325 mesh, and 0.5 micron mean diameter. In this paper, only types 1 and 2 solid fuel results are reported.

Igniter

To achieve ignition of the solid fuels, a pyrophoric liquid, triethylborane (TEB), was injected into the recirculation zone. A stainless steel tube having an outer diameter of 0.318 cm was extended slightly above the sample surface to inject TEB parallel to the top surface of the sample, at an angle approximately 60 degrees from the flow direction. TEB was turned off after the attainment of self-sustained combustion. The injection time was usually on the order of one second. In some cases, the solid fuel sample ignited without the injection of TEB, but this was highly dependent upon the free-stream conditions and fuel composition.

Real-time X-Ray Radiography and Video System

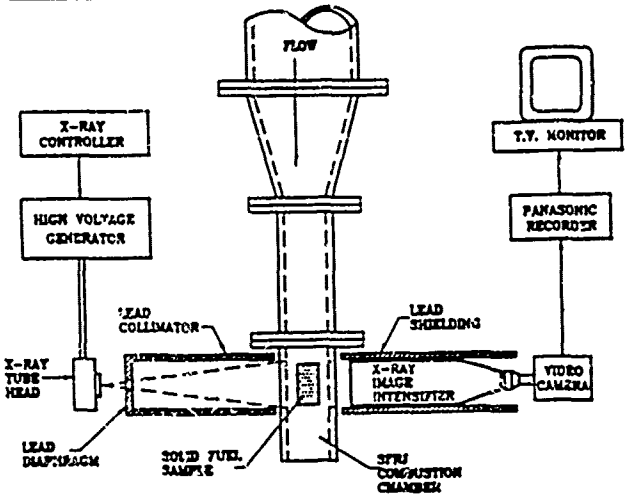


Fig. 3 Schematic diagram of the Real-time X-Ray radiography system for obtaining the fuel sample regression history

The burning phenomena of the solid fuels were studied using direct photography and real-time X-Ray radiography. The X-Ray system was used to observe the instantaneous contour of the solid fuel sample. Through its time variation, the regression rate of the sample was deduced using an image processor. The system consists of an X-Ray source, image intensifier, and video camera which viewed the fuel through two side windows on opposing sides of the test section as shown in Fig. 3. A direct video was used to capture the top view of the solid fuel through a quartz window for studying the surface ignition, flame spreading, and combustion processes. A third video camera recorded the exit plume from the combustion chamber.

III. EXPERIMENTAL RESULTS AND DISCUSSION

High-speed crossflow tests were conducted with combustion chamber static pressures from 0.26 to 0.55 MPa and free-stream temperatures from 620 to 1040 K. The high-enthalpy vitiated air entered the combustion chamber at flowrates ranging from 1.3 to 2.3 kg/s and mass fluxes ranging from 41 to 70 g/cm^{2}s. Figures 4 and 5 show typical temperature- and pressure-time traces recorded from a test firing with a boron/HTPB (10/90) solid fuel sample. The onset of solid fuel ignition is characterized by a spike in the temperature-time trace of the test section B thermocouple as shown in Fig. 4. The temperature spike is believed to be caused by the spontaneous ignition of the accumulated fuel-rich species pyrolyzed from the fuel. Combustion of the solid fuel, which lasted approximately 50 seconds, is evident in the temperature-time traces which show a significantly higher temperature in the test section than that in the aft nozzle location. The abrupt drop of the temperature near the end of the test run was caused by the shutdown of the wind tunnel.

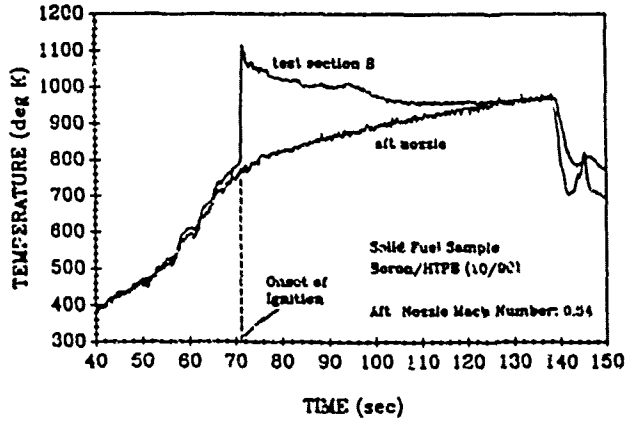


Fig. 4 A typical set of measured temperature-time traces

Figure 5 shows three separate pressure-time traces measured from the settling chamber, aft nozzle, and test section locations. As shown in the p-t traces, the onset of solid fuel ignition caused a small abrupt increase in each pressure reading. Following ignition, the pressure is steady throughout the duration of the test firing.

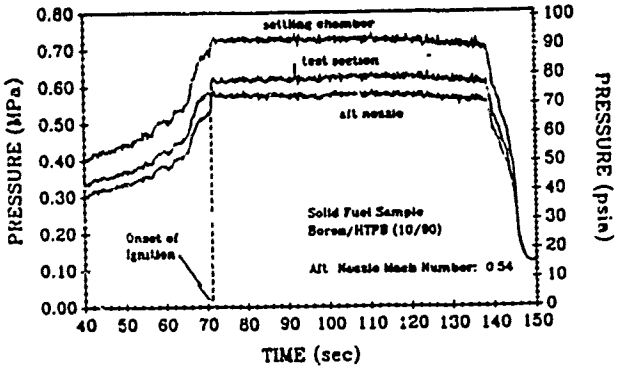


Fig. 5 A typical set of measured pressure-time traces

A series of instantaneous surface contours obtained from the X-Ray radiography system for boron/HTPB (10/90) solid fuel is shown in Fig. 6. The first 2.8 cm of the solid fuel surface was not in the X-Ray viewing area and therefore the surface contours are not plotted in this region. Following ignition, the solid fuel surface contour is plotted every 5 seconds. Burning rates were deduced at four axial positions located at 3.0, 6.0, 9.0, and 12.0 cm from the rearward facing step, as indicated in Fig. 6. As the solid fuel burns, a forward facing step is formed near the downstream end of the solid fuel. This introduces a locally high pressure region, which enhances the heat transfer to the solid fuel; thus, the downstream surface regresses faster. Because of the change in the flowfield near the downstream portion of the sample surface, only the first 15 to 25 seconds of the regression history was used to determine the burning rate of the solid fuel.

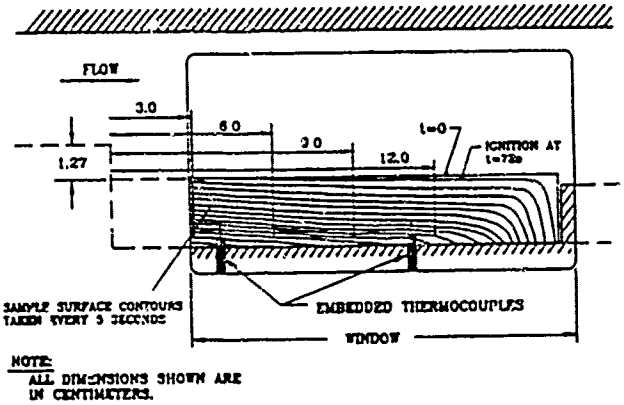


Fig. 6 Instantaneous surface contours obtained from the real-time X-Ray radiography system

Figure 7 shows the axial regression rate distributions for several HTPB-based fuels with various boron loadings. The corresponding aft-nozzle freestream temperature and pressure for each test are tabulated with temperature and pressure ranging from 730 to 830 K and 0.37 to 0.55 MPa, respectively. All of the solid fuels exhibited a faster regression rate with increasing axial distance from the rearward facing step. The increased regression rate in the downstream region is believed to be caused by the enhanced heat feedback from the diffusion flame zone in addition to the increased pressure caused by the forward facing step. The amount of heat release in the diffusion flame zone increases with axial distance, since the majority of the pyrolyzed fuel-rich species are transferred to downstream locations by the shear flow before chemical reactions occur. This implies that larger amounts of fuel-rich species are reacted near a downstream location than at an upstream station. Thus, the heat release in the diffusion flame is higher in the downstream region.

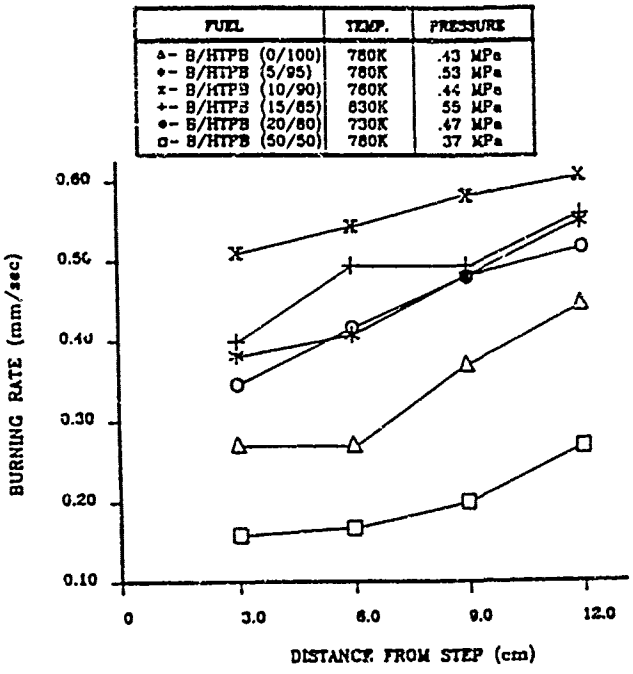


Fig. 7 Burning rate versus axial distance for HTPB-based solid fuels with various percentages of boron loading

Figure 7 also shows the effect of boron weight percentage on the burning rate. The addition of 5 and 10 percent boron to HTPB caused the burning rate to increase over the entire surface; however, further increase of boron loadings to 15, 20 and 50 percent results in a decrease in the regression rate. For a more explicit illustration, the regression rates are also plotted in Fig. 8 as a function of boron percentage. This figure clearly shows that the sample with 10 percent boron loading has the highest regression rate. The initial increase in regression rate with boron loading is believed to be caused by two factors. One is due to the heat feedback from the boron particle reactions in the flame zone, which increases the heat feedback to the sample surface. The other factor is due to the increase in radiation absorptivity of the

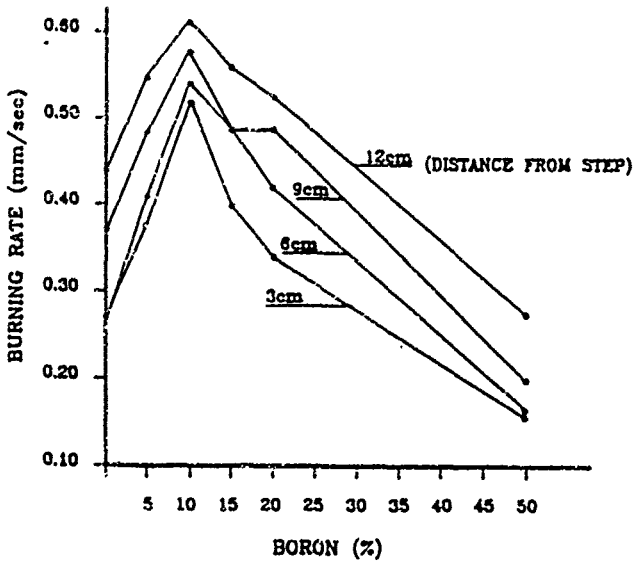


Fig. 8 Burning rate versus boron percentage at four axial locations

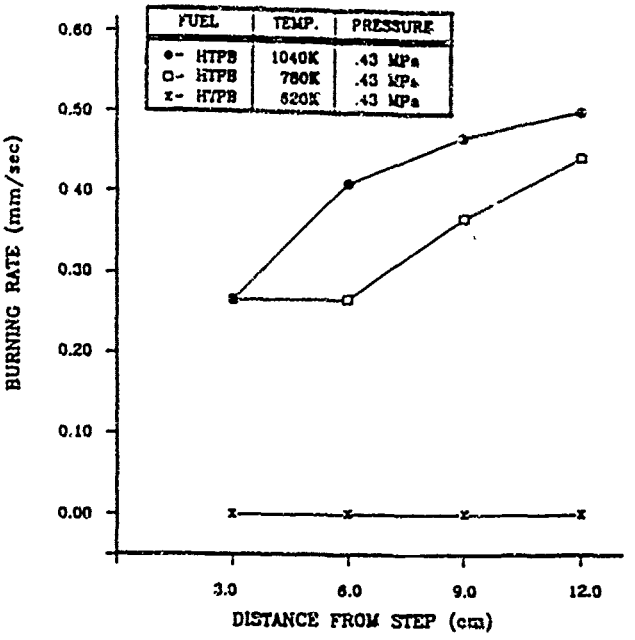


Fig. 9 Effect of freestream temperature on the regression rate of HTPB solid fuel

fuel sample with boron loading. The decrease in regression rate beyond 10 percent boron loading is attributed to several factors. When boron particles are ejected from a highly-loaded fuel sample, they absorb a significant amount of heat from the flame zone and reduce the local flame temperature, known as the "heat sink" effect[9]; thus decreasing the heat feedback to the sample surface. A large number of particles ejected with pyrolyzing gases from the sample could effectively shield the heat feedback to the surface. Accumulation of unreacted boron particles on the surface of the sample could also cover the HTPB fuel surface and reduce the pyrolysis rate. Futhermore, highly boron loaded samples contain less percentage of HTPB for pyrolysis, consequently diminishing the heat release associated with gas-phase reactions.

Figure 9 shows the influence of freestream temperature on the regression rate of an HTPB sample without boron. All tests were conducted at a constant pressure of 0.43 MPa. At 620 K, the fuel sample failed to achieve self-sustained combustion. At this temperature, the sample ignited momentarily when the pyrophoric liquid was injected above the sample; however, the sample extinguished after the igniter was turned off. Ignition and self-sustained combustion of the solid fuel was attained at temperatures of 780 and 1040 K. Under these conditions, flame spreading occured almost instantaneously over the entire fuel sample. The burning rate increased with the increase in freestream temperature due to the enhanced convective heat transfer to the fuel surface which allowed additional fuel to pyrolyze and react in the diffusion flame zone. In addition to the increased convective heat transfer, the gas-phase reaction rates are much faster at elevated temperatures.

Figure 10 shows the freestream pressure effect on the burning rate of boron/HTPB (10/90) fuel. Increasing the pressure from 0.26 to 0.44 MPa causes the burning rate to increase substantially. Two mechanisms could be attributed to the enhanced burning rate at higher pressures. First, the gas-phase kinetics are faster, thus shortening the flame standoff distance above the fuel surface and enhancing the heat feedback to the fuel surface. Second, the increase in oxidizer partial pressure promotes additional reactions with the fuel-rich species and with the condensed phase particles that are ejected from the sample surface. This results in a higher flame temperature and greater heat transfer to the fuel surface which increases the pyrolysis rate of the solid fuel.

Figure 11 shows a temperature profile for HTPB solid fuel measured from an embedded R-type thermocouple. The thermocouple bead is located 109 mm downstream of the rearward facing step and 19 mm beneath the initial sample surface. After ignition, the fuel sample begins to regress, thereby shortening the distance between the gas/solid interface and the thermocouple bead. When the fuel burns down to the location of the thermocouple bead, an interface temperature of 650 K is obtained. With further regression, the gas-phase temperature including the diffusion flame temperature were obtained. For this particular test, with HTPB burning at a freestream pressure of 0.43 MPa and

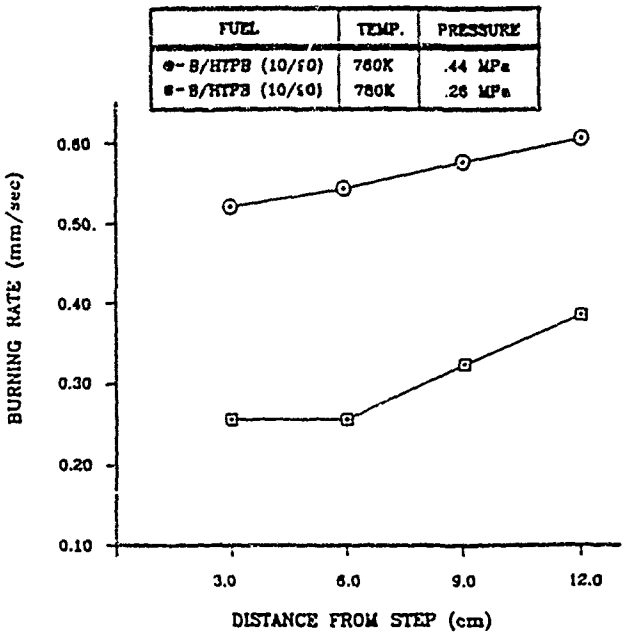


Fig. 10 Effect of pressure on the regression rate of boron/HTPB (10/90) solid fuel

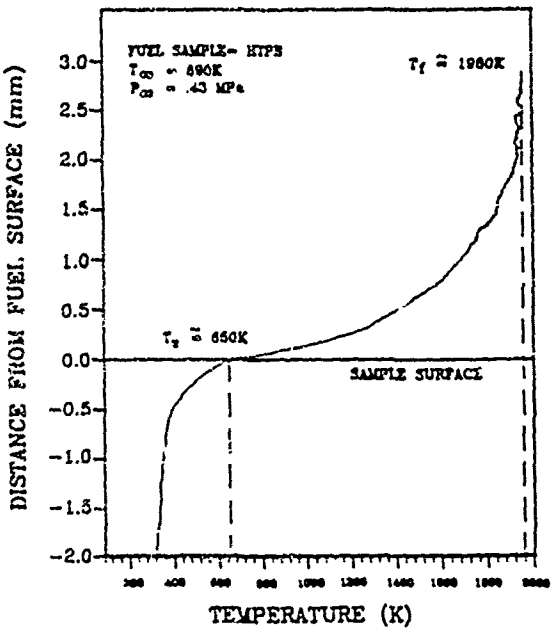


Fig. 11 Measured temperatures as a function of vertical distance from the HTPB fuel surface

temperature of 890 K, the flame temperature is approximately 1980 K with a flame standoff height of about 2.5 mm and effective thermal penetration depth of 0.5 mm.

Thermogravimetric analysis (TGA) of HTPB at a heating rate of 70 deg/min indicates that the solid fuel begins to decompose around 600 K and reaches a maximum weight loss rate at approximately 780 K[10]. The measured surface temperature of approximately 650 K, lies between these two temperatures.

IV. CONCLUSIONS

The ignition and combustion characteristics of HTPB solid fuels with various percentages of boron loadings have been studied under high-speed, high-enthalpy crossflows. All of the solid fuels tested exhibited a faster regression rate with increased distance from the rearward facing step. The increased regression rate in the downstream region is caused by enhanced heat feedback from the diffusion flame zone which supplies more heat to the sample surface as the axial distance increases.

The addition of small percentages of boron to HTPB solid fuels significantly enhances the ignition and combustion characteristics of the sample. The regression rate was found to increase with boron addition up to 10 percent. Further addition of boron causes the regression rate to decrease. The initial increase in regression rate with boron loading is believed to be caused by increased heat feedback to the surface from boron particle reactions and increased radiation absorptivity of the fuel surface. The decrease in regression rate with high boron particle loading is attributed to: 1) boron particle heat sink effect in the gas phase which reduces the flame temperature; 2) shielding of heat feedback to the surface by a large number of boron particles above the surface and; 3) reduced pyrolysis caused by the accumulation of unreacted boron on the surface and decreased gas-phase reactions due to the smaller percentage of HTPB contained in the sample.

The regression rates of the HTPB-based solid fuels were found to be a strong function of the freestream temperature and pressure. Regression rates increase with temperature because of increased convective heat transfer and faster gas-phase reaction rates. Increased regression rates with pressure are attributed to faster gas-phase kinetics and additional reactions caused by the increase in oxidizer partial pressure.

ACKNOWLEDGEMENTS

This work represents a part of the research conducted under Contract No. N00014-86-K-0468 sponsored by the Office of Naval Research, Arlington, VA, under the management of Drs. Gabriel D. Roy and Richard S. Miller. The authors would like G. Jensen of UT/CSD for providing some of the fuels used in this study. The authors

would also like to thank Bill Burdette of NWC, Prof. Vigor Yang, Prof. Tom Litzinger, Dr. Wen-Hsin Hsieh, Dave Getz, and Andrew Yang of Penn State for their assistance.

REFERENCES

1. Netzer, A. and Gany, A., "Burning and Flameholding Characteristics of a Miniature Solid Fuel Ramjet Combustor," AIAA Paper 88-3044, AIAA/SAE/ASME/ASEE 24th Joint Propulsion Conference, Boston, MA, July 1988.

2. Schulte, G., "Fuel Regression and Flame Stabilization Studies of Solid-Fuel Ramjets," Journal of Propulsion and Power, Vol. 2, No. 4, July-August, 1986, pp. 301-304.

3. Gany, A. and Netzer, D., "Combustion Studies of Metallized Fuels for Solid Fuel Ramjets," AIAA Paper 85-1177, AIAA/SAE/ASME/ASEE 21st Joint Propulsion Conference, Monterey, CA, July, 1985.

4. Jarymowycz, T., Yang, V., Kuo, K., "A Numerical Study of Solid Fuel Combustion Under Supersonic Crossflows," AIAA Paper 90-2076, AIAA/ASME/SAE/ASEE 26th Joint Propulsion Conference, Orlando, FL, July, 1990.

5. Schulte, G., Pein, R., Hogl, A., "Temperature and Concentration Measurements in a Solid Fuel Ramjet Combustion Chamber," Journal of Propulsion and Power, Vol. 3, No. 2, March, 1987, pp. 114-120.

6. Schadow, K., Gutmark, E., "Review of Passive Shear-Flow Control Research for Improved Subsonic and Supersonic Combustion," AIAA Paper 89-2786, AIAA/SAE/ASME/ASEE 25th Joint Propulsion Conference, Monterey, CA, July, 1989.

7. Snyder, T., Chen, D., Fetherolf, B., Litzinger, T., and Kuo, K., "Pyrolysis and Ignition of Boron-Based Solid Fuels for Ramjet Applications," Proceedings of the 25th JANNAF Combustion Meeting, CPIA Publication No. 498, Vol. I, October, 1988.

8. Snyder, T., Jarymowycz, T., Hsieh, W., Yang, V., and Kuo, K., "Pyrolysis and Combustion of Solid Fuels under both Subsonic and Supersonic Conditions," Proceedings of the 26th JANNAF Combustion Meeting, Pasadena, CA, October, 1989.

9. Hsieh, W.H., Peretz, A., Huang, I.T., and Kuo, K.K., "Combustion Behavior of Boron Based BAMO/NMMO Fuel Rich Solid Propellants," AIAA Paper 89-2884, AIAA/ASME/SAE/ASEE 25th Joint Propulsion Conference, Monterey, CA, July, 1989.

10. Chen, D.M., "Pyrolysis, Ignition and Combustion of Solid Fuels for Ramjet Applications," Ph.D. Thesis, The Pennsylvania State University, 1988, pp. 80-85.

CHAPTER 2
CO_2 LASER PYROLYSIS AND IGNITION

I. Introduction

The pyrolysis and ignition behavior of a solid fuel must be characterized and well understood before it can be implemented in a practical ramjet engine. However, the heterogeneous nature of solid fuels normally employed in ramjets complicates the ignition phenomena. The thermal, chemical, and physical properties of individual constituents and their interaction with each other are of particular interest. Despite the many studies conducted in the field of ignition, the understanding of the pyrolysis and ignition of solid fuels for ramjet applications remains incomplete.

In order to fully utilize the advantages of the ramjet design, a high volumetric heating value of the solid fuel is essential. Elemental boron exhibits the highest volumetric heating value at 137.5 kJ/cm^3. Solid fuels or fuel-rich solid propellants containing boron are therefore very attractive. However, the high melting point (2450 K), high boiling point (3931 K), and protective oxide layer that encases the boron particle cause serious ignition and combustion efficiency problems. In contrast, magnesium burns easily because of its relatively low melting and boiling temperatures (923 K and 1378 K, respectively) and its oxide layer is porous, thus presenting no significant resistance to oxidation of the Mg particle. The major drawback of using Mg in a ramjet fuel is its relatively low heating value (43 kJ/cm^3); however, considering the fact that it offers high combustion efficiency and low cost, it is still a desirable fuel for ramjet applications. Moreover, for a solid ducted rocket application, the mixing and burning of fluorocarbons with magnesium produces a much higher volumetric heating value than for oxidation of Mg by O_2 due to the high heat of fluorination of magnesium (60.5 kJ/cm^3).

Currently, the most popular binder used in solid fuels and conventional solid propellants is hydroxyl terminated polybutadiene (HTPB). Its many advantages include low cost, reliability, good processibility, tough mechanical properties, and long aging life. It has a heating value comparable to that of normal hydrocarbon fuels. When it is burned with boron powder, some pretreatment of the boron particles or addition of special combustion aids is required in order to attain good combustion efficiency. Recently, novel highly energetic polymeric binders based on azido and nitrate ester functionalized oxetanes have been synthesized, e.g., 3,3-bis(azido methyl) oxetane (BAMO) and 3-nitratomethyl oxetane (NMMO). These energetic materials provide good combustion efficiency and are promising solid fuels, but possess certain properties that may limit

their ramjet applications, as described in Chapter 1. Nevertheless the high energy potential of azido and nitrate groups can generate extremely high heats of combustion, and the evolved highly dynamic gases enhance the burning of the boron particles.

The laser is a desirable energy source for fundamental studies of the ignition behavior of pyrotechnics, solid fuels, and solid propellants. It offers the advantages of precise control of heating time, energy flux, and spot size on the material surface. Ignition behavior can be directly related to material properties and sample composition under such precise test conditions. A high-power CO_2 laser also allows for continuous wave heating at high levels of energy flux similar to energy levels found in larger igniter systems and in propulsive devices.

The overall objective of this research was to investigate the pyrolysis and ignition behavior of several solid fuels for use in ramjet applications. Specific objectives were: (1) to measure ignition delay times as a function of heat flux, solid fuel composition, and testing environment; (2) to investigate the luminous plume evolution and gas-phase dynamics with high-speed video photography and schlieren flow visualization; (3) to measure temperature profiles in both the gas phase and condensed phase; and, (4) to analyze gaseous product species.

II. Experimental Approach

A schematic diagram of the overall experimental setup is given in Fig. 2.1. The energy source is a CO_2 laser capable of 800 W of continuous wave power. A nearly uniform beam profile is obtained by using a mask with a 7 mm aperture to select the most uniform portion of the beam to irradiate the sample surface. A masked calorimeter was employed to measure the actual heat flux at the sample location. The solid fuel samples were tested within an aluminum test chamber that was ≈25 cm on a side. The chamber had two schlieren windows installed in opposite sides and a potassium chloride window in the top of the chamber for laser beam entrance. The pressure and gaseous composition of the initial chamber environment were controlled using a vacuum pump, a pressure/vacuum gauge, and an inert gas supply system. For gaseous species analysis, a smaller Plexiglass test chamber 10 cm long and 5 cm in diameter containing a septum port for syringe sampling was used. A schlieren flow visualization system was employed to investigate the gas phase dynamics (see Fig. 2.1). Both direct images of the flame structure and the schlieren images were recorded with a Spin Physics 2000 video recording system capable of 12,000 pictures per second. The controller permits simultaneous display of both direct and schlieren images, allowing direct comparison of the flame structure dynamics and gaseous evolution. High-resolution spatial measurements can be made with the

on-screen reticle system. A near-infrared photodiode that senses emission in the range 0.35-1.15 μm with peak sensitivity at 0.9 μm was used to measure visible and near-IR emission from which ignition delay times were obtained. The photodiode was mounted at a radial distance of 7 cm from the sample and about 2.5 cm from the laser beam centerline and aimed directly at the sample surface.

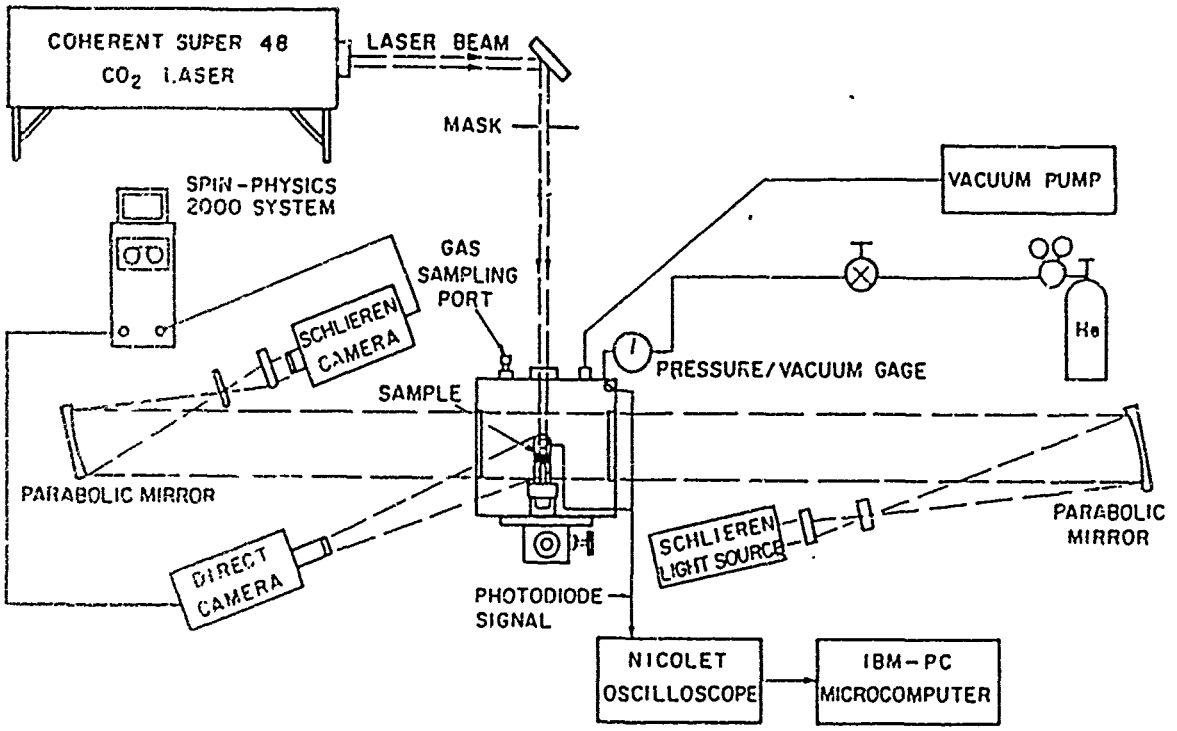


Figure 2.1. Experimental setup for laser-induced pyrolysis and ignition research

Temperature measurements were made with 25 μm and 50 μm diameter R-type thermocouples constructed of platinum and platinum/13% rhodium wires. For some of the solid fuels, condensed-phase temperature profiles were obtained by embedding the thermocouples in the fuel sample. The thermal diffusivity of several fuel samples was measured using the laser flash method.

Gaseous species analysis was achieved by using a one milliliter syringe to take gas samples from the small test chamber and inject them into either a Varian 3700 gas chromatograph or a Hewlett Packard gas chromatograph/mass spectrometer (CG/MS). The GC columns employed included a Porapak Q&R column for general species analysis and a Carbopack B/5% Flourcol column for analysis of fluorinated compounds.

Data acquired using the photodiode and the fine-wire thermocouples were recorded with a Nicolet digital oscilloscope with the thermocouple signals being amplified before transfer to the oscilloscope. The data was then transferred to a computer for processing and then to a printer for plotting.

Numerous solid fuels were tested and their compositions are listed in Table 2.1. The B-HTPB and BMT solid fuels were processed at the High Pressure Combustion Laboratory at Penn State University. The method of fabrication of the BMT samples was addressed by Fetherolf et al. (Appendix 2.1). B-HTPB fuels with a 50/50 composition were processed by Chemical System Division, United Technologies. The MTV, NWC-1, NWC-2, NWC-3, MO96, and M096T solid fuels were supplied by the Naval Weapons Center. The B-BN fuels were provided by Aerojet Propulsion Company.

Table 2.1. Compositions of Solid Fuels

Solid Fuel	Metal	Primary Binder	Various Additives
B/HTPB	Boron	HTPB	Mg, Mg/Al, CeF_3
B/BN	Boron	BAMO/NMMO	-----
MTV	Magnesium	PTFE	Viton A
BMT	Mg, Boron	PTFE	-----
NWC-1	-----	HTPB	Carbon Black
NWC-2	-----	HTPB, PCUD	PCUD
NWC-3	-----	HTPB, Zecorez	Zecorez
MO96	Magnesium	HTPB	B_4C, Comb. Aid A
MO96T	Magnesium	HTPB, PTFE	B_4C, Comb. Aid B

The ignition criterion used for measuring ignition delay times was first light emission as observed with the photodiode. It is important to note that this criterion does not always indicate the onset of ignition leading to self-sustained combustion. The MTV materials and the B/Mg/PTFE materials with above 10% boron content were the only samples tested that consistently exhibited self-sustained ignition.

III. Results and Discussion

A. B/HTPB Solid Fuels

The ignition delay behavior of several boron/HTPB fuels containing weight percentages of 1, 10, 20, 30, and 50% boron have been investigated. The effects of adding 10% Mg, Mg/Al, or CeF_3 in a 30/60/10 mixture of a B/HTPB/Additive composition were also studied. Details of this study were reported by Snyder et al. (Appendix 2.2). Gaseous species generated by pyrolyzing a pure HTPB binder were analyzed with a GC/MS in order to determine the major decomposition product species.

Figure 2.2 exhibits the ignition delay behavior of the B/HTPB solid fuels as a function of boron weight percentage and incident heat flux. For all tests, ignition was observed to take place in the gas-phase region. Following gas-phase ignition, the combustion wave propagated back down to the sample surface and enhanced the surface reactions. The delay time for first light emission was observed to decrease as boron content increased up to 20%, after which the delay time increased up to 50% boron content.

Figure 2.3 displays the effects of additives on the ignition delay behavior of boron/HTPB solid fuels. Magnesium and magnesium/aluminum powders showed a noticeable decrease in delay time. The addition of cerium fluoride to the solid fuel produced the most significant decrease in delay time, especially at low heat fluxes.

The gaseous products from pyrolysis of pure HTPB were analyzed with a GC/MS and Porapak Q and R columns in series. The major decomposition species were the monomer 1,3-butadiene along with aromatic compounds including benzene, toluene, styrene, naphthalene, and phenanthrene. These aromatic compounds are believed to play an important role in soot formation. The post-test observation revealed the formation of a black residue, which appeared in the shape of small agglomerated chains.

B. Boron-BAMO/NMMO Solid Fuels

Boron-based poly(BAMO/NMMO) fuel samples were also tested in the CO_2 laser laboratory with boron weight percentages of 0, 17.6, 29, and 39.8%. Details of this work can be found in Appendix 2.2. Figure 2.4 shows the ignition delay behavior as a function of heat flux and boron content. The data from pure BAMO/NMMO ignition tests exhibited random delay times for all heat fluxes. This random behavior is believed to be caused by the highly turbulent nature of the pyrolyzed gases evolved; the active site for first light emission varied significantly

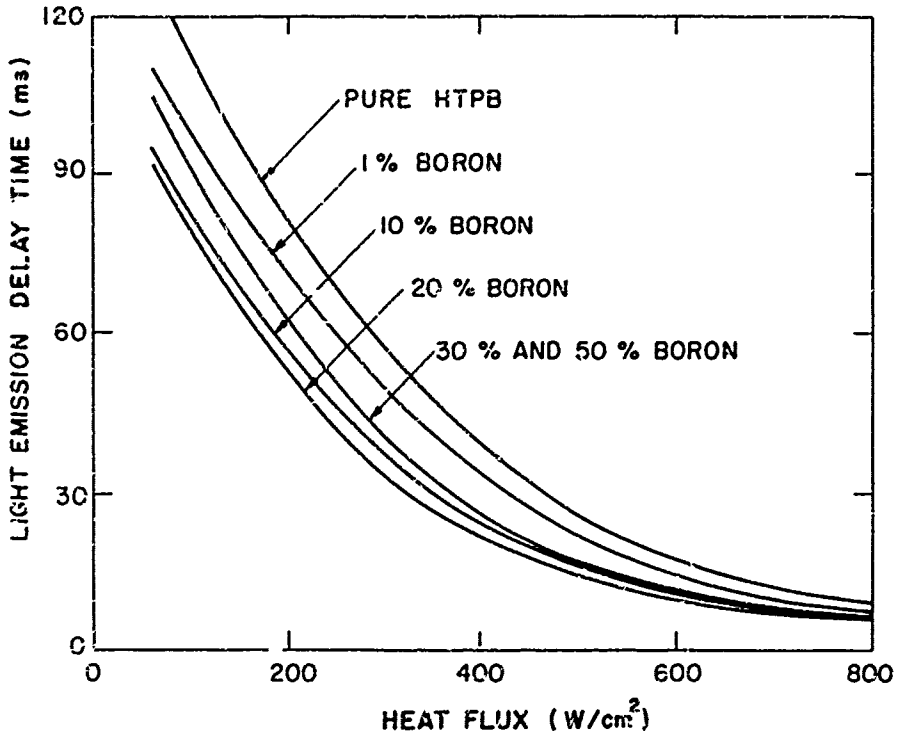


Figure 2.2 Ignition delay behavior of B/HTPB solid fuel in air at one atmosphere

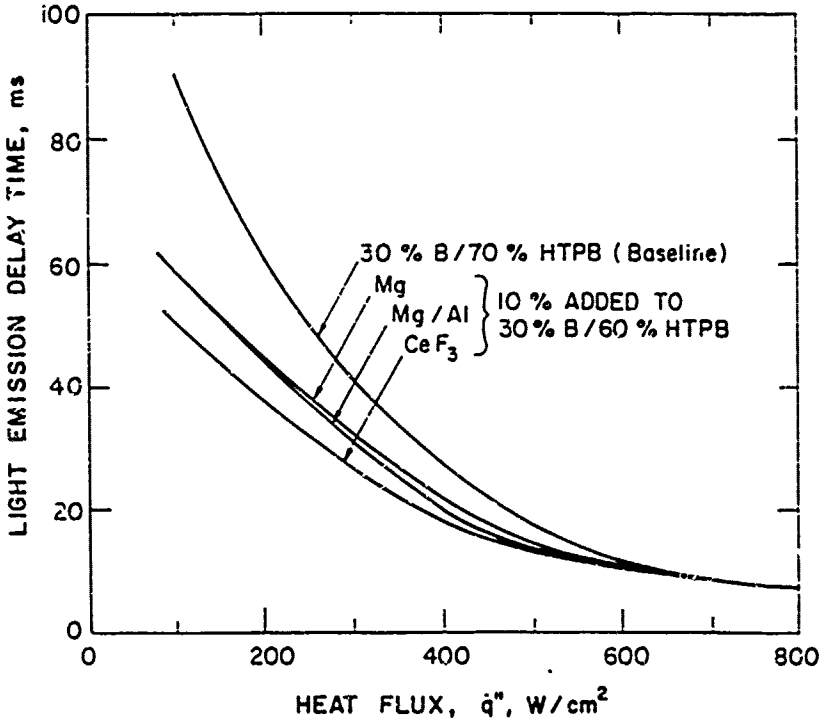


Figure 2.3 Effects of additives on ignition delay behavior of B/HTPB solid fuel

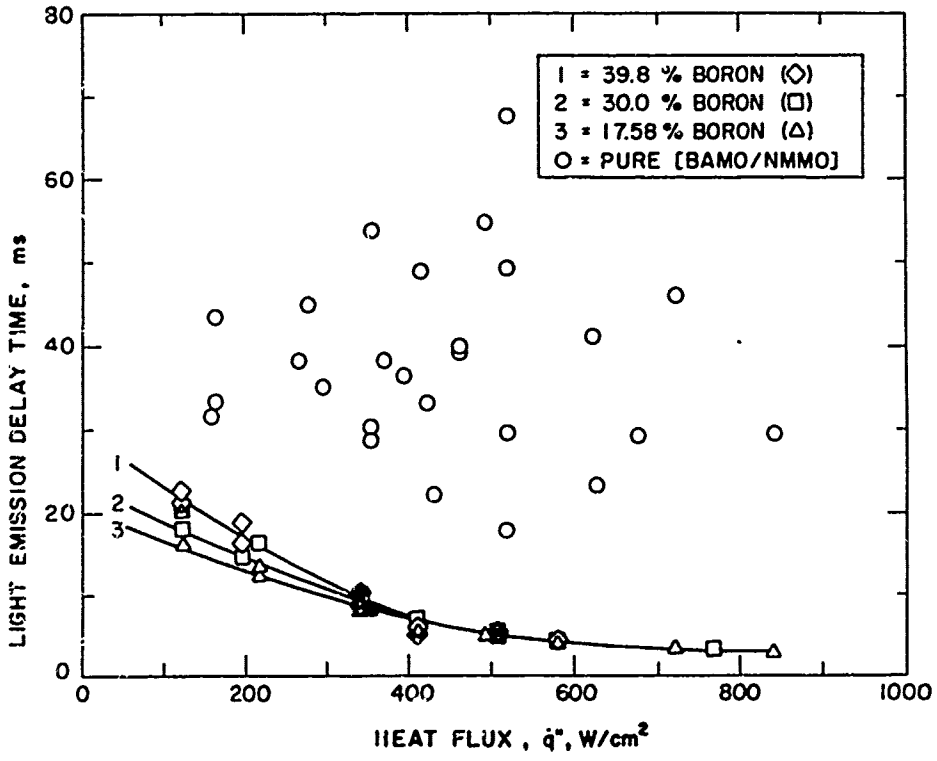


Figure 2.4 Ignition delay behavior of B/BN solid fuels in air at one atmosphere

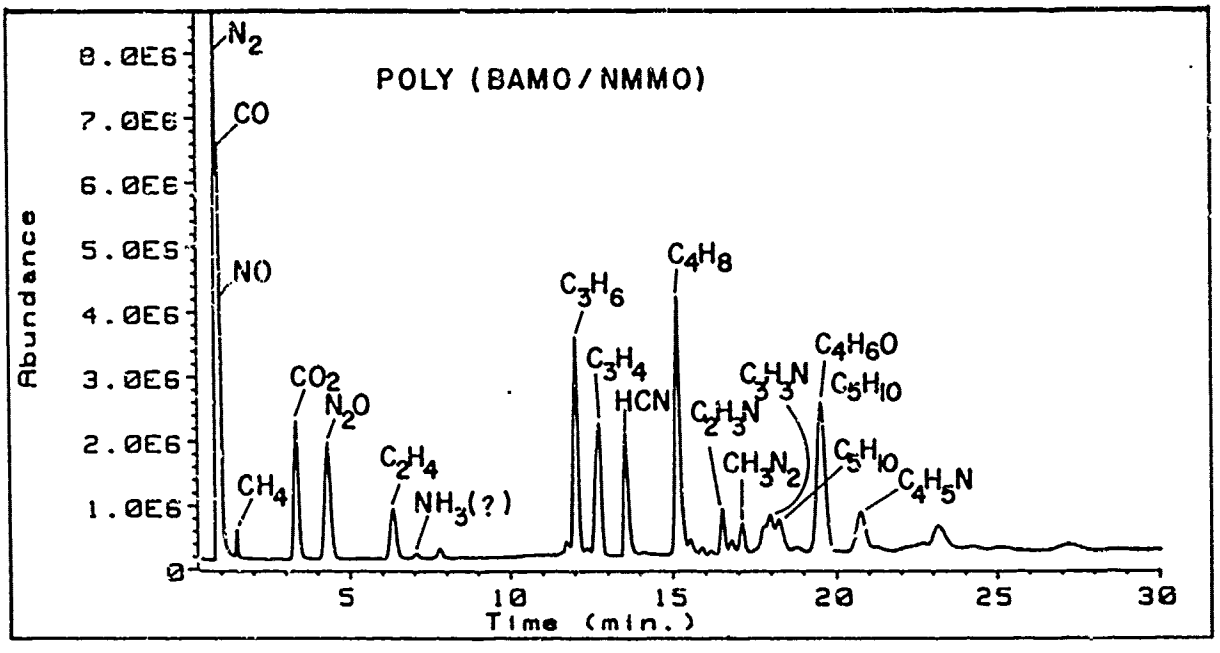


Figure 2.5 Gaseous species evolved during pyrolysis of pure BAMO/NMMO in helium at one atmosphere

from test to test. When boron particles were added to the solid fuels, this random behavior was eliminated. The delay time for first light emission decreased as incident heat flux increased for all compositions. As the boron loading percentages increased from 17.6% to 39.8%, the delay time increased slightly at low energy fluxes (below 300 W/cm^2).

Figure 2.5 is a total ion chromatogram from GC/MS analysis of the gaseous products of pure BAMO/NMMO copolymer pyrolysis in helium at one atmosphere. The most abundant species identified were N_2, CO, NO, CO_2, N_2O, C_3H_6, C_3H_4, HCN, C_4H_8, and C_4H_6O. Most of the species found in this study have been reported in the literature; however, formaldehyde, which has been reported in other studies in large amounts, was not observed. This may be attributed to the high reactivity and/or the susceptibility to degradation of formaldehyde. A sample of 30/70 B/BN was also burned under the same test conditions, and GC/MS analysis of the gaseous products indicated similar major species were produced but in significantly smaller amounts. It is believed that the boron ignites and burns vigorously with the pyrolyzed species to form some condensed phase boron compounds which cannot be properly identified by the existing analysis system.

C. Boron/Mg/PTFE Solid Fuels

The combustion characteristics and CO_2 laser ignition behavior of boron/magnesium/PTFE (BMT) solid fuels were studied be Fetherolf et al. (Appendix 2.1) as a function of weight percentages of boron and Mg. All tests were conducted in air at one atmosphere. Density measurements indicated that as the boron loading was increased the deviation between the actual density and the theoretical maximum density (TMD) increased. Figure 2.6 indicates that the ignition delay time decreased monotonically as either the heat flux or the boron content was increased. Figure 2.7 shows that only samples with a boron loading $\geq$10% achieved self-sustained combustion after removal of laser heating, and as the boron loading was increased above 10%, the burning rate decreased monotonically. The thermal diffusivity, measured by the laser flash method, decreased sharply as the boron percentage increased up to 10% and then decreased only slightly as more boron was substituted for Mg.

Several physicochemical processes were proposed to explain the ignition and combustion behavior of the B/Mg/PTFE solid fuels. The decrease in ignition delay with an increase in boron content was attributed to the absorptivity at 10.6 μm wavelength of boron being significantly higher than that of magnesium and also to the decrease in the thermal diffusivity of the solid fuel with increasing boron content, which causes the incident energy to be more concentrated at the

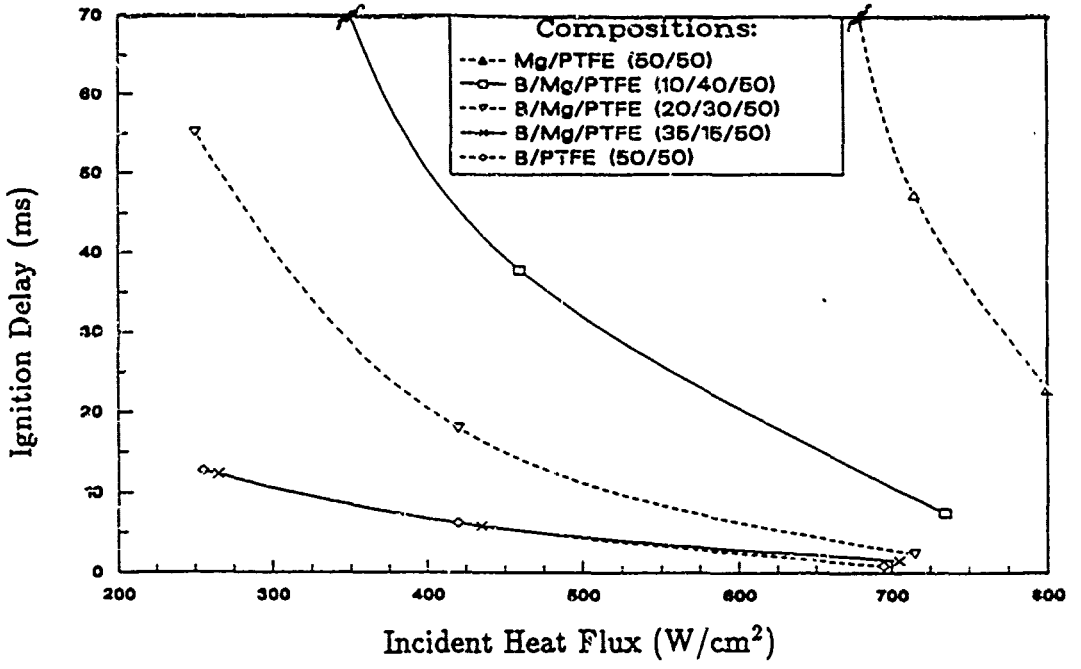


Figure 2.6 Ignition delay behavior for BMT material in air at one atmosphere

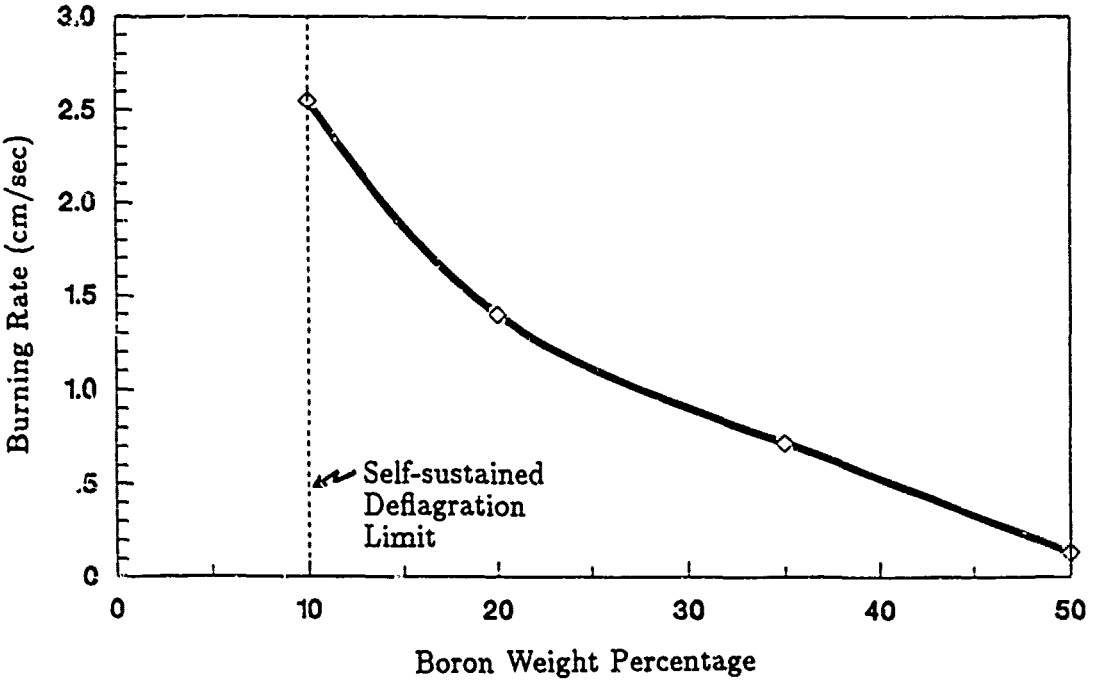


Figure 2.7 Burning rate behavior for BMT material (combustion in air at one atmosphere)

surface, thus producing a faster rise to the ignition temperature threshold. It is believed that the above 10% boron loading decrease in burning rate is due to reduction in the near-surface flame intensity (this flame is believed to be produced by the fluorination of Mg) and also due to the boron particles evolved that are below their ignition temperature acting as "heat sinks" and reducing the available energy at the fuel surface.

D. Mg/PTFE/Viton A Solid Fuels

In studies of the Mg/PTFE/Viton A (MTV) solid fuels, the effects of heat flux, pressure, and oxygen concentration have been investigated. The gaseous products of pyrolysis and combustion for each constituent and for the MTV composite were also investigated with GC/MS analysis. Details of this study can be found in Appendices 2.3 and 2.4. Figure 2.8 illustrates the effect of heat flux on the ignition delay time for heating in air at 1 and 0.1 atmospheres. Interestingly, at the lower pressure, the ignition times are shorter; this may be attributed to lower pressure or to lower oxygen concentration. The oxygen effect was investigated by performing tests at atmospheric pressure using N_2/O_2 mixtures with varying oxygen concentrations. It was observed that the ignition delay times decreased as the oxygen percentage decreased, indicating that ambient oxygen has an inhibiting effect on the ignition process. This effect is believed to be the mechanism responsible for the pressure dependency in Fig. 2.8.

The gaseous decomposition species generated by PTFE pyrolysis in inert nitrogen were analyzed with the GC/MS and a Carbopack B/5% Fluorcol column. The analysis showed a wide range of saturated and unsaturated fluorocarbon compounds; the major common compounds detected were the monomers C_2F_4, C_2F_6, C_3F_6, and C_4F_8. Analysis of the decomposition species generated by Viton A showed that a wide variety of fluorocarbons similar to those produced by PTFE were generated as were numerous hydrofluorocarbons. However, GC/MS analysis of the gaseous products of combustion of the MTV material showed evidence only of several hydrocarbons and CO and CO_2 for combustion in air, with no fluorocarbons detected. It was concluded that the primary species of PTFE and Viton A pyrolysis are consumed by combustion of the MTV material, forming undetected HF and solid MgF_2 and carbon. These condensed-phase products, along with MgO for combustion in air, were identified by an analysis using a scanning electron microscope.

Tests were also conducted to determine the amount of laser beam attenuation by the two-phase plume above a deflagrating MTV sample. The beam attenuation measuring instrument developed for these tests and the experimental results obtained are discussed by Fetherolf et

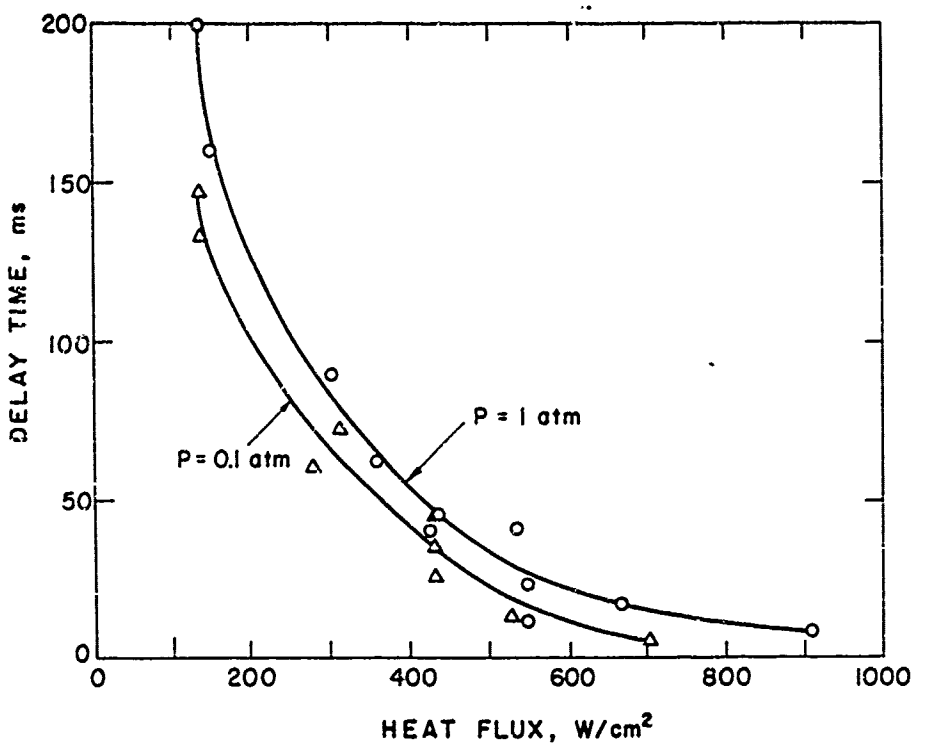


Figure 2.8 Effect of pressure and heat flux on ignition of MTV in air at one atmosphere

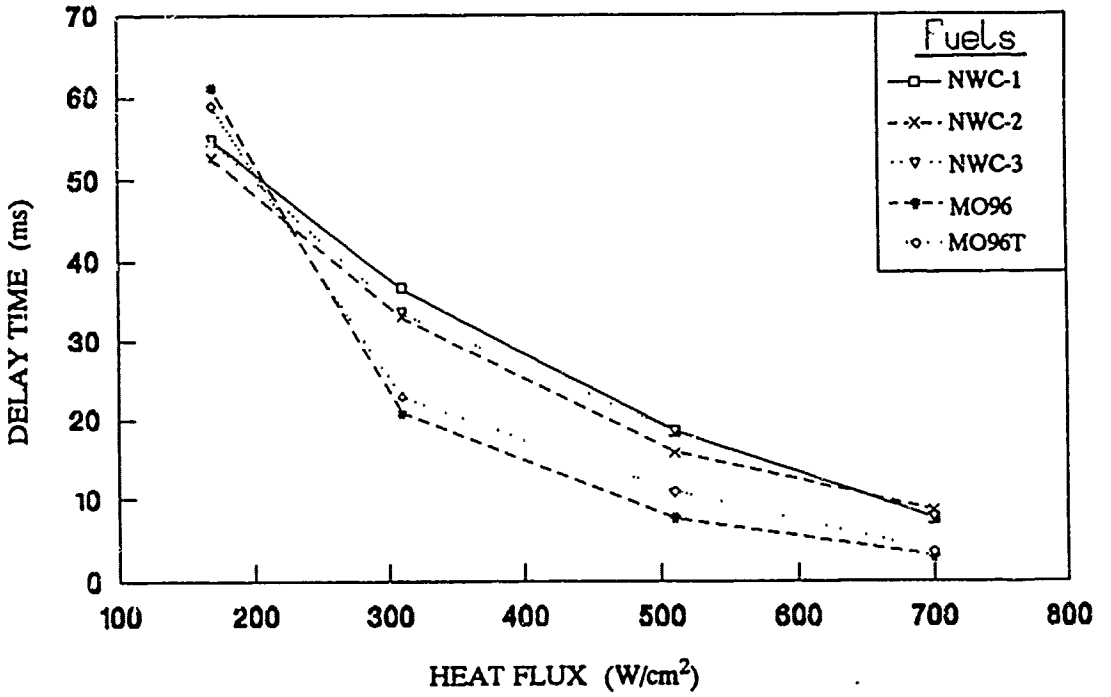


Figure 2.9 Ignition delay behavior of HTPB-based fuels in air at one atmosphere

al. (Appendix 2.5). The results showed that upon ignition of the MTV sample, the amount of heat flux passing through the two-phase plume and heating the sample surface rapidly decreased to zero with the laser beam being totally attenuated under steady-state combustion.

E. HTPB-based Solid Fuels

Ignition delay results were also obtained for five HTPB-based solid fuels received from NWC. Figure 2.9 indicates that the delay times decreased monotonically for all five fuels as the heat flux was increased. However, it was observed that at heat fluxes above 300 W/cm^2, the two fuels containing boron carbide, magnesium, and combustion aids had ignition delay times approximately 50% shorter than the other three fuels containing carbon black, PCUD, and Zecorez, which all exhibited very similar ignition delay curves.

IV. Conclusions

1. The delay time to first light emission decreases monotonically as the incident radiative heat flux increases for all solid fuels tested in this research.
2. Metal/binder compositions containing boron possess an optimum boron content value for minimizing the ignition delay time and maximizing the burning rate. This is due to the boron particles acting as "heat sinks"; that is, they do not attain their high ignition temperature, and the energy available for reaction of the other material constituents is reduced.
3. The addition of certain additives (such as Mg, Mg/Al, and CeF_3) to B/HTPB mixtures significantly shortens the ignition delay time.
4. The onset of ignition occurs in the gas phase for all solid fuels tested.
5. MTV materials ignite quicker at lower pressures due to the reduction of the effect of oxygen inhibition on the ignition process.
6. Mg reacts with the decomposition products of PTFE and Viton A in the MTV material to energetically form MgF_2.
7. The addition of B_4C, Mg, and combustion aids to HTPB-based solid fuels substantially lowered the ignition delay times at heat fluxes above 300 W/cm^2.

V. References

2.1. B. L. Fetherolf, T. S. Snyder, M. D. Bates, A. Peretz, and K. K. Kuo, "Combustion Characteristics and CO_2 Laser Ignition Behavior of Boron/Magnesium/PTFE Pyrotechnics," *Proceedings of the Fourteenth International Pyrotechnics Seminar*, RARDE and the British Pyrotechnic Industry, United Kingdom, p. 691, 1989.

2.2. T. S. Snyder, D. M. Chen, B. L. Fetherolf, T. A. Litzinger, and K. K. Kuo, "Pyrolysis and Ignition of Boron-based Solid Fuels for Ramjet Applications," *25th JANNAF Combustion Meeting*, Huntsville, AL, Oct. 24-28, 1988.

2.3. D. M. Chen, W. H. Hsieh, T. S. Snyder, V. Yang, T. A. Litzinger, and K. K. Kuo, "Combustion Behavior and Thermophysical Properties of Metal-Based Solid Fuels," AIAA-88-3041, *AIAA/ASME/SAE/ASEE 24th Joint Propulsion Conference*, Boston, Mass., July 11-13, 1988, also *Journal of Propulsion and Power*, Vol. 7, No. 2, March-April, 1991.

2.4. B. L. Fetherolf, D. M. Chen, T. S. Snyder, T. A. Litzinger, and K. K. Kuo, "Ignition and Combustion Behavior of MTV Igniter Materials for Base Bleed Applications," *The First International Symposium on Special Topics in Chemical Propulsion: Base Bleed*, Athens, Greece, November 24-26, 1988.

2.5. B. L. Fetherolf, T. A. Litzinger, K. K. Kuo, "An Instrument for Measuring High-power Laser Beam Profiles and Beam Attenuation," *The Review of Scientific Instruments*, Vol. 61, No. 1, January, 1990.

Proceedings of the Fourteenth
International Pyrotechnics Seminar,
U.K. 1989, pp. 691-711.

COMBUSTION CHARACTERISTICS AND CO_2 LASER IGNITION BEHAVIOR OF BORON/MAGNESIUM/PTFE PYROTECHNICS

B L FETHEROLF, T S SNYDER, M D BATES, A PERETZ, K K KUO
DEPARTMENT OF MECHANICAL ENGINEERING
THE PENNSYLVANIA STATE UNIVERSITY
UNIVERSITY PARK, PA, USA

ABSTRACT

The combustion characteristics and CO_2 laser ignition behavior of pressed pellets of boron/magnesium/Polytetrafluoroethylene (B/Mg/PTFE) pyrotechnic materials of varying compositions have been investigated. All tests were conducted in air at one atmosphere. Objectives of this study were to determine ignition delay times as functions of incident energy flux and sample ingredients and to measure the burning rates of samples with different compositions. Thermal diffusivities of the pyrotechnic materials were deduced using a laser flash method. While fabricating the pellets, it was observed that as the boron loading was increased, the deviation between the actual density and the theoretical maximum density (TMD) also increased. Experimental results indicated that the ignition delay time decreased monotonically as both the heat flux and the percentage of boron increased. Only samples with a boron loading $\geq$ 10% achieved self-sustained combustion, and as the boron loading was increased above 10%, the burning rate decreased monotonically. The thermal diffusivity of the materials decreased sharply as the boron percentage increased up to 10% and then only decreased slightly as more boron was substituted for Mg. Near-IR emission was found to be significantly higher for combustion of samples containing 10% and 20% boron. As the percentage of boron was increased, high frequency fluctuations observed the near-IR emission for low boron loadings decreased. Very stable combustion was observed with the 35/15/50 B/Mg/PTFE pyrotechnic material.

INTRODUCTION

Magnesium/Polytetrafluoroethylene (Mg/PTFE) and Mg/PTFE/Viton A (MTV) pyrotechnic materials have been studied in recent years for use in many applications such as rocket motor igniters [1, 2], base bleed igniters [3], and flares [4, 5]. Valenta [2] states that, "In many newer applications, MTV is replacing such traditional pyrotechnic ignition compositions as black powder, boron-potassium nitrate (B-KNO_3), and Alclo (Al-$KClO_4$) as the material of choice for many pyrotechnic and pyrogen igniters." Peretz [1] listed the following advantages of Mg/PTFE pyrotechnics for use as igniter materials: high energy content, high degree of safety in preparation, low temperature and pressure dependence of the burning rate, ease and low cost of igniter pellet and grain fabrication, favorable aging characteristics, and stable burning at low pressures. Fetherolf et al. [3] have studied the ignition behavior of MTV igniter materials for base bleed applications. They observed a thin primary flame zone attached to the burning surface of the sample in both air and inert gas environments at one atmosphere. Kubota and Serizawa [6, 7] have conducted experimental studies of the combustion of Mg/PTFE materials. They found that

the burning rate increased monotonically as the weight fraction of Mg particles increased due to the increase in heat feedback from the reaction zone to the propellant burning surface. Ladouceur [4, 5] has studied the feasibility of using an MTV material for flares in military applications. Taylor and Farnell [8] investigated a solventless process for manufacturing MTV pyrotechnic flares. Instead of being dissolved in acetone, the rubbery-like Viton A was rotor-ground by a special technique and mixed with Teflon (PTFE) powder to prevent the agglomeration of the ground powder. They claimed that the dry powder mixes flowed well under high consolidation pressures to form strong pellets and flares.

Boron is a very attractive ingredient for use in pyrotechnics and solid fuels due to its high volumetric energy density. It has long been used as a fuel in pyrotechnic delay train mixtures [9]. Numerous oxidizers have been used in conjunction with boron such as KNO_3, $NaNO_3$, Bi_2O_3, and $CaCrO_4$ to name just a few. However, when used in practical applications, boron-based solid fuels often exhibit serious combustion inefficiencies and are difficult to ignite.

Many researchers have conducted fundamental studies of the rather complex and problematic ignition and c mbustion of boron. Macek [10] and Talley [11] conducted some of the early research on the combustion of elemental boron. King has done extensive work on the ignition and combustion of boron particles and clouds [12] and has also published a review paper [13]. In 1984, Faeth [14] prepared a very comprehensive review of the status of boron combustion research. Hsieh et al. [15] have conducted an experimental investigation of boron-based BAMO/NMMO fuel rich solid propellants. They proposed an 'energy sink' hypothesis to explain the observed trend of an increase in burning rate up to a boron percentage of 20% after which the burning rate decreased. This hypothesis suggests that above a certain level of boron particle loading in the propellant, the particles may absorb a large amount of energy from the reaction zone and thereby reduce the energy feedback to the sample surface. Kuwahara and Kubota [16] investigated the role of boron in enhancing the burning rate of AP composite propellants. They found a significant increase in burning rate by the addition of small amounts of boron with an apparent limit in augmentation at 7.5% boron content. They found an increase in the temperature gradient above the burning surface with the addition of boron and concluded that the boron particles are oxidized by the decomposition gases of the AP particles, increasing the heat transfer back to the surface, with a resultant increase in burning rate.

Currently, there is very limited information available on ignition or combustion studies of the combination of boron with magnesium or with a Mg/PTFE formulation. Peretz [17] has presented some theoretical considerations of metal-fluorocarbon compositions for ramjet fuels. In that paper, he referenced work done by Zvulony, Levy, and Gany [18] where a 40/30/30 composition of a B/Mg/PTFE solid fuel was studied in a solid fuel ramjet combustor. Peretz stated that the fuel was consolidated into perforated cylindrical pellets with a fuel density 93% of the TMD and that they obtained stable combustion with certain configurations of the combustor. Tischer [19] has studied the effect of entrained air in determining optimum flare compositions. He found that as the amount of boron in a B/Mg/$NaNO_3$/Laminac flare composition was increased, the adiabatic equilibrium temperature decreased monotonically. He also concluded that the addition of small amounts of boron may influence the color of the flare plume without degrading performance. Shidlovskii and Gorbunov [20] have studied the combustion of PTFE with magnesium or boron at pressures of 10-100 atmospheres in a constant-pressure bomb containing nitro-

gen. They observed a very narrow, bright combustion zone for the burning of a Mg/PTFE material and found that B/PTFE mixtures exhibited a broad, weakly emitting flame zone without a bright combustion front. They used these observations to explain the burning rate behavior of these materials by stating that the broad flame zone of the B/PTFE composition transfers less heat back to the surface than the narrow combustion zone of the Mg/PTFE material, thus producing a lower combustion rate for the B/PTFE.

Snyder et al. [21] have investigated the effects of additives on the ignition delay behavior of boron-based solid fuels. They found that the addition of 10% Mg, Mg/Al, or CeF_3 particles to a B/HTPB formulation significantly lowered the ignition delay at lower heat fluxes but had no noticeable effect at heat fluxes above 600 W/cm^2. Previous work by the authors [3] on base bleed igniter materials indicated that the addition of boron to a Mg/PTFE formulation in moderate amounts significantly enhanced ignition and combustion behavior. They stated that further research was needed to quantify the combustion enhancement due to boron addition, particularly the burning rate as a function of boron content.

Thermal diffusivity (α) is an important parameter to be considered in studies of the ignition and combustion of pyrotechnic materials. Hermance et al. [22] developed an elaborate model to determine the thermal properties in a highly compressed pyrotechnic mixture consisting of a metal, salt, filler, and voids having close to 100% TMD. Pierce and Leith [23] also presented a simple model of thermal properties in a hot-wire initiated pyrotechnic device based on the heat diffusion equation with temperature dependent properties. They discussed the trends of the thermal conductivity and heat capacity of a composite material as a function of the packing density. Parker et al. [24] proposed a method for determining thermal diffusivities of materials termed the laser flash method or flash diffusivity method. This method was employed by Etter et al. [25] to study a material composed of $TiH_{0.65}$ and $KClO_4$. They noted that varying the blend ratio affected the thermal diffusivity nonlinearly, favoring the influence of the $KClO_4$ which had the lower α value, $\approx 1/3$ that of $TiH_{0.65}$. Etter et al. also concluded that this method is well suited for testing fragile pressed pellets and also requires only very small samples, which is desirable when working with energetic pyrotechnic materials. Snyder et al. [26] also used this method to study the thermophysical properties of metal-based solid fuels. They determined the thermal diffusivity of an MTV material to be 1.6×10^{-2} cm^2/sec.

The use of a laser for ignition studies of solid fuels, solid propellants, and pyrotechnics provides the researcher with precise control of the heating time and energy flux. Ostrowski [27] gave a comprehensive introduction in his paper on laser ignition of black powder in which he references numerous studies where lasers were used as the energy source in initiation studies of solid materials. The high-power CO_2 laser offers the advantages of continuous wave heating and a high level of beam intensity that simulates energy fluxes found in igniter systems and propulsive devices. The CO_2 laser has been employed by numerous researchers in radiative ignition studies of solid fuels, solid propellants, and pyrotechnic materials.

The literature review presented in this introduction shows that extensive research has been done on energetic materials containing magnesium, PTFE, and boron, but that few studies have been conducted on compositions containing all three of these ingredients. The overall objective of this research was to investigate the combustion characteristics and CO_2 laser ignition behavior of boron/magnesium/PTFE pyrotechnic materials as a function of the boron

loading. Specific parameters of interest included ignition delay time, burning rate, thermal diffusivity, steady-state and dynamic flame structure, two-phase plume evolution, and near infrared emission of the reaction zone.

EXPERIMENTAL SETUP

A schematic diagram of the experimental setup is given in Figure 1. The radiative energy source was a high power CO_2 laser capable of producing 800 watts of power in the continuous wave mode and 3500 watts in the pulsed mode with precise control of the lasing time and the power level. A beam profile with a relative uniformity of ±15% across the pyrotechnic surface was obtained using a mask with a 7 mm aperture placed ≈ 1 meter above the sample to allow only the most uniform center section of the beam to irradiate the surface. A masked calorimeter was employed to measure the actual heat flux at the sample location. The samples were tested within an aluminum test chamber that was ≈25 cm on each side. The laser beam entered the test chamber through a potassium chloride window, which is ≈97% transmissive to the 10.6 μm wavelength of the laser. Two high-quality glass windows were installed in opposite sides of the chamber for schlieren flow visualization, and another window in a third side provided optical access for direct photography of the flame structure dynamics. The pressure and gaseous composition of the environment within the chamber can be controlled using a vacuum pump, an oxygen analyzer, a pressure/vacuum gauge, inert gas feed lines, and control valves. However, all the tests conducted for this paper were run with initial conditions of one atmosphere of pressure in static air.

A schlieren flow visualization system was employed to investigate the two-phase plume dynamics. A parallel light beam was directed by 15 cm parabolic mirrors from a 100 watt continuous tungsten-halogen lamp through the test chamber to a high-speed camera. The light beam is shaped and directed by a rectangular aperture and a condensing lense at each end of the 'Z-type' configuration. Both direct images of the flame structure and the schlieren images were recorded with a Spin Physics 2000 video recording system. As seen in Figure 1, the system consists of a controller, video monitor, and two camera heads. The controller can display both the schlieren and direct image simultaneously, allowing direct comparison of the flame structure dynamics and the plume dynamics. Maximum recording speed is 12000 pps, but speeds of 500, 1000, and 2000 pps were employed to investigate the ignition and combustion phenomena. The Spin Physics controller also has an on-screen reticle measuring system that permits the user to make precise spatial measurements in both X and Y directions. This feature was used in conjunction with the schlieren image to measure burning rates. A SONY CCD V-9 Camcorder was also employed to obtain color images of the flame structure.

A near-infrared photodiode was employed to measure ignition delay times and also to monitor near-infrared emission. The spectral response of the photodiode is exhibited in Figure 2. The photodiode was mounted at a radial distance of 7 cm from the sample and aimed directly at the surface. The output signal was recorded with a Nicolet digital oscilloscope and then transferred to an IBM computer for processing and printing on a Hewlett Packard laserprinter.

A thermal diffusivity measuring apparatus was also fabricated. This apparatus, based on the laser flash method [24], consisted quite simply of a 75 μm Chromel-Alumel thermocouple mounted flat on a small plastic sheet with two

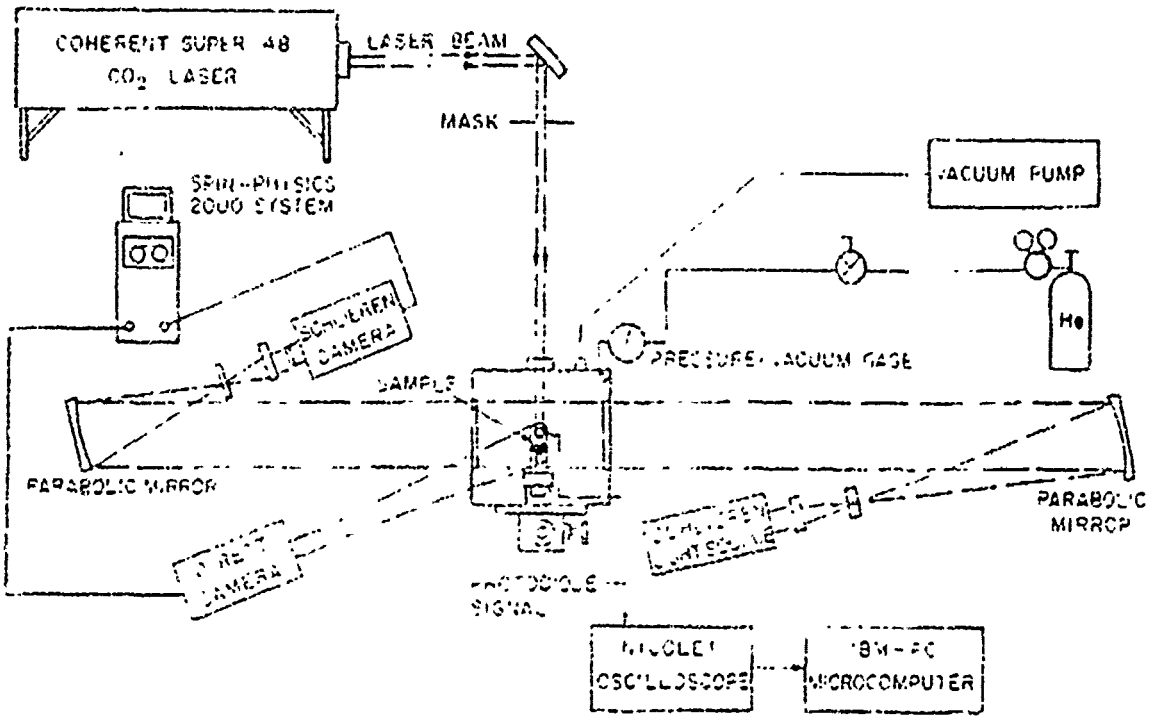


Figure 1 Experimental setup for [illegible] ignition and [illegible] studies

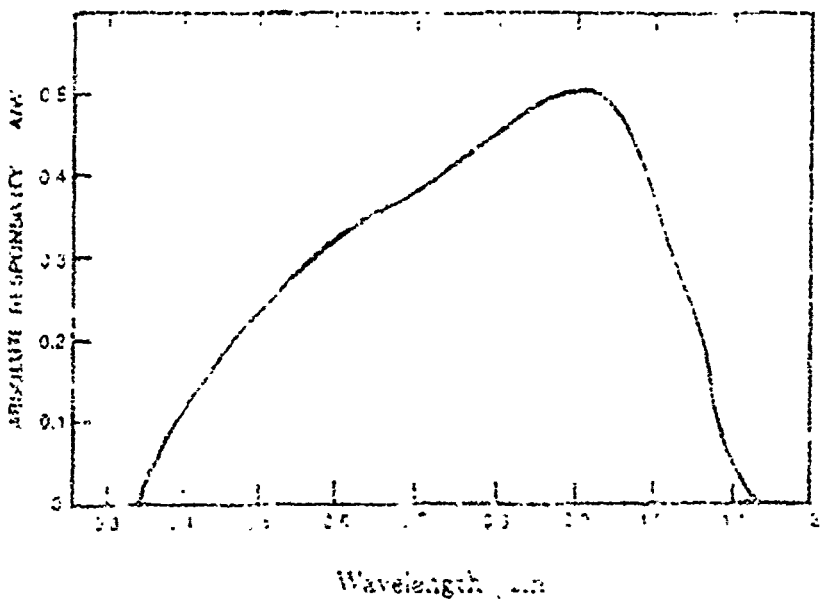


Figure 2 Spectral response of near infrared photodiode
(from EG&G Photon Devices brochure)

weighted clips mounted on either side. A thin sample of the pyrotechnic material was placed directly on top of the thermocouple bead and the two weighted clips were positioned just at the edge of the top sample surface to ensure good sample to thermocouple contact. The sample was then heated by a short laser pulse. The thermocouple on the back face of the sample produced a signal that was fed to an oscilloscope for analysis and determination of the thermal diffusivity.

PELLET FABRICATION

Samples of the B/Mg/PTFE pyrotechnic materials were consolidated into pressed pellets for testing. The ingredients used included magnesium powder of 325 mesh size and 99.8% purity; a granular resin of PTFE with a particle diameter of ≈ 30μm; and a submicron boron powder composed of 99% pure amorphous particles with a 0.15μm average size.

The fabrication process was begun by weighing out the appropriate amounts of dry powders of each of the constituents to produce 0.635 cm diameter by 1.27 cm length pellets at 100% of theoretical maximum density. A theoretical 2:1 length-to-diameter ratio was chosen to reduce the potential of any significant lengthwise density gradient. The composition was then thoroughly mixed in a low rpm fuel blender. The pellets were then consolidated in an apparatus consisting of a 2.54 cm diameter steel bar 12.7 cm long with a 0.635 cm hole through its center serving as the pellet mold. The bar was clamped tightly between two thick plates with a copper gasket on the bottom plate for sealing. A stainless steel rod 0.620 cm in diameter was used as the pressing mandrel. The mold was filled with the pyrotechnic composition and the apparatus was placed in a compression tester for pressing. The samples were pressed under a maximum force of 910 kgf (2000 lbf) producing a consolidation pressure of 140×10^6 kg/m^2 (40,000 psi). A holding time of two minutes was then employed upon reaching the maximum pressure.

Figure 3 displays the variation of the actual density from the theoretical maximum density (TMD) as a function of the boron weight percentage substituted for magnesium in the pyrotechnic materials. The consolidation pressure was held constant at the value given above. Since boron (ρ_B = 2.34 g/cm^3) is 35% more dense than magnesium (ρ_{Mg} = 1.74 g/cm^3), the TMD increases monotonically as boron is substituted for magnesium in the formulation. However, the actual density was observed to decrease as the boron loading increased. The actual density dropped significantly with only a small addition of boron up to a 10% loading and then leveled off at ≈1.70 g/cm^3 up to 35% boron. The actual density then dropped significantly again for a material with 50% boron and no magnesium. It can obviously be concluded that the substitution of boron for magnesium significantly [illegible] the packing efficiency of the pyrotechnic material even under high consolidation pressures.

It is believed that this effect may be partially explained by the 'softness' of the 20 μm magnesium particles versus the more rigid sub-micron boron particles. Under the high consolidation pressures, the magnesium particles will compact and conform more readily within the material microstructure than the boron particles, thus producing a more efficient packing. Another reason for this behavior was derived from observations by Trapp and Bingham [26] in a paper on the manufacture of consolidated pyrotechnic pellets. They state

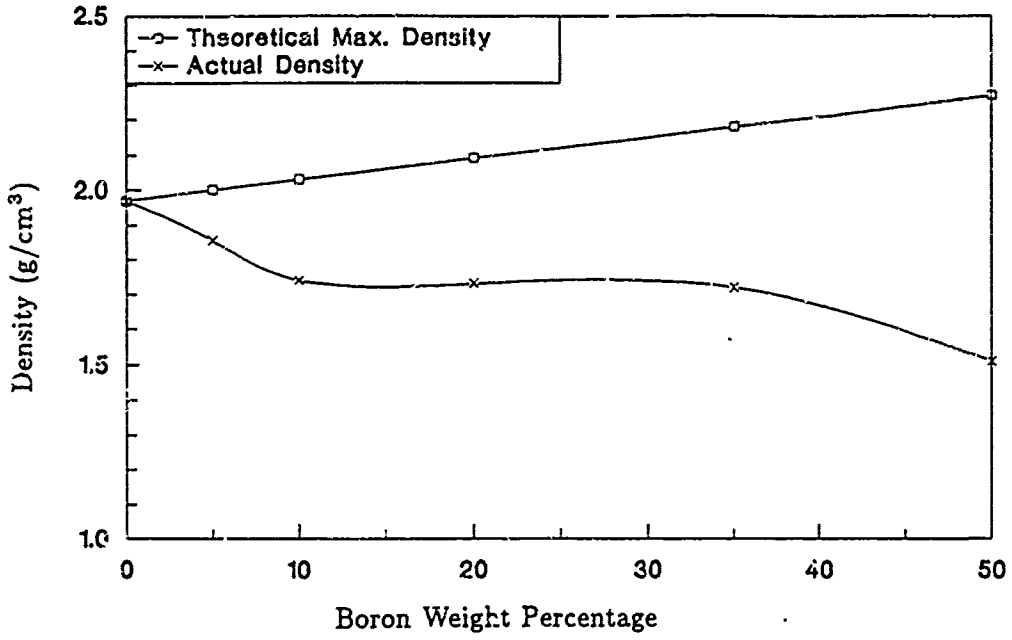


Figure 3 Comparison of actual density and TMD of the pressed pellets as a function of the boron content in the B/Mg/PTFE compositions

that, "When pressing dry powders, significant effects of friction are apparent due to (a) inter-particle friction, (b) particle to cylinder wall friction, and (c) friction during extraction." Considering item (a), the rigidity of the boron particles relative to the magnesium particles produces an increased amount of inter-particle friction as the boron loading increases. Thus, the boron-loaded material cannot flow as well or pack as efficiently, and will deviate more significantly from the TMD. Item (c) was clearly more prevalent as the boron loading was increased as it became very difficult to remove the rod from the core after pressing due to the impedance of the boron particles. Also, a considerable increase in item (b) as the percentage of boron is increased may reduce the actual force imposed on the sample and reduce the actual consolidation pressure with a corresponding reduction in the actual density.

THERMAL DIFFUSIVITY CHARACTERIZATION

The laser flash method proposed by Parker et al. [24] was employed to determine the thermal diffusivity as a function of the weight percentage of boron substituted for magnesium in the pyrotechnic formulations. Briefly, the experimental procedure involves heating a thin sample with a short-duration laser pulse and measuring the temperature rise on the back face of the sample with a thermocouple. The temperature trace exhibits a slow rise and then levels off to a steady value when the sample is uniformly heated. A simple relationship derived by Parker et al. [24] is then employed:

$$\alpha = 0.139L^2/t_{1/2}$$

where L is the sample thickness and $t_{1/2}$ is the time measured from the begin-

ning of the temperature rise to 1/2 the maximum temperature. In this study, 1.5-2.5 mm thick pressed pellets of the various compositions were used as test samples. They were heated in open air with a 300-400 watt laser pulse of 1.5-3.5 ms duration depending on the sample formulation.

The thermal diffusivity behavior of the B/Mg/PTFE pyrotechnics is given in Figure 4. The graph indicates that the substitution of small percentages of magnesium with boron in the basic 50/50 Mg/PTFE formulation produces a drastic reduction in the thermal diffusivity. The trend levels off at a boron loading of 10% and the addition of more boron up to 50% decreases the thermal diffusivity only slightly. The value of thermal diffusivity for the 50/50 Mg/PTFE formulation was $\alpha_{MT} = 3.2\times10^{-2}$ cm^2/sec. This value is twice the value obtained by Snyder et al. [26] for an MTV formulation. The densities (ρ) of these two formulations was $\rho_{MT} = 1.97$ g/cm^3 and $\rho_{MTV} = 1.84$ g/cm^3. It is believed that the presence of a significant amount of Viton A in their MTV formulation is the controlling factor producing the lower α_{MTV} value, not the slight density difference reported here.

Two explanations are proposed here for the trend observed in Figure 4. First, the thermal diffusivity of magnesium ($\alpha_{Mg} = 0.876$ cm^2/sec) is about eight times that of boron ($\alpha_B = 0.114$ cm^2/sec). Therefore, the replacement of small amounts of magnesium with boron should have a significant effect based solely on relative thermal diffusivities, and as the ratio of boron to magnesium in the formulation increases, this effect will become much less pronounced, producing a nonlinear trend overall. This agrees with the trend observed by Etter et al. [25] for a $TiH_{0.65}/KClO_4$ pyrotechnic material.

The second postulate is derived from the work of Pierce and Leith [23]. Using properties of $TiH_{0.65}$ and $KClO_4$ in their model, they presented a graph of

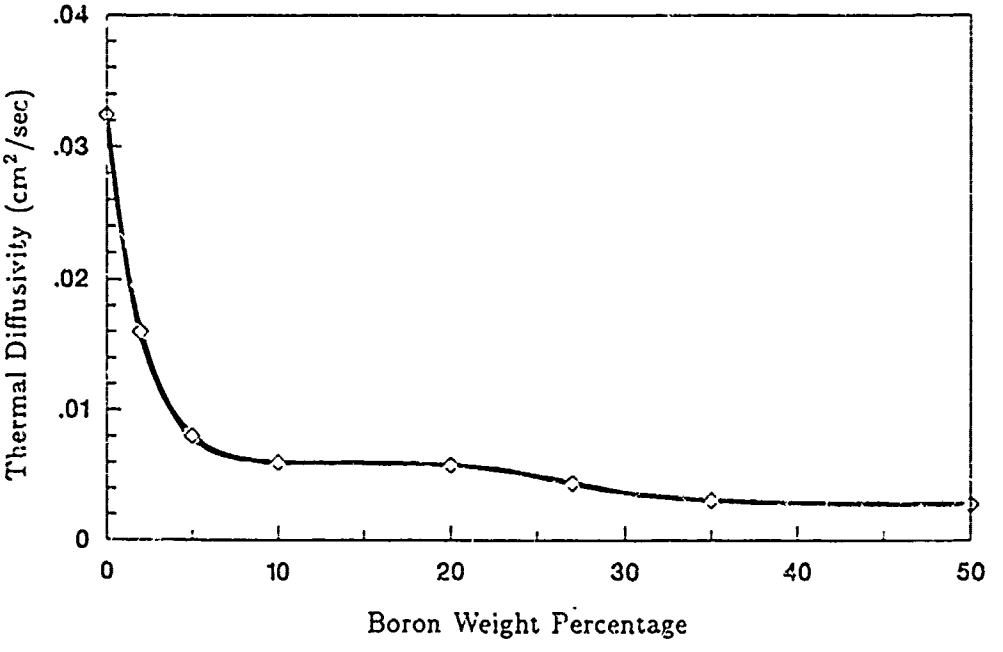


Figure 4 Thermal diffusivity as a function of boron content in the B/Mg/PTFE pyrotechnic materials

the trends of thermal conductivity (λ) and heat capacity (C) versus percent of theoretical maximum density (%TMD). The graph indicates that as the % TMD decreases, the thermal conductivity strongly decreases and the heat capacity slowly increases. Calculations made using this graph and the relation $\alpha = \lambda/\rho C$ showed that at a % TMD of 85%, the thermal diffusivity had dropped 12%. Figure 3 indicates that the 10/40/50 B/Mg/PTFE sample had a density 85.7% of the TMD, and Figure 4 indicates that the thermal diffusivity of this sample formulation had dropped 80% from the α value of the 50/50 Mg/PTFE sample. The thermophysical properties of $TiH_{0.65}/KClO_4$ and B/Mg/PTFE materials have some considerable differences, so a direct comparison of the α deviations at 85% TMD for these two materials is not feasible. However, even though the magnitude of the deviation in α at 85% TMD differs considerably, the trends coincide as both α values drop a noticeable amount. Thus, the work of Pierce and Leith [23] lends credibility to the conclusion that the trend observed in Figure 3, where the actual density drops considerably from the TMD up to a boron percentage of 10%, plays a prominent role in the significant drop in thermal diffusivity up to 10% boron content that is observed in Figure 4.

LASER IGNITION BEHAVIOR

Figure 5 exhibits the ignition delay behavior in one atmosphere of air of five different B/Mg/PTFE pyrotechnics as a function of incident heat flux. Most of the data points represent an average of several test data; average values were used to produce a more concise and readable graph since the ignition delay tests were quite reproducible and the data points at given conditions were very close to each other ($\pm$8% maximum deviation). It is also important to note that ignition of the 50/50 Mg/PTFE formulation was not sustained after removal of laser heating; thus, if ignition is defined as the onset of self-sustaining combustion, then this curve must be noted as representing the onset of laser-assisted combustion.

Figure 5 once again exhibits the trend that substituting small amounts of boron for magnesium in the B/Mg/PTFE formulations has a dramatic effect and further additions of boron above a certain level have a less significant effect. It can be seen that the ignition delay time decreases as both the percentage of boron and the incident heat flux increase. The ignition delay curves for both the 35% and 50% boron formulations are almost exactly concurrent, implying that increasing the boron percentage above 35% has almost no effect in reducing the ignition delay times. It is also quite interesting to note that the curves are roughly of exponential form. Due to the fact that the high-power CO_2 laser employed in this research was unstable below a power setting of about 130 watts, which corresponds to a heat flux of $\approx$200 W/cm^2, these lower limits of ignitability could not be explored with the current experimental setup.

Two major factors could account for this trend of ignition delay as a function of the weight percentage of boron substituted for magnesium. The first factor is the significant difference in absorptivity of magnesium and boron at the 10.6 μm wavelength of the CO_2 laser. Chen [29] reported that the available literature suggests that at this wavelength the absorptivity of magnesium is lower than 0.25, but boron exhibits a very high absorptivity. Chen used FTIR to investigate the absorptivity of boron/HTPB solid fuels at a 10.6μm wavelength. He found the absorptivity of the polymer HTPB to be only 0.2203, but a 30/70 B/HTPB formulation exhibited an absorptivity of 0.7328. Thus, it can be concluded that boron has a very high absorptivity at the 10.6 μm wavelength

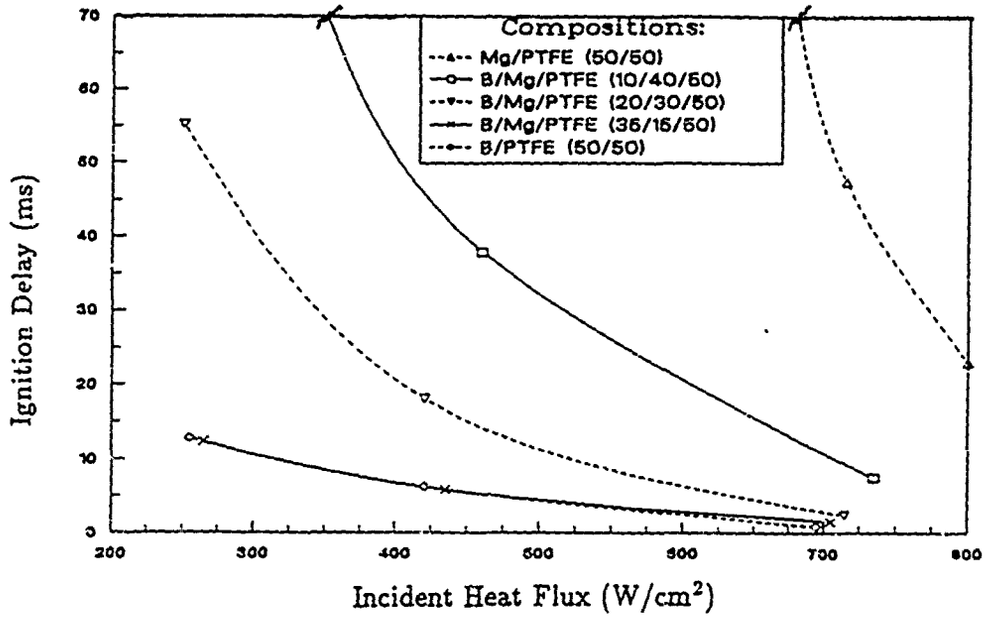


Figure 5 Ignition delay as a function of incident heat flux and sample ingredients for ignition in air at one atmosphere

of the CO_2 laser, and the actual energy flux absorbed by the sample at a given incident heat flux increases considerably as the weight percentage of boron is increased.

The second factor accounting for the trend observed in Figure 5 is the strong effect the thermal diffusivity of the test samples has on the thermal wave profile in the subsurface region during the inert heating period prior to ignition. As small amounts of boron are substituted for magnesium in the composition, the thermal diffusivity decreases dramatically (see Figure 4). Thus, the energy input to the sample surface cannot diffuse readily into the solid material. The energy becomes increasingly concentrated at the sample surface, inducing a rapid rise in surface temperature which quickly leads to the attainment of ignition. By comparing Figures 4 and 5, it can easily be conceived that the functional dependence of thermal diffusivity on boron content has a dominant effect on the ignition delay behavior of the pyrotechnic materials.

COMBUSTION CHARACTERISTICS

The principal parameter investigated in evaluating the combustion characteristics of the B/Mg/PTFE pyrotechnics was the burning rate of the test samples. Samples were heated by the CO_2 laser just long enough to produce ignition so that the subsequent combustion behavior would be independent of the laser heating. In order to observe steady-state combustion behavior beyond the ignition period, ignition delay times of the test samples were estimated from both the previous work of Fetherolf et al. [3] and the ignition delay data presented in Figure 5. The laser heating time was set as 1.5 times the estimated ignition delay at the desired heat flux to provide a margin for test variation. Thus, both a laser-induced ignition delay time as a function of incident heat flux and a laser-independent burning rate were obtained from each

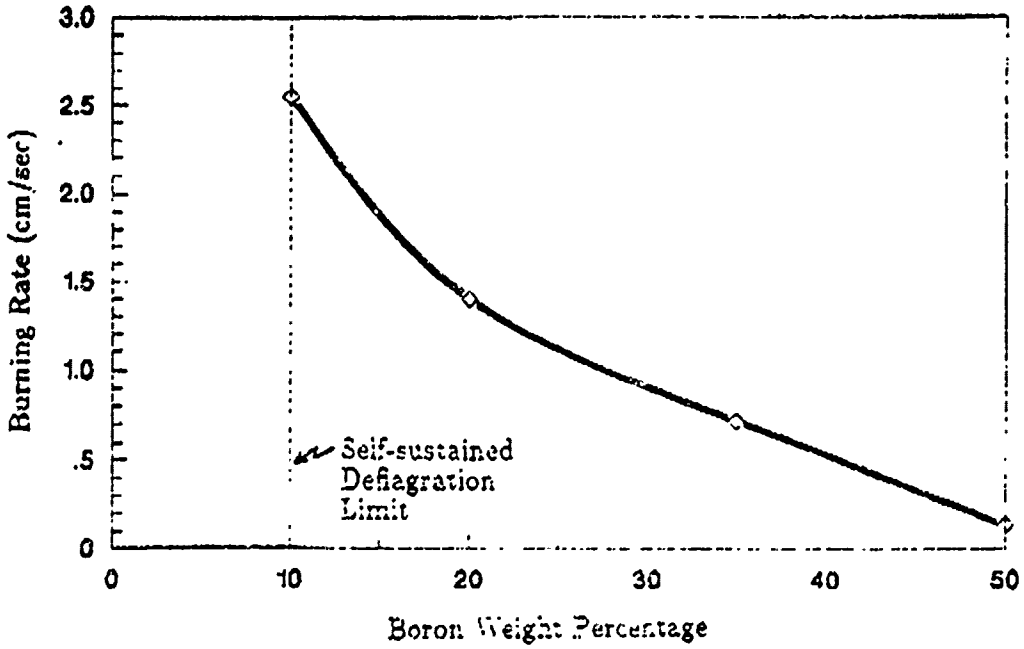


Figure 6 Burning rate as a function of boron weight percentage in the B/Mg/PTFE compositions for combustion in air at one atmosphere

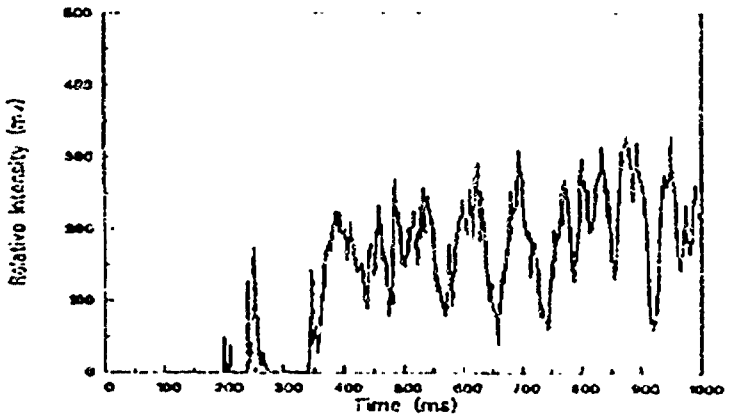
test. The burning rates obtained were found to be totally independent of the incident heat flux.

Figure 6 exhibits the burning rate behavior in one atmosphere of air of the B/Mg/PTFE pyrotechnic materials as a function of the boron weight percentage. It is important to note that there exists a self-sustained deflagration limit (SSDL) at 10% boron content below which the samples would ignite but immediately extinguish upon termination of the laser heating. Repeated experiments were conducted with samples containing 0%, 2%, and 5% boron, and no self-sustained deflagration was observed. Even if the lasing time was set at several times the estimated ignition delay time, the samples would not sustain deflagration after removal of laser heating, although a laser-induced burning rate could be observed. The trend seen in Figure 6 is quite interesting in that the 10/40/50 B/Mg/PTFE formulation which is on the border of the SSDL also has the highest burning rate, and further addition of boron above the 10% loading causes the burning rate to decrease monotonically

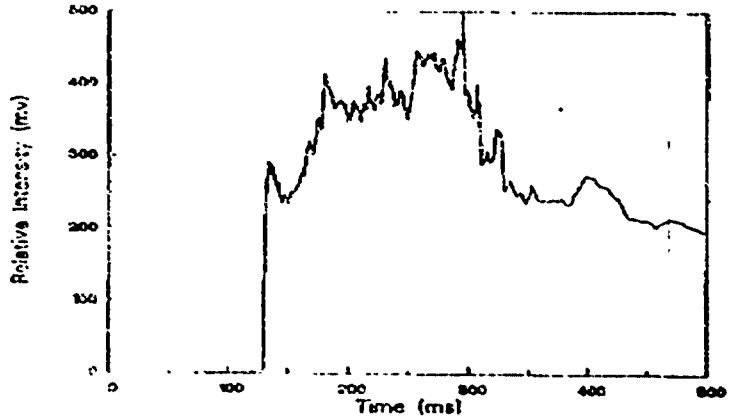
Figures 7a-7d display the near-infrared emission of four different B/Mg/PTFE compositions upon ignition. Note that the time scale of Figure 7a is different from the other three figures. It should also be noted that the near-infrared emission in Figure 7a represents laser-induced combustion as the laser remained on for the duration of that test. However, the other three figures represent self-sustained combustion after a period of laser heating slightly longer than the ignition delay of the sample.

Several trends are evident from the near-infrared emission traces in Figure 7. As discussed earlier in the paper, the length of the ignition delay time decreases as the boron loading increases Also, high-frequency fluctuations are evident in the traces, but the magnitude of these fluctuations appears to decrease as the amount of boron increases, suggesting a more stable

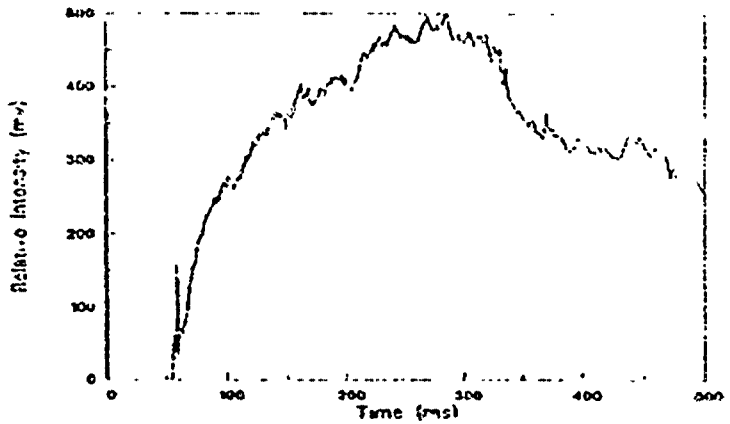
DEC 9 '91 9:46



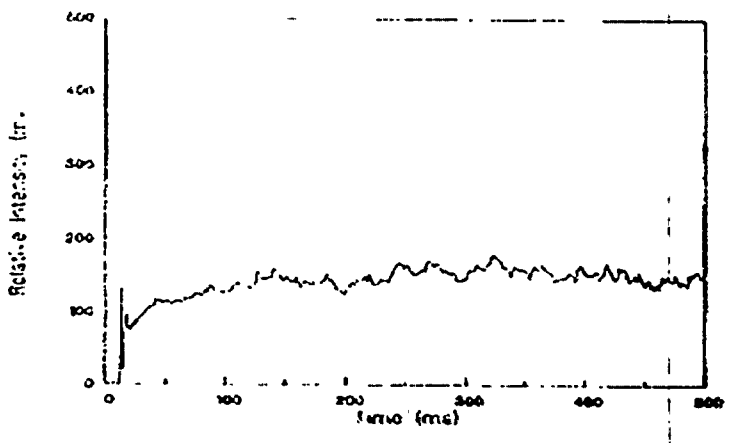
(a) 50/50 Mg/PTFE



(b) 10/40/50 B/Mg/PTFE



(c) 20/30/50 B/Mg/PTFE



(d) 35/15/50 B/Mg/PTFE

Figure 7 Near-infrared emission from combustion of B/Mg/PTFE materials in air at one atmosphere (Fig 7a: q''=420 W/cm^2; Figs 7b-7d: $q'' \approx$250 W/cm^2)

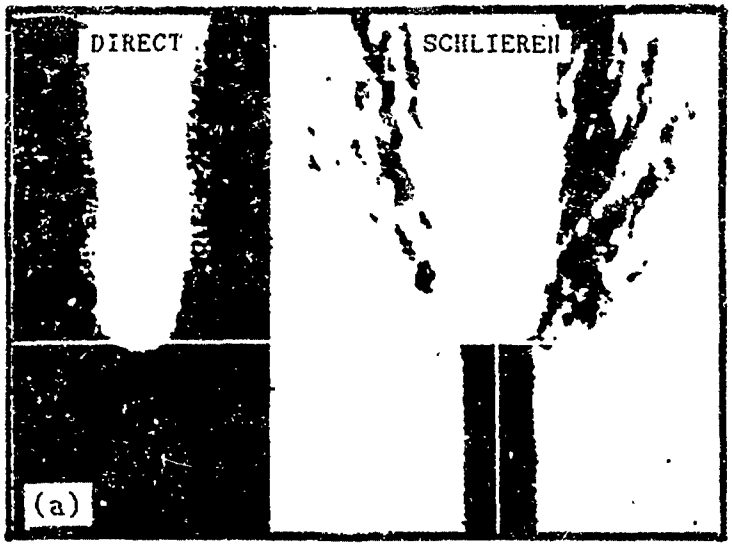
PAGE.005

combustion with an increase in boron loading. This observation was also evident in the high-speed video images as both the two-phase plume and the flame structure became more stable as the percentage of boron was increased. The high-speed videos of burning of the 35/15/50 B/Mg/PTFE formulation displayed a very stable combustion, and this stability is also evident in Fig. 7d where the near-IR emission trace is nearly a horizontal line. Wasmann [30] has studied the pulsating burning of flares and deduced that the pulsations could be due to competing chemical reactions with opposite paths, competing physical processes such as evaporation, heat flow, and heat accumulation, or a combination of both effects. It is conceivable that the pulsations observed in Figure 7 could be due to such competing processes.

It is also obvious from Figure 7 that the magnitude of the near-infrared emission is significantly higher for the intermediate boron loadings of 10% and 20% than for the low or high boron loadings. In previous work by the authors [3] employing the same photodiode setup, the maximum magnitude of near-infrared emission for the vigorous combustion of an MTV igniter/flare material was ≈200 millivolts. Therefore, it appears that the addition of intermediate amounts of boron to a Mg/PTFE composition significantly augments the near-infrared emission.

Figure 8 displays three images obtained with the Spin Physics high-speed video system. As is noted in Figure 8a, the left image is the direct view of the flame structure and the right image is the schlieren view of the two-phase plume. Figure 8a displays the on-screen reticle used to measure burning rates and also to align the sample surface at the same initial height in both images. The images were obtained at a recording speed of 1000 pictures per second. The size of the image is ≈1.5 times larger in the schlieren image than in the direct image.

Figure 8a exhibits the steady-state burning of a 20/30/50 B/Mg/PTFE sample. The high-speed videos showed numerous, glowing, fine particles being evolved from the flame. The particles are not clearly seen in this still photograph, but they comprise the 'haze' seen on both sides of the flame stem and their motion is quite evident in the high-speed movies. In the schlieren image, the particles are clearly seen evolving from the dark gradients that envelop the central stream of hot gases corresponding to the flame observed in the direct image. Fast, repetitive fluctuations in the two-phase plume were observed, but it was not distinctly evident that they corresponded to the fluctuations of the near-infrared emission seen in Figure 7c. The large amount of glowing particles being emitted from the flame may also be partly responsible for the observed fluctuations in the near-IR emission. Figure 8b is a picture of the deflagration of a 35/15/50 B/Mg/PTFE sample. Very large, glowing agglomerates are observed being evolved from the flame. The turbulence seen in the left hand side of the schlieren image corresponds to the glowing agglomerate just exiting the flame on the middle left hand side of the direct image. This agglomerate is about the median size observed being continuously evolved in the high-speed movies. Despite the size and number of these agglomerates being evolved, the burning rate of this formulation was very consistent and the combustion very stable (see Figure 7d). Figure 8c displays the rather bizarre 'burning' of a 50/50 B/PTFE formulation. The reticle indicates the location of burning; however, this is not a burning surface but a 'deflagration region' which is observed to propagate down through the pellet, leaving a glowing char behind as seen in the direct image.





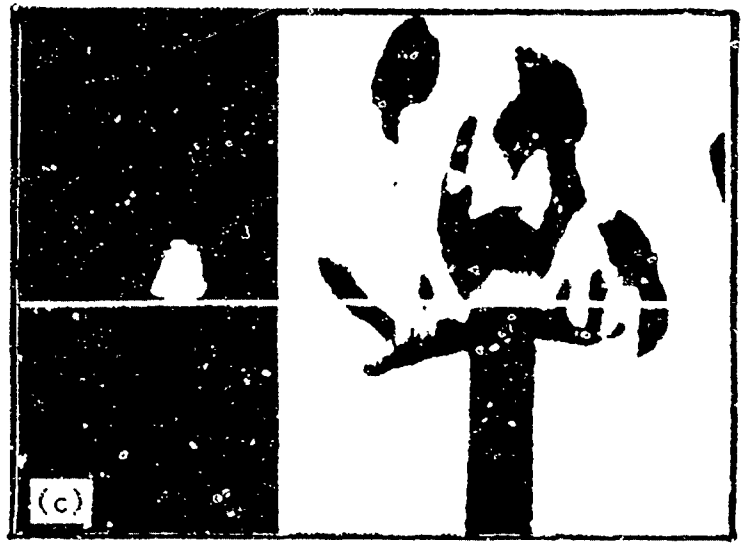


Figure 8 Direct and schlieren images of the combustion of various B/Mg/PTFE compositions in air at one atmosphere

(a) 20/30/50 B/Mg/PTFE
(b) 35/15/50 B/Mg/PTFE
(c) 50/50 B/PTFE

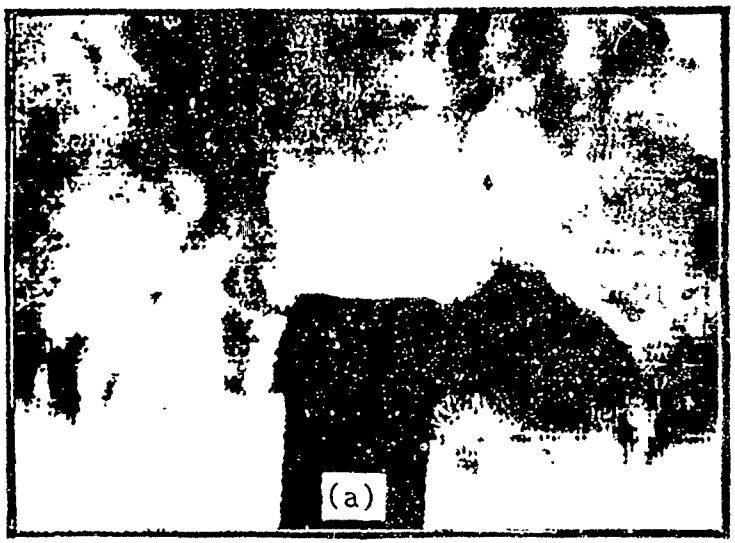
Figure 9 displays three photographs of schlieren images recorded using the Spin Physics system at 500 pps. The size of this schlieren image is slightly less than twice that of the schlieren image shown in Figure 8. A neutral density filter was employed to reduce the flame intensity observed in the schlieren images, and this permitted observation of the high-intensity, near-surface flame zone. The intensity of the near-surface flame was so strong that it overpowered the light intensity of the 100 watt tungsten-halogen lamp used as the schlieren system light source.

Figure 9a shows the burning of a 10/40/50 B/Mg/PTFE composition. Here, a relatively well-defined flame zone ≈4 mm in height was observed to stabilize on and above the sample surface throughout the steady-state deflagration. The combustion of a 20/30/50 formulation is displayed in Figure 9b, and the flame zone here appears to be slightly more diffuse with a peak about twice the height of the flame zone for the 10/40/50 sample. The fine particles being evolved in the schlieren image in Figure 8a are also quite evident in Figure 9b. The burning of the 35/15/50 B/Mg/PTFE composition seen in Figure 9c does not exhibit a well-defined, stable flame zone. Instead, small flamelets are observed dancing around within the central region of the plume. The dark regions on both sides of the plume are believed to be gradients produced by hot gases surrounding the large agglomerates being evolved by the combustion process (see Figure 8b). Some of these agglomerates, with hot gases streaming from them, are seen descending in the lower background.

Several physical and chemical processes believed to be dominant in accounting for the combustion behavior observed in Figures 6-9 will now be discussed. As was mentioned in explaining the ignition delay behavior of these materials, it is believed that the rigorous burning observed for the 10/40/50 B/Mg/PTFE composition can partially be explained by the significant lowering of the thermal diffusivity with only a 10% boron loading (see Figure 4). Since the energy input at the sample surface cannot diffuse readily into the solid material, the energy concentrates near the surface and enhances the rate of burning on the surface. However, since the thermal diffusivity changes very little as the boron loading is increased above 10%, it is apparent that other physicochemical processes are involved in the monotonic decline of the burning rate with respect to boron weight percentage.

An important heat transfer mechanism often discussed in explaining burning rate behavior [6, 15, 16, 20] is the heat feedback from the gas-phase reactions to the burning surface. Figures 9a-9c show that as the boron content in the B/Mg/PTFE compositions increases, the near-surface flame zone becomes more diffuse and less intense. Thus, there is less heat transfer from the gas-phase reactions back to the burning surface as the boron content increases, which consequently produces a decrease in burning rate as seen in Figure 6. The trend observed in Figure 7 also lends some credibility to this hypothesis as the drop in intensity from 20% to 35% boron content is clearly evident in Figures 7c and 7d. However, the photodiode cannot discriminate a drop in near-surface intensity from 10% to 20% boron content (Figures 7b and 7c) because of insufficient spatial resolution; it measures the same intensity for both flame regions seen in Figures 9a and 9b even though the flame in Figure 9b appears more diffuse than that in Figure 9a.

Several hypotheses have been developed in an attempt to understand the chemical processes occuring in the combustion of the B/Mg/PTFE pyrotechnic materials. These hypotheses refer to the following reactions:



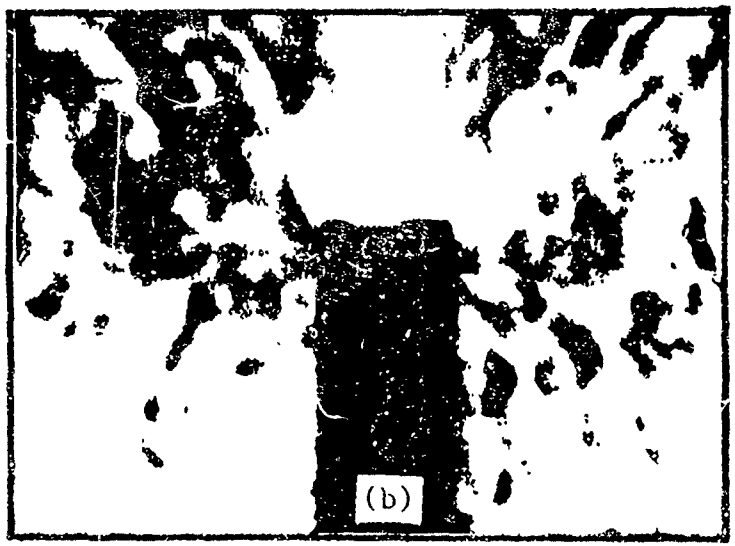




Figure 9 Schlieren images of the near-surface region for combustion of B/Mg/PTFE pyrotechnic materials in air at one atmosphere

(a) 10/40/50 B/Mg/PTFE
(b) 20/30/50 B/Mg/PTFE
(c) 35/15/50 B/Mg/PTFE

$$2Mg + \frac{1}{n}(C_2F_4)_n \longrightarrow 2MgF_2 + 2C \quad (1)$$

$$4B + \frac{3}{n}(C_2F_4)_n \longrightarrow 4BF_3 + 6C \quad (2)$$

$$\frac{an}{2}Mg + \frac{bn}{3}B + \frac{a+b}{4}(C_2F_4)_n \longrightarrow \frac{an}{2}MgF_2 + \frac{bn}{3}BF_3 + \frac{(a+b)n}{2}C \quad (3)$$

$$nO_2 + (C_2F_4)_n \longrightarrow 2nCOF_2 \quad (4)$$

$$B_2O_3 + 3Mg \longrightarrow 2B + 3MgO \quad (5)$$

$$2B_2O_3 + 6F_2 \longrightarrow 3O_2 + 4BF_3 \quad (6)$$

Reactions (1)-(3) assume ideal combustion of the metal counterparts of the B/Mg/PTFE materials with the carbon in the PTFE considered inert. In the present tests, the diffusion of ambient oxygen into the near-surface reaction zone is assumed negligible due to the high velocity of the pyrolysis and product gases evolved from the surface and reaction zone; thus, the reaction with fluorine dominates the metal combustion process [26]. Fetherolf et al. [3] observed the same near-surface flame structure and intensity for combustion of an MTV material in both air and inert environments, which supports the latter assumption. The stoichiometric weight percentages are 32.7% Mg for reaction (1) [7, 20] and 12.6% B for reaction (2) [20]. Therefore, the 50/50 B/PTFE composition has a significant excess of boron. It is believed that the unusual burning seen in Figure 8c for this composition is due to the boron acting as an 'energy sink' [15]. The boron absorbs energy from any exothermal processes occuring during sample combustion, but because the boron is present in excess, it distributes the energy and does not allow the sample to locally attain the ignition temperature of boron ($\approx$1900 K). The glowing char observed in Figure 8c is believed to be this heated boron. The 'burning' seen in Figure 8c is believed to be primarily due to reaction of pyrolyzed PTFE with the ambient oxidizer as proposed in reaction (4).

The intense flame zones observed in Figure 9 are believed to be primarily due to reaction (1). Fetherolf et al. [3] observed a flame zone $\approx$1.5 mm thick of similar structure and intensity for combustion of MTV materials using the same experimental setup. Magnesium flames have very high emissivities close to one [29], thus producing very intense emission. It is hypothesized that as the boron content increases and the Mg content decreases, the flame intensity will decrease due to reduction of the amount of Mg available for reaction in the near-surface flame zone. Also, as the boron content increases, the 'energy sink' effect of the boron particles will become more prominent and take away energy from the combustion zone. The large, glowing agglomerates in Figure 8b are 'mobile energy sinks removing useful energy from the flame zone. Both these effects of a lower flame intensity as the Mg content decreases and useful energy being constrained by the boron particles as the boron content increases contribute to the trend of lower burning rates as the boron:Mg ratio in the compositions increase above 10%. The intensity trends of Mg/PTFE and B/PTFE flames as reported by Shidlovskii and Gorbunov [20] also lend credibility to this hypothesis and substantiate the trend observed in Figure 9.

A major factor in the combustion of boron is the removal of the nonporous oxide layer (B_2O_3) which coats the elemental boron particle. This layer is on the order of 0.001-0.1 μm thick [14], and the physicochemical processes leading to its removal, permitting combustion of the clean boron particle surface, are very complex. Nemodruk and Karalova [31] state, " At high temperatures, B_2O_3 is reduced by many metals, for example Mg, to form elementary boron " They

also state," Fluorine reacts readily with B_2O_3 to form BF_3." Reactions (5) and (6) were formulated from these two statements. Reaction (5) is also known as the 'Moissan Process' and is used in industry to produce elementary boron [32]. It is hypothesized that these reactions (5 & 6) may occur in B/Mg/PTFE materials, producing a quicker and more efficient removal of the oxide layer from the boron particle so that it can react with fluorine as in reaction (2), releasing a high amount of energy to augment the burning of the B/Mg/PTFE pyrotechnic materials.

CONCLUSIONS

The combustion characteristics and CO_2 laser ignition behavior of pressed pellets of B/Mg/PTFE pyrotechnic materials were investigated as functions of boron content in the sample. All tests were conducted in air at one atmosphere. When the pyrotechnic pellets were fabricated, the actual densities of the pellets were observed to decrease as the boron weight percentage increased despite the theoretical maximum density (TMD) increasing as boron content increased. It was believed that the rigid boron particles restricted the flow of the material under the high consolidation pressure (140×10^6 kg/m^2) and increased the inter-particle friction, thus reducing the packing efficiency and causing the actual density to deviate from the TMD, with the effect being most significant at low boron contents up to 10%.

Thermal diffusivities were measured using a laser flash method. The thermal diffusivity (α) was found to decrease drastically as small amounts of boron up to 10% were added to the formulation. The α value dropped only slightly as more boron was added above 10%. Two factors were used to explain this behavior. First, α_B is about eight times less than α_{Mg}, so the addition of small amounts of boron significantly reduces the overall α value. Second, the significant reduction in % TMD as up to 10% of boron is added to the formulation is believed to be prominent in the significant reduction in the α value up to a 10% boron content.

The ignition delay times were observed to decrease as the incident heat flux increased and the boron weight percentage increased. This trend was less significant at the higher boron weight percentages. Two parameters were considered in explaining this behavior: the absorptivity at the 10.6μm wavelength of the CO_2 laser and the thermal diffusivity of the samples. The absorptivity of Mg is < 0.25 at this wavelength, but boron exhibits a very high absorptivity; thus, an increase in boron content significantly increases the effective heat flux absorbed by the samples and lowers the ignition delay. The significant decrease in the α value as boron content is increased causes the incident energy to remain concentrated at the surface, which produces a more rapid rise in surface temperature and quicker attainment of ignition.

The burning rate of the B/Mg/PTFE pyrotechnic materials dropped monotonically from its maximum at 10% boron content as the percentage of boron was increased above 10%. Interestingly, self-sustained deflagration was not observed for any formulations with lower than 10% boron content. Near-infrared emission was observed to be significantly higher for combustion of samples containing 10% and 20% boron. Fluctuations observed in the near-IR emission for low boron contents decreased as the percentage of boron was increased. High speed videos of the flame structure and the two-phase plume dynamics showed that as the boron content increased, the size of the particles evolved from the surface increased and the near-surface flame zone became more diffuse and less intense.

Several physicochemical processes were proposed to account for the observed combustion behavior. As was mentioned in discussing the ignition delay behavior, the significant decrease in the α value up to a boron content of 10% is believed to increase the level of surface energy and thus enhance the surface burning. Above 10% boron, the decrease in burning rate as boron content increases is attributed to the reduction in heat feedback from the gas-phase reactions to the sample surface evidenced by the changes in flame structure. The intense near-surface flame zone is believed to be primarily due to the fluorination of Mg. It is also believed that boron particles may act as 'energy sinks' if they cannot attain their high ignition temperature, thus reducing the energy available for other physicochemical processes in the sample. Thus, it was concluded that as the Mg content decreases and the boron content increases, the near-surface flame intensity and the energy available at the surface are both reduced, producing a decrease in the burning rate as the boron content increases. Finally, it was also concluded that with the proper conditions magnesium and fluorine may react with the nonporous oxide layer on the boron particle, causing a quicker and more efficient removal of the layer, producing a clean boron particle available for energetic reaction.

ACKNOWLEDGEMENTS

This work was sponsored by the Office of Naval Research, Contract No. N00014-86-K-0468, under the management of Drs. Richard S. Miller and Gabriel D. Roy. We would like to express our sincere appreciation to them for their support and also to Dr. T. A. Litzinger for his advice and valuable assistance in writing this paper.

REFERENCES

1. Peretz, A, "Investigation of Pyrotechnic MTV Compositions for Rocket Motor Igniters," AIAA Paper 82-1189, June 1982.

2. Valenta, F, "MTV as a Pyrotechnic Composition for Solid Propellant Ignition," Proceedings of the 13th International Pyrotechnics Seminar, Grand Junction, Colorado, July 1988.

3. Fetherolf, B L, Chen, D M, Snyder, T S, Litzinger, T A, and Kuo, K K, "Ignition and Combustion Behavior of MTV Igniter Materials for Base Bleed Applications," Proceedings of the 1st International Symposium on Special Topics in Chemical Propulsion: Base Bleed, Athens, Greece, November 1988.

4. Ladouceur, H D and Oran, E S, "Windstream Effects on IR Decoy Flares," KTA-16, Pyrotechnic Ignition Transfer Symposium, Monterey, CA, October 1985, Proceedings of the Workshop on Pyrotechnic Ignition, Naval Weapons Support Center.

5. Ladouceur, H D, "Windstream Effects on Pyrotechnic Combustion," 25th IRIS Meeting, Johns Hopkins University, April 1987.

6. Kubota, N and Serizawa, C, "Combustion Process of Pyrotechnics," *Propellants, Explosives, Pyrotechnics*, Vol. 12, 1987, pp. 145-148.

7. Kubota, N and Serizawa, C, "Combustion of Magnesium and Polytetrafluoroethylene," *Journal of Propulsion*, Vol. 3, No. 4, July-August 1987, pp. 303-307.

8. Taylor, F and Farnell, P, "New Solventless Process for Safer Manufacturing of Pyrotechnic Flares," Proceedings of the 13th International Pyrotechnics Seminar, Grand Junction, Colorado, July 1988.

9. Kelley, C M, Williams, R E, Takemoto, A, "Combustion Kinetics of Particulate Boron," Proceedings of the 2nd International Pyrotechnics Seminar, Snowmass at Aspen, Colorado, July 1970.

10. Macek, A and Semple, J M, "Combustion of Boron Particles at Atmospheric Pressure," *Combustion Science & Technology*, Vol. 1, 1969, pp. 181-191.

11. Talley, C P, "The Combustion of Elemental Boron," Progress in Astronautics and Aeronautics, Vol. 1, Solid Propellant Rocket Research, 1960, pp. 279-285.

12. King, M K, "Boron Particle Ignition in Hot Gas Streams," *Combustion Science & Technology*, Vol. 8, 1974, pp. 255-273.

13. King, M K, "Ignition and Combustion of Boron Particles and Clouds," 18th JANNAF Combustion Meeting, Vol. 3, 1982, pp. 225-241.

14. Faeth, G M, "Status of Boron Combustion Research," 21st JANNAF Combustion Meeting, CPIA-Pub-412, Vol. I, October 1984.

15. Hsieh, W H, Peretz, A, Huang, I T, and Kuo, K K, "Combustion Behavior of Boron-Based BAMO/NMMO Fuel Rich Solid Propellants," AIAA Paper 89-1189, July 1989.

16. Kuwahara, T, and Kubota, N, "Role of Boron in Burning Rate of AP Composite Propellants," *Propellants, Explosives, Pyrotechnics* 14, 1989, pp. 43-46.

17. Peretz, A, "Some Theoretical Consideration of Metal-Fluorocarbon Combustion for Ramjet Fuels," 8th International Symposium on Airbreathing Engines, Cincinnati, Ohio, June 1987.

18. Zvulony, R, Levy, Y, and Gany, A, "Experimental Investigation of a Solid Fuel Ramjet Combustor," Collection of Papers of the 27th Israel Annual Conference on Aviation and Astronautics, Israel, Feb 1985, pp. 205-209.

19. Tischer, R, "Effect of Entrained Air in Determining Optimum Flare Compositions," Proceedings of the 2nd International Pyrotechnics Seminar, Snowmass at Aspen, Colorado, July 1970.

20. Shidlovskii, A A, and Gorbunov, V V, "Combustion of PTFE Mixed with Boron, Titanium, or Magnesium," Translated from Fizika Goreniya i Vrzyva, Vol. 14, No. 1, Jan-Feb 1978, pp. 157-159.

21. Snyder, T S, Chen, D M, Fetherolf, B L, Litzinger, T A, and Kuo, K K, "Pyrolysis and Ignition of Boron-Based Solid Fuels for Ramjet Applications," 25th JANNAF Combustion Meeting, Huntsville, Alabama, Oct 1988.

22. Hermance, C E, Yovanovich, M M, and Zwart, J, "Calculation of Effective Thermal Properties in a Highly Compressed Pyrotechnic Mixture," Proceedings of the 8th International Pyrotechnics Seminar, Steamboat Springs, Colorado, July 1982.

23. Pierce, K G, and Leith, J R, "A Numerical Model of the Thermal Processes Leading to Ignition in a Pyrotechnic Device," Proceedings of the 11th International Pyrotechnics Seminar, Vail, Colorado, July 1986.

24. Parker, W J, Jenkins, R J, Butler, C P, and Acbott, G L, "Flash Method of Determining Thermal Diffusivity, Heat Capacity, and Thermal Conductivity," *Journal of Applied Physics*, Vol. 32, No. 9, 1961, pp. 1679-1683.

25. Etter, D E, Kaser, D R, and Wittenberg, L J, "Determination of the Thermal Diffusivity of Pyrotechnic Materials," Proceedings of the 6th International Pyrotechnics Seminar, Estes Park, Colorado, July 1978.

26. Snyder, T S, Chen, D M, Hsieh, W H, Yang, V, Litzinger, T A, and Kuo, K K, "Combustion Behavior and Thermophysical Properties of Metal-Based Solid Fuels," accepted for publication in *Journal of Power and Propulsion*.

27. Ostrowski, P P, "Laser Ignition Phenomena with Black Powder," Proceedings of the 7th International Pyrotechnics Seminar, Vail, Colorado, July 1980.

28. Trapp, A H, and Bingham, J F, "The Manufacture of Consolidated Pyrotechnic Pellets for Propellant Ignition System," Proceedings of the 10th International Pyrotechnics Seminar, Karlsruhe, Federal Republic of Germany, July 1985.

29. Chen, D M, "Pyrolysis, Ignition, and Combustion of Solid Fuels for Ramjet Applications," Ph.D. Thesis, Department of Materials Science and Engineering, The Pennsylvania State University, August 1988.

30. Wasmamn, F-W, "The Phenomenon of Pulsating Burning in Pyrotechnics," Proceedings of the 5th International Pyrotechnics Seminar, Vail, Colorado, July 1976.

31. Nemodruk, A A, and Karalova, Z K, Analytical Chemistry of Boron, translated by Kondor, R, Ann Arbor-Humparey Science Publishers, Ann Arbor, London, 1969.

32. Matkovich, V I, editor, Boron and Refractory Borides, Springer-Verlag Berlin Heidelberg, New York, 1977.

APPENDIX 2.2

UNCLASSIFIED

CPIA Publication 498, Vol. 1,
Oct. 1988, pp. 219 - 230.

PYROLYSIS AND IGNITION OF BORON-BASED SOLID FUELS FOR RAMJET APPLICATIONS

T. S. Snyder,* D. M. Chen,** B. L. Fetherolf,* T. A. Litzinger,+ and K. K. Kuo#
Department of Mechanical Engineering
The Pennsylvania State University
University Park, PA 16802

ABSTRACT

The ignition of two types of boron-based solid fuels, one with a hydrocarbon binder and the other with an energetic binder, have been studied, and the results suggest that the energetic binder enhances the ignition and combustion of boron. Ignition delay times for both types of solid fuels were found to decrease with the addition of boron to the pure fuels. The ignition process for both types of solid fuels began in the gas phase; then the reaction zone propagated toward the surface of the condensed phase. Both high-speed schlieren and direct photography systems were used to study the pyrolysis and ignition of the solid fuels. A physical explanation of the trends observed is given for quiescent ambient conditions and for low velocity crossflow conditions. Ignition tests with the incorporation of additives into the boron-based hydrocarbon solid fuel were also performed. Results show that cerium fluoride, magnesium, and magnesium/aluminum decrease ignition delay time with cerium fluoride having the largest effect.

INTRODUCTION

Boron continues to be a very attractive metal for use in ramjet combustion systems because of its high volumetric heating value. However, the high melting point (2450 K) and boiling point (3931 K) of elemental boron cause serious ignition and combustion efficiency problems. The ignition process of solid fuel plays a critical role during the transition from the booster motor to the ramjet mode of operation. During the transition, ram air is allowed to enter the combustion chamber to provide the necessary oxygen with adequate temperature to ignite the solid fuel. Thus, the ignition characteristics of the candidate fuels should be understood to ensure the proper operation of the ramjet engine.

Ignition based on a thermal stimulus can be caused by three different types of external sources. Convective heating of a solid fuel to ignition can be achieved with the passage of hot gases flowing over the sample surface. In laboratory studies, such kinds of flow conditions can be simulated using a shock tunnel[1] or a blowdown wind tunnel. Radiative heating of a solid fuel to ignition can be achieved by using a well-controlled external energy source, such as an arc image furnace[2] or a laser ignition system.[3] Conductive ignition can be attained through the direct contact of a solid fuel with hot solid particles, liquid droplets, or gases. Electrically heated hot wires[4] can also be used for conductive ignition purposes.

In the current study, a radiant energy source from a CO_2 laser has been used to study ignition characteristics. The CO_2 laser can deliver a desirable energy flux during a prescribed time period. One major advantage is due to its high reproducibility. Also, the laser can simulate a broad range of heat fluxes that the solid fuel would receive inside an actual ramjet engine. Furthermore, with the advancement of high-powered miniature lasers, it is foreseeable that radiative energy can be used in actual ramjet engines.

When a radiative energy source is used for ignition, the effect of attenuation of the incident radiation by the pyrolyzed gases must be considered. When gases and particles are evolved from the solid fuel surface, they will absorb and scatter some of the incident laser energy. Kashiwagi[6] observed this phenomena when igniting PMMA and red oak under radiative heating, and he measured values of 70-80 percent attenuation after five seconds. In the present study, the ignition delay time for the solid fuels are much shorter than five seconds (on the order of 7 to 120 ms). To determine the effect of laser energy-flux attenuation by the presence of pyrolysis products on the ignition process, tests were conducted with and without a low-velocity crossflow to remove a larger fraction of pyrolyzed gases from a considerable distance above the surface.

A variety of criteria have been used by other workers in the experimental determination of ignition.[7] Some of the typically used criteria include first appearance of luminosity, onset of light emission detected by a photodiode or photocell, onset of mass loss, abrupt rise in surface temperature from a thermocouple trace, and achieving sustained combustion by a go/no-go test. The criteria used here is the onset of light emission corresponding to the delay time from the start of laser heating to the onset of the first light detected by a photodiode.

---

* Graduate Assistant
**Graduate Assistant, Ph.D. Candidate
\+ Assistant Professor
\# Distinguished Alumni Professor

This document is approved for public release; distribution is unlimited.

UNCLASSIFIED

Two groups of solid fuels were investigated to observe their ignition characteristics. One consisted of hydroxyl terminated polybutadiene (HTPB) with various boron loadings. HTPB is the most popular binder used in conventional solid propellants because of its low cost, reliability, desirable mechanical properties, and long aging life. The other consisted of a copolymer of 3, 3-bis[azidomethyl] oxetane and 3-nitratomethyl-3-methyl oxetane (BAMO/NMMO) with the addition of boron.[8] BAMO/NMMO is a new, highly energetic binder which may enhance the combustion efficiency of boron significantly. The chemical structures of HTPB and BAMO/NMMO are shown in Fig. 1.

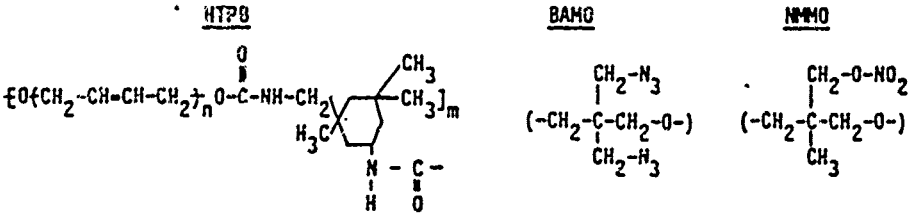


Fig. 1 Chemical Structures of HTPB Cured with IPDI and the Polymers of BAMO and NMMO

In addition to these two groups of fuels, the effects of additives on light emission delay time were also studied. The combustion of boron can be enhanced significantly by adding small amounts of magnesium and/or aluminum powders.[9,10] Another possibility for the enhancement of boron combustion, proposed by many investigators, is the addition of a fluorine compound into the fuel. The additives studied include magnesium, magnesium/aluminum, and cerium fluoride, which were mixed directly into boron/HTPB samples.

EXPERIMENTAL APPROACH

A high-powered CO_2 laser (Coherent Super 48) was used as the radiative ignition source. The laser is capable of generating 800 watts in the continuous mode of operation and 3500 watts in pulsed mode. The continuous mode was used in all ignition tests. Figure 2 shows a schematic diagram of the CO_2 laser test facility. In order to generate a relatively uniform beam, a thin sheet metal mask with a 7 mm diameter hole was utilized to allow only a uniform portion of the laser beam incident to the sample surface. The resulting spatial variation of the beam intensity was measured and found to be ± 10 percent. To ensure the level of laser energy input to the sample, the actual heat flux at the sample location was measured before each test using a calorimeter.

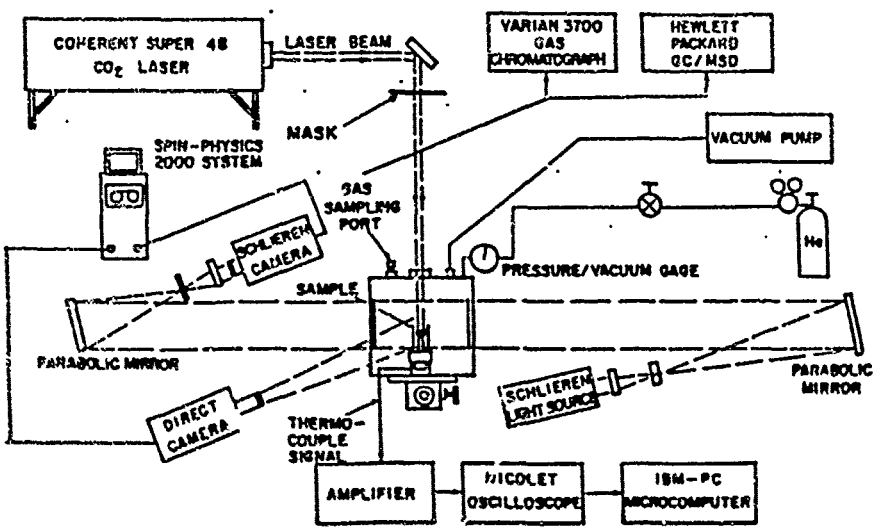


Fig. 2 Schematic of Experimental Apparatus Used in CO_2 Laser Tests

A test chamber (25 cm cube) was fabricated using 2.54 cm thick plexiglass and a 1.25 cm thick stainless steel top cover. The transparent nature of this chamber allows visual access from all directions. Two high quality glass windows were mounted on opposite sides of the chamber to facilitate schlieren photography. In order to record the light emission from the solid fuel, two near infrared photodiodes were mounted rigidly at specific locations in the chamber. One photodiode was positioned close to the sample surface (see Fig. 3) to determine the first light emission. For comparison purposes, a second photodiode was place farther away and was used to view a larger region of the plume development process during pyrolysis and ignition of the solid fuel sample. The spectral response of the photodiodes is between the wavelengths of 0.35 and 1.15 micrometers.

A high-speed video recording system (Spin Physics 2000) was used to register the dynamic behavior of the flame structure at a framing rate of 2,000 pps. The system accommodates two cameras which recorded the schlieren images and direct photographs simultaneously. The schlieren image can detect clearly the initiation of the solid fuel gasification, pyrolysis, and the subsequent ignition steps; whereas the direct photograph provides information about luminous flame development above the solid fuel sample.

The majority of testing was performed in an initially quiescent environment; however, some tests with crossflow were performed to study the effect of attenuation of the incident laser beam by the pyrolyzed gases and particles (see Fig. 3 for the location of the cross-flow nozzle). The crossflow was maintained at a specific velocity and was positioned in such a way as to remove the pyrolyzed gases without introducing convective cooling of the sample surface.

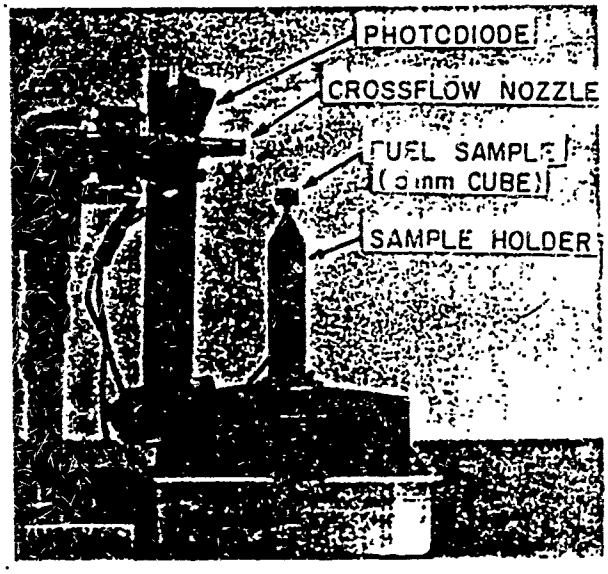


Fig. 3 Position of Near-Field Photodiode and Crossflow with Respect to the Solid Fuel Sample

EXPERIMENTAL RESULTS AND DISCUSSION

Quiescent Ambient Condition

Figure 4 shows two photodiode traces obtained for the ignition of HTPB with the addition of 30 percent boron [i.e., boron/HTPB (30/70)] at two different heat fluxes. Three important points are noted on each of the traces; first light emission (defined at an output of five millivolts from the photodiode), an abrupt increase in light emission, and maximum light intensity. As the heat flux increases, the time for each event to take place decreases. At low heat fluxes, the time from first light emission until the abrupt increase in light intensity is very long, compared to that at high heat fluxes. This important feature is believed to be caused by the time required by the pyrolyzed products to attain a sufficient temperature to induce a rapid increase in light intensity. The smaller the heating rate, the longer the time it takes to raise the local temperature of the pyrolyzed products (by the incident laser) to a critical value. In terms of the gas-phase ignition process, the onset of abrupt increase in light intensity (designated by triangular symbols) can be regarded as the ignition point.

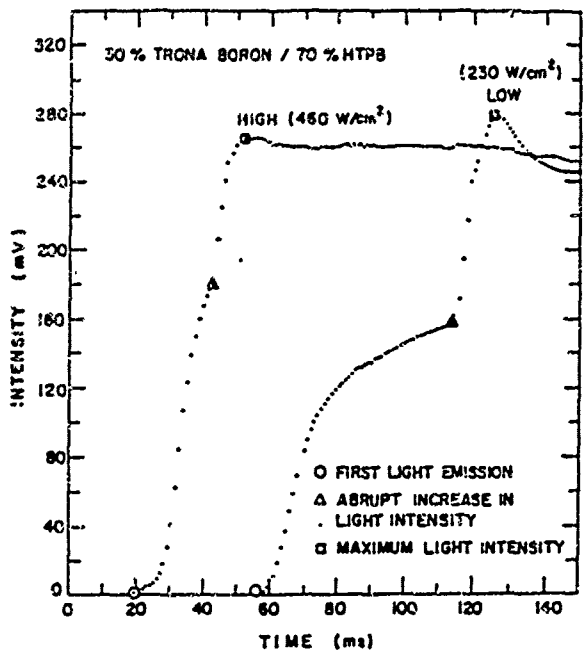


Fig. 4 Characteristic Photodiode Traces of Boron/HTPB (30/70) at High and Low Heat Fluxes

In order to understand these pyrolysis and ignition processes, the schlieren and direct motion pictures were taken. Figure 5 shows a sequence of six selected pictures for the ignition of boron/HTPB (30/70) by a 200 W/cm^2 heat flux. The first picture, composed of a direct image on the left and a schlieren image on the right, shows the evolution of pyrolyzed products in the schlieren image. The actual sample in these images is a 25 mm cube. The sample height is the same for both images; however, the direct image is slightly smaller than the schlieren due to differences in the camera magnifications. The second picture in the sequence shows the first light emission in the gas phase at 62 ms. This light intensity grows continuously and then increases rapidly at 125 ms. This abrupt increase is believed to be caused by the gas-phase reaction. During the pyrolysis and ignition event, a bright luminous zone propagates toward the sample surface, while a thermal plume with a mushroom-shaped core region and spherical outer boundary expands and rises in the vertical direction.

Figure 6 shows the effect of heat flux on delay time, defined by first light emission, for various boron percentages. Clearly, as the boron percentage increases from 0 to 20 percent, the delay time decreases. However, the delay time increases as boron loading increases from 20 percent to 30 and 50 percent. This change in trend with increasing boron loading can be explained by the absorptivity and

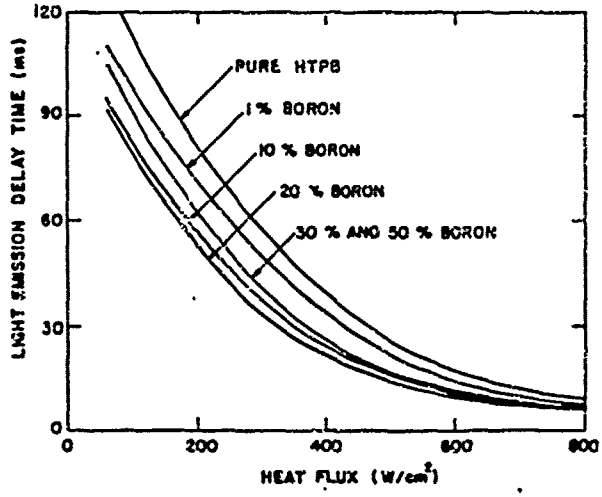


Fig. 6 Effect of Incident Heat Flux and Boron weight Percentage on Light Emission Delay Time of Boron/HTPB Solid Fuels

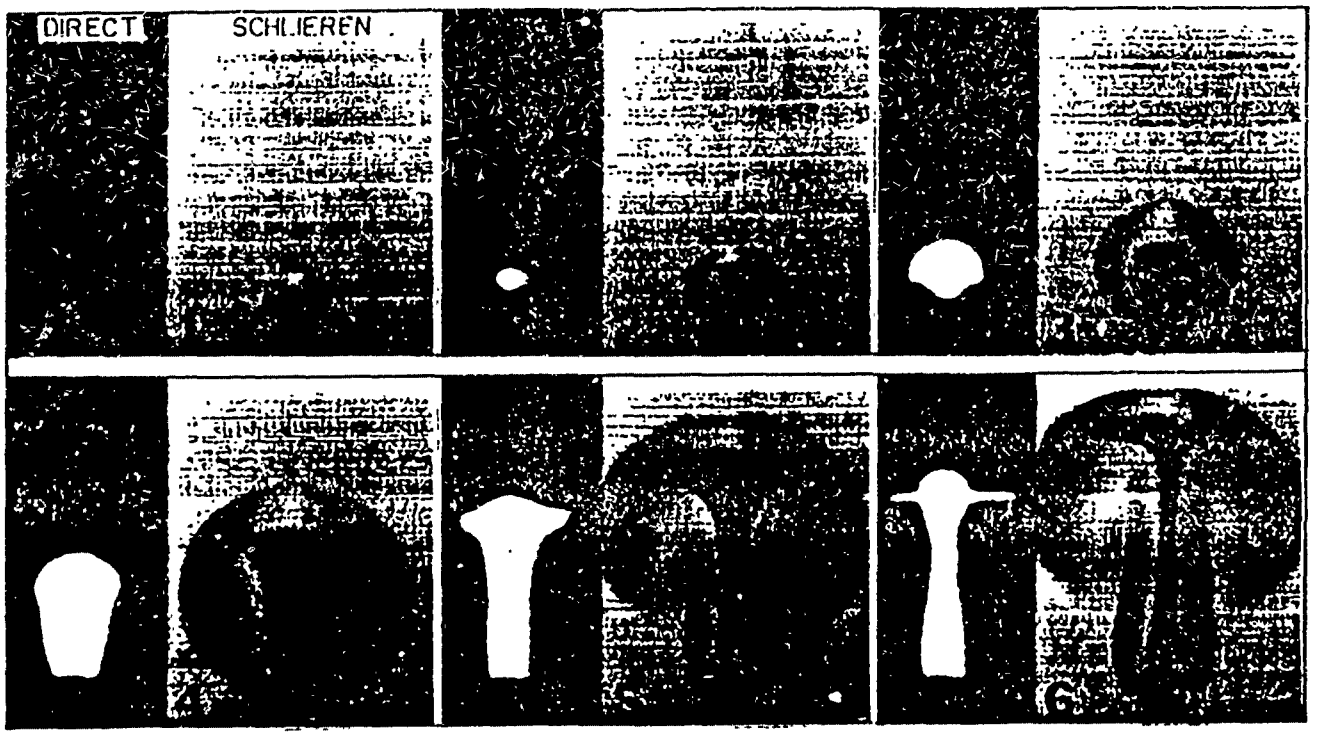


Fig. 5 Ignition Sequence of Boron/HTPB (30/70) Solid Fuel in Air with a Heat Flux of 200 W/cm^2 (The time from initial laser heating for pictures 1 through 6 are 57.5, 62.0, 87.5, 125.0, 147.5, and 158.0, respectively.)

volumetric specific heat in the plume. The rate of energy absorption $Q_{absorption}$ for a two-phase mixture containing boron particles and pyrolysis gases can be written as the sum of two terms: one for each phase, i.e.,

$$Q_{\substack{absorption \\ total}} = Q_{\substack{absorption \\ boron\ particles}} + Q_{\substack{absorption \\ pyrolysis\ gases}} \tag{1}$$

For a control volume with cross-sectional area A normal to the flow with average velocity $\bar{V}$, the two terms on the right-hand side of Eq. (1) can be written as

$$Q_{\substack{absorption \\ boron\ particles}} = \frac{4}{3}\pi r_B^3 \bar{n} A \bar{V} \rho_B C_B (T_B - T_i) \tag{2}$$

$$Q_{\substack{absorption \\ pyrolysis\ gases}} = \phi A \bar{V} \rho_g Cp_g (T_g - T_i) \tag{3}$$

where r_B is the average radius of boron particles, $\bar{n}$ the number density in the control volume, ρ_B the boron particle density, C_B the boron specific heat, T_B the average temperature of the boron in the control volume, T_i the initial temperature of the solid fuel, ϕ the void fraction, ρ_g the average gas density, Cp_g the constant-pressure specific heat of the gas phase, and T_g the average gas-phase temperature. The loaded fraction of boron particles can be written as

$$1 - \phi = \frac{4}{3}\pi r_B^3 \bar{n} \tag{4}$$

After substituting Eqs. (2)-(4) into (1), we have

$$Q_{\substack{absorption \\ total}} = A \bar{V} [(1-\phi) \rho_B C_B (T_B - T_i) + \phi \rho_g Cp_g (T_g - T_i)] \tag{5}$$

The average temperature of boron particles T_B could be different from T_g during the ignition event. To understand the role of effective volumetric specific heat, one can assume that they are roughly equal. Under such an assumption, Eq. (5) becomes

$$Q_{\substack{absorption \\ total}} = A \bar{V} (T_g - T_i) [(1-\phi) \rho_B C_B + \phi \rho_g Cp_g] = A \bar{V} (T_g - T_i) (\rho_M C_M)_{effective} \tag{6}$$

where $(\rho_M C_M)_{effective}$ is the effective volumetric specific heat of the two-phase mixture. As the boron is added in small percentages, the absorptivity of the plume increases linearly, while the volumetric specific heat of the plume changes very little (since $\phi \approx 1.0$). The increase in absorptivity causes the temperature in the pyrolysis products to rise faster with the addition of boron. At high boron loadings, the effective volumetric specific heat of the pyrolysis product mixture increases linearly as the percentage of boron increases. However, the radiation absorptivity of the mixture becomes weakly dependent on the boron concentration in the plume, since there are enough boron particles in the plume. Thus, the temperature rises more slowly due to the increase of effective volumetric specific heat with nearly constant radiation absorptivity at high boron loadings. The competition between absorptivity and volumetric specific heat directly affects the rate of increase of temperature in the plume which, in turn, affects the delay time for the onset of light emission.

The effect of incident heat flux and types of additives on the ignition delay ... boron/HTPB solid fuels is shown in Fig. 7. The delay time for all cases decreases monotonically ... ident heat flux increases. Magnesium and magnesium/aluminum powders showed a noticeable decrea ... ay time. The addition of cerium fluoride to the solid fuel produced the most significant decr ... delay time, especially at low heat fluxes.

Figure 8 shows two photodiode traces for BAMO/NMMO solid fuel with 17.58 percent boron by weight. The characteristic variations of photodiode traces are similar to those of boron/HTPB solid fuels even though the binders are quite different. However, the delay times for boron/[BAMO/NMMO] fuels are much shorter than those of boron/HTPB fuels. Again, at low heat fluxes there is a noticeable delay between the first light emission and the abrupt increase in light intensity; this is caused by the time needed by the pyrolyzed products to absorb enough laser energy to ignite.

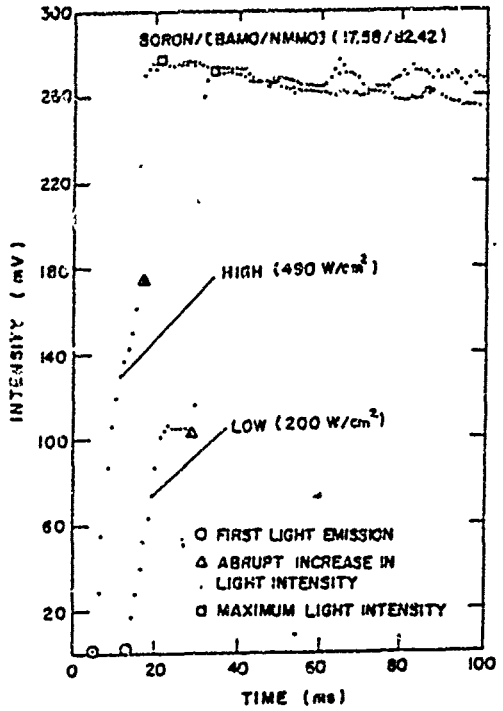


Fig. 7 Effect of Incident Heat Flux and Types of Additives on the Delay Time for First Light Emission of Boron/HTPB Solid Fuels

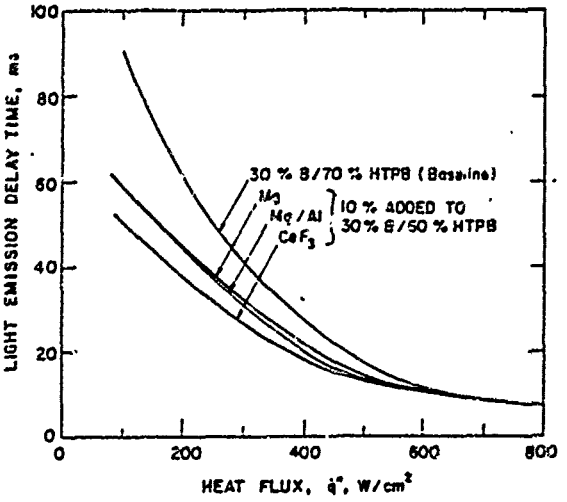


Fig. 8 Photodiode Traces for Boron/[BAMO/NMMO] Solid Fuel at High and Low Incident Heat Fluxes

Figure 9 shows a sequence of six selected pictures for the pyrolysis and ignition event of boron/[BAMO/NMMO] solid fuel at an incident heat flux of 490 W/cm^2. The pyrolyzed product velocities are much higher than those for the boron/HTPB fuels, as a result of the energetic nature of the BAMO/NMMO copolymer. The velocity was measured to be 1000 cm/sec compared to 30 cm/sec for HTPB. As a result of the high velocity plume jet, the plume is highly turbulent for the boron/[BAMO/NMMO] fuel. The first sign of visible light emission is seen in the third selected picture of the sequence at 10 ms. The light intensity grows rapidly and continuously. The luminous region expands abruptly at 17.5 ms (see picture 4). Following the gas-phase ignition, the reaction zone propagates toward the surface (see pictures 4 through 6). After the reaction zone reaches the surface, the reactions on the surface itself become apparent. Chunks of solid fuel are entrained in the plume jet resulting in bright reaction zones in the circumferential region of picture 6.

To illustrate the difference in the plume structure and surface reaction process before and after the reaction front reaches the sample surface, two sets of enlarged photographs are selected and presented in Figs. 10 and 11. These photographs are obtained from the same experiment shown in Fig. 9. Both the direct and schlieren photographs show the event of flame propagation toward the sample surface. Once the flame reaches the surface (see Fig. 11), the condensed phase reaction is enhanced immediately as seen by the flame on the sample surface and by many bright spots near the edge of the luminous plume in the direct picture. This process has been observed for boron/HTPB solid fuel as well; however, the apparent intensity of the reactions on the surface are much less. The reactions causing the luminous flame on the surface are believed to be caused by the energetic nature of BAMO/NMMO copolymer.

Figure 12 shows the effect of incident heat flux on delay time for first light emission for boron/[BAMO/NMMO] solid fuels with various boron weight percentages. The data from pure BAMO/NMMO copolymer fuel is also plotted, which exhibited random delay times for all heat fluxes. This random behavior is believed to be caused by the highly turbulent nature of the pyrolyzed gases evolved; the active site for first light emission varies significantly from test to test. The location of the active site depends upon effective absorption of the infrared energy flux from the laser and the convective heat-transfer conditions in the turbulent plume. Since the convective heat-transfer conditions are strongly effected by the randomness of the turbulence, the active site and the delay time for first light emission are highly random. When boron particles are added to the solid fuels, this random behavior is eliminated. The delay time for first light emission decreases as incident heat

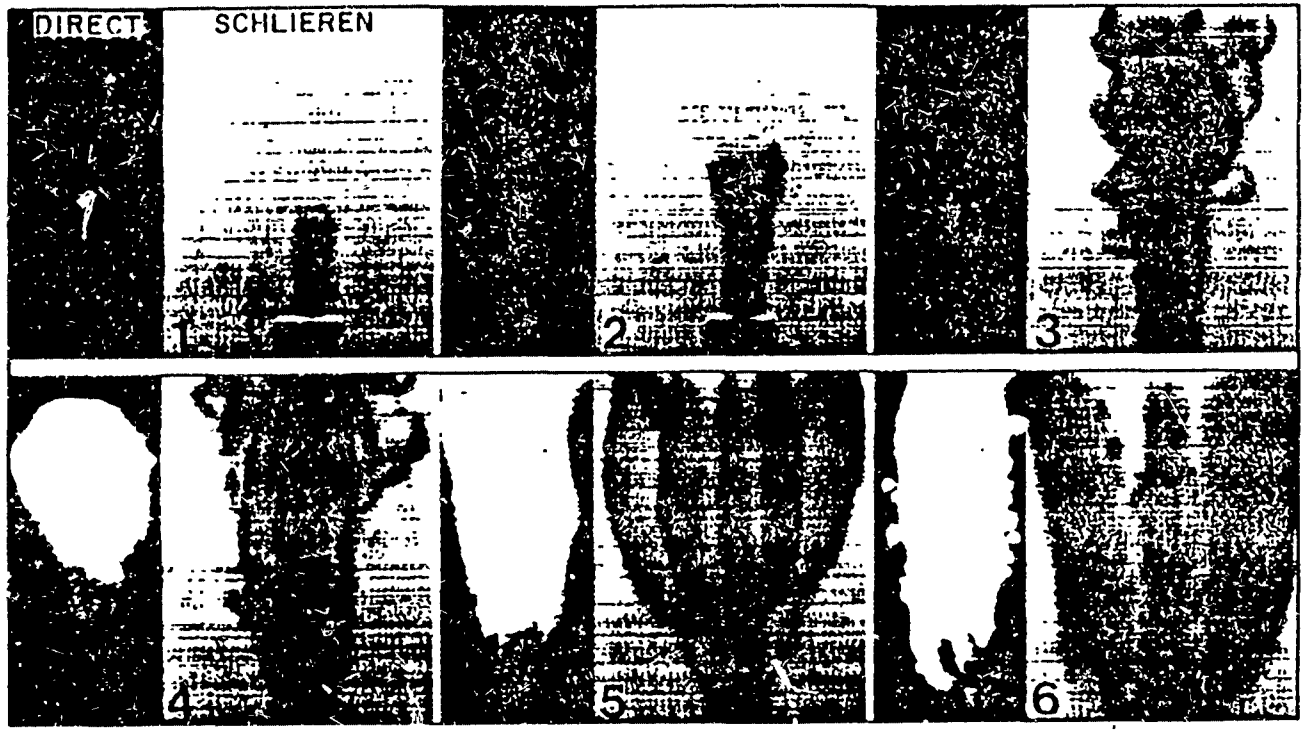


Fig. 9 Ignition Sequence of Poly(BAMO/NMMO) with 17.6 Percent Boron in Air with a Heat Flux of 490 W/cm^2 using CO_2 Laser. (The time from initial laser heating for pictures 1 through 6 are 5.0, 6.0, 10.0, 17.5, 42.0, and 140.5 ms, respectively. Ignition takes place in the gas phase region at 10.0 ms.)

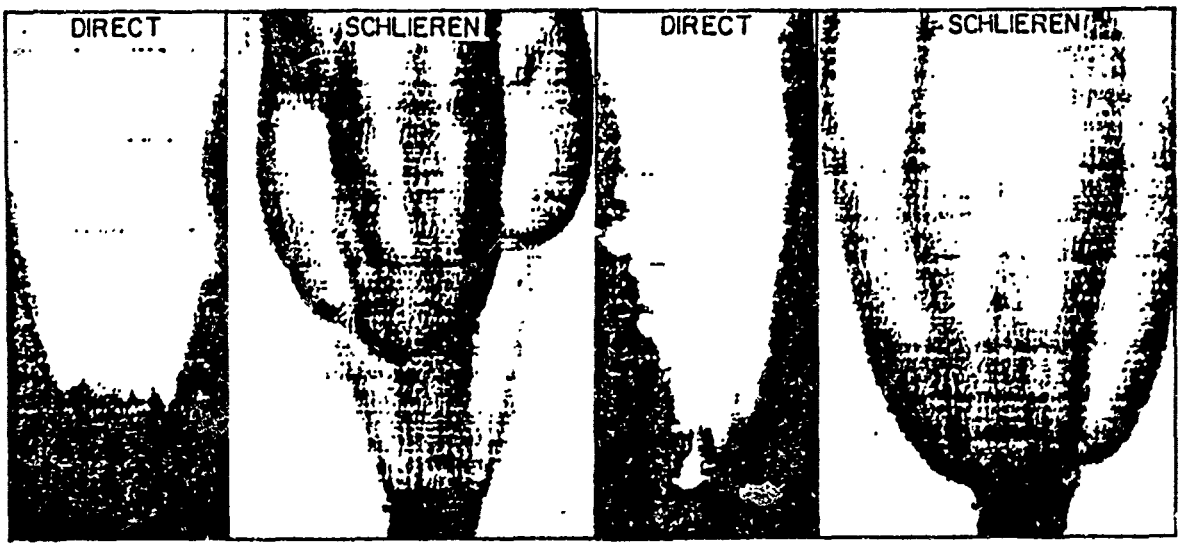


Fig. 10 Direct and Schlieren Photographs of the Plume from a Pyrolyzing Boron/[BAMO/NMMO] Solid Fuel at 37 ms Just Before the Flame Reaches the Sample Surface

Fig. 11 Direct and Schlieren Photographs of the Plume from a Burning Boron/[BAMO/NMMO] Solid Fuel at 52 ms Just After the Flame Reaches the Sample Surface

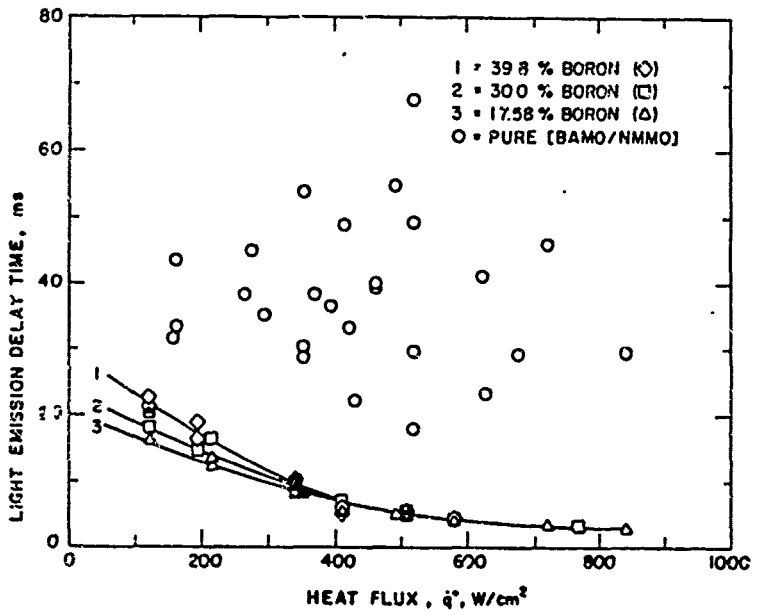


Fig. 12 Effect of Incident Heat Flux on Light Emission Delay Time for BAMO/NMMO Solid Fuels with Various Boron Weight Percentages

flux increases. As the boron loading percentage increases from 17.58 to 39.8, the delay time increases slightly at low energy fluxes (below 300 W/cm^2). Similar to the reasoning for the boron/HTPB fuels, this increase is believed to be caused by the increase of the effective volumetric specific heat due to the increase of boron weight percentage while the absorptivity changes little as boron loading increases above 17.58 percent. As a result, the effective heating rate of the plume is decreased with the increase in boron loading causing the delay time to increase.

Crossflow Ambient Conditions

All the above results were obtained under quiescent ambient conditions. It was noted that the attenuation of the laser energy flux by the pyrolysis products, especially the boron particles, could strongly influence the delay times for onset of first light emission and ignition. To study this effect, a crossflow setup for blowing particles away from the top portion of the plume was utilized. The horizontal crossflow nozzle is situated at a vertical distance far enough from the sample surface so that convective cooling of the sample surface is negligible. Under the condition of crossflow, the mixing of oxygen with pyrolysis products of solid fuel is enhanced, and the attenuation of the laser energy flux is minimized.

Figure 13 shows the schlieren and direct pictures of the ignition of pure HTPB in a crossflow at 30 ms under a laser heat flux of 760 W/cm^2. The horizontal white line in the direct image represents the surface of the sample. The location of the crossflow is shown on the left portion of the picture. After 30 ms, the first light emission was observed 7 mm from the surface of the sample, near the lower edge of the crossflow jet. The luminous flame grew very slowly, extinguished, reignited at the same location, and once again extinguished. This process repeated for the duration of the laser heating which lasted for 600 ms. During this process, an abrupt increase in light intensity was not observed because the pyrolyzed gases, in the absence of boron, did not absorb enough laser energy to cause ignition.

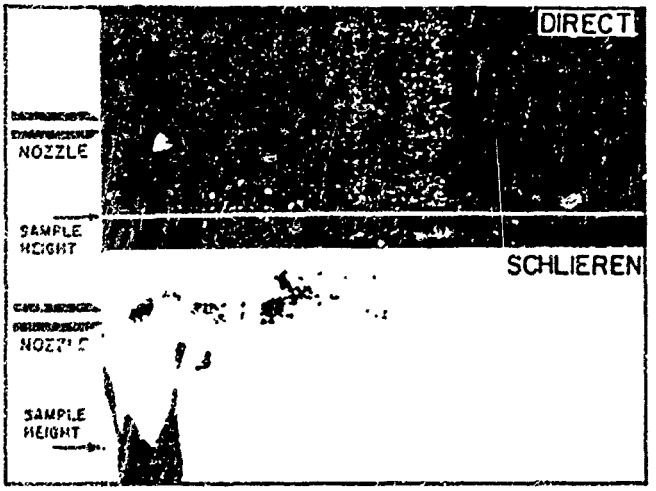


Fig. 13 Direct and Schlieren Pictures Showing the First Detection of Light Emission in the Gas Phase for Pure HTPB at 30 ms under a Heat Flux of 760 W/cm^2.

Figures 14 and 15 show the ignition of boron/HTPB (10/90) solid fuel in the crossflow with a 280 W/cm^2 energy flux. Figure 14 shows the first light emission at 35 ms. At 152 ms, an abrupt increase in light intensity was observed in a region above the sample surface. This event is followed by an intense luminous flame which lasted for 650 ms. At this time, the laser was cutoff; however, the luminous flame remained burning for an addition 140 ms. This suggests that the solid fuel sample was able to store enough thermal energy to continue the pyrolysis of gases and particles; thus the supply of fuel-rich species to the reaction zone was maintained. The eventual extinction after laser cutoff suggests that the rate of heat release from the surface and gas-phase reactions was less than the rate of heat loss.

The delay times for first light emission and an abrupt increase in light intensity for both boron/HTPB and boron/[BAMO/NMMO] solid fuels were obtained in crossflow conditions and are summarized in Table 1. The heat flux was kept constant at 280 w/cm^2 for all tests; however, the crossflow velocity had to be increased for boron/[BAMO/NMMO] solid fuel because of the high pyrolysis velocity of the material. The upstream pressure of the crossflow nozzle was set at 170 and 350 KPa for boron/HTPB and boron/[BAMO/NMMO] solid fuels, respectively. In contrast to the quiescent ambient results, the

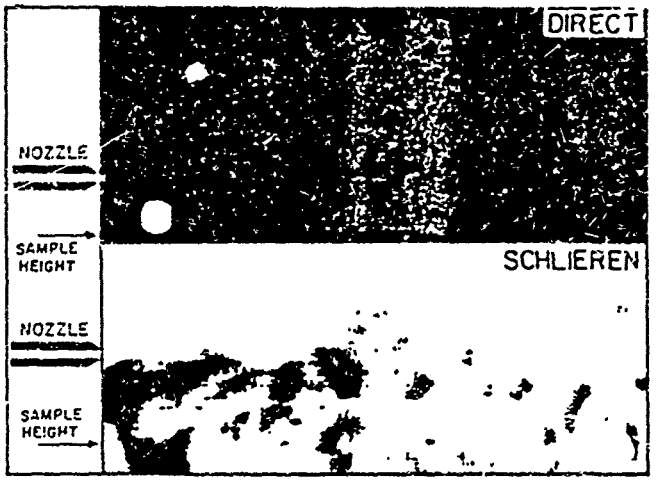


Fig. 14 First Light Emission of Boron/HTPB (10/90) Solid Fuel at 35 ms, Incident Laser Heat Flux of 280 W/cm^2

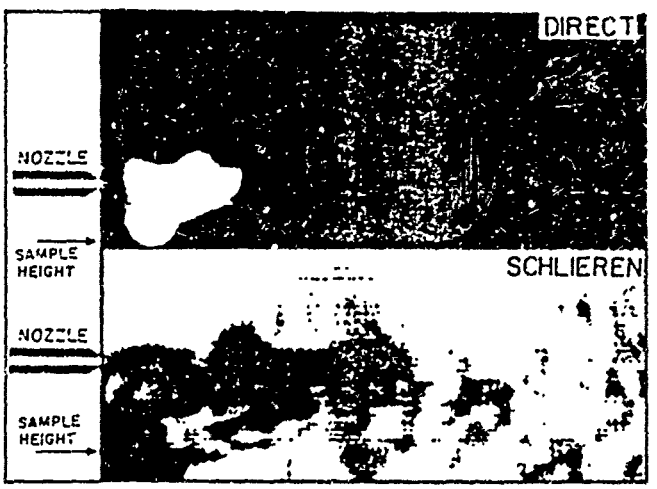


Fig. 15 Abrupt Increase in Light Emission of Boron/HTPB (10/90) After 152.0 ms in a Crossflow Laser Ignition Experiment

crossflow results show that the delay times decreased continuously for both boron/HTPB and boron[BAMO/NMMO] solid fuels as the boron weight percentage increased.

This trend is believed to be caused by the enhanced mixing of air with the pyrolysis products in the plume. The enhanced mixing of oxygen with the pyrolyzed products (specifically the boron particles) is believed to cause the boron particles to react with oxygen and to release energy to the gas-phase species. Thus, the high boron loadings continue to decrease the delay time because the absorptivity and volumetric specific heat effects are counter-balanced by the increased boron reactions. The increased boron reactions in the crossflow tests were evidenced by the appearance of glowing particles, which were not present in the quiescent tests, before the abrupt increase in light intensity associated with the gas-phase ignition.

After laser cutoff, the solid fuel samples which contained the highest boron percentage in HTPB remained burning the longest. In the case for boron/[BAMO/NMMO] solid fuel, the samples burned completely after laser cutoff due to the energetic nature of BAMO/NMMO copolymer. Whether the energetic nature of the binder actually changed the mechanisms of boron combustion, further studies are needed. In such studies, one has to determine the chemical composition and physical structure of the residues recovered.

TABLE 1 DELAY TIMES FOR HTPB AND BAMO/NMMO SOLID FUELS UNDER CROSSFLOW CONDITIONS WITH LASER ENERGY FLUX OF 280 W/cm^2

Fuel	Boron %	First Light (ms)	Abrupt Increase (ms)	Laser Cutoff (ms)	Extinction (ms)
HTPB	0	none	none		
HTPB	1	none	none		
HTPB	10	35.0	152.0	650.0	790.0
HTPB	20	33.5	30.0	664.0	791.0
HTPB	30	24.0	29.0	656.0	825.0
B/N	9	584.5	578.0	612.0	612.0
B/N	17.58	144.0	537.0	604.0	burned completely
B/N	29.06	82.5	218.0	623.0	burned completely
B/N	39.80	76.0	120.0	640.0	burned completely

CONCLUSIONS

Tests performed in quiescent conditions for boron/HTPB solid fuels show that an increase in boron weight percentage (up to 20%) causes a decrease in first light emission delay time. Further increase in boron percentage causes the delay time to increase. This change in trends can be explained by the effects of volumetric specific heat of the pyrolysis products and absorptivity of the two-phase mixture on the rate of increase of the mixture temperature. The results from crossflow tests show that the delay time decreases monotonically with increases in boron loading percentage for both types of solid fuels. With crossflow, the effects of absorptivity and volumetric specific heat are counter-balanced by the enhancement of the boron reactions with oxygen caused by the enhanced mixing of air with the plume products. For both quiescent and crossflow conditions, the ignition process initiated in the region above the sample surface and then propagated toward the surface to enhance the condensed-phase reactions.

ACKNOWLEDGMENT

This work represents a part of the research results obtained under Contract No. N00014-86-K-0468 sponsored by the Office of Naval Research, Arlington, VA, under the management of Drs. Richard S. Miller and Gabriel D. Roy. The authors would like to thank Dr. Gerald Hanser of Aerojet Propulsion Company and Dr. Gordon Jensen of the United Technology's Chemical Systems Division for providing some of the solid fuels used in this study.

REFERENCES

1. Kashiwagi, T., MacDonald, B. W., Isoda, H., and Summerfield, M., "Ignition of Solid Polymeric Fuels by Oxidizing Gases," AFOSR-TR 70-2935, 1970.

2. Beyer, R. B. and Fishman, N., "Solid Propellant Ignition Studies with High Flux Radiant Energy as a Thermal Source," Solid Propellant Rocket Research, edited by Summerfield, M., Progress in Astronautics and Aeronautics, Vol. 1, 1960, pp. 673-672.

3. Ohlemiller, T. J. and Summerfield, M., "Radiative Ignition of Polymeric Fuels in an Oxidizing Gas," AFOSR-TR 69-2147, 1969.

4. Baer, A. D. and Ryan, N. W., "Evaluation of Thermal-Ignition Models from Hot-Wire Ignition Tests, Combustion and Flame, Vol. 15, 1970, pp. 9-22.

5. Cook, J. R., "State of Pyrolaser/Fiber Optic Ignition," JANNAF Workshop on Ignition of Low Sensitivity Gun Propellant Charges, The Pennsylvania State University, April 12, 1988.

6. Kashiwagi, T., "Experimental Observation of Radiative Ignition Mechanisms," Combustion and Flame, Vol. 34, 1979, pp. 231-244.

7. Kuo, K. K., Principles of Combustion, Chapter 10, John Wiley and Sons, New York, 1986, pp. 734-788.

8. Manser, G. E., Fletcher, R. W., and Knight, M. R., "High Energy Binders," Final Report, Morton Thiokol, Inc., Contract No. N00014-82-C-0800, June 1985.

9. Childs, L. B., King, M. K., and Martin, I. D., "Improved Propellants for Throttleable Solid-Air Augmented Rockets," AFRPL-TR-71-127, Vol. II, 1971.

10. Yuasa, S. and Takeno, T., "Ignition and Combustion of Mg/Al Alloy Particle Clouds in a Hot Gas Stream," 19th Symposium (International) on Combustion, 1982, pp. 741-748.

Combustion Behavior and Thermophysical Properties of Metal-Based Solid Fuels

D. M. Chen,* W. H. Hsieh,† T. S. Snyder,‡ V. Yang,§ T. A. Litzinger,§ and K. K. Kuo¶
Pennsylvania State University, University Park, Pennsylvania 16802

Two metal-based solid fuels (magnesium-based and boron-based) have been studied to determine their combustion behavior and thermophysical properties. The burning rate for the magnesium-based (Mg/PTFE/Viton A) solid fuel was found to increase monotonically with ambient pressure and to follow the Saint Robert's law in both air and nitrogen environments. The fuel, however, burned 10% slower in air than in nitrogen. The slower burning rate in air is postulated to result from the entrained oxygen which competes with fluorine to react with magnesium. Because of the lower heat of formation of M_gO vs M_gF_2, the near-surface heat release is reduced when the oxygen is present, thus reducing the burning rate. This reasoning is also supported by results obtained from the companion pressure deflagration limit (PDL) and ignition tests, which show that the combustion of the magnesium-based fuel has a higher PDL and a longer ignition delay time in air than in nitrogen. Results from the study of ignition and combustion characteristics of boron-based solid fuels show that boron can significantly reduce the ignition delay times of poly(BAMO/NMMO). In determining the thermophysical properties of fuel samples, a subsurface temperature-measurement method was developed to quantify the temperature dependence of the thermal diffusivities of fuel samples. Results show good agreement with those obtained with the laser-flash method.

Nomenclature

PDL = pressure deflagration limit, kPa
r_b = burning rate, mm/s
p = pressure, kPa
K = thermal conductivity, W/K-cm
ρ_p = density, g/cm^3
C_p = specific heat, J/g-K
$\dot{q}_{sub}$ = net heat release from subsurface, W/g
α = thermal diffusivity cm^2/s
L = sample thickness, cm
t_c = characteristic rise time, s
τ = laser pulse time, s
t = time, s
$t_{1/2}$ = time to reach one-half of maximum value, s

Introduction

IN the search for new and improved propulsion technology, the solid-fueled ramjet engine has become an attractive candidate because of its simplicity and high performance. Among the various solid fuels that are under consideration for ramjet use, the boron-based and magnesium-based fuels are the most promising because of the high volumetric heating value of boron and the high combustion efficiency of magnesium. However, the poor ignition behavior of boron particles usually leads to lower combustion efficiency, making them impractical for use in an actual system. On the other hand, magnesium particles possess superior ignition behavior but offer considerably lower heat of reaction. Thus, methods of enhancing the combustion efficiency of boron and retaining the ignition characteristics of magnesium are essential in order to render these fuels feasible for propulsion applications.

Two types of solid fuels were considered. The first contained magnesium with polytetrafluoroethylene (PTFE) and vinylidene fluoride w/perfluoropropylene (Viton A). The second contained boron with a highly energetic binder, 3,3-bis (azidomethyl) oxetane/3-nitratomethyl 3-methyloxetane [poly-(BAMO/NMMO)]. To date, efforts to examine the fundamental ignition and combustion behavior of these fuels have been few. Peretz[1] studied various thermochemical properties of several metal/fluorocarbon fuels for ramjet applications. Results indicate that not only is magnesium a desirable metal additive for fluorocarbon solid fuels, but boron can also be burned effectively with fluorocarbons. Kubota and Serizawa[2] performed detailed experimental work on the combustion of magnesium-based solid fuels containing magnesium, PTFE, and a small amount of Viton A. They observed that the burning rate of this type of solid fuel increases with increased magnesium content but decreases with increased particle size. The significance of the exothermic reactions immediately above the burning surface on the combustion process was also addressed.

Manser et al.[3] recently developed a number of highly energetic binders. In view of the large positive value of the heat of formation associated with poly(BAMO/NMMO), they claimed that a theoretical increase of the specific impulse by 5 s is possible when this polymer is used as a binder in a minimum-smoke propellant system. The total energy release from the fuel was found to increase significantly with addition of percentages of boron to poly(BAMO/NMMO).

The major purpose of this paper is to study the fundamental ignition and combustion characteristics of Mg/PTFE/Viton A and boron/poly(BAMO/NMMO) solid fuels and to develop a convenient method for measuring the thermophysical properties of these two types of solid fuels. The specific objectives are

1) to determine the burning rates of both fuels as functions of pressure and ambient gas;

2) to characterize the ignition and combustion behavior by performing CO_2 laser ignition combustion tests, x-ray diffrac-

Presented as Paper 88-3041 at the AIAA/ASME/SAE/ASEE 24th Joint Propulsion Conference, Boston, MA, July 11-13, 1988, received Aug. 22, 1988, revision received Sept. 16, 1989. Copyright © 1988 by the American Institute of Aeronautics and Astronautics, Inc. All rights reserved.

*Associate Scientist, Chung-Shan Institute of Science & Technology, R.O.C.

†Assistant Professor, Department of Mechanical Engineering. Member AIAA.

‡Graduate Assistant, Department of Mechanical Engineering. Student Member AIAA.

§Associate Professor, Department of Mechanical Engineering. Member AIAA.

¶Distinguished Professor, Department of Mechanical Engineering. Associate Fellow AIAA.

tion analysis, low-pressure deflagration limit (PDL) tests, and microscopic examinations; and

3) to deduce the thermophysical properties from the measured subsurface temperature profiles (STP).

Experimental Approach

A windowed strand burner and a CO_2 laser facility were used to study the ignition and combustion behavior of these two types of solid fuels and to characterize their thermophysical properties under well-controlled conditions. A brief description of the test facilities is given below, followed by a discussion of results obtained for each of the metal-based solid fuels.

Strand Burner

Figure 1 shows a schematic diagram of the windowed strand burner. A fuel sample (5 mm in diameter and 77 mm in length) was mounted vertically in the chamber. Ignition of the sample was achieved by passing an electrical current into a nichrome wire which pierced through the test sample about 3 mm from the top surface. A scale was optically superimposed on the image of the solid-fuel sample, using a 75 × 75 mm semitransparent mirror. To visualize the burning process, a video-recording system was employed to photograph the motion of the burning surface inside the strand burner and the optically superimposed scale. With this technique, the burning rate could be determined precisely from the length of the sample burned in a certain time duration. In addition to the visualization study, an imbedded fine-wire thermocouple (platinum/platinum-13% rhodium) with a diameter of 50 μm was used to measure the temperature profiles in both the subsurface and surface regions. A more detailed discussion of the overall strand burner system is given in Ref. 4.

The strand burner was used to study both the steady-state burning behavior and the PDL. During each steady firing, the chamber pressure was maintained at a prescribed level by means of a computer-controlled gas supply system. For the PDL tests, the chamber was depressurized at a rate of 1.1 kPa/s. The extinguishment point could then be identified from the measured pressure-time trace. After each test firing, the solid residues were collected for microscopic examination and x-ray diffraction analysis.

CO_2 Laser Ignition/Combustion Facility

A high-powered CO_2 laser (Coherent Super 48) capable of generating 800 W in continuous wave mode was used for the ignition and combustion studies. Figure 2 shows a schematic diagram of the facility. In order to generate a relatively uniform beam, a thin piece of sheet metal with a 7 mm-diam hole was used to allow only the most uniform portion of the laser beam to reach the sample surface. The resulting spatial variation of the beam intensity was $\pm 10\%$.[5] A test chamber (25 × 25 × 25 cm) was fabricated using 2.54-cm-thick plexiglass and a 1.25-cm-thick stainless steel top cover. The transparent nature of this chamber facilitated visual access to the ignition and combustion processes from all directions. Two high-quality glass windows were mounted on opposing sides of the chamber to allow for schlieren photography. A KCl window was installed in the top of the chamber to allow the laser to pass into the chamber when pressures other than atmospheric were needed.

A high-speed video system (Spin-Physics 2000) was used to record the dynamic behavior of the flame at a framing rate of 2000 pictures/s. The system accommodates two cameras capable of recording schlieren images and direct photographs simultaneously. The schlieren image can detect clearly the initiation of fuel gasification and its subsequent processes, whereas the direct photograph provides information about luminous flame development and burning characteristics.

In addition to its role in the ignition and combustion study, the CO_2 laser system was also used to conduct laser-flash tests for measuring the thermal diffusivities of the fuel samples. A 75-μm K-type (chromel/alumel) thermocouple was bonded to the bottom of the fuel sample having a specified thickness. As the laser flash irradiated the sample surface, the temperature detected by the bonded thermocouple was recorded by a Nicolet oscilloscope and could then be used to calculate the thermal diffusivity of the fuel.

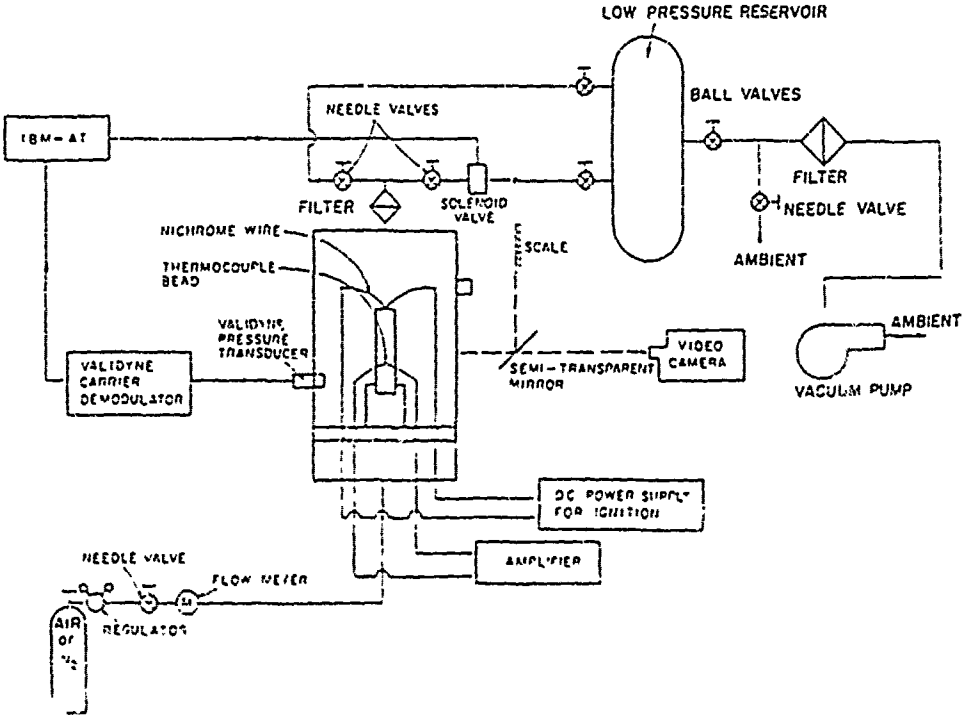


Fig. 1 Schematic of experimental apparatus used in strand-burner tests.

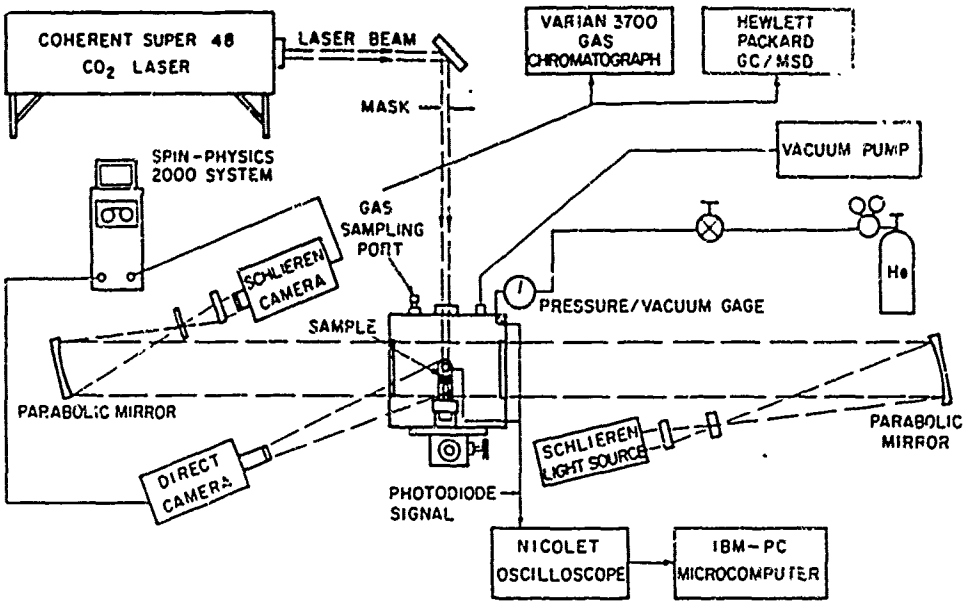


Fig. 2 Schematic of experimental apparatus used in CO_2 laser tests.

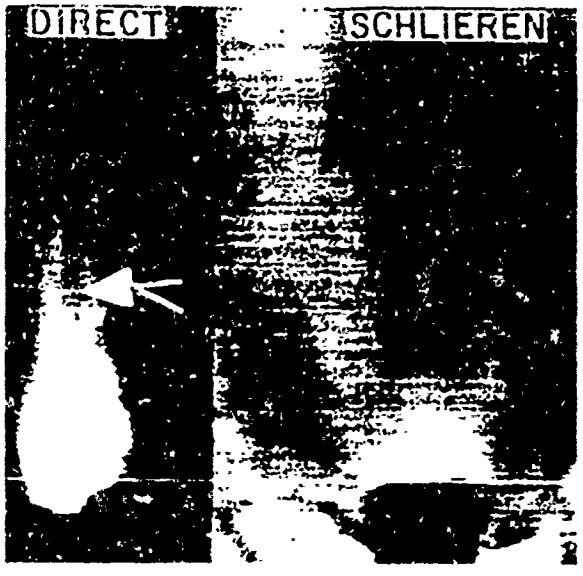


Fig. 3 Mg/PTFE/Viton A combustion in CO_2 laser test.

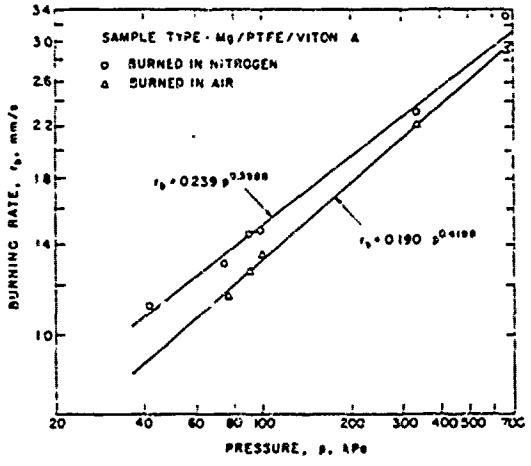


Fig. 4 Burning rate as a function of pressure for Mg/PTFE/Viton A in nitrogen and air.

Combustion Characteristics of Magnesium-Based and Boron-Based Solid Fuels

Magnesium-Based Solid Fuel

The magnesium-based solid fuels used in this study consisted of 50% fluorocarbons (PTFE and Viton A) and 50% magnesium powders with a mean diameter of 20 μm. Initial tests were performed in the CO_2 laser facility, and subsequent experiments in the strand burner. In both cases, not only did the luminous flame initiate at the surface, but it remained attached to the surface for the duration of the combustion period. Figure 3 shows a typical flame structure of the fuel following ignition. The ejection of magnesium particles from the burning surface can be observed as indicated by the arrow in the direct image. This phenomenon was also noted in the strand-burning tests using both air and nitrogen. However, the height of the luminous flame was much greater for combustion tests performed in air than for those performed in nitrogen. The ignition delay time for the magnesium-based fuel was also determined for various oxygen percentages. It increased from 43 ms to 52 ms as the oxygen concentration increased from 1.0% to 21.0%, respectively. These tests were performed at 100 kPa, with an incident heat flux of 400 W/cm^2 from the laser.

Figure 4 illustrates the dependence of the burning rate on the chamber pressure in two different gaseous environments. The burning rate was found to increase monotonically as the pressure increased, and to follow the Saint-Robert's law closely. It is interesting to note that despite the fuel-rich nature of the sample, the burning rate measured in nitrogen was consistently higher than that in air by approximately 10%. This observation is substantiated by the PDL results which show that the lowest pressures for sustaining stable combustion are 9.8 and 28.1 kPa for nitrogen and air, respectively. The fuel has a tendency to extinguish faster in air than in nitrogen. These results suggest that the burning characteristics of this type of solid fuel depend upon the composition of the ambient gas.

Figure 5 shows two temperature profiles obtained from 50-μm thermocouples imbedded in the solid fuel. The tests were performed at atmospheric conditions in both air and nitrogen. Both curves indicate a surface temperature (characterized by the inflection point in the temperature profile) in the neighborhood of 850°C, but with different spatial distributions depending on the gas environment. The temperature profile in the vicinity of the surface is steeper when the fuel was burned in nitrogen, suggesting a higher heat-transfer rate at the surface.

Based upon the above observations, it is believed that the oxygen in the air has an adverse effect on the regression rate, ignition, and extinction characteristics of the solid fuel containing magnesium and fluorocarbons. A proposed rationale to explain this phenomenon follows.

First, the surface regression is a local phenomena. The regression rate is determined mainly by the highly exothermic gas-phase and heterogeneous reactions occurring immediately above and on the surface, and the thermal properties of the solid fuel which control the thermal wave propagation. The processes away from the surface play a less significant role due to their weak effect on the local heat transfer to the surface region.

Second, the magnesium based solid fuel contained 50% magnesium, which is 17% greater than the stoichiometric ratio. Because of this, most of the magnesium powder did not burn completely in the near surface region. Instead, the powder was ejected from the surface as a result of the expansion processes of gaseous products generated by the pyrolysis and the solid-phase reaction of the fluorocarbons surrounding them.

Third, the gaseous products originating from the surface act as a freejet and entrain the ambient gas into the shear layer surrounding the sample boundary. Thus, during tests in air, oxygen can be entrained easily causing competitive oxidation and fluorination reactions with magnesium. Because the heat of oxidation for magnesium is approximately one-half of the heat of fluorination for magnesium, the total heat generated in the near-surface region is reduced when oxygen is present. This reduced heat release reduces the heat-transfer rate to the condensed phase and consequently decreases the regression rate.

This argument is substantiated by the subsurface temperature profiles measured in air and nitrogen environments (see Fig. 5). Results based upon the x-ray diffraction analysis of the combustion residues indicate that the major solid products for the case involving air were MgO, MgF_2, and carbon. However, for the pure nitrogen case, the major products were MgF_2, Mg, and carbon. Thus, the reaction of magnesium particles with oxygen in the gas phase is significant. Further investigation is needed to quantify the extent to which the oxidation reaction takes place in the near-surface region.

Based upon the above observations and the measured subsurface temperature profiles, the important physicochemical processes involved in the combustion of magnesium/fluorocarbon fuel in the presence of air can be characterized qualitatively. Figure 6 summarizes the entire process by identifying five distinct regions in both the gas and condensed phases. A thermocouple trace obtained from a test in air at 100 kPa is also included to show the approximate thermal wave profile. These five zones can be summarized as follows.

In zone 1, the temperature is below the exothermic decomposition temperature of Viton A (316 C) and only inert heating takes place. Zone 2 covers a temperature range from 316–530°C, corresponding to the decomposition temperatures of Viton A and PTFE, respectively. The thickness is about 170 μm at 1 atm. Exothermic decomposition of Viton A initiates in this zone and reaches its maximum rate at 471°C.[6] The major products from the pyrolysis of Viton A include HF, C_2F_2, C_2F_4, CHF_3, and other fluorocarbons and hydrofluorocarbons.[6] Chemical reactions between magnesium powders and the pyrolysis products of Viton A may also occur. Onset of the melting process of PTFE (330 C) occurs approximately 200 μm beneath the burning surface. However, as a result of the highly viscous nature of the molten PTFE, only restricted motions of magnesium particles are possible in this region.

Zone 3 is characterized by a rapid temperature increase

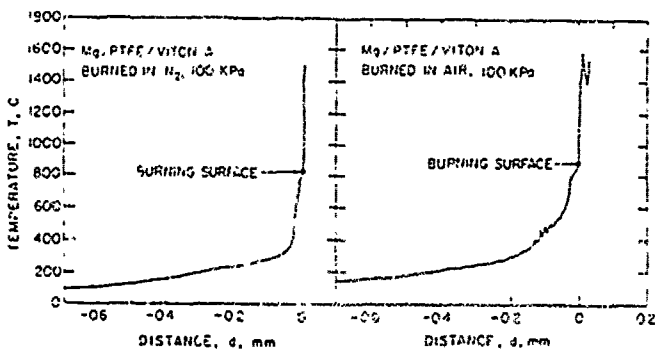


Fig. 5 Temperature profiles of Mg/PTFE/Viton A.

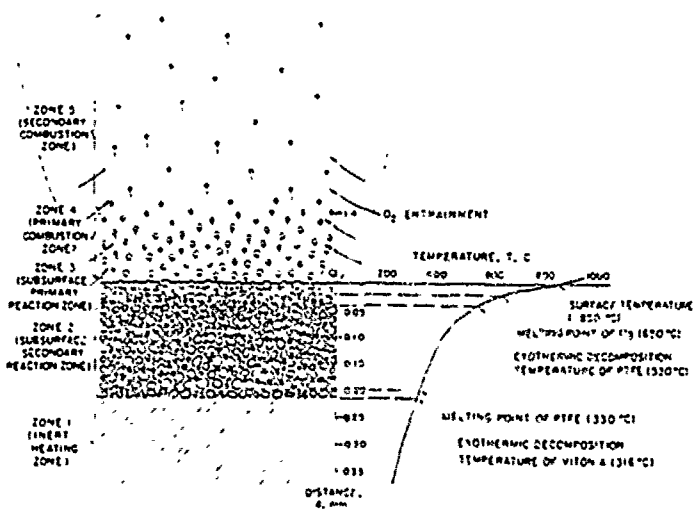


Fig. 6 Schematic showing temperature profile of subsurface region in a Mg/PTFE/Viton A sample.

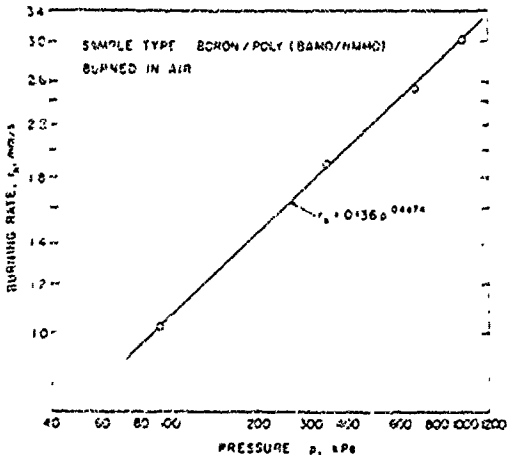


Fig. 7 Burning rate as a function of pressure for poly(BAMO/NMMO) with 17.6% boron.

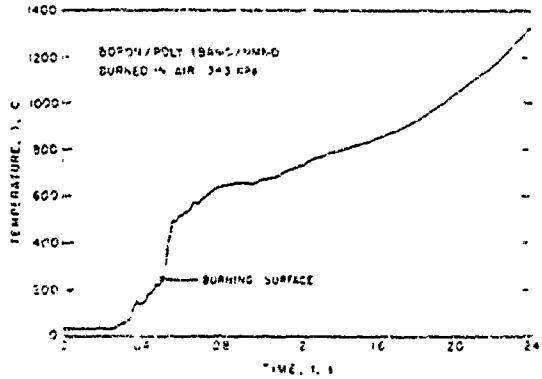


Fig. 8 Subsurface temperature profile of boron/poly(BAMO/NMMO) in air at 343 kPa.

within a thin layer of approximately 50 μm. The temperature ranges from 530°C to the surface temperature of 850°C. At 530°C, PTFE begins to decompose exothermically to liberate CF_4, C_2F_6, C_2F_4, C_3F_6, C_4F_8, other fluorocarbons, and possibly fluorine itself.[6] As the temperature further increases to 650°C, magnesium powders begin to melt. Reactions that may take place in this region are believed to be those of fluorine and fluorinated compounds with either liquid or gaseous magnesium (because the vapor pressure of magnesium at 850°C is about 50 mm Hg). These highly exothermic reactions may further enhance the gasification of PTFE, causing an imbalance of local forces. This process results in violent expulsion of magnesium particles from the surface.

Zone 4 is characterized by the high-temperature gradient in the vicinity of the burning surface. It is depicted by a bright flame associated with the exothermic gas-phase and heterogeneous reactions. As stated above, for combustion in air, oxygen may be entrained by the jet and react with molten magnesium powders near the outer region of the surface.

Zone 5 is rather far from the surface. For combustion in air, the major chemical process includes the reaction of magnesium vapor and O_2. As a result of its distance from the surface and its low flame temperature ($\sim$ 1600°C),[7] the effects of this region on surface-regression processes are insignificant.

Boron/Poly(BAMO/NMMO) Solid Fuel

In this work, the boron-based solid fuel sample contained a highly energetic copolymer, BAMO/NMMO, and 17.6% boron powder with a mean diameter of 0.5 μm. From the recorded video images, it was observed that the flame structure of the sample was affected by the testing pressure. At atmospheric conditions, only a faint gaseous flame appeared above the surface. As the ambient pressure was increased to 1034 kPa, a much brighter flame was observed, with many burning boron particles ejected from the surface.



Fig. 9 Ignition sequence of pure poly(BAMO/NMMO) in air with a heat flux of 150 W/cm^2 using CO_2 laser. Time from initial laser heating is 4.5, 5.5, 6.5, 88.0, 128.0, and 165.5 ms.

Figure 7 shows the strand-burning rate in air as a function of pressure. It followed the Saint-Robert's law with the burning rate given by $r_b = 0.136 p^{0.447}$. Figure 8 presents a measured temperature profile obtained, using a 50 μm R-type thermocouple embedded in a boron/poly(BAMO/NMMO) sample, with an ambient pressure of 343 kPa. The burning-surface temperature, indicated by a sudden temperature jump at the burning surface, was about 250°C, which was relatively low when compared to magnesium-based solid fuels. The burning-surface temperature increased monotonically with testing pressure, ranging from 220°C at 100 kPa to 310°C at 1030 kPa. The temperature-time trace presented in Fig. 8 shows several ripples between 100°C and 250°C; these are believed to be caused by the subsurface reaction of the binder.[3-10] In this particular test, the maximum measured gas-phase temperature was about 1400°C. However, in some tests, the measured temperature-time traces showed maximum temperatures higher than 1715°C.

To further enhance understanding of the ignition and combustion behavior, the boron-based fuel samples were also tested in the CO_2 laser facility. Figure 9 shows an ignition sequence of the pure poly(BAMO/NMMO) under CO_2 laser heating. The left image is a direct picture, and the right image is a schlieren picture. The magnification of the direct image is twice that of the schlieren, and the sample is a 5 mm cube.

Pyrolysis of the solid fuel was first noted after 4.0 ms in the schlieren picture. The gases formed a jet with a mean velocity of about 10 m/s. Within a distance of 8 mm from the surface, the jet appeared to be laminar in nature and became turbulent farther away from the surface. The gases gradually absorbed the incident laser energy and finally ignited after 128 ms. This ignition process is evident in the direct picture and is an indication of a gas-phase ignition process. Immediately following ignition, the flame propagated down toward the surface to further enhance the condensed phase reactions. The copolymer extinguished following laser cutoff at 200 ms.

Figure 10 shows the ignition process of poly(BAMO/NMMO) containing 17.6% boron. Gasification was noted at 4.5 ms after onset of the CO_2 laser beam. The pyrolyzed gaseous jet was less turbulent than that evolved from the pure poly(BAMO/NMMO) sample. Changes in the jet characteristics are believed to be dependent upon the boron content in the sample which acts to dampen the turbulent mixing process.[11] Because the boron is initially ejected before burning, the solid boron particles in the gas phase absorb the incident laser energy, thus raising the temperature in the gas phase to initiate chemical reaction and lead to ignition. The increase of absorption due to the presence of boron in the gas phase has been verified by laser-attenuation tests with various gases or solid-fuel samples.[5] As a result, the boron addition decreases

the ignition delay time to 10 ms, compared to 128 ms for the pure poly(BAMO/NMMO).

Picture 6 in Fig. 10 shows many boron particles burning in the gas phase following ignition. After laser cutoff, the sample extinguished momentarily and then reignited. The reignition, which was observed for the boron-containing fuels but not for the pure copolymer, is believed to be the result of an increase in thermal diffusivity caused by the boron addition, which allows the thermal wave to penetrate further into the solid fuel.

Figure 11 shows the ignition delay times for pure poly (BAMO/NMMO) and samples containing 17.6 and 30% boron as a function of heat flux. The pure poly(BAMO/NMMO) fuel exhibited random ignition characteristics for all heat fluxes. When boron was added, the delay time became shorter and reproducible. The behavior of boron/poly(BAMO/NMMO) is distinctly different from that of pure poly(BAMO/NMMO) due to the effects of boron particles on the fluid dynamics and radiative absorption. In the pure poly(BAMO/NMMO) case, the high turbulence level in the gas phase caused the pyrolyzed gases to be heated more uniformly; thus, no local high-temperature region could be established easily in the gas phase.

On the other hand, when boron is added, the gas phase becomes less turbulent due to the damping effect of submicron boron particles present in the pyrolyzed gases. This introduces a smaller heat-transfer rate within the pyrolyzed gases and causes a local high-temperature region to be established more readily. In addition, the radiative absorption by the pyrolyzed gases mixed with boron particles is significantly increased. The ignition delay time of boron/poly(BAMO/NMMO) is, therefore, much shorter than that of pure poly(BAMO/NMMO).

Thermophysical Property Characterization

Both subsurface temperature profile (STP) and laser-flash methods were used to evaluate the thermal diffusivities and conductivities of the fuel samples. Other properties, such as densities and specific heats, were obtained from the open literature. A brief description of these two measurement techniques is given below, followed by a discussion of results.

Subsurface Temperature Profile (STP) Method

In order to obtain a temperature profile of the subsurface region during combustion, an R-type fine-wire thermocouple with a diameter of 50 μm was embedded in a vertically mounted solid fuel sample. The sample was then ignited using a nichrome wire and burned down into the imbedded thermocouple. In this manner, both the subsurface and gas-phase temperature profiles were obtained. The subsurface temperature profile could be used to deduce the thermal diffusivity and conductivity as functions of temperature.

The STP method is based upon a one-dimensional heat-conduction equation. In order to simplify the analysis, a moving coordinate system was used with its origin located at the instantaneous burning surface. Using this coordinate system, the heat-conduction equation becomes[12,13]

$$\frac{\mathrm{d}}{\mathrm{d}x}K\frac{\mathrm{d}T}{\mathrm{d}x}-\frac{\mathrm{d}(\rho_p r_p C_p T)}{\mathrm{d}x}+\rho_p \dot{q}_{sub}=0 \qquad (1)$$

where $\dot{q}_{sub}$ is the net heat release in the subsurface region of the fuel sample. This term vanishes if there is no chemical reaction within this region (i.e., the inert heating region).

Integration of Eq. (1) gives

$$K\frac{\mathrm{d}T}{\mathrm{d}x}\bigg|_x - K\frac{\mathrm{d}T}{\mathrm{d}x}\bigg|_{-\infty} = \int_{-\infty}^{x}\frac{\mathrm{d}(\rho_p r_b C_p T)}{\mathrm{d}x}\,\mathrm{d}x$$

$$= \int_{T(-\infty)}^{T(x)} \rho_p r_b C_p\,\mathrm{d}T \qquad (2)$$

The density and specific heat are evaluated using a mass-averaged value of the ingredients in the solid fuel sample. Rearranging Eq. (2) and assuming that the heat flux is zero at $x = -\infty$, the thermal conductivity as a function of temperature becomes

$$K(T) = \int_{T(-\infty)}^{T(x)} \rho_p r_b C_p\,\mathrm{d}T \Big/ \frac{\mathrm{d}T}{\mathrm{d}x}\bigg|_x \qquad (3)$$

where the local temperature gradient $\mathrm{d}T/\mathrm{d}x$ can be calculated from the measured subsurface temperature profile. By definition, the thermal diffusivity can be deduced from the relation

$$\alpha(T) = K/(\rho_p C_p) \qquad (4)$$

Because the STP method was used to deduce the thermal conductivity and diffusivity of the testing sample in the inert region, the thermocouple bead did not experience rapid temperature variations and thus was able to measure the temperature profile very accurately. The characteristic time of the thermocouple used in this study was about 10 ms,[14] which is much smaller than heat-conduction time within the inert region. Measurement errors caused by velocity and radiation effects[15] are not present since the thermocouple is embedded in a solid, opaque fuel sample. Because of the small diameter of the thermocouple wire, heat losses caused by conduction from the thermocouple bead are also negligible.[15] The largest error introduced into the STP method (± 10°C) comes from the data acquisition and reduction procedures.

Laser-Flash Method

The laser-flash method[16] was also used to determine the thermal diffusivity of the solid fuel samples. In this method, a short laser pulse was given to the top surface of the sample. A thermocouple was mounted to the bottom surface of the

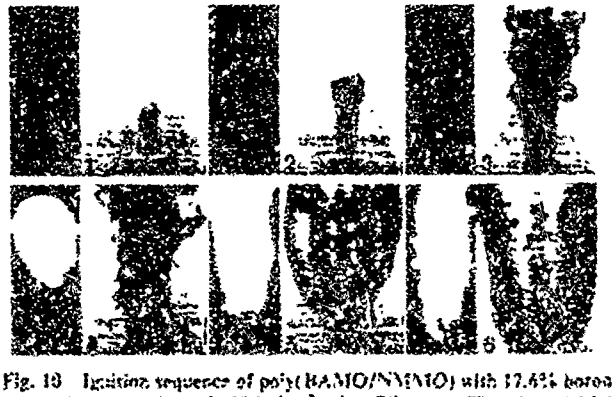


Fig. 10 Ignition sequence of poly(BAMO/NMMO) with 17.6% boron in air with a heat flux of 490 W/cm² using CO_2 laser. Time from initial laser heating is 5.0, 6.0, 10.0, 17.5, 42.0, and 140.5 ms.

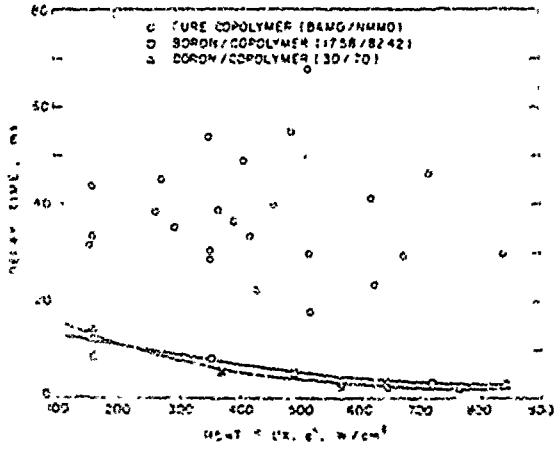


Fig. 11 Ignition delay time vs heat flux for pure poly(BAMO/NMMO) binder.

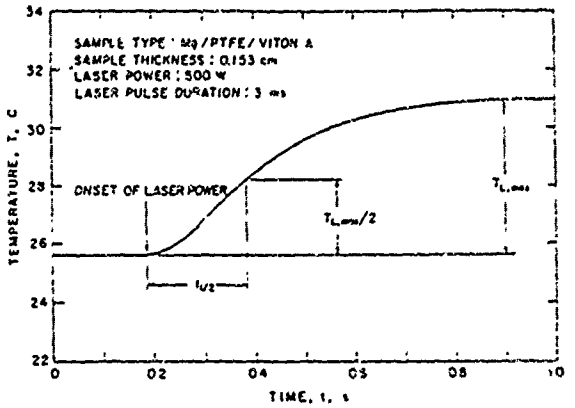


Fig. 12 Temperature-time trace from laser-flash test.

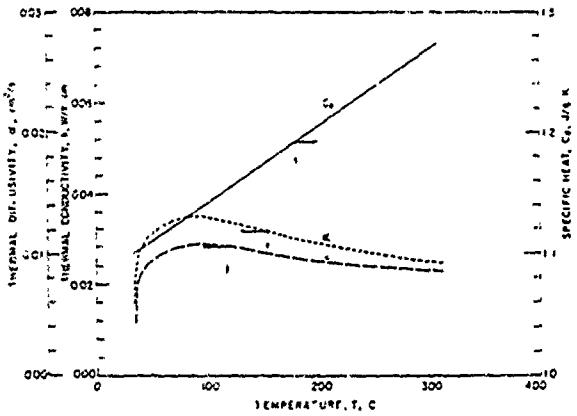


Fig. 13 Thermophysical properties of Mg/PTFE/Viton A as functions of temperature from STP method.

sample to monitor the temperature rise as the energy from the top surface was conducted through the sample (thickness of 1 mm). Figure 12 shows a typical temperature-time trace from the thermocouple on the bottom surface. The temperature rises slowly and reaches a maximum value (T_L, max) after 800 ms.

If we assume that the solid fuel sample has a uniform initial temperature distribution and that the energy from the laser pulse is instantaneously and uniformly absorbed in a thin layer on the top surface, then the temperature rise on the bottom face can be expressed as[17]

$$T(L,t) = T_{L,\max}\left[1 + \frac{1}{2}\sum_{n=1}^{\infty}(-1)^n \exp\left(-\frac{n^2\pi^2}{L^2}\alpha t\right)\right] \quad (5)$$

When $T(L,t)/T_{L,\max} = 1/2$, the dimensionless quantity $\pi^2\alpha t/L^2$ must have a value of 1.37. Consequently, the thermal diffusivity becomes

$$\alpha = \frac{1.37L^2}{\pi^2 t_{1/2}} = \frac{0.139L^2}{t_{1/2}} \quad (6)$$

where $t_{1/2}$ is the time required for the bottom face to attain one-half of its maximum temperature. Equation (6) is accurate within 1% as long as the laser-pulse length is short enough to avoid any chemical reactions and the characteristic time of the sample (defined as $t_c = L^2/\pi^2\alpha$) is greater than 50 times the laser-pulse duration.[18] The characteristic time and the pulse duration thus determine the thickness of the solid fuel sample.

Heat losses by convection from the top surface during the laser-flash method was investigated by Mendelsohn.[19] He found that the heat loss by convection depends strongly upon

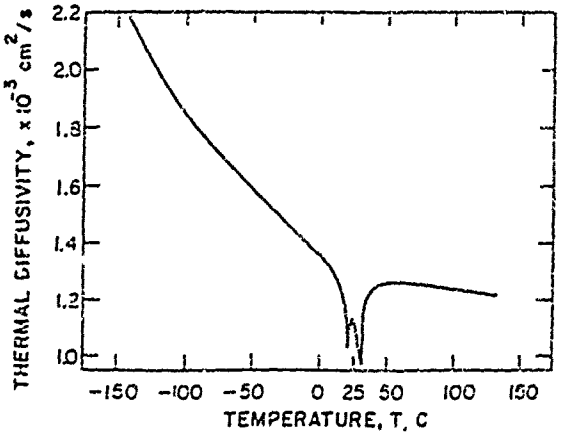


Fig. 14 Thermal diffusivity of PTFE between −140 and 125°C.[23]

the testing conditions, sample properties, and the Biot number. In order to minimize heat losses, the Biot number for the tests conducted in this study were of the order of 0.02, ensuring the reliability of the data. In addition, the sample was mounted on insulation material to minimize conductive losses from the bottom surface.

Thermophysical Properties of Magnesium-Based and Boron-Based Solid Fuels

Figure 13 shows the results obtained by the STP method for the magnesium-based solid fuel. The specific heat, thermal conductivity, and thermal diffusivity are plotted as functions of temperature. The specific heat and density of Mg, PTFE, and Viton A were obtained from Refs. 20–22, respectively. At a temperature of about 40°C, the values for both thermal conductivity and thermal diffusivity increase drastically. This sharp increase is believed to be caused by the rapid change in thermal diffusivity of PTFE that occurs near that temperature due to the crystalline transition (see Fig. 14).

To verify the measurements with the STP method, the laser-flash method was used to determine the thermal diffusivity of the magnesium-based solid fuel at 25°C. Using a sample thickness of 0.153 cm, a value of 1.6×10^{-2} cm²/s was measured; this agrees reasonably well with the value of 1.1×10^{-2} cm²/s obtained using the STP method. The laser-flash method was also used to determine the thermal diffusivity of boron/poly(BAMO/NMMO) solid fuel, and a value of 1.82×10^{-3} cm²/s was obtained at 25°C. Temperature profiles were measured for the boron/poly(BAMO/NMMO) fuel; however, the thermal diffusivity could not be calculated because the specific heat and density are not known.

Summary and Conclusions

The combustion behavior and thermophysical properties of magnesium-based and boron-based solid fuels have been studied using both a windowed strand burner and a CO_2 laser test facility. Results from strand-burner tests show that the magnesium-based fuel burns 10% faster in nitrogen than in air, indicating that oxygen has an adverse effect on the combustion behavior of this type of fuel. To verify the oxygen effect, ignition delay times were measured using different oxygen percentages. It was found that the ignition delay time decreased as the oxygen percentage decreased. PDL tests show that the fuel has a low pressure limit of 9.8 kPa for stable combustion in nitrogen, compared to 28.1 kPa in air. Subsurface temperature profiles of the magnesium-based fuel also indicate the adverse effect of oxygen on the combustion behavior.

The combustion behavior of the boron-based solid fuel was also studied in the strand burner, and its burning rate was found to have a slightly higher pressure dependence than that

for the magnesium-based solid fuel. Expressions for the burning rate of the magnesium-based fuel in air, in nitrogen, and for the boron-based fuel in air were found to be $0.190\,p^{0.42}$, $0.239\,p^{0.40}$, and $0.136\,p^{0.45}$, respectively. To investigate the effect of boron on the pure poly(BAMO/NMMO) energetic binder, ignition delay times were studied. Results showed that the random ignition delay times for the pure poly(BAMO/NMMO) became consistent when boron was added. From high-speed pictures of the ignition process, it was found that the boron particles affect the fluid dynamics for the gaseous jet. The boron also resulted in increased absorptivity in the gas phase. The combined result is a significant decrease in the ignition delay time.

An STP method was developed in order to determine the thermophysical properties as functions of temperature for these fuels, and the results were compared with those of a laser-flash method. Knowing the value for the specific heat of magnesium-based solid fuel as a function of temperature, the thermal conductivity and thermal diffusivity of the fuel were calculated from a subsurface temperature-time trace. The agreement of these two methods demonstrates the validity of the STP method.

Acknowledgments

This work represents a part of the research results obtained under Contract N00014-86-K-0468 sponsored by the Office of Naval Research, Arlington, VA, under the management of R. S. Miller and G. D. ROY. The authors would like to thank R. G. Shortridge of the Naval Weapon Supply Center and G. E. Manser of Aerojet Solid Propulsion Company for providing the solid fuels used in this study. The assistance of B. L. Fetherolf of The Pennsylvania State University is greatly appreciated in performing the CO_2 laser-ignition tests.

References

[1]Peretz, A., "Some Theoretical Considerations of Metal-Fluorocarbon Compositions for Ramjet Fuels," *8th International Symposium on Air-Breathing Engines*, AIAA, New York, 1987, pp. 398–403.

[2]Kubota, N., and Serizawa, C., "Combustion of Magnesium/Polytetrafluoroethylene," AIAA 86-1592, 1986.

[3]Manser, G. E., Fletcher, R. W., and Knight, M. R., "High Energy Binders," Final Rept., Thiokol Corp., Brigham City, UT, Contract N00014-82-C-0800, June 1985.

[4]Hsieh, W. H., "Study of Strand and Erosive Burning of NOSOL-363 Stick Propellants," Ph.D. Thesis, The Pennsylvania State Univ., University Park, PA, 1987.

[5]Fetherolf, B. L., Litzinger, T. A., and Kuo, K. K., "An Instrument for Measuring High-Power Laser Beam Profiles and Beam Attenuations," *The Review of Scientific Instruments*, Vol. 61, No. 1, 1990, pp. 7–10.

[6]Chen, D. M., Fetherolf, B. L., Snyder, T. S., Hsieh, W. H., Litzinger, T. A., and Kuo, K. K., "Ignition and Combustion Behavior of MTV Igniter Materials for Base Bleed Application," *First International Symposium on Special Topics in Chemical Propulsion: Base Bleed*, Athens, Greece, Nov. 23–25, 1988, Hemisphere, New York (to be published).

[7]Newman, R. N., and Payne, J. F. B., "The Anomalous Brightness of Magnesium-Air Flames," *Combustion and Flame*, Vol. 68, No. 1, 1987, pp. 31–41.

[8]Farber, M., Harris, S. P., and Srivastava, R. D., "Mass Spectrometric Kinetic Studies on Several Azido Polymers," *Combustion and Flame*, Vol. 55, No. 2, 1984, pp. 203–211.

[9]Oyumi, Y., and Brill, T. B., "Thermal Decomposition of Energetic Materials 14. Selective Product Distributions Evidenced in Rapid, Real-Time Thermolysis of Nitrate Ester at Various Pressures," *Combustion and Flame*, Vol. 66, No. 1, 1986, pp. 9–16.

[10]Oyumi, Y., and Brill, T. B., "Thermal Decomposition of Energetic Materials 12. Infrared Spectral and Rapid Thermolysis Studies of Azido-Containing Monomers and Polymers," *Combustion and Flame*, Vol. 65, No. 2, 1986, pp. 127–135.

[11]Snyder, T. S., Chen, D. M., Fetherolf, B. L., Litzinger, T. A., and Kuo, K. K., "Pyrolysis and Ignition of Boron-Based Solid Fuels for Ramjet Applications," *25th JANNAF Combustion Meeting*, Huntsville, AL, CPIA Pub. 498, 1988.

[12]Klein, R., Mentser, M., Von Elbe, G., and Lewis, B., "Determination of the Thermal Wave Structure of a Combustion Wave by Fine Thermocouples," *Journal of Physics and Colloid Chemistry*, Vol. 54, No. 6, 1950, pp. 877–884.

[13]Kubota, N., Ohlemiller, T. J., Caveny, L. H., and Summerfield, M., "The Mechanisms of Super-Rate Burning of Catalyzed Double Base Propellants," Dept. of Aerospace and Mechanical Sciences, Rept. 1087, Princeton Univ., Princeton, NJ, March 1973.

[14]Liperi, M., "Analisi Sperimentale Mediante Microtermocoppie Della Combustion Di Propellanti Solidi Con Proprieta Termiche Variabili," Tesi di Laurea, Dipartimento di Euregetica, Politecnico di Milano, 1986.

[15]Doebelin, E. O., *Measurement System, Application and Design*, McGraw-Hill, New York, 1975, Chap. 8.

[16]Parker, W. J., Jenkins, R. J., Butler, C. P., and Abbott, G. L., "Flash Method of Determining Thermal Diffusivity, Heat Capacity, and Thermal Conductivity," *Journal of Applied Physics*, Vol. 32, No. 9, 1961, pp. 1679–1683.

[17]Carslaw, H. S., and Jaeger, J. C., *Conduction of Heat in Solids*, 2nd Ed., Oxford Univ. Press, Oxford UK, 1959, pp. 92–101.

[18]Taylor, R. E., and Cape, J. A., "Finite Pulse-Time Effects in the Flash Diffusivity Technique," *Applied Physics Letters*, Vol. 5, No. 10, 1964, pp. 212–213.

[19]Mendelsohn, A. R., "The Effect of Heat Loss on the Flash Method of Determining Thermal Diffusivity," *Applied Physics Letters*, Vol. 2, No. 1, Jan. 1963, pp. 19–21.

[20]Chase, M. W., Jr., Davis, C. A., Downey, J. R., Jr., Frurip, D. J., McDonald, R. A., and Syverud, A. N., "JANNAF Thermochemical Tables," 3rd ed., *Journal of Physical and Chemical Reference Data*, Vol. 14 (Suppl.), No. 1, 1985, pp. 1462–1466.

[21]Marx, P., and Dole, M., "Specific Heat of Synthetic High Polymers. V. A Study of the Order-Disorder Transition in PTFE," *Journal of the American Chemical Society*, Vol. 77, Sept. 20, 1955, pp. 4771–4774.

[22]DuPont Technical Personnel, private communication, June 1988.

[23]Shelley, D. L., and Huber, S. F., "Thermal Diffusivity of Poly(tetrafluoroethylene) between −140° and 125°C," *8th Heat Conductivity Conference*, 1972, pp. 1067–1077.

IGNITION AND COMBUSTION BEHAVIOR OF MTV IGNITER MATERIALS FOR BASE BLEED APPLICATIONS

B. L. Fetherolf, D. M. Chen, T. S. Snyder,
T. A. Litzinger, and K. K. Kuo

Department of Mechanical Engineering
The Pennsylvania State University
University Park, PA 16802 U.S.A.

ABSTRACT

The pyrolysis and ignition characteristics of an igniter material composed of magnesium, Polytetrafluorethylene, and Viton A have been studied using a high-power CO_2 laser as the radiative heating source. Methods of analysis and the instrumentation employed were high-speed direct and schlieren photography to visualize the flame structure and gas-phase dynamics, near-infrared photodiodes to obtain ignition delay data, and probe sampling and a gas chromatograph/mass spectrometer to analyze the gaseous products evolved. Important test variables were incident heat flux, chamber pressure, and oxygen concentration. In addition, the effect of boron addition on the ignition behavior of the igniter charge was studied.

Ignition occurred on the sample surface under all test conditions. Experimental results indicated that the ignition delay time decreased monotonically as the incident heat flux was increased. Also, ignition times decreased as the ambient pressure or the ambient oxygen percentage was reduced; it is believed that this decrease is caused by competitive oxygen and fluorine reactions. The direct and schlieren images showed that the burning behavior was also distinctly different as the chamber pressure or oxygen partial pressure was reduced. At low pressures (~ 0.1 atm), no evident luminous plume evolution and gas-phase dynamics were observed during combustion, and the igniter material decomposed in large fragments. In an inert atmosphere, pure PTFE pyrolyzed into many fluorocarbon compounds and Viton A pyrolyzed into a variety of fluorocarbons and hydrofluorocarbons. However, for combustion of the composite MTV material in air and in an inert helium atmosphere, only hydrocarbon compounds, and CO and CO_2 for combustion in air, were observed. The addition of boron or Viton A to a basic Mg/PTFE composition significantly lowered the ignition delay time and the addition of boron also greatly enhanced combustion.

1. INTRODUCTION

The development of a reliable and efficient base bleed system to increase the range of artillery projectiles is currently of great interest. This system is designed to inject gases into the wake behind the projectile, increasing the base pressure and reducing the profile drag, which accounts for 50-75% of the total drag This reduction of the

drag will increase the range capabilities of the projectile. To insure sustained ignition of the base bleed propellant during the transition from the severe gun barrel environment to the ambient air and also during the subsequent flight, a supplementary, redundant igniter system is required. Thus, the base bleed igniter propellant must be able to sustain burning over a wide range of pressures, temperatures, and gaseous environments. It must also be durable enough to withstand the tremendous forces (~ 10,000 G's) of setback acceleration and the centrifugal forces of high-speed rotation (16,000 rpm).[1]

Most of the work to date on base bleed has concentrated on the aerodynamics and selection of candidate propellants. Several researchers have done theoretical calculations of the effect of base bleed systems on the aerodynamics of a projectile.[2-5] Experimental simulations have also been conducted to validate the effectiveness of base injection.[7,8] Kloehn and Rassinfosse have written a paper on the manufacture of base bleed propellants.[9] However, very few papers have been published to date on studies of the performance of practical base bleed motors and their supplementary redundant igniter systems.

Magnesium/PTFE/Viton A (MTV) igniter materials have been considered in solid rocket motor igniters and are now being tried experimentally in base bleed igniter systems. Peretz[10] stated that the use of magnesium as the metal counterpart is beneficial because it ignites and burns readily, thus promoting efficient combustion, and requires small amounts of oxidizing agent to burn. Viton A $(-C_5H_{3.5}F_{6.5}-)_n$, a copolymer of vynilidene fluoride and perfluoropropylene, is often added to Mg/PTFE formulations to increase homogeneity and facilitate fabrication. Because of its chemical similarity to Polytetrafluoroethylene [PTFE = $(-C_2F_4-)_n$], significant amounts of Viton A can be added without altering the combustion characteristics.

Peretz[11] listed the following advantages of the MTV formulation for use as an igniter material: high energy content, high degree of safety in preparation, low temperature and pressure dependence of the burning rate, ease and low cost of igniter pellet or grain fabrication, favorable aging characteristics, and stable burning at low pressures. He also listed several advantages of metal-fluorocarbon compositions in comparison with metal-hydrocarbon materials: higher volumetric heat release, higher rate of reaction, much higher density, excellent thermal stability (due to the high C-F bond strength), higher activation energy, and much lower production of soot due to the lower content of carbon. For magnesium, the standard gravimetric and volumetric heats of fluorination [producing $MgF_{2(s)}$] are almost exactly twice as much as those for oxidation [producing $MgO_{(s)}$].

The thermal decomposition of PTFE has been studied by Griffiths et al.[12] and Kubota and Serizawa.[13] Both groups used simultaneous DTA/TG with heating rates of 20 K/min[12] and 10 K/min.[13] Griffiths et al. observed that the decomposition of PTFE was endothermic in argon and nitrogen but was exothermic in air. However, Kubota and Serizawa observed the decomposition of PTFE in argon to be exothermic. Griffiths et al. also observed that the decomposition process became increasingly exothermic in all gaseous environments as an increasing amount of magnesium was added to the PTFE, and the nature of the decomposition in argon changed from purely endothermic for PTFE to purely exothermic for a Mg/PTFE (3:2) mix.

Kubota and Serizawa have published two of the more comprehensive papers on experimental studies of the combustion of Mg/PTFE materials.[13,14] Their material also contained 3% Viton A. Chen et al.[15] have conducted studies of the thermophysical properties and combustion of metal-based solid fuels in a strand burner, including the material that is the subject of this paper. They found that the burning rate was consistently higher in a nitrogen atmosphere than in air, and they also measured the thermal diffusivity to be 1.6×10^{-2} cm^2/sec. However, to the authors' knowledge, no experimental papers have been published to date on the ignition behavior of MTV igniter materials.

Characterization of the ignition behavior of the MTV material under a wide range of conditions is critical for determining the feasibility, applicability, and subsequent performance of the igniter. Radiative ignition has been often used in the studies of ignition behavior of solid propellants. The high-power CO_2 laser is now the prevailing choice for the radiant energy source due to its advantages of precise control of lasing time and energy flux, and a high level of beam intensity that simulates energy fluxes found in igniters and propulsive devices.

The overall objective of this research was to investigate the ignition behavior of a Mg/PTFE/Viton A igniter material under various ambient conditions, to gain a better understanding of the processes governing ignition, and to correlate this data with conditions experienced by a base bleed igniter. Specific objectives were: (1) to investigate the flame structure and gas-phase dynamics during the ignition transient under various pressures and ambient oxygen concentrations, (2) to study the variation of ignition delay time as a function of pressure, ambient oxygen concentration, and incident heat flux, and (3) to analyze the gaseous species produced during pyrolysis and ignition of the MTV material and during pyrolysis of PTFE and Viton A individually.

2. EXPERIMENTAL APPROACH

A diagram of the overall experimental set-up is given in Figure 1. The radiative energy source was a high-power Coherent Super 48 CO_2 Laser, capable of producing 800 watts of power in the continuous wave mode and 3500 watts in the pulsed mode with precise control of the power output and lasing time. A beam profile, uniform within ± 10% across the propellant sample surface, was obtained using an aperture with a diameter of 7 mm to allow only the most uniform center section of the beam to irradiate the surface. For all tests, the actual heat flux was measured with a calorimeter. A cubic Plexiglass test chamber, 25 cm on a side, with a stainless steel top cover was used for ignition delay tests and schlieren visualization. Two high-quality glass windows were installed in opposite sides of the chamber for the schlieren flow visualization. For the species sampling tests, in order to have considerable species concentrations, a smaller Plexiglass test chamber, 10 cm long by 5 cm in diameter with aluminum end caps, was employed. A septum, installed in the side of the chamber, allowed for gas sampling with a syringe. The top covers of both chambers were fitted with potassium chloride windows, which are highly transmissive in the infrared range, for beam entrance. Pressure and composition of the initial gas in the chamber was controlled using a vacuum pump, a pressure/vacuum gauge, and an inert gas supply system.

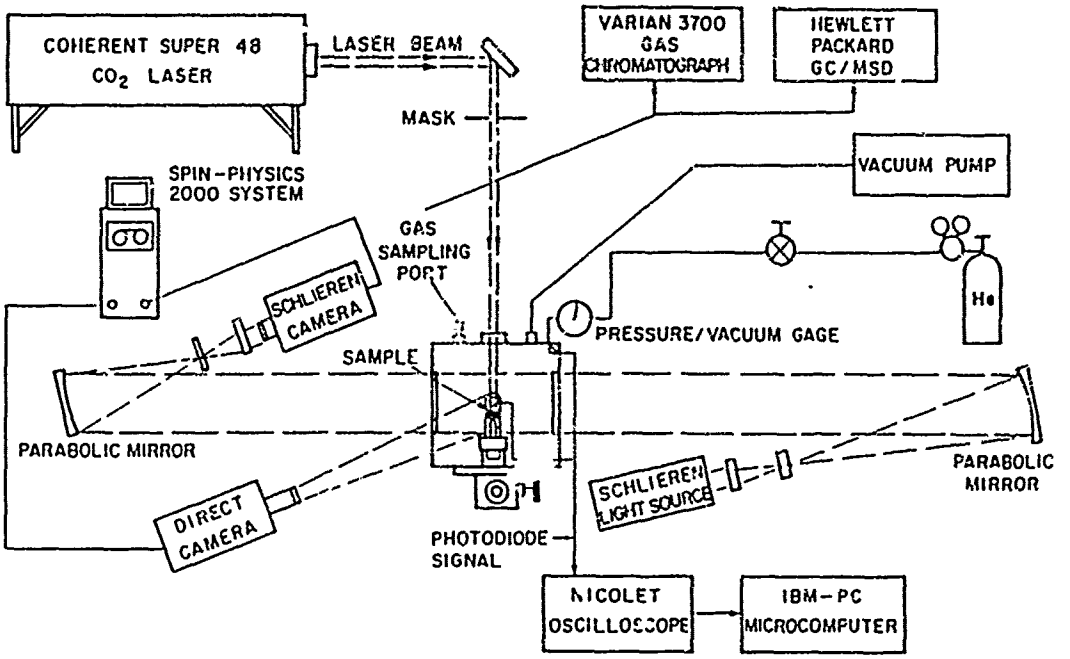


FIGURE 1. Experimental setup for CO_2 laser pyrolysis and ignition

Both the direct and schlieren images were recorded with a Spin Physics 2000 video recording system. As seen in Fig. 1, the system consists of a controller, video monitor, and two camera heads. Maximum recording speed is 12000 pps, but a 2000 pps recording rate was employed for this research. The controller can display both the schlieren and direct images simultaneously, allowing direct comparison of the flame structure and gas-phase dynamics. The schlieren system is a "Z-type" configuration, employing 15 cm parabolic mirrors to direct a parallel light beam through the test chamber from a 100 watt continuous tungsten-halogen lamp. The beam is directed and shaped by lenses and rectangular apertures at each end as it travels from the light source, through the chamber, and into the video camera at the other end.

The MTV igniter material studied in this research consisted of 50% magnesium particles of 325 mesh size and 99.8% purity. The balance of the material was composed of a granular resin of PTFE particles (dia. - 30 μm) and Viton A particles. The boron powder used in the boron/Mg/PTFE formulations was composed of 99% pure amorphous particles with a 0.5 μm average size.

Ignition delay times were determined using two near-infrared photodiodes (spectral response: 0.35-1.15 μm) to sense the first light emission from a flame or heat production from chemical reactions. One photodiode was positioned seven cm from the sample and aimed directly at its surface while the other one was positioned in an upper corner of the chamber and aimed 2.5 cm above the surface to observe the gas-phase infrared emission. To signal "zero-time" on both the photodiode traces and the direct video image, a strobe light was employed. The data was recorded on a Nicolet oscilloscope and transferred to an IBM PC for processing.

After a test, samples of gaseous products were drawn from the test chamber with a one milliliter syringe. These gaseous product species were then analyzed using a Hewlett/Packard gas chromatograph/mass spectrometer. Most of the samples were analyzed with a Carbopack B/5% Fluorocol column run isothermally at 50°C. A column with Porapak Q&R in series, used to obtain data on hydrocarbon species, was run isothermally at 50°C for the first 5 minutes and then ramped at 15°C per minute up to 200°C for the remainder of the run.

3. FLAME STRUCTURE AND GAS-PHASE DYNAMICS

Figure 2 is a sequence of images depicting the ignition transient for a sample ignited in air at 1 atmosphere. Both the direct and schlieren photographs of the ignition sequence are shown. The times below each pair of images represent the time elapsed from the onset of laser heating. In each pair of images, the sample surface is at the same height; however, the magnification of the direct image is slightly less than that of the schlieren image.

Ignition occurs in Fig. 2a after a delay time of 19 milliseconds. The faint light emission seen on the sample surface in the direct image corresponds to the abrupt rise in the photodiode signal (within 2 milliseconds) that was used as the criterion for ignition. The initial evolution of a gaseous sphere on the schlieren image occurs slightly off the center of the sample due to minor variations in the laser beam intensity profile. The gaseous sphere expands upward in Fig. 2b and a ball of flame is established within the dark outer gradients of the sphere. The flame and evolved gases continue to propagate through Figs. 2c-2f. A mushroom-shaped gas-phase structure can be seen inside the outer gradient in the schlieren picture in Fig. 2e. The cap of the mushroom is due to the formation of a vortex resulting from the

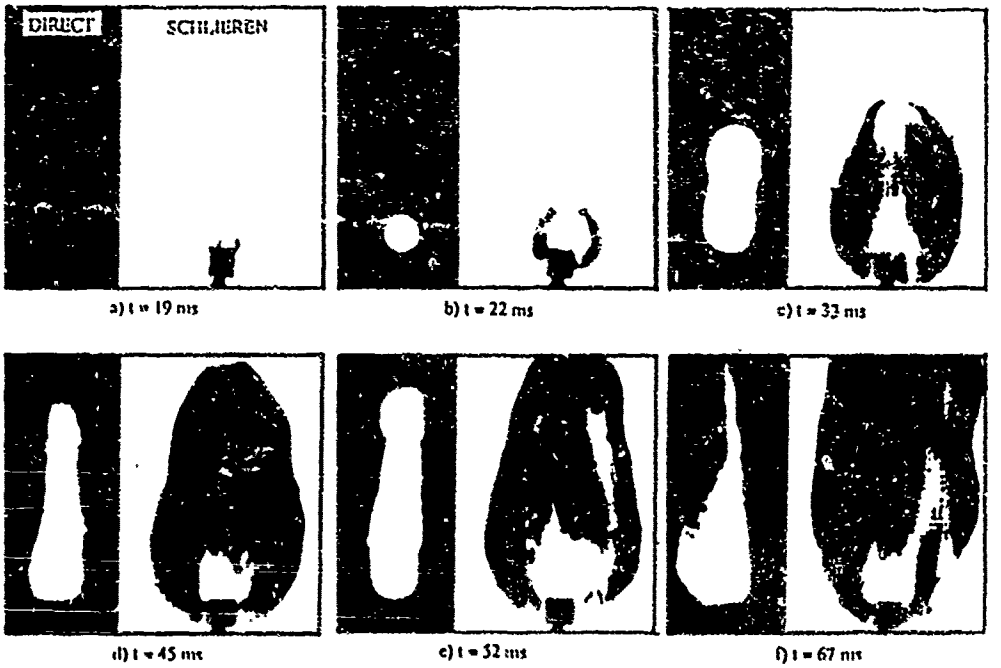


FIGURE 2. Ignition sequence of the MTV igniter material in air at 1 atmosphere ($q'' = 640$ W/cm^2)

propagation of the initial sphere of gases evolved, and the stem is formed by the continued evolution of a stream of gases normal to the surface. The actual steady-state flame shape has not yet been established in Fig. 2f, but it is quite similar in size to the inner flame region that can be seen in the schlieren image. Large particles can be seen in both the direct and schlieren images in this figure.

An ignition test conducted at a low pressure of ~ 0.1 atmosphere is displayed in Fig. 3. Clearly, this ignition process is much less vigorous than the rather explosive dynamics observed in the higher pressure ignition. The first emission of visible light does not occur until 108 milliseconds, but the photodiode signal abruptly increases at 32 milliseconds. Evidently, the rise in the photodiode signal was caused by a significant amount of heat (infrared emission) being evolved well before the visible light of a flame was observed. Thus, the ignition at low pressure is correlated with the significant evolution of heat from chemical reactions; the heat evolution does not directly correspond to the onset of a visible flame.

Two distinct phenomena observed in Fig. 3 are the abundance of very large particles and fragments evolved from the sample and the lack of any gas-phase structure in the schlieren pictures. Figures 3b and 3c depict the evolution and transport of two large fragments from the surface, and Fig. 3d shows the first sign of a substantial flame zone established on the surface. Then in Figs. 3e and 3f, huge amounts of very large particles are evolved as the sample "burns." In this test, the side surfaces of the sample were not inhibited, and particles evolved horizontally in Fig. 3f are a result of side burning. After the test, these particles fully coated the schlieren windows 15 cm from the sample and blocked the schlieren image by the time the sample had been completely burned.

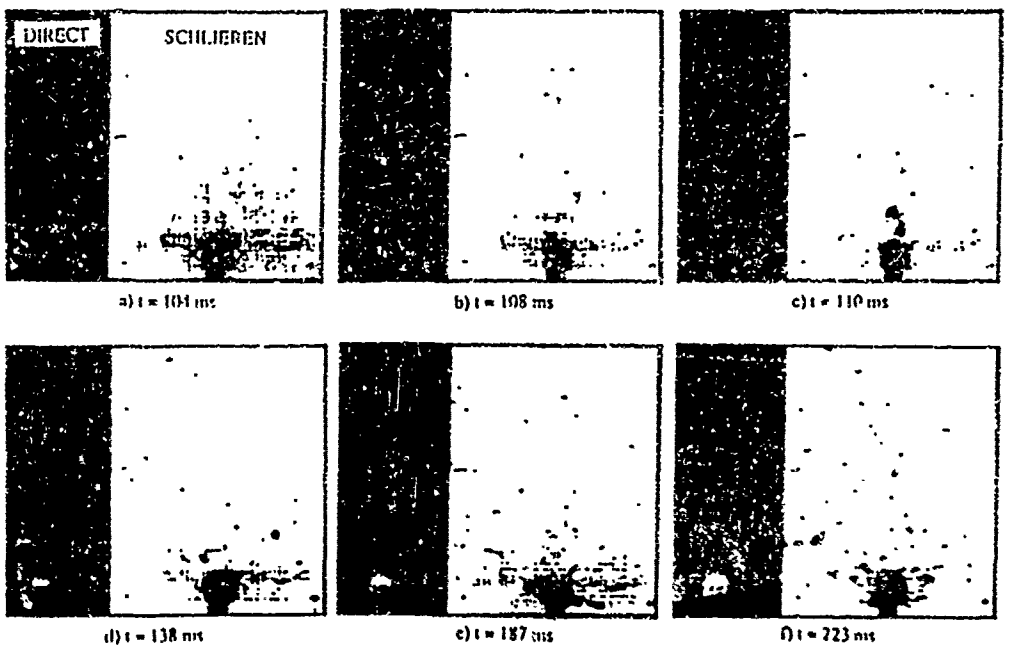


FIGURE 3. Ignition sequence of the MTV igniter material in air at ~ 0.1 atmosphere ($q'' \sim 430$ W/cm^2)

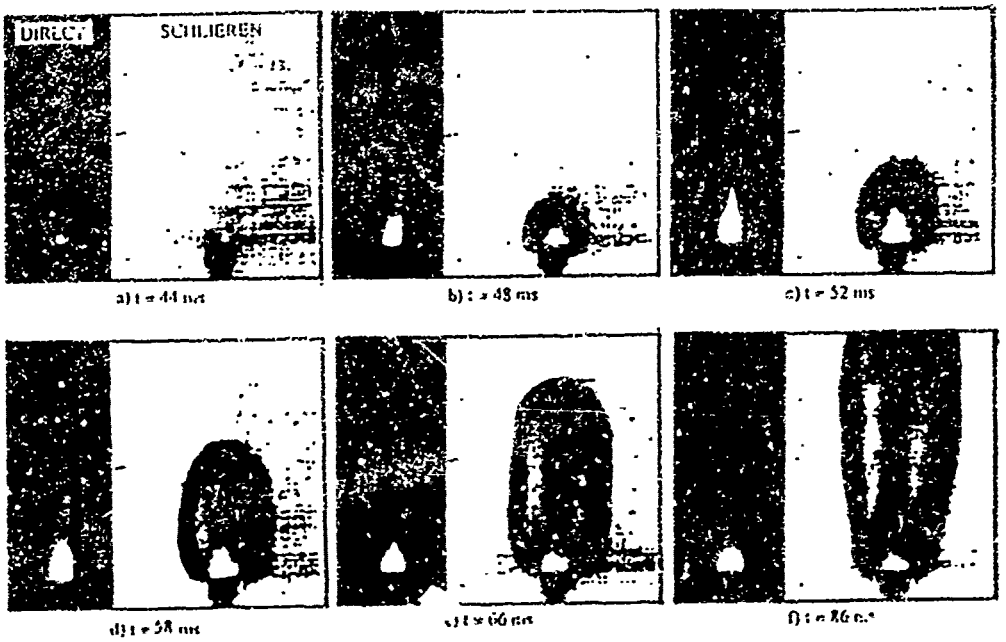


FIGURE 4. Ignition sequence of the MTV igniter material in an inert N_2 environment at 1 atmosphere ($q'' = 430$ W/cm^2)

A set of images depicting ignition in an inert atmosphere of nitrogen (~ 0.5% O_2) is given in Fig. 4. The gas-phase dynamics follow roughly the same progression as those for tests in air. The gradients are noticeably darker, though, indicating stronger density and/or temperature gradients, and the flame structure is obviously quite different from the ignition tests in air at one atmosphere. The flame initially propagates to a height around 1.0 centimeter above the sample surface and then recedes to the steady-state shape seen in Fig. 4f. Comparing Figs. 2 and 4, it can definitely be concluded that oxygen plays a significant role in the reactions that produce a large luminous plume during ignition. The final steady-state flame is also larger for the case of air.

Finally, Fig. 5 displays two schlieren images with different levels of magnification that were obtained using different focal lengths of collimating lenses in front of the camera. The lenses used for Figs. 5a and 5b provide magnifications of 1.8 and 4.5, respectively, of the images displayed in Figs. 2-4. Both images in Fig. 5 represent ignition in air at 1 atmosphere. Measurements taken from all the images, irrespective of the level of magnification, corresponded very well, confirming the accuracy and reproducibility of the schlieren system. These measurements showed that the primary flame zone established on the sample surface is 1.2-1.5 mm in height.

4. IGNITION DELAY BEHAVIOR

The ignition delay behavior of the MTV igniter material was investigated as a function of pressure, heat flux,and ambient oxygen concentration. The ignition delay times were determined from the photodiode traces as the elapsed time from the initiation of laser heating to the distinct point where the signal rose very abruptly, evidenced by the typical



(a) Magnification = 1.8, t = 90 ms (b) Magnification = 4.5, t = 90 ms

FIGURE 5. Primary flame zone attached to sample surface; two different magnifications of the size of the schlieren image in Figs. 2-4

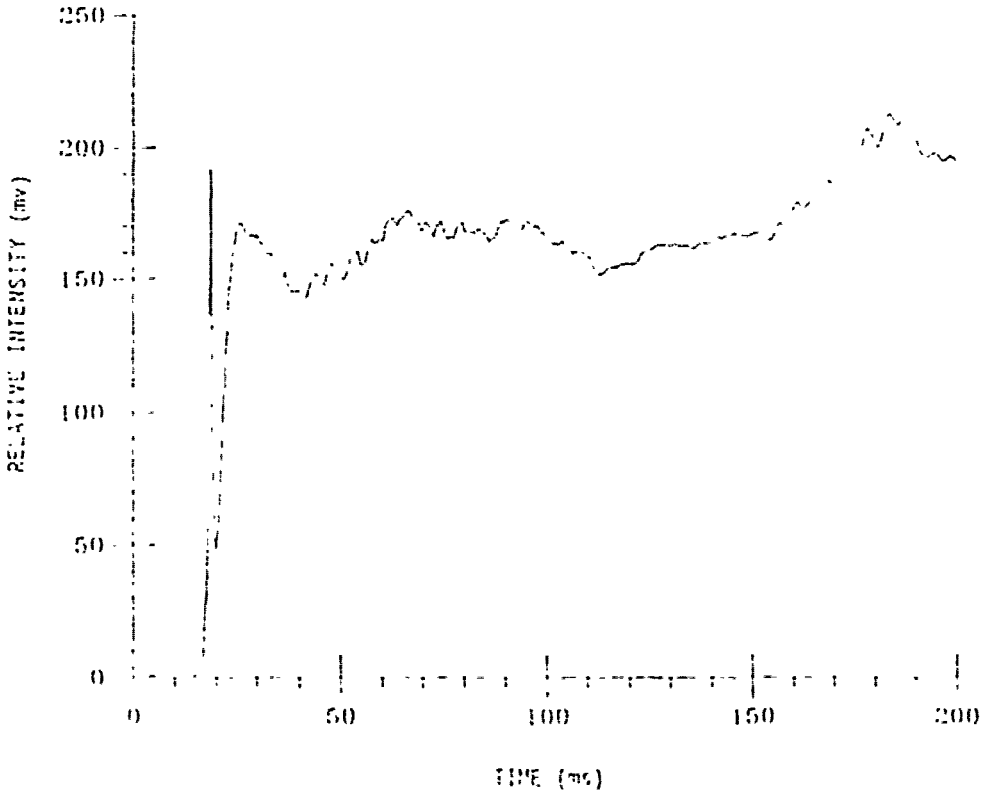


FIGURE 6. Near-field photodiode trace of ignition in air at 1 atmosphere ($q'' = 670$ W/cm^2)

photodiode trace given in Fig. 6. There is a very abrupt "spike" in the signal which drops and then rises again to a relatively steady state. This ignition delay time was normally within 2-3 milliseconds of the time elapsed until the first light emission observed in the direct image. After ignition, combustion of the samples was sustained until they were totally consumed, regardless of the ambient conditions.

Figure 7 exhibits the ignition delay behavior as a function of ambient pressure and incident heat flux. The two curves indicate the pressure dependence, one for ignition at 1 atmosphere and the other in a relative vacuum of less than 0.1 atmosphere. Most importantly, it can be seen that the ignition delay times are shorter at lower pressure. Also, the profiles of both curves as a function of the radiative heat flux from the CO_2 laser are quite similar. In other words, lowering the pressure merely serves to shift the curve down while maintaining the same flux-dependent profile. However, the reason for the shorter delays at lower pressures can most likely be explained by the results given in Fig. 8.

Figure 8 illustrates the effect of the ambient oxygen concentration on the ignition delay behavior at a constant heat flux. The curve shows that the ignition delay time increases with an increase in the ambient oxygen concentration. Although more data is needed to confirm this behavior, the trend is believed to be correct, and it represents a significant point in understanding the ignition mechanisms. This behavior is also the most likely justification for the lower ignition delays at lower pressures observed in Fig. 7, since as pressure decreases, the concentration of ambient oxygen also decreases.

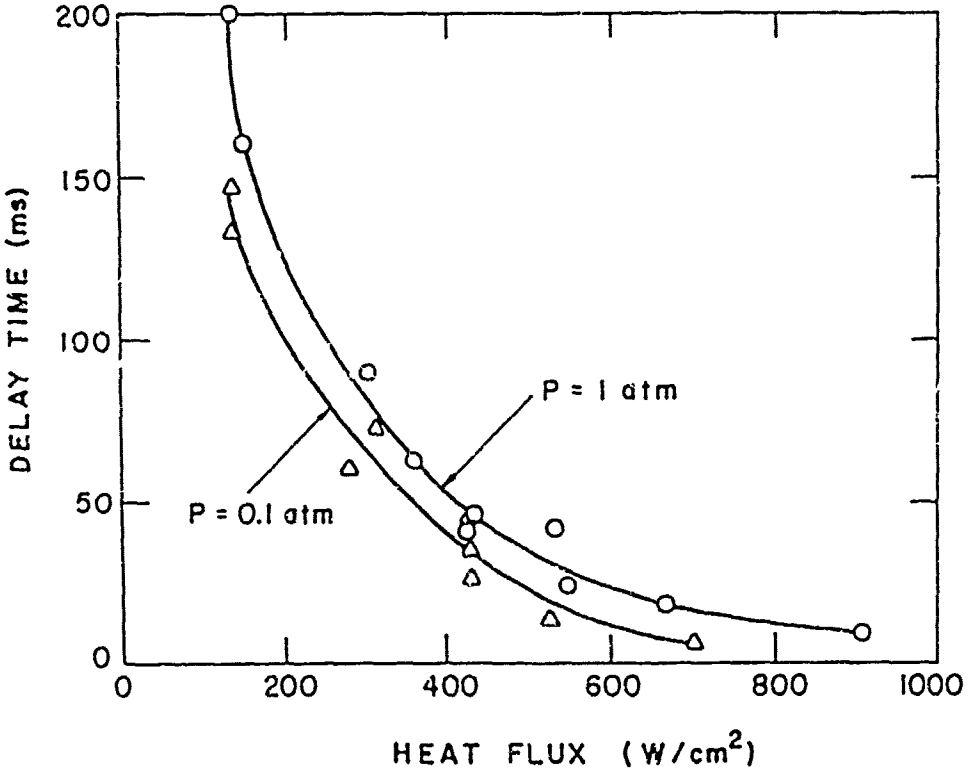


FIGURE 7. Effect of pressure and incident heat flux on ignition delay time of MTV igniter material in air

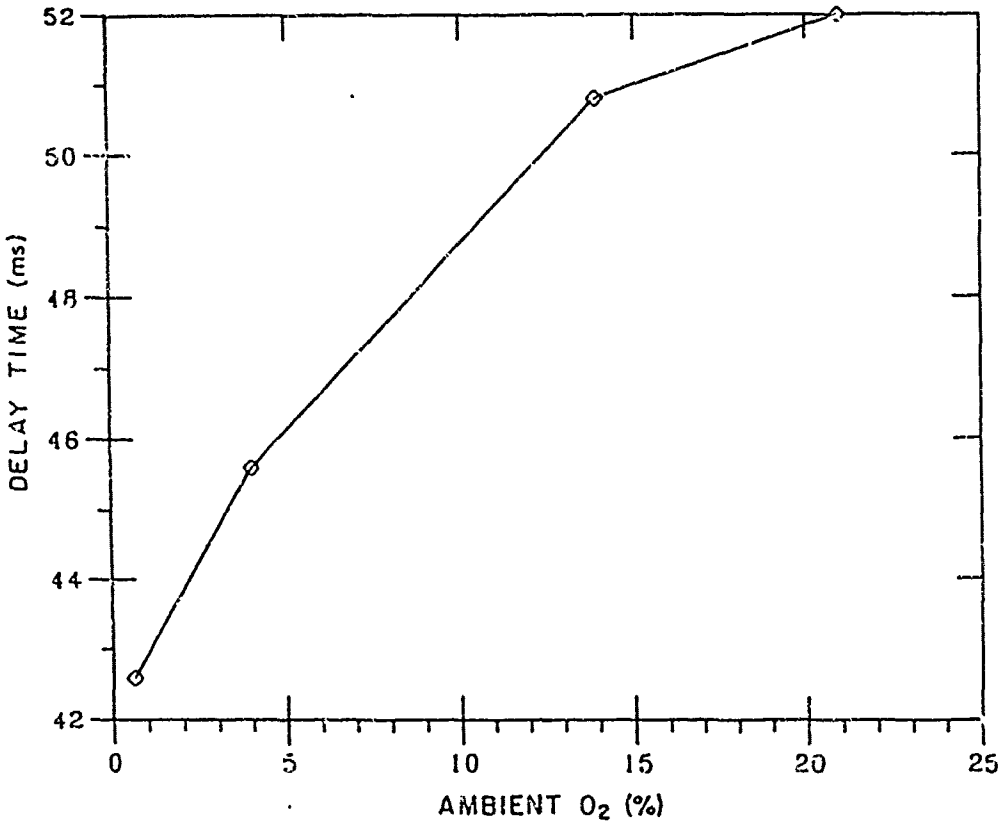


FIGURE 8. Effect of oxygen concentration on ignition delay time of MTV igniter material at 1 atmosphere ($q'' = 409$ W/cm^2)

In this work, it is believed that the inhibiting effect of oxygen observed in Fig. 8 was due to the reaction with Mg to form MgO and thus prevent the fluorine from reacting with the Mg. Since the gravimetric heats of oxidation and fluorination of Mg are 24.75 KJ/g and 46.25 KJ/g, respectively,[11] the reaction of oxygen with magnesium would generate less thermal energy than the reaction of fluorine with magnesium, producing a longer ignition delay in air. Ignition delay tests performed on a pellet composed of a 1:1 mixture of PTFE and Mg without any Viton A showed that the ignition delay was approximately twice as much as that of the MTV igniter material under the same conditions, leading to the conclusion that Viton A is the rate-controlling ingredient for the MTV formulation. Properties of these polymers that would seem to substantiate this behavior are the decomposition of Viton A at 589 K[16] versus 803 K[13] for the PTFE, and activation energies of 210 KJ/mol and 350 KJ/mol, respectively. The effect of oxygen on the ignition delay of the MTV igniter material should then be a result of its effect on Viton A, in addition to its effect on magnesium. Also, the appearance of first light emission always occurred on the surface, suggesting that heterogeneous reactions may be involved in the ignition process.

In an attempt to improve the ignition and combustion of the MTV igniter material, boron was added to several different formulations of Mg and PTFE. The ignition delay results are presented in Fig. 9. The results indicate that increasing the amount of boron in an Mg/PTFE formulation significantly reduces the ignition delay time, with the shortest delay observed for a 50/50 formulation of boron/PTFE without any magnesium.

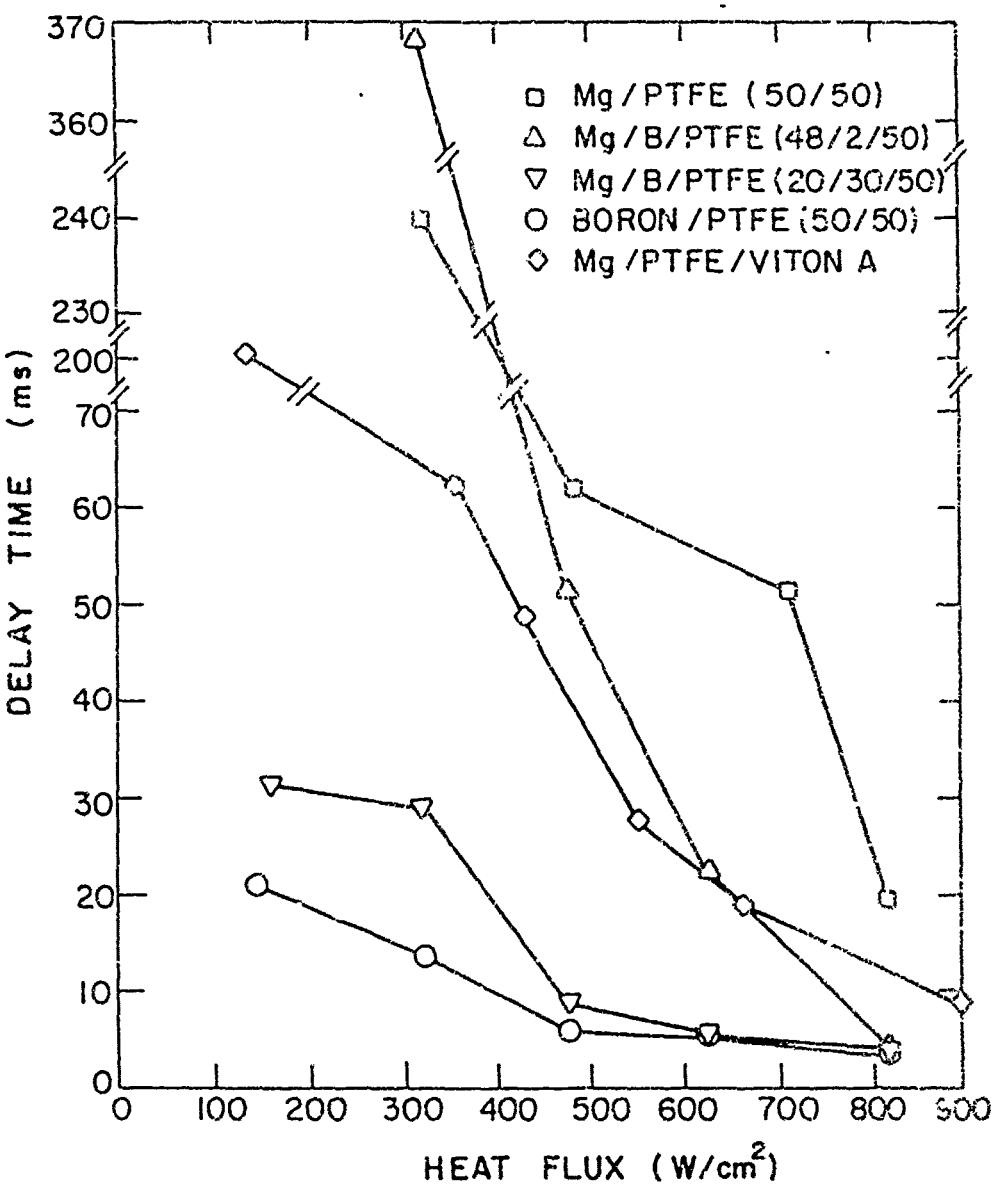


FIGURE 9. Effect on ignition delay of the addition of boron and Viton A to a Mg/PTFE material (ignition in air at 1 atmosphere)

Two factors considered in explaining this trend were radiation reflectivity at the 10.6 μm wavelength of the CO_2 laser and thermal diffusivity. The reflectivity of magnesium is about 0.75,[17] which is much greater than that of boron. Therefore, a large part of the laser energy may be reflected away from the surface of samples containing significant amounts of magnesium. It was considered that the ignition enhancement by boron observed in Fig. 9 may be an artifact of the laser and not a practical consideration for the improvement of the ignition of Mg/PTFE igniter material. However, the combustion after laser cutoff of the Mg/B/PTFE formulation with 30% boron was much more vigorous than the formulation without any boron, indicating that the addition of boron does have a significant physicochemical effect. Also, the thermal diffusivity of magnesium is 0.876 cm^2/sec, which is eight times higher than that of boron. Consequently, in a sample containing magnesium, the rate of

penetration of the thermal wave is much higher. This phenomenon lowers the rate of increase of the surface temperature, which in turn, increases the delay time to ignition.

Another important observation from Fig. 9 is that the replacement of PTFE in the 50/50 Mg/PTFE formulation with an amount of Viton A significantly reduced the ignition delay time. Kubota and Serizawa[13] reported that the addition of 3% Viton A to their Mg/PTFE formulation did not alter the burning rate. However, the MTV igniter material tested here contained a higher percentage of Viton A, and the effect on the ignition delay time was obviously significant. The lower delay times are believed to be caused by the lower decomposition temperature and lower activation energy of Viton A, in comparison with those of PTFE, which were reported earlier.

5. PYROLYSIS AND IGNITION PRODUCT SPECIES ANALYSIS

The gaseous species evolved during the pyrolysis of PTFE and Viton A, and the ignition of the MTV igniter material, were analyzed with a gas chromatograph/mass spectrometer. Tests were conducted in both an inert atmosphere and in air to investigate the role of oxygen in the ignition processes. Solid ignition products were also analyzed by X-ray diffraction.

The pyrolysis of PTFE in an inert N_2 environment at one atmosphere produced the total ion chromatograph given in Fig. 10. The sample was heated twice by a heat flux of 430 W/cm^2 for two seconds each time. The most abundant species evolved are C_2F_6, C_2F_4 (the monomer), C_3F_6 (two isomers), CF_4, and two isomers of C_4F_8. Interestingly, the most abundant species, perfluoroethane (C_2F_6), was not listed in a depolymerization/degradation chart for PTFE presented by Elias,[18] but was the most abundant compound observed in the pyrolysis of both PTFE and Vicon A.

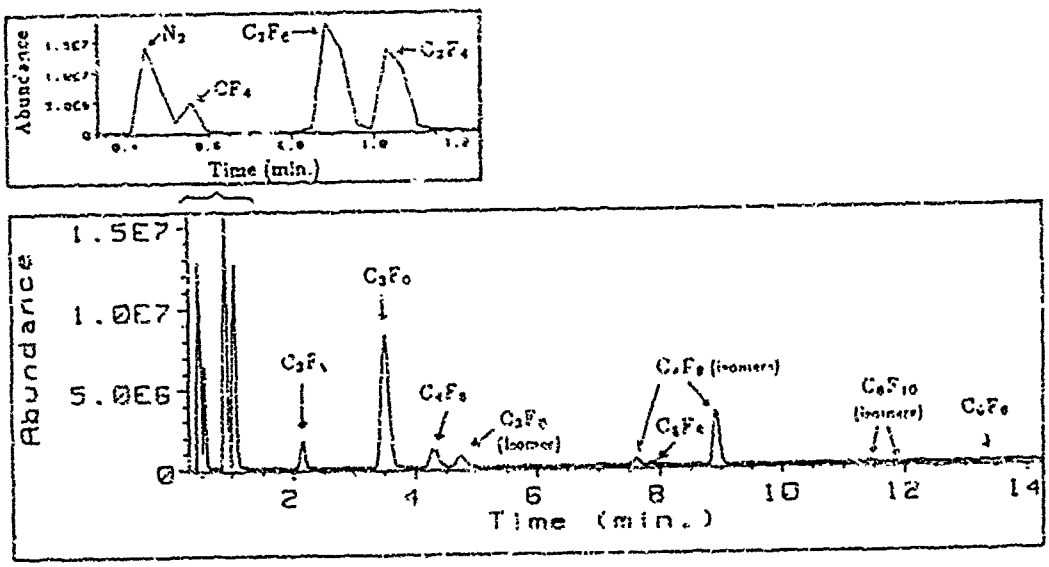


FIGURE 10. Chromatograph of the pyrolysis of PTFE in an inert N_2 environment at 1 atmosphere ($q'' = 430$ W/cm^2 for 2 heatings of 2 seconds)

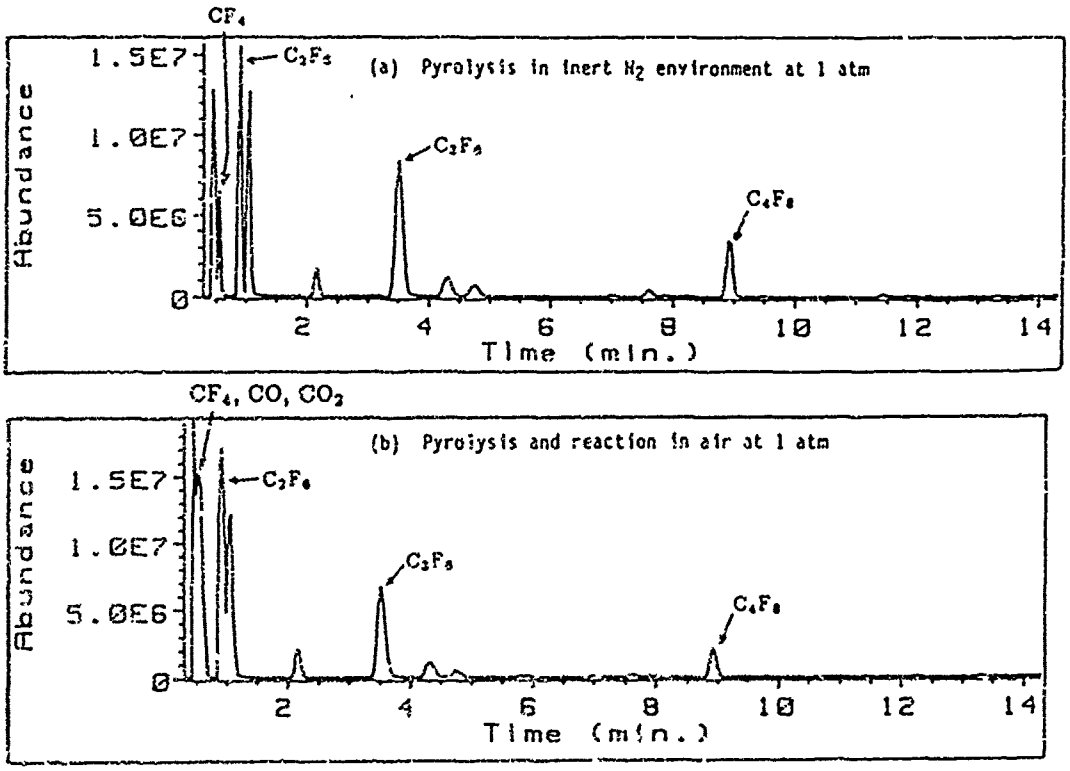


FIGURE 11. Chromatograph of the pyrolysis and reaction of PTFE in both an inert N_2 environment and air at 1 atmosphere ($q'' = 430$ W/cm^2 for 2 heatings of 2 seconds)

Figure 11 compares the inert pyrolysis of PTFE (shown in Figs. 10 and 11a) with the pyrolysis and reaction of PTFE in air at 1 atmosphere. It can be seen that the amounts of C_3F_6 and C_4F_8 decreased slightly for pyrolysis and reaction in air (Fig. 11b), compared to pyrolysis in nitrogen (Fig. 11a). The amount of C_2F_6 appeared to remain the same. The amount of CF_4 appeared to increase in Fig. 11b, but the mass spectrometric breakdown of that peak indicated that CO and CO_2 were also eluted at that time, and the three compounds could not be individually resolved. Griffiths et al.[12] reported that CO_2 and CF_2O had been found by several other researchers for the reaction of PTFE in air. However, the existence of CF_2O could not be confirmed by the present apparatus. Using a microburner to study the premixed burning of several fluorocarbon-oxygen mixtures, Natula[19] reported significant burning of mixtures containing C_3F_6 and C_4F_8. He also reported that C_2F_6-O_2 and CF_4-O_2 mixtures could not be ignited at one atmosphere of air. These results are consistent with the results presented in Fig. 11.

Figure 12 gives the total ion chromatograph for the pyrolysis of Viton A in an inert N_2 atmosphere. The major species evolved were CF_3H, C_2F_6, C_2F_4, C_2F_3H, C_2F_5H, $C_3F_4H_2$, C_3F_6, C_3F_5H, $C_4F_6H_2$, C_5F_{10}, C_5F_7H, and C_4F_6. The two most abundant species evolved were C_2F_6 and C_3F_6, which were also the most abundant species, along with the monomer, that were evolved from PTFE. The similarity of products between PTFE and Viton A substantiates the claim that the effect of oxygen on the decomposition products for Viton A and PTFE may be quite similar. Interestingly, no CF_4 was observed for Viton A, but a peak observed at the same time it is normally

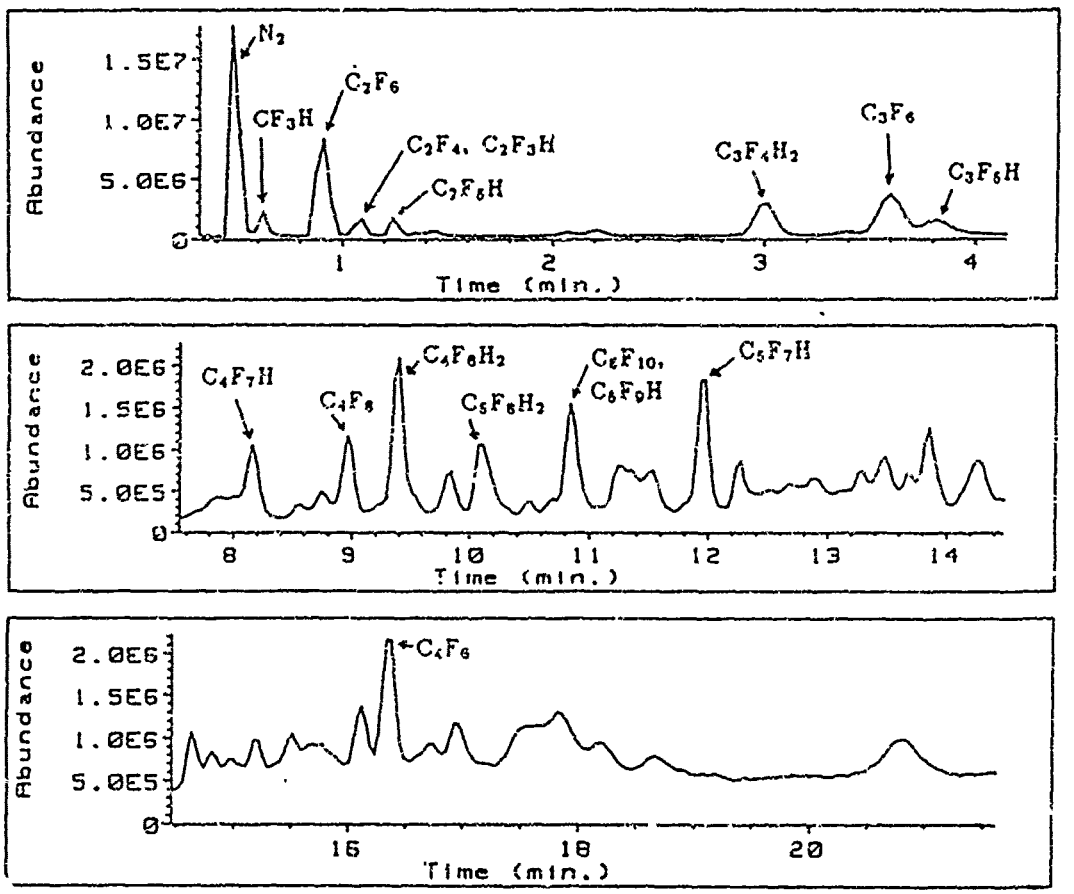


FIGURE 12. Chromatograph of the pyrolysis of Viton A in an inert N_2 environment at 1 atmosphere ($q'' = 430$ W/cm^2 for 2 heatings of 2 seconds)

eluted contained CF_3H. A trend was observed where fluorine atoms were replaced by hydrogen atoms in some of the more common C_mF_n structures (i.e., $C_3F_6 \Rightarrow C_3F_5H$).

The chromatographs of the gaseous product species evolved for the ignition and combustion of the MTV igniter material are presented in Figs. 13 and 14. Since the 5 millimeter cubes of igniter material were totally consumed after ignition and the gas samples were taken after the test was over, the species analyzed were the products of sustained combustion and not just ignition. Figure 13a displays the results of tests conducted in air, and the tests for Fig. 13b were conducted in an inert nitrogen atmosphere. Magnesium compounds were not observed in the gaseous state in either case. As was seen in Fig. 11, tests run in air also produced CO and CO_2 as well as most of the other products identified in the combustion in an inert atmosphere.

The rest of the peaks observed in these chromatographs establish an important point to be considered in the mechanisms of ignition and subsequent combustion of the igniter material. Almost all of the species observed for combustion in both air and an inert N_2 atmosphere were C_aH_b compounds, and the numerous C_mF_n and $C_xH_yF_z$ observed in the pyrolysis of Teflon and Viton A were not found in the combustion of the MTV igniter

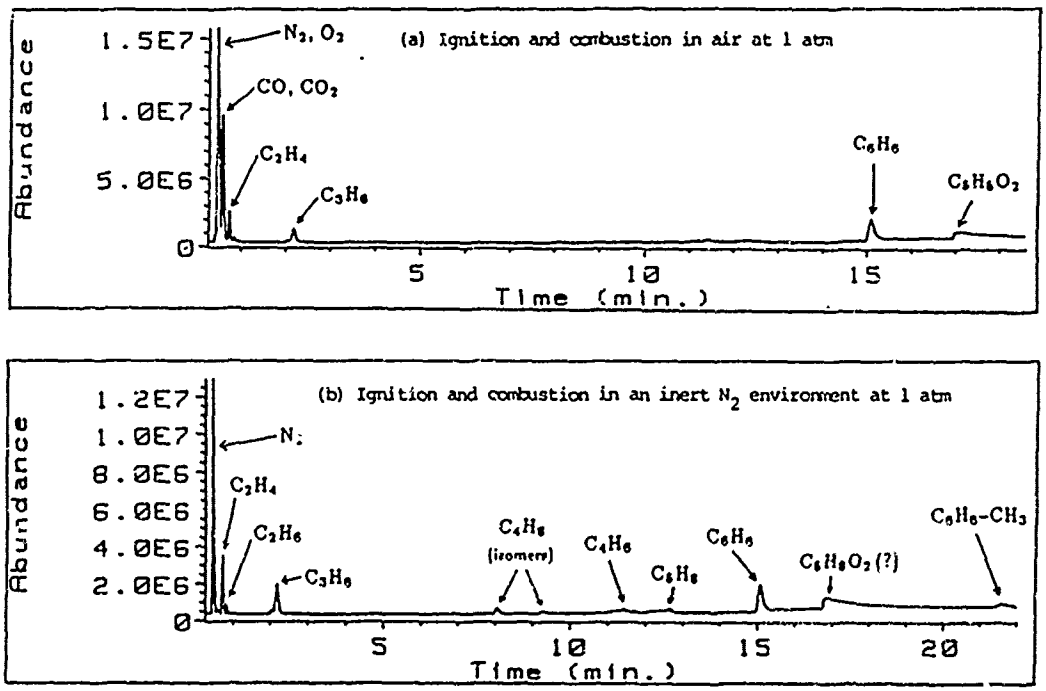


FIGURE 13. Chromatograph using Carbopack B/5% Fluorcol Column to analyze the gaseous products of ignition and combustion of the MTV igniter material (q" = 430 W/cm^2)

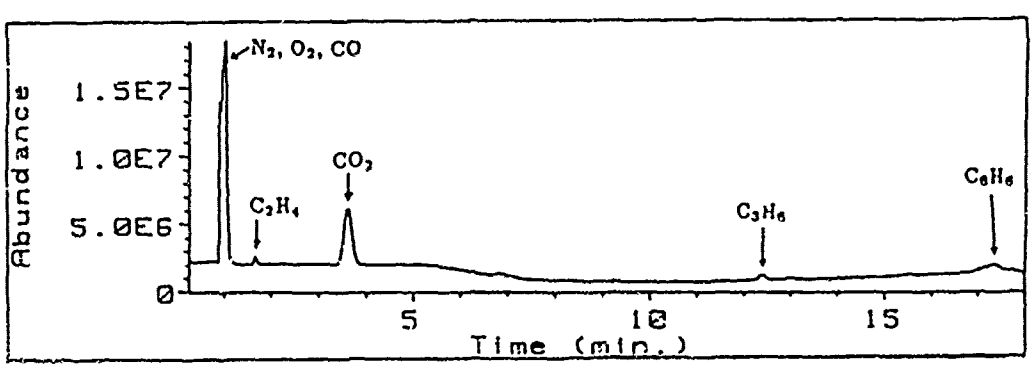


FIGURE 14. Chromatograph using a series of Porapak Q and R columns to analyze the gaseous products of the ignition and combustion of the MTV igniter material in air at 1 atmosphere (q" = 430 W/cm^2)

material. A probable explanation is that the primary pyrolysis species are consumed to form undetected HF or to form the observed MgF_2 solid products. Also, the small peaks from 8-13 minutes observed in the inert combustion tests are not evident in the combustion in air; clearly, the combustion in an inert atmosphere is not as complete as that in air.

In Fig. 14, gas samples of the MTV material ignition and combustion in air were also run through a series of Porapak Q and R columns for species identification. These columns are more applicable to detecting C_aH_b compounds. However, only small amounts of a few compounds of this type were detected, as well as significant amounts of CO and CO_2. These results verify the results given in Fig. 13a for the same experimental conditions using the Carbopack B/5% Fluorcol column for analysis.

X-ray diffraction analysis was also used to investigate the composition of the condensed-phase species evolved during the combustion of the propellant. MgF_2, MgO, and carbon were detected in varying amounts, depending on the test conditions. Of course, MgO was only detected in significant amounts for the combustion in air.

6. SUMMARY AND CONCLUSIONS

The pyrolysis and ignition characteristics of a Mg/PTFE/Viton A igniter material were studied under radiative heating by a high-power CO_2 laser. The ignition sequence was recorded by both direct high-speed video photography of the flame structure and schlieren flow visualization of the gas-phase dynamics. Ignition delay times were obtained as a function of incident heat flux, pressure, and ambient oxygen concentration. A gas chromatograph/mass spectrometer was used to analyze the pyrolysis and ignition products of the test sample and its constituents.

High-speed video photography showed that ignition always occurred on the sample surface. A primary flame zone attached to the surface with a height of 1.2-1.5 millimeters was observed in both air and inert gas environments at one atmosphere. The size of the luminous gas-phase plume above the primary flame decreased with a decrease in ambient oxygen concentration for tests conducted at one atmosphere. However, at a pressure of ~ 0.1 atmosphere, no evident plume evolution and gas-phase dynamics were observed, and the igniter material decomposed in large fragments.

Ignition delay times decreased monotonically as heat flux increased, pressure decreased, or ambient oxygen concentration decreased. The effect on ignition delay of adding boron or Viton A to a basic composition of Mg/PTFE was also investigated. The addition of boron significantly lowered the ignition delay time and greatly enhanced combustion. The addition of Viton A, which has a much lower decomposition temperature and activation energy than PTFE, greatly lowered the ignition delay time, which led to the conclusion that Viton A is the rate-controlling constituent for ignition of the MTV igniter material.

For combustion of the igniter material in both inert N_2 and air environments at one atmosphere, the only gaseous product species detected were several hydrocarbons, with the addition of CO and CO_2 in air. However, for pyrolysis of PTFE and Viton A individually in an inert N_2

environment, numerous fluorocarbon species, and hydrofluorocarbons for Viton A, were detected. It was concluded that these primary pyrolysis species are consumed to form the detected hydrocarbons, CO and CO_2 for combustion in air, undetected HF, and solid MgF_2 and carbon. These condensed phase products were identified by X-ray diffraction. Solid MgO was also observed for combustion in air.

In summary, the MTV igniter material with the addition of boron is highly recommended for base bleed applications, due to its suitable ignition behavior under various gas and low-pressure environments.

ACKNOWLEDGMENT

This work was sponsored by the Office of Naval Research, Contract No. N00014-86-K-0468, under the management of Drs. Richard S. Miller and Gabriel D. Roy. We would like to express our appreciation to them, and also to NWC for providing the igniter material that was used in this research.

REFERENCES

1. Brody, F., Snelling, L., Steinle, M., "A High Volume Cost Effective Manufacturing Process for the Production of Propellant Grains for Base Burning Artillery Projectiles," 1986 JANNAF Propulsion Meeting, CPIA Publication 455, New Orleans, LA, August 26-28, 1986.

2. Sahu, J., "Supersonic Flow Over Cylindrical Afterbodies with Base Bleed," Final Report, BRL-TR-2742, June 1986.

3. Hellgren, R., "Base Bleed Projectiles: Range Calculation Program and Efficiency Comparisons," FOA-C-20516-D2, November 1983.

4. Fox, J. H., "A Generalized Base-Flow Analysis with Initial Boundary-Layer and Chemistry Effects," Final Rept., AEDC-TR-79-46 October 1, 1976-May 18, 1979.

5. Bauer, R. C., Fox J. H., "An Application of the Chapman-Korst Theory of Supersonic Nozzle-Afterbody Flows," Final Rept., AEDC-R-76-158, July 1, 1975-Sept. 30, 1976.

6. Peters, C. E., Phares, W. J., "Analytical Model of Supersonic, Turbulent, Near-Wake Flows," Final Rept., AEDC-TR-76-127, July, 1973-Dec., 1975.

7. Strahle, W. C., Hubbartt, J. E., Walterick, R., "Base Burning Performance at Mach 3," AIAA Paper 81-1469, AIAA/SAE/ASME 17th Joint Propulsion Conference, July 27-29, 1981.

8. Kayser, L. D., "Effects of Base Bleed and Supersonic Nozzle Injection on Base Pressure," Final Rept., BRL-MR-2456, March 1975.

9. Kloehn, R., Rassinfosse, A., "Base Bleed Solid Propellants Containing Thermoplastic Elastomers as Binders," Joint Symposium (3rd) on Compatibility of Plastics/Materials with Explosives, Propellants, and Pyrotechnics Ingredients Proce..ing, Phoenix, AZ, May 31-June 2, 1982.

10. Peretz, A., "Investigation of Pyrotechnic MTV Compositions for Rocket Motor Igniters," Journal of Spacecraft and Rockets, Vol. 21, 1984, pp. 222-224.

11. Peretz, A., "Some Theoretical Considerations of Metal-Flourocarbon Compositions for Ramjet Fuels," 8th International Symposium on Air-Breathing Engines, Cincinnati, OH, June 15-19, 1987.

12. Griffiths, T. T., Robertson, J., Hall, P. G., and Williams, R. T., "Thermal Decomposition of PTFE in the Presence of Magnesium," Proceedings of the 10th International Pyrotechnics Seminar, July 2-5, 1985, Karlsruhe, Federal Republic of Germany, page 19-1.

13. Kubota, N., Serizawa, C., "Combustion of Magnesium/ Polytetrafluoroethylene," Journal of Propulsion, Vol. 3, No. 4, July-Aug. 1987, pp. 303-307.

14. Kubota, N., Serizawa, C., "Combustion Process of Mg/TF Pyrotechnics," Propellants, Explosives, Pyrotechnics, Vol. 12, 1987, pp. 145-148.

15. Chen, D. M., Hsieh, W. H., Snyder, T. S., Yang, V., Kuo, K. K., "Study of the Thermophysical Properties and Combustion Behavior of Metal-Based Solid Fuels," AIAA/ASME/SAE/ASEE 24th Joint Propulsion Conference, Paper No. AIAA-88-3041, Boston, MA, July 11-13, 1988.

16. Haaf, F., "Occasional Exothermic Decompositions During Processing of 'Viton' Fluoroelastomer," Dupont Bulletin VT-1001, April, 1983.

17. Siegel, R., Howell, J. R., Thermal Radiation Heat Transfer, 2nd Edition, McGraw-Hill, New York, 1981, pp. 129-137.

18. Elias, H. G., Organic and Macromolecular Chemistry, 1972.

19. Matula, R. A., Orloff, D. I., Agnew, J. T., "Burning Velocities of Fluorocarbon-Oxygen Mixtures," Combustion and Flame, Vol. 14, 1970, pp. 97-102.

Dr. N. E. Gunners' Question: In your paper you say that "the MTV igniter material with the addition of boron is highly recommended for base bleed applications." In conventional base bleed applications, the ignition takes place under conditions rather different from your experiments. Would you please comment on this? Do you have other information--not reported here--supporting your recommendation?

Answer: We understand that the actual conditions for ignition of the base bleed igniter material in the gun environment are quite different from the well-controlled laboratory conditions under which these experiments were conducted. In the gun environment, ignition is due to thermal energy input from hot gases, while ignition by a high-power laser is due to radiative energy input. However, in both cases, ignition of the igniter material is caused by an external thermal energy input to increase the energy in the thermal layer near the surface of the igniter material to a critical level.

The ignition delay is governed by the rate of this thermal energy input to the test sample. The rate of energy input experienced by the igniter material in the gun can be simulated by the controlled radiative energy flux from a high-power laser. In addition, the fundamental understanding of the ignition processes of the MTV igniter material can be better achieved by the well-controlled experimental setup.

Presently, we do not have additional results to support our recommendation. However, we are conducting a comparative study between convectively-induced ignition of the igniter material in a shock tunnel environment and the CO_2 laser-induced ignition.

Dr. A. Gany's Question: You relate your ignition data to the heat flux to the surface, while the heat balance may be different under practical system conditions. Did you consider a possibility that a certain surface temperature could be an ignition criterion? Is there any indication of the propellant surface temperature at the instant of ignition?

Answer: In reference to your first statement, please refer to our answer to Dr. Gunners' question. Regarding your question about a critical surface temperature, fine-wire surface thermocouples were not employed in our ignition experiments. They cannot survive the vigorous ignition of the MTV igniter material and the subsequent self-sustained flame attached to the surface. However, separate tests were conducted in a strand burner using embedded thermocouples to determine the burning surface temperature, which is believed to be comparable to the critical ignition temperature. This temperature was found to be 1000K ± 100K.

APPENDIX 2.5

An instrument for measuring high-power laser beam profiles and beam attenuation

B. L. Fetherolf, T. A. Litzinger, and K. K. Kuo

The Pennsylvania State University, Department of Mechanical Engineering, University Park, Pennsylvania 16802

(Received 26 May 1989; accepted for publication 18 September 1989)

An instrument has been developed for measuring high-power laser beam profiles and the amount of beam attenuation during radiative ignition of solid propellants. The detector houses a 1.0 mm square PZT (lead-zirconate-titanate) sensing element that responds to changes in incident laser beam intensity. A chopper wheel with three slots was employed to produce the changes in beam intensity required by the element. The resultant output signal is a series of "spikes" whose height corresponds to the level of beam intensity. Profiles of a high-power CO_2 laser beam were obtained by using the detector to acquire a series of radial data points which were then graphed to yield the beam profile. Experiments were also conducted to measure the amount of attenuation of the laser beam during the ignition of solid propellants. This was done by mounting a small sample of propellant on a thin plate above the detector, cutting a 1.5 mm hole through the propellant and the plate, and aligning the hole with the sensing element. The gases and particles evolved during ignition and subsequent combustion of the propellant attenuated the laser beam as it passed through the gaseous plume and the small hole in the sample before being measured by the sensor. The intensity measured by the sensor was then used to quantify the level of transmittance of the beam through the gaseous plume to the propellant sample surface. Results are presented and discussed for a beam profile test and two attenuation tests performed on different energetic materials.

INTRODUCTION

Several researchers in the field of solid propellant ignition and combustion have used a high-power CO_2 laser as a radiative ignition source.[1–4] For this type of research, the laser beam profile must be relatively uniform across the propellant surface. If a nonuniform profile exists, the ignition delay time and the thermal wave propagation will be governed by the high intensity regions, and the assumption of a uniform beam profile may lead to an erroneous ignition model for the propellant. Numerous methods have been employed in attempts to obtain a uniform beam profile, such as an expanding lens,[1] vibrating mirrors,[2] and kaleidoscopes and masks.[3]

Another important quantity to be considered in analyzing the ignition behavior is the amount of attenuation of the laser beam by the gases and particles evolved from the propellant sample during the ignition process. Kashiwagi[1] found that there was significant attenuation of a CO_2 laser beam by the gaseous plume in the ignition of wood (red oak) and polymethylmethacrylate (PMMA). Ohlemiller *et al.*[3] studied dynamic effects on the ignitability limits of several solid propellants under radiative ignition. They found that certain propellants extinguished immediately after laser cutoff due to the abrupt imbalance in the heat fluxes to and from the burning surface. This dynamic extinction behavior was not seen with propellants containing platonizing catalysts, and they proposed that these propellants may undergo a more gradual flux termination because they produce gaseous product species that absorb this wavelength of laser beam and consequently reduce the level of the heat flux imbalance upon laser cutoff. Thus, the effects of laser beam attenuation on the radiative ignition of solid propellants must be understood before a realistic model can be developed.

Akau *et al.*[6] studied the effects of laser beam attenuation on the weld penetration depth using a Nd:YAG laser to weld four different metals. They found that the weld penetration increased significantly when the gaseous plume evolved from the welded surface was subjected to a crossflow of argon gas.

Very few instruments are commercially available which can measure and profile the radiative intensity and the pattern of a high-power laser beam, and those available are often prohibitively expensive. Several inexpensive methods have been reported for profiling a low-power laser beam,[7,8] but the detector elements employed usually cannot withstand a high-power beam.

This article describes an instrument that was used to profile a high-power laser beam and to measure laser beam attenuation during radiative ignition of solid propellants and solid fuels. The instrument employs a PZT (lead-zirconate-titanate) detector element[9] as the high-energy beam sensor. Since this element reacts only to changes in incident intensity, the incoming beam is regulated by a slotted chopper wheel that provides three intensity peaks per one revolution of the wheel. The detector signal output is relayed to an oscilloscope for display and processing. Results of the laser beam profile and beam attenuation measurements will also be presented and discussed to substantiate the usefulness of this instrument.

I. TECHNICAL DESCRIPTION

A schematic diagram of the laser beam profile and beam attenuation measuring instrument is displayed in Fig. 1. The

 0034-6748/90/010097-04$02.00 © 1990 American Institute of Physics

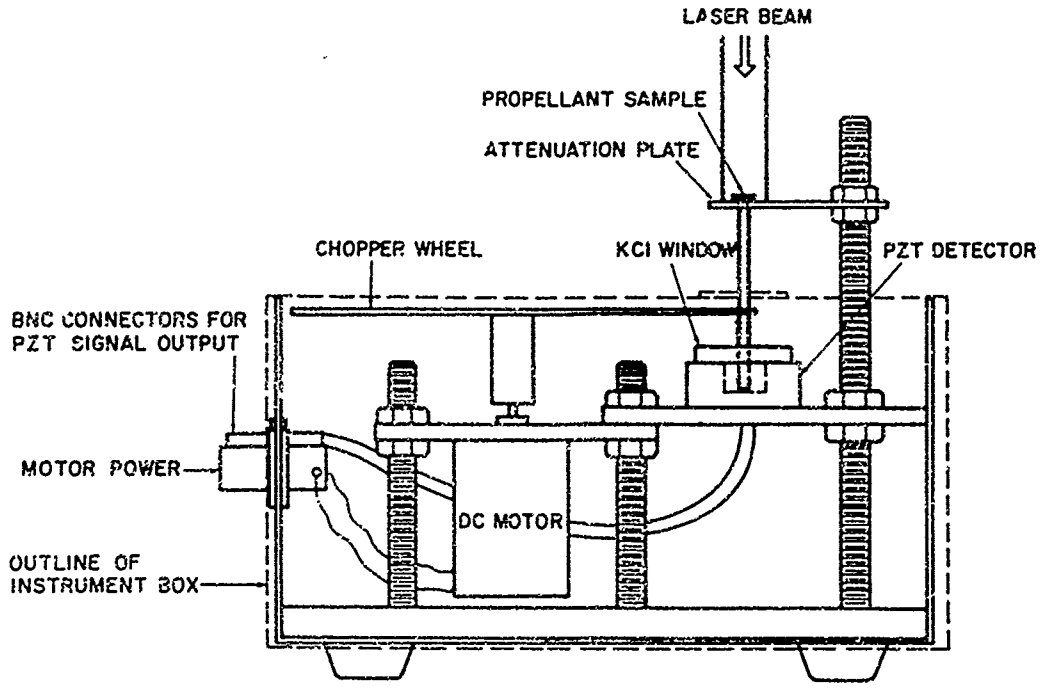


FIG. 1. Schematic diagram of instrument.

principal component of the instrument is a 350-1 PZT laser pulse detector produced by Barnes Engineering Company.[9] The sensing element is a 1.0 mm square ceramic composed of lead, zirconate, and titanate that combines the characteristics of a high Curie temperature and high mechanical strength to reduce the susceptibility to thermal shock. Advantages of using this detector include a high energy capability of up to 200 W/cm^2, a low cost of about $100, and the ability to employ the detector at room temperature. Other specifications include a very high response speed of 10 ns with a 50 Ω load and a responsivity of 1.5 μa/W. The sensing element is housed in a TO-5 package which is installed in a 2.7 cm diameter heat sink to enhance its high-power handling capability. A 2.5 cm diameter potassium chloride window, which is 97% transparent to the 10.6 μm wavelength of the CO_2 laser, was fastened to the top of the heat sink to protect the element from the gases and particles evolved during propellant ignition.

The 10.0 cm chopper wheel was made from 0.2 mm thick stainless-steel sheet, and three 1.0 cm square slots were cut in the outer edge with a 120° spacing. The wheel was bolted to a small aluminum hub, which was pressed on to the shaft of a 1.5–9 V dc motor. The voltage input to the motor was fed through a BNC cable, which was connected to a small control box. The control box was powered by a 6 V ac adapter and contained an on/off switch and a potentiometer for speed control. The 6 V input and variable resistance allowed for speed control of the chopper wheel from 0–6500 rpm. The PZT signal output was then relayed through a BNC cable to a Nicolet oscilloscope for display, processing, and storage. The entire setup was housed in a 7.5 × 10 × 15 cm instrument box, and a 1.25 cm hole was cut in the top for the entrance of the laser beam.

For beam attenuation measurements, a small sample of the solid propellant or solid fuel, 5 mm square by 1 mm thick, was glued on a plate that was fastened to two threaded rods which extend above the instrument (Fig. 1). Depending upon the mechanical properties and sensitivity of the propellant, a 1.5 mm hole was either stamped or drilled through the sample, and that hole was aligned with the sensing element. For beam profile measurements, a thin metal sheet with a 0.5 mm hole was fastened to the plate above the instrument and the hole was aligned with the center of the sensing element. Using this smaller aperture improved the spatial resolution for beam profiling.

During initial testing of the attenuation instrument, the small air movement caused by the high speed of the chopper

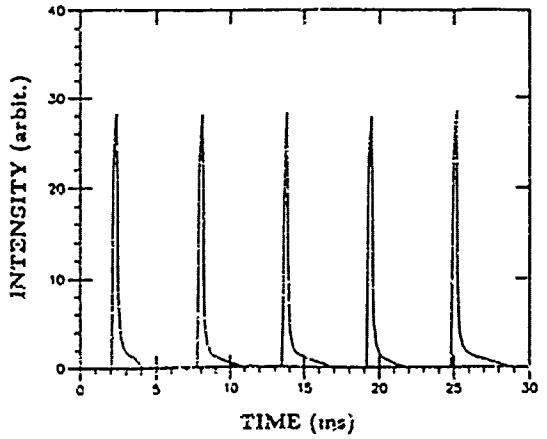


FIG. 2. Oscilloscope trace of signal from instrument (I = 125 W/cm^2, chopper speed = 3300 rpm).

wheel disturbed the gas-phase ignition processes of the propellant. A thin aluminum plate with a hole only 1 mm larger than the hole in the propellant sample was then fastened to the top of the instrument box. This eliminated the effect of the air movement induced by the chopper wheel while still allowing the beam to pass through to the sensing element.

In order to obtain the optimum signal pattern and spacing for ease of analysis of the oscilloscope trace, the rise time of the detector was modified by attaching two 2.2 kΩ resistors in parallel with the detector leads. This produced a rise time of 200 μs, which, in conjunction with the proper sampling rate setting of the oscilloscope and a chopper wheel speed of 3300 rpm, produced the pattern depicted in Fig. 2. Tests were usually run with a total oscilloscope sampling time of 200 ms, so the pattern in Fig. 2 is approximately 1/7 of the usual trace that is recorded for evaluation. Obviously, the only point of significance on each signal spike is the peak value, and the peak values are used to develop plots of beam profiles and beam attenuation curves.

A near-infrared photodiode was also employed in the attenuation tests to determine the time of ignition. Ignition was determined by the point where the photodiode signal rose very rapidly, indicating intense light emission from the developing flame. A high-speed Spin Physics video camera (12,000 pps max.) in conjunction with a schlieren flow visualization system was also employed to visualize the flow of the gases and particles evolved from the propellant sample during ignition.

II. RESULTS AND DISCUSSION

A. Beam profiling

Figure 3 illustrates a radial laser beam profile obtained with the measuring instrument. The laser employed was a high-power CO_2 laser capable of 800 W of power in the continuous wave mode and 3500 W in the pulsed mode. For beam profiling and attenuation tests using this instrument, the laser was set to produce a beam intensity of ≈200 W/cm², which is the maximum intensity rating of the sensor. This instrument is not capable of producing a full profile of the laser beam in one test. However, intensity measurements along a diameter of the beam can be obtained very quickly and then are plotted to produce the profile. To profile the beam, the instrument is first placed on a precise *X-Y* positioner. The instrument is then centered by using a short laser pulse to burn a profile on thermal paper and aligning the aperture with an axis through the center of this profile. The intensity is then measured in steps of 0.5 mm along this axis. Tests were conducted to obtain the full circular profile of the laser beam, and the data showed the beam to be axisymmetric within ± 5%. Therefore, profiles of the beam in any radial direction can be assumed to be a relatively good representation of the overall beam profile.

The instrument was used repeatedly to profile the beam during tests conducted to obtain the most uniform beam profile using various beam-modifying apparatus, and it is also used to recheck the beam profile periodically. The time required (≈7 min) to profile the beam with this instrument in comparison to real-time beam profiling instruments was not critical in this research, and the tremendous financial savings gained by using the PZT measuring instrument far outweighed the amount of time required. The total cost of this instrument was less than $120 as opposed to the $6000 price for a real-time, high-power laser beam profiler.

In summary, although this instrument takes a longer amount of time to profile the laser beam compared to the direct result obtained with a real-time beam profiler, the tremendous financial savings makes it very attractive for researchers using a high-power laser who do not need to continuously measure the laser beam profile.

B. Beam attenuation measurements

Results of a test run using the measuring instrument as an attenuation tester are presented in Fig. 4. The *X* axis represents the time elapsed during the ignition process, and the *Y* axis represents the transmittance of the laser beam through the gaseous ignition plume, which is given as the ratio of the intensity recorded by the sensor during the test to the initial beam intensity. The curves depicted in Fig. 4 were obtained during the radiative ignition of a sample of an energetic copolymer (BAMO/NMMO) and a pyrotechnic material (MTV) composed of ≈50% magnesium particles and the polymeric binders polytetrafluoroethylene and Viton A. The

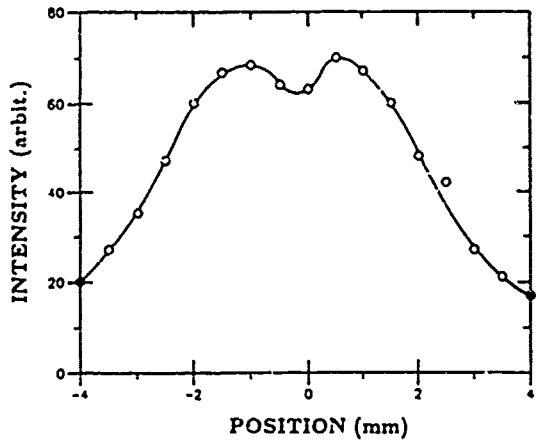


FIG. 3. Axial profile of CO_2 laser beam (I = 200 W/cm²).

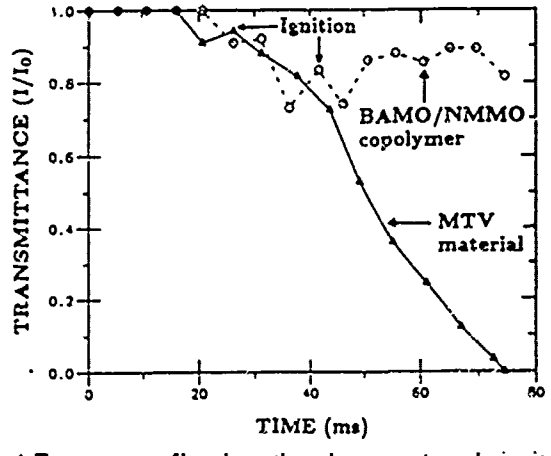


FIG. 4. Transmittance of laser beam through gaseous plume during ignition sequence of two energetic materials (I = 125 W/cm², t = 70 ms).

sensor response for the ignition of BAMO/NMMO shows several fluctuations during the ignition sequence and then becomes relatively constant at a level of about 90% transmittance. These fluctuations were caused by the turbulent plume of pyrolyzed gases evolved, which was clearly seen with the schlieren system. However, the intensity profile for the ignition of the MTV sample shows that the transmittance of the laser beam through the evolved gases and particles to the sensor, dropped rapidly to zero after the sample was ignited. The tremendous difference in the transmittance through the ignition plume for these two samples is to be expected because of the large amount of metal particles contained in the MTV sample. These particles are ejected during ignition and subsequent combustion and cause total attenuation of the laser beam.

In summary, the use of this instrument provides data to quantify the amount of laser beam attenuation during and after the ignition of energetic materials, thus answering an important question often asked of researchers doing radiative ignition studies.

ACKNOWLEDGMENTS

This work was sponsored by the Office of Naval Research under the management of Dr. Richard S. Miller and Dr. Gabriel D. Roy. Their support is greatly appreciated, and we would also like to thank Dr. Claudio Zanotti of CNPM-CNR in Milan, Italy for his assistance in developing the initial design of this instrument.

[1]T. Kashiwagi, Combust. Sci. Technol. 20, 225 (1979).
[2]T. Saito, L. Maruyama, K. Higashi, and A. Iwama, Combust. Sci. Technol. 15, 161 (1979).
[3]J. U. Kim, *Laser Ignition of Nitramine Composite Propellants*, Ph.D. Thesis, Pennsylvania State University, 1988.
[4]N. Mutoh, T. Hirano, and K. Akita, *The 17th Symposium (International) on Combustion* (The Combustion Institute, Pittsburgh, PA, 1979) p. 1183.
[5]T. J. Ohlemiller, L. H. Caveny, L. DeLuca, and M. Summerfield, *The 14th Symposium (International) on Combustion* (The Combustion Institute, Pittsburgh, PA, 1973) p. 1297.
[6]R. L. Akau, D. M. Keicher, P. W. Fuerschbach, and T. J. Lienert, Sandia Laboratories Technical Report, SAND-85-1523C, October 1985.
[7]D. Letalick, and I. Renhorn, Rev. Sci. Instrum. 58, 765 (1987).
[8]D. Sliney, and M. Wolbarsht, *Safety with Lasers and Other Optical Sources, A Comprehensive Handbook* (Plenum, New York, 1980), p. 385.
[9]Bulletin 2-230-3/4, Barnes Engineering Company, Stamford, Conn.

CHAPTER 3
NONINTRUSIVE FT-IR DIAGNOSTICS FOR SPECIES AND TEMPERATURE MEASUREMENTS OF PRODUCTS FROM SOLID PROPELLANTS

I. Introduction

The success of flame diagnostics of solid propellant combustion has so far been limited due to the extraordinary experimental and theoretical challenges that exist. For example, the stoichiometry and flow rates of the fuel and oxidizer cannot be controlled after ignition. Furthermore, the burning rates often are extremely high in laboratory settings, limiting the available times for data acquisition. On the theoretical side, many current models treat the propellant flame chemistry in a relatively limited way. The chemistry is represented by only a set of global reactions, and the overall combustion behavior is lumped into an overall momentum and energy transport problem, which only emphasizes the thermophysical behavior. The employment of several global reactions however, leads to a limited predictive capability, because the selection rules of the appropriate global reaction mechanisms are not well understood. Thus, it is clear that much more work is required.

Recognizing the potential usefulness of Fourier-Transform infrared (FT-IR) spectroscopy as an important diagnostic tool for both condensed and gas phases, a rapid-scanning FT-IR spectrometer (Nicolet 740) was acquired via ONR's support through the DoD-URIP program. The use of such a device should enable one to perform both flame diagnostics and to increase the data base of radiative properties of substances that are required in calculations of IR-signatures using advanced computer codes.

II. Objectives of Work

The overall objective of the work is to deduce species concentration and temperature profiles of products from the combustion of small strands of solid propellants and fuels, and pyrotechnics using the FT-IR spectrometer system. To successfully meet such an overall objective, the following specific objectives were devised.

1. Design and construct a transparent test chamber with optical access for the modulated beam of the spectrometer, and with pressure and purge gas control.
2. Design and construct a system for accurate control of position of burning surface relative to line-of-sight of modulated beam of spectrometer.
3. Design and construct an enclosure between transparent test chamber and spectrometer bench for protecting the modulated beam from the interference of H_2O, CO_2 and particulates.
4. Design and construct a high temperature furnace (1300°K) which is necessary to measure reference spectra of IR active gases, such as CO_2, H_2O, CO, C_mH_n, etc.
5. Design and construct a small boiler which is necessary to vaporize substances that exist as a liquid at S.T.P.
6. Assess the overall signal-to-noise of spectrometer system in order to determine the spatial resolution that can be achieved in spatial profiling measurements.
7. Perform emission and transmission measurements on plume products to assess overall system performance.
8. Perform emission and transmission profiling measurements on test samples of particular Navy interest.
9. Process and analyze data, and compare the obtained results with results that have been obtained by other workers using different measurement techniques.

Many of the above mentioned objectives have been met since the award of the DoD-URIP Grant, which started on February 15, 1989. The spectrometer itself was installed in the middle of November, 1989. In the following sections, we shall present only a short description of the setup of the spectrometer system and the type of measurements that have been conducted; the details have been elaborated in the enclosed papers in the Appendices 3.1 - 3.3.

III. Method of Approach

The FT-IF spectrometer, which is the instrument that detects the thermal radiation, is based on Michelson's principle in that a beam of radiant energy is first split up by a beamsplitter into two legs of an interferometer and then recombined to form a modulated beam (Griffiths and de Haseth, 1986). In transmission measurements, the modulated beam is incident on the test sample and the transmitted component is measured by a detector. In these measurements, the radiant energy emitted by a blackbody source is used to construct the modulated beam. In emission measurements, the emitted energy from a hot test sample (combustion products and hot surface of solid propellant) is the source of the radiant energy of the modulated beam and is measured by the detector. However, all wavelengths cannot be detected using a single detector/beamsplitter combination; instead, it is necessary to employ several different detectors and beamsplitters and repeat the experiment. The FT-IR located in the HPCL has the capability of using three different detectors. The liquid nitrogen cooled mercury-cadmium-telluride (MCT) detector covers the wavelength range between 2 and 20 μm, the lead-selenide (PbSe) detector covers 1-5 μm, and the silicon (Si) detector covers 0.67-1.1 μm. Two different beamsplitters are required: the KBr on a Ge substrate beamsplitter covers 2-20 μm and the quartz beamsplitter that covers 0.5-2.5 μm.

Measurements using the FT-IR spectrometer can be performed rapidly compared to wavelength dispersive instruments. For example, at $\Delta\nu = 4$ cm^{-1} resolution ($\Delta\lambda = 0.01$ μm at

λ = 5 μm and 4296 data points), which is often sufficient to resolve the spectral line features of most combustion product gases, such as CO_2, CO, HCl, HF, and H_2O, measurements can be performed repeatedly at the rate of 300 ms using a double-sided interferogram. The measurement time can be reduced significantly by decreasing the resolution to $\Delta\nu$ = 16 cm^{-1} and only acquiring single-sided interferograms; in this case, the measurement time is approximately 50 ms, but it is doubtful that the spectral line features of most diatomic molecules can be resolved with sufficient accuracy unless the pressure broadening effects are significant.

Currently, the FT-IR spectrometer system is being employed to determine the temperature and species profiles of the products formed during the combustion of a small (0.25 inch diameter, 1.25 inches long) propellant strand within a pressure controlled windowed test chamber (Klotz et al., 1990). The overall schematic diagram of the experimental setup is shown in Fig. 3.1. The small strand is placed on a pedestal within the windowed test chamber and ignited by using electrical resistance heating of a nichrome wire, which is inserted into the top of the propellant strand. Since the regression of propellant surface changes the measurement location relative to the instantaneous propellant surface, it is necessary to fix the position of the burning surface relative to the measurement line-of-sight location of the modulated beam generated by the FT-IR spectrometer. Such position control is achieved by using a He-Ne laser, a photodiode, a programmable linear actuator and a PC in a closed loop feedback system with proportioning-integral-derivative (PID) control. This position control system has worked very well for all the propellants that have been tested in our laboratory. The experimental setup is capable of measuring either the emitted IR energy from or the transmitted IR energy through the combustion products at a spatial resolution to within 100μm. The optical setup is shown in Fig. 3.2. To our knowledge, it is the only setup of an FT-IR spectrometer system that has a demonstrated capability to perform such experiments. Since the pyrolysis and/or final products may contain more than one phase, it is important to have the capability to perform both emission and

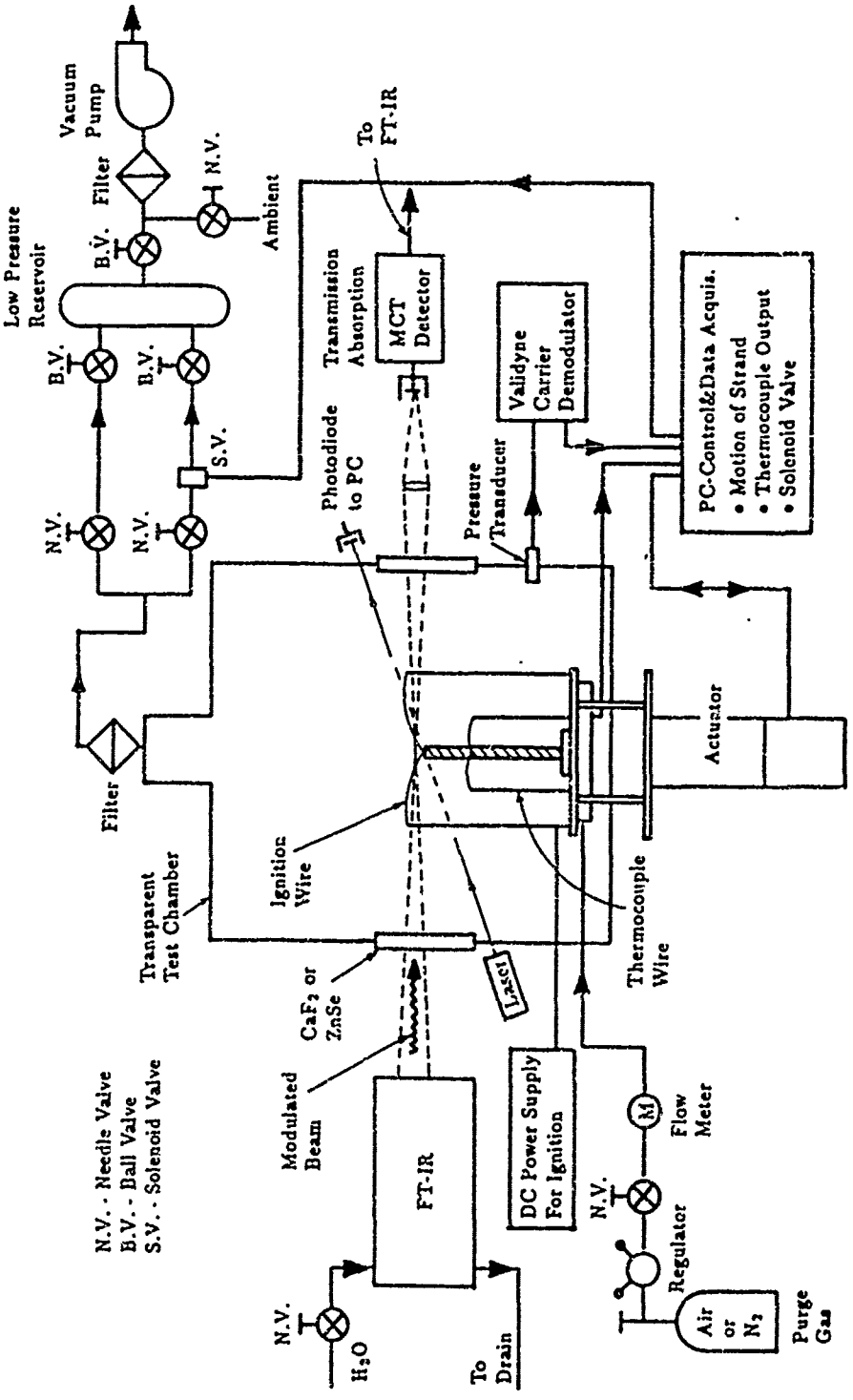


Fig. 3.1 Schematic diagram of experimental setup for combustion product studies in transparent test chamber using the FT-IR.

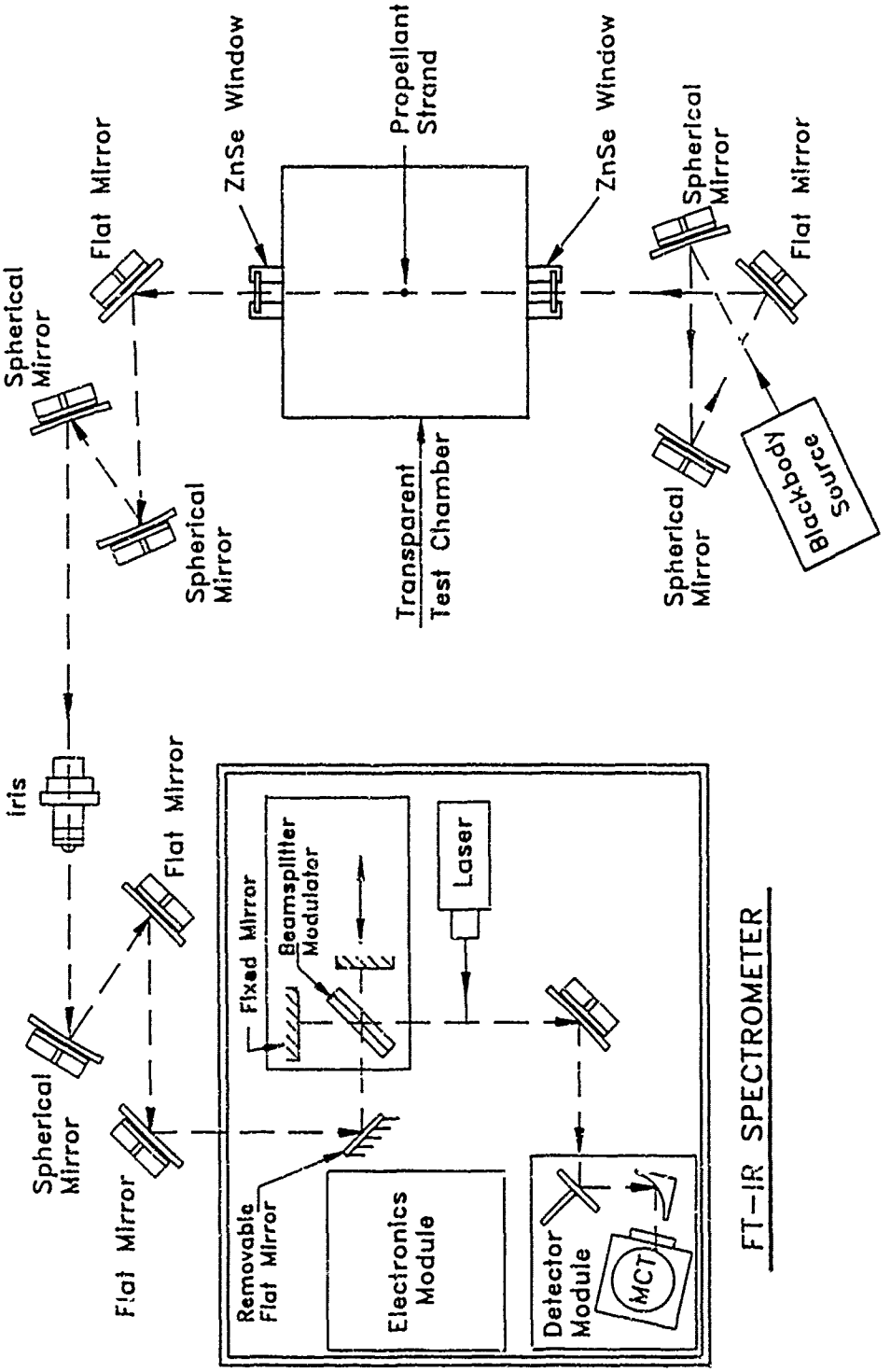


Fig. 3.2 Overall Schematic Drawing Showing the FT-IR Spectrometer and IR Beam Path from Blackbody Source, Through Test Rig (Transmission Measurement) to Spectrometer for Modulation and Detection.

transmission measurements. The importance of having such a capability is revealed during a comparison of measured spectra of combustion products from a standard solid propell[illegible] discussed in the following section.

IV. Discussion of Results

A. Emission and Transmission Measurements

Figures 3.3 and 3.4 show the spectral emissivity and transmissivity, respectively, of AP/HTPB as a result of coaddition of sixteen spectra. The data were taken at a $2cm^{-1}$ resolution with the FT-IR operating in the rapid scan mode (approximately 0.5 sec/spectra), with triangular apodization and with phase correction[11]. The measurement conditions were as follows: the strand was approximately 6mm in diameter, the center of the line-of-sight measurement location was approximately 30 mm above the burning surface, and the diameter of the spot size was about 10 mm. Inspection of the video recording shows luminous combustion products of approximately 40mm in diameter and that the combustion is somewhat unsteady at 1 atm pressure. Examination of Fig. 3.3 reveals the following. First, the achievable signal-to-noise is extremely high. This is most noticeable in the 4500 - 4000 cm^{-1} region where we observe no emitting species. Second, there appears to be almost no soot formation. The emission from soot is continuous and proportional to ν, which should reveal itself as a slightly decreasing continuous broadband which is absent in this figure. Finally, many characteristic infrared bands from the combustion products are clearly shown (Herzberg, 1968).

The strongest infrared emission bands are readily identified as CO_2, H_2O, HCl, CO and fragments of HTPB. The carbon dioxide has four strong absorption bands (at room temperature), these are located at 3716, 3609, 2349 and 667 cm^{-1} corresponding to the $(\nu_1+\nu_3)$, $(2\nu_2 + \nu_3)$, ν_3 and ν_2 vibrational modes, respectively. The carbon dioxide molecule also has two hot bands, located at 961 and 1064 cm^{-1} corresponding to the $\nu_3-\nu_1$ and $2\nu_2-\nu_1$ vibrational modes,

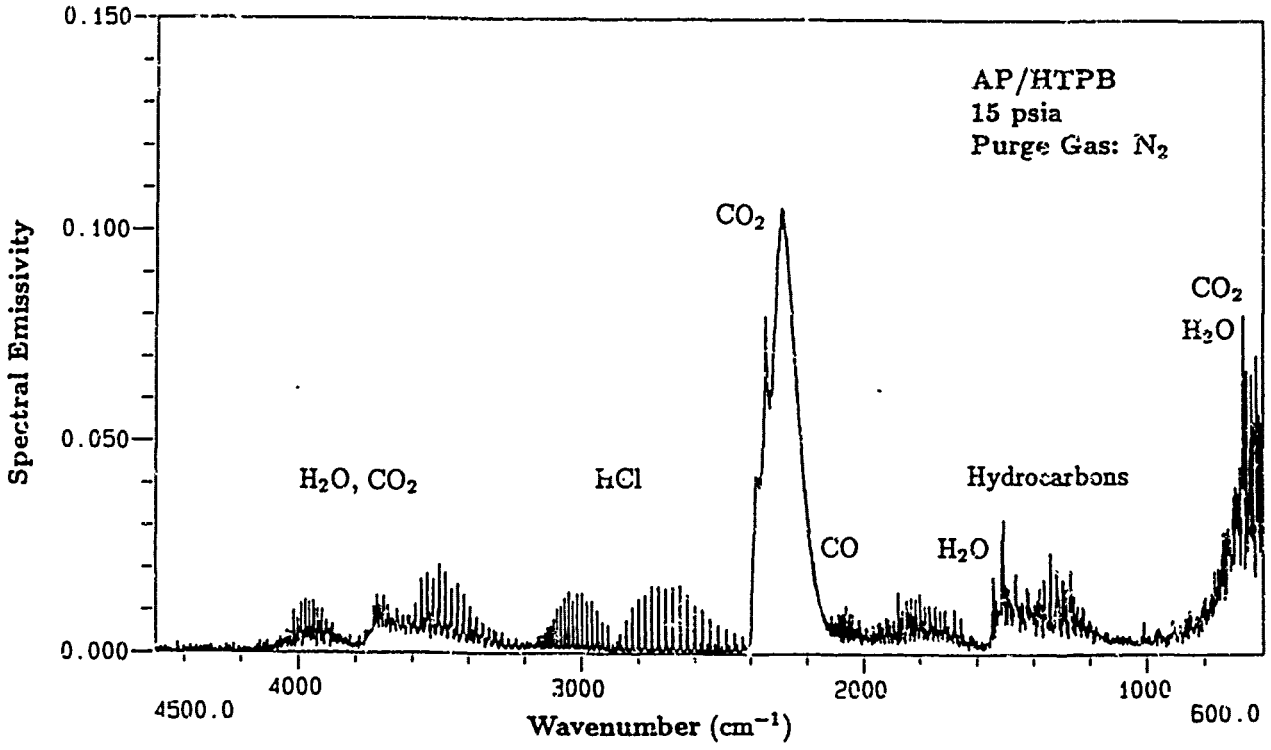


Fig. 3.3 Results of 16 coadded emission spectra of AP/HTPB evaluated according to Eq. (2) with $T_p = 1500K$

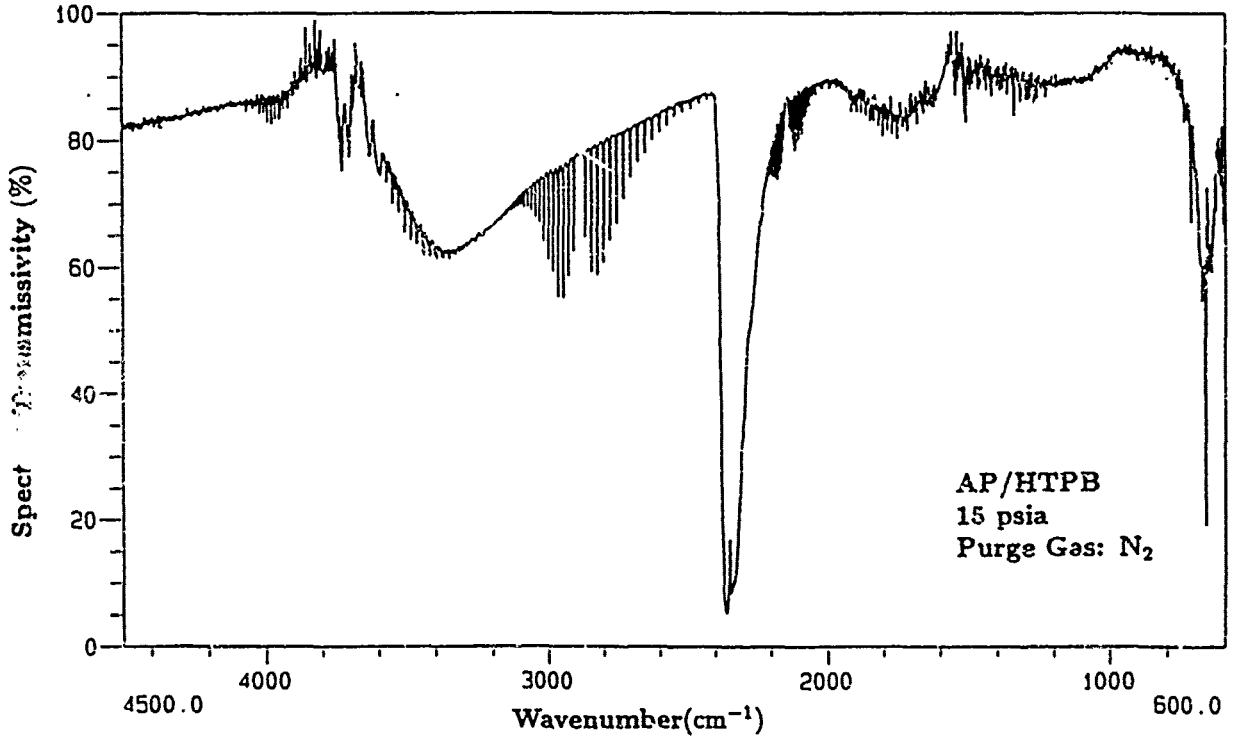


Fig. 3.4 Result of 16 coadded transmission spectra of AP/HTPB evaluated according to Eq. (3).

respectively, but these are either too weak or overlapped due to emission bands of HTPB fragments occurring at these spectral locations. In addition, the strong CO_2 band located at 2349 cm^{-1} also reveals some self absorption effects on the longer wavenumber side. This is possibly due to recirculating CO_2 within the windowed test chamber or residual CO_2 present in the otherwise well-purged path to and within the spectrometer.

The spectrum shown in Fig. 3.3 also reveals water vapor emission bands centered at 3750 and 1600 cm^{-1} and the pure rotational band continuing its emission beyond the 500 cm^{-1} cutoff of the ZnSe windows and MCT detector. Although the water vapor shows an extremely fine line structure, the 2 cm^{-1} resolution appears to reveal the presence of water vapor quite well.

Two diatomic molecules also reveal their infrared spectra, namely HCl and CO. Only the fundamental bands are clearly shown here, that is the v_1, centered at 2889 cm^{-1} for HCl and 2143 cm^{-1} for CO. The fact that both of these bands do not significantly overlap the strong CO_2 band centered at 2349 cm^{-1} or any of the water vapor bands is extremely important for concentration and temperature measurements.

Finally, thermal fragments of the HTPB (as various hydrocarbons) also appear in the figure. Fragments of the HTPB are tentatively assigned to the 1400-1200 cm^{-1} region, possibly as various CH_n and C_2H_n groups. It is evident, however, that high temperature reference spectra of the various molecular species must be measured before firm assignments can be made.

Comparison of Fig. 3.4 with Fig. 3.3 reveals that there are certain spectral regions that do not exhibit a similar spectral behavior as expected, since one should expect the combustion to be complete within the focal spot of the modulated beam. This is apparently not true and we attribute the observed results to the presence of a two-phase mixture. That is, AP particles emerge from the surface region and do not completely pyrolyze before they enter the line-of-sight region of the FT-IR. During pyrolysis, the particles and the decomposed gases are relatively cold and do not show up in the emission spectra. However, the presence of such particles is

revealed by both the continuous absorption band; a firm assignment of the strong vibration-rotation band centered near 3300 cm^{-1} cannot be made however.

B. Signal-to-Noise Analysis of High-Pressure Combustion

It is well known that the achievable signal-to-noise ratios (SNRs) of FT-IR spectrometers can be much higher than the corresponding SNR of wavelength dispersive instruments. To date, however, no analysis has been made on the effect of achievable SNR on the desired temperature and species profiling accuracy of high-pressure solid propellant combustion. A high spatial resolution is required in order to resolve the changes in species concentration and temperature in the vicinity of a propellant surface. From such extremely useful measurements, important information on the complex propellant pyrolysis and combustion chemistry will be obtained. For example, the CARS technique (Stufflebeam and Eckbreth, 1989) has employed a 200 μm diameter and 3 mm long probe volume in high-pressure combustion diagnostics.

To estimate the achievable SNRs, in which the noise is simply related to the detector noise, we follow the approach originally developed by Mattson (1978). According to a modification of his development, which is shown in the enclosed Appendix B and verified experimentally, the SNR at a given wavenumber ν (SNR_ν) can be estimated from the expression

$$SNR_\nu = C\,(1-\exp^{-\tau_\nu})\,I_{b\nu}(T)\,\theta_{slit} \qquad (1)$$

where C is a constant that depends upon many factors including, among others, the type of detector used, optical throughput of system, and wavenumber resolution; $(1-\exp^{-\tau_\nu})\,I_{b\nu}(T)$ is the spectral radiant intensity emitted by the combustion products (Ozisik, 1973), τ_ν is the optical depth and depends on the type of gas considered, $I_{b\nu}(T)$ is the Planck function for blackbody emission, and θ_{slit} is the slit height which controls the spatial resolution. In order to determine the SNR using this expression, it is necessary to determine the constant from experiments and to select an appropriate wavenumber and the type of gas considered. First, we select a

wavenumber ν=2400 cm^{-1}, which should lie somewhere in between the anticipated maximum of blackbody emission and maximum specific detectivity of the MCT detector. Near this wavenumber region, there should be several significant emission/absorption bands from numerous decomposition and equilibrium combustion products of various propellants. Since the radiative properties of CO_2 are well-known, we select this molecule for the SNR calculations, although it may not be present in significant quantities (<10%) in the combustion products near the burning surface. The optical depth is readily estimated using Edwards' well-established exponential wide-band models (Edwards, 1976) and further discussed in Appendix 3.2.

Figure 3.5 shows the SNRs that are expected to be obtained in emission measurements of combustion products containing CO_2 for three different temperatures, a slit height of 100 μm and a slit width of 6 mm. Inspection of this figure reveals that for a plume depth L=0.006 m, a total pressure p=450 psia (30 atm), and a concentration X_{CO_2}=10%, the estimated SNRs are on the order of 500 to 800 at temperatures relevant to propellant combustion. At the higher partial pressure path-lengths, the optically thick limit is approached and blackbody emission obtained. Thus the SNRs becomes independent of the partial pressure path-length. If the slit height is doubled or tripled, then the predicted SNRs also double or triple in magnitude. Hence, temperature and species profiling of combustion products from solid propellants burning at realistic pressures should be possible. We believe that this conclusion is of utmost importance for our planned future work on the continued development of the FT-IR spectrometry as a diagnostic tool for solid propellant pyrolysis and combustion.

The results shown in Fig. 3.5 are not unexpected, since FT-IRs have been employed to deduce temperatures and species concentrations on the effluents from smoke stacks, whose temperatures were relatively low (Herget, 1982). The approach for deducing temperatures from emission measurements of the hot bands of CO_2 located near 10 μm has also been studied in

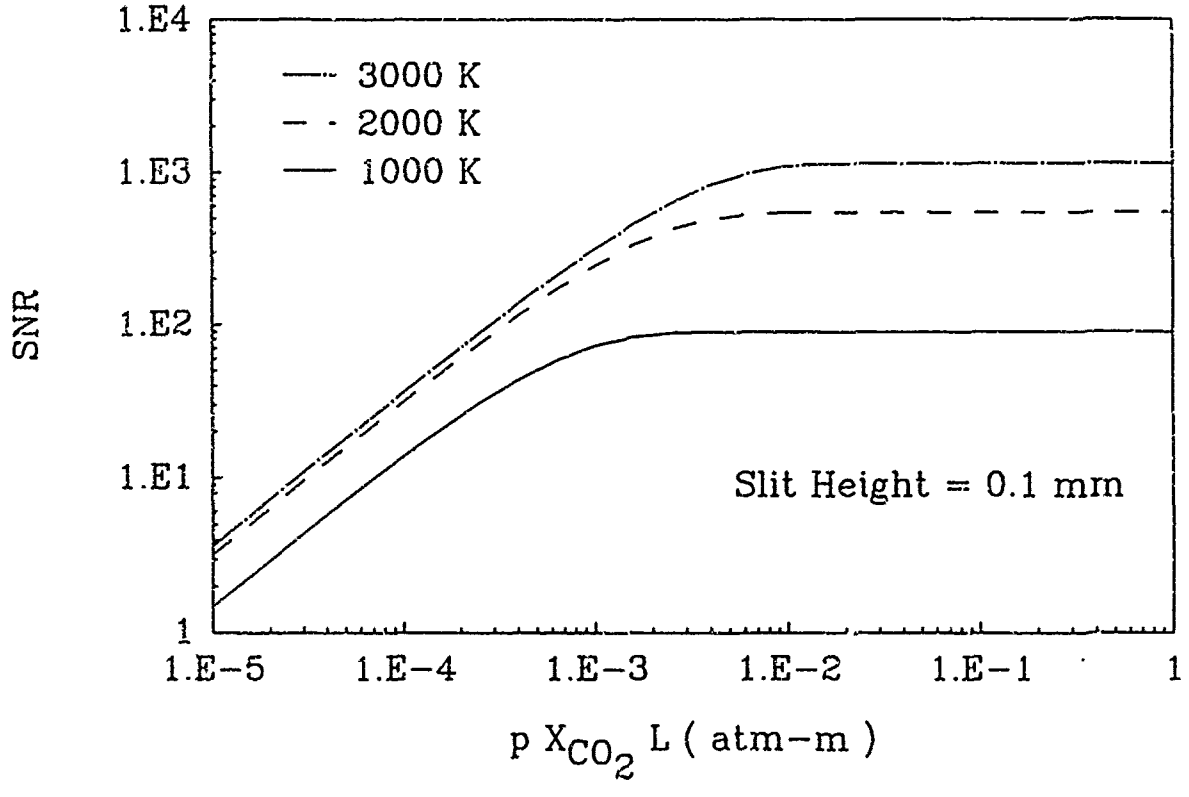


Fig. 3.5 SNR at different temperatures at a slit height of 100 μm.

laboratory settings (Gross and Griffiths, 1988a,b). In addition, it should be noted that the above value of SNR is the RMS value; the peak-to-peak value is approximately 5 times larger.

C. A New Approach to Flame Spreading Measurements

The previously described FT-IR spectrometer system has also been employed for the development of a new approach for the measurement of flame spreading over solid propellant surfaces. Traditionally, such measurements have been extremely difficult to perform using fuse wires, thin-film flux gauges, or motion picture cameras. The use of standard video techniques is also problematic due to the strong luminosity of soot and burning metal particles and emission of photons during electronic transitions within radicals. A short description of the technique is described next, with the details elaborated in the attached Appendix 3.3.

The technique is based on the assumption that the emission characteristics of a burning surface is very much different than the emission characteristics of the corresponding equilibrium products. To evaluate this assumption, a test matrix involving four different cases of emission measurements was devised and is illustrated in Fig. 3.6. Case 1 corresponds to the situation when only emission from equilibrium products is detected, Case 2 when emission from both equilibrium products and the burning surface are detected, Case 3 when emission from the burning surface alone is detected, and Case 4 when emission from the cold surface is detected. Figure 3.7 illustrates the MCT spectral detector response for these four cases of an Al/AP/HTPB (18% Al) propellant. Examination of the results shown in Fig. 3.7 reveals that the emission characteristics within the 4500 to 2400 cm^{-1} wavenumber range is significantly different (stronger) between the ignited and the unignited surfaces, although the surface is subject to a cross-flow of equilibrium combustion products from the solid propellant. Based on this result, it is suggested that standard lead-selenide detectors be employed for such measurements. The recorded output voltage from such a detector should change by about an order of magnitude

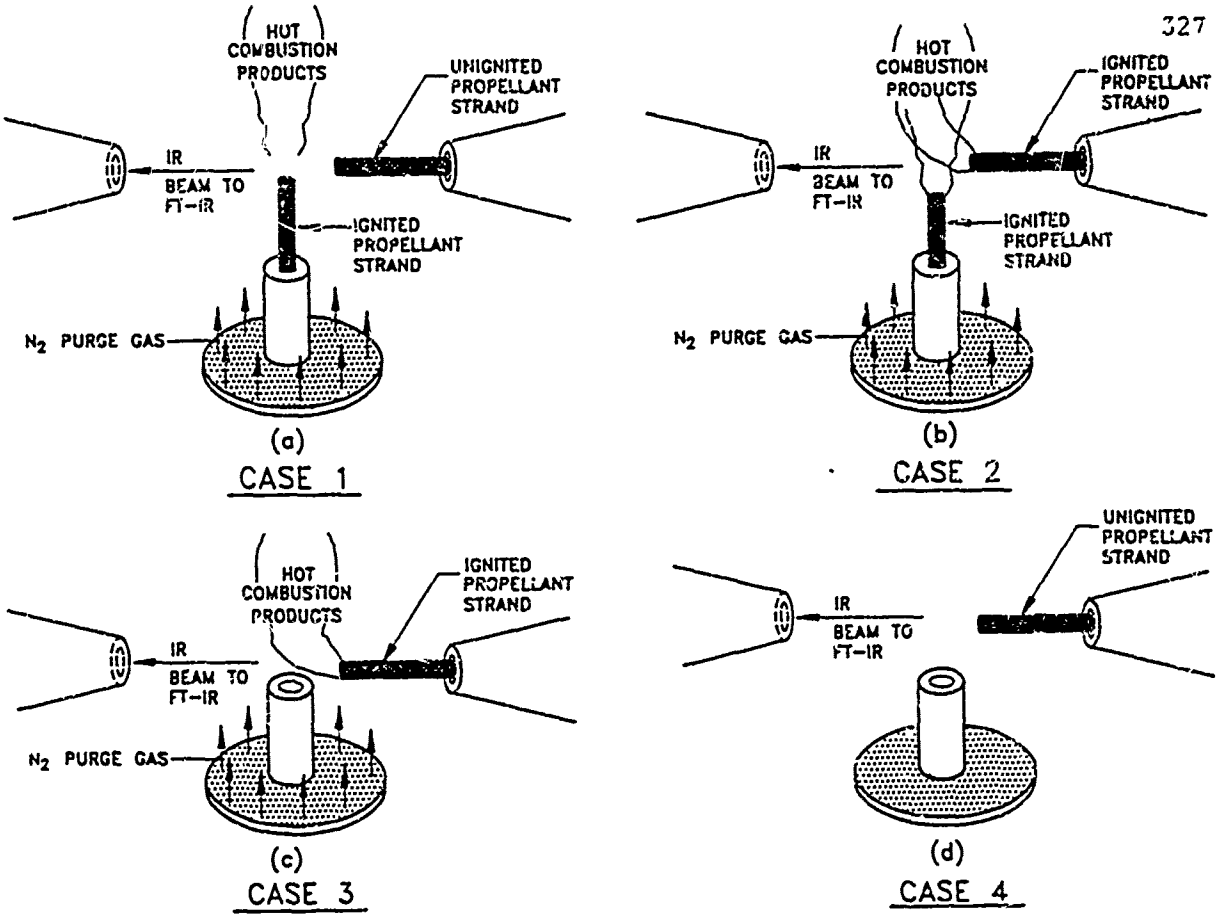


Fig. 3.6 Experimental Setup of Propellant Strands within Windowed Test Chamber for Conducting Emission Measurements Simulating Flame Spread.

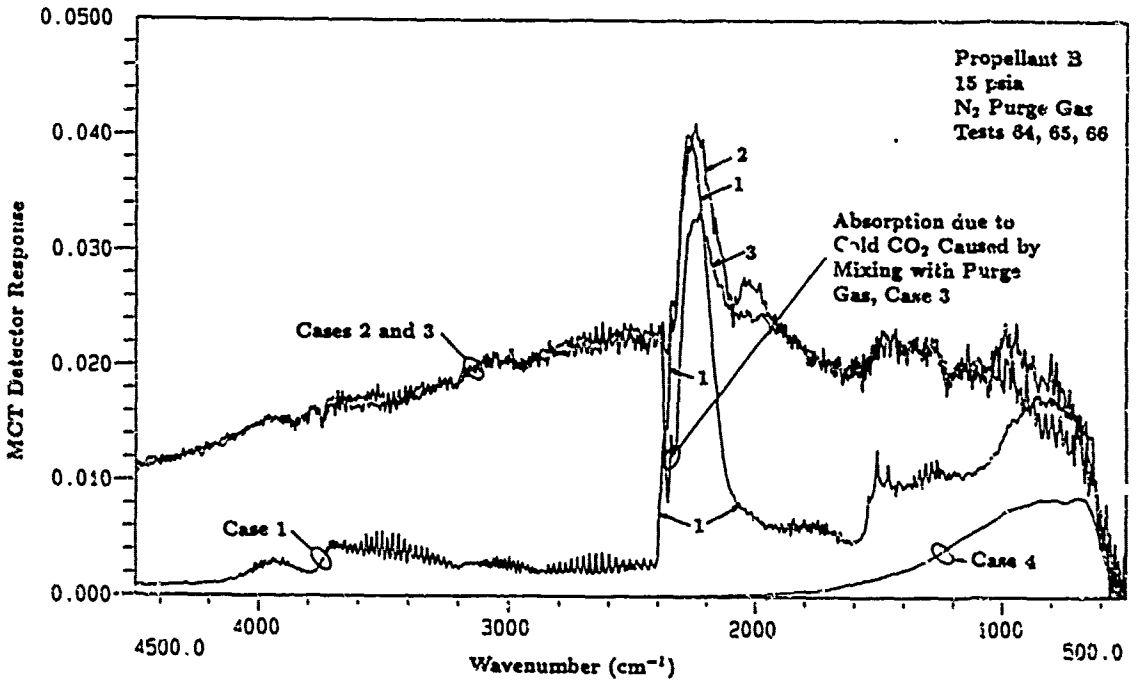


Fig. 3.7 MCT Detector Responses due to Emission According to Cases 1, 2, 3 and 4.

once the surface has ignited. In addition, other propellants have also been tested in our laboratory, but the conclusions reached are the same.

V. Conclusions

A brief summary of the major conclusions of the study involving measurements using the FT-IR spectrometer system and modeling of radiation is given below.

- A unique FT-IR spectrometer system has been established which is capable of performing simultaneous emission and transmission measurements of products from the combustion of solid fuels, solid propellants, and pyrotechnics.
- High-quality emission and transmission spectra have been obtained and used to determine the temperature and species concentration of combustion products. To authors knowledge, this is the first attempt to use FT-IR spectroscopy to perform such measurements on combustion products from solid propellants.
- A recently completed study at The Pennsylvania State University has shown that FT-IR emission spectroscopy can be performed at a spatial resolution to within 100 μm with a signal-to-noise ratio of more than 1000 at the high pressures of solid propellant combustion.
- From our pioneering work using the FT-IR spectrometer system, a new approach to the measurement of flame spreading over solid propellant surfaces has been established through a feasibility study.
- Many reference spectra of IR active gases at high temperatures and at high spectral resolutions were obtained. These measurements are not only an integral part of our experimental effort, but also provide important input to data bases of computer codes that predict iR-signature as well as for model validation of gaseous flame-zone reactions with finite-rate kinetics.

- A multi-dimensional, axisymmetric radiation code including the effects of absorbing, emitting and anisotropically scattering constituents, has been formulated and solved using exact techniques This is the first code available which has this capability.
- The first fundamental results on the effects of scattering have shown that it is possible to either enhance or inhibit the spectral plume emission. This could have a tactical value to the U.S. Navy.

VI. References

Edwards, D.K., "Molecular Gas Band Radiation," in *Advances in Heat Transfer,* edited by T.F. Irvine and J.P. Hartnett, Vol. 12, pp. 115-193, 1976.

Griffiths, P.R., and de Haseth, J.A., *Fourier Transform Infrared Spectrometry*, Wiley, New York, New York, 1986.

Gross, L.A., and Griffiths, P.R., "Temperature Estimation of Carbon Dioxide by Infrared Absorption Spectrometry at Medium Resolution," *J. Quant. Spectrosc. Radiat. Transfer*, Vol. 39, No. 2, pp. 131-138, 1988a.

Gross, L.A., and Griffiths, P.R., "Spectroscopic Temperature Estimates by Infrared Emission Spectrometry," *J. Quant. Spectrosc. Radiat. Transfer*, Vol. 39, No. 6, pp. 463-472, 1988b.

Harris, L.E., and Kuo, K.K., "Advanced Diagnostics for Gun Propellant Combustion," JANNAF Combustion SubCommittee Workshop, CPIA Publication 534, June 13-14, 1989.

Herget, W.F., "Remote and Cross-Stack Measurement of Stack Gas Concentrations Using a Mobile FT-IR System," *Applied Optics*, Vol. 21, No.4, pp. 635-641, 1982.

Herzberg, G., *Molecular Spectra and Molecular Structure. II. Infrared and Raman Spectra of Polyatomic Molecules*, van Nostrand Co., Princeton, New Jersey, 1968.

Huang, I.T., S.T. Thynell, K.K. Kuo, "Measurements and Theory of Signal-to-Noise Ratio of FT-IR Emission Spectrometry Applied to High Pressure Solid Propellant Combustion," submitted to *Applied Spectroscopy,* February, 1991.

Klotz, S., S.T. Thynell, I.T. Huang, and K.K. Kuo, "Analysis of Plumes of Solid Propellant Combustion Using an FT-IR Spectrometer," AIAA/SAE/ASME/ASEE Joint Propulsion Conference and Exhibit, Orlando, FL, July 16-18, 1990.

Mattson, D.R., "Sensitivity of a Fourier Transform Infrared Spectrometer," *Applied Optics,* Vol. 32, No. 4, pp. 335-338, 1978.

Ozisik, M. N., *Radiative Transfer and Interactions with Conduction and Convection*, Wiley, New York, New York, 1973.

Stufflebeam, J.H., and Eckbreth, A.C., "Multiple Species CARS Measurements of High Pressure Solid Propellant Combustion," Twenty-seventh Aerospace Sciences Meeting, AIAA-89-0060, Reno, Nevada, January 9-12, pp. 1-10, 1989.

Publications and Presentations

Huang, I.T., S.T. Thynell, K.K. Kuo, "Measurements and Theory of Signal-to-Noise Ratio of FT-IR Emission Spectrometry Applied to High Pressure Solid Propellant Combustion," submitted to *Applied Spectroscopy,* February, 1991.

Klotz, S., S.T. Thynell, I.T. Huang, K.K. Kuo, "Analysis of Plumes of Solid Propellant Combustion Using an FT-IR Spectrometer," AIAA Paper No. 90-1850, presented at the 26th AIAA/SAE/ASME/ASEE Joint Propulsion Conference and Exhibit, Orlando, FL, July 16-18, 1990, *AIAA J. Propulsion and Power,* (in press).

Thynell, S.T., I.T. Huang, C.S. Kuo, W.H. Hsieh, K.K. Kuo, "An Approach to Measurements of Flame Spreading over Solid Propellants," submitted to *AIAA J. Propulsion and Power,* February 1991.

Thynell, S.T., "Radiation due to CO_2 or H_2O and Particles in Cylindrical Media," AIAA Paper No. 89-1718, Presented at the 24th Thermophysics Conference, Buffalo, N.Y., June 12-14, 1989, *AIAA J. Thermophysics and Heat Transfer,* Vol. 4, No. 4, pp. 436-445.

Thynell, S.T., "The Effect of Linear-Anisotropic Scattering on the Directional and Hemispherical Emittance from a Cylindrical Plume," AIAA Paper 90-1237 presented at the AIAA 28th Aerospace Sciences Meeting, Reno, Nevada, January 8-11, 1990, *AIAA J. Thermophysics and Heat Transfer,* (in press).

Thynell, S.T., "The Integral Form of the Equation of Transfer in Finite, Two-Dimensional Cylindrical Media," *J. Quant. Spectrosc. Radiat. Transfer,* 42(2):117-136 (1989).

Thynell, S.T., "Treatment of Radiation Heat Transfer in Absorbing, Emitting, Scattering Two-Dimensional, Cylindrical Media," *Numerical Heat Transfer,* Part A, 7:449-472, (1990).

Thynell, S.T., "Radiative Transfer in Two-Dimensional Cylindrical Media With Internal Heat Generation," ASME Proceedings of the 1990 AIAA/ASME Thermophysics and Heat Transfer Conference, HTD. Vol. 137, pp. 117-124, 1990.

Venkateswaran, S., S.T. Thynell, C.L. Merkle, "A Study of Thermal Radiation Transfer in a Solar Thruster," ASME Proceedings of the 1990 AIAA/ASME Thermophysics and Heat Transfer Conference, HTD. Vol. 137, pp. 125-132, 1990; *ASME J. Heat Transfer,* (in press).

Journal Publications and Paper Presentations

Klotz, S., "Analysis of Plumes of Solid Propellant Combustion Using an FT-IR Spectrometer," M.S. Thesis, Department of Mechanical Engineering, The Pennsylvania State University, May 1990. (Cpt. S. Klotz is currently teaching at West Point, N.Y.)

Kuo, C.S., "Measurements of High Temperature Reference Spectra of H_2O and CO_2," M.S. Thesis, Department of Mechanical Engineering, The Pennsylvania State University, May 1991.

Huang, I.T., "Species Concentration and Temperature Profiling of Products from the Combustion of Solid Propellants," Ph.D. Thesis, in progress (expected completion in May 1992).

AIAA-90-1850

Analysis of Plumes of Solid Propellant Combustion Using an FT-IR Spectrometer

S. Klotz, S. T. Thynell, I. T. Huang, and K. K. Kuo
Mechanical Engineering Department
The Pennsylvania State University
University Park, PA 16802

AIAA/SAE/ASME/ASEE
26th Joint Propulsion Conference
July 16-18, 1990 / Orlando, FL

For permission to copy or republish, contact the American Institute of Aeronautics and Astronautics
370 L'Enfant Promenade, S.W., Washington, D.C. 20024

Analysis of Plumes of Solid Propellant Combustion Using an FT-IR Spectrometer

S. Klotz,* S.T. Thynell,† I.-T. Huang*, and K.K. Kuo‡

Abstract

A Fourier Transform-Infrared (FT-IR) spectrometer has been setup to study the combustion products of various solid propellants. The overall objective of the work is to perform radiation measurements using a rapid scanning FT-IR on combustion products evolved from burning a small strand in a windowed test chamber. The windowed test chamber is equipped with a computer controlled linear actuator, which is employed to fix the vertical position of the burning surface so that steady state emission and transmission/absorption measurements can be made using the spectrometer. Several experiments have been conducted to test the setup and operation of the system. The setup has operated reliably for propellants which ignite and burn under few atmospheric pressure conditions. Results presented here include emission and transmission spectra of a typical heterogeneous AP/HTPB propellant and a homogeneous NOSOL 363 triple-base propellant.

Nomenclature

$I_{b\bar{\nu}}$	Planck function ($W/m^2\,cm^{-1}\,sr$)
$I_{bg\bar{\nu}}$	background intensity ($W/m^2\,cm^{-1}\,sr$)
$I_{\bar{\nu}}$	intensity ($W/m^2\,cm^{-1}\,sr$)
$I_{s\bar{\nu}}$	blackbody source intensity ($W/m^2\,cm^{-1}\,sr$)
$I_{0\bar{\nu}}$	incident intensity ($W/m^2\,cm^{-1}\,sr$)
T_{ref}	temperature of blackbody source (K)
T_p	temperature of combustion products (K)
$W_{\bar{\nu}}$	instrument response function
$\epsilon_{\bar{\nu}}$	spectral emissivity
$\tau_{\bar{\nu}}$	spectral transmissivity
$\alpha_{\bar{\nu}}$	spectral absorptivity
$\bar{\nu}$	wavenumber (cm^{-1})
$\Delta\bar{\nu}$	wavenumber resolution (cm^{-1})

*Graduate Student
†Assistant Professor, Member AIAA
‡Distinguished Professor, Associate Fellow AIAA

Copyright © 1990 American Institute of Aeronautics and Astronautics, Inc. All rights reserved.

Introduction

The detailed combustion chemistry and radiative property determination of plumes from solid propellant combustion are topics of strong current interest[1,2]. There are several reasons for such interest. First, the understanding of structure and reaction mechanisms of solid propellant flames is limited at present. For example, the chemistry of nitrogen in flames is one area that requires further research to overcome the discrepancies between modelling prediction and experimental results. The modelling efforts of propellant performance and combustion instability should benefit significantly from a much improved understanding of the nitrogen chemistry.

Second, the determination of radiative properties is required for the estimation of species concentration and temperatures using laser and/or IR based techniques, as well as for model validation of codes that compute IR signatures. Furthermore, radiative heat transfer could play an important role in the burning of aluminized composite solid propellants as the temperatures are extremely high. In related areas, a knowledge of radiative properties is critical to proper modelling of heat transfer to insulator and nozzle surfaces in solid rocket motors[3], the analysis of radiative heat transfer back to burning propellant surface[4], and spectrally selective absorption of radiation by particles influences the melting and agglomeration of aluminum at the surface of the propellant[5]. Consequently, a significant effort has been devoted to the development of both intrusive and nonintrusive techniques that offer the possibility of measuring the species concentrations and temperatures.

Among the intrusive methods, thermocouples and probes represent the classical measurement techniques for the study of combustion of solid propellants and fuels. Some examples include microthermocouples to measure plume temperatures and thermal wave penetrations[6], and sampling probes to determine particle size distributions and concentrations[7]. However,

to obtain in a highly spatially and temporally resolved manner the species concentration and temperature profiles, a significant effort has been focussed on the development of laser based techniques. Examples of such include, among others, laser-induced-fluorescence[8,9] (LIF), and coherent anti-Stokes Raman scattering (CARS)[10]. However, laser based techniques have a few disadvantages. First, these techniques cannot be applied to highly dense systems, that is, to combustion products containing a significant amount of particulate matter; second, only a few species are measured, unless a wide variety of lasers are used simultaneously; third, the use of LIF methods to systems containing particulate matter is questionable; and, fourth, light scattering techniques requires a prior knowledge of radiative properties of the scattering constituents. Consequently, there is a need to continue the development of nonintrusive diagnostic techniques.

To fulfill such a need, the combustion group at The Pennsylvania State University (PSU) has incorporated the use of a rapid scanning FT-IR (Fourier transform infrared) spectrometer for species and temperature measurements on combustion products of solid propellants and fuels, and pyrotechnics. The FT-IR offers several important advantages over laser based techniques. First, it measures simultaneously the thermal radiation over a broad range of wavelengths (wavelength range limited by a combination of the detector response and beamsplitter transmittance); second, it can be applied to optically dense systems; third, very high signal-to-noise ratios are achievable; and fourth, data processing of interferograms is extremely rapid and data can be displayed almost instantly. Nevertheless, there are two disadvantages of using the FT-IR; one is its long measurement time (~50 ms @ 16cm^{-1} resolution) and the other is the line-of-sight approach.

The objectives of this work are to describe the details of the experimental setup and to present a preliminary analysis of the measured spectra. Specifically, the design of a transparent test chamber, with accurate control of chamber pressure and position of burning surface of propellant strand are discussed. Representative emission and transmission spectra obtained from the FT-IR spectrometer are presented.

Experimental Setup

A schematic diagram of the overall setup is shown in Fig. 1. As shown in this figure, the setup consists of two major components: a windowed test chamber and FT-IR spectrometer. These two major components are set up separately and then integrated to function simultaneously in a given experiment. Of the two computers required, one computer is an integral component of the FT-IR system and is used to communicate commands to the spectrometer bench, and to receive and display information from the spectrometer. The second, an IBM compatible computer (P/C), is used to control other non-FT-IR functional components, such as pressure control, position control, etc. The use of these two components, their overall operation and interfacing, and the setup for emission and transmission/absorbtion measurements are discussed below. In addition, since the theory of FT-IR spectroscopy is well-established, interested readers are referred to the appropriate texts on this topic[11].

Windowed Test Chamber

The propellant strand is burned in a 30*cm* x 30*cm* x 30*cm* transparent, 2.54*cm* thick plexiglass combustion chamber capable of operating between vacuum and about 2 atmospheres. The strand is placed in the center of the chamber on a platform which delivers a purge gas up and around the burning sample, thereby removing the combustion products. Additionally, the horizontal position (perpendicular to line-of-sight) of the sample is controlled accurately by manual adjustment of a micrometer to preselect propellant strand position. The chamber is fitted with two special optics holders, shown in Fig. 2, (one each on opposite sides of the chamber) which protect the beam path from IR active gases and particulates recirculating in between the sample and the chamber walls, and hold the zinc-selenide windows in place. Between the chamber and the spectrometer, radiant energy is routed through a series of external flat and parabolic mirrors all of which are enclosed in a sealed and purged path.

The test stand is also configured with a linear actuator which is attached to the bottom of the chamber so that its stroke arm extends up through the base of the chamber. The use of a laser and photodiode, which are interfaced by means of an IBM compatible computer with the actuator, enables us to control the position of the burning surface. As the sample burns down below the line-of-sight established by the laser/photodiode setup, the photodiode senses the laser energy. This process is scanned by the data acquisition board (DAS-16) within the computer. When the photodiode energy reading reaches a certain level (indicating the propellant burning surface has receded), the computer simultaneously sends a movement command string to the actuator controller, which results in an upward movement of the platform and therefore the

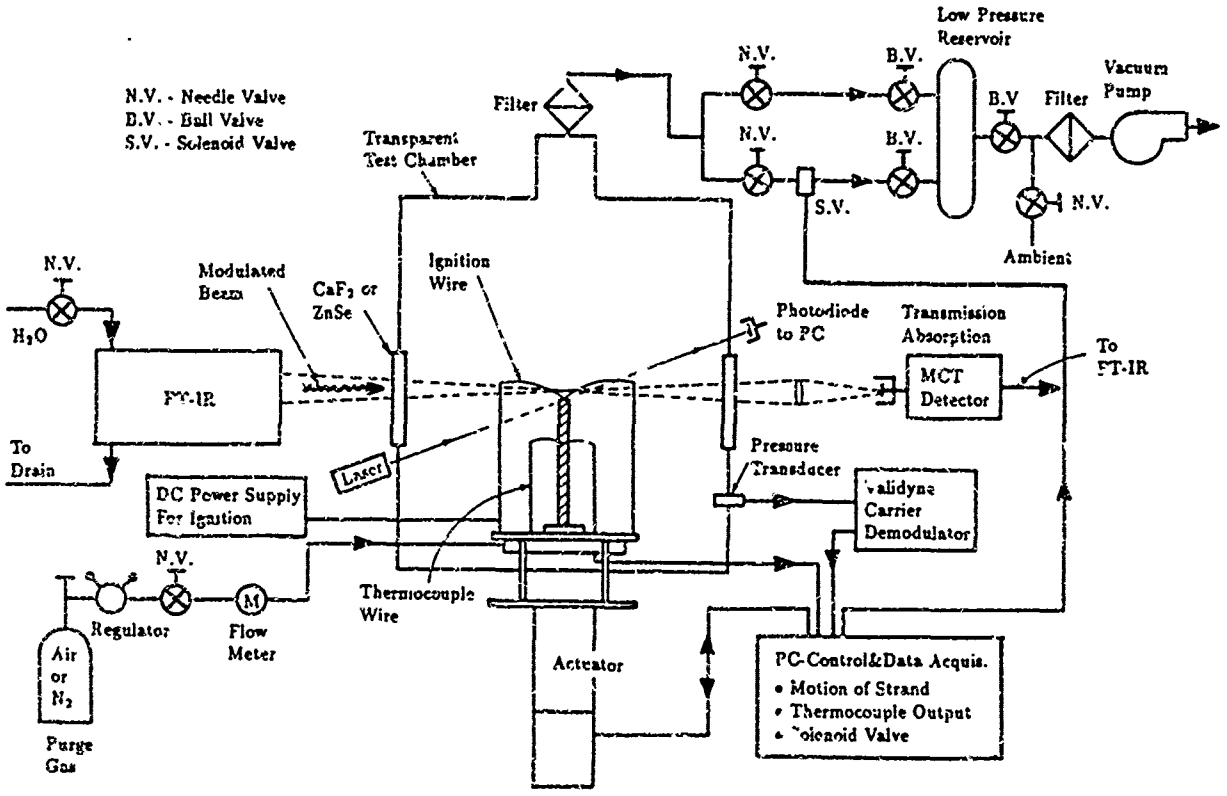


Fig. 1. Schematic diagram of experimental setup for combustion product studies in transparent test chamber using the FT-IR.

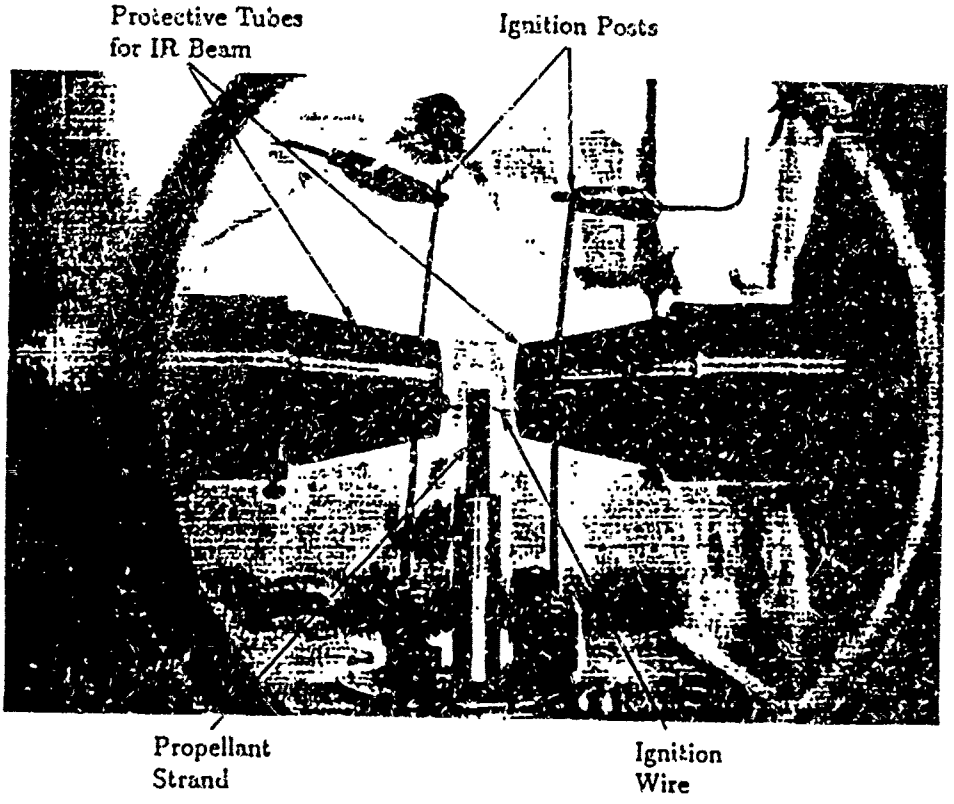


Fig. 2. Close up view of the propellant strand located within transparent test chamber.

sample burning surface. This entire process provides a closed feedback system for maintaining the burning surface at a fixed position in order to achieve desired spectroscopic measurements. Furthermore, the controller of the actuator can also be programmed to feed the sample at a predetermined rate so that the vertical species profile above the sample surface can be measured. A similar system was used by Goetz and Mann[12]. It should be noted that for combustible strands containing significant amounts of particulate matter, the laser beam cannot penetrate the combustion products and, therefore, the lased-based positioning system is not suitable. In addition to the closed loop feedback positioning system, the test rig includes an exhaust/pressure control system and thermocouple temperature measurement devices (both controlled by the DAS-16 board in the computer), and ignition control devices.

Emission Measurements

In emission measurements, the emitted radiant energy from the combustion products is measured. These types of measurements are particularly useful for the determination of the temperature of the combustion products. Figure 3 shows the emission measurement setup. The radiant energy emitted from the combustion products of the burning propellant strand travels from the chamber along the optical path indicated and enters the rear port of the spectrometer. With the removable flat mirror in place, the beam passes through the beamsplitter (B/S), is modulated by the interferometer, and is directed onto the detector module mounted inside the spectrometer. Three detector modules are available: a liquid N_2 cooled MCT-A detector for mid-IR range, and PbSe and silicon detectors for near-to mid-IR ranges. Detector and beamsplitter (KBr or quartz) combinations determine the appropriate wavenumber ranges covered.

To determine the emissivity of the combustion products, it is necessary to know the instrument response function. The instrument response function accounts for the reduction of the IR signal from the plume due to mirrors, optical windows, interferometer components, iris, detector response, etc. If the measured radiant intensity due to a blackbody source at temperature T_{ref} is denoted by $I_{s\bar{\nu}}$, then the instrument response function $W_{\bar{\nu}}$ is computed from

$$W_{\bar{\nu}} = \frac{I_{s\bar{\nu}}}{I_{b\bar{\nu}}(T_{ref})}, \tag{1}$$

where $I_{b\bar{\nu}}(T_{ref})$ is the Planck function and calculated by software. To determine the plume emissivity $\epsilon_{\bar{\nu}}$, the background intensity $I_{bg\bar{\nu}}$ must be measured prior to ignition and the apparent plume intensity $I_{\bar{\nu}}$ is measured during combustion. Finally, the plume emissivity is given by

$$\epsilon_{\bar{\nu}} = \frac{I_{\bar{\nu}} - I_{bg\bar{\nu}}}{W_{\bar{\nu}} I_{b\bar{\nu}}(T_p)}, \tag{2}$$

where T_p is the plume temperature and must be known. At this stage, it is appropriate to make two comments regarding the use of Eq. (2). First, the instrument response function should be measured at a temperature of the blackbody source that is relatively close to the temperature of the combustion products. The reason for this is related to the slight nonlinearity of the highly sensitive MCT-A detectors. Second, the temperature of the combustion products should be uniform along the line-of-sight of measurement. This is most likely the case in the combustion of propellant strands in inert environments.

Transmission/Absorption Measurements

In transmission/absorption measurements, a continuum spectrum of radiant energy (from a blackbody source) is incident on the combustion products. These types of measurements represent the standard approach for species concentration measurements. Figure 4 shows the optical measurement setup. In this case, the removable detector is placed next to the combustion chamber. Additionally, the removable flat mirror of Fig. 3 is removed. Energy from a blackbody source within the spectrometer is passed through the beamsplitter modulator and a flipper mirror, and then directed out through the second external port. With the electronically controlled external flipper mirror moved out of the path (therefore not shown in the figure), the beam is directed through the plume of the propellant strand and out of the chamber onto the detector on the opposite side of the chamber. If $I_{0\bar{\nu}}$ denotes the incident intensity, the transmissivity is determined as

$$\tau_{\bar{\nu}} = \frac{I_{\bar{\nu}}}{I_{0\bar{\nu}}}, \tag{3}$$

where $I_{\bar{\nu}}$ is the transmitted intensity. For a participating medium which contains no scattering constituents, the spectral absorptivity is

$$\alpha_{\bar{\nu}} = 1 - \tau_{\bar{\nu}}. \tag{4}$$

Discussion of Results

Background on Interpretation of IR Spectra

The combustion chemistry of solid propellants is extremely complex and in general not well understood.

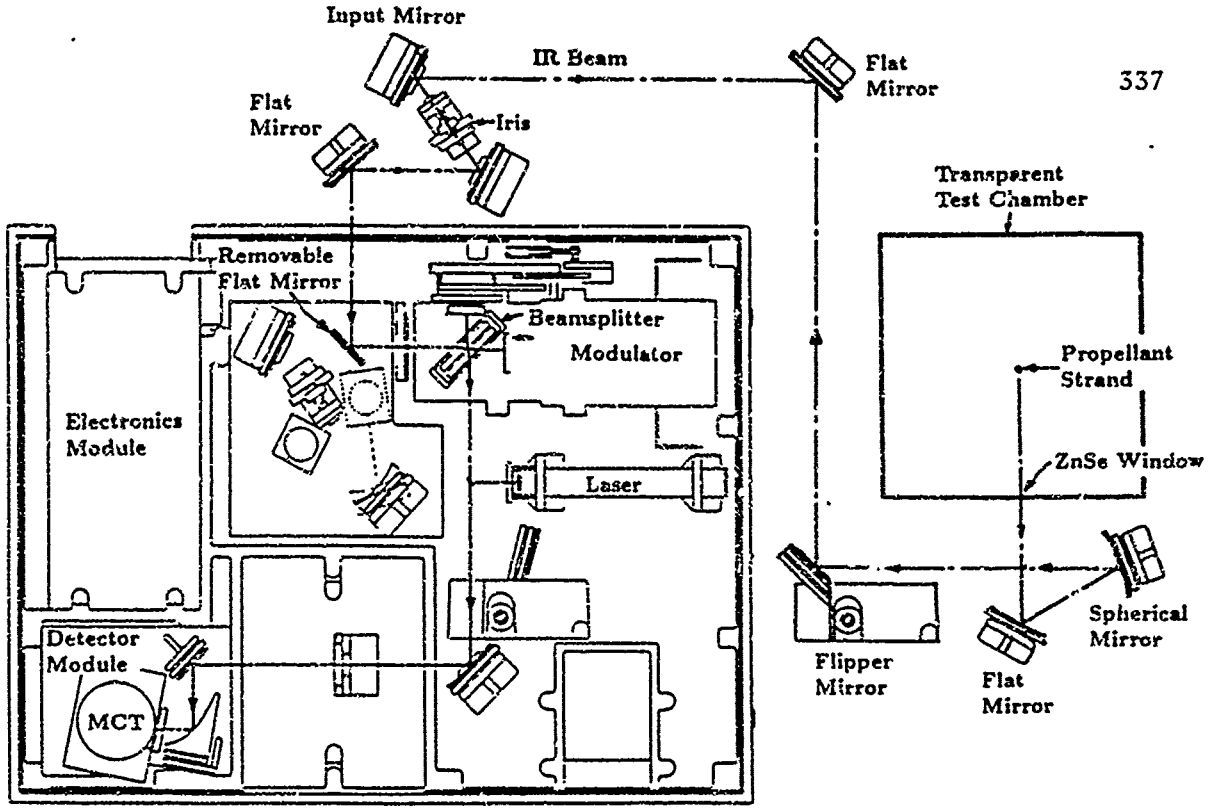


Fig. 3. Optical layout of beam paths for performing emission measurements using the FT-IR and the windowed transparent test chamber.

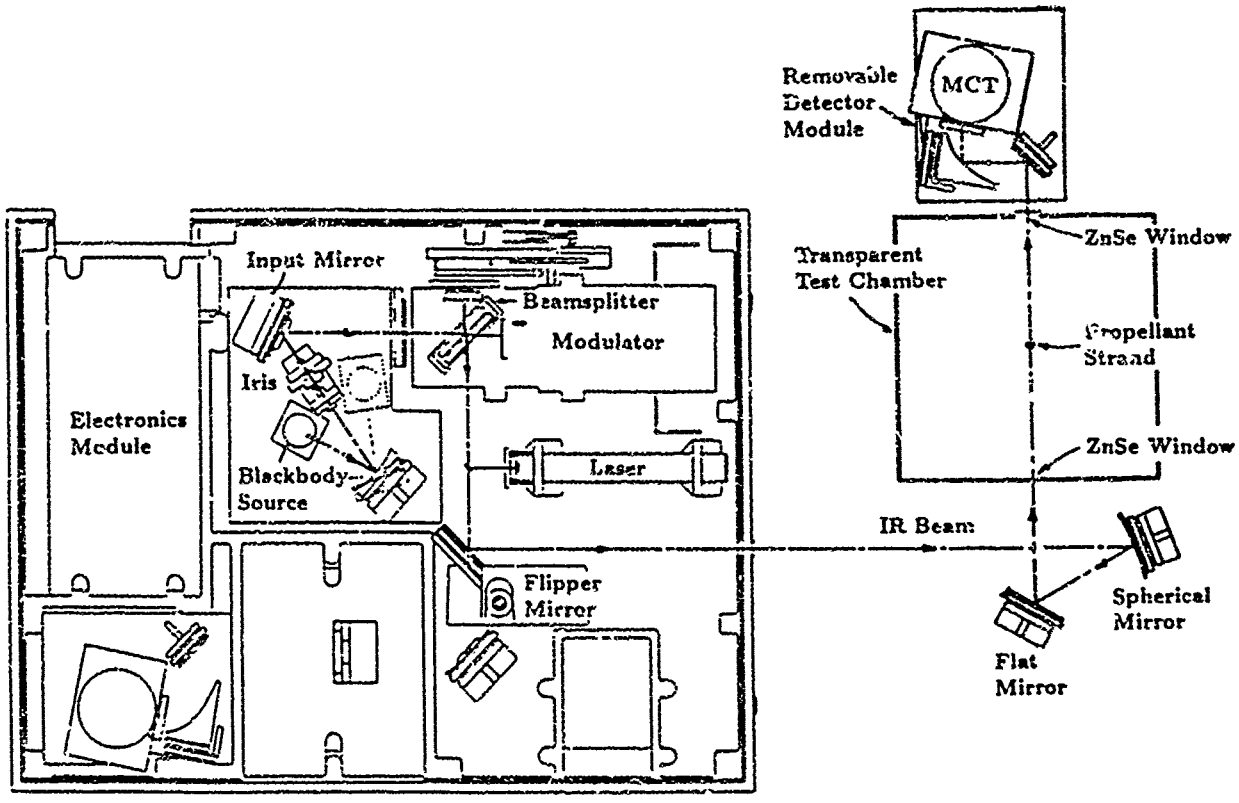


Fig. 4. Optical layout of beam paths for performing transmission/absorption measurements using the FT-IR and the windowed transparent test chamber.

One of the reasons for lack of understanding of the combustion process is related to the fact that the propellant contains complex molecules for both binder materials and oxidizers. As a result of the complex nature of solid propellant ingredients, a wide variety of chemical species are present in the flame zone. Also, it is extremely difficult to ascertain the molecular structure of the pyrolyzing species as they leave the solid surface, the heterogeneous reactions on the burning surface, the gas-phase reaction mechanism with numerious paths, and the diffusion of chemical species in the flame zone. Furthermore, solid-propellant flame structure can also be strongly affected by the operating conditions, such as pressure variation and flow field structure. In addition, a significant fraction of the combustion products are IR active.

Before proceeding to the interpretation of IR spectra of gases, however, it is important to mention that reference absorption spectra, which have been measured at room temperatures, are in general not similar to the emission spectra measured at elevated temperatures. The consequence of this difference is that an application of the Kirchhoff law may not be completely correct. There are two primary reasons for this effect. First, at elevated temperatures, it is known that higher vibrational states are populated, resulting in a band broadening, in the case of the strong CO_2 band located at 2349 cm^{-1}, the broadening shows up on the smaller wavenumber side Second, self-absorption of emitted energy produces a reduction in the observed emission spectra on the longer wavenumber side. Thus, it is difficult to employ commercially available absorption spectra over the temperature and pressure ranges for plume measurement applications, and the task of analyzing IR spectra is difficult: the emitting species types may not be exactly known and small band shifts may have occurred due to instrumental effects of the FT-IR. It would be desirable to establish a data bank of the emission/absorption behavior of IR active gases at high temperatures. Such effort is extremely tedious to perform since the radiative behavior of a molecule is not only a function of temperature and pressure, but to some extent of the type of molecules with which it interacts. Nonetheless, such effort is currently in progress at the High Pressure Combustion Laboratory of PSU.

Several experiments have been run to test the setup and operation of the system. Results have been obtained for ammonium perchlorate/hydroxyl terminated polybutadiene (AP/HTPB) and nitro-cellulose based propellants, such as NOSOL-363, including video recording of the burning event. Some specific results determined from emission and transmission/absorption measurements of AP/HTPB and NOSOL-363 propellants are presented.

Use of Laser Based Positioning System

Examination of sequential emission spectra reveals the capability of the laser based positioning system to adequately fix the position of the burning surface. Figure 5 shows four sequential AP/HTPB emission spectra measured at $2cm^{-1}$ resolution with the FT-IR operating in the rapid scan mode (approximately 0.5 sec/spectra), with triangular apodization and with phase correction[11]. The measurement conditions were as follows: the strand was approximately 6mm in diameter, the center of the line-of-sight measurement location was approximately 30 mm above the burning surface, and the diameter of the spot size was about 10 mm. Inspection of the video recording shows luminous combustion products of approximately 40mm in diameter and that the combustion is somewhat unsteady at 1 atm pressure. Examination of this figure reveals a small variation between the four spectra. We believe that this variation is most likely due to the observed unsteadiness in the burning, which is commonly observed in low pressure situations. Overall, the laser based positioning system has also adequately controlled the location of the burning surface of other relatively particulate-free propellants tested at PSU.

Emissivity and Transmissivity of AP/HTPB

Figure 6 shows the spectral emissivity of AP/HTPB as a result of coaddition of sixteen spectra; the data used comes from the same measurements as described in the preceeding paragraph for Fig. 5. Examination of this figure reveals the following. First, the achievable signal-to-noise is extremely high. This is most noticable in the 4500 - 4000 cm^{-1} region where we observe no emitting species. Second, there appears to be almost no soot formation. The emission from soot is continuous and proportional to ν, which should reveal itself as a slightly decreasing continuous broadband which is absent in this figure. Finally, many characteristic infrared bands from the combustion products are clearly shown[13].

The strongest infrared emission bands are readily identified as CO_2, H_2O, HCl, CO and fragments of HTPB. The carbon dioxide has four strong absorption bands (at room temperature), these are located at 3716, 3609, 2349 and 667 cm^{-1} corresponding to the $(\nu_1 + \nu_3)$, $(2\nu_2 + \nu_3)$, ν_3 and ν_2 vibrational modes, respectively. The carbon dioxide molecule also has two "hot" bands, located at 961 and 1064 cm^{-1} corresponding to the

Acknowledgements

The support received from Dr. R. S. Miller and Dr. G. Roy of ONR under contracts N00014-86-K-0468 and N00014-89-J-1559 is greatly appreciated.

References

[1] Edwards, T., "Investigation of High Pressure Solid Propellant Flame Chemistry," *28th Aerospace Sciences Meeting,* AIAA 90 0547, Jan. 8-11, 1990.

[2] Peretz, A., "Investigation of Pyrotechnic MTV Compositions for Rocket Motor Igniters," *AIAA Paper 82-1189,* paper presented at Eighteenth Joint Propulsion Conference, AIAA/SAE/ASME, Cleveland Ohio, pp. 1-7, July 1982.

[3] Pearce, B.E., "Radiative Heat Transfer within a Solid-Propellant Rocket Motor," *AIAA Journal of Spacecraft and Rockets,* Vol. 15, No. 2, pp. 125-128, 1979.

[4] Brewster, M.Q., "Particle Radiative Feedback in Ammonium Perchlorate Deflagration," *AIAA Journal,* Vol. 24, No. 7, pp. 1141-1147, 1986.

[5] Brewster, M.Q., and Patel, R., "Selective Radiative Preheating of Aluminum in Composite Solid Propellant Combustion," *Journal of Heat Transfer,* Vol. 109, pp. 179-184, 1987.

[6] Kubota, N., "Combustion Wave Structures of Ammonium Perchlorate Composite Propellants," *AIAA Journal of Propulsion and Power,* Vol. 2, No. 4, pp. 296-300, 1984.

[7] Forney, L.J., and McGregor, W.K., "Particle Sampling in Supersonic Streams with a Thin-Walled Cylindrical Probe," *AIAA Journal,* Vol. 25, No. 8, pp. 1100-1104, 1987.

[8] Edwards, T., "Laser-Induced Fluorescence in High Pressure Solid Propellant Flames," *Applied Optics,* Vol. 26, No. 17, pp. 3496-3509, 1987.

[9] Parr, T., and Hanson-Parr, D., "The Application of Imaging Laser-Induced Fluorescence to the Measurement of HMX and Aluminum Propellant Ignition and Deflagration Flame Structure," *23rd JANNAF Combustion Meeting,* CPIA Pub. 457, Vol. 1, pp. 249-267, 1986.

[10] Stufflebeam, J.H., and Eckbreth, A.C., "Multiple Species CARS Measurements of High Pressure Solid Propellant Combustion," *Twenty-seventh Aerospace Science Meeting,* AIAA-89-0060, Reno, Nevada, January 9-12, pp. 1-10, 1989.

[11] Griffiths, P.R., and deHaseth, J.A., *Fourier Transform Infrared Spectroscopy,* John Wiley and Sons, New York, New York, 1986.

[12] Goetz, F., and Mann, D.M., "Design and Use of a Servo-Controlled High Pressure Window Bomb in Spectroscopic Studies of Solid Propellant Combustion," *17th JANNAF Combustion Meeting,* Vol. 1, pp. 417-434, 1980.

[13] Herzberg, G., Infrared and Raman Spectra of Polyatomic Molecules, Vol. II, D. van Nostrand Company, Inc., Princeton, New Jersey, 1968.

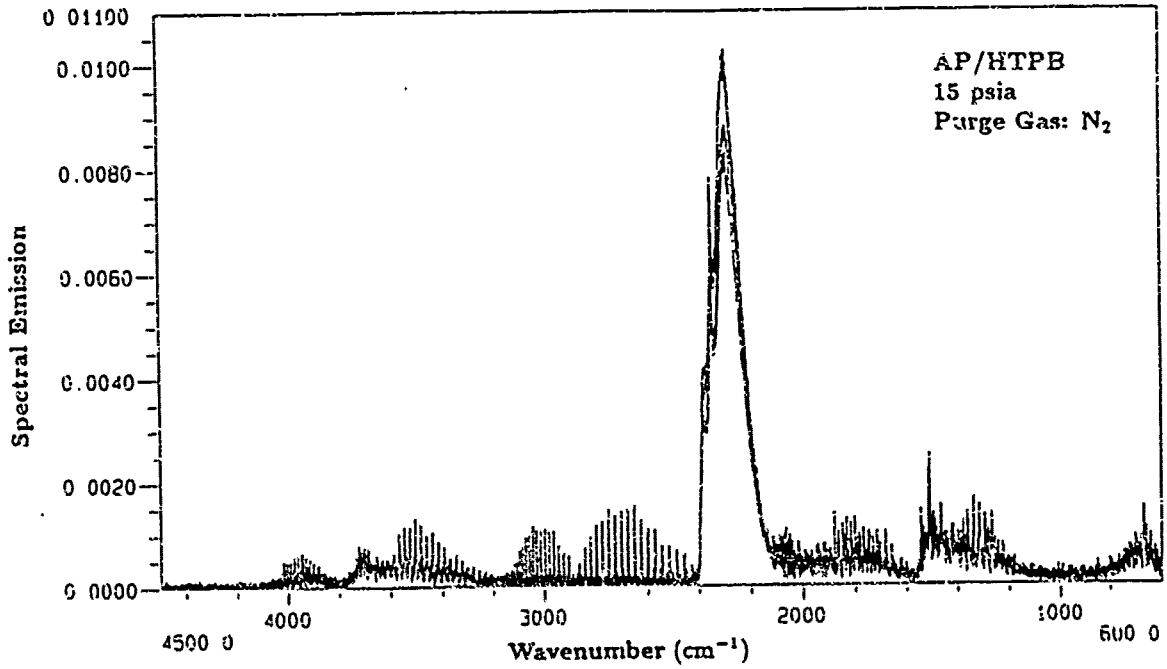


Fig. 5. Four sequential background subtracted emission spectra of AP/HTPB combustion products.

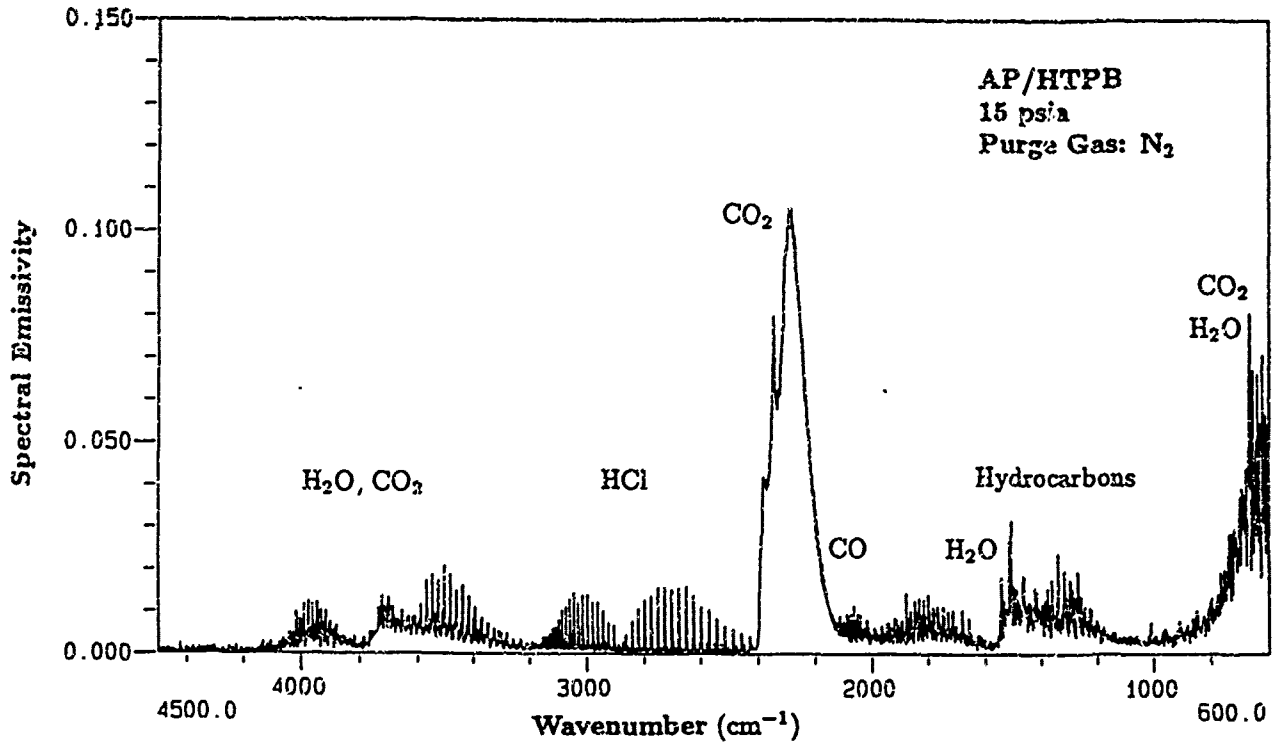


Fig. 6. Result of 16 coadded emission spectra of AP/HTPB evaluated according to Eq. (2) with $T_p = 1500K$.

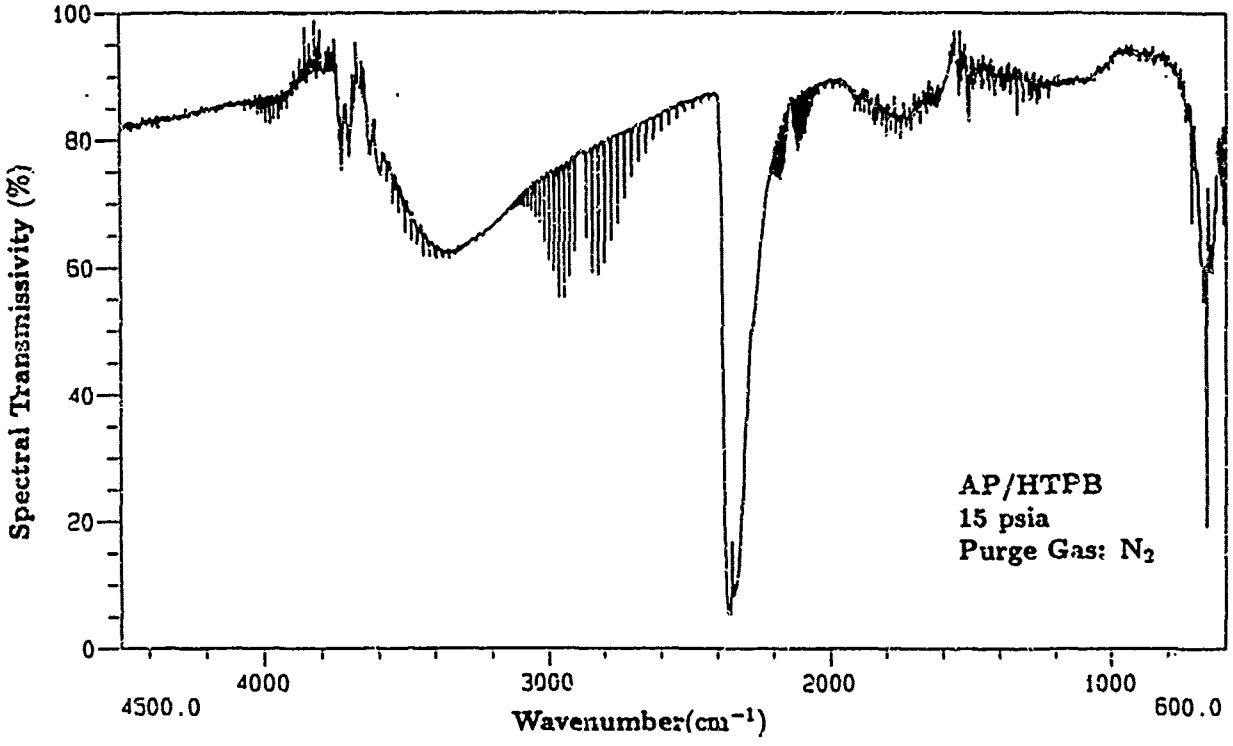


Fig. 7. Result of 16 coadded transmission spectra of AP/HTPB evaluated according to Eq. (3).

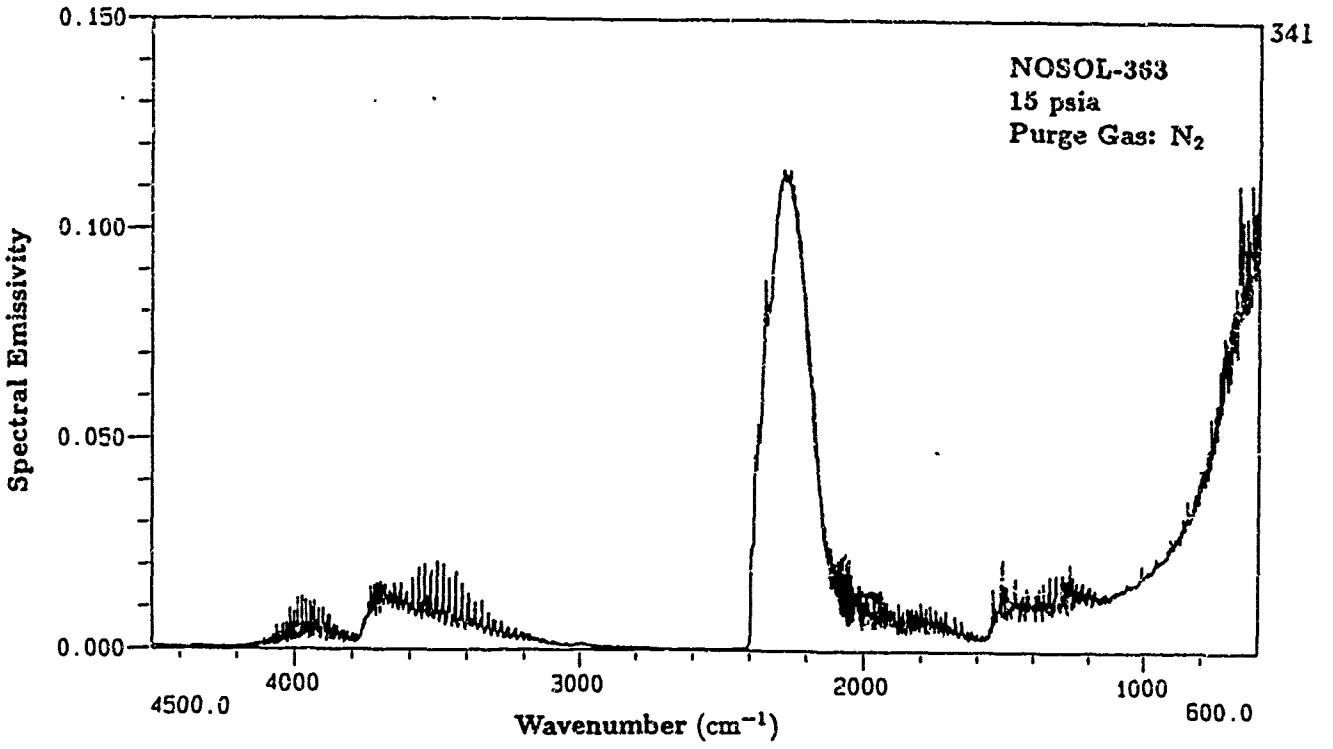


Fig. 8. Result of 16 coadded emission spectra of NOSOL-363 evaluated according to Eq. (2) with $T_p = 1500K$.

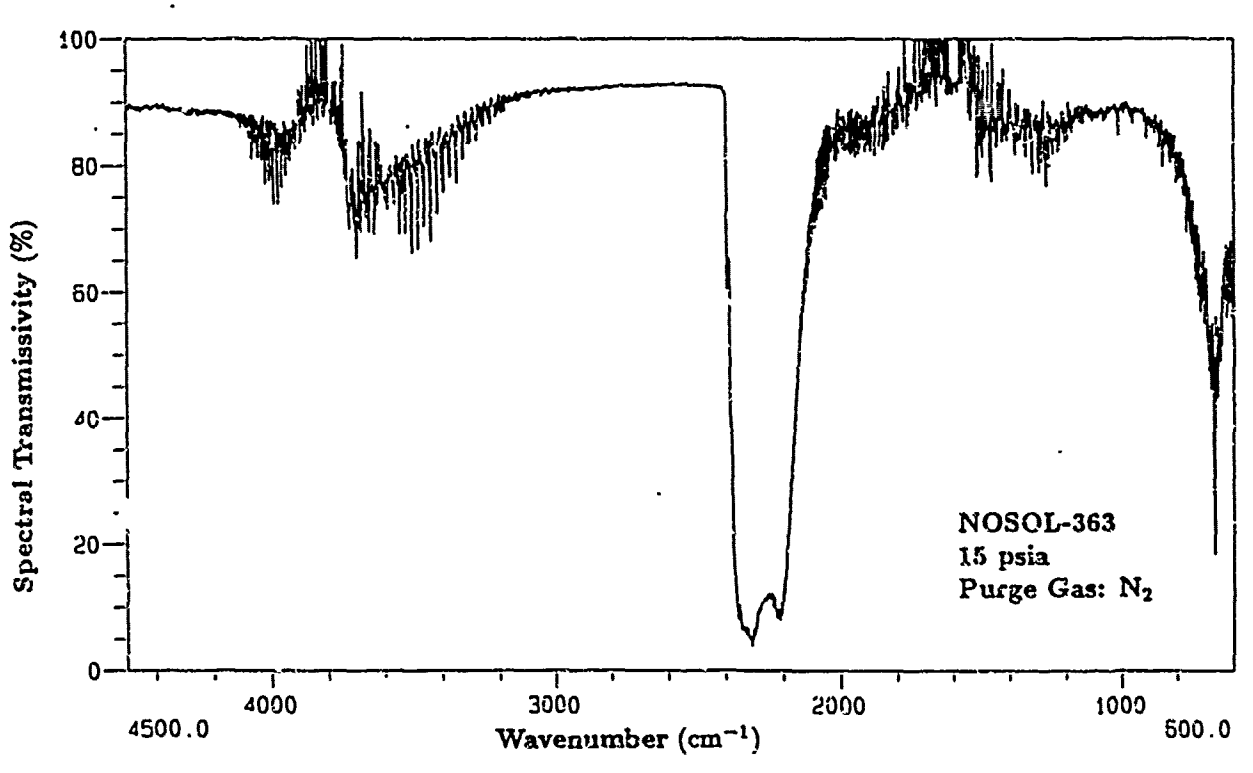


Fig. 9. Result of 16 coadded emission spectra of NOSOL-363 evaluated according to Eq. (3).

Measurements and Theory of Signal-to-Noise Ratio of FT-IR Emission Spectrometry Applied to High Pressure Solid Propellant Combustion

by

I. T. Huang, S. T. Thynell* and K. K. Kuo

Department of Mechanical Engineering
The Pennsylvania State University
University Park, Pennsylvania 16802

---

* Author to whom correspondence should be sent.

Abstract

Solid propellant combustion studies at high pressures (500-50,000 psi) must be conducted with a high spatial resolution in order to resolve the species concentration and flame temperature profiles. Such studies are often performed in specifically designed experimental facilities, including chimney type strand burners. To successfully carry out FT-IR emission spectrometry of products from the combustion of small propellant strands, it is required to perform a critical assessment of the achievable signal-to-noise ratios (SNR). In this work, an analytical expression for the SNR of FT-IR emission spectrometry limited to detector noise has been derived. The expression is specifically applied for the ν_3 fundamental band of CO_2 and in the optically thick limit verified by experiments. The results from the application of the theory show that a spatial resolution on the order of 100 μm should yield SNRs of 1000 or larger at the center of the considered band for the anticipated temperatures of high pressure solid propellant combustion. Measurements of emission spectra of combustion products of a homogeneous solid propellant, NOSOL-363, has also been performed at one atmosphere total pressure to show that a 1000 μm spatial resolution may be sufficient to deduce species concentrations and temperature.

Index Heading: Fourier Transform Infrared Emission Spectroscopy; High Pressure; Analytical Methods

INTRODUCTION

Research on solid propellant combustion has been actively pursued during the past several decades, and many of the important findings have been compiled in a document edited by Kuo and Summerfield.[1] Since then, numerous diagnostic techniques have further been advanced and applied to investigate the complex chemical kinetics of solid propellant combustion. To date, such investigations appear to have had a limited success in resolving species concentration and temperature profiles within the combustion products. However, to conduct studies in conditions simulating rocket motors or gun chambers is extremely difficult due to the high pressures (500-50,000 psi), high temperatures (to 3500 K), and short time scale of the overall event (down to milliseconds). The analysis may further be complicated by the observed fact that the flame zone is very thin ($\leq$ 100 μm in some cases), thus requiring spatially precise measurement techniques for obtaining species and temperature profiles. Consequently, a significant effort has been devoted to the development of both intrusive and nonintrusive techniques. Usually, intrusive measurements may have shortcomings, including: (1) the introduction of disturbances in the medium; (2) the consumption of the probe itself within the hostile environment; and (3) a poor temporal response and limited spatial resolution. Optical techniques have the capability of overcoming these limitations and offer the greatest potential for application to solid propellant combustion.

Of the optical methods, laser-based diagnostics have been an area of intensive research. The coherent anti-Stokes Raman scattering (CARS), laser-induced fluorescence (LIF) and planar laser-induced fluorescence (PLIF) techniques have received considerable amount of attention. The CARS[2] approach is capable of making instantaneous and spatially precise measurement of temperatures and species concentrations in high pressure environments. However, only a few species can be measured simultaneously due to the limited wavelength range of the tunable laser source unless several lasers with different ranges are used. The

LIF[3] technique is very sensitive and is frequently used to measure the flame radicals which are present in very low concentrations. The PLIF[4] method is simply the case in which the laser beam is expanded into a thin sheet. The distribution of the selected radical concentration over the cutting surface of the laser sheet can be mapped out in a single laser shot. Both LIF and PLIF techniques identify only one species at a time, and the species must have an absorption wavelength accessible to the tunable laser source. Also, both methods suffer from a quenching problem which reduces the quantity of the fluorescence and makes the quantitative analysis difficult especially at the higher pressures.[2] Consequently, there is a need to continue the development of nonintrusive diagnostic techniques.

Fourier transform infrared (FT-IR) spectrometry has been employed for studies in numerous areas of science and engineering. The major advantages offered by the FT-IR spectrometry include: (1) the thermal radiation can be measured over a broad spectral range simultaneously; (2) relatively high signal-to-noise ratios can be achieved; and (3) data processing is rapid. All these advantages indicate that FT-IR spectrometry could be a highly potential technique for high pressure solid propellant combustion diagnostics. There are many works available in the literature that have used FT-IR spectrometry as a diagnostic tool for solid propellant pyrolysis/combustion or flame emission studies. Examples of such works include, among others, thermal decomposition of energetic materials,[5] thermal fragmentation of organic compounds,[6] solid propellant performance studies,[7] and a preliminary analysis of plume products of solid propellant combustion.[8]

To apply FT-IR spectrometry for measuring radiant energy emitted from or transmitted through the products of high pressure solid propellant combustion, the difficulties, some of which were mentioned above, associated with the measurements must be identified. First, it is necessary to design and construct a vessel (strand burner) that safely can withstand high pressures (to 5,000 psi), that has optical access in several directions, and that allows for control of the position of the burning surface. Second, the measurements

should allow a spatial resolution to within approximately 100 μm in order to resolve the flame zone. Third, the data must be acquired within a short time period (typically the event lasts < 10 seconds). In view of these concerns, it is clear that one should address and try to estimate the achievable signal-to-noise ratios (SNR) prior to commencing a study on high pressure solid propellant combustion. There are three objectives of this study. First, an analytical expression of the SNR anticipated within the ν_3 fundamental band of CO_2 is developed. Second, the unknown constant appearing in this expression is determined from experiments. Finally, results are presented that can be used to estimate the SNR of emission measurements that must be performed at a required spatial resolution given that approximate values of the partial pressure of CO_2 and gas temperature are available

EXPERIMENTAL SETUP

A schematic diagram of the overall setup used to conduct the emission measurements is shown in Fig. 1. As shown in this figure, the setup consists of two major components: a Nicolet 740 FT-IR spectrometer and a transparent test chamber capable of operating at low pressures (< 1.5 atmospheres). For FT-IR diagnostics, the burning surface of the propellant must often be kept at a certain level. To fulfill this requirement, a closed-loop positioning system is employed to elevate the solid propellant strand as it burns down. The principal components of the system include a 40-mW He-Ne laser (Spectra-Physics Model 145), whose beam propagates through the products slightly above the solid propellant strand surface, a photodiode detector with a narrow band filter (Oriel, G-527-6328) sensing the laser energy, a data acquisition board (MetraByte Model DAS-16) within personal computer (Proteus Model 386/25MX) receiving signal from the detector, and a controller receiving commands from the P/C and activating a linear motor which is attached to the bottom of the test sample mount. The positioning algorithm (with proportional-integral-derivative control) is devised to keep a fraction of the laser beam blocked by the propellant strand and the remaining fraction detected by the photodiode.

In general, the positioning system keeps the burning surface of the solid propellant strand more or less at a fixed level relative to the collection volume of the optical path of the FT-IR system. In addition to the closed-loop positioning system, the control system is also integrated with a pressure transducer and a demodulator to keep the transparent test chamber pressure at a constant level.

Figure 2 shows the optical layout of the beam path for the emission measurement. The radiant energy emitted from the products of the burning solid propellant strand travels along the path indicated from the transparent test chamber to the FT-IR spectrometer. Two 18-inch focal-length, 3-inch diameter, gold coated spherical mirrors (Edmund Scientific Model 32871) are used to collect IR energy from the plume over a collection area whose size is approximately identical to the size of the rectangular slit of the iris. It is realized that the optical beam diverges along the beam path. In order to get a stronger detector signal from the plume, a 4-inch focal-length, 2-inch diameter, gold coated spherical mirror (Edmund Model 32816) is placed after the slit to condense the optical beam since the Nicolet 740 is equipped with a 1-inch diameter interferometer. Inside the spectrometer, the combinations of two beamsplitters (Quartz and Ge on KBr) and three detectors (Silicon, PbSe and liquid nitrogen cooled MCT-A) determine the spectral range covered. A ZnSe window is installed at the optical port of the transparent test chamber To avoid the effects of H_2O, CO_2 and particulates along the beam path, the external mirrors are enclosed in a sealed box. The FT-IR spectrometer and the sealed box are purged with dry air from a H_2O and CO_2 filtration system (Balston Type 75-60).

SNR - THEORY OF ESTIMATION

The following analysis assumes that the detector noise is the significant source of noise. Other sources of noise such as digitization noise, sampling noise, folding effects and fluctuation noise, are assumed to be small compared with the detector noise. The SNR of

an IR detector is defined as the ratio of the signal voltage to the root mean square (RMS) noise voltage. A practical expression of SNR have been developed by Mattson,[9] and it can be expressed as[10]

$$\mathrm{SNR} = \frac{Q\, D^{*}\, t_m^{\frac{1}{2}}}{A_D^{\frac{1}{2}}}\ , \tag{1}$$

where D^{*} is the specific detectivity of the detector ($\mathrm{cm\,Hz^{\frac{1}{2}}/W}$), t_m is the total measurement time (sec), and A_D is the active area of the detector ($\mathrm{cm^2}$). The radiant energy incident on the detector area Q (W) within wavenumber interval $\Delta\nu$ (spectral resolution) is given by

$$Q = I_\nu\, \theta\, \xi\, \Delta\nu\ , \tag{2}$$

where I_ν is the spectral intensity of the emission source ($\mathrm{W/cm^2\,sr\,cm^{-1}}$), θ is the optical throughput ($\mathrm{cm^2\,sr}$), and ξ is the overall system efficiency. Substitution of Eq. (2) into Eq. (1) yields

$$\mathrm{SNR} = \frac{I_\nu\, \theta\, \xi\, \Delta\nu\, D^{*}\, t_m^{\frac{1}{2}}}{A_D^{\frac{1}{2}}}\ . \tag{3}$$

In order to evaluate the spectral intensity of the source, which is a result of emission from the hot products within the plume, we treat the plume as an isothermal emitter with uniform concentration of gaseous species along the line-of-sight. Neglecting the scattering effect, a solution to the radiative transport problem yields[11]

$$I_\nu = I_{\nu,b}\, [\, 1 - \exp\, (\, -\kappa_\nu\, L\,)\,] \tag{4}$$

where $I_{\nu,b}$ is the Planck function of blackbody emission, κ_ν is the spectral absorption coefficient, and L is the physical plume thickness. The product of κ_ν and L is the spectral

optical depth, and it is a function of wavenumber, gas composition, pressure, temperature and plume thickness. It is beyond the scope of this work to estimate the SNR for all wavenumbers. Instead, we select to carefully analyze the SNR for one wavenumber located within the ν_3 fundamental band of CO_2. The reasons for selecting this band include: (1) it is a very active band and readily detected, (2) it lies away from the spectral region where maximum emission at typical flame temperature occurs (> 6000 cm^{-1}) and where maximum detector detectivity is located (near 1000 cm^{-1} for a typical wide band MCT detector), and (3) the high-temperature behavior of this band is well-studied. It should be noted, however, that near or below the flame zone the most significant emission may not be due to the CO_2 molecule. In this work, which emphasizes an approximate analysis, we employ the data developed by Edwards.[12]

From the previous work of Edwards,[12] the optical depth at band head of an IR active specie at high pressure can be approximated by

$$\tau_H = \kappa_\nu \, L = \frac{\alpha_0 \, \rho \, L}{\omega_0} \, , \tag{5}$$

where α_0, ρ and ω_0 represent the integrated band intensity, density of the absorbing gas and bandwidth parameter, respectively. The values due to Edwards[12] of the ν_3 fundamental band of CO_2 of α_0 and ω_0 are adopted. Applying perfect gas law for the gas mixture the Eq. (5) becomes

$$\tau_H = \frac{\alpha_0}{\omega_0} \left[\frac{T_0}{T} \right]^{\frac{1}{2}} \frac{P \, X_{CO_2}}{R \, T} \, L \, , \tag{6}$$

where P is the absolute test chamber pressure, T is the absolute gas temperature, X_{CO_2} is the mole fraction of CO_2 and R is the gas constant. Substitution of Eqs. (4) and (6) into Eq. (3) yields the SNR at 4.42 μm given by

$$SNR = I_{\nu,b} \left\{ 1 - \exp \left[-\frac{\alpha_0}{\omega_0} \left(\frac{T_0}{T} \right)^{\frac{1}{2}} \frac{P\, X_{CO_2}}{R\, T} L \right] \right\} \left[\frac{\theta\, \xi\, \Delta\nu\, D^*\, t_m^{\frac{1}{2}}}{A_D^{\frac{1}{2}}} \right] . \qquad (7)$$

The parameters in the second bracket on the right hand side of Eq. (7) are associated with the experimental setup and sampling parameters, and they are independent of the test conditions in the chamber such as pressure, gas temperature and mixture composition. It is assumed that the optical throughput is limited by the area of the slit and the 18 inches focal length of the spherical mirror We denote the optical throughput with the symbol θ_{slit}, which is equal to the product of the solid angle of the IR beam focusing on the slit, $d\omega_{slit}$, and the slit area, A_{slit}. The slit area can be changed as desired. Thus

$$\theta_{slit} = A_{slit}\, d\omega_{slit} ,$$

where $d\omega_{slit}$ can be roughly approximated by the ratio of the area of the spherical mirror to the square of the focal length of the spherical mirror. All the other unknowns in the bracket can be described by a single parameter, C, provided that the same experimental setup and sampling parameters are used. The value of C is determined from the experimental results for different slit sizes and is expected to be close to a constant.

The burning rate of solid propellant strands is in general quite high, and it typically increases with increasing pressure. The quarter-inch-diameter, two-inch-long propellant strand used in this work took about ten seconds to burn out in a nitrogen environment at one atmosphere. Thus, practically there is a short measurement period of time, about seven seconds, after the transient ignition event and before the complete combustion of the propellant strand. Within the available measurement period of time, it is desirable to perform emission/absorption measurement at several positions above the burning surface of the propellant. Thus, the number of spectra that can be taken is limited. With our spectrometer, it is possible to take four spectra within approximately 1.25 seconds at 4

cm^{-1} resolution. The SNR of the 4 coadded spectra at 4.42 μm is evaluated by the ratio of $\bar{I}$ to ΔI, where $\bar{I}$ and ΔI are the arithmetic average intensity and the root-mean-square error of experimental results, respectively. By employing a standard blackbody source (Infrared Industries, Inc. Model 463-1), the constant C is determined from

$$C = \frac{SNR}{\theta_{slit}\, I_b\,(4.42\,\mu m, 1273\,K)} . \tag{8}$$

Once C is obtained, Eq. (7) can be rewritten as

$$SNR = C\, I_{\nu,b}\, \theta_{slit} \left\{ 1 - \exp\left[-\frac{\alpha_0}{\omega_0} \left(\frac{T_0}{T} \right)^{\frac{1}{2}} \frac{P\, X_{CO_2}}{R\, T} L \right] \right\} . \tag{9}$$

RESULTS AND DISCUSSION

In this study, a liquid nitrogen cooled MCT-A detector and a Ge on KBr beamsplitter were employed. All measurements were made in the rapid-scanning mode with 4 cm^{-1} resolution. A triangular apodization function was used and phase corrected real algorithm was applied for the phase correction. None of the spectra were corrected for the background emission or instrument response. In order to determine the effect of the spatial resolution on the constant C, measurements were performed that involved 10 different slit heights ranging from 0.1 mm to 1 mm and a constant 6 mm slit width. For each slit height, 25 spectra (4 files/spectrum) were obtained, and $\bar{I}$ and ΔI of the 25 readings at 4.42 μm were calculated. In order to eliminate inconsistent data points, it was assumed that the 25 data points for each slit height obeyed a normal distribution and all the data points outside $\bar{I} \pm 3\Delta I$ were eliminated. As a result, one reading for 0.5 mm and 0.9 mm slit heights, respectively, was removed and not included in the final calculation of $\bar{I}$ and ΔI.

Input Parameters. In the theoretical calculations of the constant C, each parameter in Eq. (3) required an input value. To be consistent with the experimental results,

the Planck function at 4.42 μm and 1273 K replaced I_ν and θ_{slit} replaced θ. In estimating ξ, the rule-of-thumb value of spectrometer efficiency of 10% was reduced by accounting for the 60% transmittance of the quarter-inch-thick ZnSe window. The resulting value of $\xi = 0.06$ was further reduced by a factor of two, to account for the inefficiencies of the external mirrors; i.e., the use of spherical mirror as opposed to parabolic mirrors. Hence, the value of $\xi = 0.03$ was employed. The value of $\Delta\nu = 1.929$ cm^{-1}, which is one-half the calculated resolution since the Nyquist sampling criteria of two data points per resolution element is satisfied. The D* of the detector at 4.42 cm^{-1} is approximated by a typical value, 1×10^{10} cm Hz$^{\frac{1}{2}}$ W^{-1}. As it is difficult to estimate the actual speed of the moving mirror during data acquisition processes, the measurement time used in the theoretical calculations was obtained from the FT-IR software program. It was about 0.32 second, which includes the elapsed time from the start of data collection to the end for one scan plus the time required to write the data onto the permanent storage area. The time required for data transfer is relative short compared with the time required for data acquisition; thus the error in theoretical calculation introduced by this parameter is expected to be small. Therefore, the total measurement time t_m is 1.25 seconds. The detector area A_D is 0.01 cm^2.

Determination of SNR and C using Blackbody Source. Figure 3 shows the results of SNRs obtained from experiments and theory using the values of the various parameters described above. Inspection of this figure reveals that the theory overestimates the experiments by about a factor of five and the experimentally determined SNRs range from 150 to 1950 for slit heights of 0.1 mm and 1 mm, respectively. This discrepancy is expected, since measurements of the actual detector sensitivity and mirror reflectivities have not been performed due to the lack of appropriate equipment. Furthermore, the overall trend of the experimentally determined value of SNR follow that of the theory. However, the experimental values exhibit a slight oscillation. The oscillations of the experimentally determined SNR are related to. (1) error in measurements of the slit height, and (2) misalignment of the center of the slit rectangular area along the beam path.

The values of C, determined from the experimental SNR via Eq. (8), are shown in Fig. 4. It is noted that the parameter C is a function of the overall efficiency, characteristics of the detector and sampling paramcters. It is expected to be close to a constant regardless of the slit size. Due to the oscillation of the experimental SNR, nevertheless, the deviations of the value of C at different slit size from the average value are unavoidable. Therefore, an average value of C equal to 1.205×10^9 is employed in the following calculation.

Predicted SNR. From Eq. (9), the value of the SNR of 4 coadded spectra at 4.42 μm can be estimated provided that information of T, P, X_{CO_2}, and L are given. Typical temperatures of solid propellant combustion are in the range of 2000 to 3500 K. Figures 5 show the expected SNRs versus the partial pressure path length ($PX_{CO_2}L$) for a given temperature of our experimental setup over a broad range of experimental conditions at three different slit heights. However, the gaseous emission for the longer partial pressure path lengths approaches that of a blackbody and as a result the calculated values of SNR levels out. Examination of these figures reveal that the predicted SNRs are quite high. Even for a slit height of 100 μm, which should be sufficient to resolve the flame zone at the high pressures (1000 psi) where temperatures are 2500 K are observed, the SNR shown in Fig. 5c approaches 1000 in the optically thick case and T = 3000 K.

The obvious question that results from the predicted values shown in Figs. 5, is: What SNRs are required in order to employ the emission spectra for species concentration and temperature measurements on the products from high pressure solid propellant combustion? This question is difficult to answer, because it depends on the approach that is employed. For example, Gross and Griffiths[12] employed a spectral line ratio technique to accurately deduce the temperature of a CO_2 gas using the hot band near 10 μm. In their work, an SNR of approximately 12 was sufficient due to the fact that 32 lines were used in the data reduction procedure. At the higher pressures of solid propellant combustion, it is questionable if this technique can be applied, since significant overlapping of the spectral

lines may occur due to pressure broadening effects. A more likely approach is to employ band ratio techniques.[14] According to this technique, the ratio of two bands is employed to deduced the species concentration and temperature. Since many different bands can be employed, it could be analogous the spectral line ratio technique. To be conservative, results of species concentration and temperatures of sufficient accuracy for most engineering application should be obtainable if the SNRs of the emission spectra are on the order of 500 or better. If that is the case, then a spatial resolution 100 μm appears to be achievable. It should be pointed out that the use of parabolic mirrors instead of the spherical mirrors should offer the possibility further improving the SNR. The following discussion of results attempts to illustrate the following: (1) to estimate the SNRs expected to be obtained in emission measurements of products from the combustion of specific solid propellants at high pressures, and (2) to show the type of emission spectra that are easily measured in our low pressure transparent test chamber.

Predicted SNR of High Pressure Solid Propellant Combustion. In order to predict the SNRs of emission measurements on products from combustion of specific solid propellants, it is necessary to obtain reasonably accurate values of the species concentration and the flame temperature. To obtain such values, we employ the CET86[16] Chemical Equilibrium Transport Code. The output from this code includes the adiabatic flame temperature and the equilibrium mole fractions. Although the code includes a wide variety of chemical species, numerous assumptions were incorporated into its development. First, the code development does not consider heat losses by convection and radiation, and turbulent mixing effects between the edge of the flame zone and the purge gas. Second, only the equilibrium species are determined. Finally, the pressure deflagration limit (PDL) is not accounted for. Since the PDL is typically on the order of 10 atm for the propellants considered in this work, steady burning at 1 atm cannot be achieved. For example, NOSOL-363 is observed to exhibit a fizz-burning mode at 1 atm in a nitrogen purged environment. To obtain a steady, luminous flame zone at 1 atm for NOSOL-363, an oxidizer

rich purge gas must be employed, but uniform species concentration and temperature along the measurement line-of-sight cannot be obtained.

Table 1 shows the results from calculations using the CET86[16] Chemical Equilibrium Transport Code. Inspection of the results reveals several interesting features. First, the adiabatic flame temperatures range from about 2150 to 3300K. Second, the flame temperature and final products are essentially independent of pressure However, it is well known that the pathways of the chemical reactions are highly dependent upon pressure. As a result, the predicted signal-to-noise ratios are for all practical purposes only dependent on pressure for a given propellant. Third, CO_2 is not the dominant equilibrium product; CO and H_2O constitute in most cases more than 50product species. Significant fractions of N_2 and H_2 are also formed for the M30 triple-base and XM39 nitramine propellants. N_2, which is generally considered as an IR inactive species, could reveal itself at the higher pressures ($p > 50$ atm) due to a collision induced absorption band.[17] Finally, the estimated SNRs for the considered 100 fm slit are in all cases except one much greater than 500 for the larger pressures ($p \geq 10$ atm). Thus, in those cases for which the considered propellants have been observed to burn steadily ($p > 10$ atm), it is clear that very high signal-to-noise ratios are expected for the 100 fm slit.

Results of Plume Measurements. Results of spectral emission measurements on products from the combustion of NOSOL-363, which was burned at 1 atm in an air purged environment, using slit heights of 1000 and 300 μm are shown in Figs. 6 and 7, respectively. The shown emission spectra are the result of coaddition of 4 successive scans using the same sampling parameters as described previously. The effects from background emission have been subtracted. Examination of these figures reveals that the SNR of the spectrum in Fig. 6 is in authors' opinion quite high, whereas the SNR of the spectrum in Fig. 7 is much worse. This is most noticeable in the short-wavelength (high wavenumber) region where few emitting species are observed. Since the combustion took place at 1atm

using air as the purge gas, it is difficult to compare the SNR of the measured spectra with the predicted SNRs obtained from the previous analysis and shown in Table 1. As briefly mentioned previously, a comparison is difficult to perform because (1) the species concentration and temperature is nonuniform along the line-of-sight as result of combustion near the edge of the unburned propellant products and the oxygen rich purge gas, (2) a turbulent combustion zone between the oxidizer in the purge gas and the unburned propellant products is established which introduces additional noise in the spectra that is not accounted for in the development of the expression for SNR, and (3) the plume widens to approximately 25mm at the point of measurement, that is, there is significant radially outward diffusion of the IR active species which must be balanced by a radially inward diffusion of the species in the purge gas (both O_2 and N_2). The 6 mm wide IR collection volume (or the center of the slit) was focused at about 8 mm above the burning surface.

Nonetheless, the characteristic infrared emission bands from the expected combustion products are readily identified.[15] However, the emission spectra of combustion products measured at elevated temperature are in general not similar to the reference absorption spectra which have been measured at room temperature due to the band broadening or/and shifts caused by various reasons, such as high temperature, self absorption, etc. The identifiable emission bands in Fig. 6 include: (1) CO_2, centered at 2349 and 667 cm^{-1} corresponding to the ν_3 and ν_2 bands, respectively; (2) H_2O, centered at 3756, 3652, and 1595 cm^{-1} corresponding to the ν_3, ν_1, and ν_2 bands, respectively; and (3) CO, centered at 2143 cm^{-1} corresponding to ν_1 band which slightly overlaps the ν_3 band of CO_2 centered at 2349 cm^{-1}. In addition, some thermal fragments (as various hydrocarbons) of the incomplete combustion products also appear in the 1400-1000 cm^{-1} region.

Measurements with a smaller slit height of 100 μm were also conducted, but a considerable increase in the noise was observed as expected. A much improved value of the SNR can be achieved by employing wider strands to obtain a larger area over which the emission

occurs and by using parabolic collection mirrors to increase the amount of collected IR energy.

CONCLUSIONS

An analysis and results have been presented for the purpose of investigating the achievable spatial resolution of emission measurements of the products from solid propellants combustion using an FT-IR spectrometer. In order to extrapolate to relevant rocket motor conditions, experiments were performed to determine the unknown constant in the empirical expression for SNR. The theory of SNR assumes that the major source of noise is the detector noise. The major conclusions from this study are as follows:

(1) The expression employed for the determination of SNR has been verified by experiments in the optically thick limit.

(2) For condition applicable to high pressure solid propellant combustion, the predicted maximum SNRs are of the order of 1000 at a spatial resolution of 100 μm. It is expected that such SNRs are sufficient to apply band ratio techniques for deducing species and temperature profiles.

(3) Measurements of emission spectra of NOSOL-363 at low pressure (one atmosphere) yield an SNR that appears to be quite high using a spatial resolution of 1000μm.

(4) The SNRs of the employed experimental setup can further be increased by employing wider slit or use parabolic mirrors in the IR collection optics.

ACKNOWLEDGEMENT The support received from the Office of Naval Research under Contract No. N00014-89-J-1559 for the setup of the spectrometer system is greatly appreciated.

References

1. G. Lengellk, A. Bizot, J. Duterque, and J. F. Trubert, "Steady-State Burning of Homogeneous Propellants," and K. N. R. Ramohalli, "Steady-State burning of Composite Propellants under Zero Cross-Flow Situation," in *Fundamentals of Solid Propellant Combustion*, K. K. Kuo and M. Summerfield, Eds. (AIAA, New York, 1984), Chaps. 7 and 8.
2. J. H. Stufflebeam and A. C. Eckbreth, 25th JANNAF Combustion Meeting, 1, 113 (1987).
3. T. Edwards, D. P. Weaver, and D. H. Campbell, Appl. Opt. 26, 3496 (1987).
4. T. Parr and D. Hanson-Parr, 24th JANNAF Combustion Meeting, 1, 367 (1988).
5. Y. Oyumi and T. B. Brill, Combustion and Flame **62**, 213 (1985).
6. D. C. Tilotta, K. W. Busch, and M. A. Busch, Appl. Spectrosc. **43**, 704 (1989).
7. F. J. Shaw and R. A. Fifer, Technical Report BRL-TR-2993, 1989.
8. S. Klotz, S. T. Thynell, I. T. Huang, and K. K. Kuo, AIAA paper 90-1850, 26th Joint Propulsion Conference, (1990); also AIAA J. Propulsion and Power, (in press).
9. D. R. Mattson, Appl. Spectrosc. **32**, 325 (1978).
10. P. R. Griffiths and J. A. de Haseth, *Fourier Transform Infrared Spectrometry*, (Wiley, New York, 1986), Chap. 7.
11. M. N. Özisik, *Radiative Transfer and Interactions with Conduction and Convection*, (Wiley, New York, 1973), p. 258
12. D. K. Edwards, Advances in Heat Transfer, 12, 115 (1976).
13. L. A. Gross and P. R. Griffiths, J. Quant. Spectrosc. Radiat. Transfer, 39, 463 (1988).
14. C. C. Ferriso, C. B. Ludwig, and F. P. Boynton, Tenth Symposium (International) on Combustion, 161 (1965).
15. G. Herzberg, *Infrared and Raman Spectra of Polyatomic Molecules*, (D. van Nostrand Company, Inc. Princeton, New Jersey, 1968), Vol. II, Chap. 3.

16. S. Gordon, B. J. McBride, and F. J. Zeleznic, *Computer Program for Calculation of Complex Chemical Equilibrium Compositions and Applications, Supplement I - Transport Properties*, (NASA, 1984).

17. M. E. Thomas and M. J. Linevsky, J. Quant. Spectrosc. Radiat. Transfer, 42, 465 (1988).

LIST OF FIGURES

Fig. 1 Schematic diagram of experimental setup for combustion product studies in transparent test chamber using the FT-IR.

Fig. 2 Optical layout of beam paths for performing emission measurements using the FT-IR and the windowed transparent test chamber.

Fig. 3 Comparison of SNR from theoretical calculations and experimental results

Fig. 4 Unknown constant, C, from experimental results.

Figs. 5 SNR at different temperatures and slit heights, (a) 0.1 mm, (b) 0.3 mm, (c) 1.0 mm.

Fig. 6 Result of 4 coadded emission spectra of NOSOL-363 with a 1000 μm slit height.

Fig. 7 Result of 4 coadded emission spectra of NOSOL-363 with a 300 μm slit height.

List of Tables

Table 1. Predicted SNRs using a 100μm slit size of emission spectroscopy near the peak of the ν_3 fundamental band of CO_2. The equilibrium mole fractions and adiabatic flame temperature has been calculated using the CET86[16] code.

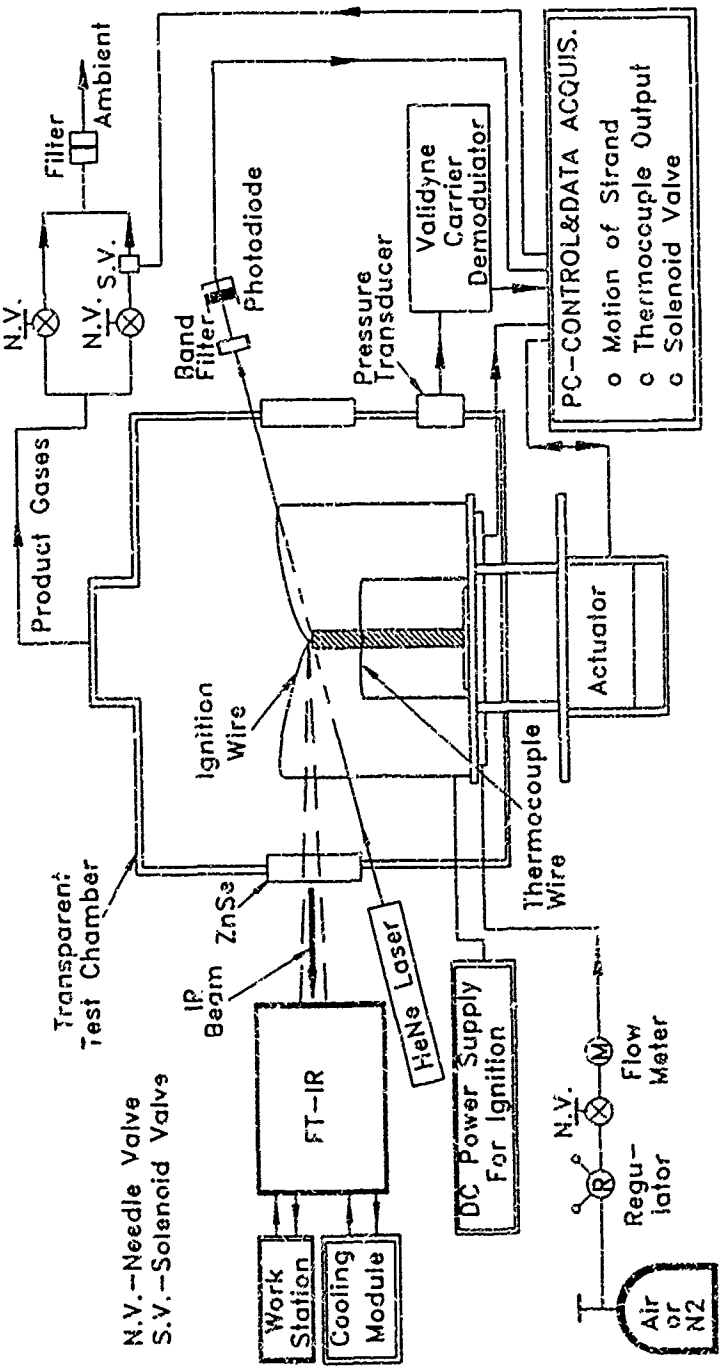


Fig. 1 Schematic diagram of experimental setup for combustion product studies in transparent test chamber using the FT-IR

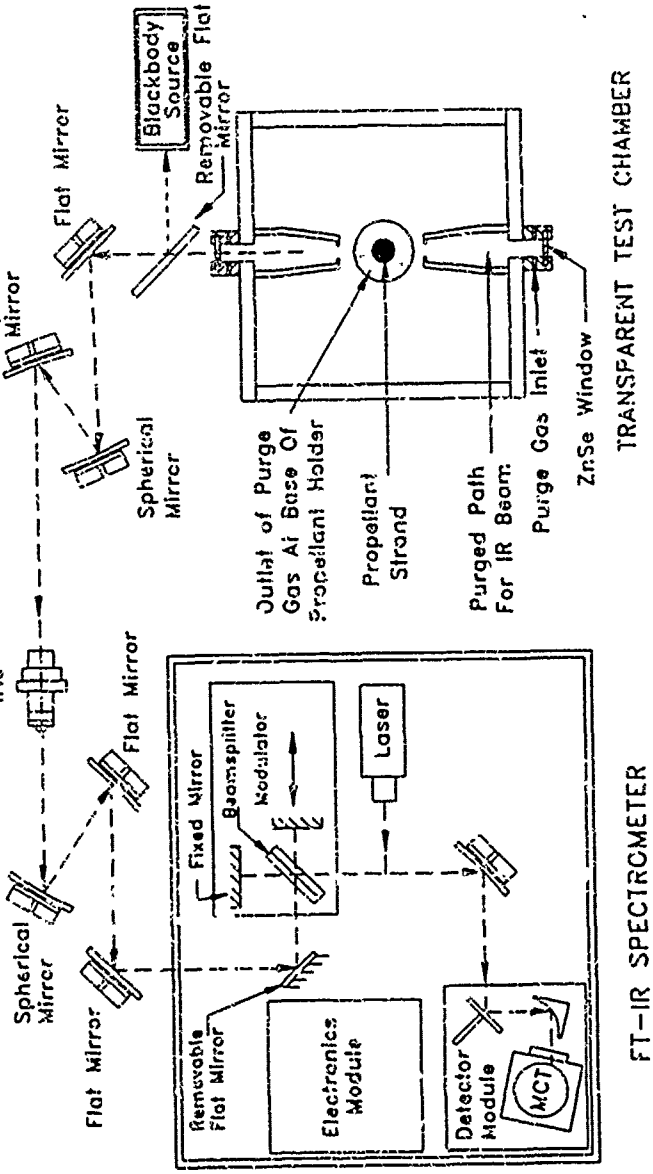
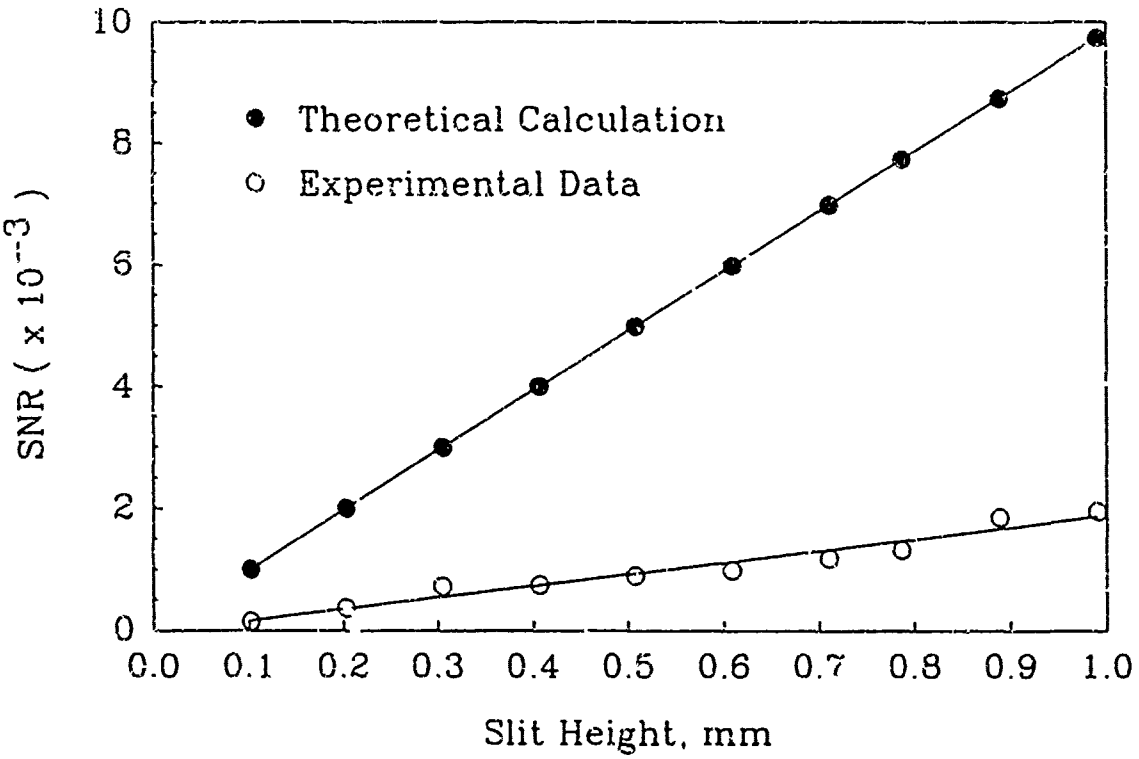
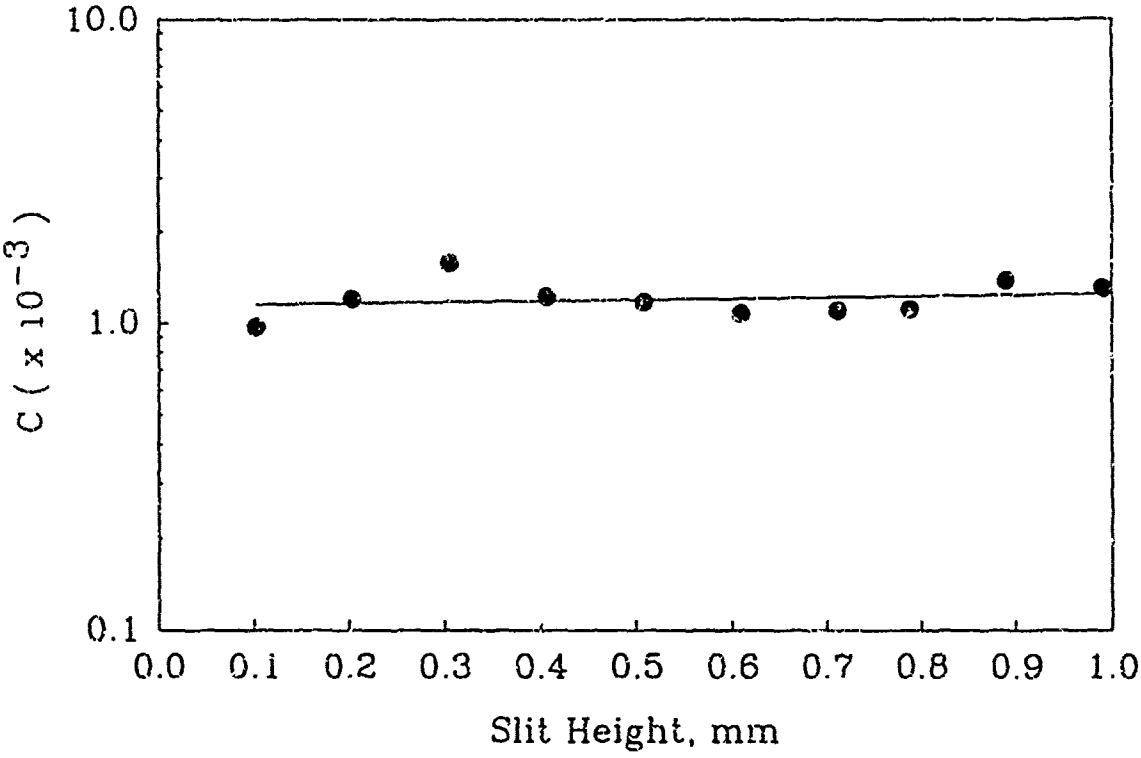
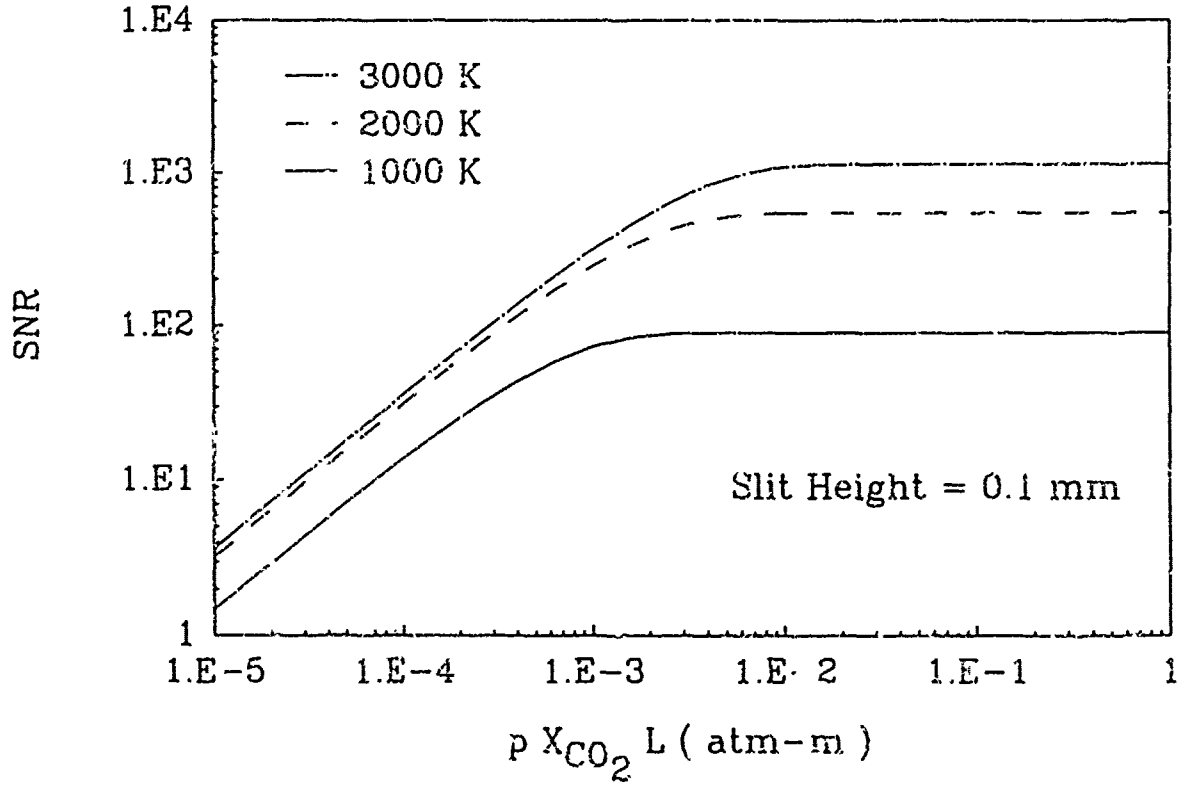
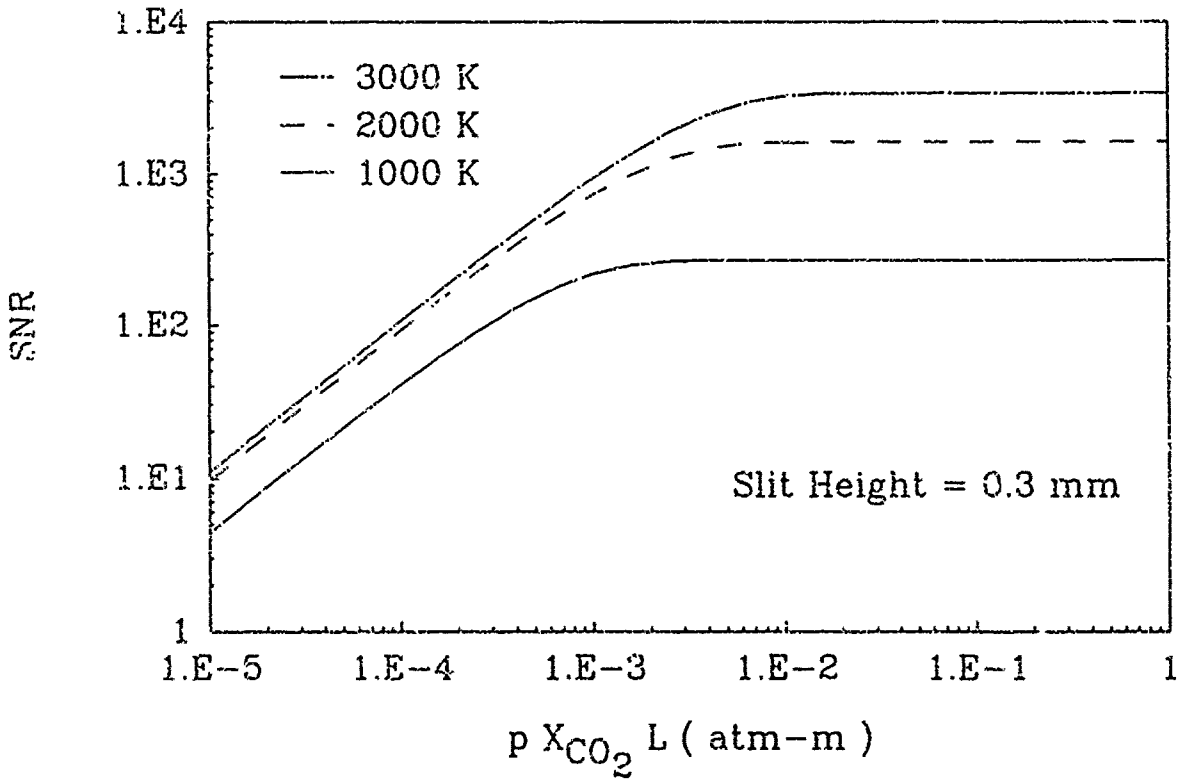


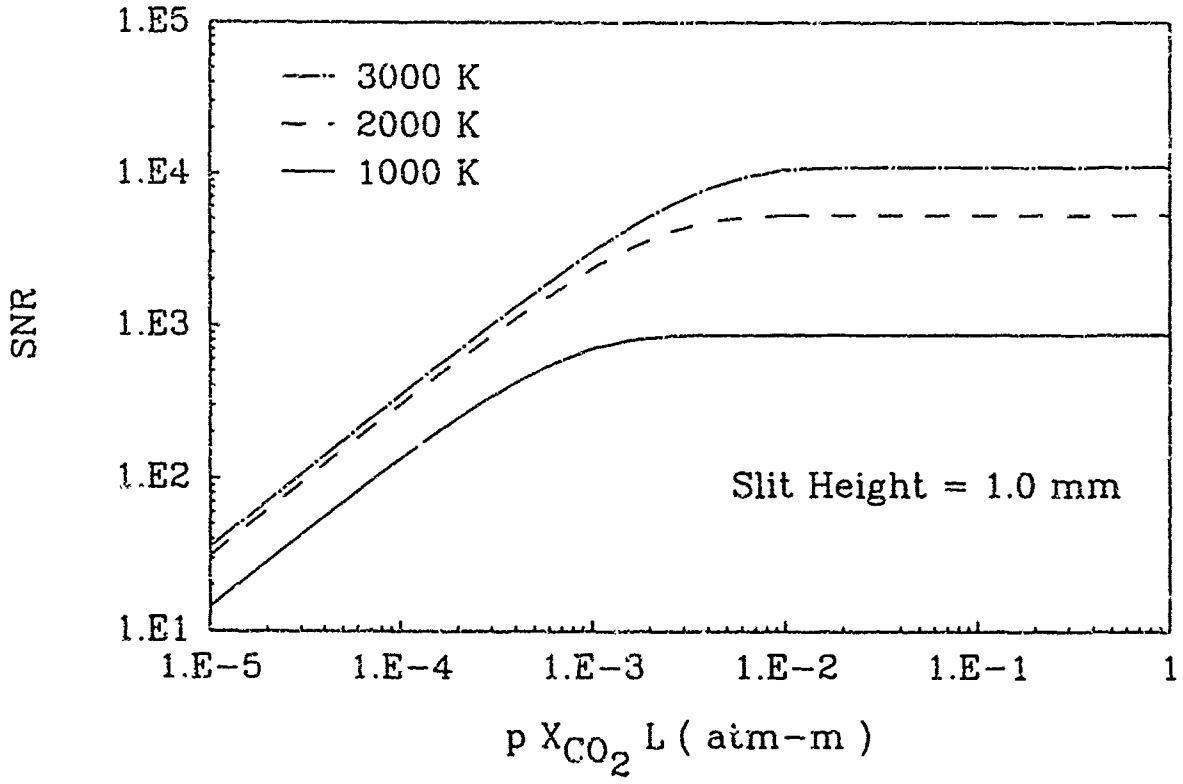
Fig. 2 Optical layout of beam paths for performing emission measurements using the FT-IR and the windowed transparent test chamber

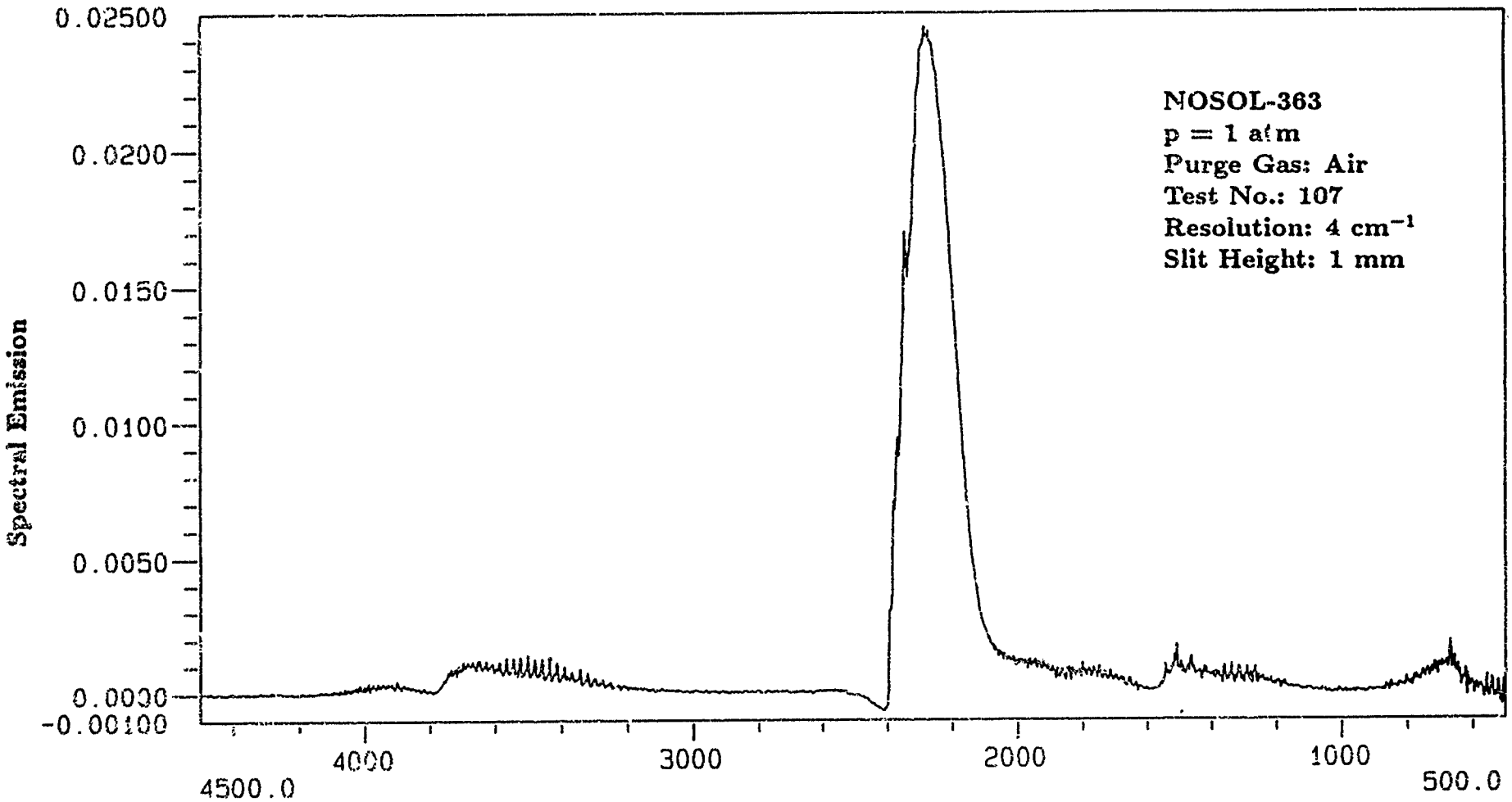

10
8
6
4
2
0
SNR (x 10^{-3})
Theoretical Calculation
Experimental Data
0.0
0.1
0.2
0.3
0.4
0.5
0.6
0.7
0.8
0.9
1.0
Slit Height, mm


10.0
1.0
0.1
C (x 10^{-3})
0.0
0.1
0.2
0.3
0.4
0.5
0.6
0.7
0.8
0.9
1.0
Slit Height, mm


1.E4
1.E3
1.E2
1.E1
1
SNR
3000 K
2000 K
1000 K
Slit Height = 0.1 mm
1.E-5
1.E-4
1.E-3
1.E-2
1.E-1
1
p X_{CO_2} L (atm-m)


1.E4
1.E3
1.E2
1.E1
1
SNR
3000 K
2000 K
1000 K
Slit Height = 0.3 mm
1.E-5
1.E-4
1.E-3
1.E-2
1.E-1
1
p X_{CO_2} L (atm-m)


1.E5
1.E4
1.E3
1.E2
1.E1
SNR
3000 K
2000 K
1000 K
Slit Height = 1.0 mm
1.E-5
1.E-4
1.E-3
1.E-2
1.E-1
1
p X_{CO_2} L (atm-m)


0.02500
0.0200
0.0150
0.0100
0.0050
0.0000
-0.00100
Spectral Emission
4500.0
4000
3000
2000
1000
500.0
Wavenumber
NOSOL-363
p = 1 atm
Purge Gas: Air
Test No.: 107
Resolution: 4 cm-1
Slit Height: 1 mm

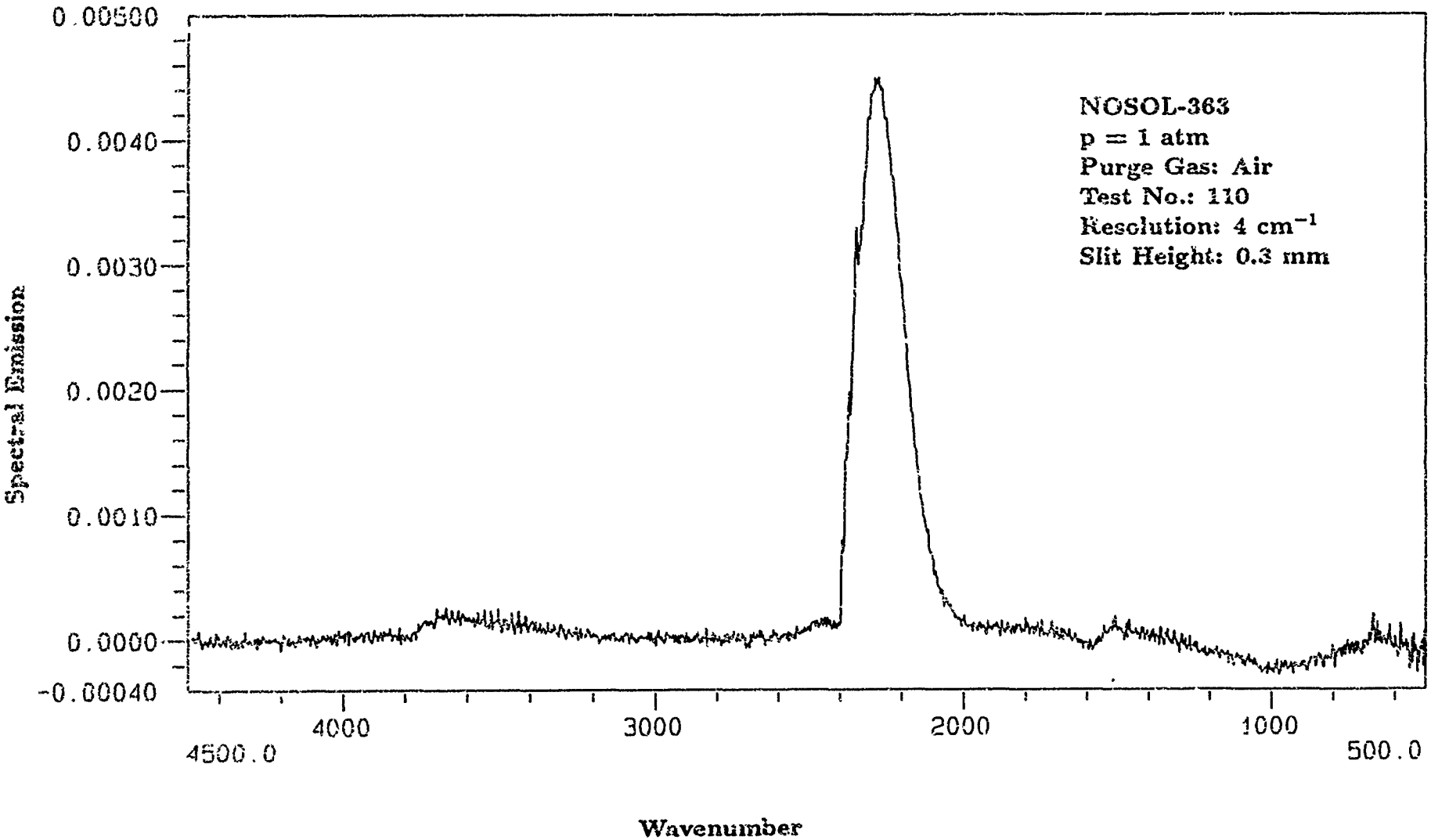

0.00500
0.0040
0.0030
0.0020
0.0010
0.0000
-0.00040
Spectral Emission
4000
3000
2000
1000
4500.0
500.0
Wavenumber
NOSOL-363
p = 1 atm
Purge Gas: Air
Test No.: 110
Resolution: 4 cm-1
Slit Height: 0.3 mm

Table 1. Predicted SNRs using a 100 μm slit size of emission spectroscopy near the peak of the ν_3 fundamental ban CO_2. The equilibrium mole fractions and adiabatic flame temperatures have been calculated using the CET86 c

Propellant	Chemical Family	Applied System Pressure (atm)	Adiabatic Flame Temperature (K)	Equilibrium Mole Fractions, X					$pX_{CO_2}L$ ($\times 10^3$ atm-m)	SNR for a 100 μm Sli
				CO_2	CO	H_2O	H_2	N_2		
M10	Single-base	1	2359	0.12	0.43	0.20	0.13	0.11	0.70	211
		10	2385	0.12	0.43	0.21	0.13	0.11	7.0	720
		100	2397	0.12	0.43	0.21	0.13	0.11	70.	753
JA-2	Double-base	1	2708	0.13	0.36	0.25	0.10	0.12	0.79	251
		10	2821	0.13	0.37	0.26	0.10	0.12	8.0	951
		100	2883	0.13	0.37	0.27	0.10	0.12	81.	1039
M9	Double-base	1	2893	0.17	0.31	0.23	0.06	0.13	1.0	313
		10	3113	0.18	0.31	0.25	0.06	0.14	11.	1140
		100	3307	0.19	0.31	0.27	0.06	0.14	114.	1297
NOSOL-363	Double-base	1	2332	0.09	0.41	0.21	0.17	0.11	0.52	162
		10	2357	0.09	0.41	0.21	0.17	0.11	5.2	671
		100	2368	0.09	0.41	0.21	0.17	0.11	52.	736
M30	Triple-base	1	2544	0.07	0.27	0.23	0.13	0.28	0.45	149
		10	2602	0.07	0.27	0.24	0.13	0.28	4.5	739
		100	2627	0.07	0.27	0.24	0.13	0.28	45.	887
XM39	Nitramine	1	2157	0.03	0.39	0.10	0.27	0.21	0.17	57
		10	2166	0.03	0.39	0.10	0.27	0.21	1.7	383
		100	2170	0.03	0.39	0.10	0.27	0.21	17.	624

TECHNICAL NOTE

An Approach to Measurements of Flame Spreading over Solid Propellants

S. T. Thynell*, I. T. Huang†, C. S. Kuo†, W. H. Hsieh*, and K. K. Kuo‡

The Pennsylvania State University, University Park

Pennsylvania 16802

*Assistant Professor, Member AIAA
†Graduate Student
‡Distinguished Professor, Fellow AIAA

Introduction

To measure the flame spreading over solid propellant surfaces, many techniques have been employed.[1] Brown et al.[2] and Jensen et al.[3] employed fuse wires and thin-film flux gages embedded in the propellant sample for measurements of ignition and ignition front propagation rates. Mitchell and Ryan[4] used a high-speed movie camera to measure flame spreading over freshly cut nonaluminized composite solid propellants. Similarly, McAlevy et al.[5] recorded the flame spreading event with a motion picture camera. However, the use of cameras for measuring flame spreading is difficult. The recorded (visible) luminosity at a specific location may be due to chemical reactions of pyrolysis products carried by the mean flow from upstream, or the luminosity could be due to glowing particulate matter, such as aluminum or boron or their oxides.

The objective of this work is to present a new approach for measuring flame spreading over solid propellant surfaces. The approach is based on the characterization of the radiant energy emitted from the combustion products of a typical solid propellant with and without a burning surface in the background. To characterize such emission, a rapid-scanning FT-IR spectrometer system has been employed for measuring the emitted energy from the combustion products of a solid propellant containing aluminum/ammonium perchlorate/hydroxyl-terminated polybutadiene (Al/AP/HTPB).

Measurement Approach

During the ignition transient, the solid propellant is subject to intense heating by convection, radiation and particle impingement up to its ignition temperature. Once the solid propellant burns, the emission of radiant energy from the burning surface and gas/particle mixture should remain nearly constant (unless the conditions within the motor change). To use the emitted energy as a means for detecting the flame spreading during the ignition transient, three important aspects must be satisfied. First, it is necessary a optical access to the

measurement location. Second, the emitted radiant energy from the burning surface must be distinguishable from the emitted radiant energy from the flowing, hot combustion products. That is, the emission of radiant energy from the hot combustion products cannot overwhelm the spectral emission characteristics of a burning surface. Finally, it is necessary that the radiation measurement system is capable of recording the rapidly changing event taking place during the flame spread. The most important component of such a system is the detector, which should have a time constant on the order of 1 μs. Examples include, among others, the mercury-cadmium-telluride (MCT), lead selenide (PbSe), or the indium antimonide (InSb) detectors.

Experimental Setup

To examine the emission characteristics of the combustion products, a preliminary engineering study was conducted using the MCT detector in an FT-IR spectrometer system and a solid propellant containing a mixture of Al/AP/HTPB (18% Al). The details of this spectrometer system have been discussed previously.[6] To simulate the flame spreading in a simple yet realistic manner, four cases were devised as shown in Fig. 1.

Case 1, which involves the burning of a single, vertical propellant strand as shown in Fig. 1(a), represents the situation that is expected to occur when the hot combustion products (from the core of the motor) flow over and heat up the propellant. Case 2, which involves the burning of both a vertical strand and a horizontal strand simultaneously, approximates th situation when hot combustion products flow over an ignited surface. Case 3 represents the situation when there are no hot combustion products flowing across a burning surface. Finally, Case 4 is the setup to determine the spectral features of the background emission.

Results and Discussion

Measurements of emission according to the four cases described above were performed using solid propellant strands of 6 mm diameter and 30 mm length. The FT-IR spectrometer was

set to take 100 double-sided interferograms at 8 cm^{-1} resolution, with each interferogram requiring approximately 300ms of measurement time (4296 data points). The top of the vertical strand was aligned within the measurement line-of-sight location to capture the ignition transient phenomena. The focal spot size of the IR measurement was adjusted to a circle of 6 mm diameter. The strand was easily ignited using electrical resistance heating of a nichrome wire inserted into the top of the strand. The burning rate was approximately 5 mm/sec in the windowed test chamber using nitrogen as purge gas at 1 atm.

As the top of the burning propellant strand recedes below the field-of-view of the detector, the emission of radiant energy is primarily due to the equilibrium combustion products, which are gases and particulates (primarily Al_2O_3). Figure 2 shows the MCT detector response average of 10 scans from Case 1 [defined in Fig. 1(a)]. During the measurement period of time, which was approximately 3 sec, the burning surface receded approximately 15 mm, but the sequential individual emission spectra (not shown) show only a 10% variation. Although the spectral resolution is only 8cm^{-1} and only 10 scans were averaged, many of the characteristic vibration-rotation bands of IR active molecules are clearly revealed.

The following identification of IR active species uses information compiled by Herzberg.[7] The major species formed during the combustion are as expected H_2O and CO_2. The water vapor has bands centered at 3700 and 1587 cm^{-1}, but the pure rotational band appears to be washed out by the continuous emission from the aluminum oxide particles and the strong fundamental band of CO_2 centered at 667 cm^{-1}. CO_2 also has another fundamental band centered at 2400 cm^{-1} and an overtone centered at 3700 cm^{-1}. HCl, CO, and NO have fundamental bands centered at 2850, 2170, and 1850 cm^{-1}, respectively. Visual examination of the floor of the windowed test chamber did not reveal any soot formation of the Al/AP/HTPB solid propellant. but white dust settled everywhere within the test chamber and thus required a

thorough clean up after each test firing. The identification and assignment of additional species require higher resolution and the availability of reference spectra at high temperatures.

The MCT detector responses of Cases 1, 2, 3 and 4 are shown in Fig. 3. The first 3 cases are the average of 10 scans following the ignition transient. The background emission according to the setup of Case 4 is included for comparison purposes. In Case 2, the vertical strand was ignited near its top, whereas the horizontal strand was ignited convectively from the hot combustion product gases evolving from the vertical strand. The ignition transient lasted approximately 1.5 sec and was dominated by continuum emission. The recorded sequential spectra, which are not included here, revealed that the emission of radiant energy remained fairly steady once the ignition transient was complete. In addition, the absorption peak near 2400 cm^{-1} of Case 3 is a self-absorption effect. That is, the hot combustion products mix with the N_2 purge gas to form relatively cold gases that partially absorb the radiation emitted by the products evolving from the burning horizontal strand.

Examination of the results shown in Fig. 2 reveals that the continuum emission from the Al_2O_3 particles is extremely small although the initial aluminum mass fraction in the propellant is large. The continuum emission is especially absent in the 5000-2400cm^{-1} region although the combustion products are at a high temperature. The reason for such low emission is attributed to the low emissivity of such particles, which are known to have a very large scattering cross-section that increases with increasing wavenumbers.[8] Once the burning surface is within the field of view of the detector, according to Cases 2 and 3 shown in Fig. 3, the continuum emission within the aforementioned wavenumber region increases significantly. The increase in the spectral detector response is possibly attributed to the emission by carbonaceous residue formed from the binder polymer fragments ejected from the burning propellant surface. Because of the low emissivity of the aluminum oxide particles, emission measurements are proposed

covering the 5000-2400 cm^{-1} region for the detection of flame spreading along the surface of a propellant containing significant amounts of aluminum. That is, the emission of radiant energy within this wavenumber region should increase significantly once the surface has ignited.

Summary and Conclusions

An FT-IR spectrometer system has been employed to measure the thermal radiation emitted from the combustion products of a solid propellant. The objective of the measurements was to ascertain the characteristics of radiant energy emitted from the combustion products with and without a burning surface in the background. Based on the findings of this preliminary study involving a propellant containing Al/AP/HTPB (18% Al), it is expected that infrared measurements covering the 5000-2400 cm^{-1} wavenumber region should enable definite detection of the arrival of the propagation of a flame front over a solid propellant surface.

Acknowledgment

The support received from the Office of Naval Research under Contract No. N00014-89-J-1559 for the setup of the spectrometer system is greatly appreciated.

References

[1]Kumar, M., and K.K. Kuo, "Flame Spreading and Overall Ignition Transient," *Fundamentals of Solid-Propellant Combustion*, eds. K.K. Kuo and M. Summerfield, Vol. 96 of Progress in Astronautics and Aeronautics, 1984, pp. 305-360.

[2]Brown, R.S., Wirrick, T.K., and Anderson, R., "Theory of Ignition and Ignition Propagation of Solid Propellants in a Flow Environment," AIAA Paper 64-157, January 1964.

[3]Jensen, G.E., Brown, R.S., Cose, D.A., and Anderson, R., "Ignition and Ignition Propagation in Solid Propellant Motors," AIAA Paper 66-677, June 1966.

[4]Mitchell, R.C. and Ryan, N.W., "Flame Spread on Solid Propellant," AIAA Paper 64-128, Jan. 1964; see also *Journal of Spacecraft and Rockets*, Vol. 2, July-Aug. 1965, pp. 610-612.

[5]McAlevy, R.F. III, Magee, R.S., Wrubel, J.A., and Horowitz, F.A., "Flame Spreading Over the Surface of Igniting Solid Rocket Propellants and Propellant Ingredients," *AIAA Journal*, Vol. 5, Feb. 1967, pp. 265-271.

[6]Klotz, S., Thynell, S.T., Huang, I.T., and Kuo, K.K., "Analysis of Plumes of Solid Propellant Combustion Using an FT-IR Spectrometer," AIAA Paper No. 90-1850, July 1990.

[7]Herzberg, G., *Infrared and Raman Spectra of Polyatomic Molecules*, Vol. II, van Nostrand Company, Princeton, New Jersey, 1968.

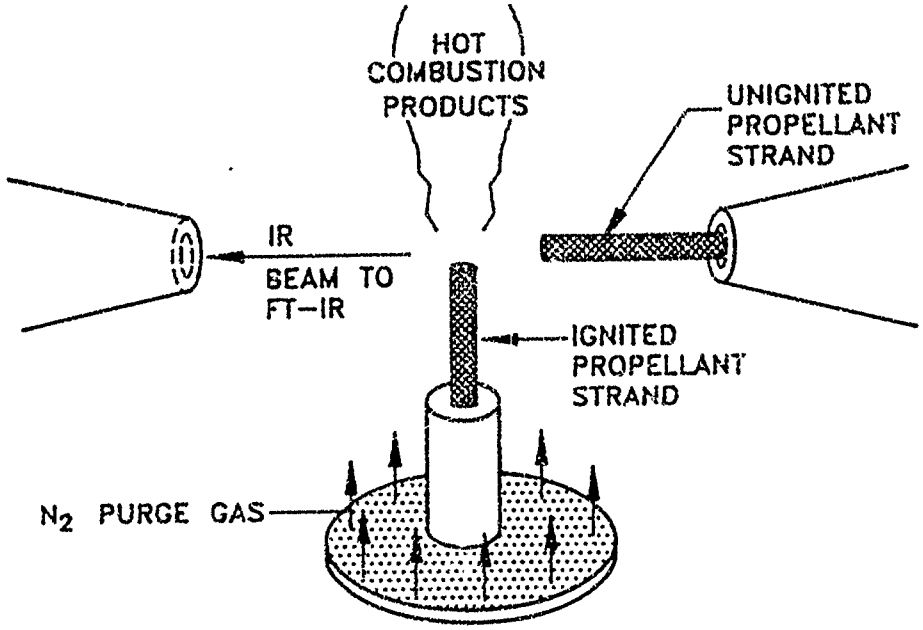
[8]Plass, G. N., "Temperature Dependence of the Mie Scattering and Absorption Cross Sections for Aluminum Oxide," *Applied Optics*, Vol. 4, No. 12, 1965, pp. 1616-1619.

List of Figures

Fig. 1 Experimental Setup of Propellant Strands within Windowed Test Chamber for Conducting Emission Measurements Simulating Flame Spread

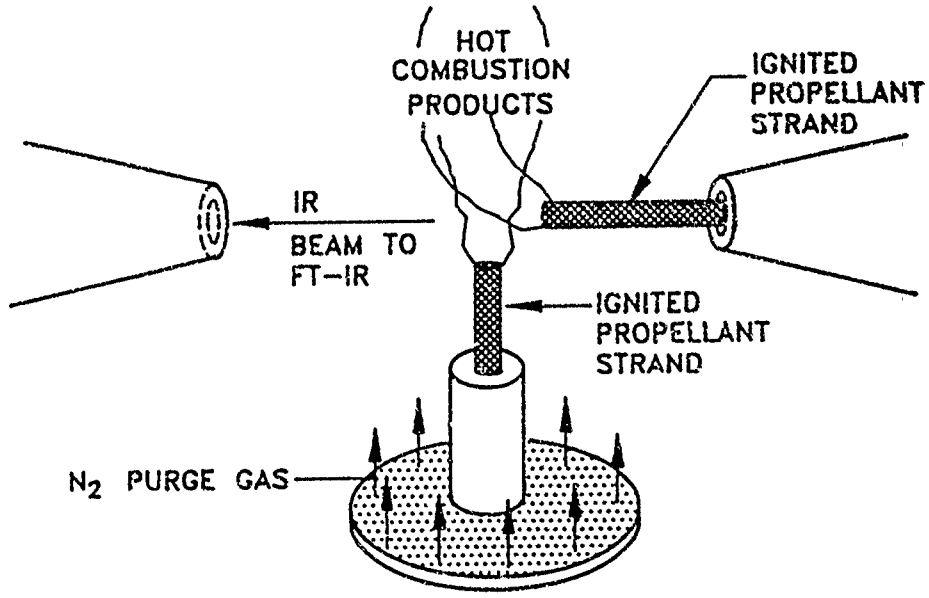
Fig. 2 MCT Detector Response due to Emission from Combustion Products of an Al/AP/HTPB Containing Propellant Strand Burned According to Case 1

Fig. 3 MCT Detector Responses due to Emission According to Cases 1, 2, 3 and 4



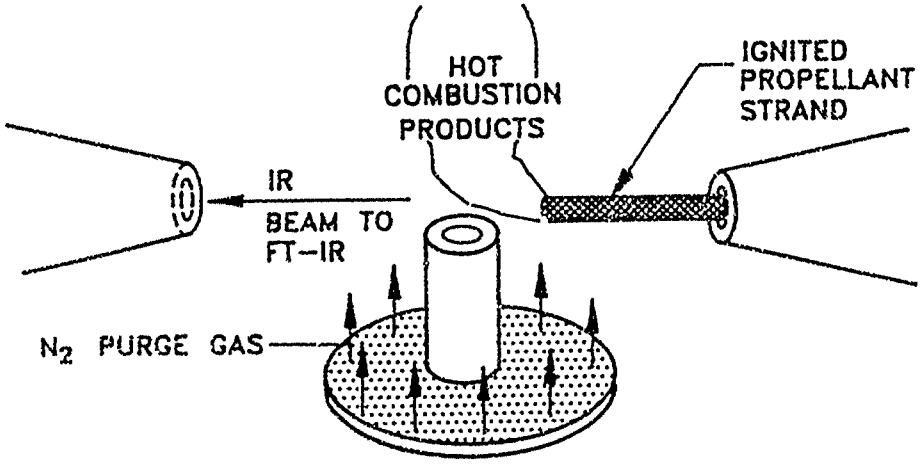
(a)

CASE 1



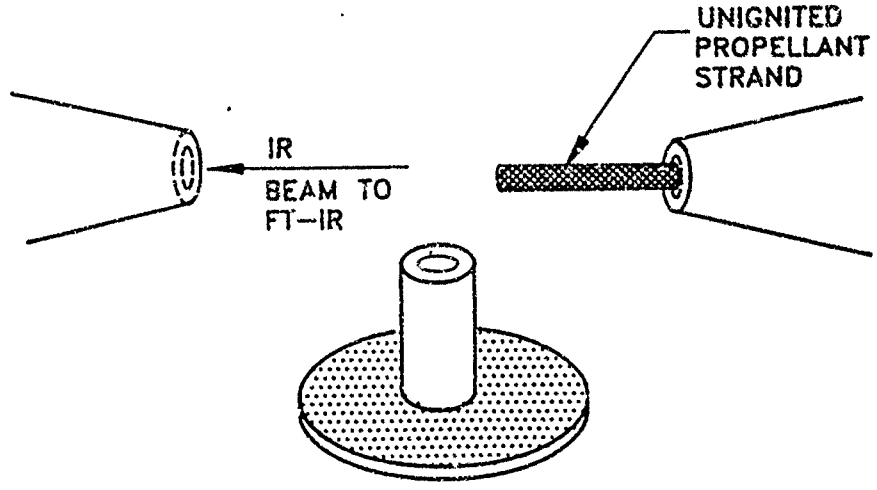
(b)

CASE 2



(c)

CASE 3



(d)

CASE 4

Fig-1

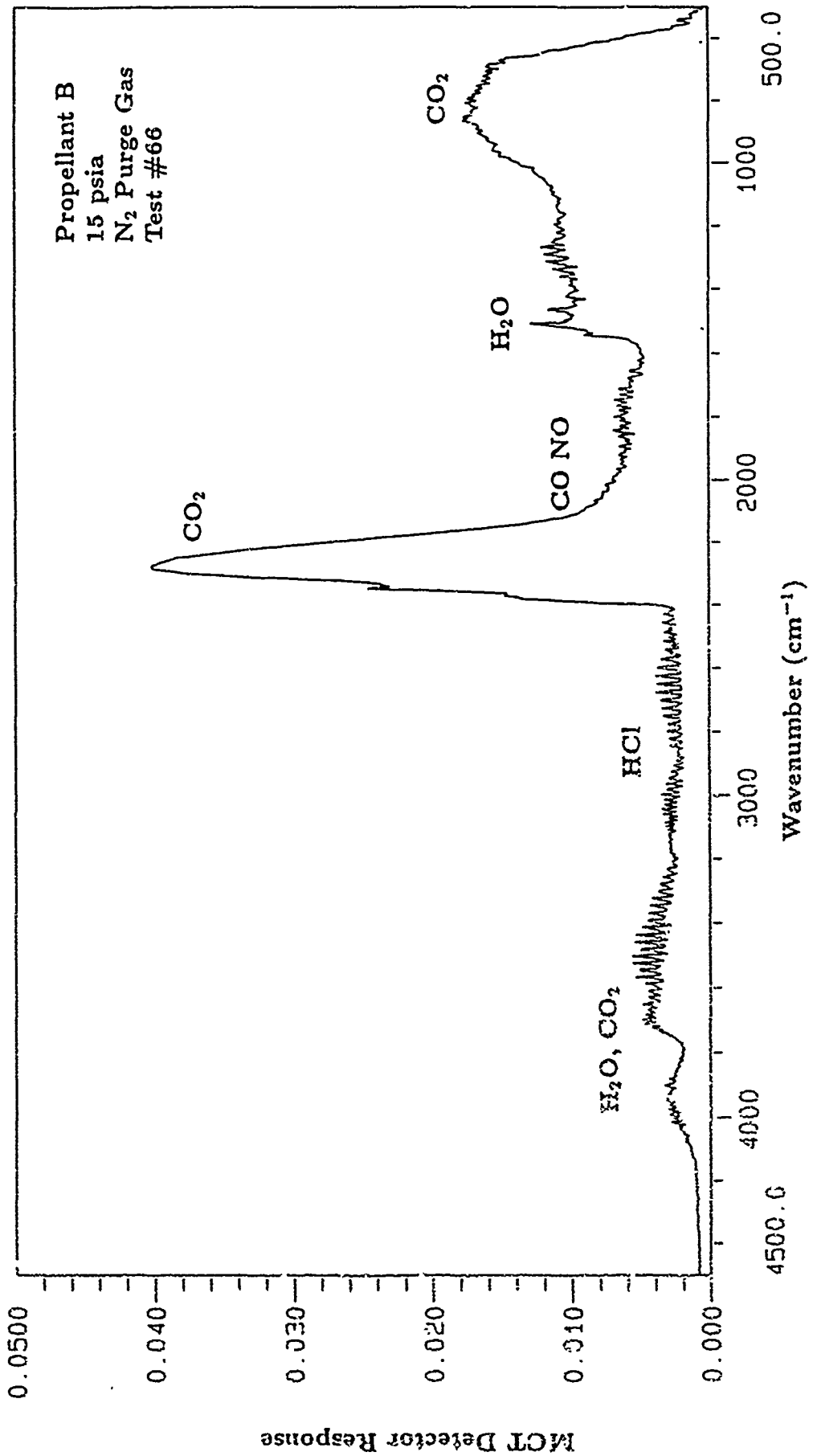

Propellant B
15 psia
N_2 Purge Gas
Test #66
CO_2
CO NO
H_2O
CO_2
HCl
H_2O, CO_2
0.0500
0.040
0.030
0.020
0.010
0.000
4500.0
4000
3000
2000
1000
500.0
Wavenumber (cm^{-1})
MCT Detector Response

Fig. 2

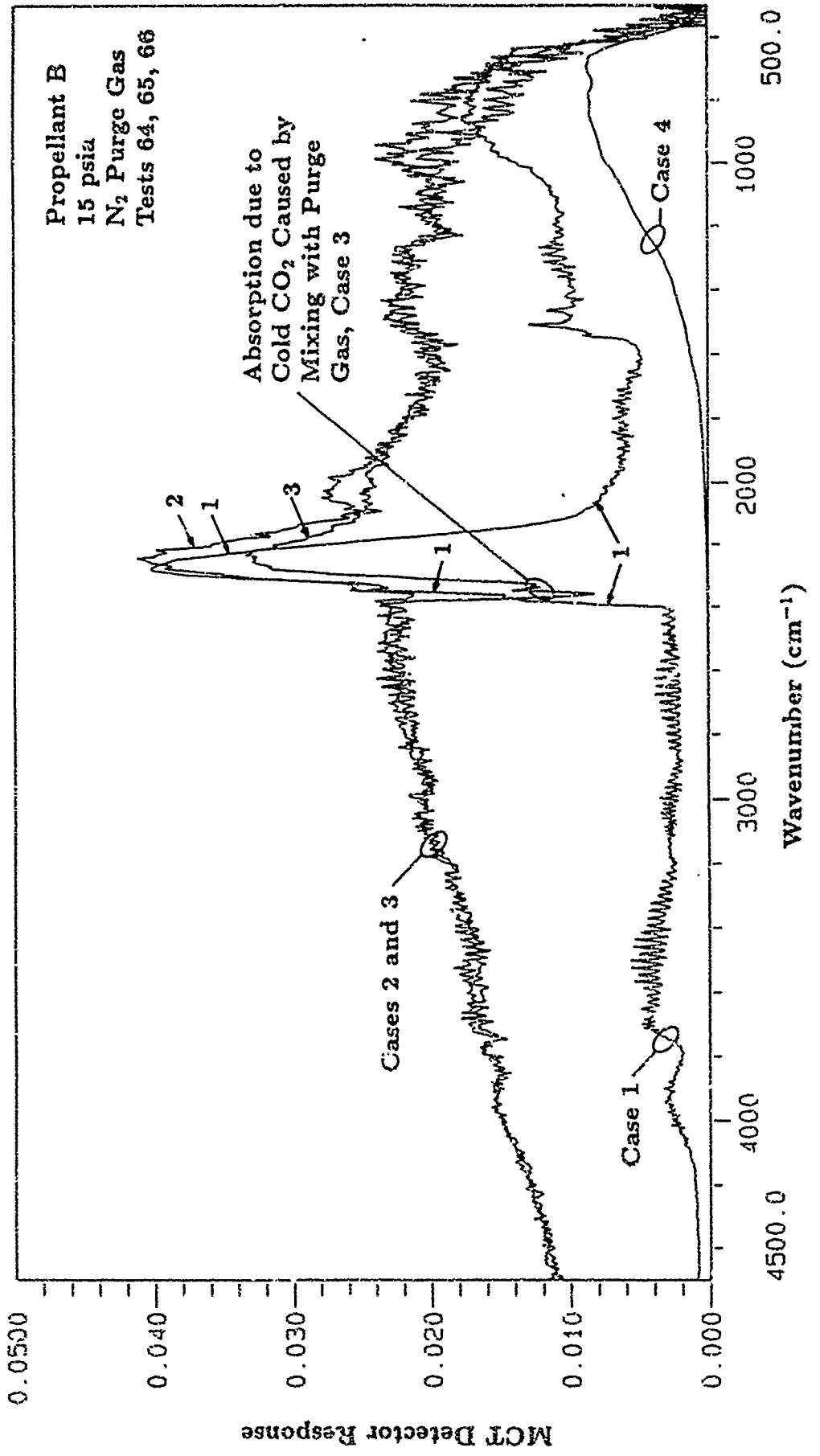

Propellant B
15 psia
N_2 Purge Gas
Tests 64, 65, 66
Absorption due to Cold CO_2 Caused by Mixing with Purge Gas, Case 3
Case 4
Cases 2 and 3
Case 1
1
2
3
MCT Detector Response
0.0500
0.040
0.030
0.020
0.010
0.000
4500.0
4000
3000
2000
1000
500.0
Wavenumber (cm^{-1})

Fig. 3

CHAPTER 4
STEADY-STATE COMBUSTION BEHAVIOR OF MG/PTFE/VITON AND BORON-BASED SOLID FUELS

I. Introduction

Basic knowledge of steady-state burning behaviors of solid energetic materials is essential for numerous applications. These behaviors include: (1) baseline regression rate as a function of pressure, initial temperature, and other operating conditions, (2) deduced activation energy and frequency factor as kinetic input parameters to computer codes, (3) low-pressure deflagration limit and temperature sensitivity, (4) flame behavior and burning surface conditions, (5) burning surface temperature, and (6) ejection of particulates from the burning surface region. Such basic data are important in the design of propulsion systems, and they are needed in the development and execution of comprehensive theoretical models of combustion processes of energetic materials.

The objective of this task is to achieve a better understanding of the above-mentioned combustion behaviors of various energetic materials by conducting experimental investigations using a temperature and pressure-controlled optical strand burner.

II. Method of Approach

A temperature- and pressure-controlled optical combustor was used in this work to study boron-based BAMO/NMMO energetic solid fuels, and magnesium/teflon/viton-a pyrotechnic materials. Figure 4.1 shows the schematic diagram of the optical combustor. The chamber pressure is measured by either a Validyne (up to 3,200 psi) or a Kistler (up to 10,000 psi) pressure transducer. The chamber pressure was kept constant by a solenoid valve of which operation was controlled by an IBM/AT personal computer. In order to investigate the effect of ambient gas composition on the combustion behavior, a purge gas with different compositions was used to pressurize the test chamber.

To heat up or cool down the test sample to a pre-specified initial temperature, both temperatures of chamber body and purge flow were kept at the same level. The chamber is surrounded by a constant-temperature bath of silicon fluid, of which the temperature can be preset at a level between -40 to 70°C. A pump is incorporated into this closed-loop system to provide a necessary driving force for circulation purpose. Through the heat transfer between the chamber wall and the above-mentioned recirculating constant-temperature bath, a uniform stable

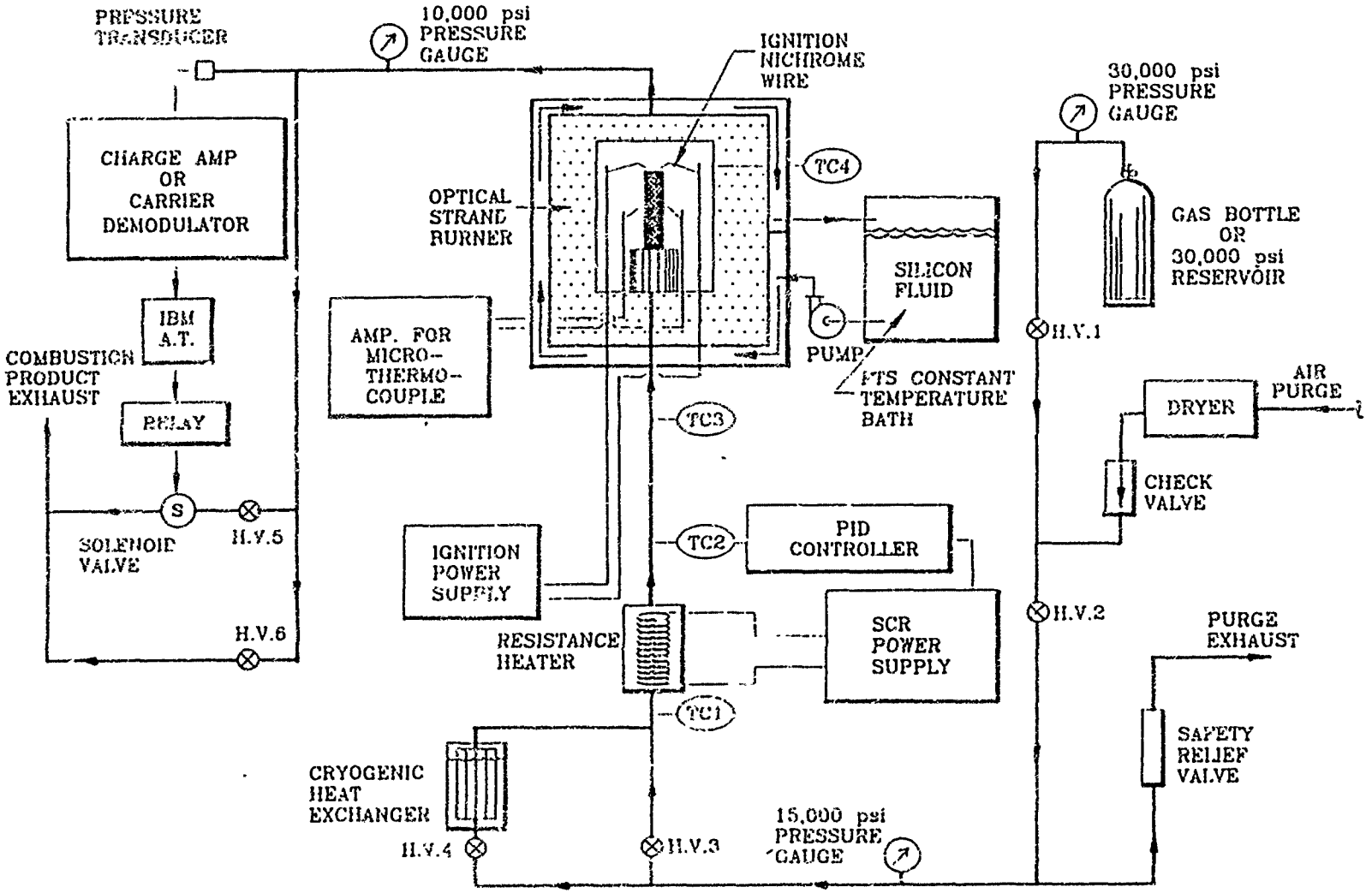


Fig. 4.1 PRESSURE & TEMPERATURE CONTROLLED OPTICAL STRAND BURNER

temperature of chamber body can be attained. In test firings with low initial propellant temperature (e.g. -10°C), the purge gas is first precooled in a cryogenic heat exchanger, operated by means of liquid nitrogen, down to the temperature which is typically 15°C lower than the pre-specified level. Then, a resistance heater, linked to a control unit consisting of a proportional integral derivative (PID) controller and a silicon controlled rectifier (SCR) power supply, inputs an appropriate amount of heat flux to the purge flow. Therefore, the chamber gas-phase temperature is increased to the preset value and remained stable at that point.

During a test, a sample of the energetic material is mounted vertically in the chamber. Ignition of the sample is achieved by sending an electrical current to a nichrome wire, pierced through the test sample about 3mm from the top surface. A scale is optically superimposed on the image of the sample by a semitransparent mirror. The length of the sample burned in a certain time span is accurately determined from both images of the scale and the test sample, which are recorded by a video recording system. From the information of the instantaneous locations of the burning surface, the burning rate of the test sample is deduced.

For the pressure deflagration limit tests, the chamber was depressurized at a rate of about 1.0 kPa/sec. The extinguishment of the test sample was indicated by a sudden chamber pressure drop and, therefore, the pressure deflagration limit can be determined from the recorded pressure-time trace.

In order to measure the burning surface temperature and thermal-wave structures in the subsurface and gas-phase region of the test sample, fine-wire thermocouples (Platinum/Platinum-13% Rhodium) with a wire diameter of 5 to 50 μm were employed in this investigation. The thermal conductivity and diffusivity of the energetic material as functions of temperature were deduced from the measured subsurface temperature profiles using the subsurface temperature profile (STP) method developed by the researchers. As mentioned above, the burning rate and burning surface temperature were measured from recorded video images and thermocouple outputs, respectively. As the burning rate and burning surface temperature data are available, the activation energy and the pre-exponential factor are then deduced using a least-square nonlinear regression analysis.

III. Discussion of Results

In this research work, combustion behaviors of Boron/(BAMO/NMMO) and MG/PTFE/VITON-A (MTV) solid fuels under different operating conditions were investigated. Results obtained from the study of B/(BAMO/NMMO) solid fuels are given in Appendices 4.1, 4.2,

The above results suggest the use of MTV solid fuels with other ingredients produces large amounts of nitrogen which facilitates the heat release and burning rate.

- The important physicochemical processes involved in the combustion of MTV solid fuels in the presence of air were qualitatively identified. Five reaction zones characterizing the combustion behavior of MTV solid fuels were envisioned for the first time. These reaction zones are inert heating, subsurface secondary reaction, subsurface primary reaction, primary combustion, and secondary combustion zones.
- The thermophysical properties, including thermal diffusivity and conductivity, were measured using a subsurface temperature profile and laser flash methods. It was found that both thermal diffusivity and conductivity are strong functions of temperature, and change drastically in the temperature range of 20-50°C. This is found to be caused by the crystalline transitions of PTFE in this temperature range.

• In the study of combustion behavior of B/(BAMO/NMMO) solid fuels with different boron weight percentages, the following important findings have been obtained:

- The burning rates of boron/poly(BAMO/NMMO) fuel-rich propellants were measured and found to depend strongly upon boron weight percentage and pressure. Burning rates of B/(BAMO/NMMO) solid fuels were found to increase with boron percentage up to the vicinity of 20% and then decrease. An "energy sink" hypothesis has been proposed to explain this dependency and is supported by thermocouple measurements of the maximum temperature of combustion products. This hypothesis suggests that as the boron particle weight percentage exceeds a critical level, they absorb a significant amount of energy from the reaction zone, thereby reducing the energy feedback to the propellant surface. Also, boron particles under such high concentration conditions may not oxidize to form the second-stage vigorous combustion zone near the burning surface.
- Formation of hexagonal crystalline boron nitride (BN) in the combustion residues of boron/poly(BAMO/NMMO) solid fuels was observed experimentally. Thermoequilibrium calculations also show the existence of BN only at high equivalence ratios. Under these conditions, some performance gains can be obtained even though the heat of reaction in forming BN is less than one-half that

of B_2O_3. This implies that boron nitridation could be important and deserves further study.

- The important physicochemical processes involved in the combustion of B/(BAMO/NMMO) solid fuels were identified from observations and measurements. Four reaction zones characterizing the combustion behavior of B/(BAMO/NMMO) solid fuels have been defined within temperature boundaries of the identified physical chemical processes.
- From the SFRJ performance point of view, there are both advantages and disadvantages to using BAMO/NMMO copolymer-based fuels compared to conventional HTPB-based fuels. The advantages are mainly due to its vigorous pyrolysis characteristics for dispersing boron particles from surface reaction zones into the main reaction zone. Therefore, high boron combustion efficiency can be expected. The second advantage can be attributed to its higher performance at lower air-to-fuel ratios, since it contains a certain amount of oxygen and thus requires less ambient oxygen to burn. The disadvantages of BAMO/NMMO copolymer-based fuels are essentially due to their lower performance at normal SFRJ operating conditions This lower performance is caused by their lower heats of reaction, resulting from lower hydrocarbon content, in comparison with conventional hydrocarbon fuels (such as HTPB), despite their high positive heats of formation.

IV. Conclusions

A unique test setup with well-controlled pressure (up to 9,000 psi) and initial temperature (from -40 to 70°C) conditions was designed and constructed. This test setup was utilized to investigate the combustion behaviors of B/(BAMO/NMMO) and MTV solid fuels. Results obtained from this research work have been applied by private industries and government laboratories. Findings on the combustion behavior of MTV propellants have been very helpful for military purposes. Similarly, results obtained from the study of B/(BAMO/NMMO) solid fuels have been useful in assessing the applicability of this type of fuel for solid fuel ramjets.

APPENDIX 4.1

Combustion Behavior of Boron-Based BAMO/NMMO Fuel-Rich Solid Propellants

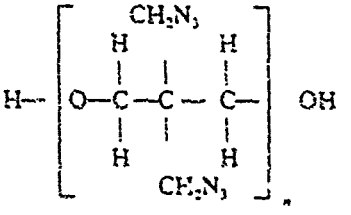
Wen-Hsin Hsieh,* Arie Peretz,† I.-Te Huang,‡ and Kenneth K. Kuo§
Pennsylvania State University, University Park, Pennsylvania 16802

Combustion characteristics of boron/poly(BAMO/NMMO) fuel-rich solid propellants have been studied due to their potential application to solid-fuel ramjets (SFRJ). For the same boron content, BAMO/NMMO copolymer-based fuels are superior to conventional hydroxyl terminated polybutadien (HTPB) fuels due to their vigorous pyrolytic characteristic for dispersing boron particles into the main reaction zone. However, their specific impulses are generally lower than that of HTPB, in spite of high positive heats of formation. Formation of hexagonal crystalline boron nitride (BN) has been found in the combustion of this family of propellants studied. Favorable conditions for the formation of BN have been identified. BN also has a significant effect on the theoretical performance for high equivalence ratio conditions. The burning rate was found to depend strongly upon pressure and nonmonotonically on boron content. An "energy sink" hypothesis is proposed to explain this observation. Fine-wire thermocouple measurements support this hypothesis.

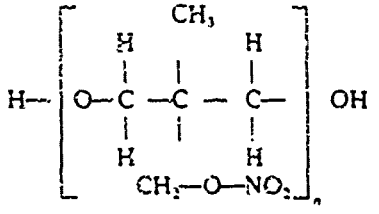
I. Introduction

THE continuous search for more energetic and denser binder materials for solid propellants and fuels has, in recent years, prompted the synthesis and development of novel polymers with azide, nitro, or nitrate groups.[1] Performance increases can be expected by replacing the conventional nonenergetic polymeric binders with polymers that could contribute energy to the formulation. These polymers are generally characterized by high positive heat of formation, high density, relatively low decomposition temperature, high nitrogen content, ease of ignition, fast pyrolysis and low oxygen consumption for combustion. In particular, copolymers of nitrate esters, such as 3-nitratomethyl-3'-methyloxetane (NMMO) with (azidomethyl)-oxetane polymers, such as 3-azidomethyl-3'-methyloxetane (AMMO) and 3,3'bis(azidomethyl)-oxetane (BAMO) have recently received much interest as potential candidates for energetic propellant fuels.[2,3] Evaluation of solid propellants, using poly(BAMO/NMMO) polyether glycol as a binder, has shown high-performance capability in terms of volumetric specific impulse and excellent mechanical properties, especially in terms of elongation.[3] The molecular structures of BAMO and NMMO polymers are

BAMO $(C_5H_8N_6O)_n$



NMMO $(C_5H_9NO_4)_n$



Boron, on the other hand, is well-known for its high heat release during oxidation or fluorination.[4] It can provide more than three times the volumetric energy density of conventional hydrocarbon solid fuels used in air-breathing ramjet propulsion systems. However, problems associated with the ignition and combustion efficiency of boron particles have been an obstacle in utilizing boron-containing solid fuels or propellants in ramjet engines. It has been shown in a recent study by Chen et al.[5] that the combined effect of very high heat release by exothermic decomposition reactions and the highly turbulent nature of the pyrolyzed gases of BAMO/NMMO copolymer binders enhances the ignition of the boron particles in BAMO/NMMO-based fuel-rich propellants. In addition, it may be expected that high performance can be obtained, due to the combination of two energetic fuel components, and also higher regression rates, caused by exothermic solid-phase or surface reactions, which is usually very desirable in solid-fuel ramjets (SFRJ).

It is known that oxidation of boron is highly exothermic. Under oxygen-rich conditions within adequate temperature and pressure ranges, the combustion products of boron will be boron oxides (e.g., B_2O_3, BO, BO_2, $HOBO$, H_3BO_3). However, when the oxygen concentration is limited, not all of the boron fuel can be oxidized. Instead of losing the heat of reaction of unoxidized boron, it is useful to consider the reaction of boron with other elements such as fluorine and nitrogen. This is why certain fluorine compounds are sometimes introduced into the formulations of solid fuels and propellants. To the best of the authors' knowledge, boron nitridation has not been considered in the performance evaluation of boron-based solid fuels. One exception is attributed to Weber and Mueller in their consideration of metal combustion in the Martian atmosphere.[6]

Presented as Paper 89-2884 at the AIAA/ASME/SAE/ASEE 25th Joint Propulsion Conference, Monterey, CA, July 10–12, 1989, received Aug. 7, 1989, revision received June 25, 1990, accepted for publication July 16, 1990. Copyright © 1989 by Kenneth K. Kuo Published by the American Institute of Aeronautics and Astronautics, Inc., with permission.

*Assistant Professor, Department of Mechanical Engineering Member AIAA.
†Visiting Professor, on sabbatical leave from Rafael-ADA, Israel Associate Fellow AIAA.
‡Graduate Student, Department of Mechanical Engineering.
§Distinguished Professor of Mechanical Engineering, Fellow AIAA.

Preliminary thermochemical calculations and strand-burner tests conducted in this study have shown that under certain conditions (e.g., high equivalence ratios) nitridation of boron can indeed take place to form hexagonal crystalline boron nitride (BN). The heat released in this reaction (23.2 kJ/g boron) is less than one-half of that released in boron oxidation. This phenomenon has surprisingly received no particular attention in the propulsion literature, as mentioned above.

The overall goal of the work described herein is to study the propulsion-related combustion behavior of the newly developed boron/poly(BAMO/NMMO) fuel-rich solid propellants with the following specific objectives: 1) assessment of the applicability of these fuel-rich propellants to SFRJ engines; 2) conduction of thermochemical and thermoanalytical studies to achieve a better understanding of the pyrolysis process, 3) determination of the burning rate as a function of the boron content and pressure by using a windowed strand burner; 4) measurement of the thermal wave structure by fine-wire thermocouples, 5) determination of the favorable combustion environment for the formation of boron nitride by examining the combustion residues with scanning electron microscope (SEM) and x-ray diffraction analyzer, and 6) identification of the source of nitrogen for boron nitridation by conducting strand-burner tests in both air and oxygen/argon atmospheres.

II. Thermochemical and Thermoanalytical Studies

Thermochemical Equilibrium and Performance Calculations

The fuel-rich propellants used in this study were synthesized and provided by G. E. Manser of Aerojet Solid Propulsion Company. They are based on the BAMO/NMMO copolymer as a binder with 70/30 mole ratio, respectively, which yields the molecular formula ($C_5H_{8.34}N_{4.30}O_{2.02}$) for the repeating unit. This energetic formulation has a heat of formation of +1,378 J/g (53 kcal/mole). The mass fractions of nitrogen and oxygen in the copolymer are 37.4% and 20.1%, respectively, with the nitrogen coming mostly from BAMO. This copolymer was mixed with a boron powder of submicron particle size (median particle diameter of 0.5 μm) at several mass fraction ratios: 0, 5, 10, 17.6, and 29% boron. In addition, a formulation containing 40% bimodal boron powder with particle sizes of 0.5 μm (30%) and 20 μm (10%) was prepared and supplied. The pure copolymer tested in this study had a density of 1.26 g/cm³.

Computer runs of the CET 86 chemical equilibrium transport code[7] for the combustion of the above-mentioned compositions with air at various equivalence ratios ϕ, combustion pressures, and air temperatures, ranging from 0.6–4.0, 0.207–1.034 MPa (30–150 psia), and 298–537°K, respectively, were conducted to evaluate the performance of these propellants in solid-fuel ramjets and obtain information on the global equilibrium combustion products.

Complete combustion of pure poly(BAMO/NMMO) with air yields N_2, CO_2, O_2, and H_2O as the major combustion product species for fuel-lean conditions ($\phi < 1$), as expected. For fuel-rich combustion ($\phi > 1$), as ϕ increases, CO_2 converts gradually into CO and unburned carbon, whereas H_2O is replaced by gaseous hydrogen. A theoretical adiabatic flame temperature of 2607°K is obtained for $\phi = 1$, a combustion pressure of 0.685 MPa, and a flight speed of Mach 2 at sea level. It was found that the effects of both pressure and air temperature are small in the range studied.

When boron is added to the poly(BAMO/NMMO) binder, the major equilibrium combustion products also contain boron oxides, mainly HOBO, B_2O_3, and B_2O_2. The CET 86 chemical equilibrium transport code reveals that as less oxygen is available for $\phi > 1$, some boron nitridation takes place. The mole fraction of boron nitride (BN) in the combustion products increases with the equivalence ratio and the boron content. Table 1 lists the major theoretical equilibrium combustion products for a composition containing 29% boron burned at 0.690 MPa and equivalence ratios of 1, 2, and 4 with air, which has enthalpy corresponding to a flight speed of Mach 2 at sea level. Crystals of hexagonal BN were found in residues from strand-burner tests in this study, as described in the following section. Boron nitridation releases 23.21 kJ/g boron, as compared to 58.74 kJ/g boron for oxidation to B_2O_3. When an SFRJ is operating under certain conditions (such as high-altitude, high angle-of-attack flight, or an accelerating climb), combustion of solid fuels will occur at high equivalence ratios. Under such conditions, the amount of heat release due to chemical reaction comes not only from boron oxidation but also from boron nitridation. Chemical-equilibrium calculations show that the portion of unoxidized boron nitridation increases with pressure, as confirmed by the experimental testing conducted in this study.

Table 1 Major products of combustion of boron/poly BAMO/NMMO) (containing 29% boron by weight) with air at 0.690 MPa (100 psia)

Combustion products, mole fraction, %	Equivalence ratio, ϕ		
	1	2	4
N_2	74.56	60.36	30.86
CO_2	5.93	0.01	—
HBO_2	5.72	0.80	0.01
H_2O	3.95	0.04	—
CO	3.06	15.29	22.46
B_2O_3	2.08	2.93	0.01
H_2	—	10.18	16.91
BN(s)	—	2.04	22.38
HBO	0.02	4.00	2.12
B_2O_2	—	2.46	0.29

Detailed studies of the finite-rate chemical kinetics of BN formation under actual fuel-rich SFRJ operating conditions should be conducted. Investigation of various researchers indicated that there are some kinetic limitations of boron nitridation.[8]

In addition to the chemical-equilibrium calculations, the CET 86 code was used to calculate the theoretical performance of an SFRJ by assuming complete equilibrium combustion. A performance comparison was made between boron-based poly(BAMO/NMMO) and HTPB fuels for the same boron mass fractions at the Mach 2 sea-level flight condition. The calculated results show that for the same equivalence ratio in the range of ϕ = 0.6–4.0, boron-based poly(BAMO/NMMO) fuels have considerably lower gravimetric specific impulses than those of boron-based HTPB fuels. This is caused by the higher heat of combustion of the HTPB binder, which overcomes the high positive heat of formation of the poly(BAMO/NMMO) binder. The difference in performance between these two types of fuels becomes much smaller in terms of volumetric specific impulse, which is very important for volume-limited propulsion systems. Figure 1 shows plots of the theoretical volumetric specific impulse as a function of equivalence ratio for pure poly(BAMO/NMMO) and HTPB fuels and the same fuels mixed with 40% boron, all burning at 0.690 MPa in an SFRJ engine at Mach 2 sea-level flight. The density and heat of formation of HTPB were taken as 0.92 g/cm³ and 0 J/g, respectively. The relatively high performance of the boron-loaded fuels at high equivalence ratios is obtained due to boron nitridation. The same performance is plotted vs air/fuel ratio in Fig. 2. The stoichiometric air/fuel ratios for various fuels are also given in Fig. 2. For low air/fuel ratios, the poly(BAMO/NMMO) fuel is superior to the pure HTPB fuel, due to the larger oxygen deficiency of the latter. As the air/fuel ratio increases, the performance of the HTPB-based fuels becomes gradually greater. It should be recalled that the hydrocarbon mass fraction of poly(BAMO/NMMO) is only 42.5%, as compared to almost 100% hydrocarbon for HTPB.

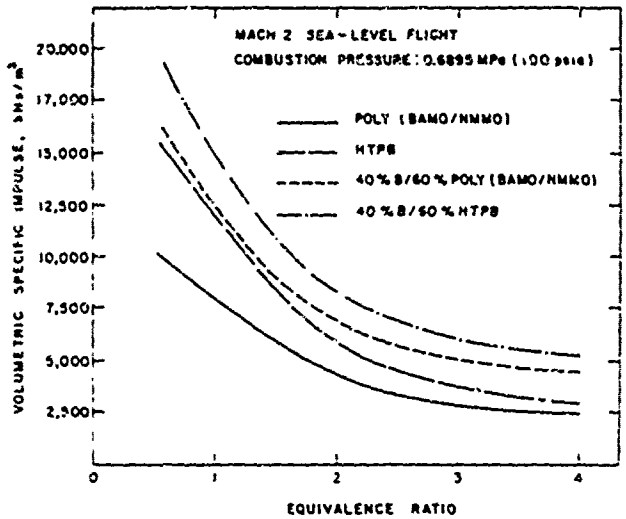


Fig. 1 Comparison of volumetric specific impulse of BAMO/NMMO copolymer and HTPB fuels with 0 and 40% boron at various equivalence ratios.

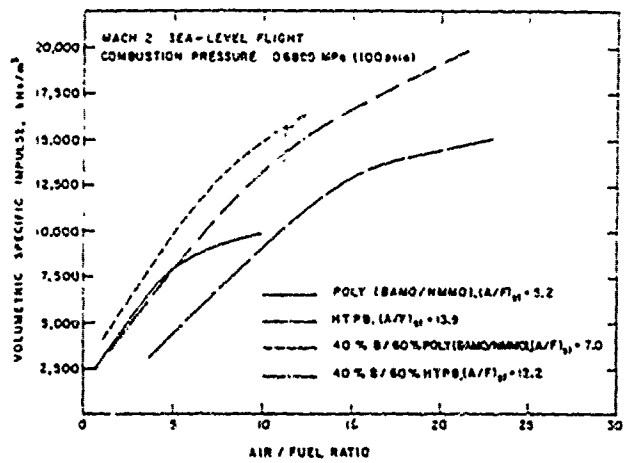


Fig. 2 Performance comparison of BAMO/NMMO copolymer with HTPB fuels containing 0 and 40% boron at various air/fuel ratios.

Thermoanalytical Studies

Extensive studies of the thermal decomposition of energetic monomers and polymers have been conducted by Farber et al.[9] and Oyumi and Brill.[2,10,11] An interesting finding by the latter with regard to poly(BAMO/NMMO) was that the two polymers decompose more or less independently despite being copolymerized. It was also revealed that pressure and heating rate exert relatively little influence on the concentration of the gaseous decomposition products. Mass spectrometric and rapid-scan Fourier-transform infrared spectroscopy (RSFTIR) tests have shown that both BAMO and NMMO polymers decompose thermally in two stages. In the first stage (primary decomposition), rupture/destruction of the side groups takes place, and in the second stage, decomposition of the polymer oxetane backbone occurs. Farber et al.[9] conducted mass spectrometric studies of the thermal decomposition of BAMO polymer at 10^{-5} Torr, and reported a start of decomposition at 130°C by release of molecular nitrogen due to the rupture or scission of the azide bond structure. Much higher rate of N_2 evolution is observed at temperatures above 160°C. The three-carbon backbone starts to decompose into small fragments, such as HCN, CH_2, OH, and CH_2O, at 160°C and the thermal decomposition rate increases rapidly with temperature. Similar results were obtained by Oyumi and Brill,[10] by slow and rapid thermolysis of BAMO at a wide range of pressures using RSFTIR. The decomposition temperature of the BAMO polymer was determined to be 463°K by slow heating at atmospheric pressure of argon.

The mass spectrometric studies of the thermal decomposition of NMMO polymer conducted by Farber et al.[12] revealed that decomposition starts at about 100°C, with the release of NO_2 and CH_2O by the rupture of the nitrate bond ($O-NO_2$) and the bond destruction in the nitrate ester side group. The onset of the oxetane backbone decomposition occurs at approximately 150°C. Oyumi and Brill[10] suggest that considerable condensed phase reactions take place in the decomposition of poly(NMMO), which is assumed by them to start with the release of CH_2O or CO. They claim that the decomposition temperature of poly(NMMO) is 187°C. Manser is quoted as suggesting that the backbone of NMMO polymer might be less thermally stable than the nitrate ester.[11,12]

Thermogravimetric analysis (TGA) tests in a 0.1-MPa argon atmosphere were conducted in this study on fuel-rich compositions with various boron content, using a Perkin Elmer TGS-2 thermogravimetric analyzer at a heating rate of 20°C/min. Weight loss of pure poly(BAMO/NMMO) samples started at 150–155°C at a very slow rate and rapid pyrolysis took place at a temperature between 205 and 210°C, leaving residues between 1 and 2%. The addition of 5, 10, and 18.3% boron did not substantially affect the temperatures of the start of weight loss and rapid pyrolysis, but the dispersion in the measured values of these temperatures was higher than that of the pure copolymer. The residue increased to between 2 and 3%. A single test with a composition containing 40% boron showed an onset of weight loss at about 120°C and rapid pyrolysis at 210°C, leaving a residue of only 1.2%. No definite conclusion for this difference can be drawn, due to the small number of experiments. However, it must be noted that in all tests, eyeball observations revealed a very rapid and violent pyrolysis process, in which the pyrolyzed gases of the copolymer dispersed the boron powder in the gas phase in the form of a brownish cream-colored cloud. A single TGA test with a sample of HTPB-based fuel with 30% boron was also conducted for comparison. In this case, the weight loss started at about 160°C and proceeded slowly until the rate was substantially increased between 420 and 480°C, leaving a black residue of 34%. The shape of the curve agrees well with published TGA thermograms for pure HTPB fuel.[13] Figure 3 shows the above-described TGA thermograms of 40% boron-containing poly(BAMO/NMMO) and 30% boron-containing HTPB fuels. In view of the close similarity of the TGA thermograms of pure HTPB[12] and the boron/HTPB fuel of this study, one may conclude that the boron content has an insignificant effect on the decomposition process of HTPB for temperatures up to the completion of decomposition (~450°C). The only noticeable effect is that the boron-containing fuel has a higher percentage of residue.

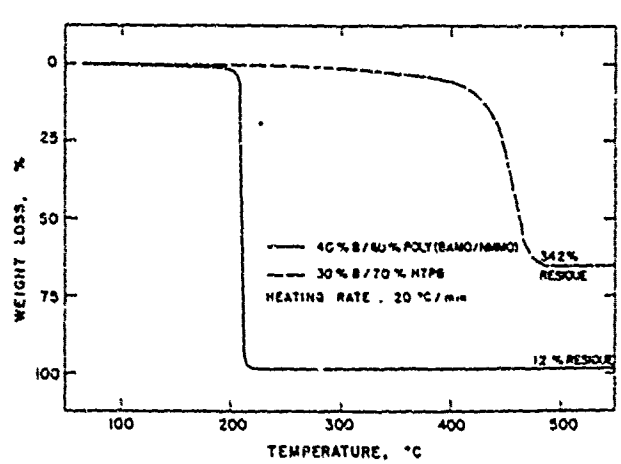


Fig. 3 TGA thermograms of poly(BAMO/NMMO) and HTPB fuels containing boron.

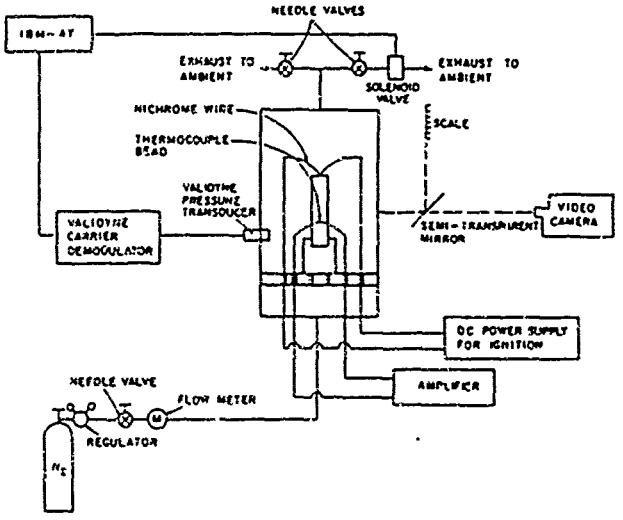


Fig. 4 Schematic diagram of experimental apparatus used in strand-burner tests.

III. Strand-Burner Tests

Experimental Approach

In this investigation, a windowed strand burner was used to study the combustion behavior of boron/poly(BAMO/NMMO) fuel-rich solid propellants. Figure 4 shows a schematic diagram of the windowed strand burner. A sample (5 mm in diameter and 60 mm in length) was mounted vertically in the chamber. Ignition of the sample was achieved by sending an electric current to a nichrome wire, pierced through the test sample about 3 mm from the top surface. To determine the burning rate of the test sample, the image of a scale was optically overlapped on that of the test sample by a semi-transparent mirror. During a test, both images of the scale and the test sample were recorded by a video-recording system. With this technique, the burning rate could be determined accurately from the length of the sample burned in a certain time duration.

Different gaseous mixtures were used to pressurize the strand burner for studying the effect of ambient gas environment on the combustion behavior of boron/poly(BAMO/NMMO) fuel-rich solid propellants. The chamber pressure was maintained at a preselected level by a computer-controlled gas supply system. Fine-wire thermocouples (platinum/platinum-13% rhodium) were embedded in the test sample to measure the thermal-wave structure. Detailed descriptions of the computer-controlled gas supply system, preparation of the fine-wire thermocouples, their embedding in the propellant samples, and the data acquisition system can be found in Refs. 14 and 15. The combustion residues from the strand-burner tests were collected and examined by an SEM. The boron compounds in the combustion residues were determined with an x-ray diffraction analysis technique.

The effect of the boron content and chamber pressure on the burning behavior of boron/poly(BAMO/NMMO) fuel-rich solid propellants was examined by testing five compositions with different boron weight percentages (0, 5, 10, 29, 40) at various pressures ranging from 0.241–1.034 MPa (35–150 psia).

Results and Discussion of Strand-Burner Tests

The measured strand burning rates in air as a function of pressure for the five compositions of test samples are shown in Fig. 5. Error bars given in this figure are defined as $\pm 2\sigma$ (standard deviation). The burning rates for all compositions increase as the pressure increases. It is interesting to note that the burning rate increases with increasing boron weight percentages up to a certain boron content and then decreases.

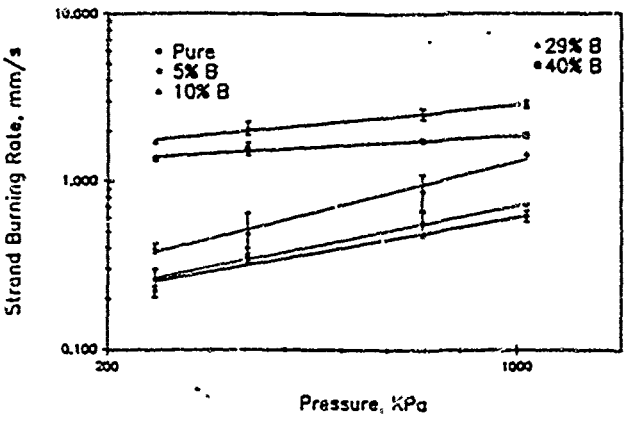


Fig. 5 Measured strand-burning rate as a function of pressure for boron/poly(BAMO/NMMO) solid fuel with different weight percentage of boron.

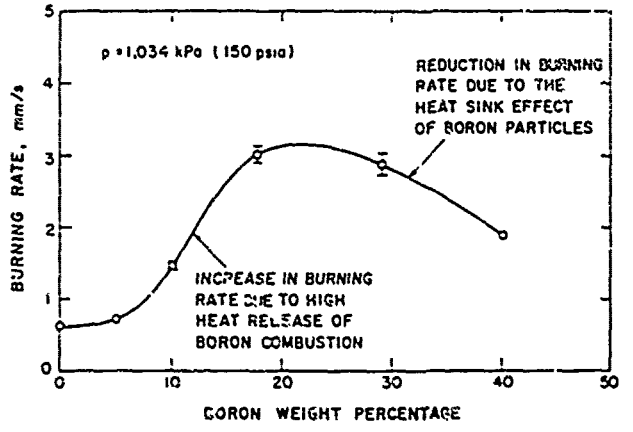


Fig. 6 Effect of boron weight percentage on burning rate of boron/poly(BAMO/NMMO) solid fuels at a fixed pressure.

In order to examine this effect, the burning rates for the five types of test samples at 1.034 MPa (150 psia) along with the burning rate data for 17.6% boron/poly(BAMO/NMMO) from Ref. 5 are plotted in Fig. 6. It was found that the highest burning rate occurs between 17.6 and 29% boron content.

Figure 7 shows the measured temperature profile obtained using a 50-μm R-type thermocouple embedded in a 29% boron/poly(BAMO/NMMO) sample, at a combustion pressure of 0.345 MPa (50 psia) in air atmosphere. The burning surface temperature, indicated by a sudden jump in the slope of temperature near the surface, was found to be 205°C. This measured burning surface temperature agrees well with the decomposition temperature of the fuel-rich propellant sample from TGA tests at a pressure of 1 atm. The burning surface temperature T_s for 29% boron/poly(BAMO/NMMO) increases monotonically with chamber pressure, ranging from 200°C at 0.24 MPa (35 psia) to 300°C at 1.03 MPa (150 psia). The burning surface temperature is also found to be a function of boron weight percentage. At 1.03 MPa, T_s is nearly constant (≈300–310°C) for samples containing 5, 10, 17.6, and 29% boron particles; it drops to 260°C for the sample with 40% boron particles. It is noted that the subsurface temperature profile shown in Fig. 7 does not follow the exponential form, which is commonly observed or theoretically derived for inert heating zones with constant thermal properties. This departure from the exponential form is believed to be caused mainly by the subsurface reactions of poly(BAMO/NMMO) binders, as discussed in the earlier section. Beyond the burning surface, the thermocouples continue to measure the temperature of the media in the two-phase reacting region. Some irregularities of the temperature-time trace are noticeable;

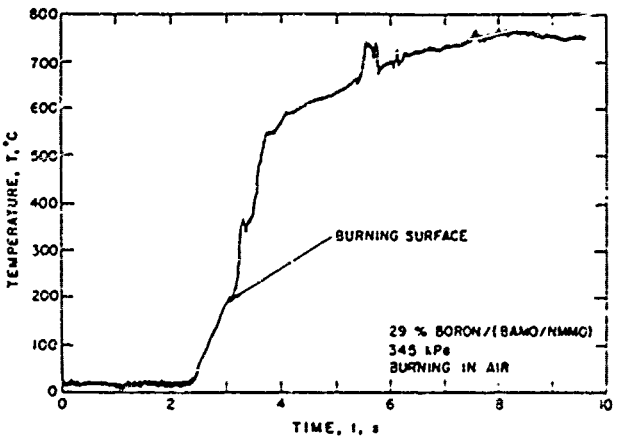


Fig. 7 A typical measured temperature-time trace from a strand-burner test using a 50-μm fine-wire thermocouple.

the irregularities could be caused by the complex structure of the reacting zone described below.

A schematic description of the physicochemical processes occurring in the combustion of boron/poly(BAMO/NMMO) fuel-rich solid propellant, together with the temperature profile in the condensed and two-phase reacting regions, is shown in Fig. 8. Several zones can be defined based upon the major physicochemical processes taking place in the specified domains. In zone 1, the condensed phase material is being heated and there are no chemical reactions whatsoever. At the boundary between zone 1 and zone 2, decomposition of BAMO polymer starts around 130°C (measured under vacuum).[9] As one approaches a higher temperature region near the "burning surface," decomposition[11] of NMMO polymer occurs near 190°C. The measured temperature of the so-called "burning surface" is around 205°C. Near the interface between the subsurface reaction zone (zone 2) and the first-stage combustion zone (zone 3), there are certain residues (containing B_2O_3, H_3BO_3, B, BN, etc.) accumulated on the "burning surface."

In the lower portion of the first-stage combustion zone, the boron particles, coated with a thin layer (on the order of tens of Angstroms)[16] of solid boron oxide, enter the hot combustion environment as low temperature solids. As described by King[17] and Faeth,[18] heat transfer from the reaction zone causes the particle temperature to rise with the B_2O_3 layer melting at roughly 455°C. Boron and/or oxygen diffuse across the oxide layer and tend to react more rapidly with the increase of particle temperature as particles move in the upward direction. This gives rise to a first-stage ignition of B/B_2O_3 particles, where reaction rates suddenly increase with appearance of luminosity. According to a number of researchers' observations summarized by Faeth,[18] this first-stage reaction appears to slow down almost immediately after the appearance of luminosity. This reduction of luminosity is believed to be caused by the thickening of the boron-oxide layer. Further increase of B/B_2O_3 particle temperature causes rates of evaporation of boron oxide to increase, thus reducing the thickness of the oxide layer. Eventually, when the evaporation rate of the oxide layer is sufficiently large to remove the oxide layer, a second-stage ignition is attained at about 1627°C. From there on, the boron particles are exposed directly to the ambient oxidizers and relatively fast boron combustion takes place. The above-mentioned processes are depicted in Fig. 8.

To explain the dependence of burning rate as a function of boron weight percentage (as shown in Fig. 6), it is useful to consider the measured temperature-time traces under various conditions. As mentioned above, the surface temperatures of the burning fuel-rich propellant sample tested in this study are quite low (~205°C). The boron particles with oxide coating, ejected into the gas phase, serve as an "energy sink" to absorb a part of the energy generated by the reaction of pyrolysis products of the energetic BAMO/NMMO binder. When the boron weight percentage is low (≤20%), the B/B_2O_3 particles can reach the second-stage ignition temperature of 1900°K (1627°C). A high amount of heat release is

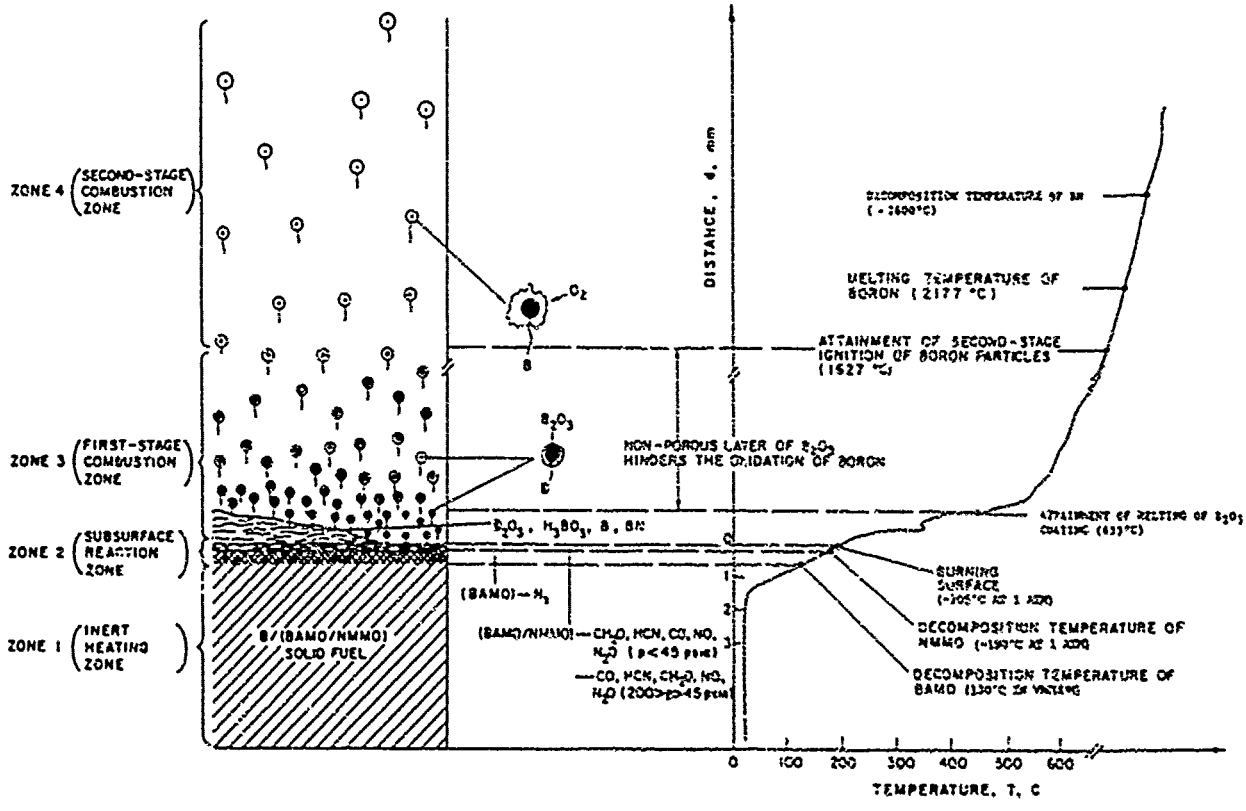


Fig. 8 Physicochemical processes in the combustion of boron/poly(BAMO/NMMO) solid fuel in air.

Table 2 Measured maximum combustion product temperatures for poly(BAMO/NMMO)-based solid fuels with various boron content (p = 1.034 MPa)

Boron weight percentage	5.0	10.0	17.6[a]	29.0	40.0
Maximum temperature, °C	>1800[b]	>1800[b]	>1800[b]	970	760

[a]From Ref. 5.
[b]During the tests, the output voltage of R-type thermocouples exceeded the calibration range.

Table 3 Presence of boron nitride in combustion residues of boron/poly(BAMO/NMMO) fuel-rich solid propellants burned in air

Boron weight percentage	Pressure, MPa			
	0.241	0.345	0.690	1.034
5.0	None	None	None	None
10.0	None	None	None	None
17.6[a]	None	None	None	Small amount
29.0	None	None	Small amount	Significant amount
40.0	None	None	None	Small amount

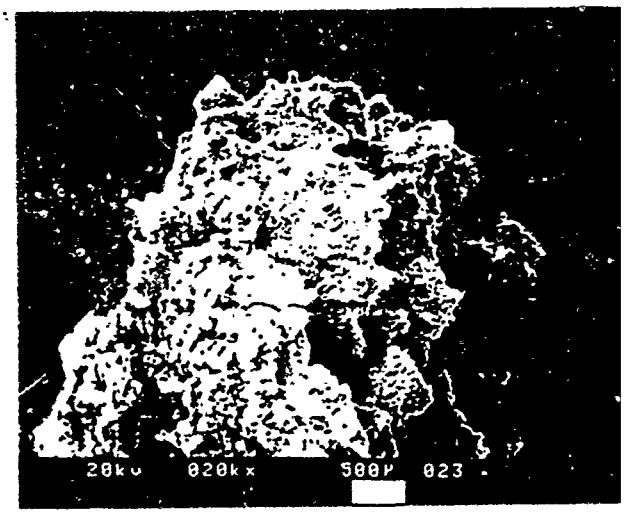
[a]From Ref. 5.

obtained due to efficient boron combustion. The heat feedback to the burning surface is high, and the burning rate is enhanced by the increase of boron content in the fuel-rich propellant. However, as the boron content exceeds a certain critical value (~20%), the "energy sink" effect becomes a dominant factor in reducing the heat feedback to the burning surface. This reduction is due either to the unattainment of the so-called second-stage ignition temperature or the extension of the active reaction zone to a much further distance from the burning surface.

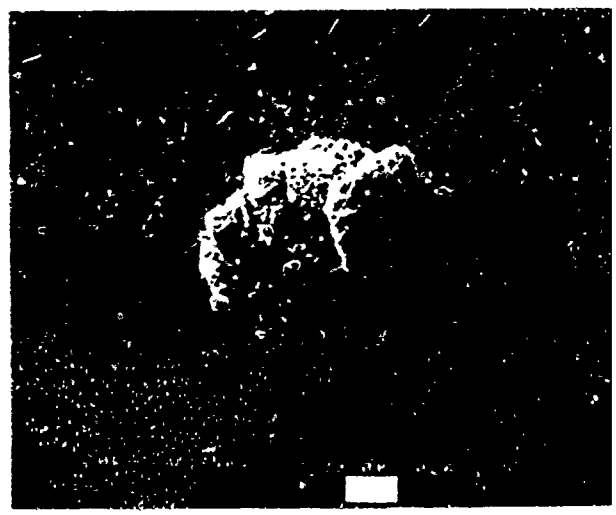
To verify the above-mentioned hypothesis, temperature measurements of the combustion products of the two-phase reacting media were made with fine-wire thermocouples. The maximum temperatures measured from the combustion of solid fuels with different amounts of boron content are listed in Table 2. It is useful to note that when the boron percentage is 17.6% or below, the measured maximum temperature exceeds the second-stage ignition temperature of boron of 1627°C. For 29 and 40% boron, the measured maximum temperatures were much lower. This finding supports the "energy sink" postulation for explaining the burning-rate behaviors of fuel-rich solid propellants with various boron contents. Besides the "heat sink" postulation, the effect of agglomerate sizes generated from fuel-rich solid propellants with different boron contents can also be used to explain part of the burning-rate behavior observed in this study. The size of the boron agglomerates, which are ejected from the surface in the burning process, may increase significantly for higher boron concentration. The large agglomerate size may result in poor ignition/combustion characteristics, and consequently in lower flame temperature, lower heat feedback, and lower burning rates. However, this agglomerate size effect can only be adopted to explain why the burning rate decreases with increased boron content, when the boron content is greater than 20%. This reasoning cannot be used to explain the fact that when the boron content is less than a critical percentage, the burning rate increases with the boron content as observed in this study.

After each strand-burner test, the combustion residues were collected for SEM examination and x-ray diffraction analysis. From the results of x-ray diffraction analysis, significant amounts of boron nitride (BN) in hexagonal crystalline form were found for the tests conducted at 1.034 MPa (150 psia) with 29% boron/poly(BAMO/NMMO). For other tests, the amounts of BN found in the combustion residues were much lower, as indicated in Table 3. Besides BN found in certain test conditions, other major boron compounds detected by x-ray diffraction analysis were B_2O_3 and H_3BO_3. These two compounds were found in residues from all test conditions listed in Table 3. The importance of this finding of BN was discussed in the earlier part of this paper. It is useful to note that the amount of residue recovered from strand-burner tests increases with the percentage of boron. No residue was found after tests with pure BAMO/NMMO copolymer. The flame is generally faint at low pressures, but at high pressures (p > 0.69 MPa), the flame becomes much brighter. Some streak lines of the burning B/B_2O_3 particles can be seen from high-speed video images.

Figures 9 and 10 are SEM pictures showing the H_3BO_3 and BN crystal structures in the combustion residues from tests with 29% Boron/poly(BAMO/NMMO) in air at 0.345 MPa (50 psia) and 1.034 MPa (150 psia), respectively. In order to identify the source of nitrogen in the formation of boron nitride, a set of strand-burner tests using Boron/poly(BAMO/NMMO) solid fuel with 40% boron were conducted with a mixture of 21% O_2 and 79% Ar (volumetric ratio) at 1.034 MPa (150 psia). In contrast to the test condition with air,

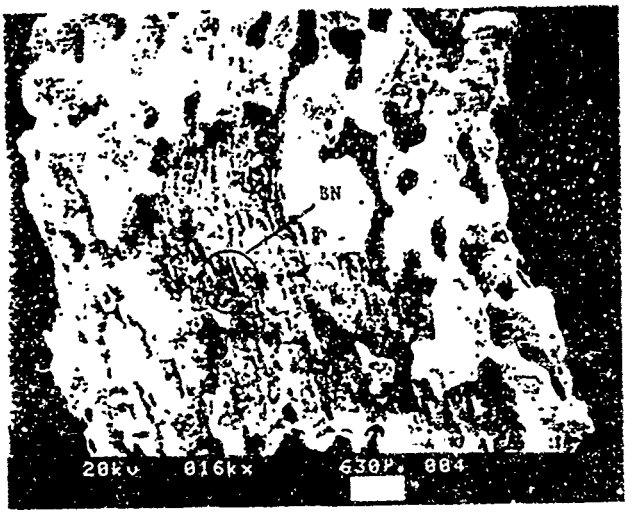


a) Magnification 20X

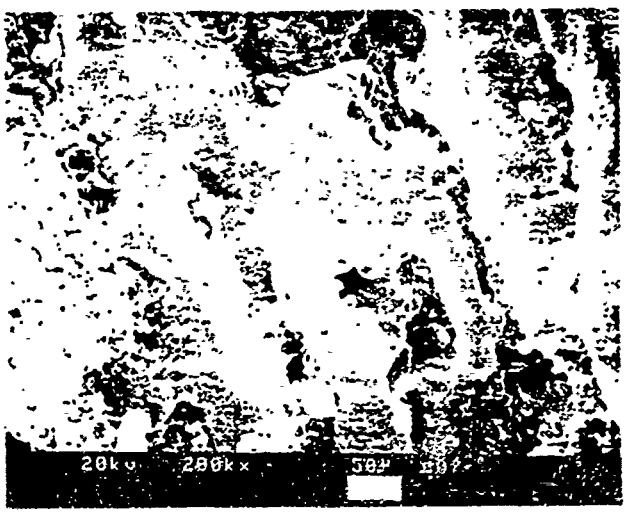


b) Magnification 350X

Fig. 9 SEM pictures showing the crystal structure of H_3BO_3 in the combustion residue of boron/poly(BAMO/NMMO) solid fuels (with 29% boron) burned in air at 0.345 MPa.



a) Magnification 16X



b) Magnification 200X

Fig. 10 SEM pictures showing the presence of boron nitride (BN) in the combustion residue of boron/poly(BAMO/NMMO) solid fuels (with 29% boron) burned in air at 1.034 MPa.

boron nitride was not found in the combustion residues from these tests. This implies that the nitrogen involved in the boron nitridation comes from the air but not from the nitrogen in the poly(BAMO/NMMO) under the testing condition. This may be explained by the fact that the release of N_2 from (BAMO/NMMO) copolymer begins at 130°C and ends at about 205°C. At these low temperatures, boron particles are not reactive with nitrogen. In principle, the gaseous nitrogen pyrolyzed from the copolymer could still react with boron in the high-temperature zones. Certain chemical reactions must occur to consume the gaseous nitrogen before reaching the high-temperature zones. Detailed chemical kinetic steps are required to understand this interesting observation.

IV. Summary and Conclusion

1) The steady-state combustion characteristics of boron/poly(BAMO/NMMO) fuel-rich solid propellants have been studied under various pressure conditions for compositions with different boron weight percentages. Thermochemical and thermoanalytical studies and strand burner tests were conducted in a systematic fashion.

2) From the SFRJ performance point of view, there are both advantages and disadvantages of using BAMO/NMMO copolymer-based fuels as compared to conventional HTPB-based fuels. The advantages are mainly due to its vigorous pyrolysis characteristics for dispersing boron particles from surface reaction zones into the main reaction zone. Therefore, high boron combustion efficiency can be expected. The second advantage can be attributed to its higher performance at lower air-to-fuel ratios, since it contains a certain fraction of oxygen and thus requires less ambient oxygen to burn. The disadvantages of BAMO/NMMO copolymer-based fuels are essentially due to their lower performance at normal SFRJ operating conditions. This lower performance is caused by their lower heats of reaction, resulting from lower hydrocarbon content, in comparison with conventional hydrocarbon fuels (such as HTPB), despite their high positive heats of formation.

3) Addition of boron particles in BAMO/NMMO copolymer fuels always increases the theoretical performance of solid fuels.

4) TGA results show that the pyrolysis characteristics of boron/poly(BAMO/NMMO) fuel-rich propellants are nearly unaffected by the percentage of boron content.

5) Formation of hexagonal crystalline boron nitride (BN) in the combustion residues of boron/poly(BAMO/NMMO) solid fuels was observed experimentally. Thermoequilibrium calculations show the existence of BN only at high equivalence ratios. Under these conditions, some performance gains can be obtained even though the heat of reaction in forming BN is less than one-half of that in forming B_2O_3. This implies that boron nitridation could be important and deserves further study.

6) The burning rates of boron/poly(BAMO/NMMO) fuel-rich propellants were found to depend strongly upon boron weight percentage and pressure. Burning rate increases with boron percentage up to the vicinity of 20% and then decreases. An "energy sink" hypothesis has been proposed to explain this dependency. Thermocouple measurements of the maximum temperature of combustion products support this hypothesis. This hypothesis suggests that as the boron particle weight percentage exceeds a critical level, they absorb a significant amount of energy from the reaction zone and thereby reduce the energy feedback to the propellant surface. Also, boron particles under such high concentration conditions may not oxidize to form the second-stage vigorous combustion zone near the burning surface.

Acknowledgments

This paper represents a part of the research work conducted under Contract N00014-86-K-0468 funded by the Office of Naval Research, Arlington, VA. The support and encouragement of Drs. Richard S. Miller and Gabriel D. Roy are highly appreciated. The authors would also like to thank Mr. Gerald E. Manser of the Aerojet Solid Propulsion Co. for providing the fuel-rich solid propellants used in this study.

References

[1]Manser, G. E., Fletcher, R. W., and Knight, M. R., "High Energy Binders, Final Report," Morton Thiokol, Inc., Bngham City, UT, Project JM101, June 1985.

[2]Oyumi, Y., and Brill, T. B., "Thermal Decomposition of Energetic Materials 14. Selective Product Distributions Evidenced in Rapid, Real-Time Thermolysis of Nitrate Esters at Various Pressures," *Combustion and Flame*, Vol. 66, No. 1, Oct. 1986, pp. 9–16.

[3]Lindsay, G. A., Talukder, M. A. H., Nissan, R. A., Quintana, R. L., Hasting, M. A. S., Yee, R. Y., Nadler, M. P., Atwood, A. I., Reed, R., and Manser, G. E., "Energetic Polyoxetane Thermoplastic Elastomers: Synthesis and Characterization," Naval Weapons Center, China Lake, CA, TP 6945, Dec. 1988.

[4]Peretz, A., "Some Theoretical Considerations of Metal-Fluorocarbon Compositions for Ramjet Fuels," *Proceedings of the 5th International Symposium on Air-Breathing Engines*, Cincinnati, OH, June 1987.

[5]Chen, D. M., Hsieh, W. H., Snyder, T. S., Yang, V., and Kuo,

K. K. "Study of the Thermophysical Properties and Combustion Behavior of Metal-Based Solid Fuels," AIAA Paper 88-3041, July 1988.

[6]Weber, J. O., and Mueller, K. H., "Metals Burning Nitrogen," *Chemical Engineering Progress*, Vol. 60, No. 2, Feb. 1964, pp. 40–41.

[7]Gordon, S., McBride, B. J., and Zeleznik, F. J., "Computer Program for Calculation of Complex Chemical Equilibrium Compositions and Applications, Supplement I—Transport Properties," NASA TM-86885, Oct. 1984.

[8]King, M. K., Atlantic Research Corp., personal communication, Jan. 1990.

[9]Farber, M., Harris, S. P., and Srivastava, R. D., "Mass Spectrometric Kinetic Studies on Several Azido Polymers," *Combustion and Flame*, Vol. 55, No. 2, Feb. 1984, pp. 203–211.

[10]Oyumi, Y., and Brill, T. B., "Thermal Decomposition of Energetic Materials 12. Infrared Spectral and Rapid Thermolysis Studies of Azide-Containing Monomers and Polymers," *Combustion and Flame*, Vol. 65, No. 2, Aug. 1986, pp. 127–135.

[11]Oyumi, Y., and Brill, T. B., "Thermal Decomposition of Energetic Materials 27. The Contrasting Effects of Pressure on the High-Rate Thermolysis of 34 Energetic Compounds," *Combustion and Flame*, Vol. 68, No. 2, May 1987, pp. 209–216.

[12]Farber, M., Harris, S. P., and Srivastava, R. D., "Mass Spectrometric Investigation of the Thermal Decomposition of Several Propellant and Explosive Ingredients," Space Sciences, Inc., Monrovia, CA, Project NR092-554, Feb. 1986.

[13]Kubota, N., Kuwahara, T., Miyazaki, S., Uchiyama, K., and Hirata, N., "Combustion Wave Structures of Ammonium Perchlorate Composite Propellants," *Journal of Propulsion and Power*, Vol. 2, No. 4, July–Aug. 1986, pp. 296–300.

[14]Hsieh, W. H., and Kuo, K. K., "Study of Erosive and Strand Burning of Stick Propellants, Pt. I. Measurements of Burning Rates and Thermal Wave Structures," *Journal of Propulsion and Power*, Vol. 6, No. 4, 1990, pp. 392–399.

[15]Hsieh, W. H., "Study of Strand and Erosive Burning of NOSOL-363 Stick Propellants," Ph.D. Thesis, The Pennsylvania State Univ., PA, Aug. 1987.

[16]Glassman, I., Williams, F. A., and Antaki, P., "A Physical and Chemical Interpretation of Boron Particle Combustion," 19th JANNAF Combustion Meeting, CPIA Publication 366, Vol. I, 1982, p. 63.

[17]King, M. K., "Ignition and Combustion of Boron Particles and Clouds," *Journal of Space and Rockets*, Vol. 19, No. 4, July–Aug., 1982, pp. 294–306.

[18]Faeth, G. M., "Status of Boron Combustion Research," 21st JANNAF Combustion Meeting, CPIA Publication 412, Vol. I, Oct. 1984, pp. 15–29.

Recommended Reading from the AIAA Progress in Astronautics and Aeronautics Series . . . AIAA

Thermal Design of Aeroassisted Orbital Transfer Vehicles

H. F. Nelson, editor

Underscoring the importance of sound thermophysical knowledge in spacecraft design, this volume emphasizes effective use of numerical analysis and presents recent advances and current thinking about the design of aeroassisted orbital transfer vehicles (AOTVs). Its 22 chapters cover flow field analysis, trajectories (including impact of atmospheric uncertainties and viscous interaction effects), thermal protection, and surface effects such as temperature-dependent reaction rate expressions for oxygen recombination; surface-slip equations for low-Reynolds-number multicomponent air flow, rate chemistry in flight regimes, and noncatalytic surfaces for metallic heat shields.

TO ORDER: Write, Phone or FAX:
American Institute of Aeronautics and Astronautics,
c/o TASCO, 9 Jay Gould Ct., P.O. Box 753, Waldorf, MD 20604
Phone (301) 645-5643, Dept. 415 • FAX (301) 843-0159

Sales Tax: CA residents, 7%, DC, 6%. For shipping and handling add $4.75 for 1–4 books (call for rates for higher quantities). Orders under $50.00 must be prepaid. Foreign orders must be prepaid. Please allow 4 weeks for delivery. Prices are subject to change without notice. Returns will be accepted within 15 days.

1985 566 pp., illus. Hardback
ISBN 0-915928-84-9
AIAA Members $54.95
Nonmembers $81.95
Order Number V-96

1988 Technical Meeting of the Easter
Section of the Comb. Inst. Dec. 5-7
Clearwater Beach, FL

APPENDIX 4.2

STRAND-BURNING CHARACTERISTICS OF ADVANCED BORON-BASED BAMO/NMMO FUEL-RICH SOLID PROPELLANTS*

W. H. Hsieh,† J. J. Cheng,+ and K. K. Kuo‡
Department of Mechanical Engineering
The Pennsylvania State University
University Park, PA 16802

I. Introduction

Due to its extremely high volumetric heating value,[1] boron has been one of the most attractive elemental metal for use in air-breathing ramjet propulsion systems. However, the low combustion efficiency of boron has always been an obstacle in utilizing boron-based fuel-rich solid propellants in ramjet engines. The low combustion efficiency of elemental boron is mainly caused by its high melting temperature of 2450°K and boiling temperature of 3931°K. In addition, the protective boron oxide layer that encloses the boron particle further hinders the reaction of boron with surrounding oxidizer. Recently, a novel and highly energetic polymetric binder, 3,3-bis(azido-methyl) oxetane (BAMO), and 3-nitratomethyl 3-methyl oxetane (NMMO), was synthesized by Manser et al.[2] to be mixed with boron. Due to the potentially high energetic azido and nitrato groups associated with their chemical structure, this type of binder can generate extremely high heat of combustion and highly turbulent pyrolysis gases to enhance the burning of boron particles. To date, no basic research has been conducted to study the combustion behavior or to characterize the thermo-chemical properties of the newly developed boron-based BAMO/NMMO fuel-rich solid propellant. The objectives of this work are: 1) to study the combustion behavior of boron/BAMO/NMMO fuel-rich solid propellants; 2) to determine the burning rates of these propellants as functions of pressure by using a windowed strand burner; 3) to measure the thermal-wave structure by fine-wire thermocouples; and 4) to examine the effect of boron weight percentage on burning rate.

II. Experimental Approach

In this study, a windowed strand burner was used to study the combustion behavior of boron/BAMO/NMMO fuel-rich solid propellants. Figure 1 shows a schematic diagram of the windowed strand burner. A sample (5 mm in diameter and 60 mm in length) was mounted vertically in the chamber. Ignition of the sample was achieved by sending an electric current to a nichrome wire, pierced through the test sample about 3 mm from the top surface. To determine the burning rate of the test sample, the image of a scale was optically overlapped on that of the test sample by a semi-transparent mirror. During a test, both images of scale and test sample were recorded by a video recording system. With this technique, the burning rate could be determined very accurately from the length of the sample burned in a certain time duration.

---

†Research Associate
+Visiting Scholar
‡Distinguished Alumni Professor

*This work represents a part of the research results obtained under Contract No. N00014-86-K-0468 sponsored by the Office of Naval Research, Arlington, VA, under the management of Drs. R. S. Miller and G. D. Roy. The authors would like to thank Dr. G. E. Manser of Aerojet for providing the fuel-rich solid propellants used in this study. The help of Mr. T. S. Snyder of PSU and Mr. H. C. Chen of BRC, in conducting some tests, is also greatly appreciated.

Either nitrogen gas or air were used to pressurize the strand burner for studying the effect of ambient gas environment on the combustion behavior of boron(BAMO/NMMO) fuel-rich solid propellant. The chamber pressure was maintained at a preselected level by a computer-controlled gas supply system, which consisted of a pressure transducer (Validyne DP 215), a carrier demodulator (Validyne CD 15), a solenoid valve (Skinner XLB 11002), and an IBM/AT personal computer.

Fine-wire thermocouples (Platinum/Platinum-13% Rhodium) were embedded in the test sample to measure the thermal-wave structure of the test sample. The thermocouples (with 50 μm wire diameter) used in this study were prepared by the authors at The Pennsylvania State University. A detailed description of the preparation of thermocouples and embedding them in the test samples is given in Ref. 3.

III. Results and Discussion

In order to examine the effect of boron weight percentage on combustion behavior, two types of boron(BAMO/NMMO) fuel-rich solid propellants were used--one containing 29% boron with a mean diameter of 0.5 μm, and the other containing 30% 0.5 μm boron powders and 10% 20 μm boron powders. Figure 2 shows the strand burning rates in air as a function of pressure for both types of test samples. The burning rate data for both types of samples follows the Saint-Robert's law very well, and can be expressed as $r_b = ap^n$, where r_b and p are in units of mm/sec and kPa, respectively; values of a and n are given in the figure. It is interesting to note that the burning rate for the test sample containing 29% boron powders is significantly higher than that of the test sample containing 40% boron powders. Near the burning surface region, the boron particles generated form the burning surface enter into the gas phase with an existing solid non-porous boron oxide coating on the surface. At this stage of combustion process, the boron particles serve as an "energy sink" to absorb the energy generated by the combustion of energetic BAMO/NMMO binders. If this favorable condition persists, the temperature of boron particles would rise continuously until it reaches first-stage ignition at 447°C, when the boron oxide layer melts to allow the boron and/or oxygen to diffuse across the oxide layer and react with each other rapidly. However, reaction rate slows down immediately following first-stage ignition, as the oxide layer thickens and rates of diffusion for boron and/or oxygen reduce. If the gas phase surrounding the boron particle can further supply the energy to the boron particle and increase the temperature of boron particle, the rates of evaporation of the relatively volatile boron oxide layer would also increase. Finally, at 1730°C, the rate of oxide evaporation is sufficiently large to remove the oxide layer, and a second-stage ignition process occurs. Then, a very rapid boron oxidation happens to relieve the large amount of heat of combustion.

However, with the test conditions used in this study, the second-stage ignition process of boron particles was not observed from the thermal-wave structure measurement (to be discussed later) due to the fact that the heat released from the combustion of BAMO/NMMO and from the first-stage ignition of boron particles was not sufficient to heat the large amount of boron particles to a temperature of 1730°C. Therefore, in the gas-phase region, boron particles actually serve as an "energy sink" without releasing a major portion of their heat of combustion. As the boron weight percentage in the boron(BAMO/NMMO) fuel-rich solid propellant increases, this "energy sink" phenomena becomes more pronounced and reduces the energy feedback from the gas phase to the solid phase; hence reducing the burning rate. A second reason for burning rate reduction at higher boron weight percentages

could be caused by the increase of thermal diffusivity of the sample at high boron weight percentage. The thermal energy at the surface layer becomes smaller as thermal diffusivity increases. Burning rate of the test sample goes down with the surface temperature reduction.

In order to further examine the effect of boron concentration, the burning rate of pure BAMO/NMMO was also measured at 345 kPa (50 psia) in air. The result indicated the burning rate was 0.36 mm for pure BAMO/NMMO, which was significantly lower than that of the test sample with 29% or 40% boron powders, as shown in Table 1. From Table 1, it is postulated that the burning rate increases as boron weight percentage increases, until an optimum value of boron weight percentage is reached; then the burning rate starts to decrease with the increase of boron weight concentration. At the optimum value of boron weight percentage, the heat released from the combustion of BAMO/NMMO is sufficient to increase the temperature of boron particles to reach 1730°C for second-stage ignition and rapid boron oxidation, and to release the huge amount of heat of combustion of boron particles in the gas phase. However, this optimum value needs further experimental verification. Also, the burning rates for fuel-rich BAMO/NMMO solid propellants with 1%, 10%, and 18% boron will be measured in the near future.

Figure 3 shows a measured temperature profile obtained using a 50 μm R-type thermocouple embedded in the 29% boron/(BAMO/NMMO) sample, with an ambient pressure of 345 kPa (50 psia). The burning surface temperature indicated by a sudden temperature jump at the burning surface, is found to be about 200°C. The maximum measured temperature was 760°C at 1.2 cm above the burning surface (5.2 sec. after the thermocouple detected the burning surface temperature). This measured maximum temperature is increased monotonically with ambient pressure, as shown in Table 2. It is noted that the measured maximum temperature does not exceed the second-stage ignition temperature of boron particles (1730°C). This implies that the combustion of boron did not reach second-stage ignition for this set of strand burner tests.

Table 1. Effect of Boron Weight Percentage on the Burning Rate at 345 kPa (50 psia) in Air

Sample Type	Pure BAMO/NMMO	BAMO/NMMO with 29% B	BAMO/NMMO with 40% B
Burning Rate (mm/s)	0.36	2.23	1.48

Table 2. Measured Maximum Temperature as a Function of Pressure

Pressure (kPa)		241	345	690	1,034
Maximum Temperature (°C)	29% B	640	760	850	970
	40% B	---	---	810	---

References

1. Peretz, A., "Some Theoretical Considerations of Metal-Fluorocarbon Composition for Ramjet Fuels," 8th International Symposium on Airbreating Engines, 1987.

2. Manser, G. E., Fletcher, R. W., and Knight, M. R., "High Energy Binders," Final Report, Morton Thiokol, Inc., Contract No. N00014-82-C-0800, June 1985.

3. Hsieh, W. H., "Study of Strand and Erosive Burning of NOSOL-363 Stick Propellants," Ph.D. Thesis, The Pennsylvania State University, 1987.

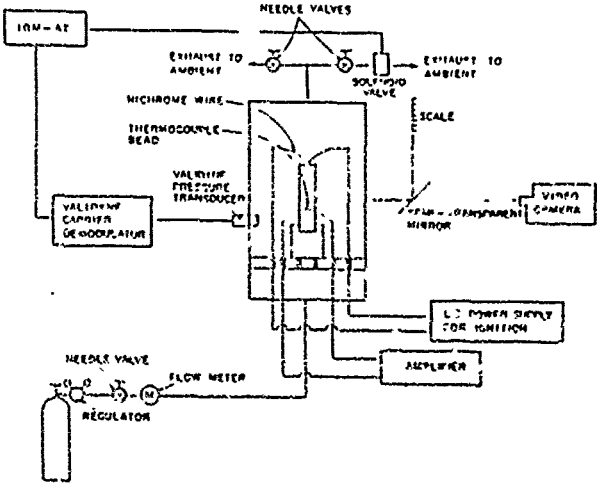


Fig. 1 Schematic Diagram of Experimental Apparatus Used in Strand Burner Tests

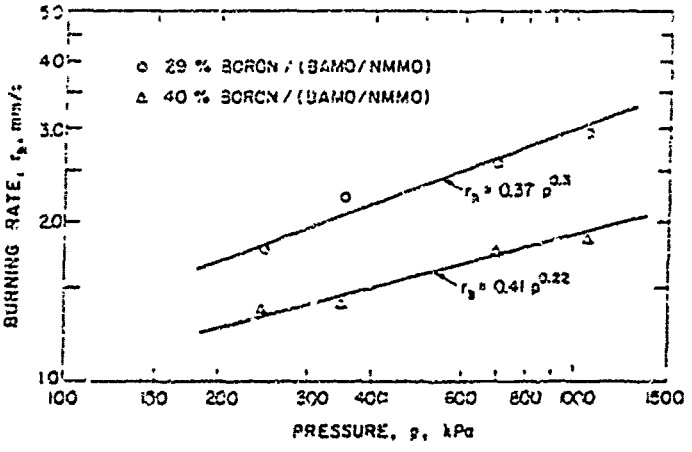


Fig. 2 Effect of Boron Weight Percentage on the Burning Rate of Fuel-Rich Solid Propellants Burning in Air

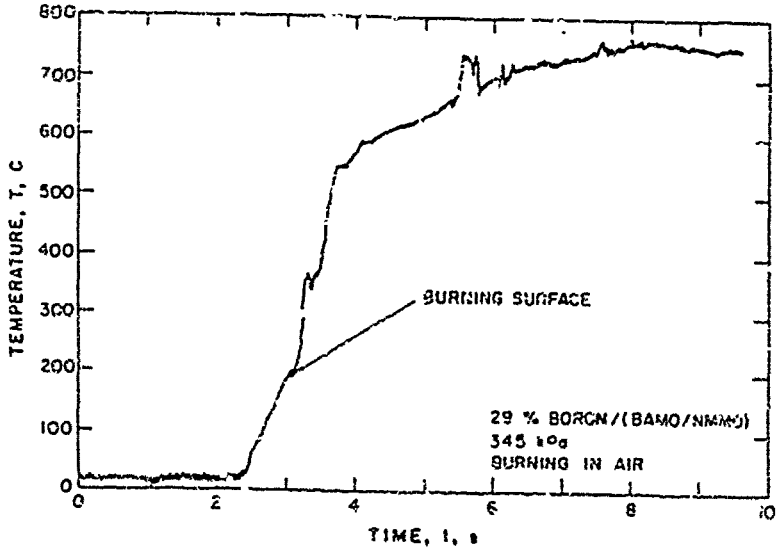


Fig. 3 Measured Temperature-Time Trace from a Strand Burner Test Using a 50 μm Fine-Wire Thermocouple

BURNING-RATE CHARACTERISTICS OF BORON/[BAMO/NMMO] FUEL-RICH SOLID PROPELLANT UNDER BROAD RANGES OF PRESSURE AND TEMPERATURE*

A. S. Yang,‡ I. T. Huang,‡W. H. Hsieh,† and K. K. Kuo§
Department of Mechanical Engineering
The Pennsylvania State University
University Park, PA 16802, U.S.A.

ABSTRACT

Burning-rate characteristics of pure and 10% boron-based 3,3 - bis (azido- methyl) oxetane (BAMO), and 3 -nitratomethyl 3 -methyl oxetane (NMMO) copolymer fuel-rich solid propellants in air atmosphere have been studied using a pressure and temperature controlled test chamber with optical windows. The temperature and pressure ranges of test firings were −10 to 60°C and 240.5 to 1030.6 KPa (35 to 150 psia), respectively. Temperature sensitivity of the burning rate, one of the most important design parameters in practical application to solid-fuel ramjets (SFRJ) and to solid- propellant ducted rockets (SDR), was deduced from the experimental data. The thermal wave structure of boron/[BAMO/NMMO] copolymer fuel-rich solid propellants under no cross flow conditions was measured by fine-wire thermocouples. From the temperature-time traces recorded at a fixed chamber pressure, the burning surface temperature was found to increase with the initial temperature. Furthermore, the combustion residues of boron/[BAMO/NMMO] copolymer samples, recovered from the tests with different initial temperatures, were examined employing a scanning electron microscope.

---

* This paper represents a part of the research work supported by the Office of Naval Research (Contract No. N00014-86-K-0468) under the management of Drs. Richard S. Miller and Gabriel D. Roy.

‡ Ph.D. Candidate

† Assistant Professor

§ Distinguished Professor

NOMENCLATURE

Symbol	Description
a	= Preexponent of Saint-Robert's burning rate law
b_0, b_1, b_2	= Coefficients, Eq. (3)
C_p	= Specific heat of propellant, cal/g-K
n	= Exponent of Saint-Robert's burning rate law
P	= Pressure, KPa
Q_s	= Net heat released at the burning surface, cal/g
r_b	= Burning rate, mm/s
$\bar{r}_b$	= Average burning rate, mm/s
$r_{b,k}$	= The k^{th} measured burning rate, mm/s
T	= Temperature, °C
T_i	= Initial propellant temperature, °C
T_s	= Burning surface temperature, °C
x	= Distance, cm

Greek Symbols

λ_g	= Thermal conductivity of gas phase, cal/cm-sec-K
ρ_p	= Density of propellant, g/cm^3
σ_p	= Temperature sensitivity, 1/K

1. INTRODUCTION

The solid-fuel ramjets (SFRJ) and solid-propellant ducted rockets (SDR) have become increasingly important for military applications due to the advantage of allowing the incorporation of high energy/high density ingredients in the solid fuels and propellants. Among various elements, boron has been one of the most attractive elements because of its extremely high volumetric heating value.[1] However, it is difficult to burn boron particles under ramjet combustion conditions, which leads to serious problems of ignition and combustion efficiency in practical application to ramjet propulsive systems. In a recent development program [2], this situation was improved significantly with the use of a highly energetic copolymer binder, 3, 3 - bis (azido - methyl) oxetane (BAMO) and 3 - nitratomethyl 3 - methyl oxetane (NMMO), which can generate high heat of combustion and strong turbulent pyrolysis gases to enhance the burning of boron particles.

Some efforts have been made to investigate the combustion behavior of boron-based [BAMO/NMMO] copolymer fuel-rich solid propellants. Chen et al.[3] examined the ignition and combustion characteristics of boron/poly [BAMO/NMMO] in detail and pointed out the high energy release from the burning surface of copolymer [BAMO/NMMO] can greatly improve the combustion efficiency of boron. Hsieh et al.[4] further addressed that [BAMO/NMMO] copolymer-based fuels are superior to conventional HTPB fuels due to their vigorous pyrolysis characteristic for dispersing boron particles into the main reaction zone. In their work, the burning rate was found to depend strongly on pressure and non-monotonically on boron content. Experimental results and thermoequilibrium calculations also showed that the existence of hexagonal crystalline boron nitride (BN) at high equivalence ratios. The heat released in the boron nitridation reaction is less than one-half of that released in boron oxidation; however, substantial performance gains still can be attained through this nitridation reaction process.

The aforementioned studies have deeply probed the fundamental mechanism governing combustion behavior of boron/[BAMO/NMMO] copolymer fuel-rich solid propellants, and have determined their burning-rate characteristics to be a function of pressure as well as boron weight percentage. However, very limited research has been conducted to study the temperature sensitivity of the burning rates of these fuel-rich propellants, even though the initial propellant temperature significantly affects burning rate, thrust, and burning time of rocket motors. The purpose of this paper is to study the effect of initial temperature on the combustion behavior of boron/[BAMO/NMMO] copolymer fuel-rich solid propellants, with the following specific objectives:

1. to determine the burning rate under different initial propellant temperatures and pressures;
2. to deduce the temperature sensitivity from measured burning-rate results;
3. to identify the favorable operating conditions of reducing the temperature sensitivity, which can decrease the variation in ballistic performance of rocket motors or SFRJs at different initial temperatures;
4. to measure the thermal wave structure by means of fine-wire thermocouples under different initial propellant temperatures; and
5. to investigate the effect of initial temperature on the formation of BN.

2. EXPERIMENTAL APPROACH

A pressure and temperature controlled test chamber with optical windows was employed to study the combustion characteristics of boron/[BAMO/NMMO] copolymer fuel-rich solid propellants. The apparatus used in this investigation is shown schematically in Fig. 1. A fuel sample of 5 mm in diameter and 60 mm in length was mounted vertically in the chamber. Ignition of the sample was achieved by sending an electrical current to a nichrome wire, pierced through the test sample about 3 mm from the top surface. A scale was optically superimposed on the image of the sample by a semitransparent mirror. The length of the sample burned in a certain time span could be accurately determined from both images of the scale and the test sample, which were recorded by a video recording system. From the information of the instantaneous locations of the burning surface, the burning rate of the test sample was deduced.

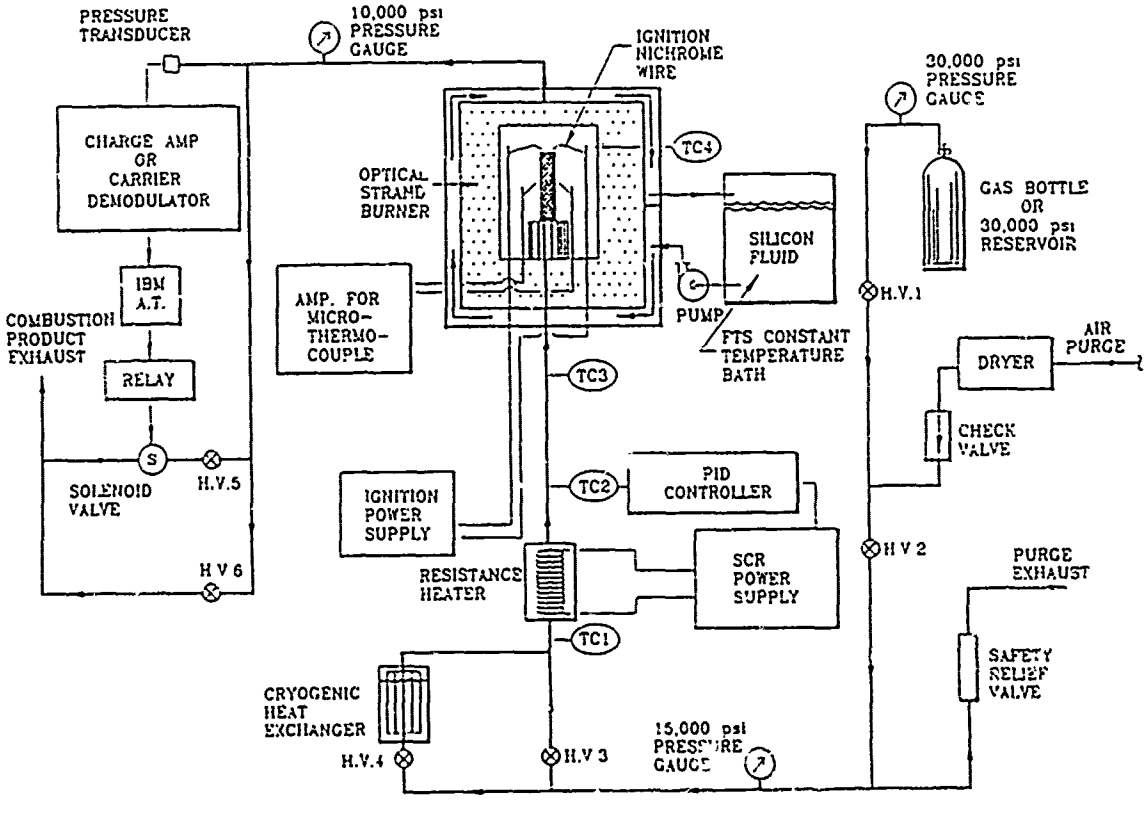


FIGURE 1. Schematic Diagram of Pressure and Temperature Controlled Test Chamber with Optical Windows

During the test, air was used to pressurize the test chamber and to remove combustion products from the test chamber. Air, instead of nitrogen, was used in this set experiments to simulate the combustion of fuel-rich samples in an oxidizer-rich environment. The chamber pressure was maintained at a prespecified level by a computer feedback-controlled gas supply system. In addition, to heat up or cool down the test sample to a prespecified initial temperature, both temperatures of chamber body and purge air flow have to be kept at the same level. The chamber was surrounded by a constant-temperature bath of silicon fluid, of which the temperature can be preset at a level between −40 to 70°C. A pump was incorporated into this closed-loop system to provide a necessary driving force for circulation purpose. Through the heat transfer between the chamber wall and the above-mentioned recirculating contant-temperature bath, a uniform stable temperature of chamber body can be attained. It took about two and half hours to heat up the chamber from 20 to 60°C. In test firings with low initial propellant temperature (e.g. −10°C), the air flow was precooled first in a cryogenic heat exchanger, operated by means of liquid nitrogen, down to the temperature which was typically 15°C lower than the prespecified level. Then, the resistance heater, linked to a control unit consisting of a proportional integral derivative (PID) controller and a silicon controlled rectifier (SCR) power supply, input an appropriate amount of heat flux to air flow. Therefore, the chamber gas-phase temperature was increased to the preset value and remained stable at that point. On the other hand, the cryogenic heat exchanger was disengaged for test firings with high initial propellant temperature (e.g. 60°C). The air flow temperature in the chamber was heated to the prespecified level by using the heating system mentioned above.

In order to measure the thermal-wave structures of boron/[BAMO/NMMO] copolymer fuel-rich solid propellants in both subsurface and surface regions, a fine-wire thermocouple (Platinum / Platinum-13% Rhodium) with a wire diameter of 50 μm was employed in this investigation. In addition, the combustion residues after each firing test were collected and examined using a scanning electron microscope (SEM). A detailed discussion of the overall system setup is given in Refs.5 and 6.

3. DISCUSSION OF RESULTS

In this work, two types of fuel-rich propellant samples were used to examine the effects of boron content and initial temperature of fuel-rich solid propellants on burning-rate characteristics. One was a pure [BAMO/NMMO] copolymer binder with 70/30 mole ratio, and the other was the same copolymer containing 0.5 μm boron powders at 10% mass fraction. The initial temperature and pressure of the test firing ranged from -10 to 60°C and 240.5 to 1030.6 KPa (35 to 150 psia), respectively. Results obtained from the tests are presented below.

3.1. Burning Rate Measurements

The measured burning rates in air under different initial propellant temperatures were shown in Figs. 2 and 3 for 10% boron/[BAMO/NMMO] and pure [BAMO/NMMO] copolymer samples, respectively. Each data point represents the average value of 4 to 12 measured burning rates with error bars specified by $\pm 2\sigma$. Here, σ is the standard deviation defined by the following equation.

$$\sigma = \sqrt{\frac{\sum_{k=1}^{N}(r_{b,k} - \bar{r}_b)^2}{N-1}} \tag{1}$$

Where N is total number of measured data at a given experimental condition; $\bar{r}_b$ is average burning rate of N measurements; and $r_{b,k}$ is k^{th} measured burning rate.

The change in chamber pressure and initial propellant temperature shows a significant effect on burning rate. Basically, the burning rate increases as the pressure and/or initial temperature increase for both types of test samples, and the relationship between burning rate and pressure under different initial propellant temperatures can be expressed in terms of Saint-Robert's burning rate law (i.e. $r_b = aP^n$). The constants a and n are given in Table 1. As the initial propellant temperature of 10% boron/[BAMO/NMMO] copolymer was decreased to -10°C, unstable combustion phenomena occurred and the burning rate decreased rapidly in the low-pressure condition [$P \leq 343.5$ KPa (50 psia)]. This implied that the initial propellant temperature had a stronger effect on the burning rate at low pressures, which resulted in a large difference in the values of exponent n for T_i= 60 and -10°C. The data shown in Fig. 2 revealed a mode that the burning-rate data

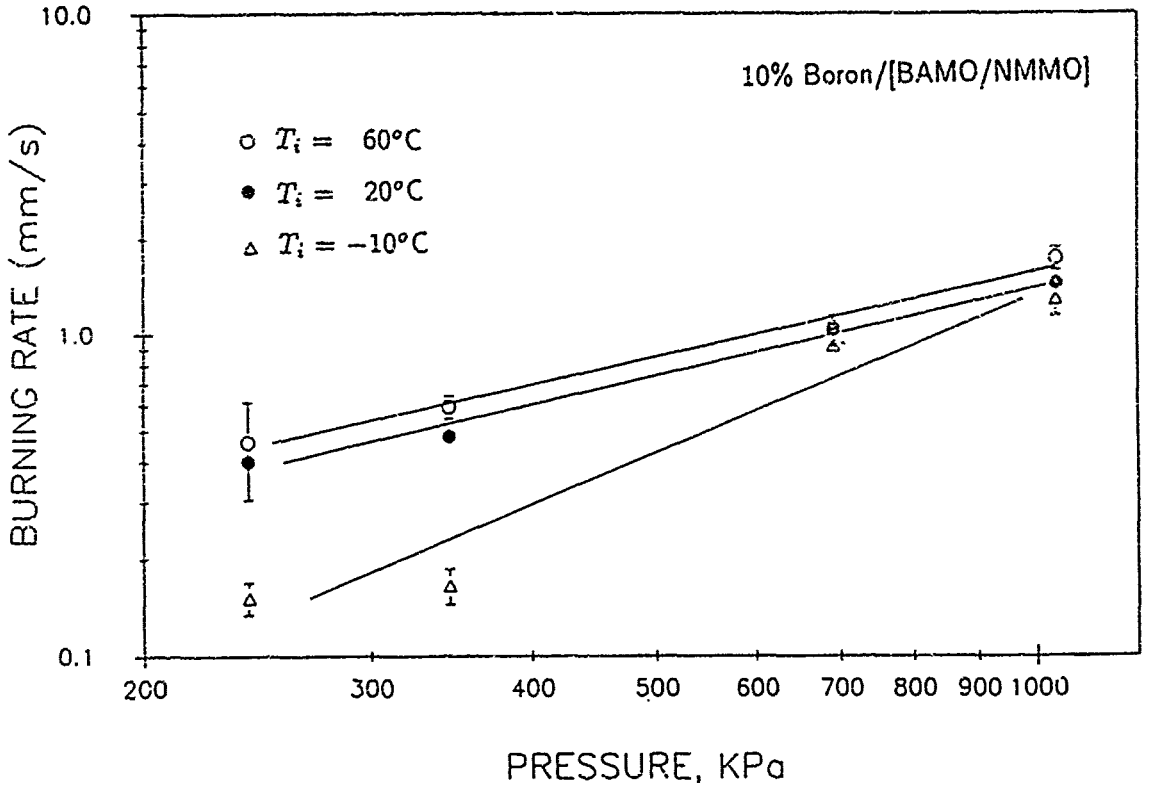


FIGURE 2. Measured Burning Rate versus Pressure for 10% Boron/ [BAMO/ NMMO] Copolymer Fuel-Rich Solid Propellant at T_i= −10, 20, and 60°C

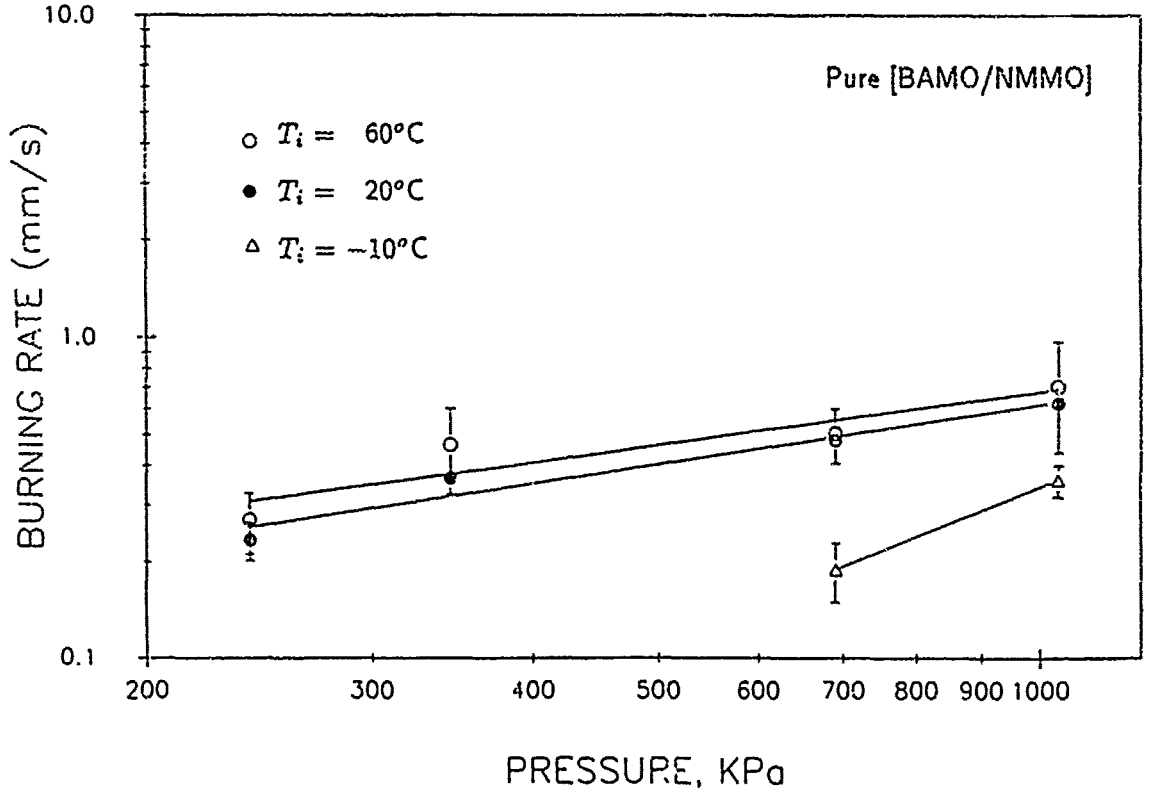


FIGURE 3. Measured Burning Rate versus Pressure for Pure [BAMO/NMMO] Copolymer Fuel-Rich Solid Propellant at T_i= −10, 20, and 60°C

points follow the Saint-Robert's law closely at high initial propellant temperatures. However, some discrepancy was observed at low initial propellant temperature of -10^{o}C. This is believed to be caused by the unstable combustion phenomena at low pressures.

TABLE 1. Saint-Robert's Burning Rate Law* for 10% Boron and Pure/ [BAMO/ NMMO] Copolymer Fuel-Rich Solid Propellant

Initial propellant	a		n	
Temperature, °C	10%B	Pure	10%B	Pure
60	3.107×10^{-3}	1.417×10^{-2}	0.9035	0.5604
20	2.284×10^{-3}	8.398×10^{-3}	0.9309	0.6222
-10	1.3583×10^{-5}	5.5808×10^{-6}	1.6660	1.5949

* $r_b = aP^n$, units: $[r_b]$=mm/s, and $[P]$=KPa.

To further study the boron mass fraction effect, the burning rates of pure [BAMO/ NMMO] in air were also measured at various initial temperatures. As shown in Fig. 3, the burning rates of pure [BAMO/NMMO] copolymer were significantly lower than those of 10% boron/[BAMO/NMMO] samples. At the low initial temperature of -10^{o}C, it was found that the test samples of pure [BAMO/NMMO] copolymer extinguished under low-chamber pressure conditions [$P \leq 343.5$ KPa (50 psia)]. This signified that the low-pressure deflagration limit (PDL) of the sample, below which no sustained stable combustion can be achieved, should lie between 343.5 and 687.1 KPa (50 and 100 psia).

3.2. Temperature Sensitivity

The temperature sensitivity of solid-propellants is defined as

$$\sigma_p \equiv (\frac{\partial ln r_b}{\partial T_i})_p \tag{2}$$

Where σ_p is the temperature sensitivity of burning rate and T_i is the initial temperature. At a given pressure, the burning rates at three initial temperatures (−10,

20, and 60°C) were computed from the Saint-Robert's law. A second-order polynomial, as shown in Eq.(3), was adopted to fit these three calculated burning rate data.

$$r_b = b_2(p)T_i^2 + b_1(p)T_i + b_0(p) \tag{3}$$

The temperature sensitivity can be calculated by differentiating Eq.(3) with respect to T_i according to Eq.(2). Using the above data reduction method with the deduced Saint-Robert's law constants, i.e., a and n shown in Table 1, the temperature sensitivity for 10% and pure [BAMO/NMMO] copolymer fuel-rich solid propellants were deduced and presented in Figs. 4 and 5, respectively. The observation of these temperature sensitivity results indicates the following trends:

1) The σ_p decreases as pressure increases for a given initial temperature. This tendency becomes more obvious at low initial temperatures, e.g., $T_i = -10°C$.
2) At a fixed chamber pressure, the σ_p decreases as initial temperature increases.
3) The σ_p of 10% boron/[BAMO/NMMO] is generally lower than that of pure [BAMO/NMMO] copolymer. This suggests that the boron particles added in [BAMO/NMMO] copolymer are helpful in reducing the temperature sensitivity of fuel-rich propellants.
4) The operating conditions of high chamber pressure and/or high initial temperature show favorable effects on reducing the temperature sensitivity.

Several theoretical works have been conducted to investigate the fundamental mechanisms affecting temperature sensitivity.[7-9] According to the statement of Kubota and Ishihara[7], the temperature sensitivity can be split into two parts: the first part is associated with the initial temperature effect on the flame structure of the gas phase and the second part is associated with the initial temperature effect on the subsurface temperature profile of the condensed phase and the surface heat release rate. These two parts can be evaluated if the detailed gas and condensed phase reactions are known. For simplicity, an analysis conducted by Glick[8] and Cohen and Flanigan[9] is adopted to probe the physical insight of the above temperature sensitivity results.

For the steady-state burning condition with constant thermal properties, the energy balance equation at the burning surface is

$$\rho_p C_p r_b (T_s - T_i) = \lambda_g \left(\frac{dT}{dx}\right)_g + \rho_p r_b Q_s \tag{4}$$

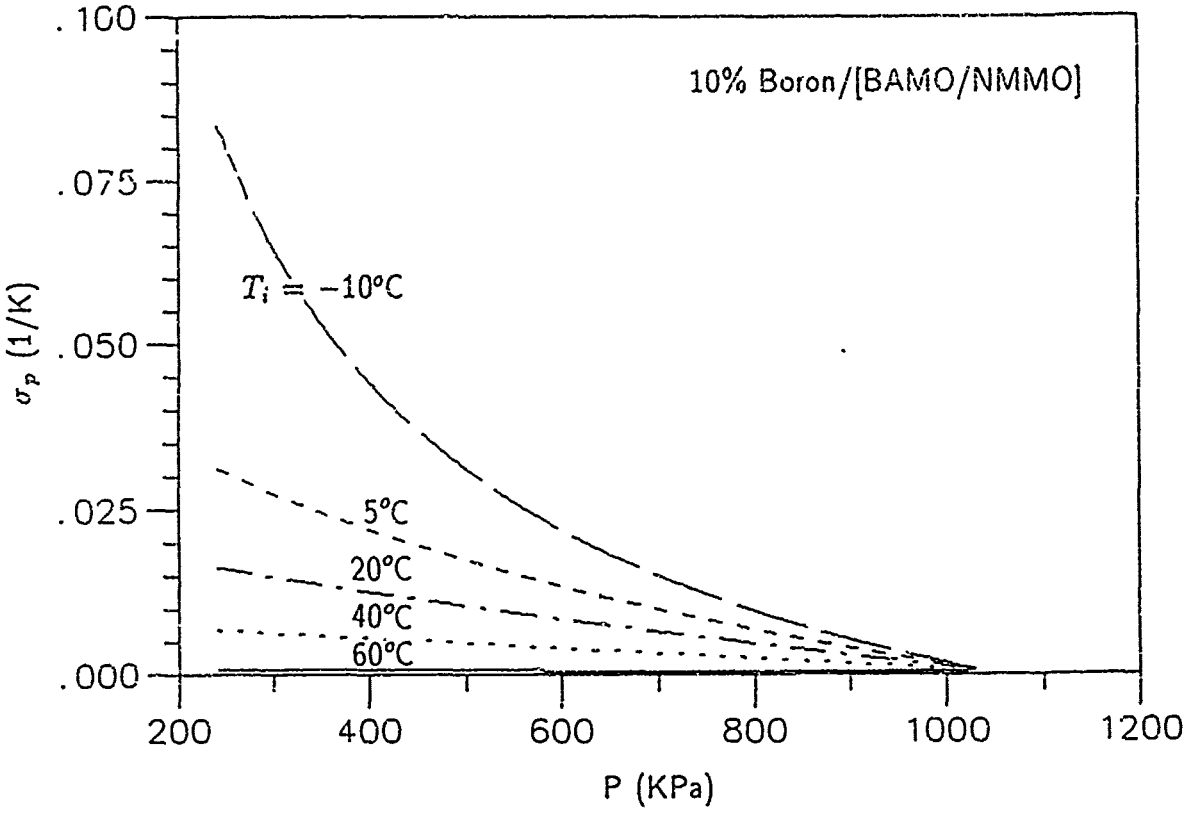


FIGURE 4. Temperature Sensitivity of Burning Rate versus Pressure for 10% Boron/[BAMO/NMMO] Copolymer Fuel-Rich Solid Propellant

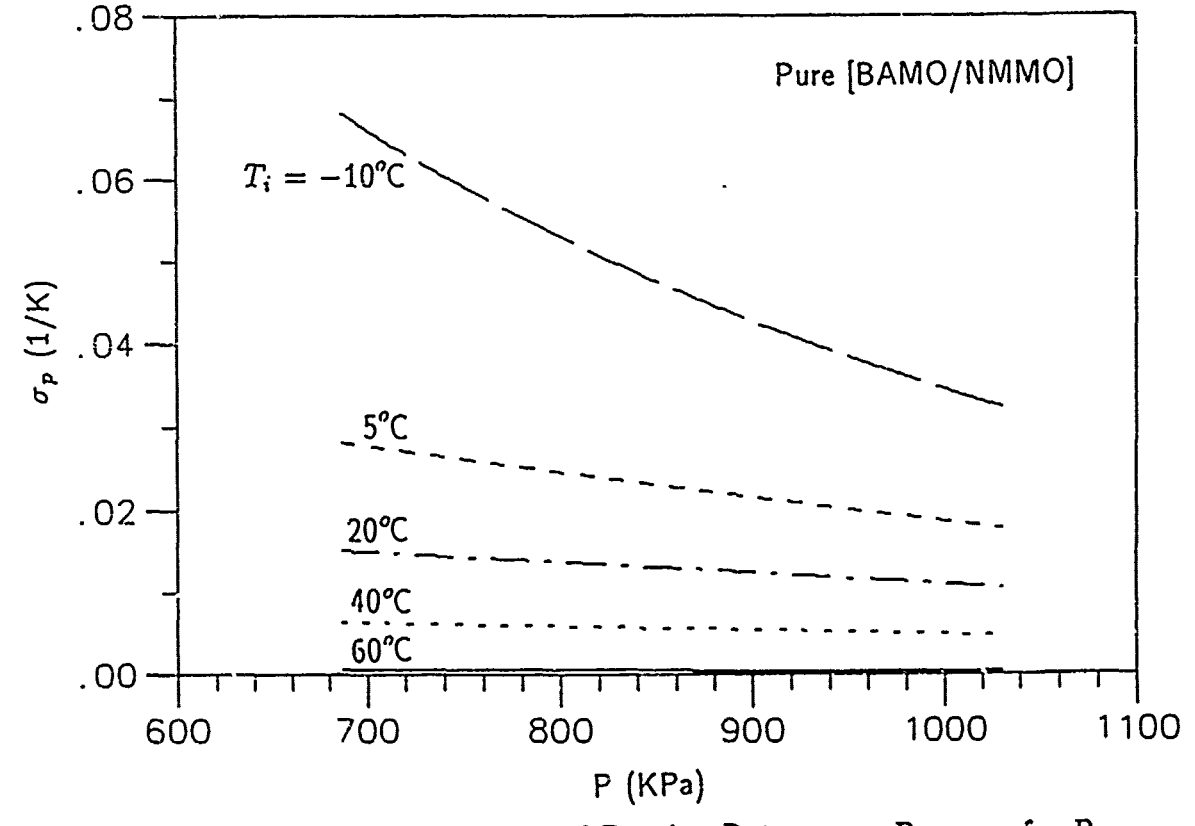


FIGURE 5. Temperature Sensitivity of Burning Rate versus Pressure for Pure [BAMO/NMMO] Copolymer Fuel-Rich Solid Propellant

Assuming T_s, Q_s and $\lambda_g(\frac{dT}{dx})_g$ are weakly dependent on T_i, the relation between the temperature sensitivity and pressure can be expressed as follows.[9]

$$\sigma_p = \frac{1}{(T_s - T_i - \frac{Q_s}{C_p})} \tag{5}$$

From the previous measurement results [3,4], the burning surface temperature increases with pressure. In addition, T_i is fixed for each particular test firing condition. It then leads to the result that the temperature sensitivity of the burning rate decreases as the pressure increases. This presumption is in good agreement with the tendency shown in Figs. 4 and 5. To further incorporate the initial temperature effect and temperature dependence of thermal properties into the theoretical analysis, a comprehensive formulation covering both condensed and gas phase reactions must be considered. Therefore, the development of a detailed combustion model, which can interpret the mechanisms of controlling temperature sensitivity of boron/[BAMO/NMMO] copolymer, is expected to be useful for future investigation.

An attempt was also made to study the relationship of temperature sensitivity with pressure and initial temperature for 10% boron/[BAMO/NMMO] copolymer samples. The correlation determined from least-square nonlinear regression analysis is shown as follows.

$$\sigma_p = (K_0 + K_1 T_i + K_2 T_i^2 + K_3 T_i^3) P^{(K_4 + K_5 T_i)} \tag{6}$$

Where

K_0= 3.9088430E+02
K_1=−1.7935820E+01
K_2=−1.9663031E-01
K_3= 0.6449711E-02
K_4=−1.4045797
K_5= 0.018839587

The units of initial temperature, pressure, and temperature sensitivity are °C, KPa and 1/K, respectively.

Results from this correlation are given in Fig. 6. In general, the data correlates reasonably well according to Eq. (6) for broad ranges of initial temperature and pressure; however, some discrepancy exists at high pressures for T_i=−10°C curve,

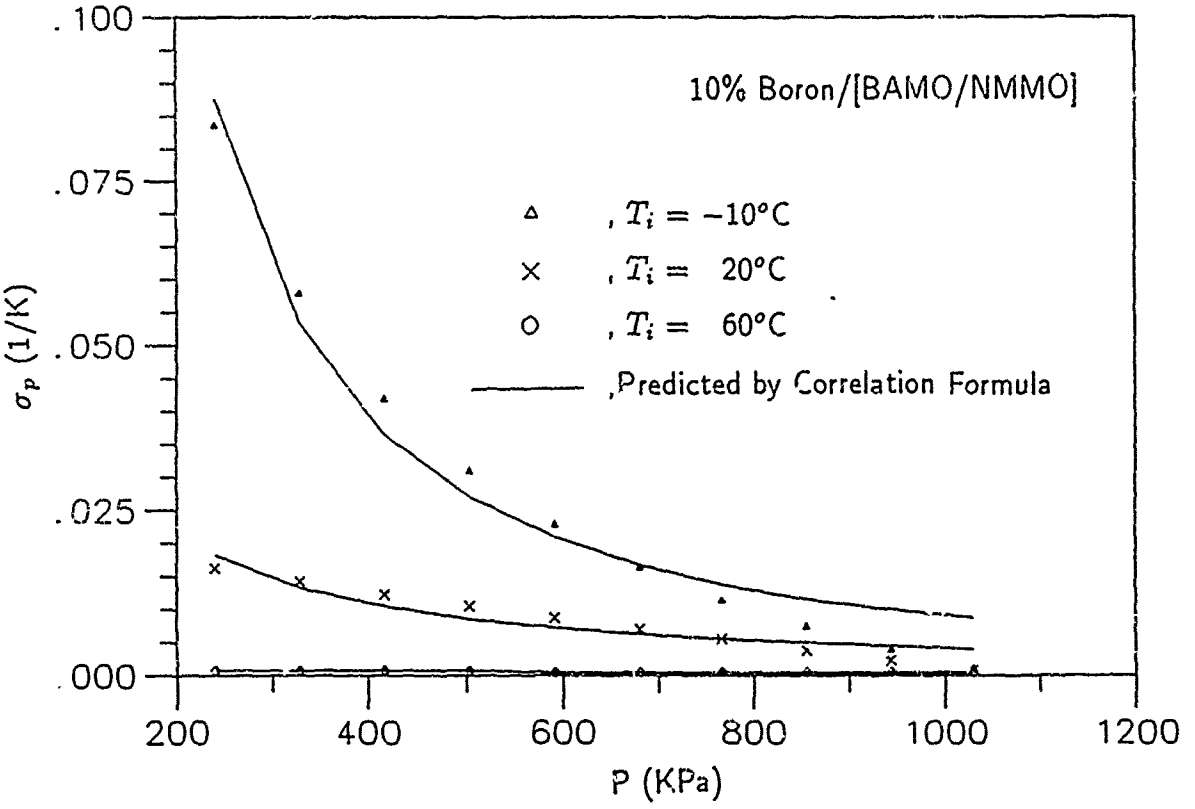


FIGURE 6. Correlation of Temperature Sensitivity with Pressure and Initial Temperature for 10% Boron/[BAMO/NMMO] Copolymer Fuel-Rich Solid Propellant

and care must be taken before applying the above equation to very low initial temperature conditions. Equation (6) could be useful for design considerations as well as theoretical analysis of propellant burning rates.

3.3. Effect of Initial Temperature on Burning Surface Temperature and Formation of Boron Nitride

The thermal wave structures of boron/[BAMO/NMMO] copolymer samples were measured to investigate the effect of initial temperature on the burning surface temperature. The burning surface temperature T_s, indicated by a sudden temperature jump with the steep slope at the burning surface, was reported to be 300°C for 10% boron/[BAMO/NMMO] copolymer under the condition of 1030.6 KPa (150 psia) and 20°C (68 F) in Ref. 4. In this study, the chamber pressure was maintained at the same level of 1030.6 KPa; T_s was measured to be about 315°C for T_i =60°C, and it dropped to 290°C for T_i = −10°C. This clearly shows the trend that the burning surface temperature increases with the initial propellant temperature.

The importance of the formation of BN has been pointed out by Hsieh et al.[4]. During the tests, no residue was found for pure [BAMO/NMMO] copolymer. The combustion residues of 10% boron/[BAMO/NMMO] copolymer samples in air under eight different firing conditions (P = 240.5, 343.5, 687.1, 1030.6 KPa and T_i =−10, 60 °C) were collected for SEM examination. Figure 7 presents the 200 × magnification photomicrographs of the combustion residues for various pressures and initial temperatures. The SEM observations show the major boron compound in the recovered samples is H_3BO_3 crystal. The grain size of H_3BO_3 crystal at low initial-temperature condition is smaller than that at high initial-temperature condition. It appears that the pressure has no pronounced effect on the microstructures of these residues. For initial temperature range tested, no BN hexagonal crystalline structure was found in the aforementioned eight test conditions.

4. CONCLUSIONS

The burning-rate characteristics of boron/[BAMO/NMMO] fuel-rich solid propellants have been investigated under different pressures and initial propellant temperatures. The burning rate increases with both the initial temperature and pressure. The temperature sensitivity was deduced from the measured burning rate results. The favorable operating conditions of reducing the temperature sensitivity of burning rate have been determined to be high pressure and/or high initial temperature. The addition of the boron element in [BAMO/NMMO] copolymer also shows positive effects on reducing temperature sensitivity. The measurement results of thermal wave structure indicate the burning surface temperature increases as the initial propellant temperature increases. For the range of initial temperature and pressure tested, no formation of BN was observed in this study.

REFERENCES

1. Peretz, A., "Some Theoretical Considerations of Metal-Fluorocarbon Composition for Ramjet Fuels," *International Symposium on Airbreathing Engines*, Cincinnati, OH., 1987.
2. Manser, G. E., Fletcher, R. W., and Knight, M. R., "High Energy Binders," Final Report, Morton Thiokol, Inc., Contract No. N00014-82-C-0800, June 1985.

3. Chen, D. M., Hsieh, W. H., Snyder, T. S., Yang, V., and Kuo, K. K., "Study of the Thermophysical Properties and Combustion Behavior of Metal-Based Solid Fuels," *AIAA-88-3041, 24th Joint Propulsion Conference*, Boston, Mass., 1988.
4. Hsieh, W. H., Peretz, A., Huang, I. T., and Kuo, K. K., "Combustion Behavior of Boron-Based BAMO/NMMO Fuel Rich Solid Propellants," accepted for publication in the *Journal of Propulsion and Power*.
5. Hsieh, W. H., "Study of Strand and Erosive Burning of NOSOL-363 Stick Propellants," Ph.D. Thesis, The Pennsylvania State University, August, 1987.
6. Salizzoni, R. M., Hsieh, W. H., and Kuo, K. K., "Regression Behavior and Temperature Sensitivity Measurements of Very High Burning Rate Propellants," *27th JANNAF Combustion Meeting*, October 1990.
7. Kubota, N., and Ishihara, A., "Analysis of the Temperature Sensitivity of Double-Base Propellants," *Twentieth Symposium (International) on Combustion*, pp. 2035-2041, 1984.
8. Glick, R. L., "Temperature Sensitivity of Solid Propellant Burning Rate," *AIAA Journal*, Vol. 5, pp. 586-587, 1967.
9. Cohen, N. S. and Flanigan, D. A., "Mechanisms and Models of Solid-Propellant Burn Rate Temperature Sensitivity: A Review," *AIAA Journal*, Vol. 23, pp. 1538-1547, 1985.



FIGURE 7 (a). SEM Pictures Showing the Crystal Structure of H_3BO_3 in the Combustion Residue of 10% Boron/[BAMO/NMMO] Copolymer Samples Burned in Air for P = 343.5 KPa (50 psia), $T_i = -10°C$, and 200 × Magnification



FIGURE 7 (b). P = 343.5 KPa (50 psia), T_i = 60°C, 200 × Magnification

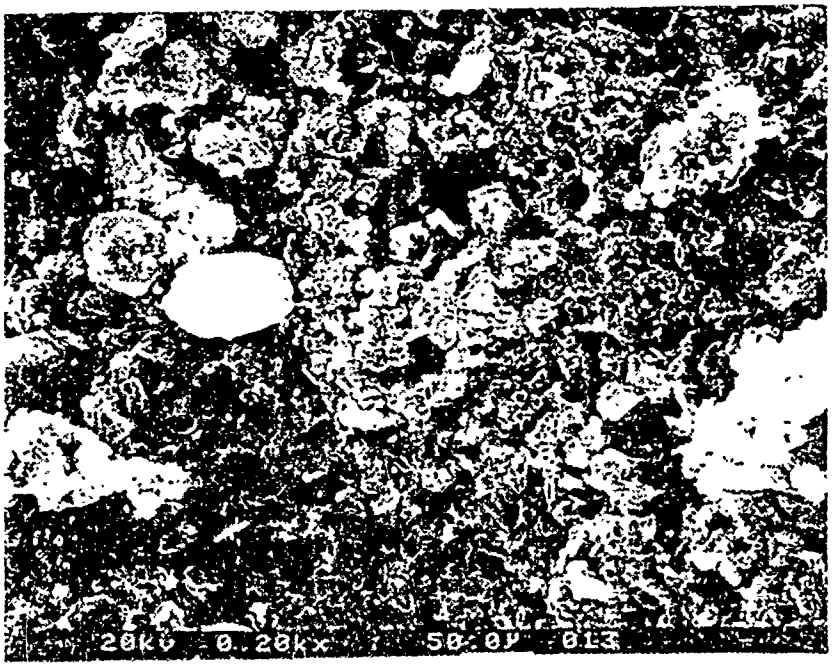


FIGURE 7 (c). P = 687.1 KPa (100 psia), T_i = 60°C, 200 × Magnification

Combustion Behavior and Thermophysical Properties of Metal-Based Solid Fuels

D. M. Chen, W. H. Hsieh, T. S. Snyder, V. Yang, T. A. Litzinger, K. K. Kuo

Reprinted from

Journal of Propulsion and Power

Volume 7, Number 2, March–April 1991, Pages 250–257

AMERICAN INSTITUTE OF AERONAUTICS AND ASTRONAUTICS, INC.
370 L'ENFANT PROMENADE, SW • WASHINGTON, DC 20024

Combustion Behavior and Thermophysical Properties of Metal-Based Solid Fuels

D. M. Chen,* W. H. Hsieh,† T. S. Snyder,‡ V. Yang,§ T. A. Litzinger,§ and K. K. Kuo¶
Pennsylvania State University, University Park, Pennsylvania 16802

Two metal-based solid fuels (magnesium-based and boron-based) have been studied to determine their combustion behavior and thermophysical properties. The burning rate for the magnesium-based (Mg/PTFE/Viton A) solid fuel was found to increase monotonically with ambient pressure and to follow the Saint Robert's law in both air and nitrogen environments. The fuel, however, burned 10% slower in air than in nitrogen. The slower burning rate in air is postulated to result from the entrained oxygen which competes with fluorine to react with magnesium. Because of the lower heat of formation of MgO vs MgF_2, the near-surface heat release is reduced when the oxygen is present, thus reducing the burning rate. This reasoning is also supported by results obtained from the companion pressure deflagration limit (PDL) and ignition tests, which show that the combustion of the magnesium-based fuel has a higher PDL and a longer ignition delay time in air than in nitrogen. Results from the study of ignition and combustion characteristics of boron-based solid fuels show that boron can significantly reduce the ignition delay times of poly(BAMO/NMMO). In determining the thermophysical properties of fuel samples, a subsurface temperature-measurement method was developed to quantify the temperature dependence of the thermal diffusivities of fuel samples. Results show good agreement with those obtained with the laser-flash method.

Nomenclature

PDL = pressure deflagration limit, kPa
r_b = burning rate, mm/s
p = pressure, kPa
K = thermal conductivity, W/K-cm
ρ_p = density, g/cm^3
C_p = specific heat, J/g-K
$\dot{q}_{sub}$ = net heat release from subsurface, W/g
α = thermal diffusivity cm^2/s
L = sample thickness, cm
t_c = characteristic rise time, s
τ = laser pulse time, s
t = time, s
$t_{1/2}$ = time to reach one-half of maximum value, s

Introduction

IN the search for new and improved propulsion technology, the solid-fueled ramjet engine has become an attractive candidate because of its simplicity and high performance. Among the various solid fuels that are under consideration for ramjet use, the boron-based and magnesium-based fuels are the most promising because of the high volumetric heating value of boron and the high combustion efficiency of magnesium. However, the poor ignition behavior of boron particles usually leads to lower combustion efficiency, making them impractical for use in an actual system. On the other hand, magnesium particles possess superior ignition behavior but offer considerably lower heat of reaction. Thus, methods of enhancing the combustion efficiency of boron and retaining the ignition characteristics of magnesium are essential in order to render these fuels feasible for propulsion applications.

Two types of solid fuels were considered. The first contained magnesium with polytetrafluoroethylene (PTFE) and vinylidene fluoride w/perfluoropropylene (Viton A). The second contained boron with a highly energetic binder, 3,3-bis (azidomethyl) oxetane/3-nitratomethyl 3-methyloxetane [poly-(BAMO/NMMO)]. To date, efforts to examine the fundamental ignition and combustion behavior of these fuels have been few. Peretz[1] studied various thermochemical properties of several metal/fluorocarbon fuels for ramjet applications. Results indicate that not only is magnesium a desirable metal additive for fluorocarbon solid fuels, but boron can also be burned effectively with fluorocarbons. Kubota and Serizawa[2] performed detailed experimental work on the combustion of magnesium-based solid fuels containing magnesium, PTFE, and a small amount of Viton A. They observed that the burning rate of this type of solid fuel increases with increased magnesium content but decreases with increased particle size. The significance of the exothermic reactions immediately above the burning surface on the combustion process was also addressed.

Manser et al.[3] recently developed a number of highly energetic binders. In view of the large positive value of the heat of formation associated with poly(BAMO/NMMO), they claimed that a theoretical increase of the specific impulse by 5 s is possible when this polymer is used as a binder in a minimum-smoke propellant system. The total energy released from the fuel was found to increase significantly with the addition of percentages of boron to poly(BAMO/NMMO).

The major purpose of this paper is to study the fundamental ignition and combustion characteristics of Mg/PTFE/Viton A and boron/poly(BAMO/NMMO) solid fuels and to develop a convenient method for measuring the thermophysical properties of these two types of solid fuels. The specific objectives are

1) to determine the burning rates of both fuels as functions of pressure and ambient gas;

2) to characterize the ignition and combustion behavior by performing CO_2 laser ignition/combustion tests, x-ray diffrac-

Presented as Paper 88-3041 at the AIAA/ASME/SAE/ASEE 24th Joint Propulsion Conference, Boston, MA, July 11-13, 1988; received Aug. 22, 1988; revision received Sept. 16, 1989. Copyright © 1988 by the American Institute of Aeronautics and Astronautics, Inc. All rights reserved.

*Associate Scientist, Chung-Shan Institute of Science & Technology, R.O.C.
†Assistant Professor, Department of Mechanical Engineering. Member AIAA.
‡Graduate Assistant, Department of Mechanical Engineering. Student Member AIAA.
§Associate Professor, Department of Mechanical Engineering. Member AIAA.
¶Distinguished Professor, Department of Mechanical Engineering. Associate Fellow AIAA.

tion analysis, low-pressure deflagration limit (PDL) tests, and microscopic examinations; and

3) to deduce the thermophysical properties from the measured subsurface temperature profiles (STP).

Experimental Approach

A windowed strand burner and a CO_2 laser facility were used to study the ignition and combustion behavior of these two types of solid fuels and to characterize their thermophysical properties under well-controlled conditions. A brief description of the test facilities is given below, followed by a discussion of results obtained for each of the metal-based solid fuels.

Strand Burner

Figure 1 shows a schematic diagram of the windowed strand burner. A fuel sample (5 mm in diameter and 77 mm in length) was mounted vertically in the chamber. Ignition of the sample was achieved by passing an electrical current into a nichrome wire which pierced through the test sample about 3 mm from the top surface. A scale was optically superimposed on the image of the solid-fuel sample, using a 75 × 75 mm semitransparent mirror. To visualize the burning process, a video-recording system was employed to photograph the motion of the burning surface inside the strand burner and the optically superimposed scale. With this technique, the burning rate could be determined precisely from the length of the sample burned in a certain time duration. In addition to the visualization study, an imbedded fine-wire thermocouple (platinum/platinum-13% rhodium) with a diameter of 50 μm was used to measure the temperature profiles in both the subsurface and surface regions. A more detailed discussion of the overall strand burner system is given in Ref. 4.

The strand burner was used to study both the steady-state burning behavior and the PDL. During each steady firing, the chamber pressure was maintained at a prescribed level by means of a computer-controlled gas supply system. For the PDL tests, the chamber was depressurized at a rate of 1.1 kPa/s. The extinguishment point could then be identified from the measured pressure-time trace. After each test firing, the solid residues were collected for microscopic examination and x-ray diffraction analysis.

CO_2 Laser Ignition/Combustion Facility

A high-powered CO_2 laser (Coherent Super 48) capable of generating 800 W in continuous wave mode was used for the ignition and combustion studies. Figure 2 shows a schematic diagram of the facility. In order to generate a relatively uniform beam, a thin piece of sheet metal with a 7 mm-diam hole was used to allow only the most uniform portion of the laser beam to reach the sample surface. The resulting spatial variation of the beam intensity was ±10%.[5] A test chamber (25 × 25 × 25 cm) was fabricated using 2.54-cm-thick plexiglass and a 1.25-cm-thick stainless steel top cover. The transparent nature of this chamber facilitated visual access to the ignition and combustion processes from all directions. Two high-quality glass windows were mounted on opposing sides of the chamber to allow for schlieren photography. A KCl window was installed in the top of the chamber to allow the laser to pass into the chamber when pressures other than atmospheric were needed.

A high-speed video system (Spin-Physics 2000) was used to record the dynamic behavior of the flame at a framing rate of 2000 pictures/s. The system accommodates two cameras capable of recording schlieren images and direct photographs simultaneously. The schlieren image can detect clearly the initiation of fuel gasification and its subsequent processes, whereas the direct photograph provides information about luminous flame development and burning characteristics.

In addition to its role in the ignition and combustion study, the CO_2 laser system was also used to conduct laser-flash tests for measuring the thermal diffusivities of the fuel samples. A 75-μm K-type (chromel/alumel) thermocouple was bonded to the bottom of the fuel sample having a specified thickness. As the laser flash irradiated the sample surface, the temperature detected by the bonded thermocouple was recorded by a Nicolet oscilloscope and could then be used to calculate the thermal diffusivity of the fuel.

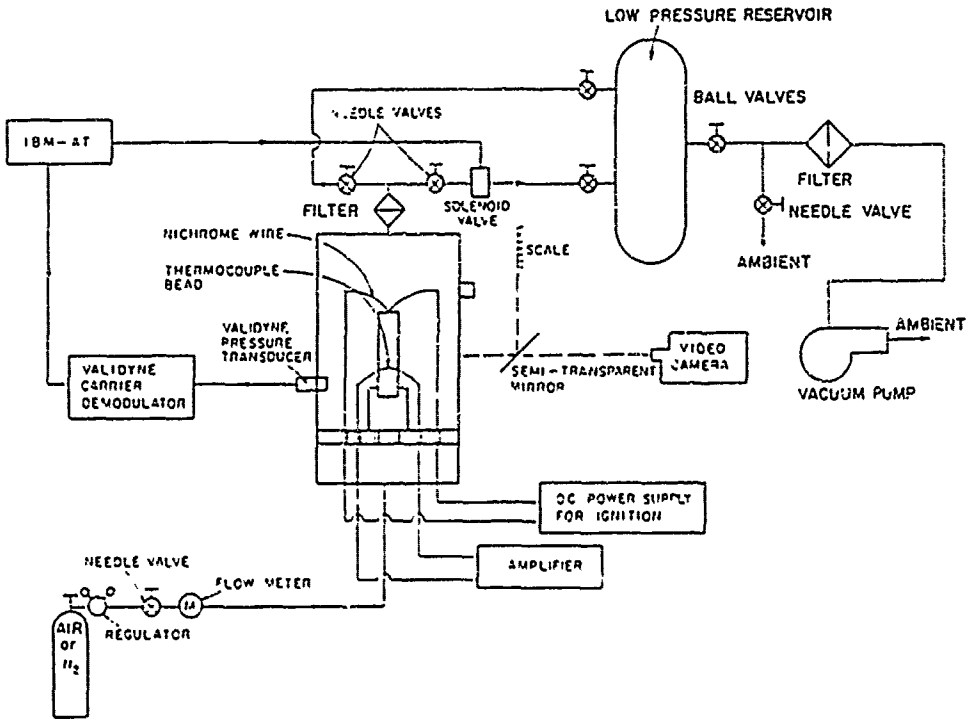


Fig. 1 Schematic of experimental apparatus used in strand-burner tests.

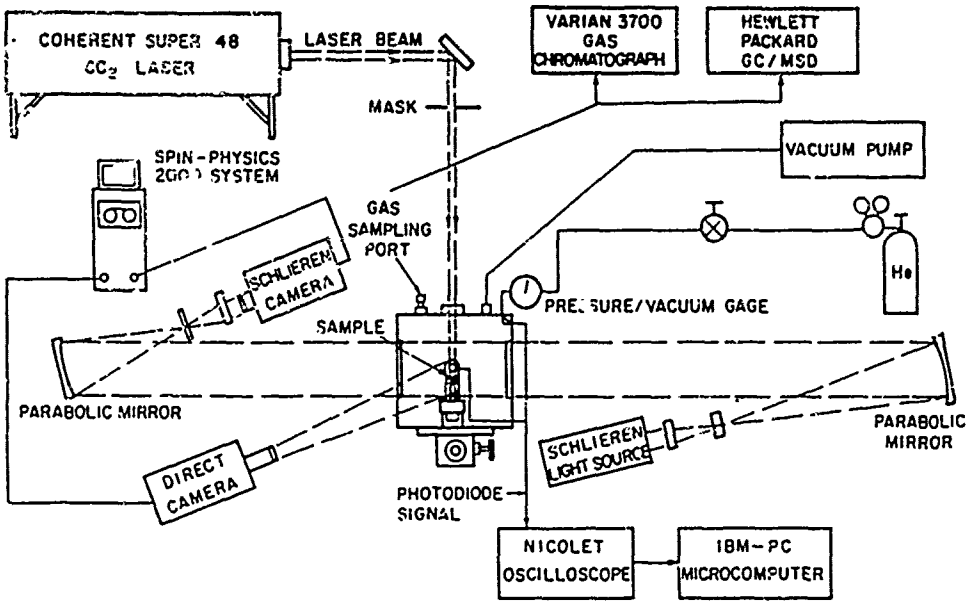


Fig. 2 Schematic of experimental apparatus used in CO_2 laser tests.

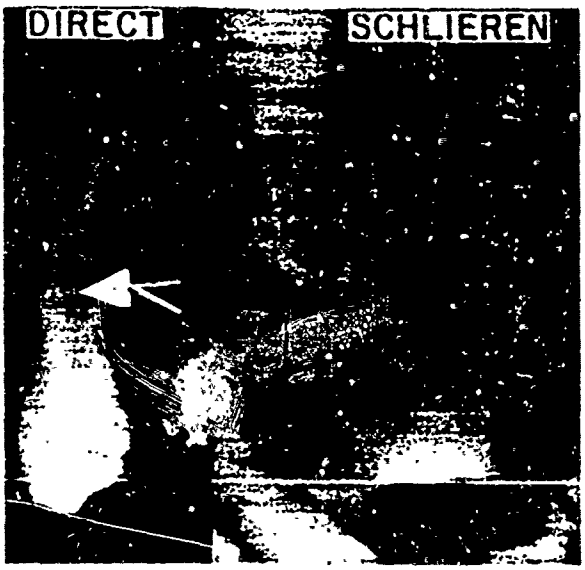


Fig. 3 Mg/PTFE/Viton A combustion in CO_2 laser test.

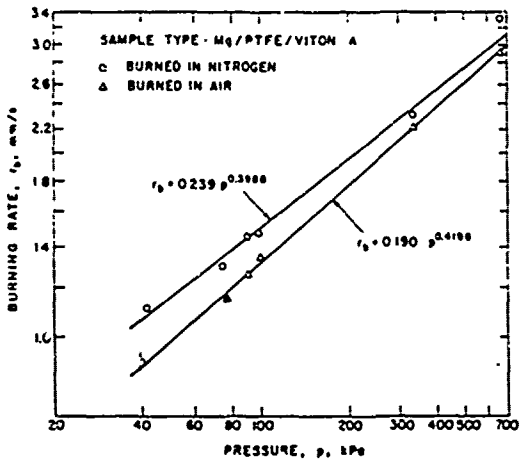


Fig. 4 Burning rate as a function of pressure for Mg/PTFE/Viton A in nitrogen and air.

Combustion Characteristics of Magnesium-Based and Boron-Based Solid Fuels

Magnesium-Based Solid Fuel

The magnesium-based solid fuels used in this study consisted of 50% fluorocarbons (PTFE and Viton A) and 50% magnesium powders with a mean diameter of 20 μm. Initial tests were performed in the CO_2 laser facility, and subsequent experiments in the strand burner. In both cases, not only did the luminous flame initiate at the surface, but it remained attached to the surface for the duration of the combustion period. Figure 3 shows a typical flame structure of the fuel following ignition. The ejection of magnesium particles from the burning surface can be observed as indicated by the arrow in the direct image. This phenomenon was also noted in the strand-burning tests using both air and nitrogen. However, the height of the luminous flame was much greater for combustion tests performed in air than for those performed in nitrogen. The ignition delay time for the magnesium-based fuel was also determined for various oxygen percentages. It increased from 43 ms to 52 ms as the oxygen concentration increased from 1.0% to 21.0%, respectively. These tests were performed at 100 kPa, with an incident heat flux of 400 W/cm^2 from the laser.

Figure 4 illustrates the dependence of the burning rate on the chamber pressure in two different gaseous environments. The burning rate was found to increase monotonically as the pressure increased, and to follow the Saint-Robert's law closely. It is interesting to note that despite the fuel-rich nature of the sample, the burning rate measured in nitrogen was consistently higher than that in air by approximately 10%. This observation is substantiated by the PDL results which show that the lowest pressures for sustaining stable combustion are 9.8 and 28.1 kPa for nitrogen and air, respectively. The fuel has a tendency to extinguish faster in air than in nitrogen. These results suggest that the burning characteristics of this type of solid fuel depend upon the composition of the ambient gas.

Figure 5 shows two temperature profiles obtained from 50-μm thermocouples imbedded in the solid fuel. The tests were performed at atmospheric conditions in both air and nitrogen. Both curves indicate a surface temperature (characterized by the inflection point in the temperature profile) in the neighborhood of 850°C, but with different spatial distributions depending on the gas environment. The temperature profile in the vicinity of the surface is steeper when the fuel was burned in nitrogen, suggesting a higher heat-transfer rate at the surface.

Based upon the above observations, it is believed that the oxygen in the air has an adverse effect on the regression rate, ignition, and extinction characteristics of the solid fuel containing magnesium and fluorocarbons. A proposed rationale to explain this phenomenon follows.

First, the surface regression is a local phenomena. The regression rate is determined mainly by the highly exothermic gas-phase and heterogeneous reactions occurring immediately above and on the surface, and the thermal properties of the solid fuel which control the thermal wave propagation. The processes away from the surface play a less significant role due to their weak effect on the local heat transfer to the surface region.

Second, the magnesium-based solid fuel contained 50% magnesium, which is 17% greater than the stoichiometric ratio. Because of this, most of the magnesium powder did not burn completely in the near-surface region. Instead, the powder was ejected from the surface as a result of the expansion processes of gaseous products generated by the pyrolysis and the solid-phase reaction of the fluorocarbons surrounding them.

Third, the gaseous products originating from the surface act as a freejet and entrain the ambient gas into the shear layer surrounding the sample boundary. Thus, during tests in air, oxygen can be entrained easily, causing competitive oxidation and fluorination reactions with magnesium. Because the heat of oxidation for magnesium is approximately one-half of the heat of fluorination for magnesium, the total heat generated in the near-surface region is reduced when oxygen is present. This reduced heat release reduces the heat-transfer rate to the condensed phase and consequently decreases the regression rate.

This argument is substantiated by the subsurface temperature profiles measured in air and nitrogen environments (see Fig. 5). Results based upon the x-ray diffraction analysis of the combustion residues indicate that the major solid products for the case involving air were MgO, MgF_2, and carbon. However, for the pure nitrogen case, the major products were MgF_2, Mg, and carbon. Thus, the reaction of magnesium particles with oxygen in the gas phase is significant. Further investigation is needed to quantify the extent to which the oxidation reaction takes place in the near-surface region.

Based upon the above observations and the measured subsurface temperature profiles, the important physicochemical processes involved in the combustion of magnesium/fluorocarbon fuel in the presence of air can be characterized qualitatively. Figure 6 summarizes the entire process by identifying five distinct regions in both the gas and condensed phases. A thermocouple trace obtained from a test in air at 100 kPa is also included to show the approximate thermal wave profile. These five zones can be summarized as follows.

In zone 1, the temperature is below the exothermic decomposition temperature of Viton A (316°C) and only inert heating takes place. Zone 2 covers a temperature range from 316-530°C, corresponding to the decomposition temperatures of Viton A and PTFE, respectively. The thickness is about 170 μm at 1 atm. Exothermic decomposition of Viton A initiates in this zone and reaches its maximum rate at 471°C.[6] The major products from the pyrolysis of Viton A include HF, C_2F_2, C_2F_4, CHF_2, and other fluorocarbons and hydrofluorocarbons.[6] Chemical reactions between magnesium powders and the pyrolysis products of Viton A may also occur. Onset of the melting process of PTFE (330°C) occurs approximately 200 μm beneath the burning surface. However, as a result of the highly viscous nature of the molten PTFE, only restricted motions of magnesium particles are possible in this region.

Zone 3 is characterized by a rapid temperature increase

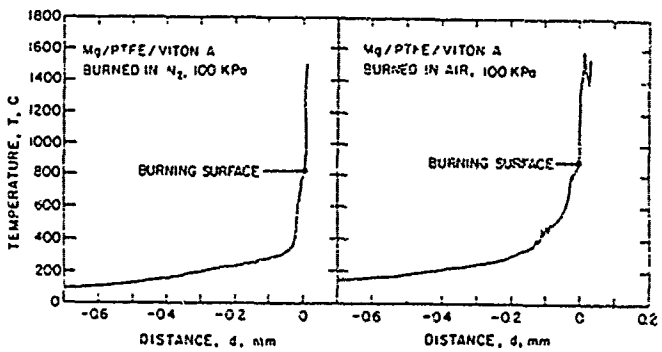


Fig. 5 Temperature profiles of Mg/PTFE/Viton A.

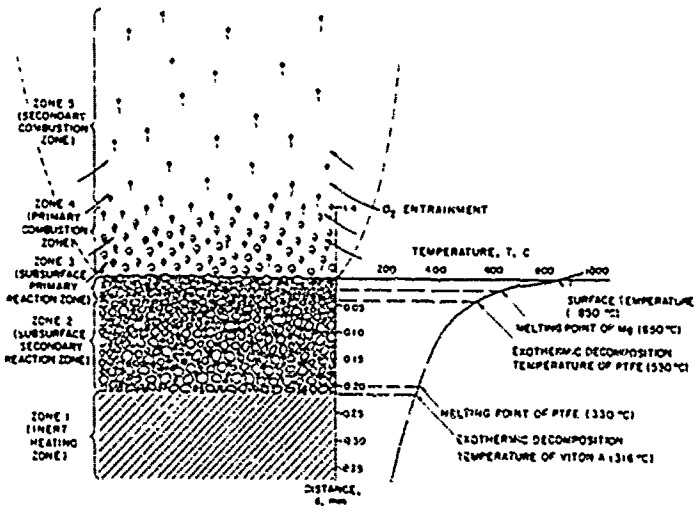


Fig. 6 Schematic showing temperature profile of subsurface region in a Mg/PTFE/Viton A sample.

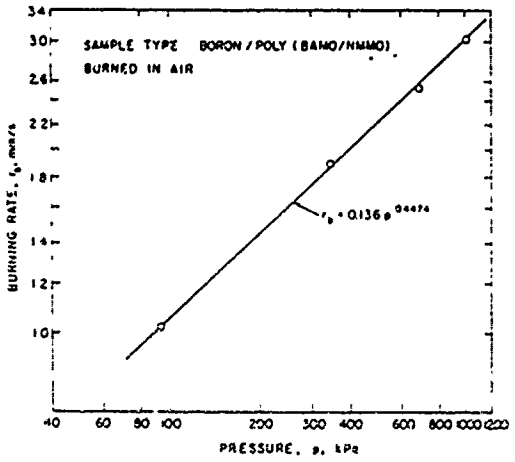


Fig. 7 Burning rate as a function of pressure for poly(BAMO/NMMO) with 17.6% boron.

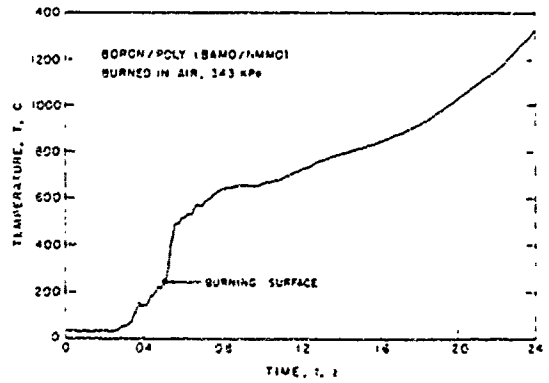


Fig. 8 Subsurface temperature profile of boron/poly(BAMO/NMMO) in air at 343 kPa.

within a thin layer of approximately 50 μm. The temperature ranges from 530°C to the surface temperature of 850°C. At 530°C, PTFE begins to decompose exothermically to liberate CF_4, C_2F_6, C_2F_4, C_3F_6, C_4F_8, other fluorocarbons, and possibly fluorine itself.[6] As the temperature further increases to 650°C, magnesium powders begin to melt. Reactions that may take place in this region are believed to be those of fluorine and fluorinated compounds with either liquid or gaseous magnesium (because the vapor pressure of magnesium at 850°C is about 50 mm Hg). These highly exothermic reactions may further enhance the gasification of PTFE, causing an imbalance of local forces. This process results in violent expulsion of magnesium particles from the surface.

Zone 4 is characterized by the high-temperature gradient in the vicinity of the burning surface. It is depicted by a bright flame associated with the exothermic gas-phase and heterogeneous reactions. As stated above, for combustion in air, oxygen may be entrained by the jet and react with molten magnesium powders near the outer region of the surface.

Zone 5 is rather far from the surface. For combustion in air, the major chemical process includes the reaction of magnesium vapor and O_2. As a result of its distance from the surface and its low flame temperature (~ 1600°C), the effects of this region on surface-regression processes are insignificant.

Boron/Poly(BAMO/NMMO) Solid Fuel

In this work, the boron-based solid fuel sample contained a highly energetic copolymer, BAMO/NMMO, and 17.6% boron powder with a mean diameter of 0.5 μm. From the recorded video images, it was observed that the flame structure of the sample was affected by the testing pressure. At atmospheric conditions, only a faint gaseous flame appeared above the surface. As the ambient pressure was increased to 1034 kPa, a much brighter flame was observed, with many burning boron particles ejected from the surface.

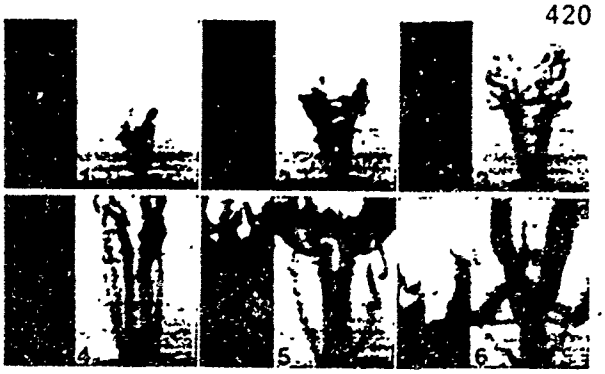


Fig. 9 Ignition sequence of pure poly(BAMO/NMMO) in air with a heat flux of 190 W/cm^2 using CO_2 laser. Time from initial laser heating is 4.5, 5.5, 6.5, 88.0, 128.0, and 165.5 ms.

Figure 7 shows the strand-burning rate in air as a function of pressure. It followed the Saint-Robert's law with the burning rate given by $r_b = 0.136\,p^{0.447}$. Figure 8 presents a measured temperature profile obtained, using a 50 μm R-type thermocouple embedded in a boron/poly(BAMO/NMMO) sample, with an ambient pressure of 343 kPa. The burning-surface temperature, indicated by a sudden temperature jump at the burning surface, was about 250°C, which was relatively low when compared to magnesium-based solid fuels. The burning-surface temperature increased monotonically with testing pressure, ranging from 220°C at 100 kPa to 310°C at 1030 kPa. The temperature-time trace presented in Fig. 8 shows several ripples between 100°C and 250°C; these are believed to be caused by the subsurface reaction of the binder.[5-10] In this particular test, the maximum measured gas-phase temperature was about 1400°C. However, in some tests, the measured temperature-time traces showed maximum temperatures higher than 1715°C.

To further enhance understanding of the ignition and combustion behavior, the boron-based fuel samples were also tested in the CO_2 laser facility. Figure 9 shows an ignition sequence of the pure poly(BAMO/NMMO) under CO_2 laser heating. The left image is a direct picture, and the right image is a schlieren picture. The magnification of the direct image is twice that of the schlieren, and the sample is a 5 mm cube.

Pyrolysis of the solid fuel was first noted after 4.0 ms in the schlieren picture. The gases formed a jet with a mean velocity of about 10 m/s. Within a distance of 8 mm from the surface, the jet appeared to be laminar in nature and became turbulent farther away from the surface. The gases gradually absorbed the incident laser energy and finally ignited after 128 ms. This ignition process is evident in the direct picture and is an indication of a gas-phase ignition process. Immediately following ignition, the flame propagated down toward the surface to further enhance the condensed phase reactions. The copolymer extinguished following laser cutoff at 200 ms.

Figure 10 shows the ignition process of poly(BAMO/NMMO) containing 17.6% boron. Gasification was noted at 4.5 ms after onset of the CO_2 laser beam. The pyrolyzed gaseous jet was less turbulent than that evolved from the pure poly(BAMO/NMMO) sample. Changes in the jet characteristics are believed to be dependent upon the boron content in the sample which acts to dampen the turbulent mixing process.[11] Because the boron is initially ejected before burning, the solid boron particles in the gas phase absorb the incident laser energy, thus raising the temperature in the gas phase to initiate chemical reaction and lead to ignition. The increase of absorption due to the presence of boron in the gas phase has been verified by laser-attenuation tests with various gases and solid-fuel samples.[5] As a result, the boron addition decreases

the ignition delay time to 10 ms, compared to 128 ms for the pure poly(BAMO/NMMO).

Picture 6 in Fig. 10 shows many boron particles burning in the gas phase following ignition. After laser cutoff, the sample extinguished momentarily and then reignited. The reignition, which was observed for the boron-containing fuels but not for the pure copolymer, is believed to be the result of an increase in thermal diffusivity caused by the boron addition, which allows the thermal wave to penetrate further into the solid fuel.

Figure 11 shows the ignition delay times for pure poly (BAMO/NMMO) and samples containing 17.6 and 30% boron as a function of heat flux. The pure poly(BAMO/NMMO) fuel exhibited random ignition characteristics for all heat fluxes. When boron was added, the delay time became shorter and reproducible. The behavior of boron/poly(BAMO/NMMO) is distinctly different from that of pure poly(BAMO/NMMO) due to the effects of boron particles on the fluid dynamics and radiative absorption. In the pure poly(BAMO/NMMO) case, the high turbulence level in the gas phase caused the pyrolyzed gases to be heated more uniformly, thus, no local high-temperature region could be established easily in the gas phase.

On the other hand, when boron is added, the gas phase becomes less turbulent due to the damping effect of submicron boron particles present in the pyrolyzed gases. This introduces a smaller heat-transfer rate within the pyrolyzed gases and causes a local high-temperature region to be established more readily. In addition, the radiative absorption by the pyrolyzed gases mixed with boron particles is significantly increased. The ignition delay time of boron/poly(BAMO/NMMO) is, therefore, much shorter than that of pure poly(BAMO/NMMO).

Thermophysical Property Characterization

Both subsurface temperature profile (STP) and laser-flash methods were used to evaluate the thermal diffusivities and conductivities of the fuel samples. Other properties, such as densities and specific heats, were obtained from the open literature. A brief description of these two measurement techniques is given below, followed by a discussion of results.

Subsurface Temperature Profile (STP) Method

In order to obtain a temperature profile of the subsurface region during combustion, an R-type fine-wire thermocouple with a diameter of 50 μm was embedded in a vertically mounted solid fuel sample. The sample was then ignited using a nichrome wire and burned down into the imbedded thermocouple. In this manner, both the subsurface and gas-phase temperature profiles were obtained. The subsurface temperature profile could be used to deduce the thermal diffusivity and conductivity as functions of temperature.

The STP method is based upon a one-dimensional heat-conduction equation. In order to simplify the analysis, a moving coordinate system was used with its origin located at the instantaneous burning surface. Using this coordinate system, the heat-conduction equation becomes[12,13]

$$\frac{\mathrm{d}}{\mathrm{d}x}K\frac{\mathrm{d}T}{\mathrm{d}x} - \frac{\mathrm{d}(\rho_b r_b C_p T)}{\mathrm{d}x} + \rho_b \dot{q}_{srb} = 0 \qquad (1)$$

where $\dot{q}_{srb}$ is the net heat release in the subsurface region of the fuel sample. This term vanishes if there is no chemical reaction within this region (i.e., the inert heating region).

Integration of Eq. (1) gives

$$K\frac{\mathrm{d}T}{\mathrm{d}x}\bigg|_x - K\frac{\mathrm{d}T}{\mathrm{d}x}\bigg|_{-\infty} = \int_{-\infty}^{x}\frac{\mathrm{d}(\rho_b r_b C_p T)}{\mathrm{d}x}\,\mathrm{d}x = \int_{T(-\infty)}^{T(x)}\rho_b r_b C_p\,\mathrm{d}T \qquad (2)$$

The density and specific heat are evaluated using a mass-averaged value of the ingredients in the solid fuel sample. Rearranging Eq. (2) and assuming that the heat flux is zero at $x = -\infty$, the thermal conductivity as a function of temperature becomes

$$K(T) = \int_{T(-\infty)}^{T(x)}\rho_b r_b C_p\,\mathrm{d}T \Big/ \frac{\mathrm{d}T}{\mathrm{d}x}\bigg|_x \qquad (3)$$

where the local temperature gradient $\mathrm{d}T/\mathrm{d}x$ can be calculated from the measured subsurface temperature profile. By definition, the thermal diffusivity can be deduced from the relation

$$\alpha(T) = K/(\rho_b C_p) \qquad (4)$$

Because the STP method was used to deduce the thermal conductivity and diffusivity of the testing sample in the inert region, the thermocouple bead did not experience rapid temperature variations and thus was able to measure the temperature profile very accurately. The characteristic time of the thermocouple used in this study was about 10 ms,[14] which is much smaller than heat-conduction time within the inert region. Measurement errors caused by velocity and radiation effects[15] are not present since the thermocouple is embedded in a solid, opaque fuel sample. Because of the small diameter of the thermocouple wire, heat losses caused by conduction from the thermocouple bead are also negligible.[15] The largest error introduced into the STP method ($\pm$10°C) comes from the data acquisition and reduction procedures.

Laser-Flash Method

The laser-flash method[16] was also used to determine the thermal diffusivity of the solid fuel samples. In this method, a short laser pulse was given to the top surface of the sample. A thermocouple was mounted to the bottom surface of the

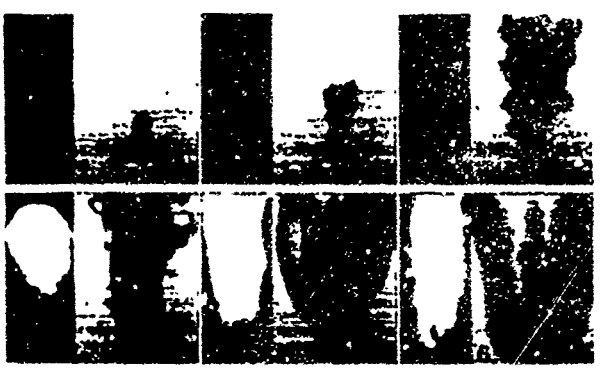


Fig. 10 Ignition sequence of poly(BAMO/NMMO) with 17.6% boron in air with a heat flux of 490 W/cm^2 using CO_2 laser. Time from initial laser heating is 5.0, 6.0, 10.0, 17.5, 42.0, and 140.5 ms.

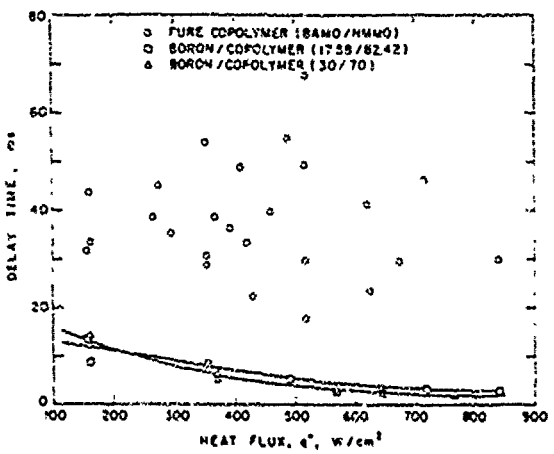


Fig. 11 Ignition delay time vs heat flux for pure poly(BAMO/NMMO) binder.

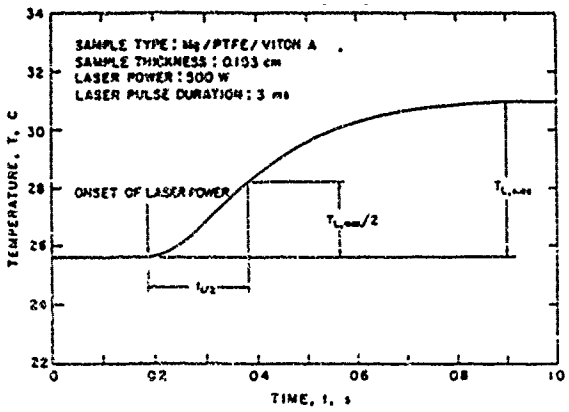


Fig. 12 Temperature-time trace from laser-flash test.

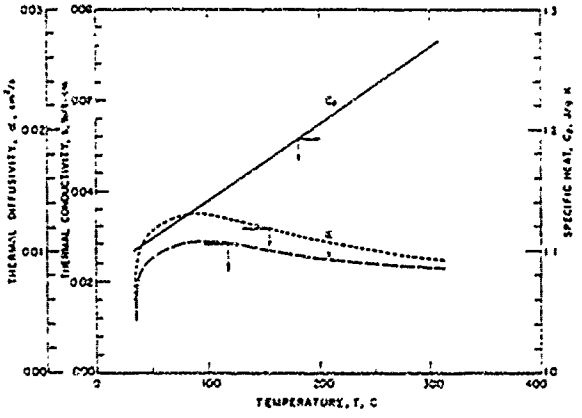


Fig. 13 Thermophysical properties of Mg/PTFE/Viton A as functions of temperature from STP method.

sample to monitor the temperature rise as the energy from the top surface was conducted through the sample (thickness of 1 mm). Figure 12 shows a typical temperature-time trace from the thermocouple on the bottom surface. The temperature rises slowly and reaches a maximum value (T_L, max) after 800 ms.

If we assume that the solid fuel sample has a uniform initial temperature distribution and that the energy from the laser pulse is instantaneously and uniformly absorbed in a thin layer on the top surface, then the temperature rise on the bottom face can be expressed as[17]

$$T(L,t) = T_{L,\max}\left[1 + \frac{1}{2}\sum_{n=1}^{\infty}(-1)^n \exp\left(-\frac{n^2\pi^2}{L^2}\alpha t\right)\right] \quad (5)$$

When $T(L,t)/T_{L,\max} = 1/2$, the dimensionless quantity $\pi^2\alpha t/L^2$ must have a value of 1.37. Consequently, the thermal diffusivity becomes

$$\alpha = \frac{1.37L^2}{\pi^2 t_{1/2}} = \frac{0.139L^2}{t_{1/2}} \quad (6)$$

where $t_{1/2}$ is the time required for the bottom face to attain one-half of its maximum temperature. Equation (6) is accurate within 1% as long as the laser-pulse length is short enough to avoid any chemical reactions and the characteristic time of the sample (defined as $t_c = L^2/\pi^2\alpha$) is greater than 50 times the laser-pulse duration.[18] The characteristic time and the pulse duration thus determine the thickness of the solid fuel sample.

Heat losses by convection from the top surface during the laser-flash method was investigated by Mendelsohn.[19] He found that the heat loss by convection depends strongly upon

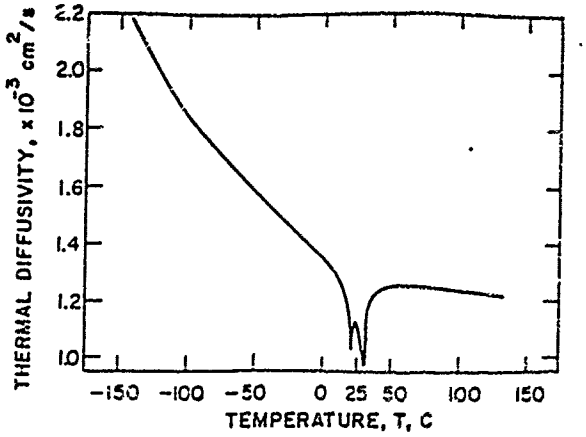


Fig. 14 Thermal diffusivity of PTFE between −140 and 125°C.[23]

the testing conditions, sample properties, and the Biot number. In order to minimize heat losses, the Biot number for the tests conducted in this study were of the order of 0.02, ensuring the reliability of the data. In addition, the sample was mounted on insulation material to minimize conductive losses from the bottom surface.

Thermophysical Properties of Magnesium-Based and Boron-Based Solid Fuels

Figure 13 shows the results obtained by the STP method for the magnesium-based solid fuel. The specific heat, thermal conductivity, and thermal diffusivity are plotted as functions of temperature. The specific heat and density of Mg, PTFE, and Viton A were obtained from Refs. 20–22, respectively. At a temperature of about 40°C, the values for both thermal conductivity and thermal diffusivity increase drastically. This sharp increase is believed to be caused by the rapid change in thermal diffusivity of PTFE that occurs near that temperature due to the crystaline transition (see Fig. 14).

To verify the measurements with the STP method, the laser-flash method was used to determine the thermal diffusivity of the magnesium-based solid fuel at 25°C. Using a sample thickness of 0.153 cm, a value of 1.6×10^{-2} cm^2/s was measured; this agrees reasonably well with the value of 1.1×10^{-2} cm^2/s obtained using the STP method. The laser-flash method was also used to determine the thermal diffusivity of boron/poly(BAMO/NMMO) solid fuel, and a value of 1.82×10^{-3} cm^2/s was obtained at 25°C. Temperature profiles were measured for the boron/poly(BAMO/NMMO) fuel; however, the thermal diffusivity could not be calculated because the specific heat and density are not known.

Summary and Conclusions

The combustion behavior and thermophysical properties of magnesium-based and boron-based solid fuels have been studied using both a windowed strand burner and a CO_2 laser test facility. Results from strand-burner tests show that the magnesium-based fuel burns 10% faster in nitrogen than in air, indicating that oxygen has an adverse effect on the combustion behavior of this type of fuel. To verify the oxygen effect, ignition delay times were measured using different oxygen percentages. It was found that the ignition delay time decreased as the oxygen percentage decreased. PDL tests show that the fuel has a low pressure limit of 9.8 kPa for stable combustion in nitrogen, compared to 28.1 kPa in air. Subsurface temperature profiles of the magnesium-based fuel also indicate the adverse effect of oxygen on the combustion behavior.

The combustion behavior of the boron-based solid fuel was also studied in the strand burner, and its burning rate was found to have a slightly higher pressure dependence than that

for the magnesium-based solid fuel. Expressions for the burning rate of the magnesium-based fuel in air, in nitrogen, and for the boron-based fuel in air were found to be $0.190\,p^{0.42}$, $0.239\,p^{0.40}$, and $0.136\,p^{0.45}$, respectively. To investigate the effect of boron on the pure poly(BAMO/NMMO) energetic binder, ignition delay times were studied. Results showed that the random ignition delay times for the pure poly(BAMO/NMMO) became consistent when boron was added. From high-speed pictures of the ignition process, it was found that the boron particles affect the fluid dynamics for the gaseous jet. The boron also resulted in increased absorptivity in the gas phase. The combined result is a significant decrease in the ignition delay time.

An STP method was developed in order to determine the thermophysical properties as functions of temperature for these fuels, and the results were compared with those of a laser-flash method. Knowing the value for the specific heat of magnesium-based solid fuel as a function of temperature, the thermal conductivity and thermal diffusivity of the fuel were calculated from a subsurface temperature-time trace. The agreement of these two methods demonstrates the validity of the STP method.

Acknowledgments

This work represents a part of the research results obtained under Contract N00014-86-K-0468 sponsored by the Office of Naval Research, Arlington, VA, under the management of R. S. Miller and G. D. ROY. The authors would like to thank R. G. Shortridge of the Naval Weapon Supply Center and G. E. Manser of Aerojet Solid Propulsion Company for providing the solid fuels used in this study. The assistance of B. L. Fetherolf of The Pennsylvania State University is greatly appreciated in performing the CO_2 laser-ignition tests.

References

[1]Peretz, A., "Some Theoretical Considerations of Metal-Fluorocarbon Compositions for Ramjet Fuels," *8th International Symposium on Air-Breathing Engines*, AIAA, New York, 1987, pp. 398–403.

[2]Kubota, N., and Serizawa, C., "Combustion of Magnesium/Polytetrafluoroethylene," AIAA 86-1592, 1986.

[3]Manser, G. E., Fletcher, R. W., and Knight, M. R., "High Energy Binders," Final Rept., Thiokol Corp., Brigham City, UT, Contract N00014-82-C-0800, June 1985.

[4]Hsieh, W. H., "Study of Strand and Erosive Burning of NOSOL-363 Stick Propellants," Ph.D. Thesis, The Pennsylvania State Univ., University Park, PA, 1987.

[5]Fetherolf, B. L., Litzinger, T. A., and Kuo, K. K., "An Instrument for Measuring High-Power Laser Beam Profiles and Beam Attenuations," *The Review of Scientific Instruments*, Vol. 61, No. 1, 1990, pp. 7–10.

[6]Chen, D. M., Fetherolf, B. L., Snyder, T. S., Hsieh, W. H., Litzinger, T. A., and Kuo, K. K., "Ignition and Combustion Behavior of MTV Igniter Materials for Base Bleed Application," *First International Symposium on Special Topics in Chemical Propulsion: Base Bleed*, Athens, Greece, Nov. 23–25, 1988, Hemisphere, New York (to be published).

[7]Newman, R. N., and Payne, J. F. B., "The Anomalous Brightness of Magnesium-Air Flames," *Combustion and Flame*, Vol. 68, No. 1, 1987, pp. 31–41.

[8]Farber, M., Harris, S. P., and Srivastava, R. D., "Mass Spectrometric Kinetic Studies on Several Azido Polymers," *Combustion and Flame*, Vol. 55, No. 2, 1984, pp. 203–211.

[9]Oyumi, Y., and Brill, T. B., "Thermal Decomposition of Energetic Materials 14. Selective Product Distributions Evidenced in Rapid, Real-Time Thermolysis of Nitrate Ester at Various Pressures," *Combustion and Flame*, Vol. 66, No. 1, 1986, pp. 9–16.

[10]Oyumi, Y., and Brill, T. B., "Thermal Decomposition of Energetic Materials 12. Infrared Spectral and Rapid Thermolysis Studies of Azido-Containing Monomers and Polymers," *Combustion and Flame*, Vol. 65, No. 2, 1986, pp. 127–135.

[11]Snyder, T. S., Chen, D. M., Fetherolf, B. L., Litzinger, T. A., and Kuo, K. K., "Pyrolysis and Ignition of Boron-Based Solid Fuels for Ramjet Applications," *25th JANNAF Combustion Meeting*, Huntsville, AL, CPIA Pub. 498, 1988.

[12]Klein, R., Mentser, M., Von Elbe, G., and Lewis, B., "Determination of the Thermal Wave Structure of a Combustion Wave by Fine Thermocouples," *Journal of Physics and Colloid Chemistry*, Vol. 54, No. 6, 1950, pp. 877–884.

[13]Kubota, N., Ohlemiller, T. J., Caveny, L. H., and Summerfield, M., "The Mechanisms of Super-Rate Burning of Catalyzed Double Base Propellants," Dept. of Aerospace and Mechanical Sciences, Rept. 1087, Princeton Univ. Princeton, NJ, March 1973.

[14]Liperi, M., "Analisi Sperimentale Mediante Microtermocopple Della Combustion Di Propellanti Solidi Con Proprieta Termiche Variabili," Tesi di Laurea, Dipartimento di Euregetied, Politecnico di Milano, 1986.

[15]Doebelin, E. O., *Measurement System, Application and Design*, McGraw-Hill, New York, 1975, Chap. 8.

[16]Parker, W. J., Jenkins, R. J., Butler, C. P., and Abbott, G. L., "Flash Method of Determining Thermal Diffusivity, Heat Capacity, and Thermal Conductivity," *Journal of Applied Physics*, Vol. 32, No. 9, 1961, pp. 1679–1683.

[17]Carslaw, H. S., and Jaeger, J. C., *Conduction of Heat in Solids*, 2nd Ed., Oxford Univ. Press, Oxford UK, 1959, pp. 92–101.

[18]Taylor, R. E., and Cape, J. A., "Finite Pulse-Time Effects in the Flash Diffusivity Technique," *Applied Physics Letters*, Vol. 5, No. 10, 1964, pp. 212–213.

[19]Mendelsohn, A. R., "The Effect of Heat Loss on the Flash Method of Determining Thermal Diffusivity," *Applied Physics Letters*, Vol. 2, No. 1, Jan. 1963, pp. 19–21.

[20]Chase, M. W., Jr., Davis, C. A., Downey, J. R., Jr., Frurip, D. J., McDonald, R. A., and Syverud, A. N., "JANNAF Thermochemical Tables," 3rd ed., *Journal of Physical and Chemical Reference Data*, Vol. 14 (Suppl.), No. 1, 1985, pp. 1462–1466.

[21]Marx, P., and Dole, M., "Specific Heat of Synthetic High Polymers. V. A Study of the Order-Disorder Transition in PTFE," *Journal of the American Chemical Society*, Vol. 77, Sept. 20, 1955, pp. 4771–4774.

[22]DuPont Technical Personnel, private communication, June 1988.

[23]Shelley, D. L., and Huber, S. F., "Thermal Diffusivity of Poly(tetrafluoroethylene) between −140° and 125°C," *8th Heat Conductivity Conference*, 1972, pp. 1067–1077.